Geophys. J. R. astr. Soc. (1984) **79**, 385–410

On approximate solutions for reflection of waves in a stratified medium

C. J. Thomson and C. H. Chapman* *Department of Physics, University of Toronto, Toronto, Ontario M5S 1A7, Canada*

Received 1983 August 2

Summary. The properties of the asymptotic and iterative solutions of the wave equation are investigated for a medium containing discontinuities. The asymptotic method involves matching different solutions on either side of a discontinuity in order to satisfy the boundary conditions. The zeroth iteration, on the other hand, is a single approximation that can be used at all depths. The full effects of discontinuities are introduced only at higher iterations via the singularities and discontinuities of a coupling parameter, which may be described as a frequency-independent differential reflection coefficient. This iterative solution, proposed by Chapman, has the attraction that time domain results are relatively simple to obtain and interpret when it is sufficient to include only the first iteration.

If a turning point and a wavespeed gradient discontinuity coincide, the coupling parameter is infinite at that point. The coupling parameter is also infinite at a first-order discontinuity. Provided the turning point does not lie at a first-order discontinuity, the iterative series for such cases takes on a limiting form in which it is easy to include many terms in the frequency domain. This amounts to an expansion of the reflection coefficient in logarithms of the material properties. However, simple time domain expressions cannot be obtained for terms beyond the first in this expansion. The iterative solution is not well suited to the case where the turning point lies at a first-order discontinuity.

Both the first-order asymptotic solution and the first iteration predict the same, step-like time domain signal from a second-order discontinuity which is well above any turning point. As the turning point nears the second-order discontinuity, the major contribution to the reflection comes from the wavespeed gradient discontinuity and can be approximated by a zeroth-order asymptotic solution.

Numerical results are obtained for a particular, geophysically relevant model meant to represent a Moho with finite thickness. The differences

*Now at: Bullard Laboratories, Department of Earth Sciences, Madingley Rise, Madingley Road, Cambridge CB3 0EZ.

between results from the two methods can be explained in some detail, often by giving a physical interpretation to terms appearing in the equations.

1 Introduction

In this paper, we consider wave propagation in elastic media where the material properties vary only with depth. Finding the motion then reduces to solving a system of coupled ordinary differential equations in the frequency-horizontal waveslowness domain. We concentrate on two approximate analytic solutions, valid when the wavefield has at most one turning point.

The first of these is an asymptotic expansion in inverse powers of frequency (Richards 1971; Chapman 1973, 1974; Woodhouse 1978). It may be regarded in the time domain as an expansion about the primary wavefront. Secondary wavefronts are not generated unless explicitly allowed for by introducing reflected and converted waves at interfaces. These interfaces are required at discontinuities in the medium parameters or their first or higher derivatives, depending on the order of the asymptotic expansion. Continuous partial reflections and conversions from smooth gradients are not included in this solution. Including higher-order terms will give the distortion of the waveform behind the wavefront, but will not generate any new wavefronts. The asymptotic series does not necessarily converge and there are some signals which cannot be represented at all by a series of inverse powers.

The second solution is iterative. The zeroth iteration is the same as the zeroth-order asymptotic approximation. The exact solution is taken to be a linear combination of the two linearly independent parts of the zeroth-order solution. Substitution in the wave equation yields a differential equation for the coefficients in the linear combination and it is this differential equation which is solved iteratively. The rate of convergence of the iterations is controlled by a 'coupling parameter' which depends on the elastic parameter gradients. Examining the phase of the first iteration shows that it may be interpreted as partially reflected or converted waves from unique depths in the medium, which are not confined to interfaces, and that the coupling parameter can be described as a differential reflection coefficient. The iterative solution has been discussed in the seismological literature by Scholte (1962), Richards & Frasier (1976), Chapman (1981) and Kennett & Illingworth (1981) and can be shown to converge (Coddington & Levinson 1955, pp. 11–13). Young (1984) has shown that the asymptotic solution may be derived from the iterative solution by a process of repeated integration by parts. There is always a remaining integral, which is ignored when using the asymptotic solution and which will contain the omitted signals referred to above.

Traditionally, a discontinuity in the medium has been treated as an interface between two different 'media'. Both the asymptotic and the iterative solutions can be used to find the fundamental matrix (Gilbert & Backus 1966) for a region between interfaces. The effects of an interface can be calculated by imposing the relevant boundary conditions on suitably general fundamental matrices defined on either side. An iterative fundamental matrix is needed if the partial reflections from smooth gradients in regions between interfaces are to be included. If an nth-order asymptotic fundamental matrix is used, the nth derivatives of the material properties must be continuous within the layer. Interfaces are therefore needed at $(n+1)$th- and lower-order discontinuities.

In order to define the fundamental matrices, turning points will in general have to be located in the two media meeting at the interface. This will usually involve analytically continuing at least one of the velocity–depth profiles into regions where it physically does not exist (Richards 1976). Kennett & Illingworth (1981) have described in detail the form of the interface solutions obtained this way. However, Chapman (1981) has pointed out that an alternative approach is possible when using the iterative solution. A single zeroth-order solution is defined for all depths and across discontinuities. There is at most one, physical turning point. First- and higher-order discontinuities in the medium cause discontinuities only in the ray directions and their derivatives, not in the tau functions which define the phase of the solution. The exact solution is found by iterating on this zeroth-order approximation. The first iteration gives partial reflections from medium parameter gradients and discontinuities. At an nth-order medium discontinuity the coupling parameter has an $(n-1)$th-order discontinuity. At a first-order discontinuity the coupling parameter is infinite, but the iterative depth integrals are still defined and do converge to the correct solution. Chapman (1981) pointed this out, but did not investigate further the convergence of the singular iterative depth integrals.

This alternative form of solution has two main attractions. Firstly, analytic continuation is unnecessary and, secondly, the first iteration can be inverse Fourier transformed to give simple time domain functions (Chapman 1981). The reflection and transmission coefficients obtained by the application of boundary conditions at interfaces are in general too complicated to inverse Fourier transform analytically. The approach described by Chapman (1981) does require the evaluation of extensive depth integrals and is only practical if the first iteration is a satisfactory approximation. Although we can always choose a single frequency high enough to ensure rapid convergence of the iterations (except possibly at a first-order discontinuity), a broad band of frequencies must be considered if accurate time domain results are to be obtained.

This paper is in part a sequel to the earlier work of Chapman (1981). It is intended not only as a comparison between the asymptotic and iterative solutions, but also as a comparison between the interface and iterative methods in media with discontinuities. This is done mainly by reference to a simple model consisting of a high gradient zone between two uniform half-spaces. The various analytic solutions are presented for comparison with the 'exact' solution obtained by the Haskell matrix method (Haskell 1953). The analytic approximations, especially the iterative solution offer more insight into the various signals observed and bring us closer to understanding the transition from a strong gradient zone to a first-order discontinuity.

When we refer to the iterative solution in the rest of this paper, we mean the solution suggested by Chapman (1981). When we refer to the asymptotic solution, we mean the solution obtained by using asymptotic fundamental matrices and applying boundary conditions at interfaces. We do not discuss the results obtained when an iterative fundamental matrix is used in a layered medium. It is understood how an iterative fundamental matrix contains partial reflections from gradients in a layer and to some extent an analysis of this solution will overlap with the other two.

2 Notation and analytic approximations

We adopt the notation of Chapman (1981), with a single but important exception. We use the more standard symbol τ, not Q, to represent the vertical slowness or phase integral. However, τ is not the delay time of a complete ray, but rather the vertical slowness integral over a portion of the ray. Cylindrical coordinates (z, x, ϕ) are used, with z positive upwards. In general, we give only the equations relating to an acoustic medium and where the results for an elastic medium are different, this is stated in the text. All quantities appearing below but not explicitly defined may be found in Chapman (1981).

The reflection/transmission properties of an interface at $z = z_I$ can be defined by (Kennett 1974)

$$\mathbf{F}(z_I - 0)\begin{pmatrix}\hat{R}_{\mathrm{U}} & \hat{T}_{\mathrm{D}} \\ 1 & 0\end{pmatrix} = \mathbf{F}(z_I + 0)\begin{pmatrix}0 & 1 \\ \hat{T}_{\mathrm{U}} & \hat{R}_{\mathrm{D}}\end{pmatrix} \tag{1}$$

where, for example, $\hat{R}_{\mathrm{D}}$ is the reflection coefficient for a downward incident wave. (For P–SV waves in an elastic medium, $\hat{R}_{\mathrm{D}}$ would be a 2×2 matrix of the four possible reflection coefficients.) We use the same symbol $\hat{R}_{\mathrm{D}}$ to denote the response relative to some reference point away from the interface (for example, due to a source and receiver at $z = 0$). In some cases, this involves only a phase shift.

$\mathbf{F}(z)$ is a fundamental matrix valid for regions between interfaces. We choose $\mathbf{F}$ so that its columns represent upward or downward travelling or standing waves at points far above the turning point. Note that the physical meaning of the reflection/transmission coefficients therefore depends on the types of wave function in the columns of $\mathbf{F}$. Several choices for $\mathbf{F}(z)$ exist:

$$\mathbf{F}(z) = \mathbf{N}(z)\left\{\sum_{n=0}^{\infty}\frac{\mathbf{P}^{(n)}(z)}{(-i\omega)^n}\right\}\exp[i\omega\mathbf{O}\tau(z)], \tag{2a}$$

$$\mathbf{F}(z) = \mathbf{L}(z)\left\{\sum_{n=0}^{\infty}\frac{\mathbf{P}^{(n)}(z)}{(-i\omega)^n}\right\}\mathbf{G}(z), \tag{2b}$$

$$\mathbf{F}(z) = \mathbf{N}(z)\exp[i\omega\mathbf{O}\tau(z)]\,\mathbf{R}(z), \tag{2c}$$

or

$$\mathbf{F}(z) = \mathbf{L}(z)\,\mathbf{G}(z)\,\mathbf{R}(z). \tag{2d}$$

The first of these is the WKBJ asymptotic expansion (Richards 1971; Chapman 1973). The second is the Langer uniformly asymptotic expansion (Chapman 1974; Woodhouse 1978). In the third and fourth, the matrix $\mathbf{R}$ is found by iteratively solving the wave equation. These are the WKBJ (Scholte 1962) and Langer (Chapman 1981; Kennett & Illingworth 1981) iterative solutions, respectively.

Adding a constant to the value of τ does not affect the final solution at a given receiver when the WKBJ solutions are used. When the Langer solution is used, unique turning points in both media meeting at the interface, z_I, are needed. In general, at least one of the velocity profiles have to be analytically continued to find a turning point. If the turning point is far from the interface then the asymptotic forms of the Airy functions can be used, i.e. the Langer solution reduces to the WKBJ solution. Therefore, since the Langer solution need be used only when a turning point lies close to the interface, the fact that analytic continuation over long distances is unstable (Morse & Feshbach 1953, p. 706) is not a problem we shall consider.

When using the iterative solution, it is easier to solve for a vector $\mathbf{r}(z)$ which satisfies the inhomogeneous wave equation rather than a fundamental matrix $\mathbf{R}(z)$ which satisfies the homogeneous equation. The elements of $\mathbf{r}$ can be related to the amplitudes of upward and downward travelling waves at points far above the turning point. The zeroth-iteration for $\mathbf{r}$ is the wave excited by the source. For example, it is usual to have an upward travelling wave above the source and a downward travelling or stationary wave below the source. The effects of discontinuities in the medium are contained in the discontinuities and singularities of the coupling parameter. This is the form of solution we discuss first. We follow on from

Chapman (1981) by analysing the first iteration for our simple model and comparing the numerical results with the Haskell matrix solution. The asymptotic solution is then discussed in the light of the analytical and numerical results from the iterative solution.

3 Example model and the exact solution

The simple structure we have chosen is shown in Fig. 1. The model parameters, velocities and densities, have reasonable values for a model of the Moho. In the high gradient zone, the inverse squares of the wavespeeds and the square of the density depend linearly on z. The wave equation reduces to Stokes equation for an acoustic medium in which the wavespeed varies in this way and the density is constant. Thus, one of the solutions discussed later is known exactly in terms of Airy functions and the others may be judged against this.

Numerically, the 'exact' solution can always be obtained by dividing the high gradient zone into many thin homogeneous layers and performing a Haskell matrix analysis (Haskell

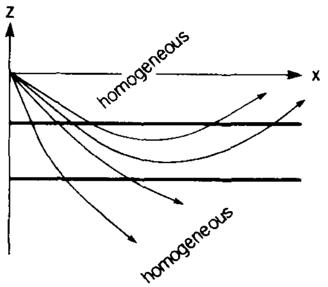

z (km)	α	β	ρ
0			
-2	6.5	3.76	2.71
-5	7.95	4.60	3.26

Figure 1. The example model. A strong gradient zone bounded by uniform half-spaces. The P-wavespeed (α km s^{-1}), S-wavespeed (β km s^{-1}) and density (ρ g cm^{-3}) have reasonable values for a model of the Moho. In the gradient zone, α^{-1}, β^{-1} and ρ vary as $\sqrt{a + bz}$, where a and b are constants. We calculate the reflection response at $z = 0$ for values of the ray parameter encompassing the rays depicted on the left.

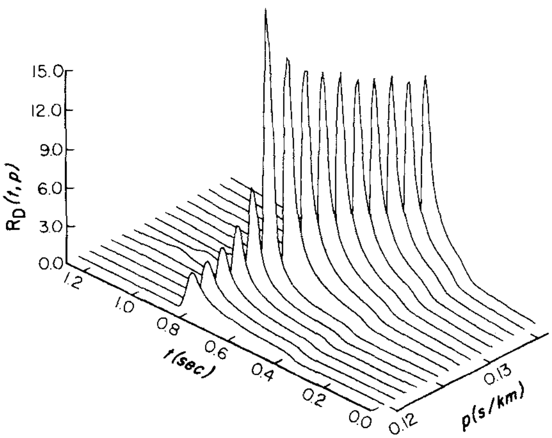

Figure 2. The Haskell matrix response for the model of Fig. 1 when $\beta = 0$ and ρ is constant. This is $R_D(t, p)$, the response at $z = 0$ due to a downgoing incident plane wave with ray parameter p which passes $z = 0$ at time $t = 0$. Some details are hidden by this projection, but this is not critical since this diagram is only given to illustrate the relative importance of the long-period corrections shown on the same scale later. The major hidden detail is the negative swing of the turning wave, part of which can be seen in Fig. 3.

1953; Gilbert & Backus 1966). The boundary condition is that only downgoing waves exist in the lower half-space. The reflected *P*-wave due to a downward incident *P*-wave of unit amplitude is inverse Fourier transformed to give the reflectivity, $R_D(t, p)$. Fig. 2 shows the acoustic reflectivity calculated this way for our Moho model when only the *P*-wavespeed varies with z. The full elastic solution is qualitatively the same and is not presented. The range of ray parameters encompasses both rays which turn in the gradient and rays which propagate through to the lower halfspace (some rays are depicted in Fig. 1).

This time domain solution has been obtained by calculating the spectral response at 64 1/1.28 Hz intervals and multiplying by a sinc-squared filter with its first zero at 25 Hz. The asymptotic time domain solutions of Section 5 have been calculated in the same way. The iterative solution of the next section is calculated in the time domain after two convolutions with the corresponding boxcar function and therefore has a comparable frequency content.

4 The iterative solution

4.1 THE ZEROTH ITERATION

The zeroth iteration reflectivity for our Moho model is shown in Fig. 3. The source and receiver are both at $z = 0$. Chapman (1981) has shown how the source wave can be constructed for an arbitrary point source in an elastic medium and has given detailed results for a pressure source in an acoustic medium. What follows here is only a brief discussion on the signals in Fig. 3.

The first five values of ray parameter p correspond to rays which propagate through to the lower homogeneous half-space without turning and so the WKBJ solution is used. The zeroth iteration consists of a downward travelling wave which departs from the source depth at time $t = 0$ and makes no contribution at the receiver. Actually, this is not strictly true, since there should be a signal at $t = 0$ due to the direct wave between source and receiver (as opposed to reflections from below either) (Chapman 1981, equation 3.44). However, this signal is not our main interest at the moment and is omitted from our (t, p) domain plots.

The higher values of p correspond to turning rays and the zeroth-order Langer solution

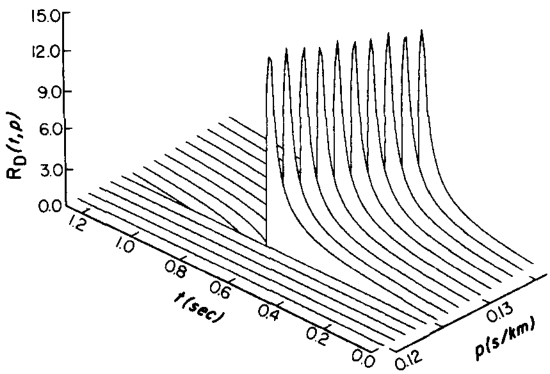

Figure 3. The zeroth iteration for $R_D(t, p)$. These signals are discussed in Section 4.1. Each of the last 10 traces is a good approximation to a smoothed Hilbert transformed delta function, which is antisymmetric about the point at which it crosses the time axis $[t = 2\tau(0)]$.

is used. An appropriate definition of the matrix $\mathbf{G}(z)$ is, for the acoustic case,

$$\mathbf{G}(z) = \left(\frac{\pi}{\omega p \xi'}\right)^{1/2} \begin{pmatrix} -i\xi' Aj'(-\xi) & -i\xi' Bj'(-\xi) \\ \omega p Aj(-\xi) & \omega p Bj(-\xi) \end{pmatrix}$$

where

$$\xi(z) = [3\,\omega\tau(z)/2]^{2/3}$$

and

$$Aj(-\xi) = Ai(-\xi), \quad Bj(-\xi) = [iAi(-\xi) + Bi(-\xi)]/2$$

(we use Aj and Bj to represent linear combinations of the Airy functions Ai and Bi which satisfy the radiation conditions of a particular problem). Far above the turning point, the first column of $\mathbf{G}$ represents a standing wave and the second column an upward travelling wave. At and below the source-receiver depth, the zeroth iteration only includes the standing wave, which turns in the gradient and decays below the turning point. Chapman (1981, section 3.5) has shown that this wave has amplitude proportional to $Bj(-\xi_0)$, where subscript zero denotes the value at $z = 0$. The constant of proportionality depends on the source moment and the material properties at the source, but it is the complex quantity $Bj(-\xi_0)$ which establishes a reference for the phase. These are the 'source terms' of Chapman (1981). The reflectivity in Fig. 3 is calculated by normalizing the standing wave so that it has amplitude one in the far field (before smoothing). At the frequencies we are using, the source and receiver are effectively far above the turning point for all values of p used in Fig. 3. Therefore, from now on we will always use the asymptotic forms of the Airy functions (Abramowitz & Stegun 1964, 10.4.60, 62, 64, 67) for the source and receiver terms. The zeroth-order Langer response then reduces to the WKBJ approximation for a turning wave,

$$\hat{R}_D(\omega, p) = -i\,\mathrm{sgn}(\omega)\exp[2i\omega\tau(0)]$$

in the frequency domain and the Hilbert transform of a delta function in the time domain,

$$R_D(t, p) = \bar{\delta}[t - 2\tau(0)] = -\frac{1}{\pi[t - 2\tau(0)]} .$$

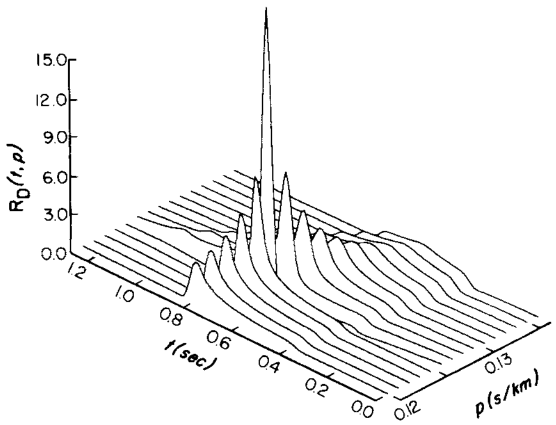

Figure 4. The long-period corrections for the acoustic, constant density Moho model, obtained by subtracting the zeroth iteration of Fig. 3 from the Haskell matrix total response of Fig. 2.

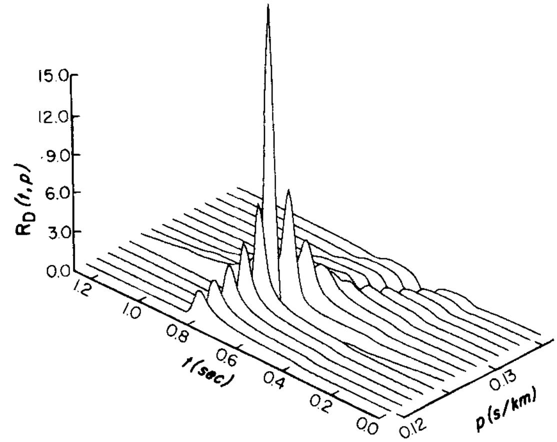

Figure 5. The long-period correction for the full elastic Moho model, obtained by subtracting the zeroth iteration of Fig. 3 from the Haskell matrix total solution for the elastic model (which is not presented).

In these expressions, $\tau(0)$ is the vertical slowness integral from the turning point $z = z_p$ to the source-receiver at $z = 0$. This is the form of solution used by the WKBJ seismogram (Chapman 1978). The zeroth iteration for *P–P* reflection in an elastic model is exactly the same, since interactions with the medium (in particular *P–SV* interactions) are not included.

Subtracting the reflectivity in Fig. 3 from the total solution in Fig. 2, leaves the 'long-period corrections' in Fig. 4. The 'corrections' for the full elastic model are shown in Fig. 5. These are the signals we are trying to interpret and calculate as simply and accurately as possible. The zeroth iteration is defined by the primary wavefront generated by the source, as opposed to secondary wavefronts generated when the primary wavefront interacts with the medium gradients and discontinuities. With this choice of zeroth iteration, the partial reflections introduced at the first iteration can be relatively easily interpreted in terms of time and depth of origin. More easily, for example, than with the fundamental matrix method with interfaces, where the primary wavefront is not always apparent and the solution depends on combinations of functions of unphysical τ integrals.

4.2 THE WKBJ FIRST ITERATION

Fig. 6 shows how the WKBJ coupling parameter, γ (Chapman 1981, equation 3.20) varies with z in our acoustic model. *P–P* scattering in the elastic model is described by the corresponding coupling parameter γ_P, for which the variation with z is qualitatively similar to the curve in Fig. 6. For simplicity, we define the arbitrary phase by choosing $\tau(0) = 0$. If the zeroth iteration contains a downgoing wave of constant amplitude which passes $z = 0$ at $t = 0$, say $\mathbf{r}^{(0)}(z) = (1,\ 0)^T$, then the first iteration introduces the improved estimate (Chapman 1981, equation 3.21)

$$\mathbf{r}^{(1)}(z) = \left(1,\ \int_{-\infty}^{z} \gamma(\zeta)\exp[2i\omega\tau(\zeta)]\,d\zeta\right)^T$$

and we may define the reflection coefficient at the receiver $z = 0$

$$\hat{R}_D(\omega, p) = \int_{-\infty}^{0} \gamma(\zeta)\exp[2i\omega\tau(\zeta)]\,d\zeta.$$

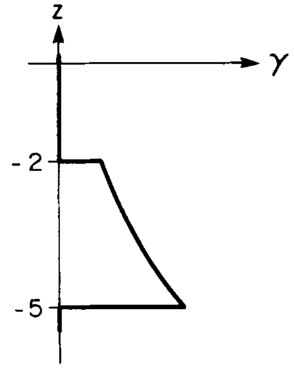

Figure 6. A sketch showing how the WKBJ coupling parameter, γ or γ_P, varies with z in our Moho model. In an elastic medium $\gamma_P = q'/2q - \rho'/2\rho + 2\mu' p^2/\rho$.

This response can be inverse Fourier transformed to give the reflectivity

$$R_D(t, p) = \int_{-\infty}^{0} \gamma(\zeta)\delta[t - 2\tau(\zeta)]\, d\zeta = \frac{\gamma}{2q}(\zeta)\bigg|_{t=2\tau(\zeta)}. \tag{3}$$

In words, this states that the reflected signal at time t is simply equal to the value of $\gamma/2q$ at $z = \zeta$ such that $t = 2\tau(\zeta)$. The approximation (3) has often been used in the interpretation of reflection seismograms (Richards & Frasier 1976) and explains why the long-period corrections for the first five traces in Figs 4 and 5 look so like the depth dependence of γ in Fig. 6. In practice, the lower limit of integration will be a point at which γ is negligibly small. Terminating the integral in a region of significant γ will cause a discontinuity in the time domain that could be confused with a reflection from a discontinuity in the model.

The value of γ at the top of the lower half-space increases without limit as p increases. When a turning ray occurs, the Langer iterative solution must be used since the corresponding coupling parameter is normally finite at the turning point (Chapman 1981). However, later we shall see that a turning point at a second-order discontinuity is a special case where neither the WKBJ nor the Langer first iterations give satisfactory results.

Equation (3) shows that the WKBJ first iteration predicts that a second-order discontinuity gives rise to a step of magnitude $[\gamma/2q]$ in the time domain, where the square brackets denote the saltus or jump in value across the discontinuity. Higher-order model discontinuities cause correspondingly higher-order time domain discontinuities. At a first-order model discontinuity the model gradients, and hence the coupling parameter, are infinite. This situation is discussed next.

4.3 THE CONVERGENCE OF THE WKBJ ITERATIVE SOLUTION

Unlike the asymptotic solution, it is possible to establish that the iterative solution converges (Coddington & Levinson 1955, pp. 11–13). The proof of convergence depends on γ being bounded; it must satisfy a Lipschitz condition with respect to z (Coddington & Levinson 1955, p. 8). The rate of convergence of the iterations depends on the magnitude of γ and the frequency. At very low frequencies, the gradient zone in our model behaves like a first-order discontinuity. By examining the convergence of the iterations as the thickness of the gradient zone tends to zero at fixed frequency, we expect to be able to estimate the error incurred by truncation after the first iteration in a finite gradient. Although $\gamma(z)$ is infinite at a first-order discontinuity, a simple change of independent variable described below shows that the iterations still converge.

We denote the upper and lower second-order discontinuitites in our model by z_1 and z_2. The reflection coefficient after three iterations is

$$\hat{R}_D(\omega, p) = \int_{z_2}^{z_1} \gamma(\zeta) \exp[2i\omega\tau(\zeta)]\, d\zeta + \int_{z_2}^{z_1} \gamma(\zeta) \exp[2i\omega\tau(\zeta)] \int_{z_1}^{\zeta} \gamma(\eta) \exp[-2i\omega\tau(\eta)]$$

$$\times \int_{z_2}^{\eta} \gamma(\nu) \exp[2i\omega\tau(\nu)]\, d\nu\, d\eta\, d\zeta.$$

The limits of integration can be made independent of the limiting process $z_1 \to z_2$ by noting that γ is a logarithmic derivative,

$$\gamma = \frac{1}{2} \frac{d}{dz} \left[\ln \left(\frac{q}{\rho} \right) \right].$$

We conveniently define $\tau(z_2)$ to be zero and omit the source and receiver terms, which involve only a phase shift. In the limit $z_1 = z_2$, q changes discontinuously from q_1 to q_2 across the first-order discontinuity, but τ is continuous. Then, in the limit $z_1 = z_2$,

$$\hat{R}_D(\omega, p) = \frac{1}{2} \ln \left(\frac{q_1 \rho_2}{q_2 \rho_1} \right) - \frac{1}{24} \ln^3 \left(\frac{q_1 \rho_2}{q_2 \rho_1} \right) + \frac{1}{240} \ln^5 \left(\frac{q_1 \rho_2}{q_2 \rho_1} \right) \ldots$$

where the first five iterations are included. Each term in the limiting form of the iterative series for $\hat{R}_D$ is a double integral of the previous term. A solely algebraic recursion scheme can be found to generate this limiting series. By comparing recursion schemes, it is possible to show that the iterative solution is the same as an expansion in logarithms of the plane wave reflection coefficient

$$\hat{R}_D(\omega, p) = \frac{(q_1 \rho_2 - q_2 \rho_1)}{(q_1 \rho_2 + q_2 \rho_1)}.$$

This series can also be obtained by inverting (Morse & Feshbach 1953, p. 411) the well-known expansion of $\ln x$ in terms of $(x-1)/(x+1)$ (Abramowitz & Stegun 1964, 4.1.27). More generally, we use the fact that q uniquely defines z for $z_2 \leqslant z \leqslant z_1$ and use this as the independent variable. In the limit $z_1 = z_2$, the equation governing $\mathbf{r}(q)$ becomes (Chapman 1981, equation 3.18)

$$\frac{d\mathbf{r}}{dq}(q) = -\mathbf{N}^{-1}(q) \frac{d\mathbf{N}}{dq}(q)\mathbf{r}(q). \qquad (q_2 \leqslant q \leqslant q_1).$$

The new function $\mathbf{r}(q)$ defines the solution just above (i.e. at $q = q_1$) and just below (at $q = q_2$) the first-order discontinuity, but its physical significance for $q_2 < q < q_1$ is obscure. The limiting series found above for $\hat{R}_D$, represents an iterative solution to this new equation when $z_1 = z_2$. This iterative solution converges so long as $q > 0$, i.e. the elements of the new interaction matrix $-\mathbf{N}^{-1} d\mathbf{N}/dq$ satisfy a Lipschitz condition with respect to q if $q > 0$. This condition is normally satisfied when the WKBJ solution is used. The exact solution of this equation is simply $\mathbf{N}(q)\mathbf{r}(q) =$ constant, from which it follows that

$$\mathbf{r}(q_1) = \mathbf{N}^{-1}(q_1)\, \mathbf{N}(q_2)\, \mathbf{r}(q_2),$$

Table 1. The plane wave reflection coefficient R_D for an acoustic Moho model consisting of a first-order discontinuity with the P-wavespeeds and densities of Fig. 1, is tabulated alongside the approximations obtained after one, three and five iterations for several values of the ray parameter.

p	R_D	$R_D^{(1)}$	$R_D^{(3)}$	$R_D^{(5)}$
0.120000	0.508722	0.561004	0.502150	0.509559
0.121057	0.539467	0.603403	0.530171	0.540837
0.122114	0.577272	0.658362	0.563242	0.579733
0.123172	0.625921	0.734682	0.602498	0.631037
0.124229	0.693851	0.855344	0.646750	0.707794
0.125286	0.811076	1.130167	0.648988	0.894827
0.125786	1.000000	∞		

a well-known result embodying the plane wave reflection and transmission coefficients for all incident waves. Note that we have not assumed the medium is acoustic.

This simple results shows that the iterative series does indeed have physical significance at first-order discontinuities. The difference between the exact result and the first few iterations at a particular first-order discontinuity for several values of p can be seen in Table 1. For reflection coefficients less than about 0.5, the fifth iteration converges to within 1 per cent of the correct result. At 0.8 the error is 10 per cent and it is infinite at 0.1. This is because the limit of the WKBJ iterative solution corresponds to pre-critical reflection. For post-critical reflection, we must study waves which turn in the corresponding high gradient zone and the Langer solution.

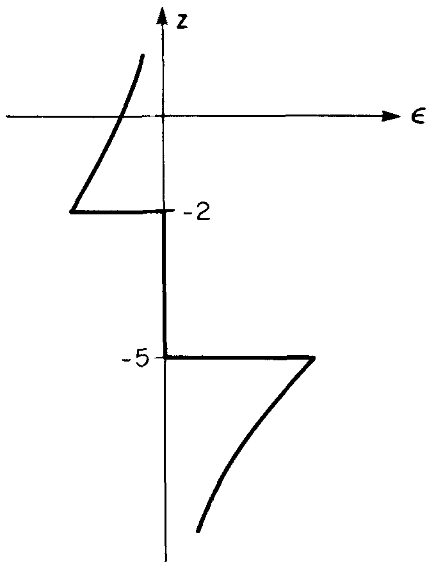

Figure 7. A sketch showing how the Langer coupling parameter, ϵ, varies with z in the acoustic, constant density model. The functional form is given in the text. Note that ϵ is largest just inside the homogeneous regions.

4.4 THE LANGER FIRST ITERATION

Chapman (1981) has discussed in great detail the interactions which can occur between a turning wave and parameter gradients. Interactions occurring below the source and receiver gives rise to upward travelling wave functions (Bj) at the receiver. For P–P scattering the relevant coupling parameter is ϵ_P and Fig. 7 shows how it varies with z in our acoustic 'Moho' model with constant density (where it is simply denoted ϵ). The analytic form is

$$\epsilon = \begin{cases} -q/6\tau & \text{if } z_1 < z \\ \gamma - q/6\tau \equiv 0, & \text{if } z_2 < z < z_1 \\ -q/6\tau & \text{if } z < z_2. \end{cases}$$

Note that ϵ is non-zero in the homogeneous regions because the Airy functions of the zeroth iteration are in general quite different to the exact solution in a homogeneous region. The partial reflections from a downward incident wave are of the three types. The first type are upward reflections from the downward incident wave. The second type are downward reflected waves from the upward travelling zeroth iteration after it has turned. These reflections themselves turn in the gradient, without suffering any further energy loss at the first iteration. For a receiver above the point of reflection they are represented by the Bj functions with a suitable time delay. The third type are reflections from below the turning point, where the evanescent wave interacts with the gradients. The first iteration also makes a correction to the zeroth iteration for the energy lost to the partially reflected waves. All these interactions are described by one piecewise continuous universal time function, $d_{21}[t/2\tau(z)]$, obtained by Chapman (1981) from its Fourier transform $\hat{d}_{21}[2\omega\tau(z)]$. Fig. 8 depicts these reflections and shows how the singularities of the d_{21}-function are related to them.

As explained in Section 4.1, the zeroth iteration for a point source can be taken to have

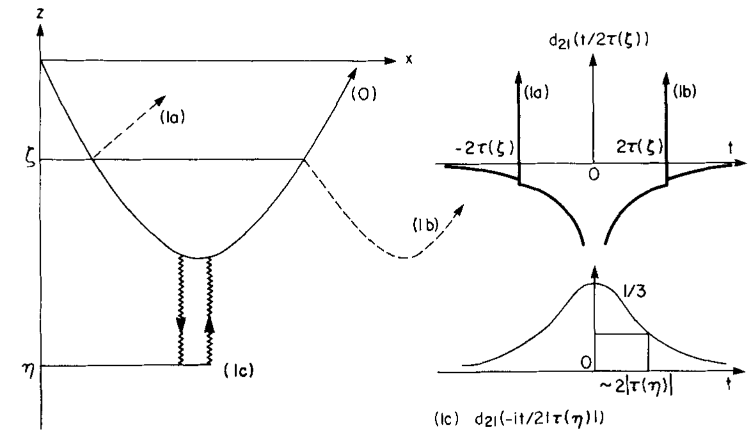

Figure 8. A ray corresponding to the zeroth iteration and the three types of interaction with the medium introduced at the first iteration. The dashed partial reflections from $z = \zeta$ are introduced at time $2\tau(\zeta)$ before and after the arrival time of the zeroth iteration ($t = 0$ on the time axis shown) by the delta function singularities (bold arrows) of the propagating d-function, $d_{21}[t/2\tau(\zeta)]$. The logarithmic singularity at $t = 0$ provides a correction to the zeroth iteration for the energy lost to partial reflections. The wiggly lines represent interactions with gradients below the turning point, which are introduced by the evanescent d-function, $d_{21}[-it/2|\tau(\eta)|]$, centred at $t = 0$.

the simplified form $\mathbf{r}^{(0)}(z) = [\![\exp[i\omega\tau(0)], 0]\!]^{\mathrm{T}}$. The first iteration introduces the improved estimate

$$\mathbf{r}^{(1)}(0) = \exp[i\omega\tau(0)]\left(1, \int_{-\infty}^{0} \epsilon(\zeta)\hat{d}_{21}[2\omega\tau(\zeta)]\,d\zeta\right)^{\mathrm{T}}$$

at the receiver. Again, the lower limit of integration will in practice be a depth at which ϵ is negligible so as not to introduce 'end point' errors. In the time domain we find that the first iteration introduces the long-period corrections (Chapman 1981, equation 3.61)

$$R_{\mathrm{D}}(t, p) = \int_{-\infty}^{0} \epsilon(\zeta)\frac{d_{21}[\![[t-2\tau(0)]/[2\tau(\zeta)]]\!]}{2\tau(\zeta)}\,d\zeta.$$

This is the function which may be compared with the results in Fig. 4 (and Fig. 5 if ϵ_{P} is used). The zeroth-order turning wave must be added to this to give the total field.

When the turning point is well below a second-order discontinuity, the effect of the discontinuity is similar to the WKBJ first iteration. The difference being that there are now two interactions with the discontinuity, one before and one after the zeroth-order wave has turned. Both interactions cause steps of magnitude $[\gamma/2q]$ in the time domain. The situation becomes more complicated as the turning point nears the second-order discontinuity. The case of a turning point exactly at a second-order discontinuity deserves a special mention.

Normally, the Langer coupling parameter is finite at the turning point $z = z_{\mathrm{p}}$. The usual expression (Chapman 1981, equation 3.29) for the term $\xi''/2\xi'$ contains singularities $(q'/2q$ and $q/6\tau)$ at this point, but these singularities cancel exactly so that (Chapman 1981)

$$\frac{\xi''}{2\xi'}(z_{\mathrm{p}}) = \frac{1}{10}\frac{d}{dz}\left(\ln\frac{dq^2}{dz}\right)_{z=z_{\mathrm{p}}} = \left(\frac{u''}{u'} + \frac{u'}{u}\right)\Big/10$$

where u is the inverse wavespeed or slowness at z_{p}. When z_{p} is also the position of a gradient discontinuity, u'' is infinite and so is ϵ. Including only the first iteration may not be sufficiently accurate for this situation. In fact, the first iteration predicts an infinite amplitude in one case. We can show this by considering a special model.

Consider two acoustic media, each with a slowness-z profile of the form $\sqrt{(a + bz)}$ and which meet at a second-order discontinuity. They have the same, constant density. For the value of p for which the turning point is at the gradient discontinuity, the coupling parameter is zero everywhere except at the discontinuity. Here it is infinite, such that

$$\int_{z_{\mathrm{p}}-0}^{z_{\mathrm{p}}+0} \frac{\xi''}{2\xi'}(\zeta)\,d\zeta = \frac{1}{2}\ln\left(\frac{\xi_1'}{\xi_2'}\right) = \frac{1}{6}\ln\left(\frac{u_1'}{u_2'}\right)$$

where subscripts 1 and 2 refer to the two sides of the discontinuity and we have used $\xi(z) = \omega^{2/3}(2uu')^{1/3}(z-z_{\mathrm{p}}) + O[(z-z_{\mathrm{p}})^2]$. The first iteration therefore introduces the correction to the zeroth-order turning wave

$$\int_{z_{\mathrm{p}}-0}^{z_{\mathrm{p}}+0} \epsilon(\zeta)\hat{d}_{21}[2\omega\tau(\zeta)]\,d\zeta = \frac{1}{6}\ln\left(\frac{u_1'}{u_2'}\right)\hat{d}_{21}(0).$$

In the time domain, this gives the long-period correction (Chapman 1981, equation B38)

$$R_{\mathrm{D}}(t, u) = \frac{1}{3\sqrt{3}}\ln\left(\frac{u_1'}{u_2'}\right)\delta[t-2\tau(0)]$$

when the source and receiver ($z = 0$) are far above the turning point. The signal attains infinite amplitude as the gradient in the lower medium tends to zero (our Moho model, for example), even when the time domain solution is smoothed. This behaviour is illustrated in the numerical results presented later and can be compared with the (exact) asymptotic solution in Section 5.1. By using ξ' rather than z as the independent variable, it is possible to show that the sum of all the iterations agrees with the asymptotic result. Instead of showing this, we prefer to proceed directly to a discussion of the Langer iterative solution at a first-order discontinuity, where similar complications arise.

4.5 THE CONVERGENCE OF THE LANGER ITERATIVE SOLUTION

The Langer coupling parameter is also infinite at a first-order discontinuity. As with the WKBJ iterative solution, this situation is of interest when estimating the error incurred by truncation in a finite gradient. The general approach adopted for the WKBJ solution may be used again, but details depend on which of two cases is considered. These are the case of a turning point above or below the strong gradient which tends to a first-order discontinuity and the case of a turning point in the strong gradient (and ultimately at the discontinuity). We will discuss first the case of a turning point away from the discontinuity. Our Moho model is not a suitable example for this situation, because the homogeneous regions cannot contain a turning point.

Since the Langer solution is exact only in special circumstances, we shall not assume ϵ is zero outside the strong gradient zone. For $z_2 < z < z_1$ we rewrite the depth integrals for $\mathbf{r}^{(k)}(z)$ as follows

$$\int_{\infty}^{z} = \int_{\infty}^{z_1} + \int_{z_1}^{z}$$

$$\int_{-\infty}^{z} = \int_{-\infty}^{z_2} + \int_{z_2}^{z} .$$

For integrals in the range $z_2 < z < z_1$ we make a change of variable. We could use q, as before, since this uniquely defines the depth. However, a better choice is ξ', which is always real. In the limit $z_1 = z_2$, ξ is continuous across the first-order discontinuity and ξ' is discontinuous with $\xi_1'/\xi_2' = q_1/q_2$. After this variable change the limit $z_1 \to z_2$ is taken. The integral from $-\infty$ to z_2 is unaffected by the limiting process. The integral from ∞ to z_1 becomes an integral from ∞ to z_2. Both of these integrals are independent of $\xi_2' < \xi' < \xi_1'$ and may be evaluated individually. Then we find that for $\xi_2' < \xi' < \xi_1'$, the limiting form of the depth integrals represents an iterative solution to the equation

$$\frac{d\mathbf{r}}{d\xi'}(\xi') = \epsilon(\xi')\mathbf{D}^{\dagger}\mathbf{r}(\xi') \qquad (\xi_2' < \xi' < \xi_1').$$

This is closely related to the equation for $\mathbf{r}(z)$ (Chapman 1981, equations 3.28, 3.31–3.34), but the new 'coupling parameter' is finite and the iterative series must converge. In this equation, $\mathbf{D}^{\dagger}$ is constant since it depends only on ξ and this is constant in the range of interest. This makes it easy to solve the new equation exactly and verify that the solution is consistent with continuity of stress and displacement.

If we denote by $\mathbf{n}^{(k)}$ the new terms introduced at the kth iteration for $\mathbf{r}$, repeated integration by parts shows that the jump in the new terms across the first-order discontinuity is

$$\mathbf{n}^{(k)}(z_1) - \mathbf{n}^{(k)}(z_2) = \sum_{m=1}^{k} \frac{(-1)^{m+1}}{m!} \mathbf{D}^{\dagger m} \left[\frac{1}{2}\ln\left(\frac{q_1\rho_2}{q_2\rho_1}\right)\right]^{m} \mathbf{n}^{(k-m)}(z_1).$$

This is the recursion scheme referred to earlier. The values of $\mathbf{n}^{(k-m)}(z_1)$ appearing on the right hand side are the total values, including contributions from non-zero values of ϵ at all other values of z. In other words, once $\mathbf{n}^{(k)}(z_1)-\mathbf{n}^{(k)}(z_2)$ is known, we must add the contribution from other depths before calculating $\mathbf{n}^{(k+1)}(z_1)-\mathbf{n}^{(k+1)}(z_2)$. This point also applies to the limiting form of the WKBJ iterations, if γ is significant at points away from the discontinuity. This recursion scheme contains all the multiple interactions which can occur between the turning wave and discontinuity. For example, if we assume ϵ is negligible at points away from the discontinuity, the reflection coefficient for a source and receiver above the discontinuity can be written

$$\hat{R}_{\mathrm{D}}(\omega,p)=\frac{1}{2}\ln\left(\frac{q_1\,\rho_2}{q_2\,\rho_1}\right)\hat{d}_{21}(2\omega\tau)-\frac{i}{4}\ln^2\left(\frac{q_1\,\rho_2}{q_2\,\rho_1}\right)\hat{d}_{21}(2\omega\tau)\,\hat{d}_{11}(2\omega\tau)$$

$$-\frac{1}{24}\ln^3\left(\frac{q_1\,\rho_2}{q_2\,\rho_1}\right)[\hat{d}_{21}(2\omega\tau)+3\hat{d}_{21}(2\omega\tau)\,\hat{d}_{11}(2\omega\tau)\,\hat{d}_{11}(2\omega\tau)]\ldots$$

where three iterations have been included explicitly and τ is evaluated at z_2. In the time domain, the multiples are contained in the repeated convolutions of the d_{21}-function by the d_{11}-function. This can be seen from Chapman (1981, fig. 12), from which diagrams it is also clear how higher iterations correct lower iterations for energy loss. Unfortunately, the d-functions are sufficiently complicated that simple time domain expressions cannot be found for the convolutions.

The situation is more difficult when the turning point lies within the strong gradient zone which tends to a discontinuity. The matrix $\mathbf{G}$ is designed to be accurate near turning points in smoothly varying media. Then, as $q\to 0$ so does τ such that the ratio $q/\tau^{1/3}$ is finite. However, if the turning point lies at a first-order discontinuity, then this ratio is in general infinite at z_1 and z_2 since q is finite and τ is zero. The stress-displacement vector must be finite and so there have to be compensating terms in the vector $\mathbf{r}$. A further complication is that although in the limit $z_1=z_2$ we have $\tau(z_1)=\tau(z_2)=0$, the ratio $\tau(z_1)/\tau(z_2)$ is not unique and depends on the form of the velocity–depth profile in $z_2<z<z_1$ as the limit is taken. Once again, the total solution can have no such dependence and all such terms must eventually cancel. It is possible to proceed as before, with an arbitrary profile is $z_2<z<z_1$, but a meaningful series for $\mathbf{r}$ alone cannot be found because of the singularities. A tedious derivation is necessary in order to ensure that all the relevant terms are retained in the limiting series for the stress-displacement vector. Instead, we shall only give a relatively quick demonstration that the solution for a particular model is consistent with the continuity of stress and displacement.

For our acoustic, constant density Moho model, $\epsilon=0$ for $z_2<z<z_1$. Hence, it follows that $\mathbf{r}(z_1)=\mathbf{r}(z_2)$ and this is true even in the limit $z_1=z_2$. For the $\sqrt{a+bz}$ waveslowness profile, it may be shown that

$$\frac{\tau(z_1)}{\tau(z_2)}=\frac{q_1^3}{q_2^3},$$

which is independent of b and so is also true as $b\to\infty$ (i.e. $z_1\to z_2$). This ratio is all that is required to show that

$$\lim_{z_1\to z_2}\mathbf{G}^{-1}(z_1)\,\mathbf{G}(z_2)=\mathbf{I}$$

from which it follows that the stress-displacement vector $\mathbf{y}=\mathbf{LGr}$ is continuous. If the density (i.e. $\mathbf{L}$) were not continuous, the longer derivation would be necessary.

This simple example hides the fact that in the homogeneous regions on either side of the first-order discontinuity, ϵ behaves like $-1/6(z-z_2)$. It would be singular even if these media were not homogeneous. As a result, **r** varies rapidly with z and the first iteration will not be adequate even where the gradients are low. The matrix **G** is not a good first approximation to use in this case. The problems arise from the term $\xi''/2\xi'$ and therefore affect the elastic as well as the acoustic solution.

4.6 NUMERICAL RESULTS WITH THE FIRST ITERATION

We have calculated the long-period corrections for our Moho model assuming the source-receiver depth is well above the turning point. The first iteration for the acoustic, constant density model is shown in Fig. 9. The capital letters (A, AA, etc.) in Fig. 9 denote the arrival times of signals associated with the ray paths shown, with P representing the zeroth-order primary wave.

The WKBJ first iteration is used for the first five values of p. The response is zero until the time of arrival (A) of the step discontinuity from the upper gradient discontinuity. The signal then has the form $\gamma/2q$ until the time of arrival (B) of the signal from the lower gradient jump, which is of opposite sign and larger (q is smaller). From then on the response is zero. Comparing closely with Fig. 4 shows that the WKBJ first iteration is adequate both qualitatively and quantitatively for lower values of p.

The sixth value of p corresponds to the first ray which turns in the gradient. The turning point is very close to the lower gradient discontinuity and $-q/6\tau$ is very large just inside the lower half-space. This is approaching the limiting case in which the turning point is at the gradient discontinuity and the first iteration fails (Section 4.4). Whereas the first iteration results for smaller and larger values of p are generally good, near this value the signal amplitude is too high. As expected, the waveform in Fig. 9 is then quite distinct from that in Fig. 4. The iterative waveform is symmetric about the time of arrival of the zeroth-order

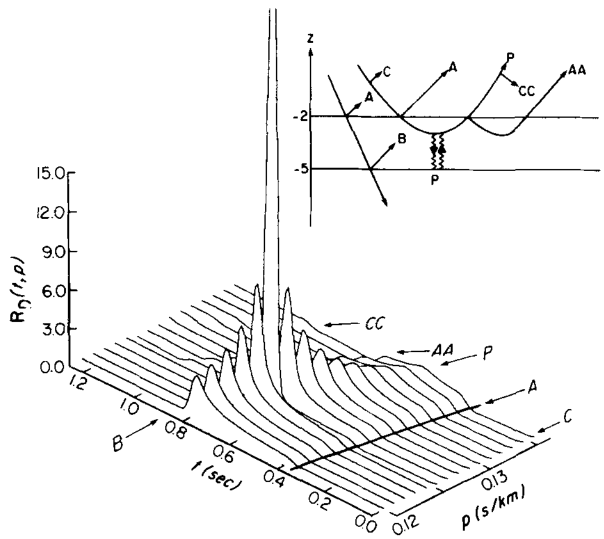

Figure 9. The new terms introduced by the first iteration or long-period corrections for our acoustic, constant density model. The letters indicate the time of arrival of signals corresponding to the virtual rays shown. The τ–p curve for reflection A is shown by the solid line.

wave, whereas the exact solution has a strong antisymmetric component (Fig. 4 and Section 5.1). This feature must be contained in higher iterations.

The coupling parameter for turning rays is zero in the gradient zone for our acoustic, constant density model. As the turning point moves upwards the relative contributions from the homogeneous regions changes from lower dominant to upper dominant. The reflections from the lower half-space are described by the evanescent d_{21}-function. The sixth and later traces in Fig. 9 show clearly how these evanescent reflections decay and broaden as the turning point moves upwards. The reflections from the upper half-space cause a negative signal at times before A and after AA. The signal is increasingly negative on going from C to A and from CC to AA, in accordance with the depth behaviour of ϵ (Fig. 7). The jumps at A and AA are of equal size and step from a negative value to zero. In contrast, the two jumps in the exact solution are unequal (although this may be difficult to see without overlaying the diagrams). In fact, the exact solution and first iteration are in relatively good agreement until about the time P, after which the exact solution is noticeably higher in amplitude. This may be understood in terms of the second iteration. Considering the ray path lengths shows that the signals introduced at the second iteration have accumulated τ values at least that of the primary wave. There is an extra turning point involved and the tails of the Hilbert transform that ensues do actually cause the second iteration signal to contribute at all times. However, the main contribution comes from the $1/t$ singularity at times greater than P and would improve the agreement between Figs 4 and 9 in this region. The small jumps at C and CC are examples of the effect of terminating the integral in regions of non-zero ϵ. These small jumps can be reduced by moving the source-receiver further from the turning point. However, changing the source-receiver position will not alter the first iteration after C or before CC.

The full elastic solution is shown in Fig. 10. The WKBJ coupling parameter is now smaller in magnitude. The reduction in signal amplitude is qualitatively in agreement with the difference between the acoustic and elastic Haskell matrix solutions (Figs 4 and 5). Another difference between the elastic and acoustic solutions is that ϵ_P is non-zero in the gradient zone (it is sketched in Fig. 10). This has the effect of reducing the magnitude of the discontinuities at A and AA and as a result the total amplitude of the signal in between. Hence, it

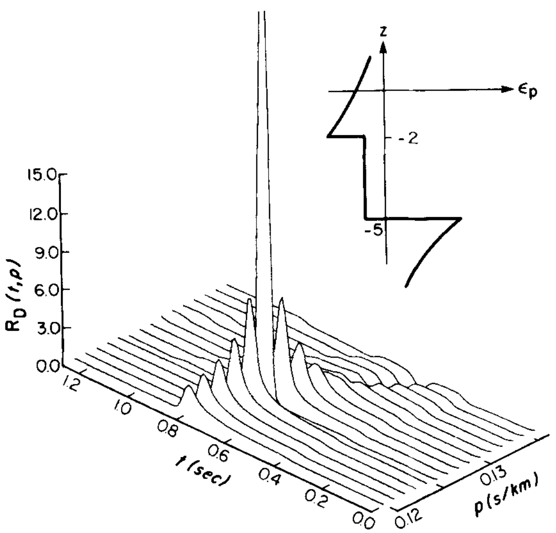

Figure 10. The first iteration for the elastic model.

appears that the evanescent reflections are less significant than in the acoustic case. What we are seeing is the sum of positive evanescent reflection and the negative reflections from ϵ_P in the gradient. The major qualitative difference between the acoustic and elastic solutions is the energy lost by the zeroth-order turning wave (i.e. the trench introduced at P by the logarithmic singularity of the d_{21}-function). This effect is much more significant now than in the acoustic case, where the remaining low amplitude evanescent reflections still dominate even for the largest value of the ray parameter. It can only be interpreted as a correction for energy lost to *SV*-waves.

5 The asymptotic solution

5.1 THE REFLECTION COEFFICIENT

In order to use the asymptotic solution, it is necessary to have interfaces at the discontinuities of the medium. The nth-derivative of the model parameters must be continuous for the nth term in the asymptotic expansion to be found. If only the zeroth-order term is retained, it is only necessary that the model parameters be continuous, not their gradients, and interfaces are always introduced at first-order discontinuities. It is well known that the frequency-independent plane wave coefficients apply to the zeroth-order WKBJ asymptotic solution at first-order discontinuities. The reflection/transmission properties of the zeroth-order Langer solution at first-order discontinuities have been discussed in detail by Richards (1976) and Kennett & Illingworth (1981). We shall proceed directly to second-order discontinuities.

Consider the more general Langer solution at a second-order discontinuity. We take the case of a downward incident wave with turning point below the interface introduced at the second-order discontinuity. Initially, we shall ignore the turning wave in the lower medium, and impose a downward-only radiation condition there. This is expected to give useful results in the time domain if $2\tau \gg 2\pi/\omega$ at the interface in both media, where ω is a characteristic frequency of the signal. This is similar to but less stringent than the condition that the asymptotic forms of the Airy functions may be used, namely $\xi = (3\omega\tau/2)^{2/3} \gg 1$. A suitable redefinition of the **G** matrix is obtained with

$$Aj = (Ai + iBi)/2, \quad Bj = (iAi + Bi)/2.$$

Far above the turning point, the first column now represents a downward travelling wave and the second column an upward travelling wave. The reflection coefficient found from (1) is

$$\hat{R}_D(\omega, p) = \frac{q_{D_1} - q_{D_2}}{q_{D_2} + q_{U_2}} \cdot \frac{Aj(-\xi_1)}{Bj(-\xi_1)}$$

where subscripts 1 and 2 refer to $z_l + 0$ in the upper and $z_l - 0$ in the lower medium respectively, and

$$q_D = \frac{-i\xi' Aj'(-\xi)}{\omega Aj(-\xi)}, \quad q_U = \frac{i\xi' Bj'(-\xi)}{\omega Bj(-\xi)}$$

are generalized vertical slownesses (Kennett & Illingworth 1981). When multiplied by the wavespeed they are known as generalized cosines (Richards 1976). From the asymptotic forms of the Airy functions we have that

$$q_U \approx q_D^* \approx q\left(1 + \frac{i}{6\omega\tau}\right)$$

to first order in $1/\omega\tau$. Thus,

$$\hat{R}_D(\omega, p) = \left[\frac{1}{\tau}\right] \frac{\exp(-2i\omega\tau_1)}{-12i\omega} + O\left(\frac{1}{(\omega\tau)^2}\right)$$

where [ ] denotes the saltus $1/\tau_1 - 1/\tau_2$. The factor $1/-i\omega$ corresponds to an integration in the time domain, so that for an impulsive incident wave the reflection is a step function. The amplitude decreases as the turning point recedes from the interface and, as is well known, the zeroth-order WKBJ asymptotic solution predicts no reflection from a second-order discontinuity. Note that the amplitude of this arrival does not agree with the correct (to first order) discontinuity described in Section 4.2.

The fact that all terms $O(1)$ have cancelled in the reflection coefficient suggests that, to be mathematically consistent, first-order asymptotic fundamental matrices should be used. Again the asymptotic forms of the Airy functions may be used to show that when this is done

$$\hat{R}_D(\omega, p) = \left(\left[\frac{1}{6\tau}\right] + \left[\frac{\epsilon}{q}\right]\right) \frac{\exp(-2i\omega\tau_1)}{-2i\omega} + O\left(\frac{1}{(\omega\tau)^2}\right)$$

$$= \left[\frac{\gamma}{2q}\right] \frac{\exp(-2i\omega\tau_1)}{-i\omega} + O\left(\frac{1}{(\omega\tau)^2}\right).$$

Unlike the zeroth-order result, this reflection coefficient depends on the density and does not vanish as τ_1 and τ_2 tend to infinity. It agrees with the result in Section 4.2.

Thus, at large $\omega\tau$, the first-order asymptotic solution and the first iteration predict the same step discontinuity in the time domain. However, at times before and after this step, the iterative solution depends on $\gamma/2q$ at points above and below the gradient discontinuity. The asymptotic solution does not depend on $\gamma/2q$ at these points and is therefore expected to give approximately the same waveform as the iterative solution provided $\gamma/2q$ does not vary rapidly in these regions. Thus, when using the asymptotic method, an interface should be introduced whenever $\gamma/2q$ varies rapidly in comparison with a characteristic wavelength of the radiation.

It is interesting that the integral terms in the first-order asymptotic $\mathbf{P}^{(1)}$ matrix do not make a contribution to $\hat{R}_D$, at least when $\omega\tau$ is large. This is consistent with our later interpretation of these integral terms as energy lost by the primary (turning) wave to the partial reflections. Since we have ignored the turning wave in the lower medium, these integral terms are not relevant to the present definition of $\hat{R}_D$. (The form of the asymptotic $\mathbf{P}^{(1)}$ matrix for an elastic medium is given in the notation of Chapman (1981) in the Appendix.)

When the turning point in the lower medium is close to the interface, the $\mathbf{G}$ matrix there must be redefined because the turning wave cannot be ignored. The Bj functions remain the same and we take $Aj = Ai$, the standing wave that decays below the turning point. The asymptotic forms of the Airy functions cannot be used and there are terms $O(1)$ in the reflection coefficient. These terms $O(1)$ would be obtained if zeroth-order asymptotic fundamental matrices were used to find $\hat{R}_D$. They generate an upward travelling wave in the upper medium due to the turning wave in the lower medium. The amplitude of this upward travelling wave is, of course, affected by the second-order discontinuity, but it is not simply a reflection 'from' the discontinuity. There are also multiple reflections from below the interface and which can only be separately identified for large $\omega\tau$. Using first-order asymptotic fundamental matrices introduces new terms in which the coefficient of $1/\omega$ is proportional to $[\epsilon/2q]$. The net reflected signal is the interference of these different components and we cannot perform a simple analysis of the response when the turning point lies just below the interface.

The case when a turning point and second-order discontinuity coincide was found to be inadequately modelled by the first iteration of the Langer iterative solution. If we return to the simple model discussed at the end of Section 4.4, we can calculate the asymptotic result. In fact, the zeroth-order asymptotic fundamental matrices in the two media are exact in this model. The arguments of the Airy functions in equation (1) are zero because the turning point and interface coincide. The solution in the upper medium consist of the turning wave $Ai(-\xi)$ of amplitude unity, together with an upward travelling wave $Bj(-\xi)$ of amplitude

$$\hat{R}_D(\omega, u) = -2\left(f - \frac{1}{f}\right)\left[f(\sqrt{3} + i) + \frac{1}{f}(\sqrt{3} - i)\right]^{-1}$$

where $f = (u_2'/u_1')^{1/3}$, u_1' and u_2' being the slowness gradients on either side of the interface. The reflection coefficient is independent of frequency and complex. The time domain response far above the turning point is therefore a linear combination of a delta function and its Hilbert transform. For the special case of $u_2' = 0$, we find that

$$R_D(t, u) = \frac{\sqrt{3}}{2}\,\delta[t - 2\tau(z)] - \frac{1}{2}\,\bar{\delta}[t - 2\tau(z)]$$

is the "long-period correction" for source and receiver at $z \gg z_p$, where the bar denotes a Hilbert transform. This combination of a symmetric and antisymmetric signal characterizes the waveform seen in Fig. 4 and is quite different to the first iteration (Fig. 9 and Section 4.4).

Finally, we should discuss the case when the turning point lies above the second-order discontinuity, since this case is quite prominent in the examples. The wave functions do not need to be redefined. Far below the turning point, $Aj = Ai$ decays exponentially and Bj is dominated by an exponentially growing term $(Bi/2)$. The reflection coefficient behaves asymptotically like

$$\hat{R}_D(\omega, p) = \left[\frac{\gamma}{2|q|}\right]\frac{\exp(-|\omega||\tau_1|)}{|\omega|}.$$

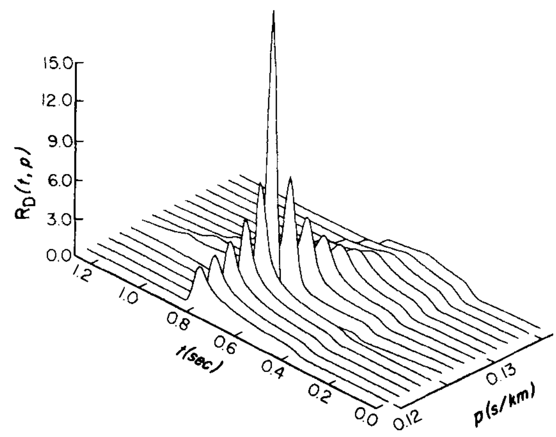

Figure 11. The long-period corrections calculated by the zeroth-order asymptotic method. In the homogeneous regions the fundamental matrix is known exactly and in the gradient layer the zeroth-order Langer approximation is used (which is also exact in the acoustic, constant density model). Equation (1) yields the total P–P reflection. The zeroth iteration of Fig. 3 is then subtracted to leave the corrections shown. Compare with Fig. 4, where the gradient zone was divided into many thin homogeneous layers.

From Chapman (1978, table 1c, e, f and table 2h), the time domain solution is seen to vary as $-\ln(t^2/|\tau_1|^2+1)$. This describes the relative variation for small values of $\pm t$, since it is only the inverse transform of a high-frequency approximation to the true reflection coefficient. However, the shape agrees qualitatively with the reflections from below the turning point seen in the numerical examples. It is impossible to compare this function directly with the evanescent d_{21}-function, because the iterative reflectivity is a superposition of simultaneous contributions from a range of z-values and the shape of the d_{21}-function varies with z.

At higher-order model discontinuities, using higher-order asymptotic fundamental matrices introduces higher-order time domain discontinuities. These signals are less important geophysically than those from first- and second-order discontinuities, which are commonly observed.

5.2 NUMERICAL RESULTS WITH THE ASYMPTOTIC SOLUTION

The zeroth-order asymptotic fundamental matrices are exact in the acoustic, constant density Moho model used in this paper. This can be seen numerically by comparing the asymptotic long-period corrections in Fig. 11 with the Haskell matrix results in Fig. 4. There is perfect agreement between the two figures.

The zeroth-order asymptotic results for the elastic model are identical to the results for the acoustic model. Thus, comparing Fig. 11 with Fig. 5, we see that there are noticeable differences between the zeroth-order result and the exact elastic solution. For low values of p, the pulse shapes have the same form, but the amplitudes differ significantly. At larger values of p the true elastic solution has a quite different waveform. The trench along the τ–p curve for the turning wave in Fig. 5 has already been attributed to energy lost by the turning wave to SV-waves (Section 4.6) and it is not modelled by the zeroth-order asymptotics. Fig. 12 shows the results using a first-order asymptotic solution when the integral terms in the $\mathbf{P}^{(1)}$ matrix are omitted. For low values of the ray parameter, the effect of including the first-order terms has been to reduce the amplitude of the zeroth-order signals by the necessary amount. Figs 12 and 5 are in good agreement in this region. However, for larger values of p the energy lost to SV-waves is not represented in Fig. 12. When the integral terms containing ϵ_P are included, the results in Fig. 13 are obtained. Now the

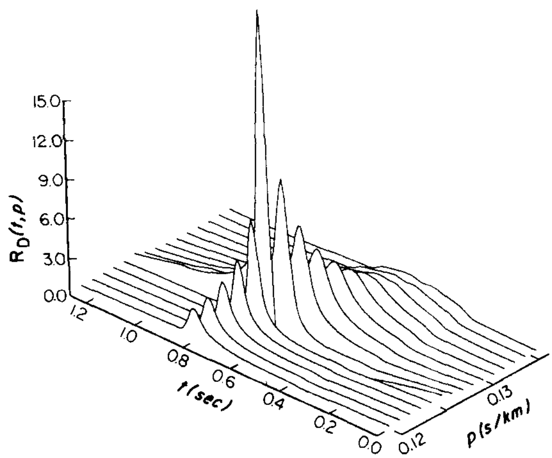

Figure 12. The first-order asymptotic long-period corrections for the elastic model. The integrals appearing in the first-order terms (given in the Appendix) have not been included.

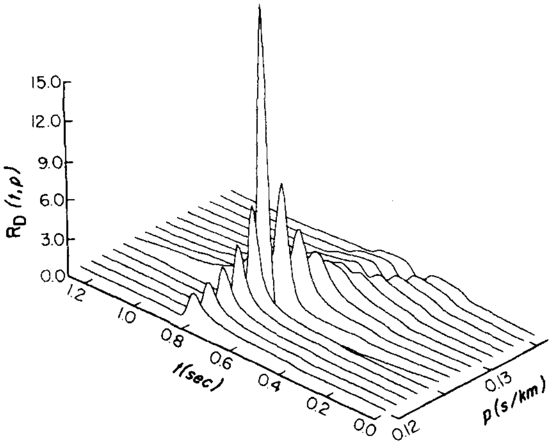

Figure 13. The first-order asymptotic long-period corrections for the elastic Moho model when the integral terms containing ϵ_P are included. The integral terms depending on ϵ_V make no significant contribution to the P–P reflection coefficient.

energy loss is more satisfactorily modelled. A close comparison with Fig. 5 shows that for the larger values of p the asymptotic solution in Fig. 13 has a very long-period component giving it a consistently higher amplitude than the exact solution. This is an example of the well-known property of asymptotic approximations, that they only describe the relative variations for short time intervals (Morse & Feshbach 1953, p. 462). In this case, the steps previously denoted A and AA are accurately modelled, but not overall (dc) level of the signal.

6 Conclusions

The two methods of finding the impulse response of a medium containing discontinuities have been compared both analytically and numerically. Although the results are not exhaustive, it is hoped that the most important details have been discussed.

The numerical results for the elastic 'Moho' model can be summarized as follows. The first-order asymptotic solution gives the best results for the smaller ray parameters used. For very low values of the ray parameter, the turning point in the middle layer (found by analytic continuation) lies far below the lower interface. The first-order asymptotic solution and the first iteration then agree that the amplitude of the reflected wave depends on the jumps in $\gamma/2q$. As the ray parameter increases and the turning point approaches the lower interface from below, a zeroth-order Langer asymptotic solution may be considered adequate. This is because the P-wavespeed gradient discontinuity then dominates the first-order result via the singular term $q'/2q$. This term is of the same order as $q/6\tau$ (because their difference is small like ϵ), which controls the signal amplitude at high frequencies when a zeroth-order asymptotic solution is used. The first-order asymptotic solution must be used if more exact results are needed or if the turning point in the middle layer is well below the lower interface (i.e. for the WKBJ asymptotic solution) or if converted waves are to be studied. However, it is not necessary to include the integrals appearing in the first-order terms. These integrals have been interpreted as a correction for energy lost by the primary wave and are therefore only significant for turning waves. The first iteration accurately predicts the reflection for the lowest values of the ray parameter. As the critical value at which the ray just turns in the gradient is approached, the first iteration generates a signal of infinite amplitude. The coupling parameter is always infinite at the turning point when that turning point coincides with a second-order discontinuity in the wavespeed. The first iteration cannot be relied upon to give accurate results in this case and is infinite in our particular model. For yet higher values of the ray parameter, corresponding to rays which turn in the gradient zone, both approximate methods involve errors which are important relative to the true long-period corrections. The first-order asymptotic solution suffers from a very long-period displacement, giving it too high an amplitude. The first iteration gives noticeably better results for times before the arrival of the zeroth iteration, but there is a need to include the second iteration at later times. The integral terms must be included if the first-order asymptotic solution is to include the effects of energy lost to P–SV conversions, which is significant for 'grazing rays'.

The numerical results are inevitably restricted by the model used and we have been able to include only one example. It may be said, for instance, that the presence of the two homogeneous regions in which the fundamental matrix is known exactly gives an advantage to the asymptotic solution. Only further applications of the methods will clarify the generality or otherwise of the conclusions drawn.

The iterative solution is still valid as the strong gradient zone tends to a first-order discontinuity. Provided that a turning point does not lie at this discontinuity, the iterative solution takes on the form of an expansion in logarithms of the reflection coefficient. Although this expansion contains the multiple interactions between a turning wave and the discontinuity in an obvious fashion, simple time domain results are not forthcoming for terms above the first. This restriction is quite severe, since the numerical results with a finite gradient indicate that the first iteration will not suffice. When the turning point lies at a first-order discontinuity, the usual Langer iterative solution is very awkward to apply. The coupling parameter is always large at points beside the discontinuity and so multiple depth integrals will always be needed. Another zeroth iteration may be more suitable, but implies treating this situation as a special case and, although other choices may exist, it seems unlikely that simple time domain expressions will be obtainable. The traditional interface method (Richards 1976; Kennett & Illingworth 1981) with analytic continuation and numerical inverse Fourier transformation must remain the preferred way of dealing with first- and sometimes second-order discontinuities.

The asymptotic and iterative solutions predict the same 'type' of time domain discontinuities resulting from discontinuities in the medium. For example, both predict that a second-order model discontinuity well above the turning point will give rise to a step in the time domain, with magnitude proportional to the gradient jumps. The asymptotic solution does not depend on the gradients at points away from the interface. Hence, interfaces should be introduced where the gradients, in fact $\gamma/2q$, change rapidly or discontinuously so as to cause significant high-frequency or discontinuous time domain signals that would otherwise be missed by the asymptotic solution. If a first- and second-order model discontinuity coincide, the zeroth-order asymptotic solution will not properly represent the low-frequency distortion caused by the second-order discontinuity.

The first iteration shows that in the time domain the partial reflection is effectively governed by the coupling parameter at a unique depth. However, in deciding whether or not to bother with the first iteration, it may not be sufficient to look simply at the values of the gradients. The danger is that, although the partial reflections have insignificantly low amplitudes, their combined energy represents a significant loss to the zeroth iteration. The first iteration of the Langer solution includes a correction for this energy loss, but the WKBJ solution does not. It is therefore possible, in principle at least, for the first iteration of the

WKBJ solution to be considered negligible but not the second iteration (which corrects the zeroth iteration for energy loss). The total energy scattered depends on the integral over time, or equivalently depth, of the coupling parameter and it is this integral which should be negligible. Thus, we are led to the criterion obtained by Kennett & Illingworth (1981, equation 3.51) by bounding the depth integrals in the frequency domain. The time and frequency domain arguments are connected by Parseval's theorem. More general conditions, such as reciprocity of the total wavefield, may not be as useful, because the range of possible signal amplitudes is so large. In our model, for example, the turning wave clearly dominates. It would be satisfactorily represented by a zeroth-order asymptotic solution and this view would be supported by arguments based on reciprocity. If the long-period corrections are to be adequately modelled though, a first-order asymptotic solution or the first iteration is needed. The correction terms do not satisfy reciprocity or energy conservation, but may model significant arrivals satisfactorily. The safe approach seems to require an awareness of the types of signal (delta-function, step-function, etc.) which can be produced and the factors controlling their amplitudes.

Consider a model with a thick zone of high gradients for which the above criterion fails. A practical alternative is to subdivide the region and use the interface method with asymptotic solutions. By introducing thin gradient zones separated by second-order discontinuities, it may be possible to satisfy the above criterion in each subdivision. Then it is tempting to use the zeroth-order solution in each layer. However, a first-order asymptotic solution must be used if, for example, the effects of density gradients are to be approximated by this method. Consider, for instance, the partial reflections for small p as described in Sections 4.2 and 5.1. Although the effects of the gradient changes have been spread over many interfaces, the overall partial reflections will be described by the total change of $\gamma/2q$ in a small depth (time) range. The zeroth-order asymptotic solution will only model the changes in $1/\tau$ not $\gamma/2q$. To avoid using first-order asymptotic solutions, we must introduce first-order discontinuities into the model. This approach has been suggested by Kennett & Illingworth (1981). We must remember, though, that the effect of gradient discontinuities, even at first-order discontinuities, will not be modelled consistently using zeroth-order solutions.

We have not investigated the solution obtained when an iterative fundamental matrix is used with the interface method. This would presumably give the best results of all, but involves much extra work as the depth integrals are frequency-dependent. The effect of an nth-order model discontinuity is still to cause an $(n-1)$th-order time domain discontinuity, but now the coupling parameters away from the interface do influence the results. The statement that the asymptotic solution depends only the coupling parameter at the extremeties of a layer has recently heen expanded upon by Young (1984). Young has shown how the WKBJ asymptotic solution can be developed from the iterative solution, essentially by integrating by parts. It is necessary to use the second iteration if all the first-order terms in $1/\omega$ are to be included. This is to be expected because the second iteration corrects the zeroth for energy lost at the first iteration, whereas this energy loss is included in the integrals of the first-order asymptotics. The corresponding results for the Langer solution will will be more intricate, because the first iteration does contain a correction for energy loss.

Acknowledgment

This work has been supported by the Office of Naval Research under contract number N00014-82-G-0001.

References

Abramowitz, M. & Stegun, I. A., 1964. *Handbook of Mathematical Functions*, Dover, New York.

Chapman, C. H., 1973. The Earth flattening transformation in body wave theory, *Geophys. J. R. astr. Soc.*, **35**, 55–70.

Chapman, C. H., 1974. The turning point of elastodynamic waves, *Geophys. J. R. astr. Soc.*, **39**, 613–621.

Chapman, C. H., 1978. A new method for computing synthetic seismograms, *Geophys. J. R. astr. Soc.*, **54**, 481–518.

Chapman, C. H., 1981. Long-period corrections to body waves: theory, *Geophys. J. R. astr. Soc.*, **64**, 321–372.

Coddington, E. A. & Levinson, N., 1955. *Theory of Ordinary Differential Equations*, McGraw-Hill, New York.

Gilbert, F. & Backus, G. E., 1966. Propagator matrices in elastic wave and vibration problems, *Geophysics*, **31**, 326–332.

Haskell, N. A., 1953. The dispersion of surface waves on multilayered media, *Bull. seism. Soc. Am.*, **43**, 17–34.

Kennett, B. L. N., 1974. Reflections, rays and reverberations, *Bull. seism. Soc. Am.*, **64**, 1685–1696.

Kennett, B. L. N. & Illingworth, M. R., 1981. Seismic waves in a stratified half-space – III. Piecewise smooth models, *Geophys. J. R. astr. Soc.*, **66**, 633–675.

Morse, P. M. & Feshbach, H., 1953. *Methods of Theoretical Physics*, McGraw-Hill, New York.

Richards, P. G., 1971. Elastic wave solutions in stratified media, *Geophysics*, **36**, 798–809.

Richards, P. G., 1976. On the adequacy of plane-wave reflection/transmission coefficients in the analysis of seismic body waves, *Bull. seism. Soc. Am.*, **66**, 701–718.

Richards, P. G. & Frasier, C. W., 1976. Scattering of elastic waves from depth-dependent inhomogeneities, *Geophysics*, **41**, 441–458.

Scholte, J. G. J., 1962. Oblique propagation of waves in inhomogeneous media, *Geophys. J. R. astr. Soc.*, **7**, 244–261.

Woodhouse, J. H., 1978. Asymptotic results for elastodynamic propagator matrices in plane-stratified and spherically-stratified earth models, *Geophys. J. R. astr. Soc.*, **54**, 263–280.

Young, R. M., 1984. Formal power series and iterative methods for wave vectors, *Geophys. J. R. astr. Soc.*, **77**, 531–547.

Appendix

Here we give the matrix $\mathbf{P}^{(1)}$, needed for the first-order Langer uniformly asymptotic solution. In order to be complete, we give the results for a self-gravitating Earth using spherical polar coordinates $(r,\ \theta,\ \phi)$. The notation follows Chapman (1981, section 5), where the sixth-order spheroidal and second-order toroidal differential systems can be found. We ease the transition from the rest of the paper by using the symbol p_s to denote the combination ap/r appearing in the spherical equations. The corresponding results for cylindrical coordinates, used earlier in the paper, can be derived from those below by neglecting gravity, replacing p_s by p and letting $r \to \infty$ elsewhere.

SPHEROIDAL MOTION

The 6×6 matrices $\mathbf{L}$ and $\mathbf{G}$ have been given by Chapman (1981, section 5.3), where the coupling parameters ϵ_P, ϵ_V, ϵ_a, ϵ_b and ψ can also be found. The non-zero elements of $\mathbf{P}^{(1)}$ are:

$$P_{12} = -\frac{\epsilon_P}{p_s} + \frac{q_\alpha}{2p_s}\, Y_\alpha$$

$$P_{21} = \frac{p_s}{2q_\alpha}\, Y_\alpha$$

$$P_{24} = P_{31} = \frac{1}{p_s} \frac{[(\epsilon_a - \epsilon_b)/\beta^2 + 2\epsilon_b p_s^2]}{(\beta^{-2} - \alpha^{-2})}$$

$$P_{13} = P_{42} = \frac{1}{p_s} \frac{[(\epsilon_a - \epsilon_b)/\alpha^2 + 2\epsilon_b p_s^2]}{(\beta^{-2} - \alpha^{-2})}$$

$$P_{34} = -\frac{\epsilon_V}{p_s} + \frac{q_\beta}{2p_s} Y_\beta$$

$$P_{43} = \frac{p_s}{2q_\beta} Y_\beta$$

$$P_{16} = -P_{52} = -\frac{\psi}{p_s}$$

$$P_{35} = -P_{64} = \psi$$

$$P_{56} = -\frac{1}{2rp_s^2}$$

$$P_{65} = -\frac{1}{2r}$$

where

$$Y_\alpha = \int_{r_p}^{r} \frac{p_s}{q_\alpha} \left[\frac{d}{dr}\left(\frac{\epsilon_P}{p_s}\right) - \frac{\epsilon_P}{p_s} [\epsilon_P + 2(\epsilon_a + s)] \right.$$
$$\left. + (\epsilon_a + \epsilon_b) P_{13} + \frac{q_\alpha^2}{p_s^2} (\epsilon_a - \epsilon_b) P_{24} + \psi^2 \right] dr$$

$$Y_\beta = \int_{r_p}^{r} \frac{p_s}{q_\beta} \left[\frac{d}{dr}\left(\frac{\epsilon_V}{p_s}\right) - \frac{\epsilon_V}{p_s} [\epsilon_V + 2(\epsilon_a - s)] \right.$$
$$\left. - (\epsilon_a + \epsilon_b) P_{24} - \frac{q_\beta^2}{p_s^2} (\epsilon_a - \epsilon_b) P_{13} - \psi^2 \right] dr$$

and

$$s = \frac{1}{r} + \frac{1}{2r}\left(\frac{\lambda - 2\mu}{\lambda + 2\mu}\right).$$

TOROIDAL MOTION

The matrix **L** and coupling parameter ϵ_H are given in Section 5.4 of Chapman (1981). The non-zero elements of $\mathbf{P}^{(1)}$ (2×2) are:

$$P_{12} = -\frac{\epsilon_H}{p_s} + \frac{q_\beta}{2p_s} Y_H$$

$$P_{21} = \frac{p_s}{2q_\beta} Y_H$$

where

$$Y_H = \int_{r_p}^{r} \frac{p_s}{q_\beta} \left[\frac{d}{dr}\left(\frac{\epsilon_H}{p_s}\right) - \frac{\epsilon_H}{p_s}\left(\epsilon_H - \frac{\mu'}{\mu} - \frac{3}{r}\right)\right] dr.$$

Geophys. J. R. astr. Soc. (1984) **79**, 411–423

Pore pressure and oceanic crustal seismic structure

Nikolas I. Christensen *Department of Geosciences, Purdue University, West Lafayette, Indiana 47907, USA*

Received 1984 January 5

Summary. Marine refraction studies during the past decade have found considerable lateral variability in the seismic properties of the upper basaltic regions of the oceanic crust. In many localities, compressional and shear-wave velocities are quite low at the top of the basalt section and velocities increase rapidly with depth. It is concluded that pore pressure may be at least in part responsible for the low upper crustal velocities and contribute significantly to the lateral variability. This is supported by compressional and shear-wave velocity measurements as functions of confining pressure and pore pressure for basalt from the Juan de Fuca ridge and dolerite from the Samail ophiolite, Oman. Within the oceanic crust, regions of overpressure and underpressure will possess anomalous velocities, the magnitude of which will depend upon the porosity and the deviation of the pore pressure from hydrostatic. The influence of pore pressure on velocities is expected to diminish with depth and is unlikely to be significant at lower crustal depths where porosity is extremely low. Of significance, Poisson's ratio is shown to be dependent on pore pressure as well as confining pressure. At constant confining pressure, Poisson's ratio increases with increasing pore pressure. Thus, overpressured regions within the upper oceanic crust are likely to have relatively high Poisson's ratios as well as low compressional- and shear-wave velocities.

1 Introduction

Beginning in the early 1950s, the seismic structure of the oceanic crust has been the subject of numerous investigations. The results of early refraction studies at sea often showed a simple three-layered crustal model with relatively uniform velocities and thickness of individual layers (Raitt 1963). More recent seismic experiments using multichannel seismic techniques have determined detailed velocity–depth structures through the oceanic crust at several locations. Of particular significance, it has been found that the uppermost basalt of the oceanic crust has relatively low velocities, usually between 3.6 and 4.8 km s^{-1} (Houtz & Ewing 1976), which increase rapidly with depth giving rise to compressional wave velocity gradients in the upper 2 km of the crust averaging between 0.5 and 2.0 s^{-1} (Kennett 1977;

Whitmarsh 1978; Houtz 1980; Spudich & Orcutt 1980). In addition, recent refraction profiles recorded on ocean bottom seismometers by Au & Clowes (1984) confirm similar low shear-wave velocities in the upper basaltic crust followed by a rapid increase in velocity with depth. The low velocities and their variability in the upper oceanic crust immediately underlying deep sea sediments are generally attributed to the presence of high porosity, rubbly pillow basalt and breccia zones at shallow depths (e.g. Hyndman & Drury 1976) with the rapid increases in velocities with depth originating from decreasing porosity.

Marine heat flow observations, electrical soundings and geophysical logging have established that the pores and cracks are water saturated and often likely to be interconnected (Lister 1972; Kirkpatrick 1979; Hermance, Nur & Bjornsson 1972). This presence of pore water within the upper oceanic crust influences a wide range of properties including fracture strength, electrical conductivity and seismic velocities (Raleigh & Paterson 1965; Brace & Orange 1968; Christensen 1970). These properties are likely to depend not only on the external confining pressure at depth, but also on the fluid pressure within the rock cavities.

The question arises as to what extent pore pressure may be responsible for lowering velocities within the upper oceanic crust, as well as producing the observed variability in upper crustal seismic velocities. Laboratory velocity measurements on high porosity sedimentary rocks (Wyllie, Gregory & Gardner 1958; King 1966; Domenico 1977) and granite (Todd & Simmons 1972) under both controlled confining pressure and pore pressure have found that increasing pore pressure at constant confining pressure significantly lowers compressional wave velocity. This also has been experimentally verified for shear-wave velocities in sedimentary rocks (Banthia, King & Fatt 1965). Clearly similar results for oceanic basalt would demonstrate the importance of pore pressure as a parameter influencing oceanic crustal seismic properties.

In this study, compressional- and shear-wave velocities have been measured under controlled pore and external pressures for oceanic basalt and dolerite. It is concluded, as shown from these measurements, that any interpretation of crustal velocities in terms of composition, crack porosity or density must take into account pore pressure.

2 Experimental details and data collection

The basalt sample selected for the velocity measurements, a tholeiitic pillow basalt, was dredged from the western edge of the median valley of the Juan de Fuca ridge at a water depth of 2470 m. A modal analysis from a single thin section is as follows: 40 per cent plagioclase (An_{58-65}), 41 per cent clinopyroxene, 6 per cent opaque and 13 per cent basaltic glass and alteration products. Compressional-wave velocities measured from cores cut from the same pillow (Christensen 1970) demonstrate no significant anisotropy, but a marked dependence of velocity on the degree of water saturation within the rock.

A virgin sample approximately 2.5 cm in diameter and 5 cm long was cored from the basalt pillow. The ends were trimmed normal to the axis and parallel to 0.02 mm. The wet bulk density of the sample calculated from its dimensions and water saturated weight is $2.91\ \mathrm{g\ cm^{-3}}$. Porosity occurring as connected microcracks and small vesicles calculated from wet and dry bulk densities is 4.0 per cent.

The dolerite was collected from the central portion of the sheeted dike section of the Samail ophiolite, Oman near Wadi Jizi at an estimated depth of 2.4 km beneath the sediment–basalt contact. The stratigraphic position of the sample within the ophiolite complex, as well as the laboratory measured velocities, place the sample within the lower portion of layer 2 of the oceanic crust (Christensen & Smewing 1981). Thus the velocity data should provide information on the influence of pore pressure on elastic properties of rocks from intermediate crustal depths.

The dolerite sample has been metamorphosed to the greenschist facies through the circulation of sea water at a mid-ocean ridge (Gregory & Taylor 1981). Mineral percentages by volume are: 48 per cent plagioclase (altered), 25 per cent clinopyroxene, 5 per cent opaque and 22 per cent alteration products consisting of albite, chlorite, epidote, actinolite, sphene and quartz. The wet bulk density of the sample is 2.8 g cm^{-3} and its porosity is 1.1 per cent.

The samples were encircled by thin shell aluminium containment cylinders (Fig. 1) containing 16 shallow longitudinal slots on their inside surface which are ported to the pore pressure pumping system, thereby exposing the circumferential surface of the sample to a controlled pore pressure. Each containment cylinder has a full length narrow opening filled with epoxy which allows closure with increasing confining pressure and assures unrestricted hydrostatic pressure on the sample. The electrodes and transducers are placed on the sleeved

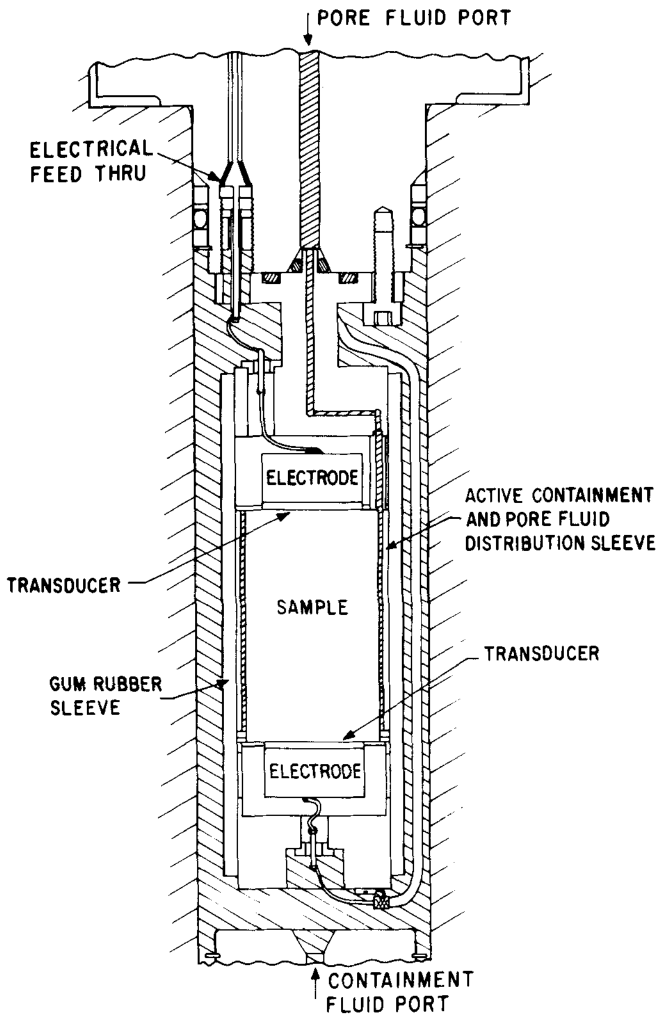

Figure 1. Diagram of sample assembly.

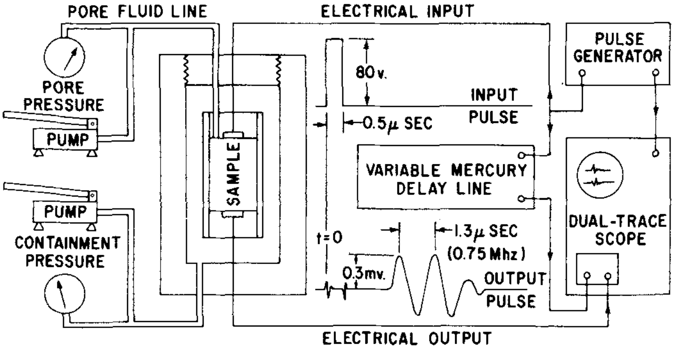

Figure 2. Schematic diagram of pressure system and electronics.

samples and jacketed with gum rubber tubing to prevent interaction of the containment and pore fluids. The mechanical configuration of the transducer electrodes, the electrical feed-throughs and the porting for pore and confining pressures are shown in Fig. 1.

A schematic diagram of the electrical and hydraulic systems designed for the velocity measurements is shown in Fig. 2. A rectangular pulse of approximately 80 V and 0.5 μs in width drives a sending transducer on one end of the rock core Lead-zirconate trans-

Table 1. Compressional wave velocities (V_p), shear wave velocities (V_s), and Poisson's ratios (σ) at various confining pressures (P_c) and pore pressures (P_p) for Juan de Fuca ridge basalt.

P_c(kbar)	P_p(kbar)	V_p(km/s)	V_s(km/s)	V_p/V_s	σ
0	0	4.601	2.110	2.181	0.367
0.1	0	4.859	2.299	2.114	0.356
0.2	0	5.034	2.441	2.062	0.346
0.4	0	5.258	2.682	1.960	0.324
0.4	0.2	5.074	2.444	2.076	0.349
0.6	0	5.396	2.814	1.918	0.314
0.6	0.2	5.293	2.689	1.968	0.326
0.6	0.4	5.103	2.452	2.081	0.350
0.8	0	5.556	2.928	1.898	0.308
0.8	0.2	5.430	2.822	1.924	0.315
0.8	0.4	5.307	2.704	1.963	0.325
0.8	0.6	5.147	2.450	2.101	0.353
1.0	0	5.660	3.012	1.879	0.303
1.0	0.2	5.598	2.936	1.907	0.310
1.0	0.4	5.458	2.822	1.934	0.318
1.0	0.6	5.359	2.704	1.982	0.329
1.0	0.8	5.184	2.458	2.109	0.355
1.0	1.0	4.810	-	-	-
1.2	0.4	5.603	-	-	-
1.5	0	5.888	3.200	1.840	0.290
1.5	0.5	5.723	3.041	1.882	0.303
1.5	0.7	5.648	2.953	1.913	0.313
1.5	0.9	5.529	2.844	1.944	0.320
1.5	1.1	5.430	2.721	2.000	0.333
1.5	1.3	5.280	2.469	2.139	0.360
1.6	1.6	4.950	-	-	-
2.0	0	5.980	3.305	1.809	0.280
2.0	1.0	5.773	3.057	1.888	0.306

Table 2. Compressional wave velocities (V_p), shear wave velocities (V_s), and Poisson's ratios (σ) at various confining pressures (P_c) and pore pressures (P_p) for Oman dolerite.

P_c(kbar)	P_p(kbar)	V_p(km/s)	V_s(km/s)	V_p/V_s	σ
0	0	5.960	3.230	1.845	0.292
0.05	0	5.979	3.243	1.844	0.292
0.2	0	6.031	3.290	1.833	0.288
0.2	0.15	5.986	3.251	1.841	0.290
0.4	0	6.078	3.333	1.824	0.285
0.4	0.35	5.991	3.253	1.842	0.291
0.6	0	6.121	3.369	1.817	0.283
0.6	0.2	6.088	3.340	1.823	0.285
0.6	0.55	5.998	3.253	1.844	0.292
0.8	0.4	6.100	3.344	1.824	0.285
0.8	0.75	6.002	3.261	1.841	0.290
1.0	0	6.185	3.409	1.814	0.282
1.0	0.6	6.108	3.353	1.822	0.284
1.0	0.95	6.017	3.263	1.844	0.292
1.3	0	6.232	3.448	1.807	0.279
1.3	0.3	6.201	3.413	1.817	0.283
1.3	0.9	6.118	3.355	1.824	0.285
1.3	1.25	6.026	3.276	1.839	0.290
1.5	0	6.252	3.452	1.811	0.280
1.5	0.5	6.210	3.418	1.817	0.283
1.5	1.1	6.127	3.360	1.824	0.285
1.5	1.45	6.036	3.281	1.840	0.290
1.7	0.7	6.224	3.422	1.819	0.284

ducers are used for transmitting and receiving compressional waves, whereas AC-cut quartz and lead-zirconate transducers generate and receive the shear waves, respectively. The electrical output from the receiving transducer is displayed on one trace of a dual trace oscilloscope. The transit time of the pulse through a sample is measured by superimposing the signals from the sample and a calibrated variable length mercury delay line (Birch 1960).

The containment and pore pressure pumps have operating pressure ranges of atmospheric to 2.7 kbar (270 MPa). Pressures are each monitored with identical Heise gauges with operating pressure ranges of 0–2.5 kbar and accuracies of 0.1 per cent of full scale.

Distilled water, which is used as the pore pressure medium, is introduced after the sample and the pore pressure plumbing have been evacuated for several hours. Data points are taken while holding a constant differential pressure (confining pressure minus pore pressure). The confining pressure and the corresponding pore pressure, required to maintain a constant differential pressure, are increased and decreased at random for each constant differential pressure data set. The average time required to reach equilibrium at each data point is approximately 12 hr. The repeatability is 0.5 per cent of the measured velocity. The accuracy of a given velocity measurement is 1 per cent.

Compressional- and shear-wave velocities, the ratio of compressional- to shear-wave velocity, and Poisson's ratios calculated from the velocities are given in Tables 1 and 2 for the basalt and dolerite. In Figs 3–6, the velocities are plotted as a function of confining

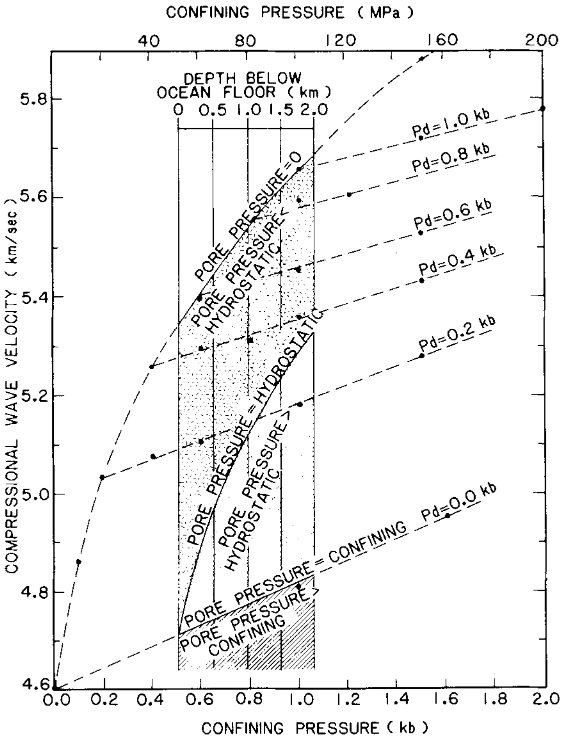

Figure 3. Basalt compressional-wave velocity as a function of confining pressure. Lines are shown for constant differential pressure (P_d).

pressures. The solid curves in Figs 5 and 6 show the variation of velocity with confining pressure at zero pore pressure and the data points beneath these curves represent velocities measured at elevated pore pressures. The dashed lines are lines of constant differential pressure, defined as confining pressure minus pore pressure. At a constant confining pressure, velocities decrease with increasing pore pressure along a vertical path in the figures (at any given point, the pore pressure is simply obtained by subtracting the differential pressure from the confining pressure).

3 Differential versus effective pressure

In addition to illustrating the dramatic decreases in velocities which accompany increasing pore pressure in oceanic rocks at fixed confining pressures, Figs 3–6 show that compressional- and shear-wave velocities are not constant at constant differential pressures. Over the pressure ranges of the measurements presented here, velocities increase at constant differential pressure as confining pressure is increased.

Several theoretical papers on acoustic wave propagation in fluid saturated porous elastic solids (Brandt 1955; Biot 1956, 1962; Biot & Willis 1957; Geertsma 1957; Fatt 1958) have concluded that seismic velocities are a function of an effective pressure $P_c - nP_p$ rather simple differential pressure $P_c - P_p$, where P_c is confining pressure, P_p is pore pressure and $n < 1$. Thus to maintain a constant velocity when confining pressure is increased, it is necessary to increase internal pore pressure an amount greater than the confining pressure.

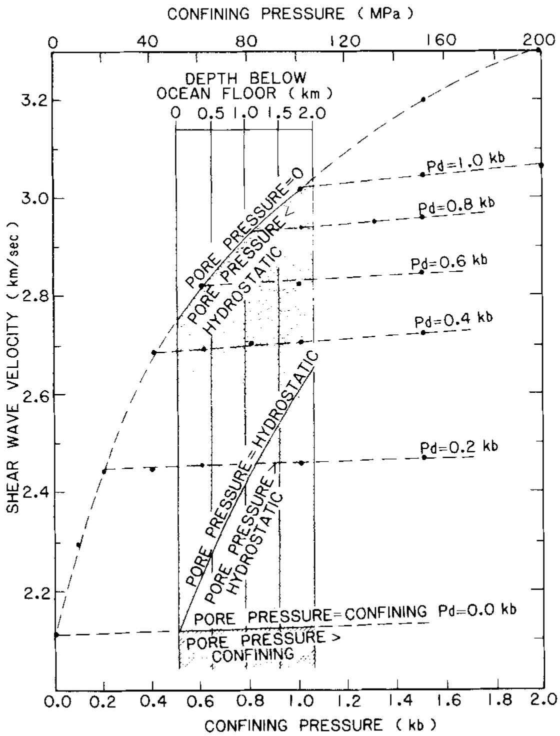

Figure 4. Basalt shear-wave velocity as a function of confining pressure. Lines are shown for constant differential pressure (P_d).

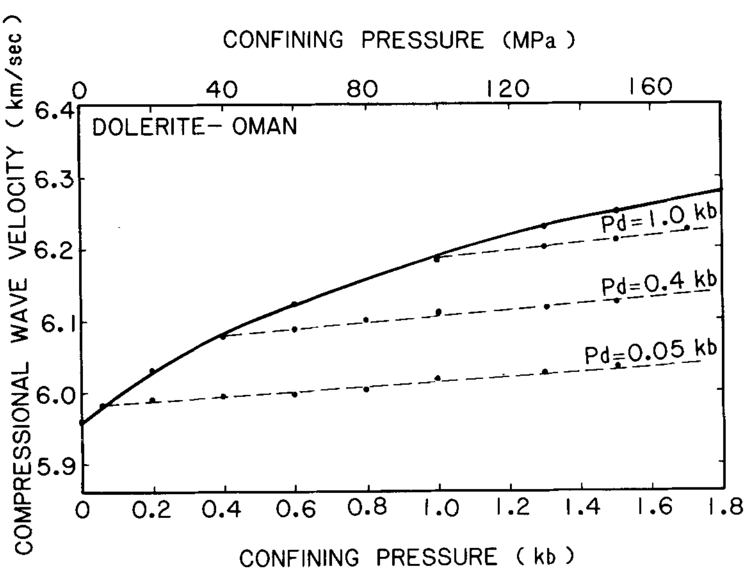

Figure 5. Dolerite compressional-wave velocity as functions of confining pressure and differential pressure (P_d).

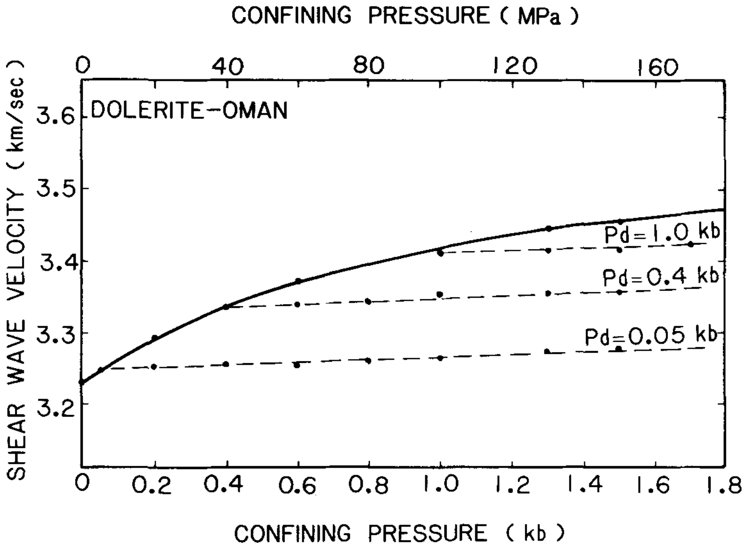

Figure 6. Dolerite shear-wave velocity as functions of confining pressure and differential pressure (P_d).

Early laboratory measurements of compressional-wave velocities in cores of sandstone (Wyllie *et al.* 1958; King 1966) suggested that velocity depends only on differential pressure; that is, $n = 1$. However, Banthia *et al.* (1965) found that for shear velocities in sandstones n is less than unity. Similar results were reported for compressional-wave velocities in low porosity samples of Chelmsford granite and Trigg limestone (Todd & Simmons 1972). More recently, Domenico (1977) has shown experimentally that velocities in unconsolidated Ottawa sand also depend on effective pressure. Of significance, n was found to be less than unity and greater for shear than compressional-wave velocities.

If we define differential pressure (P_d) as $P_c - P_p$ and effective pressure (P_e) as $P_e = P_c - nP_p$, values of n from our velocity studies can be calculated from the following relationship at constant velocity:

$$\Delta V = \left(\frac{\partial V}{\partial P_d}\right)_{P_p} \Delta P_d + \left(\frac{\partial V}{\partial P_p}\right)_{P_d} \Delta P_p = 0.$$

Since

$$\frac{\Delta P_d}{\Delta P_p} = -\frac{(\partial V/\partial P_p)_{P_d}}{(\partial V/\partial P_d)_{P_p}}$$

and for

$$\Delta P_e = 0$$

$$\Delta P_c - n\Delta P_p = 0,$$

it follows that

$$n = 1 - \frac{(\partial V/\partial P_p)_{P_d}}{(\partial V/\partial P_d)_{P_p}}.$$

Values of n calculated from the above relationship are given in Tables 3 and 4. The results show that both compressional- and shear-wave velocities depend on effective pressure rather than differential pressure and n is greater for shear than compressional-wave velocities. At constant differential pressure n remains fairly constant over a wide range of pore pressure, whereas at constant pore pressure n decreases with increasing differential pressure.

4 Seismic velocities in the upper oceanic crust

The application of the data presented here to the interpretation of oceanic crustal velocities is significant. It is clear that if oceanic rocks have pore pressures approximating the hydrostatic pressure produced by the overlying column of seawater, their velocities and related elastic properties will be much different from laboratory measured properties in which pore pressures are zero.

Near ridge crests and other oceanic regions devoid or nearly devoid of sediment cover where cracks extend to the surface, the pore pressure at a given depth is likely to equate to the weight of a column of water extending to sea-level. In some regions of the upper oceanic crust, the pore pressure may be less than hydrostatic, as has recently been reported in the Costa Rica rift region by *Glomar Challenger* drilling (Anderson & Zoback 1982). In many regions it is also probable that pore pressure is in excess of hydrostatic and thus velocities are likely to be significantly depressed. It has been well established that overpressuring in sedimentary sections can have many origins, some of which may be applicable to basaltic regions of the oceanic crust. For example, tectonic processes (Fertl 1976; Gretener 1976), the smectite to illite transformation, which releases water during diagenesis (Burst 1969),

Table 3. Values of n for compressional (V_p) and shear-(V_s) wave velocities as a function of pore pressure (P_p) and differential pressure (P_d) for Juan de Fuca ridge basalt.

P_p(kb)	P_d = 0–0.2 kb		P_d = 0.4–0.6 kb		P_d = 08–1.0 kb	
	V_p	V_s	V_p	V_s	V_p	V_s
0	0.90	0.99	0.80	0.96	0.79	0.91
0.4	0.90	0.99	0.77	0.96	0.79	0.92
0.8	0.89	0.99	0.77	0.95		
1.2	0.89	0.99	0.75	0.95		

Table 4. Values of n for compressional-(V_p) and shear-(V_s) wave velocities as a function of pore pressure (P_p) and differential pressure (P_d) for Oman dolerite.

P_p(kb)	P_d = 0–0.2 kb		P_d = 0.4–0.6 kb		P_d = 08–1.0 kb	
	V_p	V_s	V_p	V_s	V_p	V_s
0	0.90	0.93	0.77	0.87	0.64	0.76
0.4	0.91	0.93	0.78	0.86	0.64	0.76
0.8	0.92	0.93	0.83	0.85		
1.2	0.92	0.93	0.85	0.85		

and rapid accumulation of low permeability shale, which hinders dewatering of underlying sediments (Gretener 1976), can all produce excess pore pressures. In tectonically active regions, such as subduction zones, high pore pressure may be developed in water saturated basalt by active folding and faulting. Likewise, the release of water accompanying relatively low grade metamorphic reactions in basalt may result in excess pore pressure. Regions in which impermeable sediments are interlayered with basalt may constitute seals, which would facilitate the development of high pore pressure.

The changes in compressional- and shear-wave velocities with increasing pore pressure are substantially greater for the basalt sample than the dolerite. This is presumably related to the higher porosity of the basalt and complicated by the presence of vesicles in addition to microcracks in the basalt. The importance of pore shape on elastic moduli and seismic velocities has been well demonstrated (Walsh 1965; O'Connell & Budiansky 1974; Toksoz, Cheng & Timur 1976). The following discussion will be primarily concerned with the effects of pore pressure on velocities in the upper basaltic regions of the oceanic crust and the data from the Juan de Fuca ridge sample will be used for illustrative purposes. It is assumed that the cracks and pores in the sample formed during cooling and were open *in situ*, as has been found for Iceland basalt (Kowallis *et al.* 1982).

In Figs 3 and 4, the basalt velocity data are shown as functions of confining pressure and differential pressure. In the upper portions of the figures, confining pressures have been equated to depth below the sea floor assuming a model consisting of a 5 km seawater column ($\rho = 1.03\,\mathrm{g\,cm^{-3}}$) overlying fresh basalt ($\rho = 2.85\,\mathrm{g\,cm^{-3}}$). The variations of velocities with depth are illustrated for zero pore pressure, as well as for pore pressure equal to hydrostatic in which the pore pressure is assumed to be a function of the weight of a column of free seawater extending to sea-level. The regions between these curves give compressional- and shear-wave velocities for oceanic crustal underpressure (i.e. pore pressure < hydrostatic pressure). Likewise, velocities below the pore pressure equal to hydrostatic curves represent crustal conditions of overpressure (pore pressure > hydrostatic). Variations of velocity with depth for pore pressures equivalent to confining pressures (differential pressure = 0) are also shown in these figures. This latter line for shear velocity at zero differential pressure was obtained using the zero confining pressure data and assuming a slope parallel to the 0.2 kb differential pressure line. Finally, Figs 3 and 4 predict extremely low velocities in oceanic crustal regions in which pore pressures exceed confining pressures.

Since increasing pore pressure at constant confining pressure has a greater effect on shear velocities than compressional velocities, Poisson's ratio (σ) calculated from the relation

$$\sigma = \frac{1}{2}\,\frac{(V_p/V_s)^2 - 2}{(V_p/V_s)^2 - 1}$$

increases for the basalt sample with increasing pore pressure. This is illustrated in Fig. 7. Examination of this figure also shows that if pore pressure is equivalent to hydrostatic in the upper 2 km of the oceanic crust, Poisson's ratio will decrease with increasing depth. Also, Poisson's ratio depends on an effective pressure, $P_e = P_c - nP_p$, where $n > 1$.

It should be emphasized that the behaviour of velocities with confining and pore pressure obtained in this study is expected to vary for different basalts. Critical to this will be the percentage of connected pore space in a given sample and the pore geometry. Also, the measurements do not take into account the presence of large fractures and rubble zones which have been shown to be abundant within the upper basaltic regions of the oceanic crust. For a highly fractured basaltic region, the effects of pore pressure on seismic velocities may well be of greater importance than observed in this study.

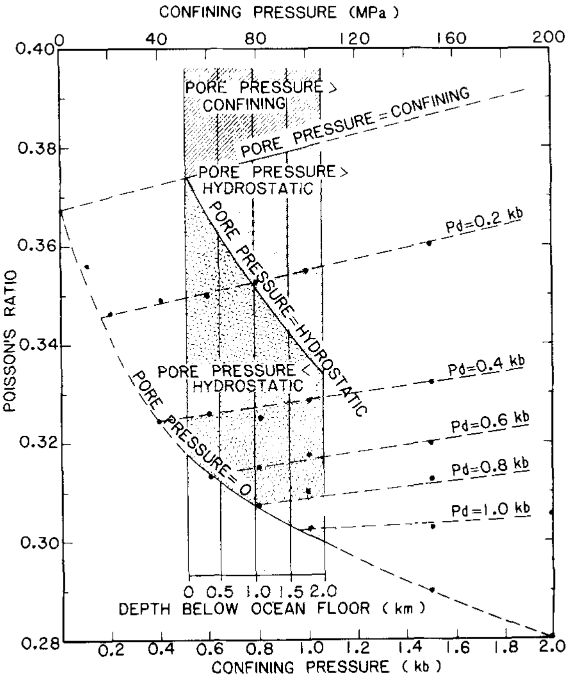

Figure 7. Poisson's ratio calculated from V_p and V_s for oceanic basalt as a function of depth within the crust and pore pressure.

5 Conclusions

Pore pressure is concluded to play an important role in influencing the velocities and elastic moduli of the oceanic crust. At constant confining pressure, compressional- and shear-wave velocities are significantly lowered by increasing pore pressure. Regions of overpressure and underpressure will possess anomalous velocities, which are dependent on depth, porosity, pore geometry and the deviation of the pore pressure from hydrostatic. Since porosity is likely to be extremely low in the lower oceanic crust, pore pressure is expected to have a greater effect on velocities in the upper few kilometres of crust.

Since pore pressure has little effect on bulk rock density, but can change velocities significantly, it becomes apparent that velocity–density relationships obtained from rocks under conditions of low pore pressure must be used with caution when applied to upper oceanic crustal velocities. For a given velocity, density is likely to be underestimated and porosity overestimated.

For oceanic basalt and dolerite, velocities are found to depend upon an effective pressure rather than simple differential pressure. When both confining pressure and pore pressure are varied, velocity increases with increasing confining pressure at constant differential pressure. Thus, the relationship $P_e = P_c - nP_p$ holds and $n < 1$. The value of n is less for compressional-wave velocities than shear-wave velocities and is not constant for a given rock.

The experimental results also show that Poisson's ratio is dependent on pore pressure as well as confining pressure. At constant confining pressure, Poisson's ratio increases with increasing pore pressure. This observation may prove significant in detecting overpressured and underpressured regions within the upper oceanic crust.

Acknowledgments

I would like to thank R. Ramananantoandro, J. Schultz, and H. Wang for their help during this study. The support of the Office of Naval Research Contract N-00014-80-C-0252 is gratefully acknowledged.

References

Anderson, R. N. & Zoback, M. D., 1982. Permeability underpressure and convection in the oceanic crust near the Costa Rica Rift, eastern equatorial Pacific, *J. geophys. Res.*, **87**, 2860–2868.

Au, D. & Clowes, R. M., 1984. Shear-wave velocity structure of the oceanic lithosphere from ocean bottom seismometer studies, *Geophys. J. R. astr. Soc.*, **77**, 105–123.

Banthia, B. S., King, M. S. & Fatt, I., 1965. Ultrasonic shear-wave velocities in rocks subjected to simulated overburden pressure and internal pore pressure, *Geophysics*, **30**, 117–121.

Biot, M. A., 1956. Theory of propagation of elastic waves in a fluid-saturated porous solid: 1. Low frequency range, 2. Higher frequency range, *J.acoust. Soc. Am.*, **28**, 168–191.

Biot, M. A., 1962. Generalized theory of acoustic propagation in porous media, *J. acoust. Soc. Am.*, **34**, 1254.

Biot, M. A. & Willis, D. G., 1957. The elastic coefficients of the theory of consolidation, *J. appl. Mech.*, **24**, 594–601.

Birch, Francis, 1960. The velocity of compressional waves in rocks to 10 kilobars, Part 1, *J. geophys. Res.*, **65**, 1083–1102.

Brace, W. F. & Orange, A. S., 1968. Further studies of the effects of pressure on electrical resistivity of rocks, *J. geophys. Res.*, **73**, 5407–5420.

Brandt, H., 1955. A study of the speed of sound in porous granular media, *Trans. Am. Soc. mech. Engrs*, **22**, 479–486.

Burst, J. F., 1969. Diagenesis of Gulf Coast clayey sediments and its possible relation to petroleum migration, *Bull. Am. Ass. Petrol. Geol.*, **53**, 73–93.

Christensen, N. I., 1970. Compressional wave velocities in basalts from the Juan de Fuca Ridge, *J. geophys. Res.*, **75**, 2773–2775.

Christensen, N. I. & Smewing, J. D., 1981. Geology and seismic structure of the northern section of the Oman ophiolite, *J. geophys. Res.*, **86**, 2545–2555.

Domenico, S. N., 1977. Elastic properties of unconsolidated porous and reservoirs, *Geophysics*, **42**, 1339–1368.

Fatt, I., 1958. Compressibility of sandstones at low to moderate pressures, *Bull. Am. Ass. Petrol. Geol.*, **42**, 1924–1957.

Fertl, W. H., 1976. *Abnormal Formation Pressures*, Elsevier, New York.

Geertsma, J., 1957. The effect of fluid pressure decline on volumetric changes of porous rocks, *Soc. Petrol. Eng.*, **210**, 331–340.

Gregory, R. T. & Taylor (Jr), H. P., 1981. An oxygen isotope profile in a section of cretaceous oceanic crust, Samail ophiolite, Oman: evidence for $\delta^{18}O$ buffering of the oceans by deep (>5 km) seawater-hydrothermal circulation at mid-ocean ridges, *J. geophys. Res.*, **86**, 2737–2755.

Gretener, P. E., 1976. Pore pressure: fundamentals, general ramifications and implications for structural geology, *Am. Ass. Petrol. Geol. Educ. Course Note Series No. 4*, 87 pp.

Hermance, J. F., Nur, A. & Bjornsson, S., 1972. Electrical properties of basalt: relation to laboratory to *in situ* measurements, *J. geophys. Res.*, **77**, 1424–1429.

Houtz, R. E., 1980. Crustal structure of the North Atlantic on the basis of large-airgun-sonobuoy data, *Bull. geol. Soc. Am.*, **91**, 406–413.

Houtz, R. E. & Ewing, J., 1976. Upper crustal structure as a function of plate age, *J. geophys. Res.*, **81**, 2490–2498.

Hyndman, R. D. & Drury, M. J., 1976. The physical properties of oceanic basement rocks from deep drilling on the mid-Atlantic Ridge, *J. geophys. Res.*, **81**, 4042–4052.

Kennett, B., 1977. Towards a more detailed picture of the oceanic crust and mantle, *Mar. geophys. Res.*, **3**, 7–42.

King, M. S., 1966. Wave velocities in rocks as a function of overburden pressure and pore fluid saturants, *Geophysics*, **31**, 56–73.

Kirkpatrick, R. J., 1979. The physical state of the oceanic crust: results of downhole geophysical logging in the mid-Atlantic ridge at 23° N, *J. geophys. Res.*, **84**, 178–188.

Kowallis, B. J., Roeloffs, E. A. & Wang, H. F., 1982. Microcrack studies of basalts from the Iceland Research Drilling Project, *J. geophys. Res.*, **87**, 6650–6656.

Lister, C. R. B., 1972. On the thermal balance of a mid-ocean ridge, *Geophys. J. R. astr. Soc.*, **26**, 515–535.

O'Connell, R. J. & Budiansky, B., 1974. Seismic velocities in dry and saturated cracked solids, *J. geophys. Res.*, **79**, 5412–5426.

Raitt, R. W., 1963. The crustal rocks, in *The Sea*, **3**, 85–102, ed. Hill, M. N., Wiley, New York.

Raleigh, C. B. & Paterson, M. S., 1965. Experimental deformation of serpentinite and its tectonic implications, *J. geophys. Res.*, **70**, 3965–3985.

Spudich, P. K. & Orcutt, I., 1980. A new look at the seismic velocity structure of the oceanic crust, *Rev. Geophys. Space Phys.*, **18**, 627–645.

Todd, T. & Simmons, G., 1972. Effect of pore pressure on the velocity of compressional waves in low-porosity rocks, *J. geophys. Res.*, **77**, 3731–3743.

Toksoz, M. N., Cheng, C. H. & Timur, A., 1976. Velocities of seismic waves in porous rocks, *Geophysics*, **41**, 621–645.

Walsh, J. B., 1965. The effect of cracks on the compressibility of rock, *J. geophys. Res.*, **70**, 381–389.

Whitmarsh, R. B., 1978. Seismic refraction studies of the upper igneous crust in the North Atlantic and porosity estimates for layer 2, *Earth planet. Sci. Lett.*, **37**, 451–464.

Wyllie, M. R. J., Gregory, A. R. & Gardner, G. H., 1958. An experimental investigation of factors affecting elastic wave velocities in porous media, *Geophysics*, **23**, 459–493.

Geophys. J. R. astr. Soc. (1984) **79**, 425–437

Inversion of seismic data: accuracy and convergence of an iterative scheme based on acoustic imaging

Philip M. Carrion, John T. Kuo and Waldo A. Patton
Aldridge Laboratory of Applied Geophysics, Henry Krumb School of Mines, Columbia University, NYC, NY 10027, USA

Received 1984 March 1; in original form 1983 May 19

Summary. This paper describes the accuracy, stability and convergence of a new iterative inversion scheme based on acoustic imaging. The scheme first decomposes the observed data (seismogram) into plane waves (PWD); then it continues the PWD data downwards. The downward continuation can take place in the time or the frequency domains. The data are continued by finding the solution of the acoustic wave equation for a trial velocity selected from a class of admissible functions. Next the downward continued data are projected on to the plane of horizontal slowness p versus depth z. The imaging principle used to recover the velocity is based on finding the maximum of the projected wavefield energy, which corresponds to the critically reflected and refracted arrivals. This maximum must coincide with the true velocity profile in the p–z domain. If not, the trial velocity function is adjusted to be closer to the maximum of the transformed data and the procedure is restarted. Examples with synthetic and real data are presented.

Introduction

Several inversion techniques which can be applied to large offset data have been presented recently. An iterative method based on downward continuation of the observed data and using as a criterion for convergence, the stationarity of the output wavefield with respect to the velocity was presented in the paper by Clayton & McMechan (1981). Schultz, Pieprzak & Loh (1983) and Diebold & Stoffa (1981) presented methods based on analysis of the locus of the travel-time curves in the domain of intercept time, τ, versus horizontal slowness, p (the slant stack domain). These methods have the advantage over 'near offset' methods that they are able to recover the velocity profile to greater depths since they utilize wide angle arrivals. However, most inversion methods ignore amplitude information and use only the phase shifts of the recorded data. It is well known that the utilization of the amplitude information not only makes the inversion more accurate but also allows the elimination of the necessity for such inconvenient procedures as subjectively picking the travel-time curves.

Carrion, Kuo & Stoffa (1984) presented a method which incorporates the amplitude information in the analysis of large offset data. Carrion (1983) and Carrion & Kuo (1984) proposed a method for the recovery of the compressional velocity based on an optimization procedure, which utilizes the energy and the phase shifts of wide aperture seismic data.

In this paper we formulate the problem of the recovery of the velocity profile in terms of acoustic imaging and of an imaging principle for the selection of a solution. The acoustic imaging involves the downward continuation of the observed data and subsequent projection of the continued wavefield into the plane of depth versus horizontal slowness. The imaging principle states that the maximum of the projected wavefield energy, corresponding to the critically reflected arrivals, should coincide with the true velocity profile.

Synthetic and real data have been processed. The synthetic example is for an elastic horizontally stratified medium. Each layer is characterized by its compressional velocity, its density, and its Poisson ratio. The real data include both the horizontal and the vertical components of the measured particle velocities. The real data were kindly provided to us by AMOCO. The convergence, accuracy, and stability of the inversion scheme are illustrated by these examples.

Definitions

In this part, we define several terms which we will use later in this paper. Let us consider two normed spaces H_1 and H_2 and an operator A (in general, non-linear), which projects the space H_1 into H_2.

$$Ax = y \in H_2, \qquad x \in H_1. \tag{1.1}$$

Stability: the stability of any numerical or analytical scheme, which finds the x in (1.1) can be defined as the existence of an inequality:

$$\| x \|_{H_1} \leqslant M \| y \|_{H_2}, \tag{1.2}$$

for all $y \in H_2$, where M is a constant independent of x.

Existence and uniqueness: it is obvious that obtaining a solution of (1.1) in general defines an inverse operator A^{-1}:

$$A^{-1} y = x. \tag{1.3}$$

In addition we will require that the solution be unique. It is true that if A is linear, properties (1.3) and (1.2) are sufficient to guarantee the uniqueness of the solution. Let us assume that x_1 and x_2 are two solutions of (1.1). Then we will call the difference:

$$e = x_1 - x_2 \tag{1.4}$$

and apply the linear operator A to (1.4)

$$Ae = 0. \tag{1.5}$$

Now we will use property (1.2):

$$\| e \|_{H_1} \leqslant M \| 0 \|_{H_2} = 0 \tag{1.6}$$

from which immediately follows:

$$x_1 = x_2. \tag{1.7}$$

This proves that if the operator A is linear the uniqueness of the solution follows automatically from (1.2)–(1.3). However, for non-linear operators this is not true in general.

Convergence: let us assume that $\{P_k\}$ is a sequence of projection operators:

$$P_k x = x_k \in H_1 \tag{1.8}$$

where:

$$\lim_{k \to \infty} \| P_k x \|_{H_1} = \| x \|_{H_1}.$$

Let us take any element $x^* \in H_1$. We will say that $x_k \to x^*$ if

$$\lim_{k \to \infty} \| x_k - P_k x^* \|_{H_1} = 0. \tag{1.9}$$

Also, the speed of convergence may be defined by:

$$\| x_k - P_k x^* \|_{H_1} \leqslant M \left(\frac{1}{k} \right)^N , \tag{1.10}$$

where k is a large number, $M > 0$ and does not depend on k. N is the rate of convergence. The same definitions apply to the space H_2.

Accuracy: the accuracy can be defined by:

$$\| x_{\mathrm{T}} - x_k \|_{H_1} \leqslant M \left(\frac{1}{k} \right)^{N_{\mathrm{a}}} \tag{1.11}$$

where x_{T} is the true solution of (1.1) and N_{a} is the order of accuracy. Actually, (1.11) and (1.10) are equivalent if and only if $x^* = x_{\mathrm{T}}$.

Basic derivations

Let us consider an acoustic medium, occupying the lower half-space $0 \leqslant z < \infty$. The propagation of a dilitational stress can be represented by the following system of partial differential equations:

$$\begin{cases} -\rho \dfrac{\partial^2 W(r, z, t)}{\partial t^2} = \nabla P(r, z, t) & (2.1) \\ -P(r, z, t) = \rho c^2 \nabla \cdot W(r, z, t), & (2.2) \end{cases}$$

where $P(r, z, t)$ is the pressure field and W is the displacement vector. Assuming that density $\rho(z)$ and velocity $c(z)$ are functions of depth only, we will derive now the reflectivity equations using (2.1)–(2.2) which will facilitate further analysis.

For this reason we will apply the Fourier–Hankel transform to (2.1–2.2) in the following form:

$$\begin{Bmatrix} \overline{P} \\ \overline{W} \end{Bmatrix} = \int_0^\infty \int_0^\infty J_0(\omega p r) \begin{Bmatrix} P \\ W_z \end{Bmatrix} \exp(-i\omega t)\, r dr dt \tag{2.3}$$

which yields after some algebra the following equations:

$$\begin{cases} \dfrac{1}{\rho(z)} \dfrac{\partial \overline{P}}{\partial z} = \omega^2 \overline{W} & (2.4) \\ -\overline{P} = \dfrac{\rho(z)\, c^2(z)}{\cos^2 \alpha} \dfrac{\partial \overline{W}}{\partial z} & (2.5) \end{cases}$$

where $\cos^2 \alpha = 1 - p^2 c^2(z)$ and α defines the propagation angle. (p is the horizontal slowness or ray parameter).

Let us introduce now a new variable:

$$y = \int_0^z \frac{\cos\alpha}{c(\xi)}\, d\xi = \int_0^z \frac{\sqrt{1 - p^2 c^2(\xi)}}{c(\xi)}\, d\xi. \tag{2.6}$$

Since the acoustic impedance I is:

$$I(y) = c(y)\,\rho(y) \tag{2.7}$$

equations (2.4)–(2.5) can be represented as follows:

$$\begin{cases} -\bar{P} = \dfrac{I(y)}{\cos\alpha} \dfrac{\partial \bar{w}}{\partial y} & (2.8) \\[2ex] \dfrac{\partial \bar{P}}{\partial y} = \omega^2 \dfrac{I(y)}{\cos\alpha}\, \bar{W}. & (2.9) \end{cases}$$

Differentiating (2.9) with respect to y and using (2.8) yields:

$$\left\{\frac{\partial^2}{\partial y^2} + \frac{\partial}{\partial y} \ln\left(\frac{\cos\alpha}{I(y)}\right) \frac{\partial}{\partial y} + \omega^2\right\} \bar{P} = 0. \tag{2.10}$$

A similar equation can be obtained for the displacement $\bar{W}$ or particle velocity $\bar{V}$ ($V = \dot{W}$)

$$\left\{\frac{\partial^2}{\partial y^2} - \frac{\partial}{\partial y} \ln\left(\frac{\cos\alpha}{I(y)}\right) \frac{\partial}{\partial y} + \omega^2\right\} \bar{V} = 0. \tag{2.11}$$

The solution of (2.10) or (2.11) can be presented in 3-D space R^3_ω: (y, p, ω). The second term of the operators presented in the brackets in (2.10)–(2.11) has a logarithmic singularity when $\alpha \to 90°$. This corresponds to the turning points of the critically reflected (refracted) arrivals and is equivalent to the condition $p = 1/c(z)$. Therefore in the space R^3_ω: (ω, p, y) or in the space R^3_τ: (τ, p, y) we can identify a hypersurface on which the scattering potential (second term in the brackets in 2.10–2.11) is singular and the amplitude of the pressure or particle velocity field is at a maximum. Since the equation of the hypersurface $[p = 1/c(z)]$ does not depend on frequency or time it is more convenient to consider the two-dimensional space R^2: (p, y) which can be obtained by projection of the R^3 on to R^2. In the frequency domain R^2 can be obtained from R^3 by summation over all frequencies which means a sum of contributions of monochromatic waves (frequency stack).

Downward continuation and acoustic imaging

We assume that multichannel seismic data (MCS) are acquired at the Earth's surface and presented as CSP (common shot point) or CMP (common mid-point) gathers. The raw data can be plane wave decomposed (PWD) using the Fourier–Hankel transform. Next we consider the acoustic wave equation (2.10) or (2.11) and choose a class of admissible velocity functions $c(z) \in \Omega$. Then we continue downwards the plane wave decomposed observed data. Let us return now to equations (2.10)–(2.11). We see that the second term in the brackets can be neglected in two cases. The first case is when frequencies are high enough. The second case when the logarithmic gradients of the acoustic impedance are small. In both cases the acoustic equation becomes the so-called 'two-way' acoustic equation since its solution can be represented in terms of upcoming and downgoing waves:

$$\bar{P} = U \exp(-i\omega y) + D \exp(i\omega y), \tag{3.1}$$

where U and D are coefficients which define the amplitudes of the upcoming and downgoing waves respectively. Considering the upcoming waves only and substituting the PWD pressure field by its slant stack:

$$\bar{P}(-k_r, \omega, p) = S(p, \omega, y), \tag{3.2}$$

where $S(p, \omega, y)$ is the slant stack of the observed wavefield. It has been shown that the slant stack is equivalent to the PWD procedure (see Chapman 1981, Treitel, Gutowsky & Wagner 1982). Therefore after inserting (3.2) into (3.1) and applying the inverse Fourier transform we can obtain:

$$\bar{S}(\tau = 0, p, z) = \frac{1}{2\pi} \int_{-\infty}^{\infty} S(p, \omega) \exp(-i\omega y)\, d\omega \tag{3.3}$$

where τ is set to zero, and $S(p, \omega) \equiv U$.

This expression was used by Clayton & McMechan for the recovery of the velocity profile using the stationarity of the wavefield with respect to velocity curve $c(z)$.

Let us now formulate our imaging principle based on the maximum amplitude of the PWD wavefield projected on to the p–z plane. First we will solve equations (2.10) or (2.11) and locate the maximum of the amplitude of the slant stacked wavefield. The numerical scheme we use is:

$$S_{j+1} - S_j = \left(1 - \frac{1}{2} \ln \frac{\cos^2 \alpha_{j+1} c_j}{\cos^2 \alpha_j c_{j+1}}\right) (S_j - S_{j-1}) - \omega^2 (\Delta y)^2 S_{j-1} \tag{3.4}$$

where S_j is the slant stack of the pressure field corresponding to the 'j' layer.

We can formulate the recovery of the solution of (3.4) in terms of the solution of the Cauchy problem. For this reason boundary conditions should be introduced:

$S(p, \omega, y = 0)$ is the slant stack of the recorded data.

$$S_1 - S_0 = \frac{W(\omega) \Delta y}{\sqrt{u_1^2 - p^2}} \quad (y = 0)$$

where u_1 is the slowness of the near surface layer (assumed to be known). We see that in order to solve the Cauchy problem knowledge of the source wavelet is required. In exploration geophysics, however, we do not know the source wavelet exactly. Therefore in some situations wavelet processing becomes necessary. However, wavelet processing in many cases is not able to provide us with a reliable estimate of the wavelet.

We will avoid the problem of wavelet estimation by setting the first derivative at $y = 0$ to zero. This is certainly an approximation, which gives good numerical results if Δy is small near the origin $y = 0$. Let us now return to the determination of the convergence and the accuracy of the solution.

The solution of equation (3.4) can be presented in three-dimensional space:

$\text{supp}\, S_j = R^3 : (\omega, p, y)$.

Integration over the bandwidth of the data spectrum yields:

$$\bar{S}(p, z) = \int S(p, \omega, y) \Big|_{c(z)} d\omega. \tag{3.5}$$

Now we can consider a norm similar to (1.9):

$$\lim_{k \to \infty} \| c_k(z) - P_k S(p, \omega, y) \|_{(.)} = 0 \tag{3.6}$$

where norm (3.6) defines the distance between the two functions $c_k(z)$ (admissible velocity function) and the projection of the total wavefield into the $p-z$ plane. Operator P_k in (3.6) defines an acoustic imaging principle. If we require stationarity of the wavefield with respect to $c(z)$, then the iterative procedure will be similar to the Clayton & McMechan procedure. We will choose the imaging principle, based on the analysis of the amplitude of the total wavefield. Then the problem can be formulated as: find the projection of the hypersurface $p = 1/c(z)$ in the space R^3: (ω, p, y) into the $p-z$ plane. If the estimated velocity approaches the true velocity, the distance between the projection of the hypersurface in the $p-z$ domain and the velocity will be small. Therefore we chose P_k as follows:

$$P_k S(\omega, p, y) = \max_{p,z} \int S(\omega, p, y) \Big|_{c(z)} d\omega \tag{3.7}$$

which corresponds to critical arrivals and condition $p = 1/c(z)$ (equation of the hypersurface).

Similar to accuracy criterion (1.11) we can determine the desired accuracy in terms of a 'window' Λ:

$$\| c_T - c_k \| < \Lambda, \tag{3.8}$$

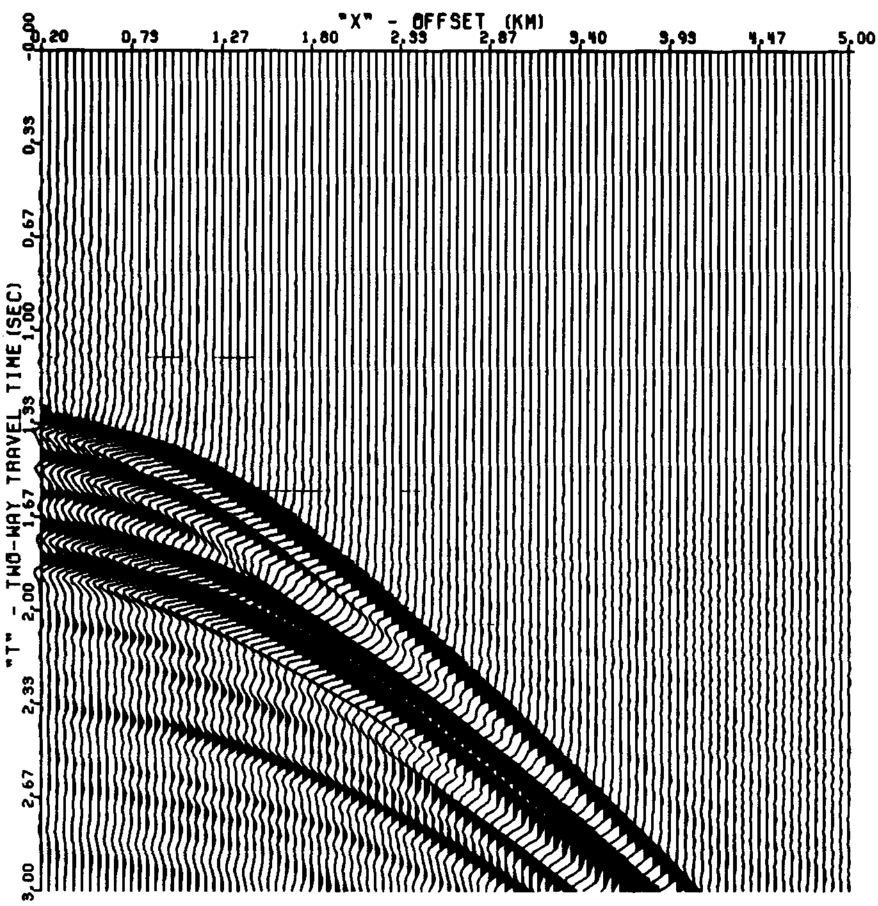

Figure 1. Synthetic seismogram, which corresponds to the model.

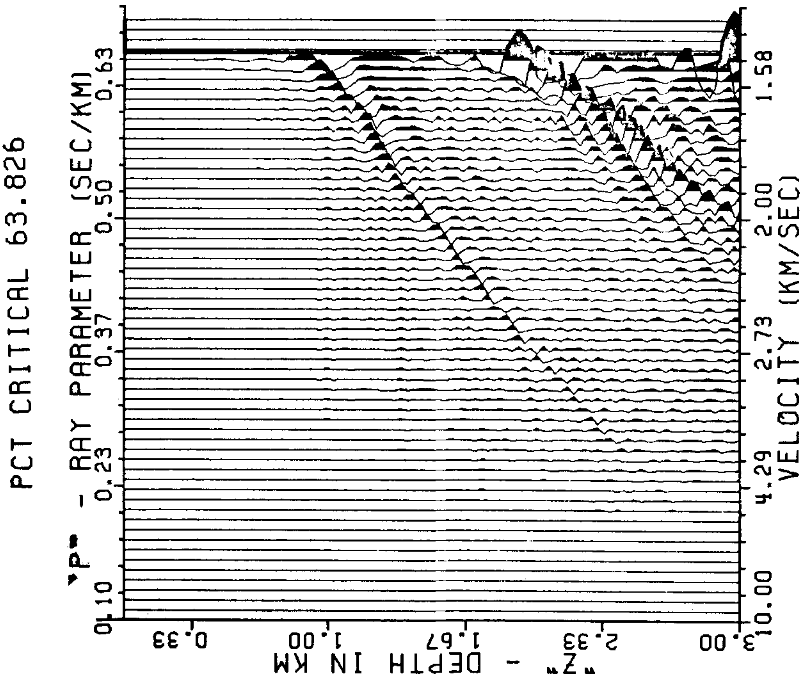

Figure 3. The wavefield image after the first iteration.

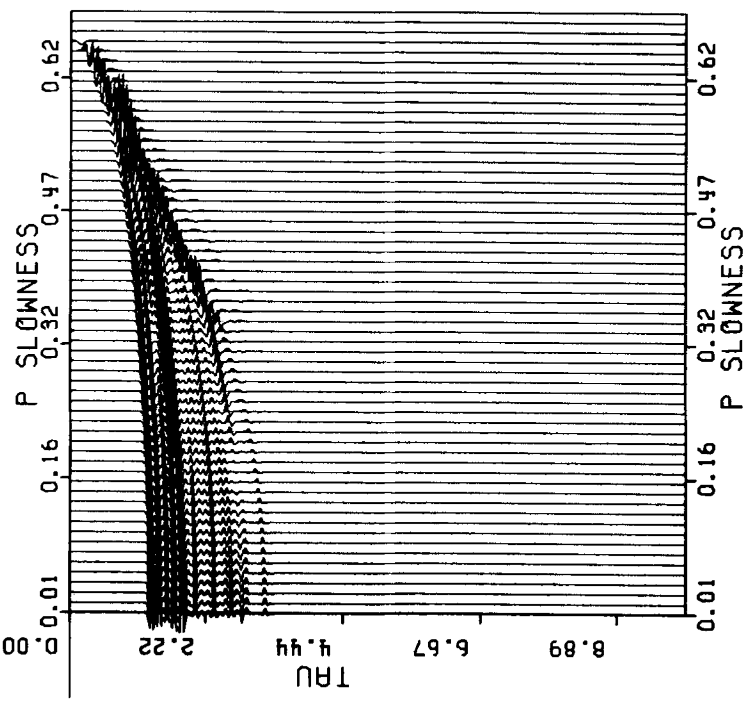

Figure 2. Slant stack of the synthetic seismogram.

where c_T is the true velocity. Actually (3.8) with a chosen window will determine the rate of convergence.

The computational procedure requires the solution of (3.4) for the chosen velocity profiles and subsequent summation over all available frequencies. Then the distance of the chosen velocities to the projection of the hypersurface is checked within the desired window Λ. The computations can be done purely automatically. If the window is narrow then the number of iterations increases.

Synthetic example

A synthetic example was chosen which presents an elastic medium, horizontally stratified into 22 layers (compressional and shear velocities presented in Table 1). A seismogram, which corresponds to this model is presented in Fig. 1. Fig. 2 is its slant stack. Fig. 3 depicts the projection of the total field on to the p–z plane after the first iteration. The chosen velocity for the first iteration coincides with the average velocity of the ocean [$c_1(z) = 1.5\ \mathrm{km\ s^{-1}}$]. Figs 4 and 5 are the images of the total wavefield after 11 and 19 iterations respectively. Fig. 5 is the coherency plot which shows the location of the reflectors and the solid line is the final velocity profile. Table 2 is the recovered velocity profile presented in Fig. 5. Comparing Tables 1 and 2 one can see that the accuracy of the solution is quite good.

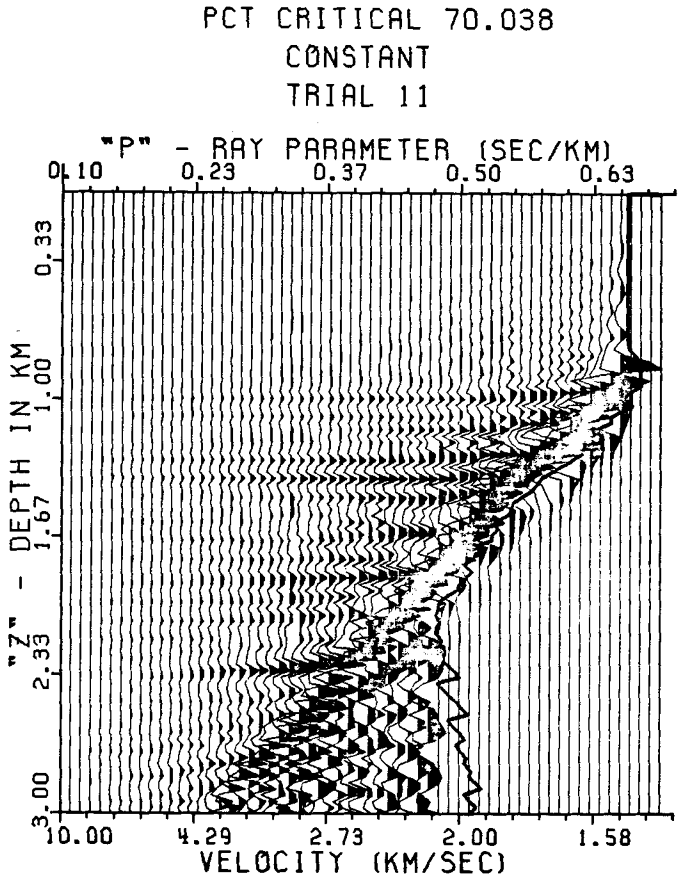

Figure 4. The wavefield image after the second iteration. Approximately 70 per cent of the total energy is concentrated near the input velocity (solid line).

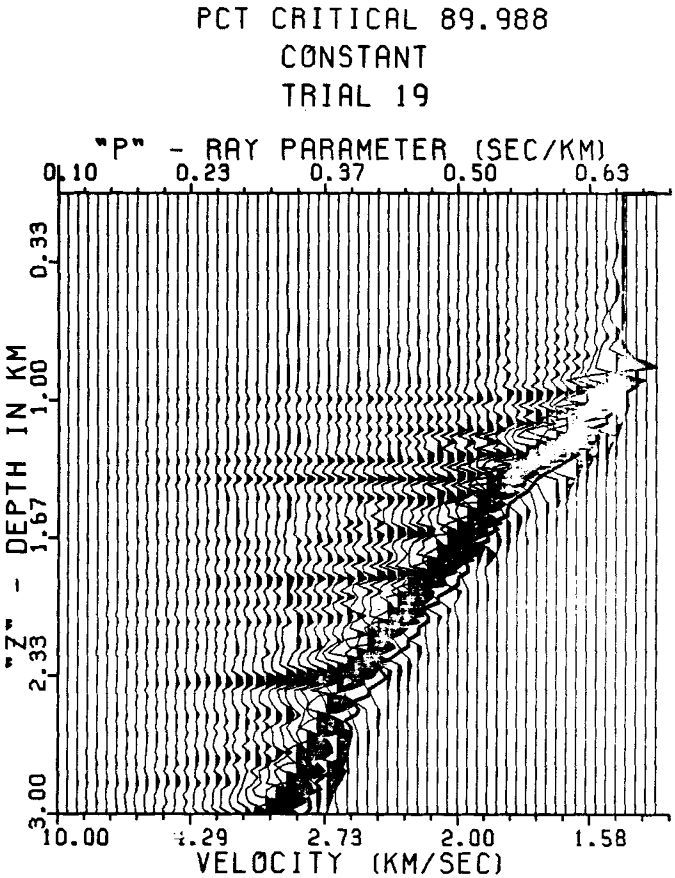

Figure 5. The image of the wavefield after 19 iterations.

Table 1. The model which represents an elastic medium, stratified into 22 horizontal layers.

	Depth	Thickness	P - Velocity	S - Velocity	Density
1	0.00	1.000	1.5000	0.0010	1.0000
2	1.00	0.100	1.5300	0.3000	1.1000
3	1.10	0.100	1.5890	0.5000	1.2000
4	1.20	0.100	1.6000	0.7000	1.3000
5	1.30	0.100	1.7000	0.8000	1.5000
6	1.40	0.100	1.8000	0.9000	1.9000
7	1.50	0.100	1.8500	0.9000	1.9000
8	1.60	0.100	1.9000	1.0000	2.0000
9	1.70	0.100	1.9500	1.0000	2.0000
10	1.80	0.100	2.0000	1.0000	2.0000
11	1.90	0.100	2.1000	1.0000	2.1000
12	2.00	0.100	2.1500	1.0000	2.1000
13	2.10	0.100	2.2000	1.0000	2.2000
14	2.20	0.100	2.3500	1.2000	2.3000
15	2.30	0.100	2.3800	1.3000	2.4000
16	2.40	0.100	2.5000	1.0000	2.0000
17	2.50	0.100	2.6000	1.3000	2.1000
18	2.60	0.100	2.6500	1.3300	2.1000
19	2.70	0.100	2.7000	1.4000	2.1000
20	2.80	0.100	2.7800	1.4000	2.1000
21	2.90	0.100	2.8000	1.4000	2.4000
22	3.00	0.100	2.9000	1.5000	2.4000

An example with real data

Fig. 7 depicts land seismic common shot point (CSP) data (the vertical component of the particle velocity). It is well known that conventional velocity analysis can give erroneous results when applied to CSP data. The method describes in this paper was used to obtain the

Table 2. The comparison between the recovered velocity and the model.

DEPTH (KM)	MODEL	COMPUTED VELOCITY
1.Ø	1.5	1.5
1.1	1.53	1.5385
1.2	1.58	1.5773
1.3	1.6Ø	1.6393
1.4	1.7Ø	1.7241
1.5	1.8Ø	1.8133
1.6	1.85	1.8519
1.7	1.9Ø	1.9455
1.8	1.95	1.96Ø9
1.9	2.ØØ	2.ØØØØ
2.Ø	2.1Ø	2.Ø834
2.1	2.15	2.1735
2.2	2.2Ø	2.2227
2.3	2.35	2.3612
2.4	2.38	2.4348
2.5	2.5Ø	2.493Ø
2.6	2.6Ø	2.5465
2.7	2.65	2.6Ø95
2.8	2.7Ø	2.6767
2.9	2.78	2.8Ø33
3.Ø	2.8Ø	2.868Ø

TABLE II

velocity profile. First the PWD of the seismogram (Fig. 7) was obtained. Fig. 8 is the time domain transform of the PWD. The velocity–depth profile (Fig. 9) was generated by the method described above.

A similar procedure applied to a common mid-point (CMP) gather was described by

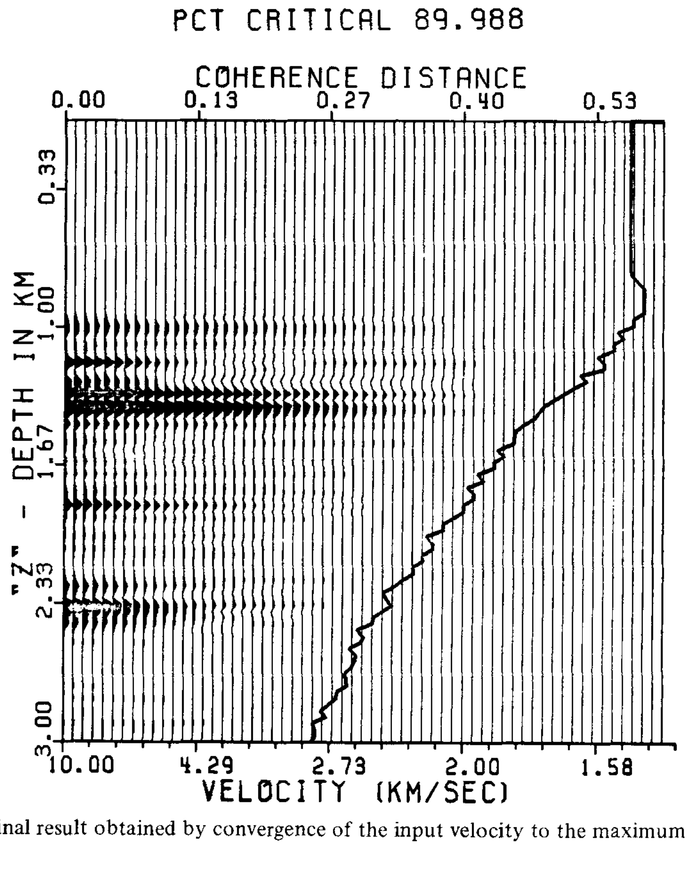

Figure 6. The final result obtained by convergence of the input velocity to the maximum of the projected wavefield.

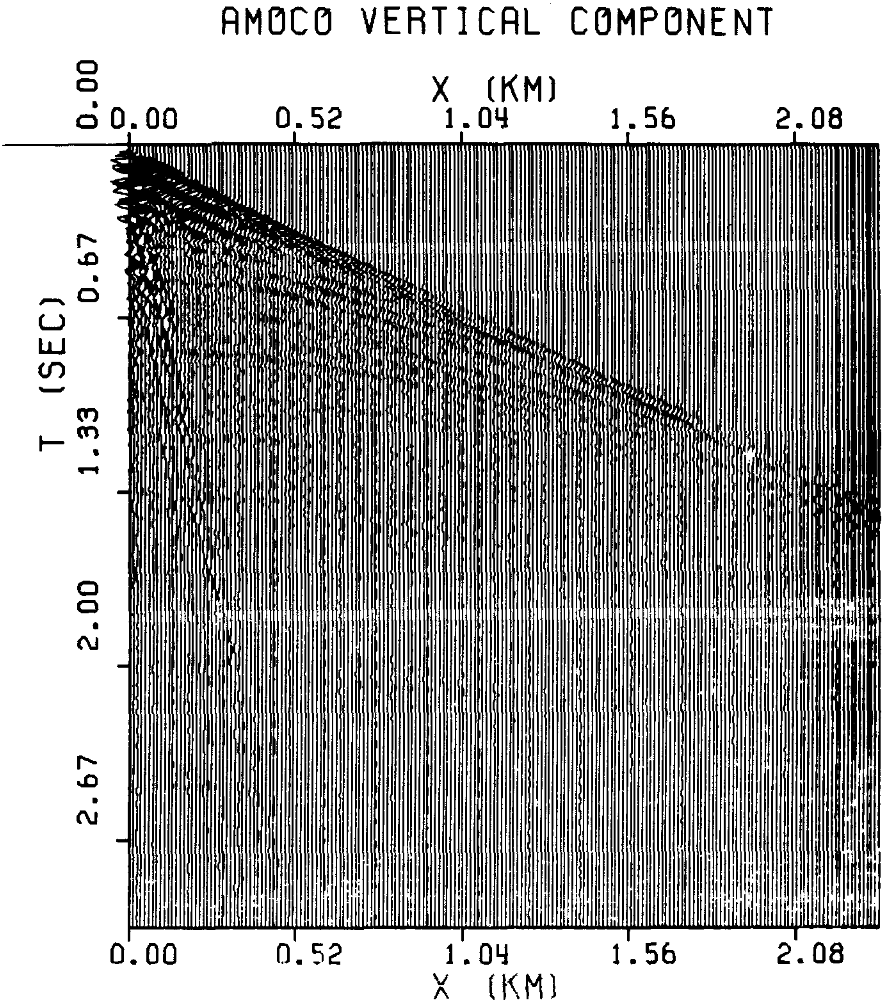

Figure 7. The vertical component of the particle velocity. CSP gather.

Carrion (1983). In that example, an additional criterion on convergence was imposed using the coherency of the phase shifts in the p–z domain. (For CMP data the images of the reflectors in the p–z domain are straight lines.) This additional criterion was not used in the present example (Fig. 9).

Conclusions

An iterative inversion technique based on acoustic imaging of the observed wavefield is presented. This technique finds the velocity profile by automatically adjusting the estimated velocity to approach the critical path (the projection of the hypersurface $p = 1/c(z)$ into the p–z domain). The estimated velocity determines the acoustic imaging based on the solution of the acoustic wave equation. Convergence occurs when the estimated velocity is equal to the critical path within a desired window. The number of iterations depends on the width of the window and on the depth at which velocities are to be found.

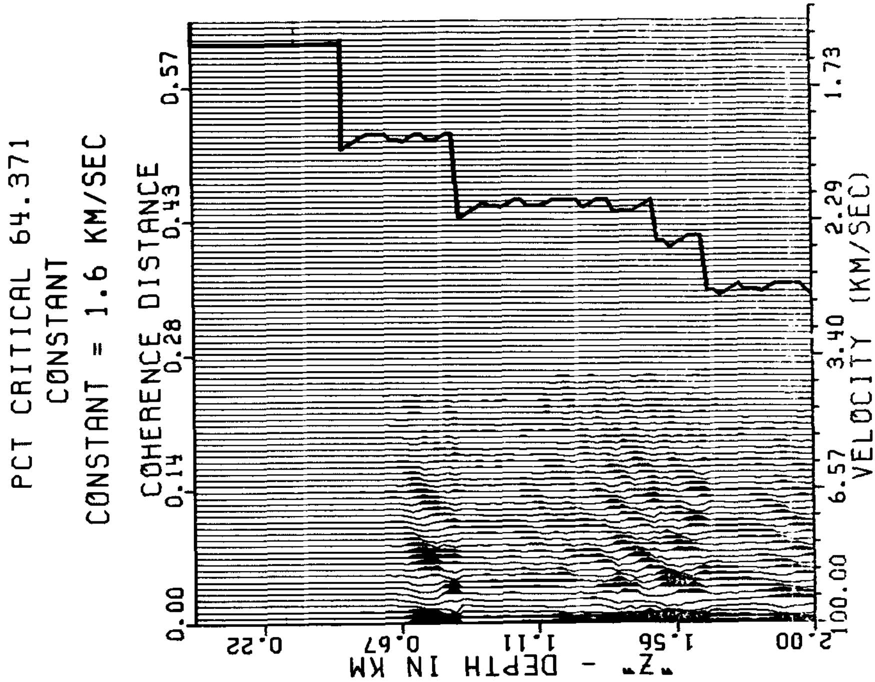

Figure 9. Recovered velocity profile (solid line).

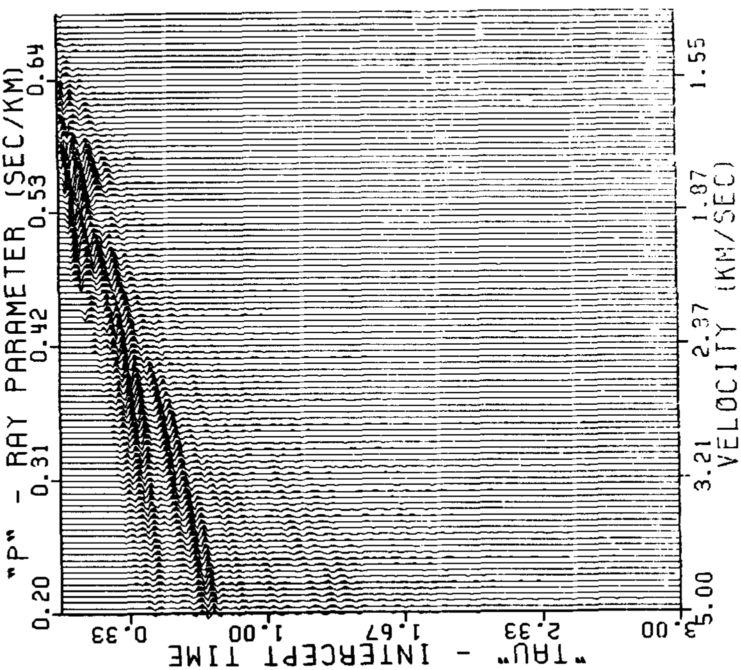

Figure 8. Slant stack of the CSP gather presented in Fig. 7.

The obvious advantage of this method is that it does not require many operations which are necessary ingredients of some inversion techniques (wavelet deconvolution for example). Its disadvantage is that the method allows only small lateral inhomogeneities.

Acknowledgments

The authors are grateful to the sponsors of Project Midas for their support of this research. We also thank Dr Sven Trietel for valuable comments. We thank AMOCO Production Company for supplying us with real seismic data and for permission to publish them.

References

Carrion, P., 1983. Minimization technique for inversion of large seismic records by double spatial transformation, *Proc. IGARSS' 83 Symp.*, pp. 41–43.

Carrion, P. & Kuo, J. T., 1984. A method for computation of velocity profiles by inversion of large offset records, *Geophysics,* **49,** 1246–1256.

Carrion, P., Kuo, J. T. & Stoffa, P., 1984. Inversion method in the slant stack domain using amplitudes of reflection arrivals, *Geophys. Prospect.*, **32,** 375–391.

Chapman, C., 1981. Generalized Radon transform and slant stacks, *Geophys. J. R. astr. Soc.*, **66,** 445–453.

Clayton, R. & McMechan, G., 1981. Inversion of refraction data by wave field continuation, *Geophysics,* **46,** 860–868.

Diebold, J. & Stoffa, P., 1981. The travel time equation, tau–*p* mapping and inversion of common mid-point data, *Geophysics,* **46,** 860–868.

Schultz, P., Pieprzak, A. & Loh, E. K. L., 1983. A case for larger offsets, *Geophysics,* **48,** 238–245.

Treitel, S., Gutowsky, P. & Wagner, D., 1982. Plane wave decomposition of seismograms, *Geophysics,* **47,** 1375–1401.

Geophys. J. R. astr. Soc. (1984) **79**, 439–467

An investigation of seismic anisotropy due to cracks in the upper oceanic crust at 45° N, Mid-Atlantic Ridge

R. S. White *Bullard Laboratories, Department of Earth Sciences, Madingley Rise, Madingley Road, Cambridge CB3 0EZ*

R. B. Whitmarsh *Institute of Oceanographic Sciences, Brook Road, Wormley, Godalming, Surrey GU8 5UB*

Received 1984 March 8; in original form 1983 September 13

Summary. A detailed seismic refraction survey using three 3-component ocean bottom seismographs over young (1.1–3.4 Ma old) Mid-Atlantic Ridge at 45° N recorded compressional wave velocity anisotropy in the upper crust of about ±5 per cent and associated particle motion deviations of up to ±8°. The magnitudes and azimuths of these anisotropic variations suggest that they are generated by sets of subparallel near-vertical water-filled cracks in layer 2. The directions of the cracks cannot be determined uniquely but they lie between the seafloor spreading and the ridge axis directions, in the range ±(30–60)° with respect to the ridge axis. We explain this unexpected crack orientation by the occurrence of cracking and fracturing induced in the upper crust as it moves away from the spreading axis. The principal horizontal stresses responsible for this fracturing are parallel and perpendicular to the ridge axis. The apparently negligible seismic influence exerted by ridge-parallel sets of (shallow?) cracks observed at the ridge axis is explained by their infilling by sediment and hydrothermal precipitates and by their closure under ridge-normal compression.

We find a normal oceanic crustal velocity structure that can be explained by decreasing numbers of open cracks with increasing depth through the upper 2 km of the crust. Lateral variability across the 25 km square survey is limited in magnitude (typically ±0.05 s variations in delay times), and the observed travel times are consistent with a model of the crust in which the isovelocity surfaces at depth are a subdued copy of the basement topography.

1 Introduction

The uppermost oceanic crust has a strong tectonic fabric approximately parallel to the axis of the parent spreading centre. Near-bottom observations of oceanic crust and studies of subaerial 'spreading centres' in Iceland and Afar frequently show sets of fissues (gjas) near the active rift which are subparallel to the spreading axis (e.g. Ballard, Van Andel &

Holcomb 1982; Harrison, Bonatti & Stieltjes 1975; Francheteau *et al.* 1980). Sidescan sonars detect highly elongated targets, orientated parallel to spreading axes, which are frequently interpreted to be fissures and inward-facing normal fault scarps (Ballard & Van Andel 1977; Luyendyk & Macdonald 1977; Laughton & Searle 1979). Fissures in the FAMOUS area at 37° N on the Mid-Atlantic Ridge are vertical and typically a few centimetres to a few metres wide and 10–2000 m long. Their vertical extent is unknown. The average spacing of faults and fissures is about 30 m in the inner rift valley. An average extension of 5–10 per cent is inferred from the width of the initially unfilled voids (Ballard & Moore 1977; ARCYANA 1978). Central zone faults are vertical but larger normal faults dipping at 50–60° and spaced a few kilometres apart become active on the sides of the median valley.

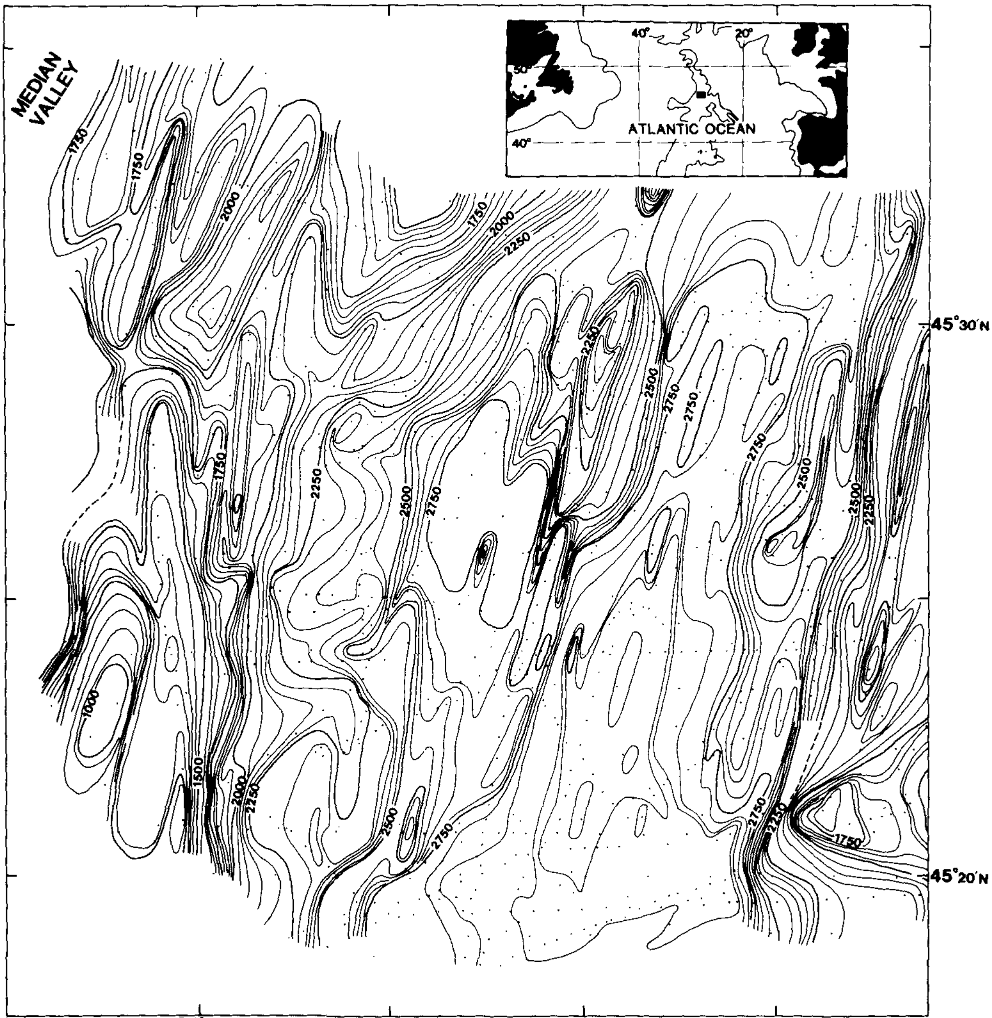

Figure 1. Contoured bathymetry and location (inset) of the survey area. Depths are in corrected metres with contour interval of 50 m. Dots indicate individual soundings. The contouring is constrained by the GLORIA mosaic shown in Fig. 2. The top of the east slope of the median valley is located in the extreme NW corner of the chart.

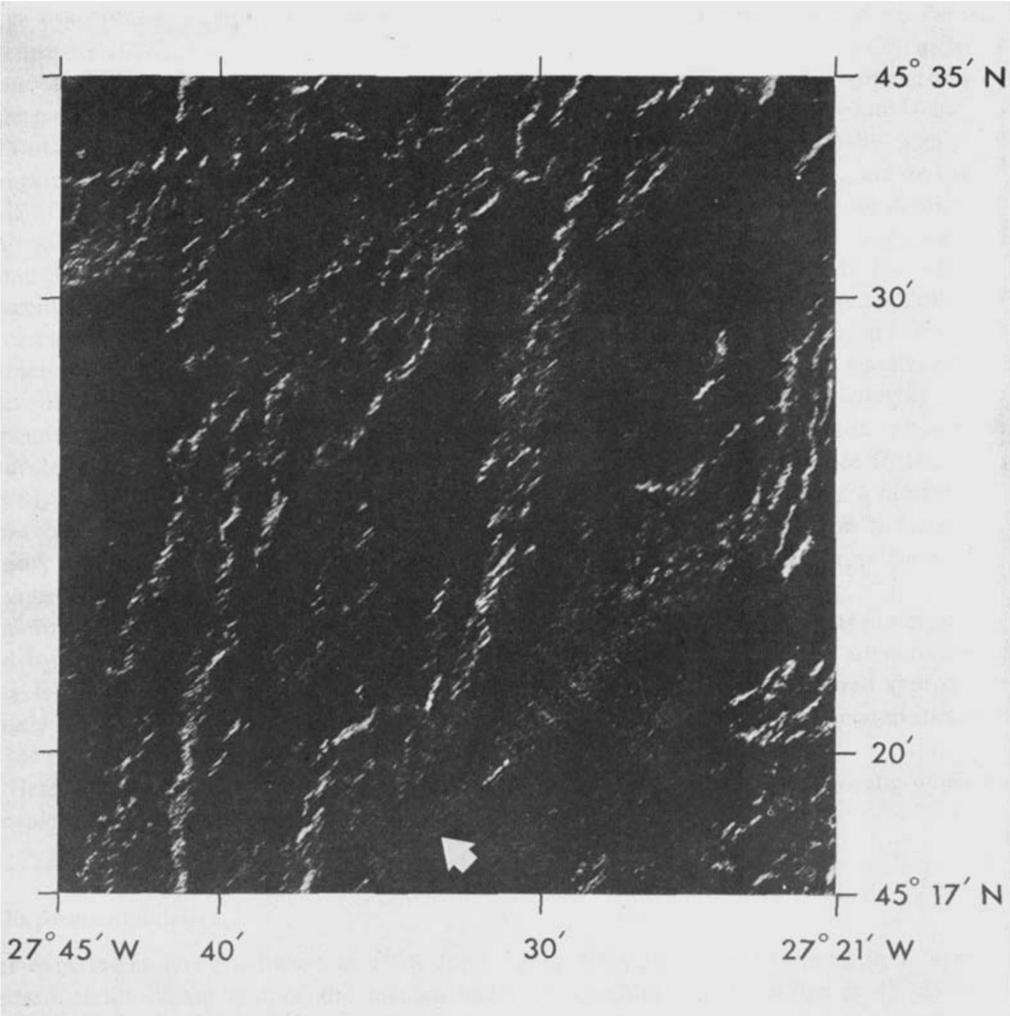

Figure 2. GLORIA sonograph mosaic for the survey area in Fig. 1. Targets shown in white. Direction of insonification was from the SE.

[*facing page* 440]

Borehole televiewer pictures in young igneous crust have been interpreted to suggest a high proportion of voids in basalt pillows as well as frequent horizontal or subhorizontal 'fractures' (Zoback & Anderson 1982). Fine, mostly randomly orientated and non-vertical cracks found in cores from the upper igneous crust may have been produced during rapid cooling of flows (Johnson 1980). Porosities near the top of the oceanic crust are high; Becker *et al.* (1983) found 12 per cent porosity in Deep Sea Drilling Project hole 504B while some porosity estimates based on seismic refraction measurements exceed 30 per cent (Whitmarsh 1978). Towards the base of seismic layer 2 the seismic velocities are similar to those expected from uncracked basalt at the appropriate pressures and temperatures (Whitmarsh 1978; Stephen, Louden & Matthews 1980; Spudich & Orcutt 1980; White 1984).

Thus, young upper oceanic crust possesses a tectonic fabric dominated by highly-elongated, often vertical or near-vertical voids (fissures and faults) whose widths are on the scale of centimetres to metres. Many of the voids parallel the spreading axis. Theory predicts that parallel vertical cracks in an otherwise isotropic matrix give rise to a body-wave azimuthal anisotropy. Garbin & Knopoff (1973, 1975) developed equations for weak concentrations of disc-shaped cracks in an isotropic medium. These equations are applicable to cases, such as the upper oceanic crust, where the extent of the cracked volume far exceeds the seismic wavelength and where the crack dimensions are much less than this wavelength. A medium with dry cracks exhibits quite large velocity anisotropy with a roughly 2θ dependence, where θ is the horizontal azimuth of the wave propagation direction, whereas saturated cracks give rise to smaller anisotropy with a roughly 4θ dependence (Crampin 1978). The anisotropy is also critically dependent on the crack density. Thus, a measurement of body-wave anisotropy in the oceanic crust not only places limits on the crack density but also indicates whether it is likely that there is a substantial proportion of unsaturated cracks.

Seismic experiments on land by Bamford & Nunn (1979) in the Carboniferous Limestone and by Park & Simmons (1982) in a variety of igneous rocks found *P*-wave anisotropies of a few tens of per cent due to aligned cracks. At sea Stephen (1981) inferred approximately 30 per cent *P*- and *S*-wave anisotropy in 109 Ma old upper crust from observations of the polarization of particle motion and of shear wave splitting.

Here we describe an experiment designed to study crack anisotropy in young upper oceanic crust at 45° N in the Atlantic Ocean.

2 Experimental design

The experiment was conducted in 1978 June during *RRS Discovery* Cruise 93 in an area centred about 28 km east of the median valley of the Mid-Atlantic Ridge at 45° 25′ N (Fig. 1, inset). The crust here is young (1.1–3.4 Ma old using the 11 mm yr^{-1} spreading rate of Loncarevic & Parker 1971) with minimal sediment cover. No clear bathymetric or magnetic discontinuities indicative of fracture zones cross our survey area. Although Loncarevic & Parker (1971) and Woodside (1972) tentatively proposed a minor transform fault at 45° 26′ N, a GLORIA mosaic (Fig. 2) shows north–south continuity of the ridges crossing the area, suggesting that the 5 km bathymetric offset previously interpreted as a transform is an artefact generated by inadequate navigational control of the older profiles. It is important that no fracture zones are present in our survey because they typically exhibit anomalous crust (e.g. Detrick & Purdy 1980; Detrick *et al.* 1982; Sinha & Louden 1983; White 1984; White *et al.* 1984). The bathymetry was recontoured on the basis of the GLORIA mosaic and all available soundings (Fig. 1) and was used subsequently in the analysis of the seismic data.

The receivers were three 3-component ocean-bottom seismographs (OBS) with hydrophones (Kirk, Langford & Whitmarsh 1982). Two 16 l (1000 in^3) airguns used as seismic sources were towed from either end of a 1 m beam and fired at 11 MPa (1600 psi) once every 2 min (approximately 250 m), giving a total of 406 shots. The shooting track (Fig. 3) gave even azimuthal coverage at ranges of 4–10 and 13–17 km, producing body-wave first arrivals from layer 2 and from the lower crust, respectively. An example of the hydrophone data is shown in Fig. 4. Clear compressional-wave first arrivals are often observed but weak later body-wave arrivals occur only intermittently.

3 Data reduction

3.1 SHOT AND RECEIVER POSITIONS

The horizontal range from each shot to each OBS was calculated from the direct water-wave

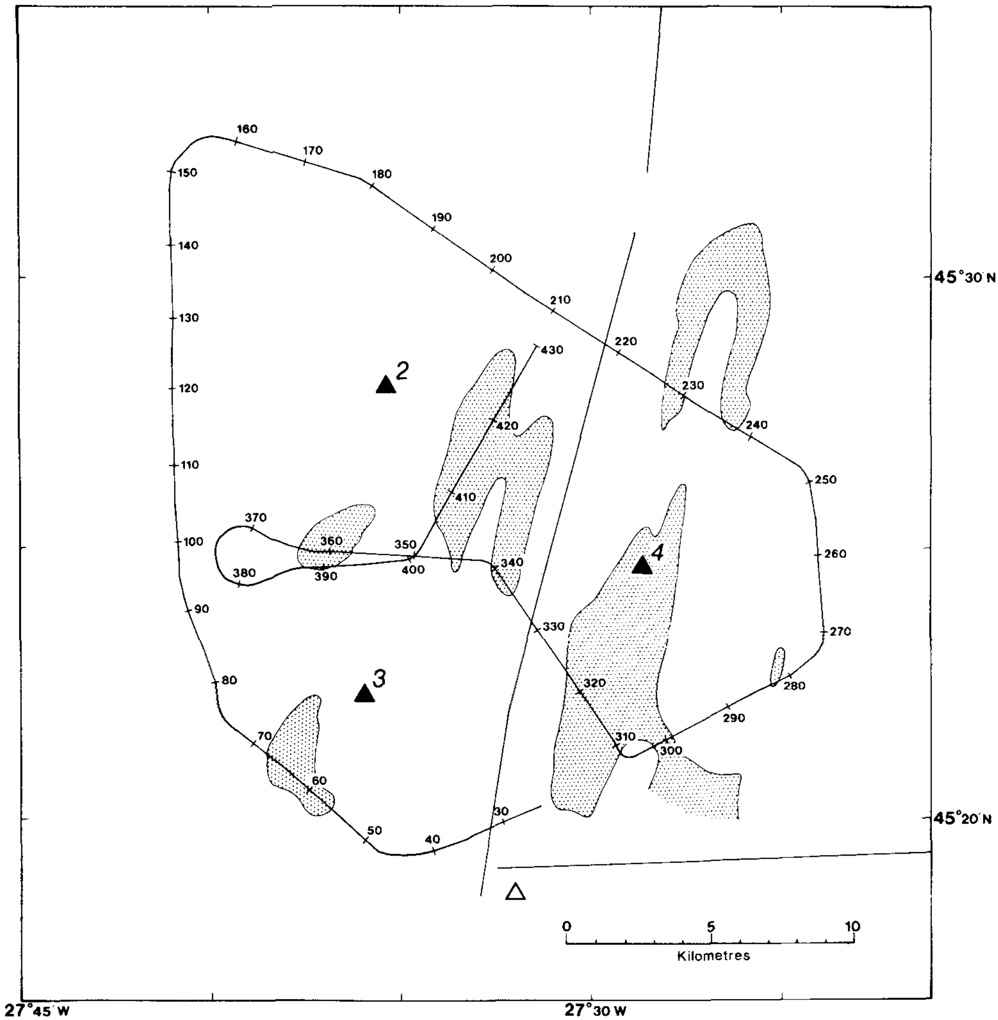

Figure 3. Track along which the airgun shots (numbered) were fired at 2 min intervals in the anisotropy experiment. Positions of the three OBS are shown by solid triangles. The N–S and E–W tracks represent other refraction profiles discussed in the text recorded by an OBS at the hollow triangle. Stipple indicates sediment ponds.

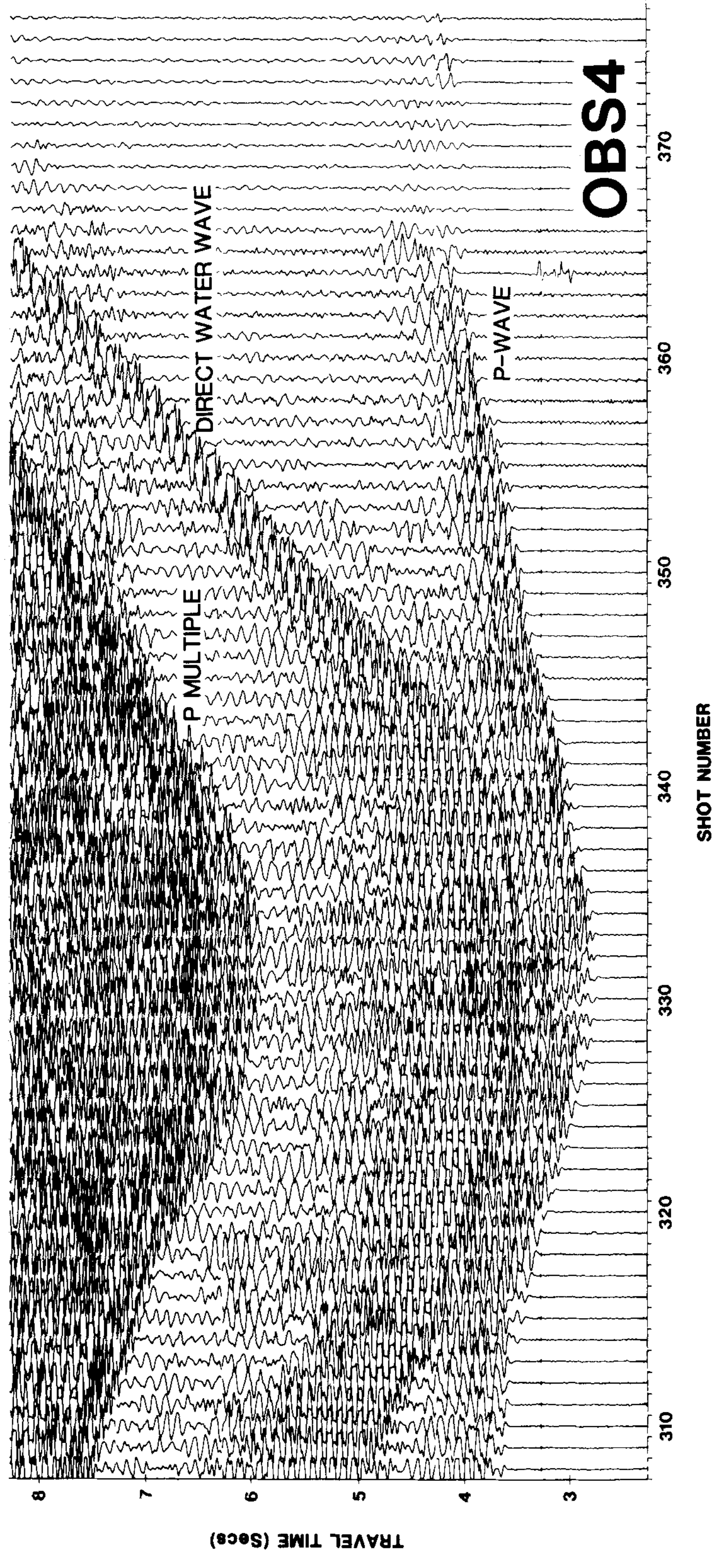

Figure 4. Example of hydrophone records from OBS 4 for shot numbers 308–376. High pass 2 Hz filter, shot-to-OBS azimuths 008°–098°, range 4.2–14.4 km.

by ray-tracing through a model of the velocity–depth structure in the water column [from station B23 (summer) of Fenner & Bucca 1971] until the theoretical and observed travel times matched to within ±0.005 s. Relative positions of the shots and OBSs were optimized using the distances between the OBS and the horizontal shot-to-OBS ranges. The OBS separations were estimated from the minimum sum or the maximum difference of shot-to-OBS ranges along tracks which cut across the line between each pair of OBS or its extrapolation, respectively. The absolute position of the OBS with the best satellite fix was taken as correct, as was the azimuth from this OBS to the second best located OBS, and the best position for each shot relative to the OBS array was then found from the centroid of the triangle (or 'cocked hat') formed by the intersection of the three shot-to-OBS range circles. Small systematic errors in the OBS positions of a few tens of metres became evident from a scrutiny of the cocked hats and were minimized during further iterations of the shot location procedure. Finally, a self-consistent set of absolute shot and OBS positions was obtained in which the rms discrepancy between the water wave ranges and the ranges from the adjusted shot positions was only 20 m, indicating the accuracy of the sound speed-depth model.

3.2 BODY-WAVE ARRIVALS

All four channels of the OBS analogue recordings (three orthogonal geophones plus hydrophone) were digitized at a 2.4 or 4 ms sampling rate and record sections (e.g. Fig. 4) were constructed. First arrival travel times were picked off the hydrophone records which were the least noisy; the consistent airgun source signature facilitated phase correlations across adjacent shots. Second arrivals, seen intermittently preceding the water-wave on some of the record sections, are interpreted as shear waves doubly converted from/to compressional waves at the water–basement interface. Their sporadic appearance is attributed to variations in velocity structure of the topmost basement beneath the shotpoints (White & Stephen 1980).

3.3 TOPOGRAPHIC CORRECTIONS

The water depth varies considerably across the survey area, from less than 1400 to almost 3000 m (Fig. 1). Variations in the water depth at the shot ray-entry points exert a much stronger influence on travel times than do any of the perturbations in crustal velocity structure which we are investigating, so it is important to make accurate corrections for them.

We have used a water delay type of correction which subtracts the water delay from the observed travel time but maintains the same shot–receiver range (e.g. Orcutt, Kennett & Dorman 1976; Detrick & Purdy 1980; White & Matthews 1980; White & Purdy 1983). This correction method assumes that: (1) the function $p(x)$, which describes the variation of ray parameter with range, is known; (2) the water velocity structure is known; and (3) the seabed is plane and horizontal in the vicinity of the ray entry point. The function $p(x)$ was found from a smooth cubic spline fitted to the first arrival times from all OBSs (Fig. 5). This was iteratively refined using improved estimates of the topographic correction and by applying 'static' corrections for delays under each of the OBSs caused mainly by different sediment thicknesses. All arrivals from shotpoints over sediment ponds (Fig. 3) were omitted so that all the data came from shots over exposed basement.

The greatest uncertainty in the topographic correction term is the water depth at the ray entry point. This arises for two separate reasons: firstly, the relief over this young crust is

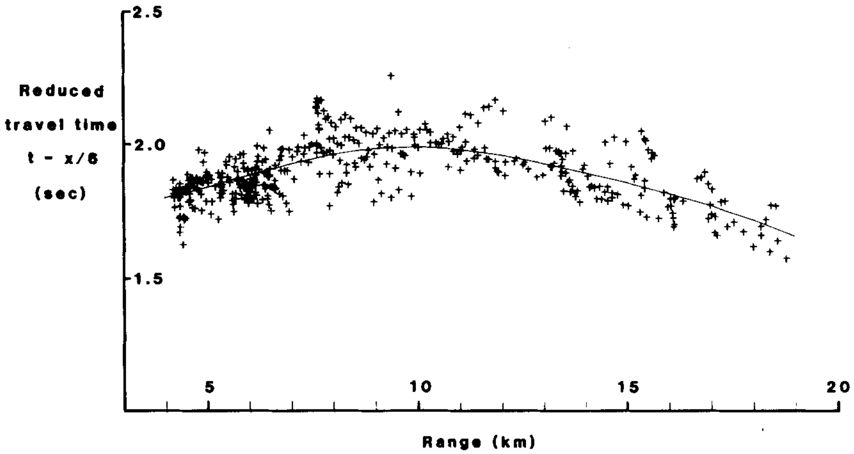

Figure 5. Travel times versus range of first arrivals with good signal to noise ratio from shots over low or moderately dipping seafloor. Times have been corrected for varying water depths at the ray entry points and for receiver delays. Heavy line shows spline fit used in calculating velocity–depth structure shown on Fig. 6.

rugged and generates numerous hyperbolic echoes on the broad beam 10 kHz ship's echo sounder causing ambiguity in the depth. Secondly, because the shooting tracks circled around the receivers (Fig. 3), most ray entry points lay about 0.6 km off the ship's track, so we have to estimate the depths.

Where the ray path lay along the shooting track (as for the radial shooting lines in Fig. 3) we calculated the offset along the ship's track using the $p(x)$ curve and read the ray-entry depth directly from the bathymetric profile. Where the ray entry point did not lie under the shooting track, we used the ship's echo sounder to find the depth beneath the shotpoint and the bathymetric chart (Fig. 1) to determine the local seafloor gradient in the shot-to-OBS direction. We then calculated the ray-entry depth from the shotpoint depth, the seafloor gradient and the offset calculated from the $p(x)$ curve.

3.4 UNCERTAINTIES AND ERRORS

Uncertainties arise through imprecision in the first arrival pick, the range and the topographic correction. We kept a record of the estimated uncertainty of each of these factors for each arrival pick and were thus able to choose different subsets of the data for analysis which lay within specified uncertainty limits. In general, where the seafloor is flat, and we can therefore calculate the topographic correction accurately, we also find that the arrivals are impulsive and can be picked with little uncertainty. However, where the seafloor near the shotpoint is rugged, making the water depth and hence the topographic correction uncertain, we usually find that the arrival is emergent and difficult to pick, presumably because the rugged topography causes defocusing and multi-pathing. We tried many different subsets of the data in our analysis but found similar results from all of them.

Typical values of the uncertainties and errors are as follows. The first arrival has a dominant frequency of about 8 Hz (i.e. a period of 0.13 s). Impulsive arrivals can be picked to within ± 0.02 s, emergent arrivals to within ± 0.07 s. Shot instants are accurately known because the airgun was triggered electrically. We used the range calculated from the water wave arrival which is accurate to within ± 20 m. The single most important cause of uncertainty is the ray-entry point depth. If the water depth is wrong by 100 m, the topographic correction will be wrong by 0.06 s. Uncertainties in the water depths are typically ±2.5 m, increasing to perhaps +100 m in the areas of most rugged relief. Errors in the $p(x)$ curve are of much less importance; if the apparent velocity at any range is incorrect by as much as 1 km s^{-1}, only 0.015–0.030 s error is introduced. If the seafloor at the ray-entry point is dipping, rather than horizontal as assumed in calculating the topographic correction term, errors of typically 0.005, 0.020 and 0.040 s will be introduced by dips of 5°, 10° and 15° respectively. The average seafloor slope without regard to sign is 6° ± 5° but, since the number of up-dip slopes is roughly the same as the number of down-dip slopes, the overall effect is simply to increase the spread of the travel times with as many being early as late.

4 Crustal velocity structure

The mean *P*-wave velocity–depth structure was found from the topographically corrected travel time–range data. From the shooting tracks running radially from each OBS over ranges of 4–14 km (Fig. 3) we calculate velocities in layer 2 of 5.5 to 5.8 km s^{-1} by least squares linear regression (Fig. 6). The remaining, roughly circular parts of the track yielded 900 shot-receiver travel times spanning ranges of 4–20 km. Weighted linear regression on the arrivals into each OBS gives the 'staircases' of homogeneous velocity layers shown in Fig. 6. However, the upper crustal velocity structure is represented better by velocity gradients than by uniform layers, so we next inverted the spline fitted to the corrected data (Fig. 5) to give the smooth velocity–depth curve shown by the heavy line on Fig. 6.

An independent determination of the velocity–depth distribution within the survey area was made from two OBS seismic refraction profiles, one parallel and one perpendicular to the structural strike (Fig. 3). Sources were 16 l airgun shots from 0 to 25 km range and explosive charges from 25 to 50 km range. Sediment thicknesses were found from concurrent seismic reflection profiles. Arrival times were modelled by ray-tracing (McMechan & Mooney 1980), assuming that crustal isovelocity layers parallel the basement and that the Moho is flat. The velocity–depth profile (dashed line, Fig. 6) satisfactorily fits data from both refraction lines and is in agreement with the structure determined from inversion of the spline fitted to the arrivals in the anisotropy experiment.

The overall picture of the velocity structure is of low velocities at the top of the basement (about 3.7 km s^{-1}) increasing with a gradient of 1.0–1.2 s^{-1} through the topmost 2.5 km. This is typical of layer 2 in very young crust, reflecting the downwards decrease in crack density. In the lower crust the velocity gradient is much lower (about 0.2 s^{-1}), again typical of results from elsewhere, although layer 3 here is rather thinner (*c.* 1.5 km) than is normal. The amplitudes of the arrivals yielded no useful additional information on the velocity structure because, at the relatively short ranges of most of the data, fine details of the amplitude variations are controlled more strongly by the seafloor topography than by the velocity structure (White & Purdy 1983).

5 Inversion of travel-time residuals

5.1 METHOD

Scatter of the topographically corrected travel times about the spline fit (Fig. 5) exceeds the estimated uncertainties in the data, indicating that the velocity–depth structure is not invariant across the survey area. The most likely causes of the scatter that we have considered are:

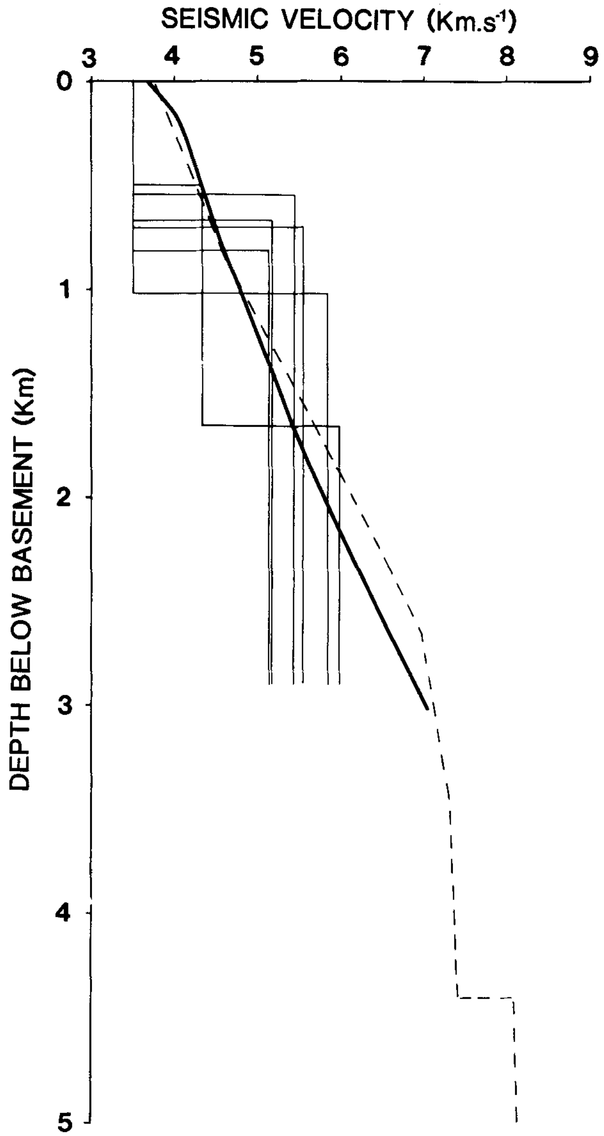

Figure 6. Velocity versus depth functions calculated from water-path corrected range–travel-time data. Stepped solid lines are from plane-layer least-squares fits to arrivals at individual OBS, from online (radial) and from offline (circular) shooting tracks. Heavy line is calculated by inversion from the spline fit to the water-path and receiver delay corrected data from all three OBS combined (Fig. 5). Broken line is best fit to separate refraction lines across the survey area modelled by ray-tracing to match the arrival times. Note the low velocities at the top of the basement (approximately 3.7 km s^{-1}) and the steep velocity gradient (approximately 1.0 s^{-1}) in the upper crust.

(a) Lateral variability in the velocity structure.

(b) Systematic travel-time variations correlated with the relief of the top of the basement beneath the shot-points, reflecting the degree to which isovelocity surfaces at depth parallel the top of the basement.

(c) Horizontal velocity anisotropy in layer 2.

The shots and receivers were not sufficiently well distributed to allow a stable inversion of the travel times for lateral variability across the survey area. As discussed in Section 5.2, there is evidence that lateral inhomogeneity is restricted in magnitude within this area. This is in agreement with results from detailed refraction surveys elsewhere in the North Atlantic (Purdy 1983; White & Purdy 1983) which indicate that lateral travel-time variations are small over regions tens of kilometres in extent away from the anomalous crust formed at fracture zones.

The dataset is, however, well distributed for investigating systematic variations in travel times associated with the basement relief because the seafloor varies greatly in depth, and for studying azimuthal anisotropy, because the shooting tracks approximate to a circle about each OBS. We assume that any travel-time perturbations caused by the basement relief will (within a certain range interval) be directly proportional to the deviation, at the ray entry point, of this relief from the mean seafloor depth. The constant of proportionality is called the *dt/dh* coefficient. We also assume that velocity perturbations due to horizontal velocity anisotropy are small and can be described by a sum of $\sin 2\theta$, $\cos 2\theta$, $\sin 4\theta$ and $\cos 4\theta$ terms (Backus 1965). Therefore, we carried out a multiple regression analysis with the seafloor ray-entry depth and shot-to-receiver azimuth as independent variables. The dependent variable was chosen to be not travel time but the travel-time residual (Δt) from the smooth spline fitted to all the data in Fig. 5. This approach overcame the complication of including a range-dependent apparent velocity in the analysis. The travel time in the presence of anisotropy can be written (Raitt *et al.* 1969),

$$T_{AB} \simeq \frac{X}{G} + \frac{(2F-X)}{G^2}(A\sin 2\theta + B\cos 2\theta + C\sin 4\theta + D\cos 4\theta) + \tau_A + \tau_B \tag{1}$$

where X is range,
G is the mean refractor velocity,
F is the ray offset between the sources or receiver and the refractor,
θ is azimuth,
$\tau_{A,B}$ are time-terms.

If subscripts A and B refer to the shots and OBS respectively, we assume

$$\tau_A + \tau_B = \tau_{0A} + \tau_{0B} + \frac{dt}{dh}(h_A + h_B - 2\bar{h})$$

where τ_{0A} = constant.

h_A, h_B, $\bar{h}$ are the depths at the ray-entry point, at the OBS, and the along-profile mean, respectively and τ_{0B} = constant for a given OBS.

Thus, the travel-time residual Δt is given by

$$\Delta t \simeq \frac{(2F-X)}{G^2}(A\sin 2\theta + B\cos 2\theta + C\sin 4\theta + D\cos 4\theta) + \frac{dt}{dh}(h_A + h_B - 2\bar{h}). \tag{2}$$

The values of F and G are strictly not constant in the case of rays passing through a region of strong velocity gradients such as the upper crust. This may cause some error in the estimated *dt/dh* values. However, the azimuths of velocity maxima and minima, around which our arguments centre, depend only on the ratios of coefficients A, B and C, D. The regression coefficients in equation (2) were determined by inverting an overdetermined matrix (Lawson & Hanson 1974). A mean value of 5 km s^{-1} was used for G. Lateral inhomogeneity was assumed to be small and to simply add noise to the data. A series of solutions with differing numbers of independent variables was made, testing at each stage to ensure that the addition of extra terms significantly improved the fit of the data.

From the complete dataset we were able to choose different subsets for inversion to test the stability of the result. Here we show results divided into two range bands: 4–10 and 10–20 km. Arrivals from 4–10 km are from the upper 2.5 km of layer 2 and are generally the most numerous and accurate since the signal-to-noise ratio is better at short ranges. The arrivals from 10–20 km range are from the lower crust.

5.2 LATERAL VARIABILITY OF VELOCITY STRUCTURE

There are two main ways of estimating the magnitude of travel-time variations due to lateral variability in the velocity structure of the upper crust. Firstly, the relative delays due to local structure beneath the three OBSs can be estimated from the differences in arrival time at two or more OBSs from the same shotpoint after allowing for the different range to each OBS. This method has the advantage of being independent of between-shotpoint inhomogeneities but it does not exclude the effects of any anisotropy. Relative delays beneath OBS 2, OBS 3 and OBS 4 of −0.07, 0.06 and 0.01 s (Table 1) were found by this method. Although we did not obtain a seismic reflection profile directly across the site of OBS 3 there is a strong suggestion from nearby profiles that the OBS lay over a small sediment pond up to 140 m thick which could account for the later arrivals it recorded. When the effect of the pond is subtracted, the residual variation in delay times attributable to inhomogeneity in the igneous basement beneath the receivers has a maximum range of less than 0.1 s.

A second way of estimating the magnitude of travel-time variations due to lateral variability is from the scatter of arrivals at individual OBSs from groups of adjacent shots having similar ranges, azimuths and seafloor ray-entry depths. Again, variations of the order of ±0.05 s are observed for shots spread over lateral distances of 3–4 km.

5.3 CORRELATIONS OF TRAVEL TIMES WITH SEAFLOOR DEPTHS (dt/dh)

The regression coefficient, dt/dh, which indicates how much travel-time variations depend on the relief of the seafloor (which here, in the absence of sediments, means the top of layer 2), gives information about the shape of crustal isovelocity surfaces.

If the wavelength of the topography is large compared to the offset of the seismic ray as it travels from the ray entry point to the crustal refractor at depth, then it is easy to predict dt/dh; if the isovelocity surfaces are conformable with the seafloor then the rays everywhere travel through the same crustal thickness and so dt/dh will be zero; if the sub-bottom interfaces are flat then the thickness over the refractor is least where the seafloor is deepest and so dt/dh will be negative with its magnitude dependent on the crustal velocities. Unfortunately, in practice, the typical wavelength of the topographic relief, particularly for young crust formed at a slow-spreading ridge, is not dissimilar to the crustal ray offsets, and so this simple interpretation breaks down. It is necessary to ray-trace through a model structure with the same seafloor relief and velocity–depth distribution in order to calculate the effect of short-wavelength topography on dt/dh (White & Purdy 1983). Where the sub-bottom layers are flat they give approximately the same value of dt/dh whatever the topographic wavelength, and this is the maximum value we can expect. Where the sub-bottom isovelocity surfaces mimic the seafloor relief the dt/dh ratio changes from zero to progressively more negative as the wavelength of the topographic variations decreases.

We find a negative dt/dh from our survey data of about half the magnitude predicted for flat sub-bottom layers. Arrivals from the upper crust (4–10 km), yield dt/dh values between −0.10 and $-0.14\ \mathrm{km\ s^{-1}}$, with a mean of $-0.10\ \mathrm{km\ s^{-1}}$ (Fig. 7 and Table 1). This is less

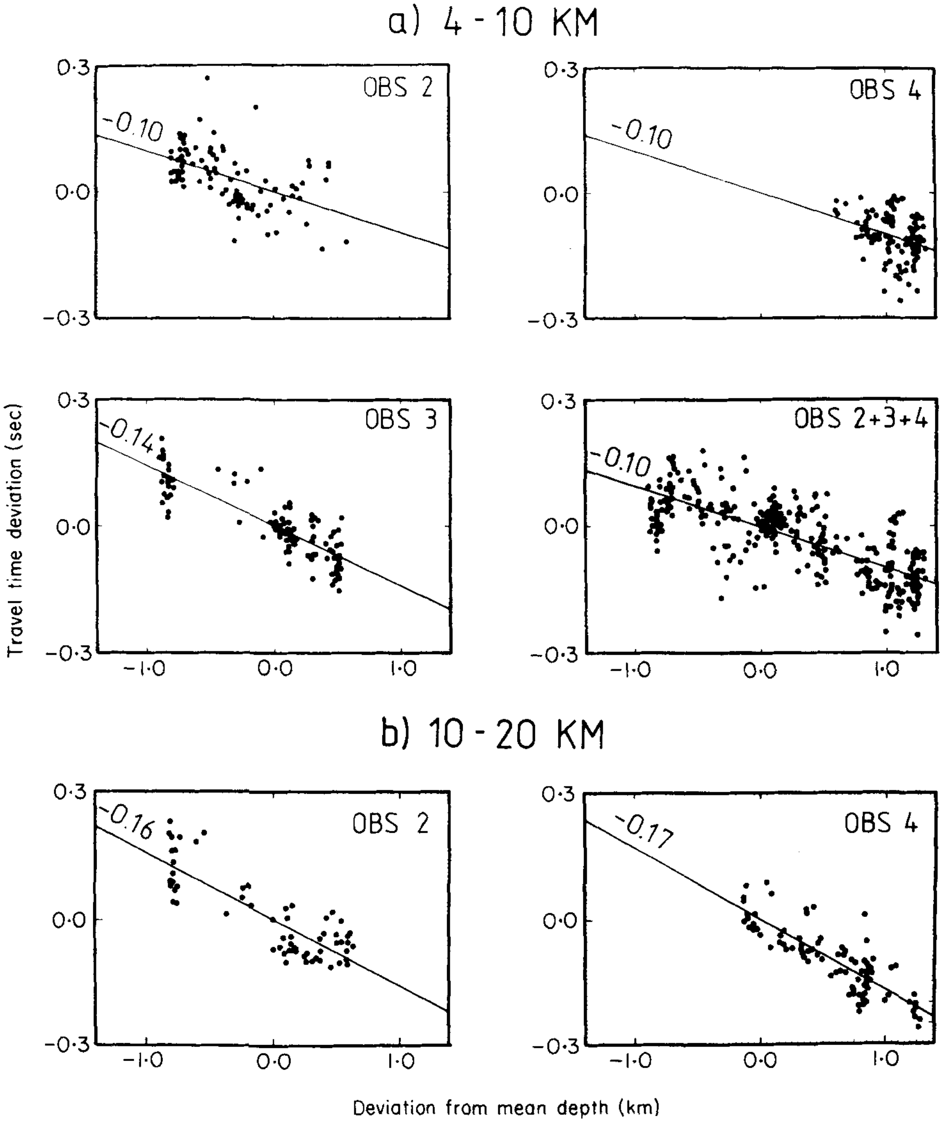

Figure 7. Plots of travel-time residual versus deviation of seafloor depth at the ray entry point from the mean depth of 2.25 km, using data with good signal to noise ratio from shotpoints over regions of low to medium seafloor dips. Arrivals from (a) upper crust at ranges of 4–10 km, (b) lower crust at ranges of 10–20 km. Times have been corrected for varying water depths at the ray entry points, for receiver delay and for upper crustal velocity anisotropy shown by solid lines in Figs 8 and 9. The gradient of the best fitting straight line is annotated on each graph.

than for horizontal isovelocity surfaces in layer 2 but is rather greater than for isovelocity surfaces in layer 2 conformable to the seafloor. Although the resolution is not very good, this suggests that the topography of isovelocity surfaces within layer 2 decreases with increasing depth, but still reflects a subdued version of the seafloor relief.

Arrivals from the lower crust (10–20 km) exhibit dt/dh values of -0.16 to $-0.17\,\mathrm{km\,s^{-1}}$ (Fig. 7 and Table 1). The higher dt/dh magnitudes than those found from the upper crust result from the smaller ray parameter (p) of the lower crustal returns. However, the higher

Table 1. Values of regression coefficients fitted to travel-time residuals for curves illustrated in Figs 7 and 8.

Data range (km)	OBS	No. of points	OBS delay time (s)	dt/dh (s km^{-1})	Anisotropic velocity deviations Azimuths of minima* (degrees)		Peak deviations (km s^{-1})		Standard error of estimate (s)
					2θ terms	4θ terms	2θ terms	4θ terms	
4–10	2	91	−0.07	−0.10	079	015, 105	0.24	0.13	0.062
	3	108	0.06	−0.14	026	−008, 082	0.26	0.23	0.042
	4	100	0.01	−0.10	103	0.19, 109	0.04	0.10	0.052
	2+3 +4	299		−0.10	063	007, 097	0.11	0.11	0.061
10–20	2	62	−0.08	−0.16	099	007, 097	0.10	0.07	0.055
	4	86	0.10	−0.17	027	010, 100	0.22	0.14	0.045
	2+4	148		−0.14	055	015, 105	0.10	0.08	0.053

* Azimuths are only listed for their occurrence in the range 000° – 180°, measured from north.

velocities in the lower crust mean that similar sized thickness changes produce smaller travel-time perturbations than in the upper crust, thus reducing still further our resolution of the relief of isovelocity surfaces in the lower crust. The observed dt/dh values are consistent with models of the lower crust in which the isovelocity surfaces follow a subdued copy of the basement relief, or in which they become flat towards the base of the crust.

5.4 AZIMUTHAL VARIATIONS IN VELOCITY

The anisotropic velocity curves fitted to arrivals from the upper and lower crust are shown in Fig. 8 and their coefficients are listed in Table 1. In Fig. 8 arrivals with shot-to-receiver azimuths in the range 180–360° have been added to those from 0° to 180°, since the 2θ and 4θ curves repeat over these intervals. Velocity deviations of up to ±0.4 km s^{-1} are apparent. In all cases where 2θ and 4θ terms were included they were statistically very significant (greater than 99 per cent level using Snedecor's F-test). The 4θ terms almost always had a greater significance than the 2θ terms. Furthermore, the coefficients of the 2θ and 4θ curves fitted separately were little different from those illustrated here from a combined fit of 2θ and 4θ terms simultaneously.

The major uncertainty in interpreting these apparent velocity variations as due to horizontal velocity anisotropy in the crust is that systematic lateral inhomogeneity potentially could produce similar effects if its distribution happened to cause appropriate travel-time perturbations. Indeed, we believe that crustal inhomogeneity causes travel-time deviations of the order of ±0.05 s within the survey area but we assume that it is distributed randomly so that it will simply contribute random scatter to the travel-time inversions. The best evidence that the apparent anisotropy is not due to lateral inhomogeneity is the consistency of the velocity deviations when data from different receivers and from different range bands are used in the inversion (Fig. 8 and also Fig. 11 where the curves are superimposed).

The curves derived from the 4θ terms display remarkable consistency between different data sets, both in their amplitude and phase (e.g. Fig. 11b). Apart from the upper crustal arrivals at OBS 3, which appear to be perturbed by lateral inhomogeneity for some of the short-range shots, the 4θ curves exhibit peak velocity deviations of ±0.07 to ±0.14 km s^{-1} and velocity minima over the narrow range of azimuths between 007° and 019° (Table 1).

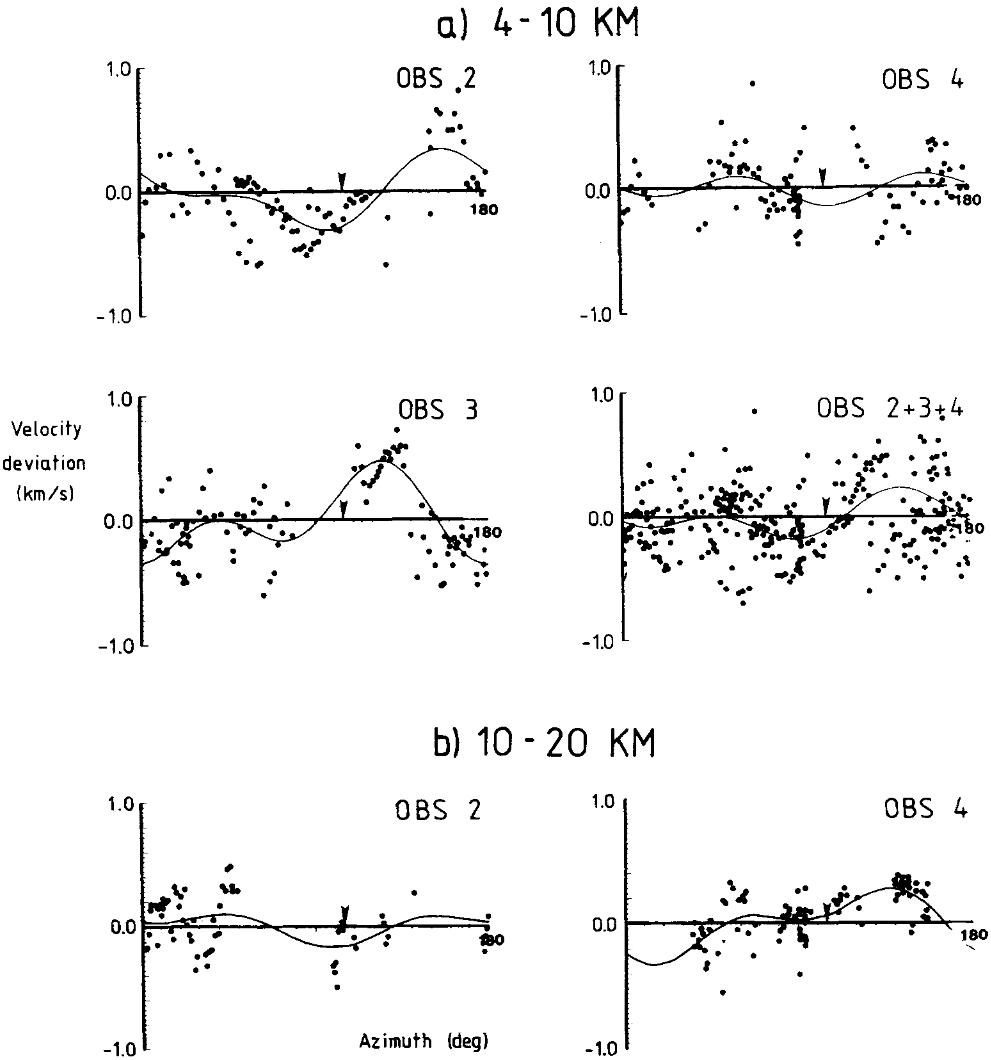

Figure 8. Velocity deviation versus shot-to-receiver azimuth for arrivals returned from (a) the upper crust (ranges 4–10 km), and (b) the lower crust (ranges 10–20 km). Solid lines shows best fitting velocity anisotropy curve defined by the 2θ and 4θ terms listed in Table 1. Data from azimuths (measured clockwise from north) greater than 180° has been combined with that from 0° to 180°. Times have been corrected for varying water depths at the ray entry points, for receiver delays and for the dt/dh correlation shown by solid lines in Fig. 7. Arrowhead shows the ridge spreading direction.

Curves derived from the 2θ terms are less consistent (Fig. 11a) with amplitudes varying from ± 0.04 to ± 0.26 km s^{-1} and minima at azimuths between 026° and 103° (Table 1). In the last section of this paper we discuss the interpretation of this observed velocity anisotropy in terms of orientated sets of cracks in the oceanic crust.

6 Particle motion evidence for anisotropy

In an anisotropic medium the particle motion of compressional waves is not generally in the ray (source-to-receiver) direction but deviates from it systematically with the source-to-receiver azimuth. The ocean crust may be considered *a priori* as a transversely isotropic medium in which the symmetry axis is horizontal and normal to a single set of vertical parallel cracks in an isotropic medium. In this case the crust possesses hexagonal symmetry and the horizontal plane is a plane of symmetry. Crampin, Stephen & McGonigle (1982) have calculated polarization direction deviations for several saturated-crack models applicable to the above situation. The maximum deviation of polarization direction is small (less than 10°). Systematic particle motion deviations, consistent with a system of vertical cracks, were found from the two horizontal geophones in OBS 3 and OBS 4 (OBS 2 failed to record data from two of its geophones).

The seafloor orientation of the geophones of OBS 3 was found from the polarization of the direct water wave arrival. The mean azimuth $\bar{\theta}$ in the XY-plane of the first 0.2 s of the water wave particle motion was determined from the individual sample-to-sample vectors,

$$\bar{\theta} = \frac{\Sigma \theta_i \cdot L_i}{\sum_{i=1}^{n} L_i} \tag{3}$$

where $0^\circ < \theta_i < 180^\circ$

$$L_i^2 = (X_{i+1} - X_i)^2 + (Y_{i+1} - Y_i)^2.$$

X_i, Y_i represent the ith samples from the X and Y geophones respectively. The 180° ambiguity inherent in θ was resolved from the direction of first motion of the water-wave arrival. Unfortunately, the azimuth of the OBS 4 geophones could not be determined by this method because at short ranges the water-wave had been clipped during the recording process while, at longer ranges, it could not be distinguished from body wave arrivals because the sediment pond on which this receiver sat caused very 'ringy' multiple reflected and converted arrivals.

The calculated azimuths of the OBS 3 geophones were found to differ by almost 10° when water-wave arrivals from two orthogonal directions were used. This is probably caused by a difference in the amplifier gains, coupling or sensitivity of the two horizontal geophone channels. Random component variations cause an estimated standard error of ± 0.17 in the unity ratio of the amplifier gains of the horizontal channels; geophone sensitivities can vary by up to ± 10 per cent; coupling differences are unknown. If the Y-geophone amplitudes are increased by 20 per cent then there is no difference in calculated azimuths and the standard deviation of all the determinations of geophone orientation is reduced to 2.3°.

Once the orientation of the geophones had been determined, the horizontal particle motion was plotted for the first 0.2 s of the P-wave arrival with respect to the radial and transverse directions (Fig. 9). Consistent linear particle motions were found from the first 1–1.5 cycles of the arrival but, in some arrivals, interference of reflected or other refracted phases caused marked changes in particle motions beyond this. On those particle motion plots with sufficient signal amplitude the principal direction of motion was determined visually and its deviation from the radial direction was measured, yielding 90 points from OBS 3.

The particle motion deviations as a function of shot-to-OBS azimuth (Fig. 10a) give a strong ($\sin\theta$, $\cos\theta$) dependence, which is unexpected because anisotropy due to cracks should contain dominantly 2θ and 4θ terms. Only systematic deviation errors would be produced by instrumental effects such as tape-head skew, phase-differences between geophone amplifiers and filters, between-channel time delays during digitizing or errors in determining the geophone orientation. Non-orthogonality of the geophones gives only 2θ errors unlikely to exceed 5°. The previously mentioned uncertainty in the ratio of the X

or Y channel gains could cause a 2θ, but not a θ, variation of azimuth less than $\pm 5.5°$ in almost every case. Possible explanations of the strong ($\sin\theta$, $\cos\theta$) variation of Fig. 10(a) are tilt of the geophones (Tréhu 1984) or dip of isovelocity surfaces in the immediate region beneath OBS 3. The horizontal geophones produce distorted signals when tilted more than about 3°. In the absence of sediment or dip under the OBS the angle of incidence will always exceed 30° (for ray-parameter $p = 0.135\,\mathrm{s\,km^{-1}}$). Nevertheless, a 5° tilt can cause azimuthal errors as large as $\pm 8.6°$, sufficient to explain about half of the $\pm 17°$ ($\sin\theta$, $\cos\theta$) variation in Fig. 10(a). However, this variation can also be explained by a $5.0\,\mathrm{km\,s^{-1}}$ refractor dipping at 18° in a direction 320° locally beneath OBS 3. Probably

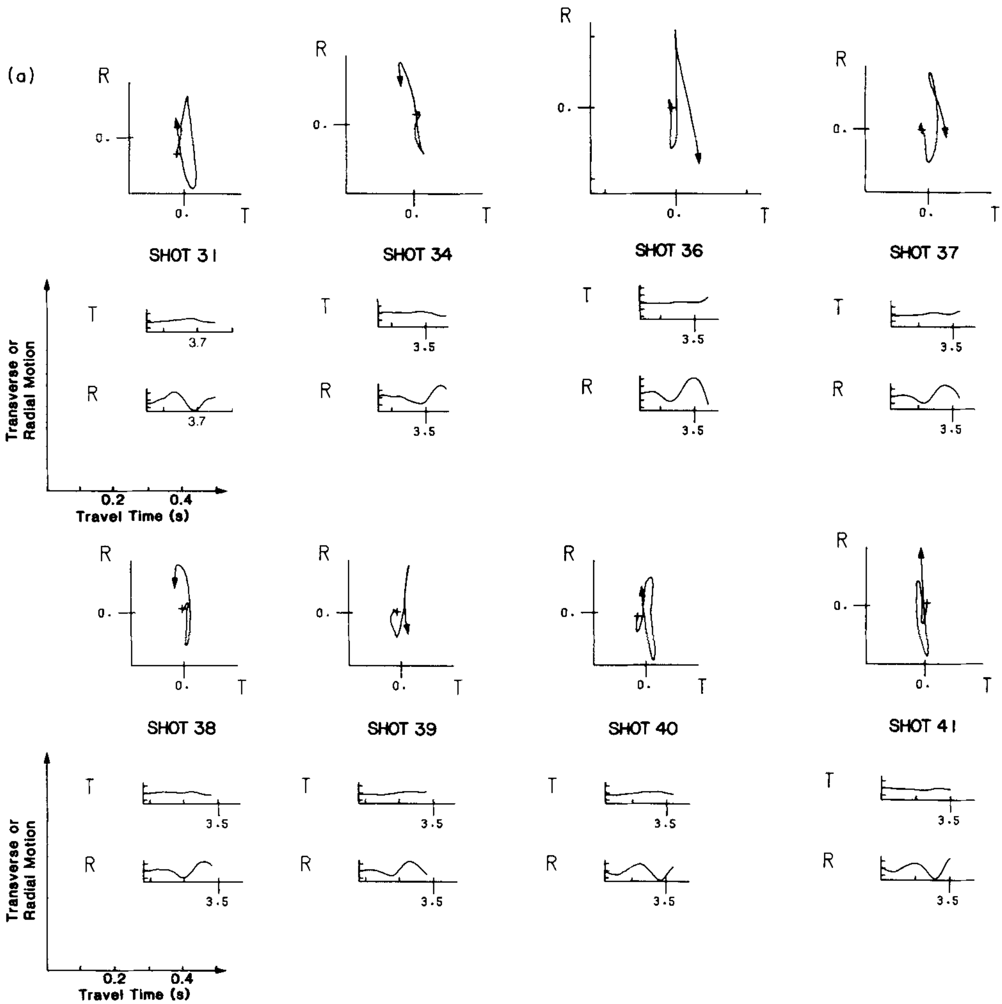

Figure 9. (a) Examples of particle motion (beginning at the +) in the horizontal plane for the first 0.2 s of the compressional wave arrival from shots 31, 34 and 36 to 41 recorded by OBS 3. The data have been passed through a 5–20 Hz digital bandpass filter. R = radial component, T = transverse component. Amplitude scales in arbitrary units; ticks every 0.1 s along the time axis. (b) Particle motion plots in the SV/T plane normal to the upcoming ray under OBS 3 for shots 109 (range 9.8 km, azimuth 138°) 110 (10.1 km, 139°), 111 (10.3 km, 140°), and 112 (10.5 km, 141°). The T-axis represents horizontal transverse motion. The SV and T components are plotted separately under each particle motion plot and the arrows are estimates of the qSV and qSH arrivals.

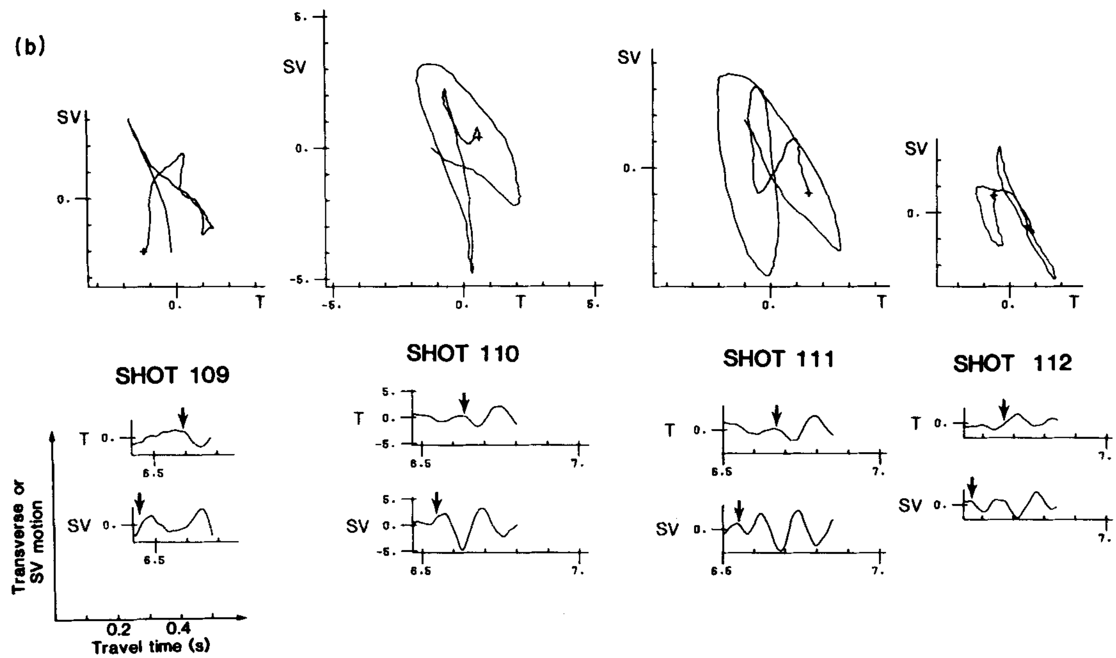

Figure 9 – *continued*

the strong θ variation results from a combination of geophone tilt and local structure. It is interesting that both factors are more significant for OBSs laid on sediment, due to the smaller angle of incidence, than on bare rock.

Multivariate analysis was used to search for statistically significant 2θ or 4θ dependence of the particle motion deviations on azimuth (summarized in Table 2), with the Y-geophone amplitudes increased by 20 per cent in accord with our analysis of the direct water-wave arrivals. The addition of both 2θ and 4θ terms decreased the variance very significantly (greater than 99 per cent using Snedecor's F-test). The 4θ terms, if indicative of anisotropy, indicate axes of symmetry at azimuths of 059° and 149°, directions mid-way between the Mid-Atlantic Ridge axis trend and the spreading direction. The amplitude of the 4θ particle motion deviations is ± 6° (Table 2). The phase of the 2θ function depends on the accuracy of the Y-amplitude correction. Its amplitude is about ± 3°.

Because the orientation of the OBS 4 horizontal geophones could not be determined, particle motions in the horizontal plane had to be measured with respect to an arbitrary fixed direction (due north) rather than the radial direction. Unfortunately, OBS 4 received weak arrivals from the east so our azimuthal coverage is poorer than for OBS 3. Nevertheless, the analysis of 69 arrivals indicates marked azimuthally dependent particle motion deviations (Fig. 10b; Table 2). Allowing for the location of OBS 4 on a sediment pond, the ($\sin\theta$, $\cos\theta$) terms can be explained by isovelocity surfaces dipping at about 15° in a direction 350° or, in part, by 5° tilt of the geophones which would produce an azimuth-dependent error of up to ± 21.5° for arrivals with ray-parameter 0.135 s km^{-1}. The addition of both 2θ and 4θ terms decreased the variance very significantly, as much as for PUBS 3. The 4θ deviations if indicative of anisotropy, indicate axes of symmetry at 064° and 154°, within 5° of those deduced from OBS 3, with peak deviations of ± 8°. The 2θ terms of OBS 3 and OBS 4 are in poor agreement but, since they may be strongly affected by instrumental

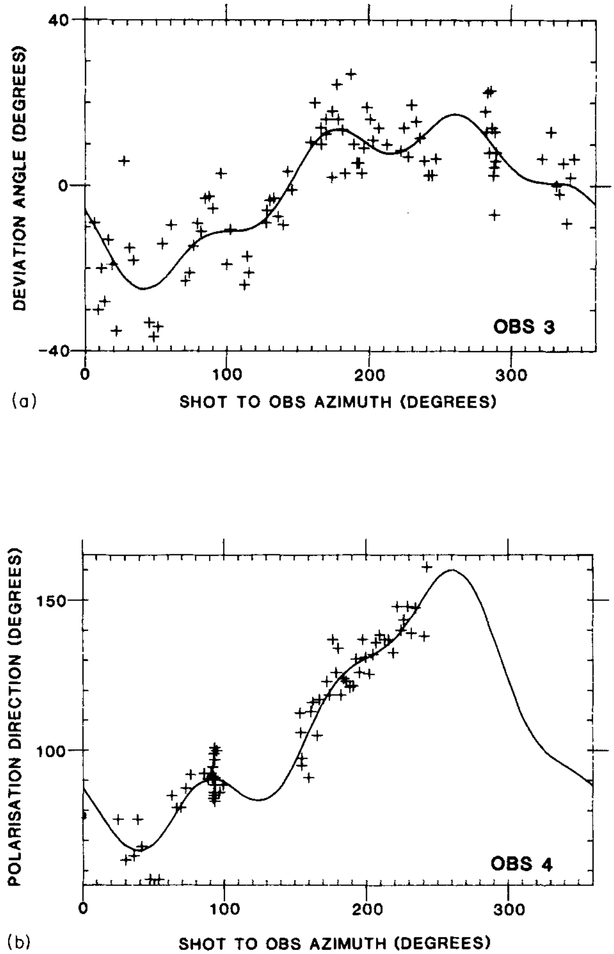

Figure 10. (a) Plot of particle motion deviations for 90 first arrivals at OBS 3, plotted against shot-to-OBS azimuth. The curve fitted by least squares corresponds to solution 3 in Table 2. (b) Plot of particle motion deviations with respect to due north for 69 first arrivals at OBS 4 against shot-to-OBS azimuth. The curve fitted by least squares corresponds to solution 6 in Table 2.

effects such as the different gains of the horizontal channels, we cannot in any case place great reliance on them. One of the distinctive characteristics of an anisotropic medium is shear-wave splitting, with the vertical and horizontal quasi-shear waves travelling at different group velocities. Our data yielded only a few shear wave arrivals which could be used to study this effect, partly because, as discussed earlier, conversion to shear waves was only sporadic, and partly because the very large and long-lasting direct water wave obscures shear wave arrivals at ranges up to 8–10 km (Fig. 4). The best shear-wave arrivals were all received at OBS 3 at shot-to-OBS azimuths of about 140° (Fig. 9b). Initial vertical shear motion is followed 0.08–0.14 s later by transverse shear motion, indicating that the velocity of the SV component is up to 0.06 km s^{-1} faster than the velocity of the SH component. This is consistent with the shear-wave splitting that would be caused by vertical, parallel sets of cracks with normals at 059° and 149° as suggested by compressional-wave particle motion deviations (Table 2; also see fig. 4a of Crampin 1978).

Table 2. Amplitudes and phases of regression functions, fitted to plots of deviation angle against shot-to-OBS azimuth, which may represent azimuthal anisotropy.

Solution	OBS	Azimuths of zero crossings* (degrees)		Peak deviation values† (degrees)		Standard error of estimate (degrees)
		2θ terms	4θ terms	2θ terms	4θ terms	
1‡	3	041.4 (±10.5)	–	±3.9 (±1.4)	–	9.3
2‡	3	–	058.7, 148.7 (±3.1)	–	±6.4 (±1.4)	8.9
3‡	3	047.0 (±11.9)	058.7, 148.7 (±3.2)	±3.1 (±1.3)	±6.0 (±1.4)	8.6
4	4	125.4 (±9.3)	–	±11.1 (±2.0)	–	7.4
5	4	–	063.7, 153.7 (±2.4)	–	±11.1 (±2.5)	8.7
6	4	123.3 (±10.1)	064.0, 154.0 (±2.9)	±10.1 (±2.1)	±8.1 (±2.0)	6.7
7‡	3 + 4	170.9 (±32.5)	059.3, 149.3 (±3.7)	±3.0 (±1.4)	±5.0 (±1.3)	10.4

* Azimuths are given only for those zero crossings where the sign of the slope of the 2θ or 4θ function indicates a possible symmetry axis direction according to Crampin *et al.* (1982). Values in brackets are standard errors.
† All solutions included ($\sin\theta$, $\cos\theta$) terms not shown here. Values in brackets are standard errors.
‡ Solutions for which the Y-geophone samples of OBS 3 were increased by 20 per cent.

7 Discussion

7.1 LATERAL AND VERTICAL VARIATIONS IN SEISMIC STRUCTURE

The random lateral variability across the survey area is relatively small, generating deviations from the mean travel times of up to ±0.05 s. In order to generate detectable variations in travel times the inhomogeneities in the crust must be several wavelengths in extent; the variations we observe from shot to shot are on a horizontal scale of typically 3–4 km (about five wavelengths). Undoubtedly, there are other smaller-scale inhomogeneities caused by local tectonic and petrologic variations that we cannot resolve.

We cannot say whether variations in travel time are due to lateral velocity or thickness changes, and probably both effects occur. However, the magnitude of these variations is consistent with, for example, 0.5 km of extra relief in the volcanic layer, such as might be 'frozen' into the crust at an axial volcano, or with the variations in velocity caused by serpentinite bodies intruded into the crust, or with the alteration of upper crustal velocities by the effects of large-scale hydrothermal circulation. These variations are minor compared to the regions of grossly abnormal crust which characterize fracture zones. Also, it is only because the travel-time perturbations caused by lateral inhomogeneities are so small that we are able to recognize in our data the equally small systematic deviations caused by horizontal anisotropy in the crust, discussed in Section 7.3.

We find negative dt/dh values consistent with a model of the crust in which the relief of the isovelocity surfaces decreases with increasing depth below the seabed. The seabed relief is governed primarily by growth faulting occurring within, and on the walls of, the median valley. The relief of the upper crustal isovelocity surfaces probably mimics the seabed topography because the upper crust is faulted into coherent blocks within the median valley and because the decrease of pore space with increasing pressure at depth is the major control on the shallow crustal velocities. However, deeper crustal material may lie beneath the sole zone of the spreading-centre listric faults and so may not suffer the same degree of vertical fault movement as the shallow layer 2 material. Furthermore, the deeper isotherms are probably smoother than the surface expression of the median valley and will, therefore, impose a smoother shape on the isovelocity surfaces resulting from metamorphic reactions in the deep crust.

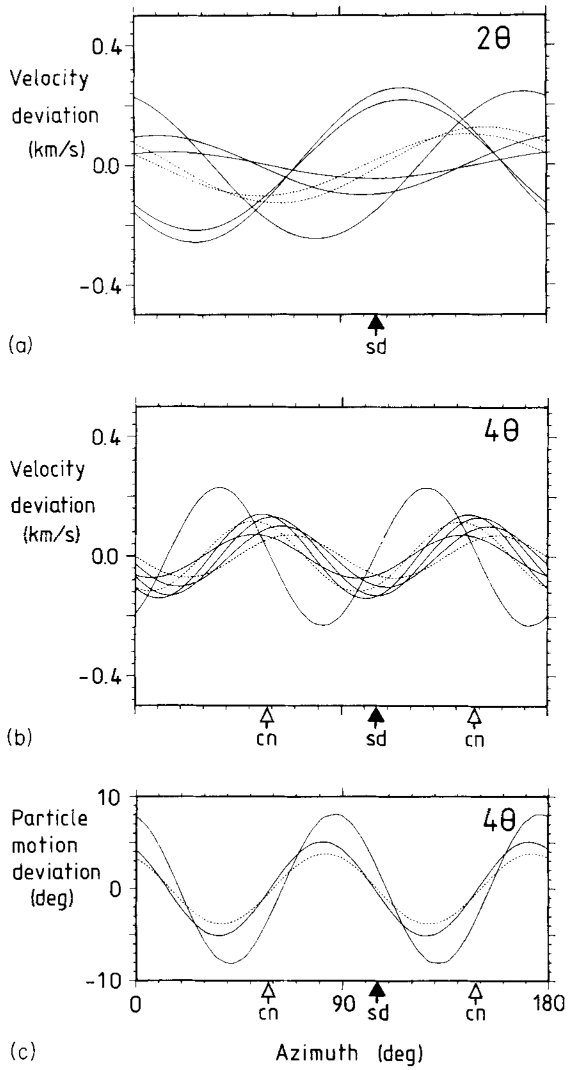

Figure 11. Summary of curves from velocity and particle motion deviations listed in Tables 1 and 2 and plotted in Figs 7 and 8, plotted against azimuth from north. (a) 2θ terms of velocity deviations, (b) 4θ terms of velocity deviations, (c) 4θ terms of particle motion deviations. Broken lines denote results from inversions of summed datasets from different receivers. Arrowheads mark Mid-Atlantic Ridge spreading direction (sd) and azimuths of inferred crack normals (cn).

7.2 UPPER CRUST POROSITY ESTIMATES

The downwards velocity increase in layer 2, with an average velocity gradient of around $1.0\ s^{-1}$, is typical of normal oceanic crust. In the upper 1 or 2 km of the crust, the decrease of porosity with depth exerts an overriding influence on the velocity gradient while, in the lower part of the crust, the porosity is very low and more subtle velocity changes reflecting petrologic differences can be detected. It is impossible to infer bulk porosity precisely from the reduced seismic velocity of the rock, even if the uncracked elastic moduli of the rock are known, because the effective moduli of the cracked rock depend not just on the amount of pore space but also on the nature of the infilling fluids, the orientations, shape and size spectra of the cracks and on whether some, or all, of the voids are interconnected. For example, it is easy to see, *reductio ad absurdum*, that a network of extensive but infinitesimally thin parallel cracks could completely disconnect the matrix and markedly affect the seismic propagation velocities, yet possess negligible porosity. The tightest general constraints that can be placed on the porosity of a cracked rock, if the elastic moduli of the rock and fluid phases are known, but making no assumptions about the crack geometry, are provided by the Hashin–Shtrikman (H–S) bounds (Watt, Davies & O'Connell 1976). Assuming a basaltic matrix with water-filled voids, the H–S bounds suggest that 3–50 per cent porosity (with a mean of about 15 per cent) is required at the top of layer 2 in order to lower the compressional-wave velocities to those we observe, and that the porosity decreases steadily with depth through layer 2.

7.3 OBSERVED AZIMUTHAL ANISOTROPY IN LAYER 2

In earlier sections we showed that 4θ curves fitted to both velocity and particle-motion deviation data from two or three OBSs, individually and to the combined data from all OBSs, are remarkably consistent particularly in their phase (Table 3). This is true both for layer 2 and for deeper crustal arrivals. The consistency of these results is even more surprising since the particle motion deviations depend on the properties of the crust within a few wavelengths (about 1 km) of each receiver whereas the velocity anisotropy depends on the mean properties of the crust averaged over the shot-to-receiver paths, typically 10 km long. The most plausible explanation for our observations is that they are caused by widespread near-vertical aligned saturated cracks in the upper oceanic crust. Theory

Table 3. Summary of azimuths of normals to wet cracks inferred from 4θ terms from velocity and particle motion deviations.

Data range (km)	OBS	Azimuths of crack normals* (degrees)	
		From velocity deviations	From particle motion deviations
4–10	2	060, 150	–
	3	037, 127	059, 149
	4	064, 154	064, 154
	2+3+4	052, 142	059, 149
10–20	2	052, 142	
	4	055, 145	
	2+4	060, 150	

*Observed 4θ variations may be caused by sets of wet cracks with their normals along either or both of the listed azimuths.

predicts that, for a single set of such cracks, the anisotropy is expressed approximately by 4θ velocity and particle motion deviation curves; the crack normals correspond to the azimuths of the maximum velocity and of the negative-to-positive zero crossing, respectively (Fig. 12). The last sentence is strictly correct only for propagation along straight rays in planes containing the crack normal. In reality rays are curved due to refraction by velocity gradients. The fact that low-angle short-range rays give the same 4θ result as more steeply dipping long-range rays leads us to suspect ray curvature is of secondary importance.

There is close agreement in our data between the crack normal directions (058° and/or 148°) inferred from the observed velocity and particle motion deviations (Fig. 11b, c). Both these directions are almost exactly mid-way between the spreading and ridge axis directions of the adjacent Mid-Atlantic Ridge (Fig. 13). However, on the basis of the two curves in Fig. 11(b, c) alone, it is not possible to distinguish between the effects of a single set of aligned cracks and, say, two orthogonal sets of aligned cracks. Indeed, calculations for the two cases give virtually indistinguishable curves (Crampin, private communication). Other sets of cracks can also be proposed which will fit the observations (Crampin, McGonigle &

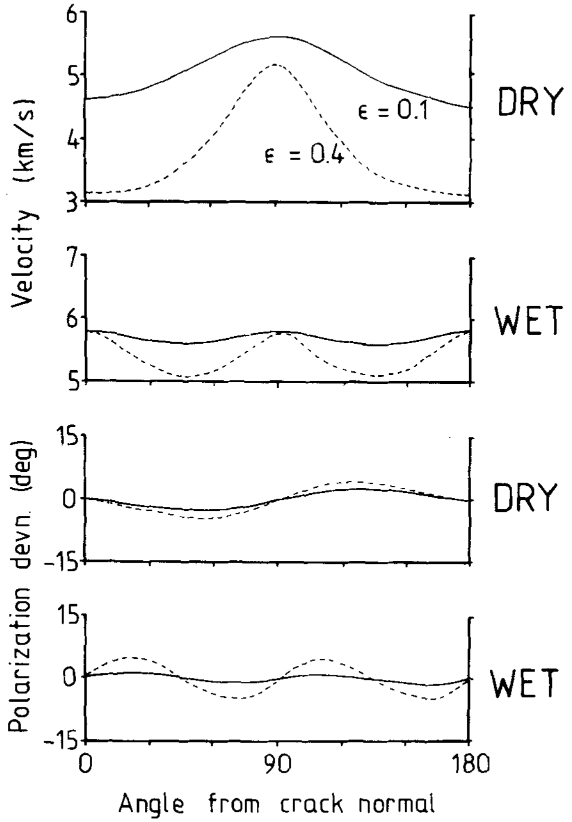

Figure 12. Variation of the group velocity and particle-motion deviations in planes through the symmetry axes of distributions of thin parallel cracks in an isotropic solid (*P*-wave velocity = 5.8 km s^{-1}, *S*-wave velocity = 3.349 km s^{-1}). Solid lines show results from cracks with density $\epsilon = 0.1$, and broken lines from cracks with density $\epsilon = 0.4$ (after Crampin *et al.* 1982). Dry cracks give dominantly 2θ variations and saturated cracks give predominantly 4θ variations in velocity and particle motion deviations. The particle motion deviation is measured from, and plotted against, direction of the ray (group velocity) arrival.

Bamford 1980). The amplitudes of the velocity deviations suggest that, if caused by a single set of cracks, the layer 2 crack density is approximately 0.1. It is even possible for two orthogonal sets of aligned near vertical dry cracks to generate 4θ *P*-wave velocity deviations (Crampin *et al.* 1980). This is unlikely to be the cause of the anisotropy we observe but, even if it were, the maxima of the 4θ curves would lie in the same directions as the crack normals, so our important inference that there are near-vertical cracks orientated obliquely to the spreading and ridge-axis directions would remain.

The compilation (Fig. 11) of all the curves fitted to the velocity and uncontaminated polarization data (Tables 1 and 2) highlights the consistency of the 4θ terms and the scatter in the 2θ terms. This suggests that the cracks are mostly saturated, since the velocity and polarization deviations generated by dry cracks are described mainly by 2θ terms while wet cracks cause dominantly 4θ terms (e.g. Fig. 12, after Crampin *et al.* 1982).

What, then, do the observed 2θ terms in the velocity deviations represent? It is possible that they are merely reflecting perturbations caused by lateral variability beneath the shotpoints because the 2θ terms are more susceptible to errors introduced by random lateral inhomogeneity than are the 4θ terms. This is because it is more likely that any lateral inhomogeneity beneath the shotpoints, of which we have taken no account in our inversions, will by chance be distributed bilaterally around the receiver causing an apparent 2θ dependence, than that it will by chance be distributed quadrilaterally so as to generate a strong 4θ dependence. One method for reducing the effects of random inhomogeneity is to sum the data from several receivers. When this is done (dotted lines on Fig. 11a), the amplitudes and phases of the summed 2θ curves from the upper (4–10 km) and the lower (10–20 km) crust are almost identical. Furthermore, the velocity minima, which for dry cracks lie in the same direction as the crack normals (Fig. 12) are at 055° and 063° for the upper and lower crustal arrivals respectively, in close agreement with the direction of one set of crack normals inferred from the 4θ velocity and polarization deviations (Fig. 11). The amplitude of the

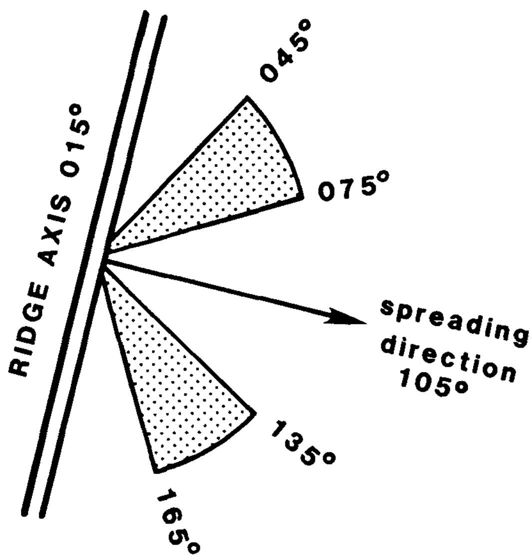

Figure 13. Sketch of the simplest set of symmetric orientations of the spreading ridge axis and cracks which generate the azimuthally dependent particle motion and velocity deviations observed in the survey area (see also Table 3). The stippled sectors denote the range of conjugate sets of saturated cracks which can give rise to the observed anisotropy.

velocity deviations from the summed curves, which is about $\pm 0.10\,\mathrm{km\,s^{-1}}$, can be used to estimate crack density (Crampin *et al.* 1980). If the 2θ velocity deviation terms are caused by a single set of vertical dry cracks then the cracks must have a very low crack density ($\epsilon = 0.01-0.02$) an order of magnitude smaller than the crack density we infer for saturated cracks from the 4θ velocity deviations.

We conclude that if aligned near-vertical dry cracks are present, then their crack density is about an order of magnitude lower than that of the saturated cracks but that their 149° orientation is consistent with one of the inferred sets of aligned near-vertical saturated cracks, suggesting a common genesis.

Other reports of anisotropy observed in the upper oceanic crust are by Stephen (1981) who used a three-component borehole seismometer in DSDP hole 417D to study velocity and polarization deviations and by Shearer & Orcutt (1982) who infer the presence of velocity anisotropy and/or lateral inhomogeneity in the shallow oceanic crust from particle motion deviations. Stephen fitted 2θ curves with maximum compressional wave deviations from 4.0 to 5.5 $\mathrm{km\,s^{-1}}$ and polarization deviations of ±6°. He made measurements along only two azimuths, parallel and perpendicular to the spreading direction, so his anisotropic curves are not tightly constrained. Although it may therefore be fortuitous, and it goes unremarked by Stephen in his paper, the curves he shows as his best fits indicate crack normals aligned at 157°, exactly 45° from the local spreading direction of 112°. This oblique orientation of cracks is identical to that inferred from our results.

7.4 SEISMIC ANISOTROPY OF THE UPPER CRUST AND RIDGE CREST TECTONICS

So far the discussion of crack systems has been in terms of either a single set or an orthogonal set of cracks orientated at about 45° to the ridge axis but, in fact, there is a whole range of sets of biplanar saturated cracks which give rise to 4θ velocity deviations similar to our observations (see fig. 2b in Crampin *et al.* 1980). In this section, therefore, we seek plausible crack geometries, in the light of current mid-ocean ridge tectonic models, which can cause the observed anisotropy. It seems clear that oblique cracks will feature in such models. On the other hand the apparently weak or negligible influence of ridge-parallel cracks, which our seismic observations indicate, is a surprise in view of the general observation of ridge-parallel cracks, fissures and other structural and volcanic features on the seafloor in the axial region of spreading centres.

Sets of parallel normal faults sometimes occur associated with, and oblique to, transform or wrench faults (Whitmarsh & Laughton 1976). Such faults have been detected with side-looking sonar up to 10 km from transform faults (Searle 1984) but GLORIA results show that there are no such transforms within the region of our experiment.

The main forces acting on normal oceanic lithosphere away from anomalous features and away from the zone of accretion are likely to be the stress associated with cooling and the forces associated with plate motion.

The upper 25 km of the lithosphere behaves elastically below about 300°C. Cooling, perhaps associated with underplating, will produce ridge-parallel tension and ridge-normal compression of about 2 kbar a few tens of kilometres from the ridge axis (Sykes & Sbar 1973; Turcotte 1974).

Solomon, Richardson & Bergman (1980) tried a variety of models of plate-driving forces to explain mid-plate first motion solutions (which mostly indicate compression), *in situ* stress measurements and the strikes of stress sensitive geological features. The best fitting global stress models have stress magnitudes comparable to the horizontal compressive stress (200–300 bar) exerted by ridge elevation. In the NE Atlantic Ocean, close to our experiment, the direction of the principal horizontal compressive stress is estimated by Solomon *et al.* (1980) to be about ESE and, therefore, approximately normal to the ridge axis.

More direct evidence of ridge normal compression was provided by Stein & Wiens (1983) and Wiens, Helm & Stein (1983) who concluded from a study of focal mechanisms of earthquakes in the oceanic lithosphere that compressive stress in the spreading direction is practically ubiquitous. Bergman & Solomon (1983), in a similar study of 28 events, found almost twice as many strike-slip (horizontal minimum principal compressive stress axis, $P_{\min}$) as thrust (vertical $P_{\min}$) events.

In areas where $P_{\min}$ is horizontal there is evidence that conjugate sets of oblique vertical cracks or shear joints will result. Experimental and field data indicate that an isotropic material, when subjected to uniaxial compressive stress, tends to fail along shear planes orientated at about 30° to the compression axis. In anisotropic rocks the angle of shear fracture varies considerably. Donath (1961) experimented on samples of slate and shale. When the principal axis of stress was inclined more than about 30–45° (but less than 90°) to the planes of cleavage or fissility in the specimens, the shear fractures appeared at 40–60° to this axis (slate) or at about 30° to this axis (shale). If we an extrapolate these results to the ocean crust, equating the cleavage or fissility with the ridge parallel cracks, then sets of conjugate vertical shear joints at ±(30–60°) to the ridge axis are predicted.

Due to the symmetry of the 4θ velocity variations certain sets of conjugate faults which are not orientated 45° to the ridge axis can give rise to a velocity variation which appears to be due to a single set of 45° cracks (e.g. cracks at ±30° to the ridge axis are indistinguishable from two sets of cracks at 30° and 60° clockwise from the axis; both cases give a velocity maximum 45° clockwise from the axis). In practice, the possible sets of conjugate faults are limited by realistic crack densities and by the observed velocities. Calculations using the formulae of Crampin *et al.* (1980) show that the observed velocities can be fitted by sets of conjugate cracks orientated between ±(30–60)° to the ridge axis with crack densities of up to 0.17. These angles are consistent with those predicted by the above experimental studies.

However, it is not certain that either lithospheric cooling or the effect of 'ridge-push' will exert sufficient horizontal stress in the top few kilometres of the oceanic crust and within a few tens of kilometres of the ridge axis to crack the crust and we sought more direct evidence of such cracking.

Jefferis & Voight (1981) conducted an extensive analysis of surface fractures in part of SW Iceland within 5–37 km of the Mid-Atlantic Ridge plate boundary. A set of NE fractures (020–040°) was shown to be closely parallel to the normal faults and dykes in the study area and to the faults and fissures of the nearby plate boundary. Fracture traces (linear features on air photographs generally up to 2 km long) had a mean trend of 035°. A second set of fractures strikes generally east–west or at a high angle to the NE set. A third set of fractures is present at many stations, in which case the second and third sets are arranged symmetrically about the NE set. In 14 out of 16 cases, the NE set of fractures were older than the east–west set (the remainder were contemporaneous) and seem to have formed after some cooling of the area had occurred. Although the study region lay just north of the so-called Reykjavik fracture zone, so that the east–west fractures might be thought to indicate the influence of sinistral shear, Jefferis & Voight (1981) report that the extension across these fractures is inconsistent with this hypothesis. They argue instead that as the crust spread away from the accretion zone, cooling produced a rearrangement of the stress field with compression normal to this zone. Indeed, nearby hydrofracturing experiments which indicate a north–south to NE–SW trending dilation axis, are compatible with this explanation (Haimson & Voight 1977; Haimson 1979; Voight 1979).

The above Icelandic example therefore supports our suggestion of oblique cracks. Unfortunately, at present no data are published from the upper oceanic crust away from spreading centres on the orientation of near-vertical cracks from successful hydrofracturing experiments or from other downhole observations.

Although cooling of the lithosphere, or ridge-push forces, seems able to provide suitably orientated (ridge-normal) compression to generate cracks which can cause the anisotropy we observe, the inferred relative paucity of ridge-parallel cracks in the top kilometre of crust a few tens of kilometres from the ridge axis must also be explained. Two processes are probably at work. The greater age of the ridge-parallel cracks, suggested by Icelandic data, means they will have experienced greater infilling by hydrothermal precipitates. Secondly, the same compressive ridge-normal stresses which generate the oblique cracks in ridge flank areas will tend to close up the ridge-parallel cracks, particularly since these stresses increase with depth in the crust (Jefferis & Voight 1981). These two processes together may be sufficient to explain the apparent insignificance of ridge-parallel cracks in our survey area. The formation of oblique cracks must occur soon after the crust is elevated out of the tensional regime of the median valley. As the lithosphere begins to thicken, stresses in the young crust will be high and likely to induce cracking but, as the lithosphere continues to thicken and move away from the spreading centre, the stresses will decrease as they are distributed over a larger cross-sectional area. If the above explanation of seismic anisotropy is correct and a new set of connected cracks is generated, it provides a mechanism for profoundly influencing the flux and pathways of hydrothermal circulation in young crust.

8 Conclusions

(1) Significant azimuthal variations of seismic velocity and particle-motion deviation angle have been recognized at 45° N in 1.1–3.4 Ma old upper oceanic crust.

(2) The anisotropy can be described by 2θ and 4θ terms. The amplitude and phase of the 4θ terms remain the same whichever data-type, OBS or range of observations (4–10, 10–20 km) is used to calculate them. The 2θ velocity variations show considerable scatter; the 2θ particle-motion deviations are contaminated by instrumental effects.

(3) The 4θ anisotropy is consistent with it being caused by sets of aligned, near-vertical saturated cracks in the upper crust. If this explanation is correct, the cracks are not parallel to the ridge axis but must lie oblique to it.

(4) Current tectonic models of young oceanic lithosphere favour horizontal ridge-normal compression. If the least compressive stress axis is also horizontal (as suggested by the majority of compressive focal mechanisms), then conjugate sets of vertical cracks orientated in the range $\pm(30-60)^\circ$ with respect to the ridge axis are predicted. Such cracks would generate the observed anisotropy.

(5) The lack of seismic influence of ridge-parallel cracks, fissures, etc. which are observed at mid-ocean ridge crests may be due either to their insignificant vertical extent or to their subsequent closure by ridge-normal compression and by deposition of hydrothermal minerals.

Acknowledgments

We are grateful to the Master, Officers and crew on *RRS Discovery*, Cruise 93, for their assistance. We also thank our scientific colleagues at sea, particularly those who operated the OBS (J. J. Langford, R. E. Kirk and D. Grohmann) and the airgun team (R. Bonner, C. Flewellen, B. Knowles). The data were digitized by C. E. Davies and by M. Saunders who also contributed to the programs used to study particle motion. We thank Stuart Crampin and Ralph Stephen for discussion and advice and Charlotte Keen for providing soundings. The words were processed by Pat Hancock, Marion Jeffery, Ann Rayner and Gabrielle Mabley. This work was supported by the Natural Environment Research Council, Department of Earth Sciences, Cambridge, Contribution No. 421.

References

ARCYANA, 1978. *FAMOUS – Photographic Atlas of the Mid-Atlantic Ridge: rift and transform fault at 3000 m depth,* Gauthiers-Villars, CNEXO, 128 pp.

Backus, G. E., 1965. Possible forms of seismic anisotropy of the uppermost mantle under oceans, *J. geophys. Res.,* **70,** 3429–3439.

Ballard, R. D. & Van Andel, Tj. H., 1977. Morphology and tectonics of the inner rift valley at lat. 36° N on the Mid-Atlantic Ridge, *Bull. geol. Soc. Amer.,* **88,** 507–530.

Ballard, R. D. & Moore, J. G., 1977. *Photographic Atlas of the Mid-Atlantic Rift Valley,* Springer-Verlag, New York.

Ballard, R. D., Van Andel, Tj. H. & Holcomb, R. T., 1982. The Galapagos Rift at 86° W 5. Variations in volcanism, structure, and hydrothermal activity along a 30 km segment of the rift valley, *J. geophys. Res.,* **87,** 1149–1161.

Bamford, D. & Nunn, K. R., 1979. *In situ* seismic measurements of crack anisotropy in the Carboniferous limestone of northwest England, *Geophys. Prospect.,* **27,** 322–338.

Becker, K., Langseth, M. G., Von Herzen, R. P. & Anderson, R. N., 1983. Deep crustal geothermal measurements, hole 504B, Costa Rica Rift, *J. geophys. Res.,* **88,** 3447–3457.

Bergman, E. A. & Solomon, S. C., 1983. Source studies of near-ridge earthquakes: implications for the early evolution of oceanic lithosphere (abstract), *Eos,* **64,** 759.

Crampin, S., 1978. Seismic-wave propagation through a cracked solid: polarization as a possible dilatancy diagnostics, *Geophys. J. R. astr. Soc.,* **53,** 467–496.

Crampin, S., McGonigle, R. & Bamford, D., 1980. Estimating crack parameters from observations of *P*-wave velocity anisotropy, *Geophys,* **45,** 345–360.

Crampin, S., Stephen, R. A. & McGonigle, R., 1982. The polarization of *P*-waves in anisotropic media, *Geophys. J. R. astr. Soc.,* **68,** 477–486.

De Sitter, L. U., 1964. *Structural Geology,* McGraw-Hill, New York.

Detrick, R. S., Cormier, M. H., Prince, R. A. & Forsyth, D. W., 1982. Seismic constraints on the crustal structure within the Vema fracture zone, *J. geophys. Res.,* **87,** 10 599–10 612.

Detrick (Jr), R. S. & Purdy, G. M., 1980. The crustal structure of the Kane fracture zone from seismic refraction studies, *J. geophys. Res.,* **85,** 3759–3777.

Donath, F. A., 1961. Experimental study of shear feature in anisotropic rocks, *Bull. geol. Soc. Am.,* **72,** 985–990.

Fenner, D. F. & Bucca, P. J., 1971. The sound velocity structure of the North Atlantic Ocean, *USNOO Int. Rept 71-13.*

Francheteau, J., Needham, D., Juteau, Th. & Rangin, C., 1980. *Cyamex-Naissance d'un ocean sur la dorsale du Pacifique est,* Centre National pour l'Exploitation du Oceans, Paris.

Garbin, H. D. & Knopoff, L., 1973. The compressional modulus of a material permeated by a random distribution of circular cracks, *Q. appl. math.,* **50,** 453–464.

Garbin, H. D. & Knopoff, L., 1975. Elastic models of a medium liquid-filled cracks, *Q. appl. math.,* **33,** 301–303.

Haimson, B. C., 1979. New stress measurements in Iceland reinforce previous hydrofracturing results: H_{max} is perpendicular to the axial rift zones, *Eos,* **60,** 377.

Haimson, B. C. & Voight, B., 1979. Crustal stress in Iceland, *Pure appl. Geophys.,* **115,** 153–190.

Harrison, C. G. A., Bonatti, E. & Stieltjes, L., 1975. Tectonism of axial valleys in spreading centres: data from the Afar Depressions of Ethiopia, Vol. 1 (eds Pilger, A. & Rosler, A.). *Inter-Union Commission on Geodynamics, Sci. Rept. no. 14,* pp. 178–198.

Jefferis, R. G. & Voight, B., 1981. Fracture analysis near the mid-ocean plate boundary Reykjavik-Hvalfjordur area, Iceland, *Tectonophys.,* **76,** 171–236.

Johnson, D. M., 1980. Crack distribution in the upper oceanic crust, *Init. Rep. Deep Sea Drill. Proj.,* **51, 52, 53,** pt 2, 1479–1490, US Government Printing Office, Washington DC.

Kirk, R. E., Langford, J. J. & Whitmarsh, R. B., 1982. A three-component ocean bottom seismograph for controlled source and earthquake seismology, *Mar. geophys. Res.,* **5,** 327–341.

Laughton, A. S. & Searle, R. C., 1979. Tectonic processes on slow-spreading ridges, in *Deep Drilling Results in the Atlantic Ocean: Ocean Crust*, pp. 15–32, ed. Talwani, M. *et al.*, American Geophysical Union.

Lawson, C. L. & Hanson, R. J., 1974. *Solving Least Squares Problems*, Prentice-Hall, New Jersey.

Loncarevic, B. D. & Parker, R. L., 1971. The Mid-Atlantic Ridge near 45° N. XVII. Magnetic anomalies and ocean floor spreading, *Can. J. Earth Sci.*, **8**, 883–898.

Luyendyk, B. P. & Macdonald, K. C., 1977. Physiography and structure of the inner floor of the FAMOUS rift valley: Observations with a deep-towed instrument package, *Bull. geol. Soc. Am.*, **88**, 648–663.

McMechan, G. & Mooney, W., 1980. Asymptotic ray theory and synthetic seismograms for laterally varying structures: theory and application to the Imperial Valley, California, *Bull. seism. Soc. Am.*, **70**, 2021–2036.

Orcutt, J. A., Kennett, B. L. N. & Dorman, L. M., 1976. Structure of the East Pacific Rise from an ocean bottom seismometer survey, *Geophys. J. R. astr. Soc.*, **45**, 305.

Park, S. & Simmons, G., 1982. Crack-induced velocity anisotropy in the White Mountains, New Hampshire, *J. geophys. Res.*, **87**, 2977–2983.

Purdy, G. M., 1983. The seismic structure of 140 My old crust in the western central Atlantic ocean, *Geophys. J. R. astr. Soc.*, **72**, 115–138.

Raitt, R. W., Shor, G. G., Francis, T. J. G. & Morris, G. B., 1969. Anisotropy of the Pacific upper mantle, *J. geophys. Res.*, **74**, 3095–3109.

Searle, R. C., 1984. Multiple, closely-spaced transform faults in fast-slipping fracture zones, *Geology*, **11**, 607–610.

Shearer, P. & Orcutt, J., 1982. Use of horizontal component data from ocean bottom seismographs, *Eos*, **63**, 1025.

Sinha, M. C. & Louden, K. E., 1983. The Oceanographer Fracture Zone – I. Crustal structure from seismic refraction studies, *Geophys. J. R. astr. Soc.*, **75**, 713–736.

Solomon, S. C., Richardson, R. M. & Bergman, E. A., 1980. Tectonic stress models and magnitudes, *J. geophys. Res.*, **85**, 6086–6092.

Spudich, P. & Orcutt, J., 1980. A new look at the seismic velocity structure of the oceanic crust, *Rev. Geophys. Space Phys.*, **18**, 626–645.

Steinn, S. & Wiens, D. A., 1983. Implications of oceanic intraplate seismicity for intraplate stresses, plate driving forces and mantle viscosity (abstract), *Eos*, **64**, 759.

Stephen, R. A., 1981. Seismic anisotropy observed in upper oceanic crust, *Geophys. Res. Lett.*, **8**, 865–868.

Stephen, R. A., Louden, K. E. & Matthews, D. H., 1980. The oblique seismic experiment on DSDP leg 52, *Geophys. J. R. astr. Soc.*, **60**, 289–300.

Sykes, L. R. & Sbar, M. L., 1973. Intraplate earthquake, lithospheric stresses and the driving mechanism of plate-tectonics, *Nature*, **245**, 298–302.

Tréhu, A. M., 1984. Lateral velocity variations in the Orozco Transform Fault inferred from observed incident angles and azimuths of *P*-waves, *Geophys. J. R. astr. Soc.*, **77**, 711–728.

Turcotte, D. L., 1974. Are transform faults thermal contraction cracks?, *J. geophys. Res.*, **79**, 2573–2577.

Voight, B., 1979. Structure and stress history of new hydrofracturing measurement sites near the 'Mid-Ocean' plate boundary, *Eos*, **60**, 377.

Watt, J. P., Davies, G. F. & O'Connell, R., 1976. The elastic properties of composite materials. *Rev. Geophys. Space Phys.*, **14**, 541–563.

Wiens, D. A., Helm, G. A. & Stein, S., 1983. Intraplate seismicity and stresses in young oceanic lithosphere (abstract), *Eos*, **64**, 759.

White, R. S., 1984. Atlantic oceanic crust: seismic structure of a slow-spreading ridge, in *Ophiolites and Oceanic Lithosphere*, eds Gass, I. G., Lippard, S. J. & Shelton, A. W., *Spec. Publ. geol. Soc. Lond.*, **13**, 101–111, Blackwell Scientific Publications, Oxford.

White, R. S. & Matthews, D. H., 1980. Variations in oceanic upper crustal structure in a small area of the north-eastern Atlantic, *Geophys. J. R. astr. Soc.*, **61**, 401–436.

White, R. S. & Purdy, G. M., 1983. Crustal velocity structure on the flanks of the mid-Atlantic Ridge at 24° N, *Geophys. J. R. astr. Soc.*, **75**, 361–386.

White, R. S. & Stephen, R. A., 1980. Compressional to shear wave conversion in oceanic crust, *Geophys. J. R. astr. Soc.*, **63**, 547–566.

White, R. S., Detrick, R. S., Sinha, M. C. & Cormier, M. H., 1984. Anomalous seismic crustal structure of oceanic fracture zones, *Geophys. J. R. astr. Soc.*, **79**, in press.

Whitmarsh, R. B., 1978. Seismic refraction studies of the upper igneous crust in the north Atlantic and porosity estimates for layer 2, *Earth planet. Sci. Lett.*, **37**, 451–464.

Whitmarsh, R. B. & Laughton, A. S., 1976. A long-range sonar study of the Mid-Atlantic Ridge crest near 37° N (FAMOUS area) and its tectonic implications, *Deep-Sea Res.*, **23**, 1005–1023.

Woodside, J. M., 1972. The Mid-Atlantic Ridge near 45° XX. The gravity field, *Can. J. Earth Sci.*, **9**, 942–959.

Zoback, M. D. & Anderson, R. N., 1982. Ultrasonic borehole televiewer investigation of oceanic crustal layer 2A, Costa Rica Rift, *Nature*, **295**, 375.

Geophys. J. R. astr. Soc. (1984) **79**, 469–488

Physical links between crustal deformation, seismic moment and seismic hazard for regions of varying seismicity

Ian G. Main *Natural Environment Research Council, British Geological Survey, Murchison House, West Mains Road, Edinburgh EH9 3LA, and University of Edinburgh, Department of Geophysics, James Clerk Maxwell Building, Mayfield Road, Edinburgh EH9 3JZ, Scotland*

Paul W. Burton *Natural Environment Research Council, British Geological Survey, Murchison House, West Mains Road, Edinburgh EH9 3LA*

Received 1984 March 8; in original form 1984 January 13

Summary. Seismic moment release rates $\dot{M}_0$ inferred from a Weibull frequency–magnitude distribution and its extreme value equivalent are compared with observation. The seismotectonically diverse regions studied all exhibit the curvature of a log-linear frequency magnitude plot associated with applying a maximum magnitude to earthquake recurrence statistics. The inferred seismic moment release rates are consistent with available crustal deformation data within uncertainties resulting from the line fit and in magnitude determination. The uncertainties for the regions studied (Southern California, the New Madrid seismic zone, the Central and Eastern Mediterranean and mainland UK) vary from at worst an order of magnitude down to a factor of 2 or 3.

This agreement can be used to justify the extrapolation of frequency–magnitude statistics beyond the historical and instrumental era in seismic hazard studies as a test of the stationarity of short-term statistics against long-term effects.

A striking example of a bimodal seismicity distribution is observed in the New Madrid zone. This can be interpreted as being due to the superposition of two distinct seismogenic source types observed in the area. A quantitative analysis of the separate orders of seismicity observed in the frequency–magnitude statistics – comparing the different maximum magnitudes and inferred seismic moment release rates with those observed – supports this hypothesis. Superposition of many such seismogenic sources can explain the linearity observed in global frequency versus seismic moment magnitude statistics.

Introduction

The incorporation of crustal deformation into analyses of seismic hazard has given useful insight into probabilities of the largest events associated with long time periods. By linking the observed statistical magnitude occurrence with a physical parameter – seismic moment – a means is provided to test an extrapolation from short-term historical and instrumental reports against an average of crustal deformation observed over geological time. Examples of observed deformation would come from plate tectonic models, from observed rates of slip along faults which break the surface, or from geodetically determined strain rates in more complex tectonic regions. Some knowledge of the dimensions of the fault zone (extent and depth) and appropriate elastic constants are required to convert slip or strain rates to seismic moment. This information also places deterministic constraints on an important parameter in any seismicity distribution – the largest earthquake consistent with the finite breaking strength of the Earth and the finite extent of the fault zone.

In previous work on this subject (e.g. Anderson 1979; Papastamatiou 1980) this largest earthquake specifies a truncation of the two parametered Gutenberg–Richter frequency relation (equation 2 below) in order to avoid problems such as an infinite rate of strain energy release (Knopoff & Kagan 1977). This effectively introduces a third parameter to the assessment of seismic hazard, and is consistent with the simple geometric seismicity model of Kanamori & Anderson (1975).

A more complex model of seismicity (Caputo 1977), which includes the effect of variable and limited stress drop as well as source dimension shows that such arbitrary and sudden truncation is not physically valid, and rather that we might expect a gradual roll-off both in the number density and the cumulative frequency asymptotic to a maximum earthquake at zero probability. (Incidentally the model also requires a similar roll-off at very small magnitudes.) This roll-off appears as curvature on a log-linear frequency–magnitude plot. For the cumulative form, such curvature has been observed in the laboratory by Burridge & Knopoff (1967) and King (1975) for earthquake models, and also in a theoretical model by Kuznetsova, Shumilana & Zavialov (1981), which considered inhomogeneities along a fault. This behaviour has already been observed in seismicity distributions around the world – for example by Botti, Pasquale & Anghinolfi (1980) in the Western Alps, Burton *et al.* (1982) in Turkey, Makjanik (1980) in Yugoslavia, Makropoulos (1978) in Greece and by Cosentino & Luzio (1976). There is also experimental evidence that the distribution of microfracture events in stressed San Marco gabbro also shows curvature asymptotic to a maximum size at low frequencies (Scholz 1968). Analogous curved distributions have been observed elsewhere in nature, for example in the yield strength and fatigue life of steel (Weibull 1951), and are commonly used in meteorological analysis (Jenkinson 1955).

The Weibull distribution can be usefully extended to analyse preferentially the largest events associated with curvature because of its simple form. The largest events in this case consist of a subset of the frequency distribution – namely the largest value in any unit time interval. This distribution of extreme values has been used in seismic hazard analysis (Burton 1979) and also in order to assign a maximum magnitude to events on a global basis (Yegulalp & Kuo 1974). There follows a discussion on crustal deformation compatible with curvature in both the cumulative frequency distribution and that of the extreme values, with application to different tectonic regimes.

Curved cumulative frequency distributions

The most commonly used seismicity distribution is the log-linear Gutenberg–Richter law

$$\log N(x \geqslant m) = a - bm \tag{1}$$

where N is the number of times a magnitude m is equalled or exceeded and a and b are regionally varying positive constants. (The symbol m is used in the theoretical discussion for a general magnitude in order to avoid confusion with the seismic moment M_0. Elsewhere M_L, M_s, M_w and m_b have their usual meanings.) b is commonly observed to be close to 1 in accordance with the geometrical model of Kanamori & Anderson (1975). If we define a number density distribution $n = -dN/dm$ and rearrange (1) then

$$n(m) = p \exp(-b'm); \quad \begin{matrix} b' = b \ln 10 \\ p = b' 10^a. \end{matrix} \tag{2}$$

Caputo's (1977) model introduces a third parameter to the distribution at high magnitudes, above m_2 say, and defines a maximum value for m via the relation

$$n(m) = p \exp(-b'm) - q \tag{3}$$

where p, b' and q can be related to constants specifying the distribution of fault dimension and stress drop, and to maximum values of these parameters. The model also indicates that $b \approx 1$. Equation (3) is therefore a simple generalization of (2), or we can regard (2) as the limit in which $q \to 0$ or the equivalent maximum magnitude (ω) tends to infinity, since $q = p \exp(-b'\omega)$.

Jenkinson's (1955) general solution for a cumulative frequency distribution related to the extreme values takes the form

$$N(x \geqslant m) = [(\omega - m)/(\omega - u)]^{1/\lambda}$$

and is equivalent to the Weibull distribution for positive, non-zero λ. ω is the maximum magnitude, $u < \omega$ is a characteristic value associated with unit time, and $\lambda < 1$ is a measure of the curvature of the distribution. As $\lambda \to 0$ (4) reduces to the form (1) (Gumbel 1958). This form of the distribution in (4) is chosen as the most convenient for the present work. In both cases curvature in N and n asymptotic to a maximum value is reflected by three parameters, rather than the two of (1).

An alternative attempt to limit the distribution is to define $N(m) = 0$ at a finite maximum magnitude, given a normalized form of (2). The form, after Cosentino & Luzio (1976) is the truncated Gutenberg–Richter law

$$N(x \geqslant m) = \frac{\exp(-b'm) - \exp(-b'\omega)}{\exp(-b'u) - \exp(-b'\omega)} \tag{5}$$

where ω and u are defined as in the Jenkinson notation and $b' = b \ln 10$. In this case the number density distribution $n(m)$ is *not* curved although the *cumulative* frequency is (Båth 1981a), so there is a philosophical difference between (5) and the forms (3) and (4). Finally, the effects of both a lower and an upper bound to earthquake occurrence can be combined in the single equation

$$P(m) = (1 - K) + K \exp[b'(m - m_0)] \tag{6}$$

where P is the fraction of earthquakes greater than m, K is $\{1 - \exp[-b'(\omega - m_0)]\}^{-1}$ and m_0, ω are lower and upper bounds to the seismicity distribution (Cornell & Vanmarcke 1969). Normally the effects of a lower bound on earthquake statistics are negligible and can be safely ignored. The relationship of this form of the seismicity distribution to crustal deformation rates was analysed by Papastamatiou (1980) directly in terms of seismic moment.

In summary, the inclusion of a third parameter which limits the seismicity distribution gives a more general form than the open-ended Gutenberg–Richter law, and in a form in common use outside seismology. The main parameterizations are outlined above, although others are possible, but in the present work the form used will be that of (4), because this form allows us to compare both the initial distribution (N) and the extreme value distribution (P) discussed below.

Extreme value distributions

The theory of extreme values has been covered extensively by Gumbel (1958). For our purpose the most important relation is

$$P(x \leqslant m) = \exp\left[-N(x \geqslant m)\right] \tag{7}$$

where P is a probability of non-exceedance in unit time of a magnitude m – or alternatively that m is an extreme value. This relation follows from a Poissonian assumption that different events are unrelated, in the limit as the total number of events analysed $\rightarrow \infty$. A derivation of the form of N (and hence P) consistent with certain assumptions pertinent to the extreme values gave equation (4). The form of this distribution which reflects an upper bounded magnitude is defined as Gumbel's third distribution of extreme values:

$$P(x \leqslant m) = \exp\left\{-\left[(\omega - m)/(\omega - u)\right]^{1/\lambda}\right\} \tag{8}$$

where $0 < \lambda < 1$, $u < \omega$ as for the Weibull distribution.

Knopoff & Kagan (1977) have objected to the use of extreme value statistics of the first type (related to equation 1) because methods which analyse the whole data set in this case generally give more accurate results in earthquake statistics. However, the curvature consistent with Caputo's physical model is usually emphasized to a greater degree in the extreme value case for a type three distribution because it deals preferentially with the largest events where such curvature is to be expected. Gumbel's third distribution of extreme values may well be the best available method of extrapolating to earthquake occurrence at low probabilities from an existing catalogue of events, particularly when it is incomplete, although where possible the predictions should be checked against known physical parameters such as slip rate. The theoretical means of carrying this out is derived in the next section.

Crustal deformation

The measure of crustal deformation is taken to be the seismic moment M_0. This can be related to slip rates ($\dot{s}$) on individual faults, or strain rates ($\dot{e}$) over a more diffuse area by the equations

$$\dot{M}_0 = \mu A \dot{s} \tag{9}$$

$$\dot{M}_0 = 2.5\,\mu V \dot{e} \tag{10}$$

where μ is the rigidity modulus, A is the area of slip and V is the crustal volume of the zone of deformation. Equation (10) is derived in Papastamatiou (1980).

Two models are used to estimate the rate of crustal deformation, following from (I) the cumulative frequency of occurrence (whole process) and (II) from the extreme value probabilities (part process).

MODEL I

An average value for the rate of release of seismic moment is given by integration over the range $(0, M_{0\omega})$ where $M_{0\omega}$ is the largest moment which might be released in a single event for a particular region

$$\bar{\dot{M}}_0 = \int_0^{M_{0\omega}} M_0 n(M_0)\, dM_0 \tag{11}$$

$n(M_0)\, dM_0$ is the number of earthquakes occurring in an interval dM_0 per unit time with $n = -dN/dM_0$. N is given by the cumulative frequency relationship, but is normally expressed in terms of magnitude, since moment is still a fairly rare observational parameter. To convert between the two we may use the relationship

$$M_0(m) = 10^{A+Bm} \tag{12}$$

where $B = 3/2$ for the M_W scale follows from Kanamori & Anderson's (1975) theoretical considerations on fault geometry as well as from empirical fits to available data. The most recent work on this conversion from seismic moment, M_0, to seismic moment magnitude, M_W, indicates the following values for A and related stress drops $\Delta\sigma$:

interplate events = 16.1, $\Delta\sigma$ = 30 bar

intraplate events = 15.7, $\Delta\sigma$ = 76 bar

average value = 15.85, $\Delta\sigma$ = 52 bar

California = 15.83

(from Singh & Havskov 1980).

By an appropriate change of variables, and using (4) to define $n(m) = -dN/dm$, it can be shown from (11) and (12) that

$$\bar{\dot{M}}_0 = \frac{M_{0\omega}\Gamma(1 + 1/\lambda)}{[\beta(\omega - u)]^{1/\lambda}} \tag{13}$$

where $\bar{\dot{M}}_0$ and u are expressed per unit time interval, and $\beta = B \ln 10$. Γ is the usual symbol for the Gamma function.

MODEL II

Forming a probabilistic expectation value

$$\langle \dot{M}_0 \rangle = \int_0^{M_{0\omega}} M_0\, p(M_0)\, dM_0 \tag{14}$$

where

$$P(X \leqslant M_0) = \int_0^{M_0} p(X)\, dX$$

is the extreme value distribution following from the normalized probability density p. After a suitable change of variables involving (8) and (12)

$$\langle \dot{M}_0 \rangle = M_{0\omega} \int_0^1 \exp\,[-\beta(\omega - u)(-\ln x)^{\lambda}]\, dx. \tag{15}$$

In the present work this equation is evaluated numerically.

Thus in both models the seismic moment release per unit time interval is expressed as a fraction of the maximum moment $M_{0\omega}$, for all values of (ω, u, λ) consistent with a

Gumbel's third extreme value distribution and its initial Weibull distribution. We can also show that $\langle \dot{M}_0 \rangle / \bar{\dot{M}}_0 < 1$ for appropriate values of the parameters and if (7) holds.

In evaluating parameters of the distribution (8) the unit time interval must sometimes be taken to be i yr rather than annually, in order to reduce problems associated with intervals devoid of any recorded events. If this is the case u and λ are appropriate for this scale, and we can convert to annual rates via

$$\langle \dot{M}_0 \rangle_i = i \langle \dot{M}_0 \rangle_1 \tag{16}$$

where $\langle \dot{M}_0 \rangle_i$ is the seismic moment released per i yr.

(13) and (15) then define the rate of release of seismic moment in terms of the statistically determined parameters (ω, u, λ) – the link to the physical process of strain or slip rates being represented by the terms $M_{0\omega}$ and β.

UNCERTAINTIES IN $\bar{\dot{M}}_0$, $\langle \dot{M}_0 \rangle$ AND $M_{0\omega}$

Because (ω, u, λ) are subject to (often large) statistical error we have to allow for this in predictions of $\dot{M}_0$. This can be done by the equation

$$\delta(\langle \dot{M}_0 \rangle, \bar{\dot{M}}_0) = \left\{ \sum_{i=1}^{3} \sum_{j=1}^{3} \frac{\partial^2 (\langle \dot{M}_0 \rangle, \bar{\dot{M}}_0)}{\partial p_i \, \partial p_j} \sigma_{ij}^2 \right\}^{1/2} \tag{17}$$

which represents a complete covariance error in $\langle \dot{M}_0 \rangle$ and $\bar{\dot{M}}_0$ respectively. $p_{i,j}$ takes on values (ω, u, λ) and σ_{ij} is the statistically determined covariance error in these parameters. The covariance matrix ϵ is defined by

$$\epsilon = \begin{pmatrix} \sigma_\omega^2 & \sigma_{\omega u}^2 & \sigma_{\omega\lambda}^2 \\ \sigma_{u\omega}^2 & \sigma_u^2 & \sigma_{u\lambda}^2 \\ \sigma_{\lambda\omega}^2 & \sigma_{\lambda u}^2 & \sigma_\lambda^2 \end{pmatrix} \tag{18}$$

as in Burton (1979). This is the most complete method of allowing for error, because in general the parameters ω and λ are dependent on each other. A large ω leads to less curvature (lower λ) and vice versa. This manifests itself in a negative contribution from $\sigma_{\omega\lambda}^2$, or a reduction in the error compared to the variance method (a sum of the diagonal elements σ_i^2).

The uncertainty in ω is often unusually large (Burton 1979), and in many cases may be reduced where limitations on stress drop (usually in the range $1 < \Delta\sigma < 100$ bar), fault dimension and fault type place an upper bound on $M_{0\omega}$ through the general expression

$$M_{0\omega} = C \Delta\sigma_{\max} \, l_{\max}^3 \tag{19}$$

where C is a dimensionless constant which depends on the type of fault, and $l_{\max}$ is the maximum fault dimension (Kanamori & Anderson 1975). Alternatively we may use this value to compare $M_{0\omega}$ obtained by $l_{\max}$ and $\Delta\sigma_{\max}$ with statistically determined values of ω via (12).

Saturation

It is well known that curvature of the form (3), (4) or (5) may be artificially present for magnitudes above $M_S = 7.5$ to 8.0 because of instrumental saturation of the magnitude scale (Howell 1981). Chinnery & North (1975) have shown that when M_S values are

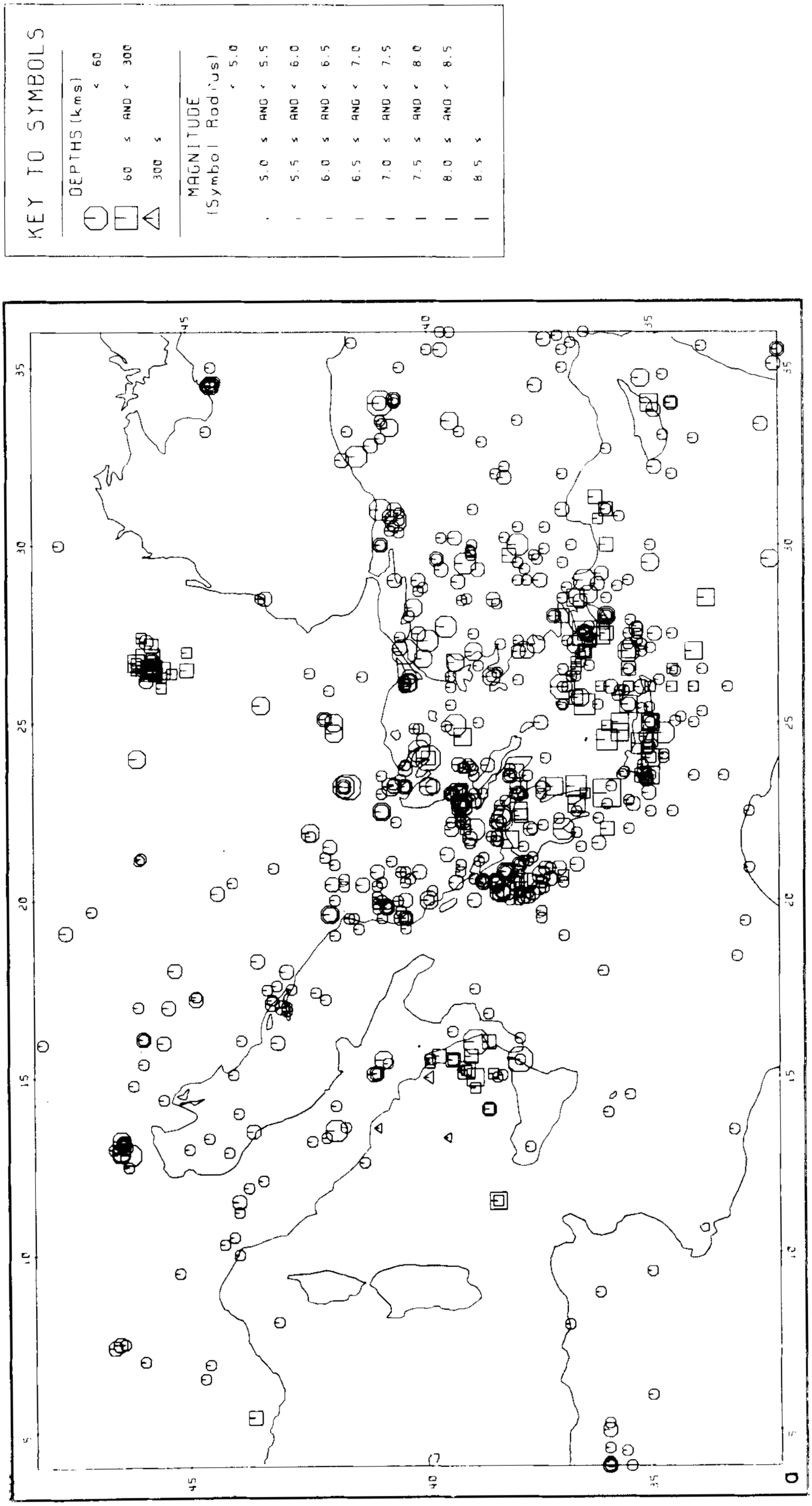

Figure 1. (a) Seismicity of the Central and Eastern Mediterranean area. Only those events of $M_S \geqslant 5$ are shown for economy of plotting. The tectonic interaction is composed of a collision between Africa and Eurasia, with seismic energy being released mainly along the arcuate trend of the Hellenic arc south and west of Greece.

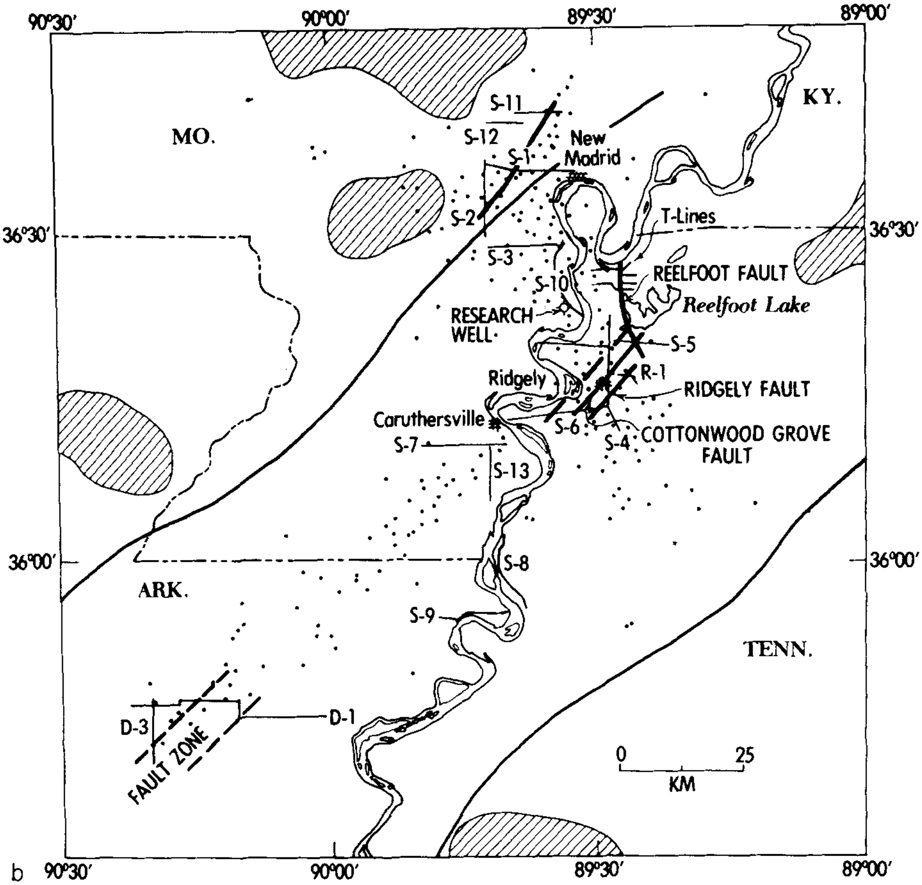

Figure 1. (b) Tectonic setting of the area around the New Madrid seismic zone (after Zoback *et al.* 1980), showing microearthquake epicentres (dots), locations of seismic profiles (e.g. S-7) and principal faults inferred from the data. The continuous heavy black lines are rift boundaries, and igneous plutons are represented by the hatched areas. There are three main seismicity trends: (1) a 100 km long stretch running SW–NE from the SW corner, (2) a section running SSE–NNW at the terminus of (1), and (3) the smallest trend SW–NE near New Madrid. Copyright 1980 by the American Association for the Advancement of Science.

corrected to what is, in effect, Kanamori's (1978) M_W on a global level then (1) is the best description of world seismicity, but concede that there are no convincing theoretical arguments for such linearity. There are, moreover, several examples of non-linearity below the threshold of curvature due to instrumental saturation when events on a more local scale are grouped together as well as a solid body of theoretical and experimental backing for such behaviour (for references see the Introduction). It may well be that the linearity observed on a global scale is due to the *superposition* of many curved distributions. For example Duda (1965) and Makropoulos (1978) found a poor fit to (1) and (8) respectively for the Aleutians–Alaska arc. Båth (1981b) and Singh, Rodriguez & Esteva (1983) have also observed such behaviour in Turkey and Mexico. A further example is cited in this paper. In many cases the superposition of two or more earthquake populations offer a plausible explanation for this apparently anomalous behaviour.

For this reason care has been taken in the following section to investigate any possible curvature which may result from such instrumental saturation. In effect, this would amount to using Chinnery & North's (1975) empirical method for converting from M_S to a seismic moment magnitude, M_w – a much more meaningful description of the 'size' of the seismic source. For the areas considered in the present work this turns out to be unnecessary.

It is not even clear that such correction is always appropriate, since Kanamori's (1977) tabulation of M_S/M_w for large events shows that M_S is commonly greater than M_w for large events – the opposite effect of that of saturation. This anomaly may be ironed out as more data become available, but can be partially included in the method of line fitting by assuming an uncertainty in each magnitude value of the same order as any saturation

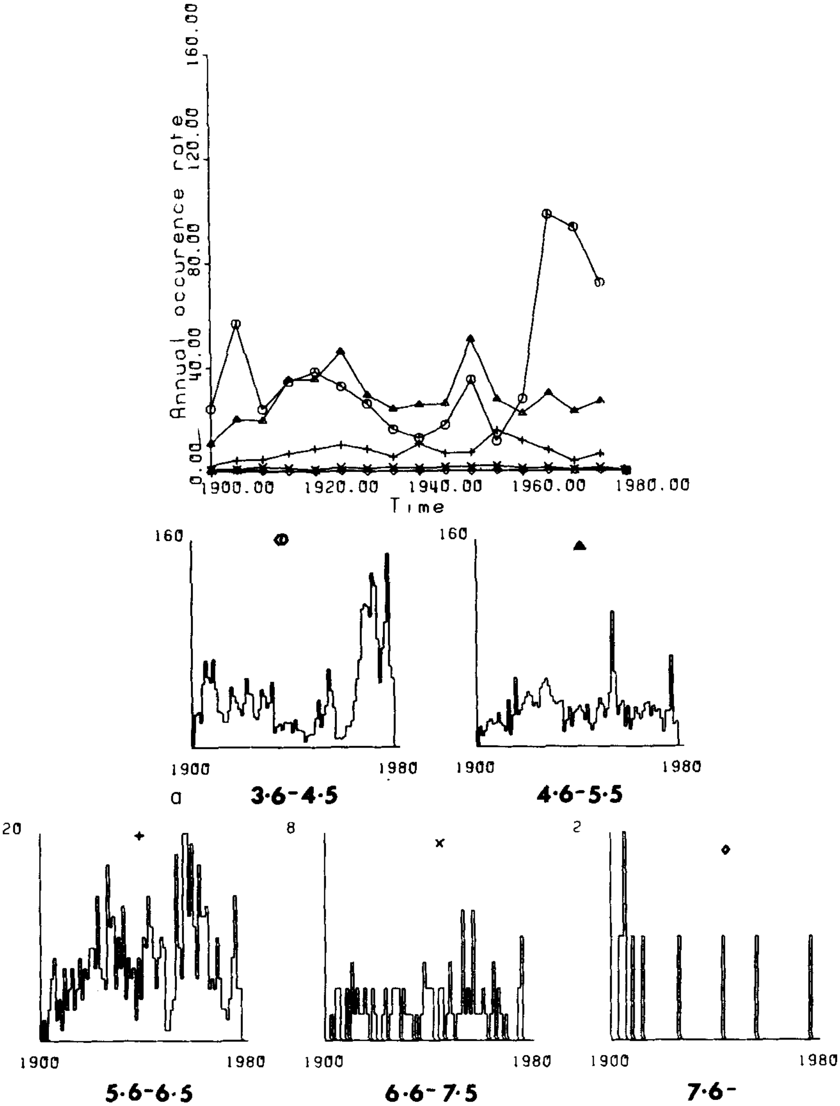

Figure 2 – (a)

Figure 2. Completeness testing. (a) The Central and Eastern Mediterranean. The roughly constant frequency of events in the range (4.6, 5.5) since 1920 or so, compared to the sudden jump in the range (3.6, 4.5) around 1963 indicates that the former is complete for the time span analysed (1943–1971). (b) Southern California. Again the roughly constant frequency of events in (4.0, 4.9) indicates a completeness threshold of 4.0.

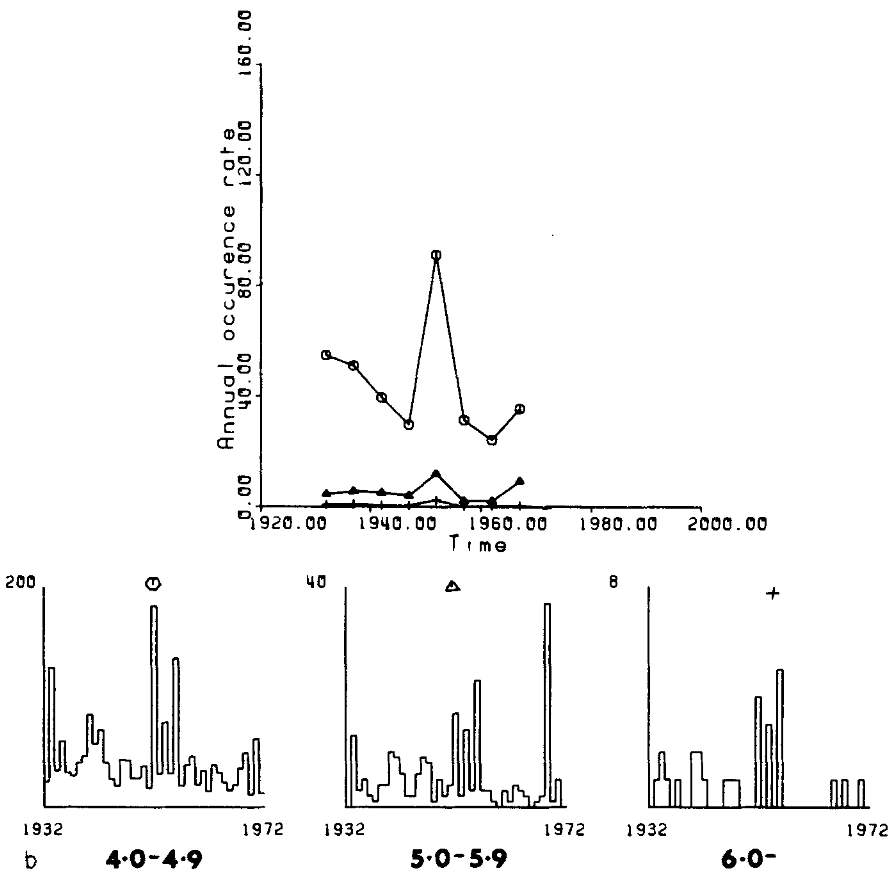

Figure 2 – (b)

correction. In the present work this value is taken to be ±0.5 of a magnitude unit, which includes estimates of measuring uncertainty, conversion to seismic moment as well as possible saturation effects in the final value of $\dot{M}_0$.

Results and discussion

Empirical line fits to establish $\dot{M}_0(\omega, u, \lambda, A, B)$ were attempted for four diverse tectonic regions: (a) the Central and Eastern Mediterranean, (b) the New Madrid seismic zone, (c) Southern California, and (d) mainland UK. The results are summarized in Tables 1 and 2 and in Figs 1–4. This section investigates in detail the areas tentatively assessed in Main & Burton (1981).

(a) THE CENTRAL AND EASTERN MEDITERRANEAN (32°–48°N, 4°–36°E)

North (1977) has tabulated seismic moment values for this area of diffuse, plate boundary seismicity. From his table 4 the total seismic moment released in this area for the period 1943–1971 was 70×10^{26} dyne cm or a rate $\dot{M}_0 = 24 \times 10^{25}$ dyne cm yr^{-1}. A more complete picture from 1963–1970 (his table 1) gives a rate 46×10^{25} dyne cm yr^{-1} which may be regarded as a minimum value.

A seismicity map of the area concerned is given in Fig. 1(a) and an excellent summary of the complex geo-tectonic setting is given in Horvath & Berckhemer (1982). The histograms of Fig. 2(a) show that the catalogue used (Burton 1978) is complete for the time range analysed (1943–1971) above mag 4.5. The range (3.6, 4.5) is not complete – as can be

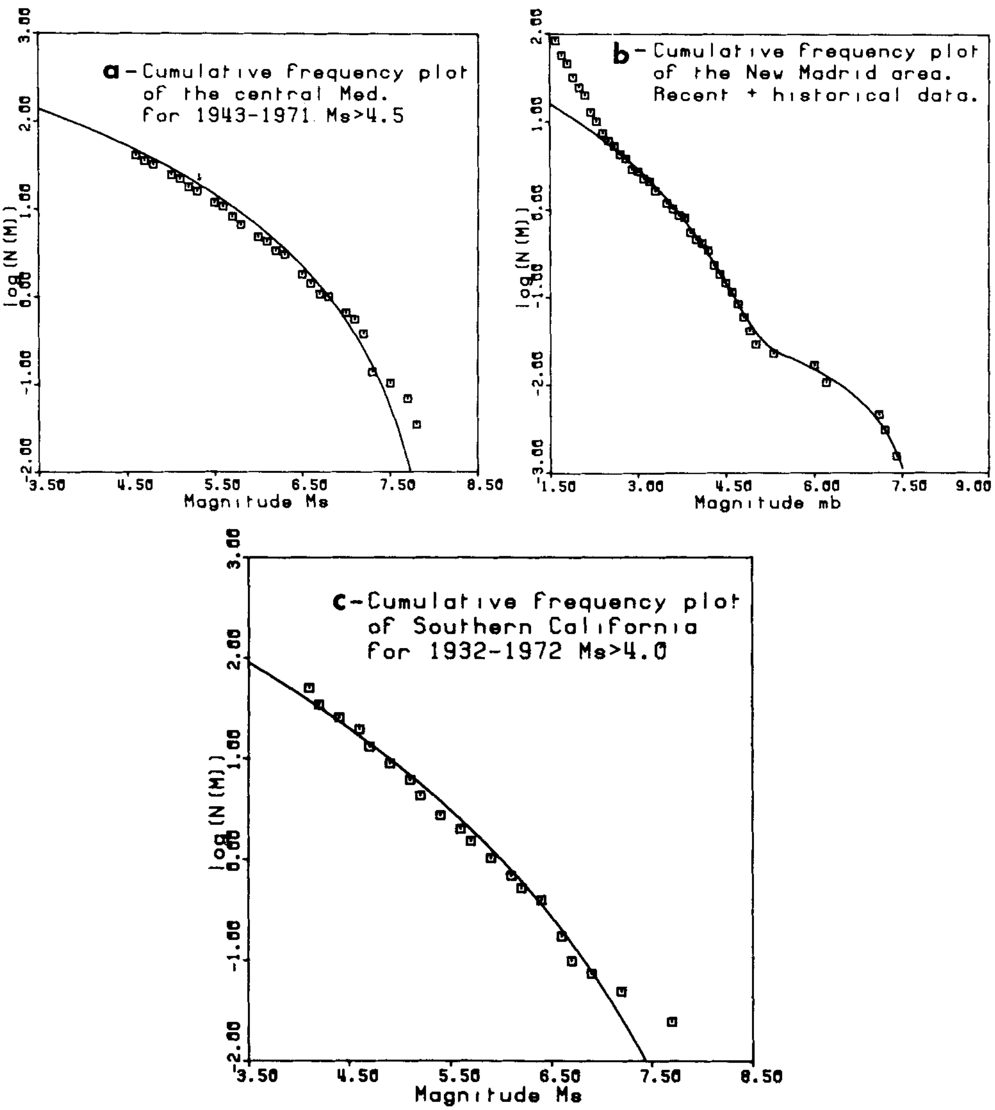

Figure 3. Cumulative frequency line fits to the distribution $N(m) = [(\omega - m)/(\omega - u)]^{1/\lambda}$. The parameters and their covariance error matrices are given in Table 1. (a) The Central and Eastern Mediterranean. In this case there seems to be a high autocorrelation error – there being a systematic trend in the positioning of the data points relative to the line. It would be difficult to justify a linear fit of the form (1) in this case, the curvature being so marked at high magnitudes. (b) The New Madrid area. Here the most successful fit was obtained by splitting the magnitude range into two segments – above and below 5, and fitting the line separately. The New Madrid events were repositioned at average repeat times $T = 650$ years ($N = 1/T$). (c) Southern California. In this case the line fit seriously underestimates the occurrence rate of the largest events which have occurred. A line fit of the form (1) would in this case give a better fit at these magnitudes, but again there seems to be some evidence of a bimodal distribution, the ranges meeting at $M_L \approx 6.7$ or so.

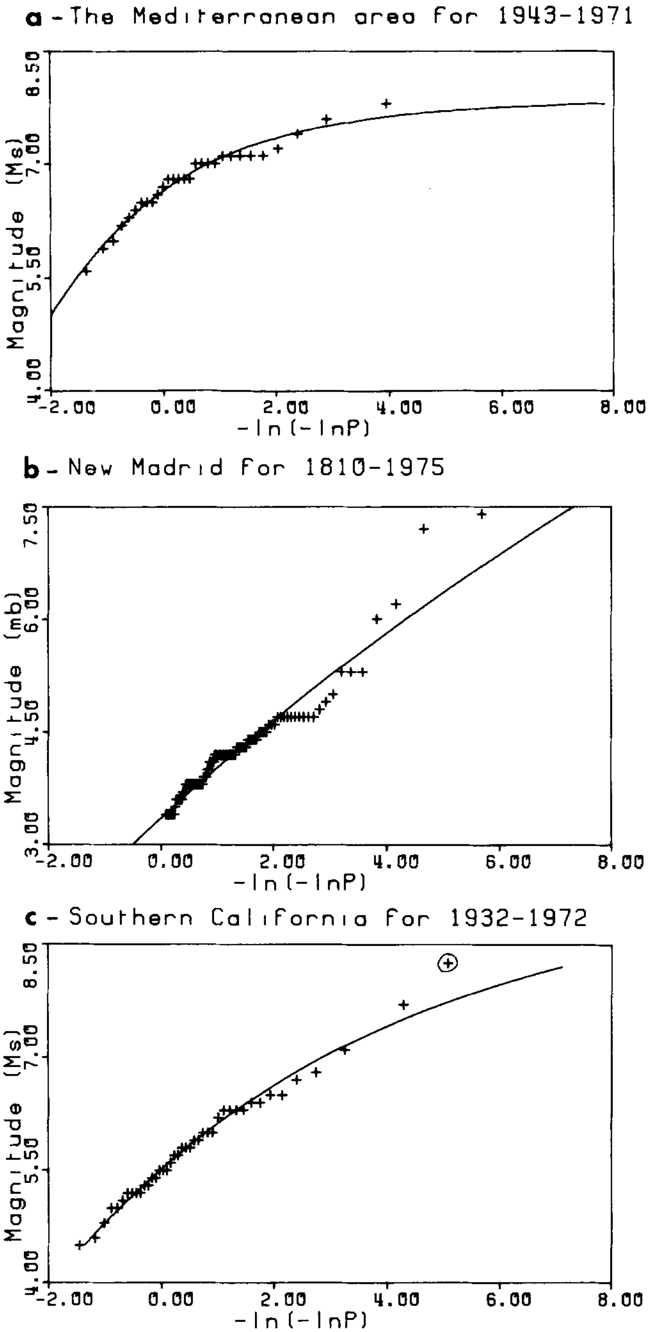

Figure 4. Extreme value line fits to the distribution $P = \exp\{-[(\omega - m)/(\omega - u)]^{1/\lambda}\}$. The parameters and their covariance error matrices are given in Table 2. (a) The Central and Eastern Mediterranean. Curvature and a maximum magnitude are well established. (b) The New Madrid area. The line fit is effectively straight – implying a moment release rate which is deterministically several orders of magnitude too high. A bimodal distribution as in Fig. 3(b) is apparent, but in this case the data could not be separated into the two portions successfully, because of their scarcity in the higher range. (c) Southern California. The curvature is enhanced compared to Fig. 3(c), but again the occurrence of the largest magnitudes is underestimated. The ringed data point has been inferred from Sieh's (1978) work which indicates $M_S = 8.25$ and $T = 163$ yr, with $P = 1 - 1/T$.

Table 1. Moment release rates predicted by cumulative frequency line fits to $N(m) = [(\omega - m)/(\omega - u)]^{1/\lambda}$ (model I and Fig. 3).

Area*		Parameters (ω, u, λ)	Covariance error matrix ϵ			Local values for A, B		$\bar{\dot{M}}_0(\omega, u, \lambda, A, B)$ $\times 10^{25}$ dyne cm yr^{-1}	$\dot{M}_0$ observed or estimated $\times 10^{25}$ dyne cm yr^{-1}
(a)		(8.16, 6.80,	0.855	−0.031	−0.119				
		0.251)	−0.031	0.018	0.008	16.0	1.5	87^{+110}_{-48}	⩾46
		M_S	−0.119	0.008	0.018				
(b)	Range	(7.81, −23.4,	1.43	71.1	−0.752				
	(5.0, 7.5)	0.680)	71.1	4179.0	−42.5	15.58	1.5	$1.2^{+12}_{-1.1}$	≈0.6
		$m_b^\dagger$	−0.752	−42.5	0.437				
(b)	Range	(5.61, 3.63,	1.00	−0.084	−0.154				
	(2.5, 5.0)	0.263)	−0.084	0.019	0.015	15.58	1.5	$4.0^{+23.5}_{-3.4}$	≈10^{-4}–10^{-2}
		$m_b^\dagger$	−0.154	0.015	0.025			($\times 10^{-4}$)	
(c)		(9.26, 6.00,	9.54	−0.304	−0.340				
		0.126)	−0.304	0.026	0.012	15.83	1.5	8^{+26}_{-6}	≈16
		M_S/M_L	−0.340	0.012	0.012				

* Areas are: (a) the Central and Eastern Mediterranean, (b) the New Madrid seismic zone, and (c) Southern California.
† Refer to text for m_b/M_S conversion.

Table 2. Moment release rates predicted by extreme value line fits to $P(m) = \exp[-(\omega - m)/(\omega - u)]^{1/\lambda}$ (model II and Fig. 4).

Area*		Parameters (ω, u, λ)	Covariance error matrix ϵ			Local values for A, B		$\dot{M}_0(\omega, u, \lambda, A, B)$ $\times 10^{25}$ dyne cm yr^{-1}	$\dot{M}_0$ observed or estimated $\times 10^{25}$ dyne cm yr^{-1}
(a)		(7.84, 6.64,	0.484	−0.044	−0.200				
		0.435)	−0.044	0.014	0.021	16.0	1.5	43 + 26	⩾46
		M_S	−0.200	0.021	0.093			−16	
(b)	Range	(19.4, 3.36,	1123.00	2.54	−3.20				
	(3.0, 7.5)	0.042)	2.54	0.013	−0.007	15.58	1.5	–	≈0.6
		$m_b^\dagger$	−3.20	−0.007	0.009				
(c)		(9.11, 5.46,	3.70	−0.062	−0.219				
		0.182)	−0.062	0.008	0.004	15.83	1.5	8.5 + 16.2	≈16
		M_S/M_L	−0.219	0.004	0.013			−5.6	
(d)		(5.46, 4.58,	0.190	−0.026	−0.134				
		0.59)	−0.026	0.015	0.026	15.7	1.5	2.2 + 1.0	≈34
		$m_b^\dagger$	−0.134	0.026	0.113			−0.7	($\times 10^{-3}$)
								($\times 10^{-3}$)	

* Areas are: (a) the Central and Eastern Mediterranean, (b) the New Madrid seismic zone, (c) Southern California, and (d) mainland UK.
† Refer to text for m_b/M_S conversion.

inferred from the sudden jump in the number of events reported on introduction of the WWSSN network in 1963. Fig. 3(a) shows the cumulative frequency line fit to these data and Fig. 4(a) the Gumbel plot, both of whose parameters were calculated using the method described in Burton (1979). The parameters and covariance errors (which include an allowance for ±0.5 uncertainty in the magnitude measurement) can be seen in Tables 1 and 2. Note that in some cases the actual values of (ω, u, λ) for N and P differ slightly as expected by Makjanik (1980).

To convert to moment release rates we refer to North's table 4 again, where we find for this area that an average stress drop is 38 bar. This converts to $A = 16.0$ using Singh & Havskov's (1980) formulation, and with $B = 1.5$ leads to a good linear fit to North's (1974) fig. 4, right up to the highest magnitudes. This last point indicates that there appears to be no instrumental saturation effect.

Both predictions of the moment release rates agree with that expected to within a factor 2 or so, which is in both cases within the expected uncertainty. This consistency, where we have reasonable error in (ω, u, λ) and some knowledge of a local stress drop or A value shows that the model proposed is quantitatively adequate well within the limits of statistical uncertainty.

Further inspection of this uncertainty shows the following relative effects of the three Gumbel parameters

$$\frac{\partial\langle \dot{M}_0\rangle}{\partial\omega} : \frac{\partial\langle \dot{M}_0\rangle}{\partial u} : \frac{\partial\langle \dot{M}_0\rangle}{\partial\lambda} = 1.3:1:1.8$$

$$\frac{\partial\langle \dot{M}_0\rangle}{\partial\omega}\sigma_\omega : \frac{\partial\langle \dot{M}_0\rangle}{\partial u}\sigma_u : \frac{\partial\langle \dot{M}_0\rangle}{\partial\lambda}\sigma_\lambda = 7.7:1:14.7.$$

This result shows that u is the best-determined parameter and that ω and λ have a dominant effect on the total uncertainty in this case. This effect is tempered by their interdependence already discussed above, and highlights the need to include the off-diagonal elements of the covariance error matrix in any attempt to quantify an error in $\langle \dot{M}_0\rangle$.

Finally, note from the tables that the error in $\langle \dot{M}_0\rangle$ is less than that for $\bar{\dot{M}}_0$ (60 per cent compared with 126 per cent).

The comments of the last three paragraphs were all found to apply qualitatively to the following areas of study, the actual values being quoted in this subsection for illustration only.

(b) THE NEW MADRID SEISMIC ZONE (35°–37°N, 89°–90.5°W)

This area of mid-plate seismicity has received much attention in recent years for reasons both practical and theoretical. Zoback *et al.* (1980) summarized the available geological and geophysical data, and concluded that the area consists of three main seismic trends (see Fig. 1b), set in a reactivated graben structure. Why the seismicity should largely follow the axis of the graben is not clear.

Practical interest is stimulated by the possibility of a repeat of the 1811–1812 sequence of major events (m_b 7.1–7.4) in an area of relatively low seismic attenuation and high population density, and theoretical interest comes from the breakdown of the classical theory of rigid plate tectonics. Because the seismicity trends are situated in a zone primarily of EW compression (Zoback & Zoback 1980) we would expect right lateral strike-slip motion along the trends (1) and (3) of Fig. 2(b) and thrust on section (2). Russ (1981) showed that this is borne out to a large extent by the few fault plane solutions available, and that section (2) may result from reactivated dip-slip faulting. Together with Schilt & Reilinger (1981), he also indicates that such evidence as there is favours 5 mm yr^{-1} of uplift occurring in and around the northern part of the active zone. There is some evidence that some of this motion is taken up by aseismic creep since earthquakes in Schilt & Reilinger (1981) did not produce enough movement to account for all of the uplift detected in a later levelling survey.

The catalogues analysed are described by Nuttli (1979) and Johnston (1981) quoting m_b values inferred from macroseismic intensities and recent microseismic data, so there are no problems associated with instrumental saturation. All events from Johnston's (1981) data set for $m_b > 2.5$ were included in the analysis. The most successful line fit came from considering the range (2.5, 5.0) and (5.0, 7.5) separately as in Fig. 3(b), which plots the superposition of these two separate distributions. There may also be a third component in the range of (1.6, 2.5). This superposition can also be seen in the extreme value case (Fig. 4b), but due to the scarcity of data in the higher portion the two ranges cannot be separated. In this case the line fit is effectively straight, even though systematic bimodal curvature is evident from the figure. For this reason no realistic $\dot{M}_0$ could be obtained with the impossibly high value of ω obtained in Table 2(b).

In arriving at the entries in Table 1(b) for $\dot{M}_0$ the magnitude conversions

$$M_s = 1.59\, m_b - 3.97 \qquad 6.5 < M_s < 8.0 \tag{20}$$

$$M_s = 1.93\, m_b - 4.8 \qquad 4.0 < M_s < 6.0 \tag{21}$$

from results summarized in Marshall (1970) were used to match the ranges above and below 5.0 respectively. There is some evidence that the stress drops in this area are relatively high, so a value $\Delta\sigma = 100$ bar was chosen to define A via Singh & Havskov's (1980) formulation. Considering the large error involved in converting from epicentral intensities I_0 to m_b (Burton, Main & Long 1983) and then to M_S it is not surprising that the final error quoted in $\dot{M}_0$ is as high as a factor 10 or so.

In Fig. 3(b) for the range $m_b > 5.0$ the largest events ($m_b > 7$) were moved to positions consistent with average repeat times of 650 years (Russ 1981). This gave agreement within a factor 2 with the estimated moment release rate from three fault areas modelled as one fault 20 km deep (Nuttli & Herrmann 1978) by 200 km long moving at 0.5 cm yr^{-1}, if $\mu = 3 \times 10^{11}$ dyne cm^{-2}.

For the range (2.5, 5.0), using a circular fault model (Kanamori & Anderson 1975) the maximum fault size (for $\omega = 5.6$) was found to be $\approx 150\,\text{km}^2$, with $\dot{s} \approx 9 \times 10^{-2}$ mm yr^{-1}. This typical movement on what are supposed to be a collection of several subsidiary faults compares favourably with that observed on one such fault ($\sim 1.2 \times 10^{-2}$ mm yr^{-1} from Zoback *et al.* 1980) on the Cottonwood Grove fault. We can see that the seismicity represented by the range (2.5, 5.0) contributes only a minor fraction of the stress release.

The conclusion here is that bumps in the cumulative frequency distribution have been numerically related to the superposition of two different orders of observed faulting.

(c) SOUTHERN CALIFORNIA (31°–38°N, 114.5°–121°W)

This well-researched area of high seismicity on a plate boundary is very different from the previous example. It includes the site of the 1952 Kern Co event and the 1971 San Fernando earthquake, as well as the 400 km long 'locked zone' which previously ruptured in 1857 with an estimated M_S of 8.25 or greater and an average repeat time of 163 yr (Sieh 1978).

The catalogue used was that of Hileman, Allen & Nordquist (1973), whose publication also gives excellent maps of the seismicity and the tectonic setting. The analysis of Fig. 2(b) shows that for the period concerned (1932–1972) magnitudes above 4.0 or so are completely reported.

Anderson (1979) indicated a moment release rate of 12×10^{25} dyne cm yr^{-1} for a 500 km long fault, but this catalogue contains a 650 km stretch of the San Andreas fault and its offshoots, so $\dot{M}_0 \approx 16 \times 10^{25}$ dyne cm yr^{-1} may be more appropriate. These figures assume a depth of the brittle zone of 15 km and $\mu \approx 3 \times 10^{11}$ dyne cm^{-2}, with a movement from plate tectonic constraints of 5.5 cm yr^{-1}. Since the movement on surface faults is of the order 1–3.7 cm yr^{-1} the deformation must taken place in a broad zone around the main fault trend.

Fitting the Weibull distribution to the data proved to be unsuccessful above magnitude 6.7 (Fig. 3c). The line fit seems to follow curvature apparent in the range (4.0, 6.7) and seriously underestimates the occurrence of the highest magnitudes. It may be that the activity above 6.7 is a separate distribution as in the New Madrid area, but with only three or four data points this cannot be tested from the current catalogue. Singh & Havskov (1980) give $A = 15.83$ for this area, which implies a moment release rate of the right order only at the expense of allowing a value for ω of 9.3 – one magnitude higher than Sieh's (1978) deterministic estimate.

Hanks, Hileman & Thatcher (1975) indicate that M_0 for the Kern Co (1952) event was 200×10^{25} dyne cm and $M_S = 7.7$. Using $A = 15.83$, we find $M_w = 7.65$ so there are no grounds for supposing instrumental saturation is important.

The extreme value line fit (Fig. 4c) gives a similar value for ω, but u is significantly different (even considering its error). Curvature does seem to be enhanced by this method (higher value for λ) but once more there is a poor fit at the highest magnitudes and the possibility of two separate curved distributions is evident. The ringed data point is inferred from Sieh's (1978) estimates of M_S and the average repeat time T, with $T = 1/(1-P)$. As in sections (a) and (b) the moment release rates inferred from the line fit are in agreement with those observed within a factor less than the estimated uncertainty (a factor of 2, cf. 3 or 4) but in this case it is evident that the parameters of the line fit may be significantly improved upon.

(d) MAINLAND UK

This area of relatively low intraplate seismicity differs from the New Madrid area in that no catastrophic events are documented in historical times. Burton (1981) analysed the area in terms of the third distribution of extreme values and produced the (ω, u, λ) set in Table 2(d). The unit time for this set was 6 yr. The m_b/M_s relation (21) is thought appropriate because of the typical range of events.

Using equation (12) $M_{0\omega} = 2.0 \times 10^{24}$ dyne cm for $A = 15.7$ for an intraplate area, and if we model this as a circular fault via (19) the maximum fault area would be ≈ 350 km^2 for a corresponding typical stress drop of 76 bar. Since $\langle \dot{M}_0 \rangle = 2.2 \times 10^{22}$ dyne cm yr^{-1} and $\mu = 3 \times 10^{11}$ dyne cm^{-2}, a typical fault movement of 0.2 mm yr^{-1} is expected.

Unfortunately there is very little direct tectonic information as yet on UK seismicity. However, King's (1980) results showed that the fault area for the Carlisle event of 1979 December 26 was of the order of 40 km^2 for an event of m_b 5.0. Very little information exists on contemporary fault movement rates, although some unconfirmed evidence of surface movement directly following glacial unloading does exist (Sissons & Cornish 1982). The thrust mechanism of the Carlisle event (King 1980), and the strike-slip solution for the

Kintail earthquake swarm of 1974 (Assumçao 1981) are both compatible with compressive intraplate tectonics.

King (1980) assumes $\Delta\sigma = 30$ bar might be appropriate for the UK. In this case $A = 16.1$, $M_{0\omega} = 5.13 \times 10^{24}$ dyne cm, the maximum fault area $= 1200\,\text{km}^2$, $\dot{s} = 0.06\,\text{mm yr}^{-1}$. King's results are consistent in themselves, but if $\Delta\sigma = 30$ bar, we should expect fault planes of an order higher than those which have been observed so far. A more realistic picture might be to interpret the maximum fault area as representing a sum of several smaller faults of the order of tens of km^2, moving at rates $\approx 0.1\,\text{mm yr}^{-1}$. This speculative interpretation is compatible with the spread of UK seismicity around small, localized centres such as at Comrie and in pockets in the north-west of England and South Wales, and the absence of catastrophic events such as in the New Madrid area.

A deterministic estimate of the movement between the sinking south of England and the relative uplift consistent with glacial unloading of the north of England and Scotland is $1.5\,\text{mm yr}^{-1}$ (Rossiter 1972). If the depth of the UK seismogenic zone is ~ 5 km, and its width is modelled as of the order 200 km, then $A \approx 1000\,\text{km}^2$ and $\dot{M}_0 \approx 3.4 \times 10^{23}$ dyne cm yr^{-1}. This area favours King's choice of $\Delta\sigma$ and comparison of the values of $\dot{M}_0$ and $\langle \dot{M}_0 \rangle$ indicate that over 90 per cent of the observed movement occurs aseismically.

Conclusion

In most cases where moment release rates were available the distributions N and P successfully modelled both the observed curvature at high magnitudes and the predicted moment release rates from models I and II. The exceptions tended to be in areas where there was evidence that the distribution was bimodal – being most striking in the New Madrid area (Fig. 4b).

Careful quantitative comparison of $\dot{M}_0 \pm \delta\dot{M}_0$ can be used as a method of distinguishing areas where the line fit is deficient at the higher magnitudes. Incorporation of deterministic values for the maximum magnitude (from seismicity trends or geological zoning), and geological estimates of their average repeat times will also improve the quality of the line fit at these magnitudes as better quality data become available.

Typical uncertainties in $\dot{M}_0$ were found to be a factor of 2–4 or so, with the Gumbel estimates giving slightly lower uncertainties, and agreement within this range with observed moment release rates from (1) a short-term catalogue for an internal consistency check in the Mediterranean and (2) long-term geological estimates in Southern California is encouraging.

A serious drawback of the distribution used is that $n(\omega) = 0$. For a cyclic input and release of strain energy we might expect $n(\omega)$ to be some non-zero value, implying a repeat time $T = 1/N(m)$ which is not infinite as $m \to \omega$. Work is currently progressing in this area to generalize (2) to allow curvature in the density distribution without requiring $n(\omega) = 0$. This will imply a less severe curvature at magnitudes just below ω, and thereby offset the underestimation of observed occurrence rates to which the Weibull and Gumbel's third distribution seems to be prone.

Acknowledgments

This work was supported by the Natural Environment Research Council and is published with the approval of the Director of the British Geological Survey (NERC). We are also indebted to Dr Arch Johnstone of the Tennessee Earthquake Information Centre for providing the cumulative frequency data used to plot Fig. 3(b).

References

Assumçao, M., 1981. The NW Scotland swarm of 1974, *Geophys. J. R. astr. Soc.*, **67**, 577–586.

Anderson, J. G., 1979. Estimating the seismicity from geological structure for seismic risk studies, *Bull. seism. Soc. Am.*, **69**, 135–158.

Båth, M., 1981a. Earthquake magnitude – recent research and current trends, *Earth Sci. Rev.*, **17**, 315–398.

Båth. M., 1981b. Earthquake recurrence of a particular type, *Pageoph*, **119**, 1063–1076.

Botti, L. G., Pasquale, V. & Anghinolfi, M., 1980. A new general frequency-magnitude relationship, *Pageoph*, **119**, 196–206.

Burridge, R. & Knopoff, L., 1967. Model and theoretical seismicity, *Bull. seism. Soc. Am.*, **57**, 341–371.

Burton, P. W., 1978. The IGS file of seismic activity and its use for hazard assessment, *Seism. Bull. Inst. geol. Sci.*, No. 6, HMSO, London.

Burton, P. W., 1979. Seismic risk in Southern Europe through to India examined using Gumbel's third distribution of extreme values, *Geophys. J. R. astr. Soc.*, **59**, 249–280.

Burton, P. W., 1981. Variation in seismic risk parameters in Britain, *Proc. 2nd int. Symp. Anal. Seismicity and Seismic Hazard*, Vol. 2, pp. 495–530, Liblice, Czechoslovakia, May 18–23, Academia, Prague.

Burton, P. W., McGonigle, R. W., Makropoulos, K. C. & Ucer, S. B., 1982. Preliminary studies of seismic risk in Turkey, and the occurrence of upper bounded and other large earthquake magnitudes, *Proc. int. Symp. Earthquake Prediction in the North Anatolian Fault Zone*, Istanbul, Turkey, 1980 March 31–April 5, in *Multidisciplinary Approach to Earthquake Production*, pp. 143–172, eds Mete Isikara, A. & Vogel, Andreas, Braunschweig, Wiesbaden, Vieweg.

Burton P. W., Main, I. G. & Long, R. E., 1983. Perceptible earthquakes in the central and eastern U.S., *Bull. seism. Soc. Am.*, **73**, 497–518.

Caputo, M., 1977. A mechanical model for the statistics of earthquakes, magnitude, moment and fault distribution, *Bull. seism. Soc. Am.*, **67**, 849–861.

Chinnery, M. A. & North, R. G., 1975. The frequency of very large earthquakes, *Science*, **190**, 1197–1198.

Cornell, A. & Vanmarcke, E., 1969. The major influences on seismic risk, *Proc. 4th W.C.E.E.*, Santiago, Chile.

Cosentino, P. & Luzio, D., 1976. A generalisation of the frequency magnitude relation in the hypothesis of a maximum regional magnitude, *Annali Geophis.*, **4**, 3–8.

Duda, S. J., 1965. Secular seismic energy release in the Circum-Pacific Belt, *Tectonophys.*, **2**, 409–452.

Gumbel, E., 1958. *Statistics of Extremes*, Columbia University Press, New York.

Hanks, T. C., Hileman, J. A. & Thatcher, W., 1975. Seismic moments of the larger earthquakes of the Southern California region, *Bull. geol. Soc. Am.*, **86**, 1131–1139.

Hileman, J. A., Allen, C. R. & Nordquist, J. M., 1973. Seismicity of the Southern California region 1st Jan. 1932 to 31st Dec. 1972, *Contr. Div. Geol. planet. Sci., Calif. Inst. Techn., No. 2385.*

Horvarth, F. & Berckhemer, H., 1982. Mediterranean back-arc basins, *Alp. Med. Geol. Ser.*, **7**, 141–173.

Howell, B. F., (Jr), 1981. On the saturation of earthquake magnitude, *Bull. seism. Soc. Am.*, **71**, 1401–1422.

Jenkinson, A. F., 1955. The frequency distribution of the annual maximum or minimum values of meteorological elements, *Q. Jl R. met. Soc.*, **87**, 158–171.

Johnston, A. C., 1981. On the use of the frequency–magnitude relation in earthquake risk assessment, *Proc. Conf. Earthquakes and Earthquake Engineering – the Eastern U.S.*, pp. 161–181, Vol. I, ed. Beavers, J., Ann Arbor Science Ltd., the Butterworth group.

Kanamori, H., 1977. The energy release in great earthquakes, *J. geophys. Res.*, **82**, 2981–2987.

Kanamori, H., 1978. Quantification of earthquakes, *Nature*, **271**, 411–414.

Kanamori, H. & Anderson, D. L., 1975. Theoretical bases of some empirical relations in seismology, *Bull. seism. Soc. Am.*, **65**, 1073–1095.

King, C., 1975. Model seismicity and faulting parameters, *Bull. seism. Soc. Am.*, **65**, 245–259.

King, G., 1980. A fault plane solution for the Carlisle earthquake, 26 December 1979, *Nature*, **286**, 142–143.

Knopoff, L. & Kagan, Y., 1977. Analysis of the theory of extremes as applied to earthquake problems, *J. geophys. Res.*, **82**, 5647–5657.

Kuznetsova, K. I., Shumilina, L. S. & Zavialov, A. D., 1981. The physical sense of the magnitude–

frequency relation, *Proc. 2nd int. Symp. Analysis of Seismicity and on Seismic Hazard,* Vol. 1, pp. 27–46, Liblice, Czechoslovakia, 1981 May 18–29, Academia, Prague.

Main, I. G. & Burton, P. W., 1981. Rates of crustal deformation inferred from seismic moment and Gumbel's third distribution of extreme values, *Proc. Conf. Earthquakes and Earthquake Engineering – the Eastern U.S.,* Vol. 2, pp. 937–951. ed. Beavers, J., Ann Arbor Science Ltd, the Butterworth group.

Makjanik, B., 1980. On the frequency distribution of earthquake magnitude and intensity, *Bull. seism. Soc. Am.,* **70,** 2253–2260.

Makropoulos, K. C., 1978. The statistics of large earthquake magnitude and an evaluation of Greek Seismicity, *PhD thesis,* University of Edinburgh.

Marshall, P. D., 1970. Aspects of the spectral differences between earthquakes and underground explosions, *Geophys. J. R. astr. Soc.,* **20,** 397–416.

North, R. G., 1974. Seismic slip rates in the Mediterranean and Middle East, *Nature,* **252,** 560–563.

North, R. G., 1977. Seismic moment, source dimensions and stresses associated with earthquakes in the Mediterranean and Middle East, *Geophys. J. R. astr. Soc.,* **48,** 137–162.

Nuttli, O. W., 1979. Seismicity of the Central United States, *Geol. Soc. Am. Rev. Engrg. Geol.,* **IV,** 67–93.

Nuttli, O. W. & Herrmann, B., 1978. Creditable earthquakes for the central U.S, *State of the art for assessing earthquake hazards in the U.S., U.S. Army Engrng. Wat. Ways Exp. Station, Rep. 12, paper S-73-1.*

Papastamatiou, D., 1980. Incorporation of crustal deformation to seismic hazard analysis, *Bull. seism. Soc. Am.,* **70,** 1321–1335.

Rossiter, J. R., 1972. Sea level observations and their secular variation, *Phil. Trans. R. Soc.,* **272,** 131–139.

Russ, D. P., 1981. Model for assessing earthquake potential and fault activity in the New Madrid seismic zone, *Proc. Conf. Earthquakes and Earthquake Engineering – the Eastern U.S.,* Vol. 1, pp. 309–335, ed. Beavers, J., Ann Arbor Science Ltd, the Butterworth group.

Schilt, F. S. & Reilinger, R. E., 1981. Evidence for contemporary vertical fault displacement near the New Madrid zone, *Bull. seism. Soc. Am.,* **71,** 1933–1942.

Scholz, C. H., 1968. The frequency-magnitude relation of microfracturing in rock and its relation to earthquakes, *Bull. seism. Soc. Am.,* **58,** 399–415.

Sieh, K. E., 1978. Prehistoric large earthquakes produced by slip on the San Andreas fault at Pallet Creek, California, *J. geophys. Res.,* **83,** 3907–3939.

Singh, S. K. & Havskov, J., 1980. On moment magnitude scale, *Bull. seism. Soc. Am.,* **70,** 379–383.

Singh, S. K., Rodriguez, M. & Esteva, L., 1983. Statistics of small earthquakes and frequency of occurrence of large earthquakes along the Mexican subduction zone, *Bull. seism. Soc. Am.,* **73,** 1779–1796.

Sissons, J. B. & Cornish, R., 1982. Rapid localised glacio-isostatic uplift at Glen Roy, Scotland, *Nature,* **297,** 213–214.

Weibull, W., 1951. A statistical distribution function of wide applicability, *J. appl. Mech.,* **18,** 293–297.

Yegulalp, T. M. & Kuo, J. T., 1974. Statistical prediction of the occurrence of maximum magnitude earthquakes, *Bull. seism. Soc. Am.,* **64,** 393–414.

Zoback, M. D., Hamilton, R. M., Crone, A. J., Russ, D. P., McKeown, F. A. & Brockman, S. R., 1980. Recurrent intraplate tectonism in the New Madrid seismic zone, *Science,* **209,** 971–976.

Zoback, M. L. & Zoback, M., 1980. State of stress in the conterminous United States, *J. geophys. Res.,* **85,** 6113–6159.

Geophys. J. R. astr. Soc. (1984) 79, 489–493

Spectral properties of the Newtonian potential field and their application in the interpretation of the gravity anomalies

M. Zadro *Istituto di Geodesia e Geofisica, University of Trieste, Via dell'Università N.7, Trieste 34100, Italy*

Received 1984 March 12; in original form 1984 February 20

Summary. Some spectral properties of the Newtonian potential field and of fields related to it by derivation processes are examined. Corresponding spectral techniques are proposed to treat several geophysical problems connected with the study of local gravity perturbation fields. In particular it is shown that, given the perturbing masses, such techniques allow the Bouguer and isostatic anomalies, the deflections of the vertical, as well as their upward and downward continuation, the geoidal height variations and, in general, the undulations of gravity equipotential surfaces, all to be obtained.

1 Introduction

Spectral techniques are already widely used in gravity interpretation problems, mostly for the separation of different wavelength bands in the gravity anomaly field and for the upward and downward continuation of the field itself.

Nowadays, owing to the availability of large-memory fast computers, more sophisticated spectral techniques may be usefully employed for the computation of the Newtonian potential field of a given perturbing mass distribution as well as the derivatives of the potential itself for any order of derivation and along any selected direction. Since the results are automatically available both inside and outside the perturbing mass, the method enables the Bouguer anomalies, the isostatic anomalies, their upward and downward continuation, the deflections of the vertical in the whole considered space, the geoidal height variations and, more generally, the undulations of gravity equipotential surfaces caused by the perturbing mass itself, all to be calculated.

The purpose of the present paper is to illustrate such techniques. The algorithms and the package of programs needed for geophysical applications are being developed and a second paper mainly concerned with the computational aspects is in preparation.

2 Spectral properties of the Newtonian fields in 3-D

The Newtonian potential $U(P)$ produced at a point P by a distribution of mass densities $\rho(P_0)$ with P_0 inside a certain volume V is given by

$$U(P) = G \int_V \frac{\rho(P_0)}{r}\, dv \tag{2.1}$$

where G is the gravitational constant and $r = |P_0 - P|$ in an x, y, z Cartesian orthogonal coordinate system.

The Newtonian force $g_t(P)$ exerted on a unitary point mass in P along the direction of the unit vector $\mathbf{t}$ is given by:

$$g_t(P) = \mathbf{t} \cdot \operatorname{grad} U(P). \tag{2.2}$$

The relationship (2.1) can be interpreted as a convolution product in the 3-D space:

$$U(P) = G \frac{1}{r} * F(P)$$

where

$$F(P) = \begin{cases} 0 \text{ for } P \text{ outside } V \\ \rho(P) \text{ for } P \text{ inside } V. \end{cases}$$

On taking Fourier transforms, it follows that:

$$\phi(\alpha, \beta, \gamma) = G\, \mathrm{FT}\left[\frac{1}{r}\right] \mathrm{FT}\,[F(P)] \tag{2.4}$$

where

$$\phi(\alpha, \beta, \gamma) = \mathrm{FT}[U(P)]$$

and α, β, γ are coordinates in the wavenumber space, corresponding to an x, y, z Cartesian coordinate system. Obviously the Fourier transforms $\mathrm{FT}[1/r]$ and $\mathrm{FT}[F(P)]$ are 3-D Fourier transforms.

As far as the $\mathrm{FT}[1/r]$ is concerned, the Fourier transform of a function of r only is a function of ν only, being $\nu = (\alpha^2 + \beta^2 + \gamma^2)^{1/2}$ (Sneddon 1951, pp. 63–65). Then (Watson 1962, pp. 391–392):

$$\mathrm{FT}\left[\frac{1}{r}\right] = \sqrt{\frac{\pi}{2}} \frac{1}{\nu^2} \tag{2.5}$$

so that

$$\phi(\alpha, \beta, \gamma) = G \sqrt{\frac{\pi}{2}} \frac{1}{\nu^2}\, \mathrm{FT}\,[F(P)]. \tag{2.6}$$

Let us now consider the 3-D Fourier transform $\psi(\alpha, \beta, \gamma)$ of the Newtonian force $g_t(P)$. Taking into account the relationship between the Fourier transform of the derivative of a function and the Fourier transform of the function itself,

$$\psi(\alpha, \beta, \gamma) = i\sigma\phi(\alpha, \beta, \gamma) \tag{2.7}$$

where σ is the wavenumber along the same direction in the α, β, γ coordinate system as the $\mathbf{t}$ vector in the original x, y, z space (Arsac 1961, pp. 116–119).

Therefore

$$\psi(\alpha, \beta, \gamma) = G\sqrt{\frac{\pi}{2}}\frac{i\sigma}{\nu^2}\ \mathrm{FT}[F(P)]. \tag{2.8}$$

More generally, it is evident that the Fourier transform of higher-order derivatives can be easily obtained by simply multiplying the function $\phi(\alpha, \beta, \gamma)$ by the products of the corresponding wavenumber and by $(-i)^k$, where k is the order of the derivative.

3 The 2-D case

The same rules apply to the 2-D, with the only modification that the FT$[1/r]$ becomes $1/\nu$. Obviously, in that case, the $F(P)$ density distribution is a planar one, $r = \sqrt{x^2 + y^2}$ and $\nu = (\alpha^2 + \beta^2)^{1/2}$.

Particular 3-D distributions can be treated by utilizing bidimensional techniques. Consider cylindrical distributions of masses, with $F(P) = F[(y^2 + z^2)^{1/2}]$, for $-\infty \leqslant x \leqslant +\infty$. In that case the 3-D FT$[F(P)]$ becomes zero everywhere in the α, β, γ wavenumber space, except on the $\alpha = 0$ plane, where it has the same values as the bidimensional FT of the plane distribution of masses on any plane x = constant, normal to the cylinder axis. Instead of

$$\phi(\beta, \gamma) = G\,\frac{1}{[\beta^2 + \gamma^2]^{1/2}}\,\mathrm{FT}[F(P)] \tag{3.1}$$

resulting from the 2-D case corresponding to the planar distribution, one obtains for the 3-D case:

$$\phi(\beta, \gamma) = G\sqrt{\frac{\pi}{2}}\,\frac{1}{\beta^2 + \gamma^2}\,\mathrm{FT}[F(P)]. \tag{3.2}$$

Looking at the convolution properties, it can be seen that on a profile normal to the cylinder axis, the 3-D potential corresponds to the convolution of the bidimensional potential with the $1/r$ (bidimensional) function.

4 Practical applications

The practical applications of the formulae above in the study of the gravity anomalies produced by perturbing masses are immediately evident when considering that the inverse Fourier transform of the functions $\phi(\alpha, \beta, \gamma)$ and $\psi(\alpha, \beta, \gamma)$ give the Newtonian potential and its derivative along a selected direction respectively. Higher-order derivatives may be easily computed using analogous procedures.

From the computational point of view the steps are as follows:

(a) The given perturbing density distribution has to be considered in a right rectangular prism with the base parallel to the horizontal (x, y) plane in such a way that a region of zero density borders the whole mass. Taking suitable Δx, Δy, Δz sampling intervals (usually it will be convenient to have $\Delta x = \Delta y$), the $F(P)$ mean contrast density distribution function of equation (2.3), multiplied by the elementary volume $\Delta x\ \Delta y\ \Delta z$ and the G constant has to be given numerically at the central points of the elementary prisms, thus creating the grid.

(b) The 3-D array representing the sampled $GF(P)\ \Delta x\ \Delta y\ \Delta z$ function has to be Fourier transformed.

(c) The 3-D complex array resulting from the above process has to be multiplied by the spectral function corresponding to the desired field ($\sqrt{\pi/2}\ 1/\nu^2$ for the potential, $\sqrt{\pi/2}\ 1/\nu^2\ i\sigma$ for the derivative along the selected direction, etc.).

(d) The inverse Fourier transform of the above array furnishes the required field sampled at all the nodal points of the initial grid.

5 Numerical aspects

Special attention must be paid to the numerical aspects of the problem. The most important one is the border effect (see for instance, for a slightly different but numerically equivalent problem, Kanaseqich 1981, p. 56).

The border effect mainly depends upon the fact that the original density distribution function $F(P)$, as a consequence of the space truncation, appears infinitely repeated in adjacent prisms, so that the consequent Newtonian effect, through the convolution product, is added to the original expected field. Such a perturbing effect obviously becomes more and more remarkable when approaching the borders of the prism. It has to be reduced to a maximum allowed level of contribution in the zone where the solution is required, by a suitable enlargement of the 3-D array representing the density distribution with the addition of zeros. Particular algorithms (many of them are already available; see for instance Anderson 1980), whenever necessary, can be adopted in order to avoid computer memory problems.

Other effects like those deriving from the Gibbs phenomenon in the truncation of the spectral image of the weighting function, as well as from its anisotropy, can be minimized applying suitable windows and filters in the wavenumber space (Zadro 1969).

Moreover, as usual in 1- and 2-D cases, aliasing effects have to be considered in the selection of the Δx, Δy, Δz sampling intervals.

6 Conclusions and discussion

For sufficiently limited regions of the Earth, where the Earth's curvature can be disregarded and the surrounding distribution of masses produces negligible, or otherwise computable, effects, the method proposed produces, both inside and outside the perturbing masses, the Newtonian potential field as well as all the fields tied to it by derivation processes in whatever direction.

Although other numerical methods are widely used in gravity interpretation problems in order to compute, point by point, the Newtonian potential and the gravitational effects produced by given perturbing masses generally modelled by a sum of elementary right rectangular prisms, the method proposed gives directly the complete 3-D map of the potential field as well as maps of fields tied to it by derivation processes. Moreover, for the solution of the inverse problem, the bidimensional spectrum of the Bouguer observed gravity anomalies can be compared with the corresponding spectrum computed for the selected model. Regional or local properties of the model can be adjusted by comparing the two spectra on the basis of the wavelengths involved.

Besides the cases above, it appears that two problems of great geophysical interest could be easily solved following the procedure proposed here.

The first one is concerned with the gravitational shear stress computed on faults of given orientation and depth in tectonically active areas. Indeed, having computed four independent normal stresses at the fault, one vertical and assumed to be the principal one, and the other three in three directions on the horizontal plane, the shear stresses on the fault may be obtained.

The second one is concerned with the isostatic compensation depth according to the Airy model. In fact, for a given crustal thickness, the crust–mantle discontinuity relief is considered as a mirror image of the topographic relief, with a scale factor depending upon the density contrast as well as upon the isostatic degree of equilibrium. With the z Cartesian coordinate axis vertical, and the γ coordinate axis corresponding to it in the wavenumber space, modifications of scale factor in the original Cartesian space, do not change the shape of the spectral image of the density distribution function, but its wavenumbers along the γ coordinate, with a law inversely proportional to the scale factor itself. Thus, having computed the FT for a first approximation density distribution, several cases can be evaluated for different scale factors, multiplying the FT itself by the spectral image of the corresponding weighting function, which is analytically given as wavenumber function. The most reliable amplification factor can be found using a suitable optimization process. Moreover, horizontal shifts, sometimes occurring between the isostatic compensation surface and the topographic relief, can be taken into account by suitable operations on the spectral image of the density distribution function, for selected bands of wavelengths, according to the information given by the gravity observational data.

Acknowledgments

Thanks are due to Professor F. Bocchio, G. F. Panza and to Dr C. Ebblin for their valuable suggestions given after reading the first draft of the paper.

The research was supported by the contract CNR no. 83.02432.

References

Anderson, G. L., 1980. A stepwise approach to computing the multidimensional fast Fourier transform, *IEEE Trans. ASSP,* **28,** 280–284.

Arsac, J., 1961. *Transformation de Fourier et Théorie des Distributions*, Dunool, Paris.

Kanasewich, E. R., 1981. *Time Sequence Analysis in Geophysics*, 3rd edn, University of Alberta Press.

Sneddon, I. N., 1951. *Fourier Transforms*, McGraw-Hill, New York.

Watson, G. N., 1962. *A Treatise on the Theory of Bessel Functions*, Cambridge University Press.

Zadro, M. B., 1969. An ideal bidimensional filter and its application in the interpretation of gravity anomalies, *Studia Geophys. Geod.,* **13**.

Geophys. J. R. astr. Soc. (1984) **79**, 495–511

Two-dimensional analysis of the effect of subsurface anomalies on the free surface response to incident *SH*-waves

Joel M. Crichlow *Computer Centre, University of the West Indies, St Augustine, Trinidad and Tobago, West Indies*

David Beckles *Department of Mathematics, University of the West Indies, St Augustine, Trinidad and Tobago, West Indies*

William P. Aspinall *Seismic Research Unit, University of the West Indies, St Augustine, Trinidad and Tobago, West Indies*

Received 1984 March 16; in original form 1983 May 18

Summary. Two-dimensional finite element modelling of subsurface anomalies at shallow depth has been done to obtain the response to incident *SH*-waves. Vertically incident *SH* and obliquely incident *SH* have been examined. Power spectral ratios were studied to determine the effect on the surface seismograms of the position, shape, depth, size and material composition of the anomaly. A number of relationships between the surface response and the anomaly has been identified. These relationships may be used in solving the inverse problem: given the seismic motion of the ground surface, determine the physical properties of the underground structure.

Introduction

The effect on the surface motion of the structural variations both at the surface and at shallow depth has been studied by several scientists.

Analytical techniques were used by a number of these researchers. Some of these are Aki & Larner (1970) who investigated the effect caused by irregular layer properties; Trifunac (1971) who examined the nature of the surface motion in and around a semi-cylindrical alluvial valley; Wong & Trifunac (1974) who considered the response of a semi-elliptical canyon to incident *SH*-waves, and Sabina & Willis (1975) who studied the scattering of plane *SH*-waves by a rough half-space of arbitrary slope.

A numerical technique was, however, chosen for this research since the analytical methods are usually restricted to regular geometries and/or long waves.

An inspiration for this study came from the work of Bolt & Smith (1976) who used the finite element method to model a few underground structural anomalies and, by considering the spectral shapes of the surface response, demonstrated that a relationship between the spectra and the anomaly may be established.

Other numerical techniques have been used in wave propagation problems. Some representative works include Boore (1972) who used the finite difference method to study the effect of topography on seismic *SH*-waves. A singular Fredholm integral equation of the second kind was developed and solved numerically by Sills (1978) in order to examine the scattering of *SH*-waves by an arbitrary surface irregularity. The same problem was considered by Sanchez-Sesma, Herrera & Aviles (1982) who applied a numerical boundary method using the notion of C-completeness after Herrera (1981).

The main aim of this research was to determine the effect on the surface motion of the shape, depth, size, and material composition of the underground structure. Lysmer & Drake (1971), Drake (1972) and Smith (1975) had already demonstrated that the finite element technique produces satisfactory results. Therefore the finite element programme designed by Smith (1975) was used by Crichlow (1982) to study a range of underground structures.

Only vertically incident *SH*-waves were studied in determining the response of anomalies whose rigidity was greater than that of the surrounding medium.

It was demonstrated that the physical properties of the underground structures may be identified in the ground surface response. This earlier study has been extended to include anomalies with rigidity less than the surrounding medium. The incident motion includes vertically and non-vertically incident *SH*-waves. The results from the earlier study are combined with those from the later research in order to present some conclusive relationships between the response and the structure.

Numerical technique and modelling

Fundamentals of the finite element method can be found in a number of texts (e.g. Zienkiewivz 1977; Norrie & De Vries 1978). The time domain formulation uses the Euler–Lagrange equation

$$\mathsf{M}\ddot{\mathbf{u}} + \mathsf{C}\dot{\mathbf{u}} + \mathsf{K}\mathbf{u} = 0 \tag{1}$$

where M is the mass matrix, C is the damping matrix, K is the stiffness matrix and $\mathbf{u}$ the displacement vector (Crichlow 1982).

A mesh of square elements is used in this study to model the physical structure. The size of element must be chosen very carefully since unwelcome attenuation and dispersion effects result from elements that are too large relative to the wavelengths considered (Smith 1975; Balytschko & Mullen 1978). A minimum of eight elements per wavelength has been recommended.

A fourth-order Runge–Kutta algorithm was used to solve the system of differential equations, (1). However, for the calculation to remain numerically stable the time step must be less than the time for energy to propagate across one element.

In order to examine the effect of the underground structure two solutions are generated. One with only the host medium and the other with the underground structure in the host medium. The ratio of the two solutions is then taken. This not only serves as a calibration technique to remove the spectral character of the input pulse but at the same time displays the effect of the inclusion.

Correcting techniques have to be used in other numerical approaches also in order to recover from the errors introduced through discretization and other approximation methods (Aboudi 1978). Although other techniques may require less computer time and storage, one major advantage of the finite element method is the ease with which different types of topological and material approximations can be used within the same mesh.

The discrete Fourier transform of the displacement seismogram was obtained by using the fast Fourier transform technique of Cooley & Tukey (1965). Power spectral ratios were computed by dividing the power spectral response when an anomaly is present by the response when there is no underground structure.

The preliminary modelling, done on a CDC 7600, included damping. These results, discussed by Crichlow (1982), did not differ significantly from the results obtained from pure elastic modelling performed by Bolt & Smith (1976). The inclusion of damping also increases the computer memory requirements. Because this part of the study was done on a smaller machine, an ICL 1901T, no damping was included. The available memory size also restricted the range of modelling. Therefore some results of interest could not be generated. However there was sufficient modelling to allow meaningful conclusions.

A rectangular anomaly was included in a rectangular medium which measured 1 km across by 0.4 km down. The entire area was divided into elements of 40 m square. At eight elements a wavelength this allowed resolution up to a maximum of 10 Hz for a 3.2 km s^{-1} S velocity. The properties of the media were systematically varied to determine the effect on the surface response. Reflections from the base and sides of the host medium were not admitted in the solution (see Smith 1974) in order to model the half-space.

The vertically incident *SH*-wave was modelled by inputting a square pulse at all the nodes on the base of the model and propagating it upwards. Oblique incidence was generated by pulsing the boundary nodes in sequence, i.e. at each successive time step the displacement at the next node or pair of nodes was set to the pulse amplitude.

Analysis of free surface response

VERTICALLY INCIDENT *SH*

Anomalies with rigidity greater than the surrounding medium returned the same pattern of response as was communicated earlier (Crichlow 1982). The peak response over the centre of anomaly is at Fd = 0.25, where Fd is dimensionless frequency: (depth of anomaly below surface)/(wavelength in host medium of incident wave). When the response at Fd = 0.5 is computed it is a minimum (see Figs 1, 2 and 3).

Anomalies with rigidity less than the surrounding medium returned a minimum response over the centre of anomaly at Fd = 0.25 (Fig. 4). The response at Fd = 0.5 was not computed.

This response over the centre of an anomaly was compared with the surface amplification for a layer over a half-space computed from the formula (Trifunac 1971):

$$\text{amplification} = 1\Big/\left[\cos^2\frac{\omega H}{\beta_s}+\frac{(\mu_s\beta)}{\mu\beta_s}\sin^2\frac{\omega H}{\beta_s}\right]^{1/2} \tag{2}$$

where H is the thickness, μ_s is the rigidity and β_s the S velocity of the surface layer; μ, β are the rigidity and the S velocity respectively of the half-space; ω is the angular frequency. Figs 5 and 6 show the amplitude distribution for three layers over a half-space plotted against the dimensionless frequency, Fd where Fd is (layer thickness)/(wavelength in layer). The pattern of the response agrees with the results from the modelling, i.e. where the rigidity of the layer is less than the half-space the peak response is at Fd = 0.25 and the minimum is at Fd = 0.5; and this is reversed in the cases where the rigidity of the layer is greater than the half-space.

This relationship of the amplitude distribution with depth, frequency and rigidity may be explained in the following way.

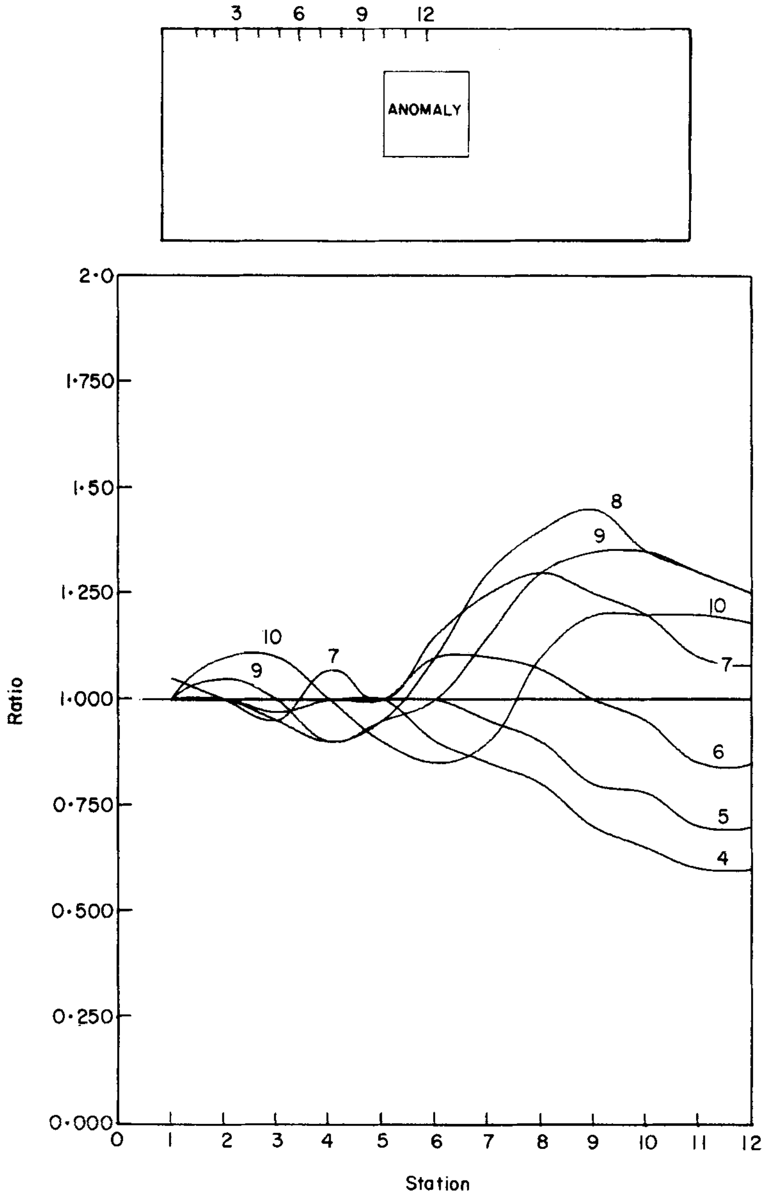

Figure 1. Response to the anomaly 160 X 160 m, 80 m below the surface. The anomaly has β = 3.5 km s^{-1} and ρ = 4.2 g cm^{-3}. The host medium has β = 3.2 km s^{-1} and ρ = 2.8 g cm^{-3}. The top diagram gives the position of the anomaly relative to the stations which are 40 m apart. The integer on the curve is the frequency value in Hz.

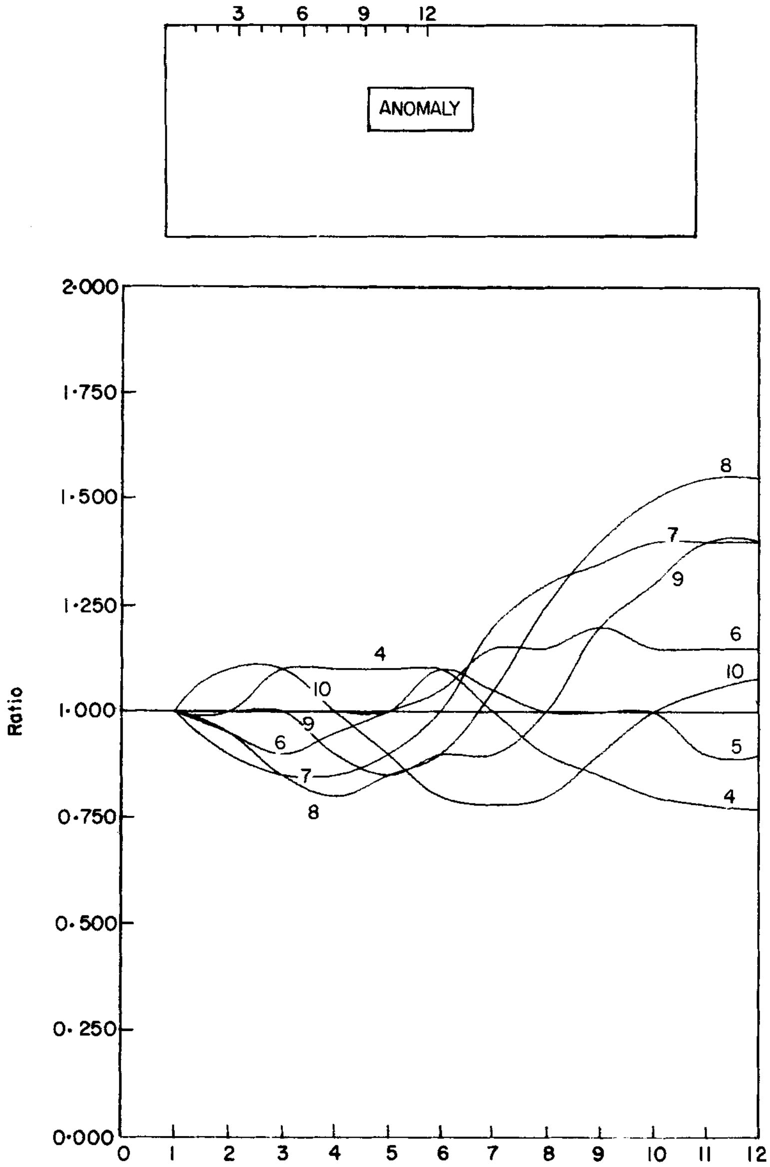

Figure 2. Response at stations 1–12 to the rectangular anomaly 200 X 80 m, 120 m below the surface. Other details are as in Fig. 1.

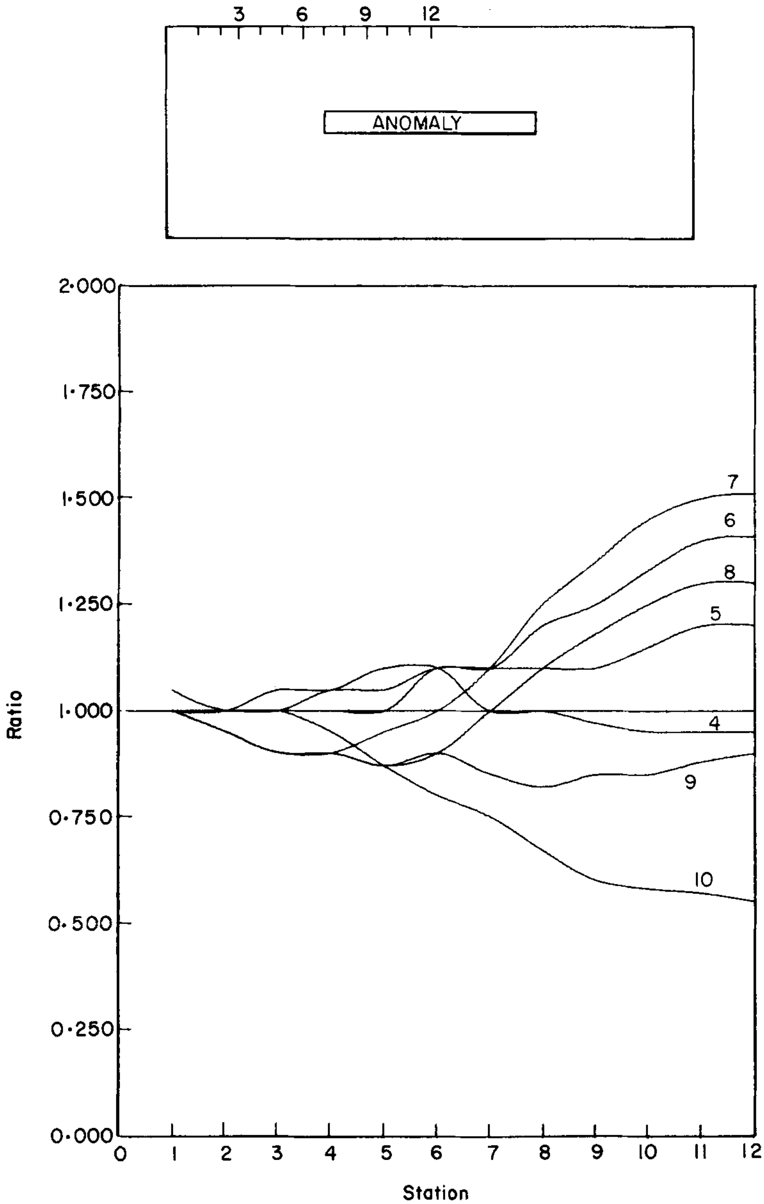

Figure 3. Response to anomaly 400 × 40 m, 160 m below the surface. Other details are as in Fig. 1.

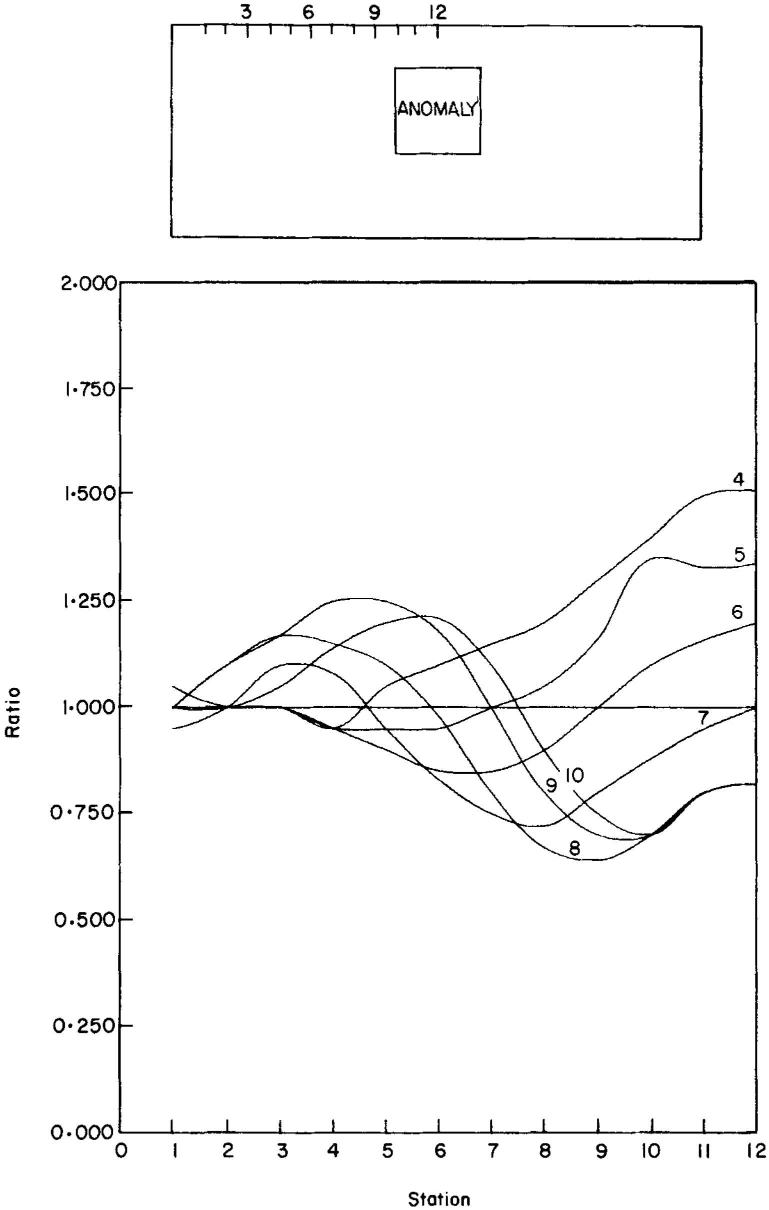

Figure 4. Response to anomaly 160 × 160 m, 80 m below the surface. The anomaly has $\beta = 3.2\,\mathrm{km\,s^{-1}}$ and $\rho = 2.8\,\mathrm{g\,cm^{-3}}$. The half-space has $\beta = 3.5\,\mathrm{km\,s^{-1}}$ and $\rho = 4.2\,\mathrm{g\,cm^{-3}}$. Other details are as in Fig. 1.

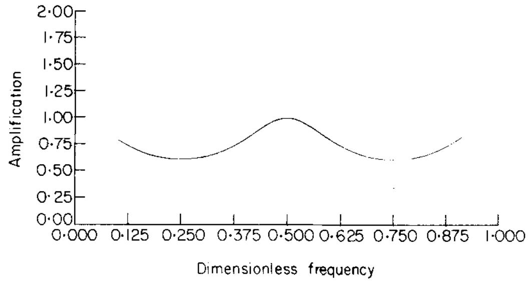

Figure 5. Amplification in the surface layer due to a vertically incident *SH*-wave of unit amplitude. This is plotted against the dimensionless frequency, Fd where Fd is (layer thickness)/(wavelength in layer). Three layers (80, 120 and 160 m thick) were considered. The responses are identical over the intersecting frequencies. In each case the surface layer has 4.2 g cm^{-3} density and 3.5 km s^{-1} *S* velocity. The half-space has a density of 2.8 g cm^{-3} and *S* velocity of 3.2 km s^{-1}.

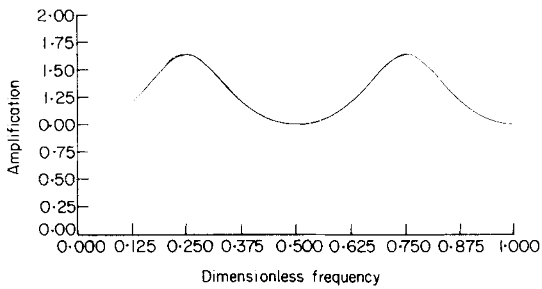

Figure 6. Amplification in the surface layer due to a vertically incident *SH*-wave of unit amplitude. This is plotted against the dimensionless frequency, Fd where Fd is (layer thickness)/(wavelength in layer). Three layers (80, 120 and 160 m thick) were considered. The responses are identical over the intersecting frequencies. In each case the surface layer has 2.8 g cm^{-3} density and 3.2 km s^{-1} *S* velocity. The half-space has 4.2 g cm^{-3} density and 3.5 km s^{-1} *S* velocity.

For vertically incident *SH* (far away from corner effects)

$$\text{Refl} = \frac{(\mu_0 v_1 - \mu_1 v_0)}{\mu_0 v_1 + \mu_1 v_0} I \qquad \text{(Bullen 1963)}, \tag{3}$$

where μ_0, v_0 are the rigidity and the *S* velocity of the half-space; μ_1, v_1 that of anomaly;

Refl, the amplitude of the reflected wave and I, the amplitude of the incident wave (see Fig. 7).

From equation (3) Refl has the same sign as the incident wave, I, if

$\mu_0 v_1 > \mu_1 v_0$,

i.e. when

$\rho_0 v_0 > \rho_1 v_1$; (ρ_0, ρ_1 are the densities of the half-space and the anomaly respectively),

and Refl has the opposite sign if

$\rho_0 v_0 < \rho_1 v_1$.

Assume that the incident motion has a positive amplitude (see Fig. 8). If $\rho_0 v_0 > \rho_1 v_1$ and the positive reflection from the top edge of the anomaly arrives at the surface (a)

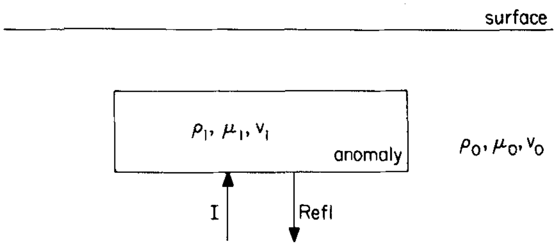

Figure 7. I is the incident wave, Refl is the reflected wave, ρ is the density, μ is the rigidity and v is the S velocity.

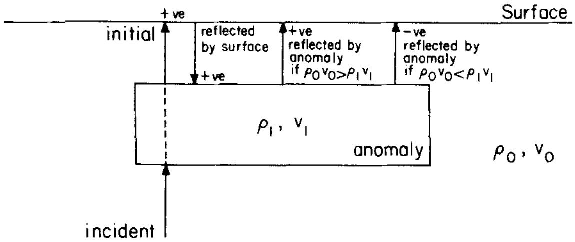

Figure 8. The effect on the sign of the amplitude due to the reflecting medium.

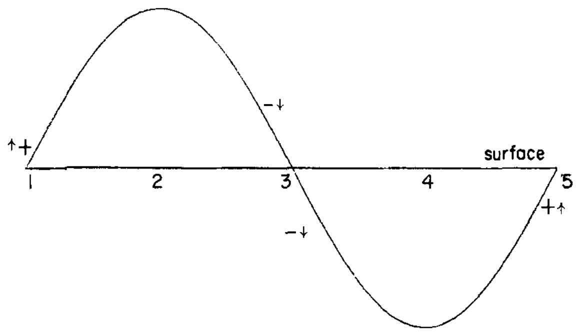

Figure 9. One cycle of surface motion with the direction of disturbance indicated.

between points 1 and 2 or 4 and 5 in Fig. 9 there will be an amplitude increase due to the sum of like signs; (b) between points 2 and 4 there will be an amplitude decrease, due to the sum of unlike signs.

The arrival time of the reflection is affected by depth. Therefore a depth of one-quarter of a wavelength in this case will produce an intersection of opposite sign at the node point, 3, thus producing a relative minimum (Figs 4 and 5).

If $\rho_0 v_0 < \rho_1 v_1$ and the negative reflection (see Fig. 8) from the top edge of the anomaly arrives at the surface (a) between points 1 and 2 or 4 and 5 there will be an amplitude decrease, due to the sum of unlike signs; (b) between points 2 and 4 there will be an amplitude increase, due to the sum of like signs.

Therefore, if the anomaly is one-quarter of a wavelength below the surface or the layer is one-quarter of a wavelength thick, the arrival will be at node point, 3 where a relative maximum will be produced (Figs 1 and 6).

This shows that one can use the energy distribution over the centre of anomaly, where the corner effects may be negligible, to not only estimate the depth, but to determine a relationship between $\rho_0 v_0$ and $\rho_1 v_1$.

In addition it can be shown that for a point on the surface directly above the rectangular anomaly, if the energy ratio value is less than one for all frequencies computed, then the anomaly may be a liquid or its depth is greater than one-half of the largest wavelength at which the response is computed.

Let I be the amplitude of the vertically incident wave; R_1 the amplitude of the refracted wave in the anomaly and R_2 the amplitude of the refracted wave into the area above the anomaly. The effect of corners will be ignored here. This is safe since for (a), an anomaly with velocity greater than the surrounding medium, the effect of the corner will not be seen in the initial disturbance at the points in the shadow of the anomaly; (b) where the velocity is less than the surrounding medium the corners will be assumed to be far enough apart to permit an undisturbed initial effect.

For vertically incident *SH* (see Fig. 10)

$$R_1 = (2\mu_0 v_1 I)/(\mu_0 v_1 + \mu_1 v_0), \qquad \text{(Bullen 1963)}$$

$$R_2 = (2\mu_1 v_2 R_1)/(\mu_1 v_2 + \mu_2 v_1) = (4\mu_0\mu_1 v_1 v_2 I)/[(\mu_0 v_1 + \mu_1 v_0)(\mu_1 v_2 + \mu_2 v_1)].$$

$R_2 < I$ implies that

$$4\mu_0\mu_1 v_1 v_2 < (\mu_0 v_1 + \mu_1 v_0)(\mu_1 v_2 + \mu_2 v_1).$$

Now

$$\mu_0 = \mu_2 \qquad \text{and} \qquad v_0 = v_2,$$

therefore

$$2\mu_0\mu_1 v_0 v_1 < \mu_0^2 v_1^2 + \mu_1^2 v_0^2.$$

$$\mu_0 = \rho_0 v_0^2, \mu_1 = \rho_1 v_1^2$$

therefore

$$2\rho_0 v_0^3 \rho_1 v_1^3 < \rho_0^2 v_0^4 v_1^2 + \rho_1^2 v_1^4 v_0^2.$$

Dividing throughout by $v_0^2 v_1^2$ gives

$$2\rho_0\rho_1 v_0 v_1 < \rho_0^2 v_0^2 + \rho_1^2 v_1^2, \qquad \text{i.e. } (\rho_0 v_0 - \rho_1 v_1)^2 > 0$$

which will hold whenever $\rho_0 v_0 \neq \rho_1 v_1$.

It therefore follows that larger energy values on the surface will be due to multiple reflections off the top edge and scatter by the corners of the anomaly.

If the depth is greater than one-half of the wavelength for the lowest frequency computed the reflection off the top edge will not arrive on the surface within that frequency cycle. There will therefore be no contribution from that reflection.

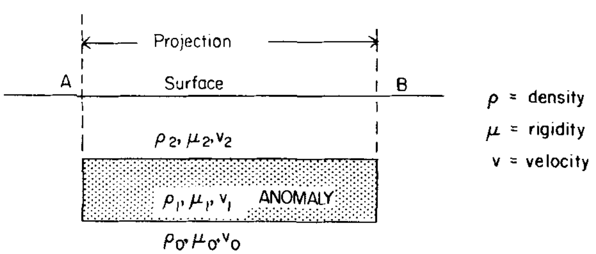

Figure 10. Rectangular anomaly. AB is the shadow area on the surface.

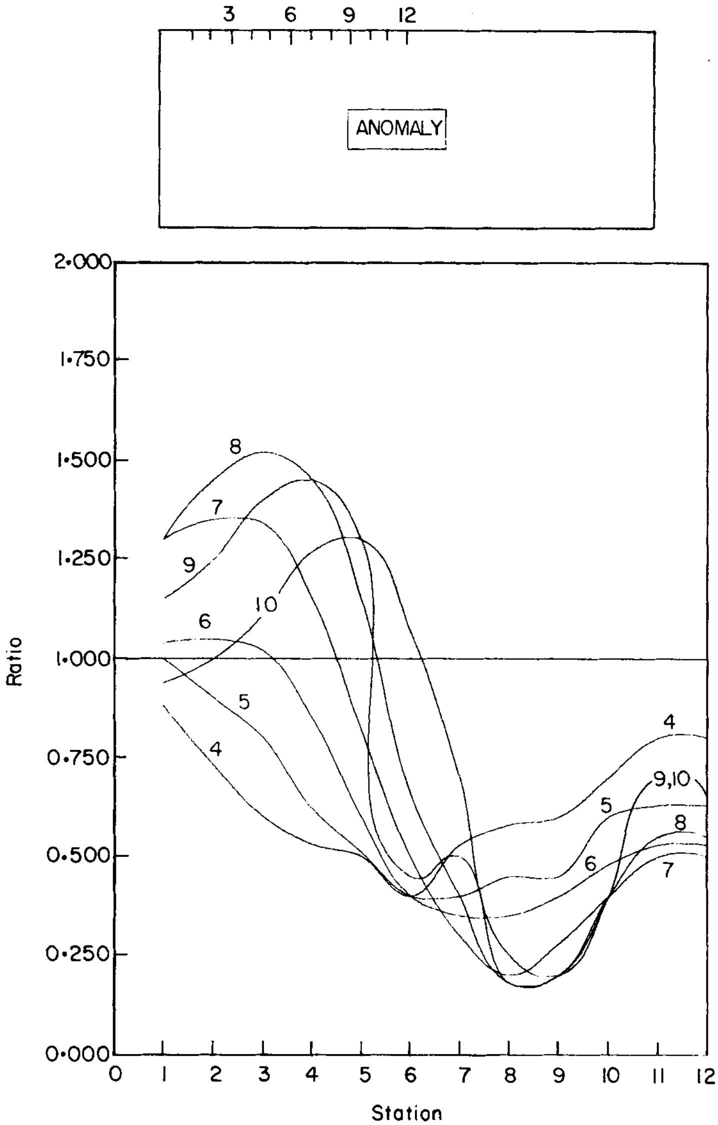

Figure 11. Response to liquid body, 200 × 80 m, 160 m below the surface. The host medium has $\beta = 3.2\,\mathrm{km\,s^{-1}}$ and $\rho = 2.8\,\mathrm{g\,cm^{-3}}$. Other details are as in Fig. 1.

The *SH*-wave does not propagate through a liquid body therefore a surface energy response less than one for all frequencies may indicate a liquid anomaly (Fig. 11).

NON-VERTICALLY INCIDENT *SH*

The models showing the response to the vertically incident *SH*-wave will be used to demonstrate the expected surface response of the rectangular anomaly to oblique incidence. Two computer models were constructed in order to show the extent of agreement with the projections.

The distribution of the response on the surface to the rectangular anomaly in Fig. 12 should take the following form. The response R_1 in region 1 may be expressed as

$$R_1 = R_i + R_r + R_s + R_t \quad (4)$$

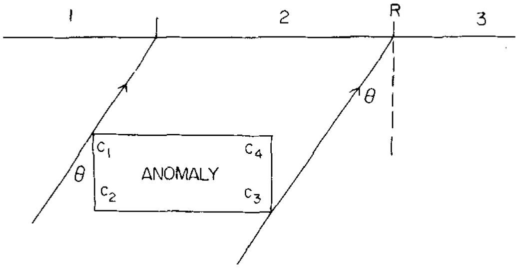

Figure 12. Rectangular anomaly with edges parallel to the surface. θ is the angle of incidence of the *SH*-wave.

where R_i is due to the incident wave,
R_r, the reflection off the left edge,
R_s, the scatter by the corners c_1 and c_2,
and R_t, the wave transmitted through the anomaly.

The particular energy ratio values recorded will depend on the frequency of the wave, depth and dimensions of anomaly, and material composition of media. The principles governing this response should be the same as discussed earlier. That is, the ratio value is determined by:

(1) the point of arrival of subsequent or secondary waves relative to the wavelength of the initial or primary waves, and
(2) the sign of the amplitudes of subsequent waves relative to the sign of the amplitude of the initial wave.

Larger ratios should be observed in the neighbourhood of the point directly above the corner, c_1.

The response R_2 in region 2 in Fig. 12 may be expressed as:

$$R_2 = R_r + R_s + R_t \tag{5}$$

where R_r is the reflection off the top edge,
R_s is the scatter by corners c_1, c_3, c_4,
R_t is the wave transmitted through the anomaly.

It may be safe to assume that the maximum values recorded here will be less than those maxima in region 1.

The response R_3 in region 3 in Fig. 12 may be expressed as:

$$R_3 = R_i + R_s + R_t \tag{6}$$

where R_i is the incident wave,
R_s is the scatter by corners c_1, c_3, c_4,
R_t the wave transmitted through the anomaly.

Since there are contributions from R_i in equation (6) it is likely that for some incident angle θ, maxima in R_3 may be greater than maxima in R_2.

An approximate estimate of the depth of the anomaly may be obtained by examining the response at the point P in Fig. 13. The relationship between arrival times of initial pulses at stations in region 1 compared to stations in region 2 will indicate whether or not $\beta_1 > \beta_0$.

Choose the frequency, f, at which the energy ratio recorded at P is maximum relative to the other ratios recorded at P.

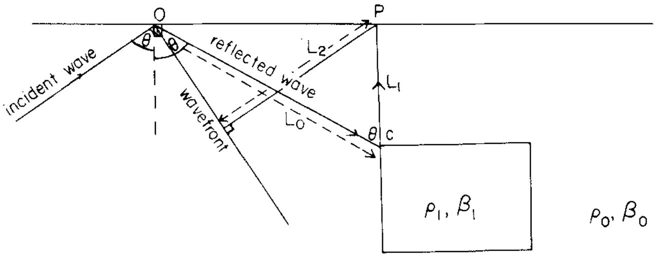

Figure 13. Rectangular anomaly with edges parallel to the surface. θ is the angle of incidence of the *SH*-wave.

If $\rho_1\beta_1 > \rho_0\beta_0$ then it can be assumed that the arrival of the second disturbance at P takes place when the first disturbance at P has completed one-half of a wavelength, as discussed before. This second disturbance could be assumed to be the reflection from 0 scattered by the corner c. Therefore

$$L_0 + L_1 = L_2 + \tfrac{1}{2}\,(\text{wavelength at } f),$$

i.e.

$$L_0 + L_1 = L_2 + \tfrac{1}{2}(\beta_0/f)$$

therefore

$$L_1 \sec\theta + L_1 = L_1 \tan\theta \sin\theta + \tfrac{1}{2}(\beta_0/f). \tag{7}$$

Since θ, β_0 and f are known, L_1 can be easily obtained. A similar operation could be performed for the case $\rho_0\beta_0 > \rho_1\beta_1$.

MODELS

(a) A square anomaly 160×160 m at a depth of 80 m and with edges parallel to the surface is subjected to a plane non-vertically incident wave. The angle of incidence is 45°. The anomaly has an S velocity of 3.5 km s^{-1} and a density of 4.2 g cm^{-3}. The half-space has an S velocity of 3.2 km s^{-1} and a density of 2.8 g cm^{-3}.

Fig. 14 shows the response at the numbered stations which are 40 m apart, with station 10 directly above the left edge of the anomaly. Regions 1, 2 and 3 as in Fig. 12 are denoted. The distribution is as anticipated. The larger energy ratios are recorded in the neighbourhood of the stations over the corners of the anomaly.

Equation (7) is applied at station 10 in Fig. 14.

$L_1 = 80$ and $\theta = 45$

therefore

$$80\,\frac{(2\sqrt{2})}{2} + 80 = 80\,\frac{(\sqrt{2})}{2} + \tfrac{1}{2}(\beta_0/f).$$

Since $\beta_0 = 3.2$ km s^{-1}, then f is approximately 11 Hz.

This implies that the maximum response at this station should be recorded at 11 Hz and the minimum at 5 or 6 Hz. The physical constraints of the model did not allow computation of the results for 11 Hz, however the expected minimum at 5 Hz was obtained.

(b) A rectangular anomaly 200×80 m at a depth of 120 m and with edges parallel to the surface is subjected to an *SH*-wave incident at 45°. The material properties are the same as in case (a).

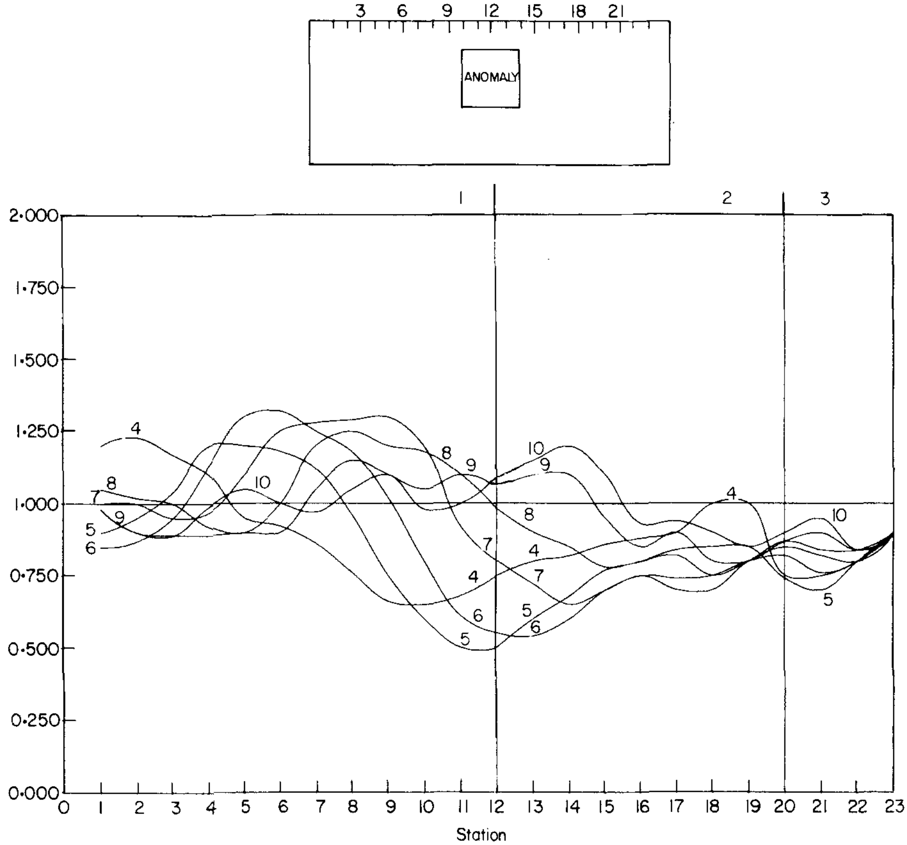

Figure 14. Response of square anomaly 160 X 160 m, 80 m below the surface to the *SH*-wave incident at 45°. The anomaly has $\beta = 3.5\,\mathrm{km\,s^{-1}}$ and $\rho = 4.2\,\mathrm{g\,cm^{-3}}$. The host medium has $\beta = 3.2\,\mathrm{km\,s^{-1}}$ and $\rho = 2.8\,\mathrm{g\,cm^{-3}}$. The top diagram gives the position of the anomaly relative to the stations which are 40 m apart. The integer on the curve is its frequency value in Hertz.

Fig. 15 shows the response which follows the same pattern as case (a).

Equation (7) is applied at station 9 in Fig. 15.

$L_1 = 120$ and $\theta = 45$

therefore

$$120\frac{(2\sqrt{2})}{2} + 120 = 120\frac{(\sqrt{2})}{2} + \tfrac{1}{2}(\beta_0/f)$$

with

$\beta_0 = 3.2\ \mathrm{km\ s^{-1}}$. This gives $f = 8$ Hz.

This implies that the maximum response at this station should be recorded at 8 Hz and the minimum response at 4 Hz. The figure gives this result.

One may use the arrival times of the initial pulse in the shadow area, the angle of incidence and an approximate value for the S velocity of the anomaly to estimate the vertical thickness of the subsurface structure. In particular if n is the number of stations at

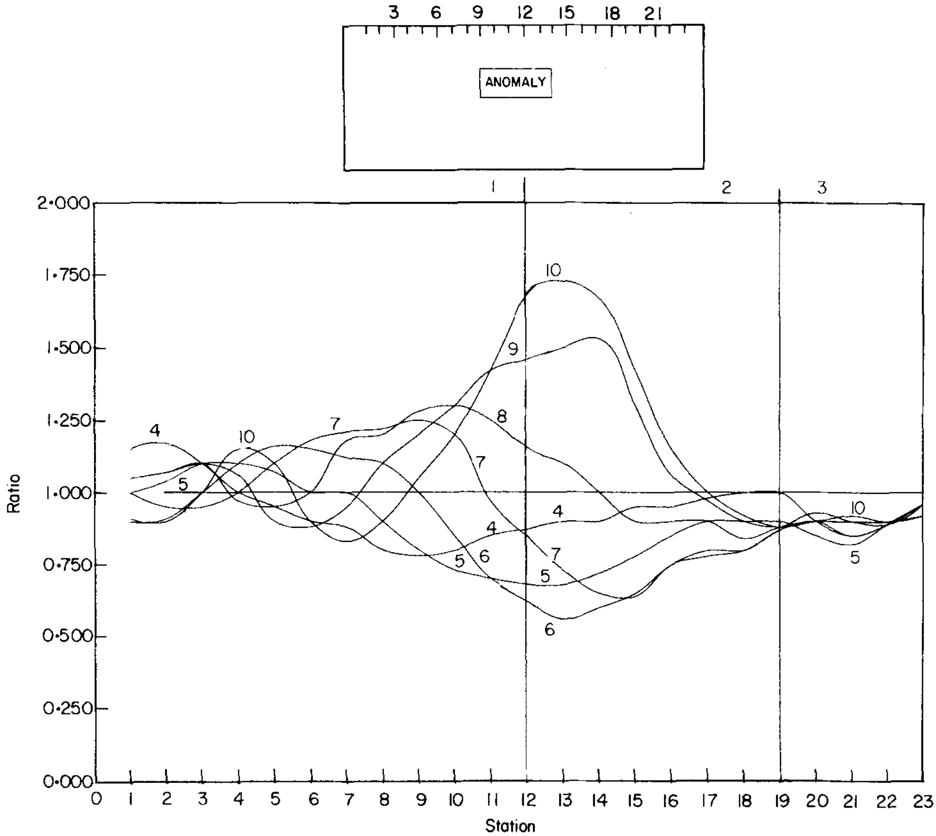

Figure 15. Response of the rectangular anomaly 200 × 80 m, 120 m below the surface to the *SH*-wave incident at 45°. Other details are as in Fig. 14.

which the response is recorded, d is the distance between stations, β_h is the S velocity of the half-space, β_a the approximate S velocity of the anomaly and θ the angle of incidence then the thickness T is given by:

$$T \leqslant \beta_a\beta_h * \Delta t / |\beta_a - \beta_h|$$

where

$$\Delta t = \max |At_1 + (i * d \sin\theta)/\beta_h - At_i|, \qquad i = 2\text{–}n;$$

and At_i is the arrival time of the incident wave at station i.

This formula can also be applied to the vertically incident case.

Conclusion

Several relationships have been identified which may be used in determining the physical characteristics of the anomaly when given the free surface response.

The horizontal length of the anomaly may be approximated from the distance on the surface between the largest peaks of response. The relative material composition of the anomaly can be deduced from the arrival times of the initial pulse at points in the shadow area along the surface, and from the distribution of the response over frequency. The depth can be obtained from the frequency value of maximum and minimum response. The displacement seismogram can be used in the estimation of the vertical thickness of the subsurface anomaly.

In this study the density and velocity values were chosen to provide an acoustic mismatch at the boundaries which was sufficiently sharp to facilitate resolution in the frequency spectrum used. Some cases in which the density contrast was not so great were also modelled. The response displayed a consistent pattern, but the degree of sensitivity to the change in parameters was not quantified. This may be a useful area in which to pursue further study.

Acknowledgments

The helpful comments from Professor Bruce A. Bolt, Dr J. Shepherd and Dr D. Morgan are gratefully acknowledged. Thanks too to an anonymous referee who suggested improvements to the original submission.

References

Aboudi, J., 1978. Numerical methods in elastodynamics, in *Modern Problems in Elastic Wave Propagation*, eds Miklowitz, J. & Achenbach, J. D., Wiley, London.

Aki, K. & Larner, K., 1970. Surface motion of a layered medium having an irregular interface due to incident plane *SH* waves, *J. geophys. Res.*, **75**, 933–954.

Balytschko, T. & Mullen, R., 1978. On dispersive properties of finite element solutions, in *Modern Problems in Elastic Wave Propagation*, eds Miklowitz, J. & Achenbach, J. D., Wiley, London.

Bolt, B. A. & Smith, W. D., 1976. Finite element computation of seismic anomalies of arbitrary shape, *Geophysics*, **41**, 145–150.

Boore, D. M., 1972. A note on the effect of simple topography on seismic *SH* waves, *Bull. seism. Soc. Am.*, **62**, 275–284.

Bullen, K. E., 1963. *An Introduction to the Theory of Seismology*, 3rd edn, Cambridge University Press.

Cooley, J. W. & Tukey, J. W., 1965. An algorithm for the machine calculation of complex Fourier series, *Math. Comp.*, **19**, 297–301.

Crichlow, J. M., 1982. The effect of underground structure on seismic motions of the ground surface, *Geophys. J. R. astr. Soc.*, **70**, 563–575.

Drake, L. A., 1972. Love and Rayleigh waves in non horizontally layered media, *Bull. seism. Soc. Am.*, **62**, 1241–1258.

Herrera, I., 1981. Boundary methods for fluids, *Finite Elements for Fluids IV*, ed Gallagher, R. H., Wiley, London.

Lysmer, J. & Drake, L. A., 1971. The propagation of Love waves across non-horizontally layered structures, *Bull. seism. Soc. Am.*, **61**, 1233–1251.

Norrie, D. H. & De Vries, G., 1978. *An Introduction to Finite Element Analysis*, Academic Press, New York.

Sabina, F. J. & Willis, J. R., 1975. Scattering of *SH* waves by a rough half-space of arbitrary slope, *Geophys. J. R. astr. Soc.*, **42**, 685–703.

Sanchez-Sesma, F. J., Herrera, I. & Aviles, J., 1982. A boundary method for elastic wave diffraction: application to scattering of *SH* waves by surface irregularities, *Bull. seism. Soc. Am.*, **72**, 473–490.

Sills, L. B., 1978. Scattering of horizontally polarised shear waves by surface irregularities, *Geophys. J. R. astr. Soc.*, **54**, 319–348.

Smith, W. D., 1974. A non-reflecting plane boundary for wave propagation problems, *J. comp. Phys.*, **15**, 492–503.

Smith, W. D., 1975. The application of finite element analysis to body wave propagation problems, *Geophys. J. R. astr. Soc.*, **42**, 747–768.

Trifunac, M. D., 1971. Surface motion of a semi-cylindrical alluvial valley for incident plane *SH* waves, *Bull. seism. Soc. Am.*, **61,** 1755–1770.

Wong, H. L. & Trifunac, M. D., 1974. Scattering of plane *SH* waves by a semi-elliptical canyon, *Int. J. Earthquake Eng. Struct. Dyn.*, **3,** 157–169.

Zienkiewicz, O. C., 1977. *The Finite Element Method*, 3rd edn, McGraw-Hill, London.

Geophys. J. R. astr. Soc. (1984) 79, 513–538

Intraplate lithosphere deformation and the strength of the lithosphere

N. J. Kusznir and R. G. Park *Department of Geology, University of Keele, Keele, Staffordshire ST5 5BG*

Received 1984 March 19; in original form 1983 October 4

Summary. The intraplate deformation of continental lithosphere in response to applied stress has been investigated using a mathematical model which incorporates the elastic, ductile and brittle response of lithosphere material. Ductile deformation is assumed to be controlled in the crust by dislocation creep in quartz, and in the mantle by dislocation creep and plasticity in olivine. Brittle failure is predicted using modified Griffith theory. A fundamental feature of the model is the redistribution of stress within the lithosphere following stress release by both ductile and brittle deformation. This redistribution produces high levels of stress in the middle or lower crust immediately above the elastic-ductile or brittle-ductile transition.

Lithosphere deformation is shown to be critically dependent on the temperature structure of which surface heat flow is a convenient indicator. For higher geothermal gradients, the release of stress in the lower lithosphere by ductile deformation is more rapid and complete and results in large stress levels in the upper lithosphere. For sufficiently large applied stresses or steep geothermal gradients, the stress levels in the upper and middle crust will cause complete fracture of the upper lithosphere. *Whole lithosphere failure* (WLF) then results, by continued brittle and ductile deformation, causing geologically significant strains.

The critical value of applied stress required to give WLF has been calculated for both tensional and compressional deformation as a function of surface heat flow. The predicted lithosphere bulk strength is then compared with expected levels of intraplate stress arising from plate boundary forces and isostatically compensated loads, which are thought to give net stress levels in the continental lithosphere in the range +0.25 to −0.25 kB. Using these expected maximum stress levels, the model predicts significant extensional deformation in regions of moderate heat flow with $q > c.\ 60\,\mathrm{mW\,m^{-2}}$ (e.g. Central Europe) as well as for areas of high heat flow like the Basin-and-Range Province. Significant compressional deformation is predicted for areas of high heat flow with $q > c.\ 75\,\mathrm{mW\,m^{-2}}$ but only for restricted conditions of stress combination. These results are in good agreement with the observed rather widespread incidence of extensional intraplate deformation and the restricted occurrence of compressional deformation which may be confined to areas of unusually high heat flow or weak crust.

The model may also be used to calculate the depth of the brittle-ductile transition which is shown to become shallower with increase in heat flow, in good agreement with seismic evidence.

1 Introduction

The lithosphere plate as originally conceived by the early proponents of the plate tectonics model was regarded as part of a relatively strong layer which exhibited no significant internal lateral distortion over time periods of the order of tens or hundreds of Ma. Evidence for lack of distortion was the exactness of fit of the severed passive continental margins of the Atlantic (Bullard, Everett & Smith 1965) and the general applicability to relative plate motions of the concept of tectonics on a sphere (McKenzie & Parker 1967 and Le Pichon 1968). Significant lithosphere deformation was thought to be confined to plate boundaries.

This view is now regarded as oversimplified in the light of more recent discoveries of the importance of deformation within the interior of continental plates – for example, the large areas of recent deformation in Central Asia attributed by Molnar & Tapponnier (1975) to the India–Asia collision, and the many cases of extensional tectonics associated with the formation of graben, rifts and sedimentary basins found within all the major continental plates. Studies of extensional basins stimulated in part by the conceptual model of McKenzie (1978) envisage local crustal extensions of 100 per cent or more over time periods of the order of tens of Ma. Structural studies of the currently active extensional zone of the Basin-and-Range Province of the western USA (e.g. Zoback, Anderson & Thompson 1981 and Wernicke *et al.* 1982) have revealed previously unrecognized large horizontal strains of the order of 100 per cent over *c.* 30 Ma. Compressional intraplate tectonics in contrast appears to be much less common – many examples being probably due to the reversal of movements on previous extensional fault systems (*cf.* Zeigler 1982). The best known examples of active intra-plate compressional tectonics are in Central Asia north of the Himalayas plate boundary (see Molnar & Tapponnier 1975).

In contrast to the behaviour of continental plates, oceanic intraplate deformation appears to be neither pervasive nor extensive and is generally confined to brittle deformation in the upper crust associated with insignificant strains or to lithosphere flexure associated with sediment or sea-mount loading (e.g. Bodine, Steckler & Watts 1981).

The magnitude of the stresses involved in intraplate deformation must clearly be large enough to promote frequent though localized extensional failure in continental lithosphere but too small to promote compressional failure except under unusual circumstances. This paper is an attempt to quantify these stresses and to investigate the conditions required for significant lithosphere failure.

The sources and distribution of tectonic stress in the lithosphere have been investigated by Forsyth & Uyeda (1975), Turcotte & Oxburgh (1976) and Richardson, Solomon & Sleep (1976). The most important sources responsible for significant tectonic stress arise from plate boundary forces and from isostatically compensated loads (Bott & Kusznir 1984). The sources and estimated stress levels are summarized in Table 1 and are discussed in greater detail later. The average stress levels within present continental plates arising from these sources seem likely to lie within the range -0.25 to $+0.25$ kB if distributed over the whole lithosphere plate. However measured and calculated stresses in the upper and middle parts of the crust are much larger – Heard (1976) suggests a maximum value for the stress

Table 1. Contributions to tectonic stress.

Source of Tectonic Stress	Expected Stress Magnitude distributed over lithosphere in OCEANIC† LITHOSPHERE	in CONTINENTAL$^{\times}$ LITHOSPHERE
Plate Boundary Forces		
(a) Ridge Push	0.2-0.3 kb (compression)	0.1-0.15 kb (compression)
(b) Slab Pull*	0-0.5 kb (mainly tension)	0-0.25 kb (mainly tension)
(c) Subduction Suction	0-0.3 kb (tension)	0-0.15 kb (tension)
Compensated Load Forces		
(a) Continental Margin	0 (but up to 0.2 kb compression)	0.1 kb (tension)
(b) Plateau Uplift	-	0-0.3 kb (tension)

* Slab Pull Stress is the net resultant of slab pull, subduction resistance and collision resistance forces.
† For oceanic lithosphere – 80 km thick.
$^{\times}$ For continental lithosphere – 150 km thick.

difference of *c*. 3 kB. Uniaxial compressive fracture strengths of common rocks are in the range 1–4 kB and tensile strengths approximately 1/8 of these values. The comparatively low levels of expected intraplate stress must therefore be reconciled with levels of upper lithosphere stress large enough to cause significant though localized crustal failure. The explanation for this apparent discrepancy lies in the ductile nature of the lower part of the lithosphere which causes redistribution of a stress applied to the whole lithosphere and its amplification in the more brittle upper part of the lithosphere.

This process of *stress amplification* has been investigated mathematically for various types of lithosphere (Kusznir & Bott 1977; Bott & Kusznir 1979; Mithen 1982; Kusznir & Park 1982). The instantaneous response of the lithosphere to the application of an applied external stress will take the form of elastic deformation with strains of the order of 0.01 per cent. Creep in the lower ductile lithosphere causes stress decay and associated stress redistribution and amplification in the upper lithosphere, leading to an increase in the elastic strains there. If the amplified stress in the upper lithosphere is sufficiently large, fracture will occur in the topmost brittle part of the lithosphere. Associated stress release further increases the stress levels in the remaining competent elastic core (Fig. 1). For sufficiently high levels of applied stress, the whole of the upper brittle lithosphere may fracture, leading to stress release and transfer to the lower ductile lithosphere where further creep and upward transfer then occurs. Thus a cyclic process of upper lithosphere fracture and lower lithosphere creep is established which results ultimately in complete failure throughout the competent elastic core when the stress levels everywhere exceed the failure strength (Fig. 1). This development is defined as *whole lithosphere failure* (WLF) after which extensive lithosphere deformation with large horizontal strains will take place.

The temperature structure of the lithosphere, because of its effect on lithosphere rheology, is critically important in controlling not only the time taken for complete failure to occur, but also the rate at which subsequent deformation takes place (Kuznir & Park 1982). This may be illustrated for example by the relative weakness of lithosphere with a Basin-and-Range type geotherm compared with lithosphere with a typical continental shield

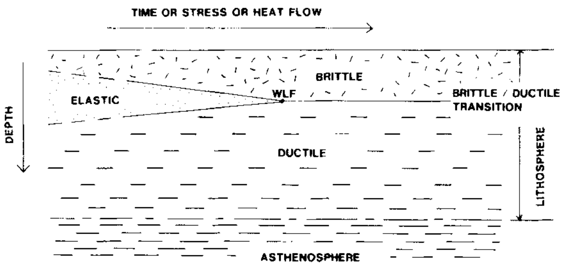

Figure 1. A diagrammatic representation of the regions of brittle, elastic and ductile behaviour in visco-elastic lithosphere under an applied lateral stress. With increase in time, given a large enough applied stress, the elastic core will be reduced to zero as the regions of brittle and ductile deformation extend downwards and upwards respectively. The point in depth at which this occurs corresponds to the brittle/ductile transition. *Whole lithosphere failure* (WLF) occurs when the elastic layer disappears. An increase in heat flow has a similar effect to increasing stress.

geotherm. Using the mathematical model described below, the critical values of applied stress may be found which will cause WLF and significant lithosphere deformation, with geologically appropriate strain rates in the range 10^{-14}–10^{-15}, for a series of different geotherms (represented by their surface heat flow values).

The main purpose of this paper is to establish a relationship between critical applied stress and heat flow which may then be applied to specific geological situations (e.g. Basin-and-Range Province, Western Europe, Central Asia) where a comparison can be made between expected anc theoretical stress values.

2 The lithosphere deformation model

The mathematical model examines the elastic, ductile and brittle response of the lithosphere to lateral applied stress. Fundamental to the model is the conservation of the total horizontal force arising from that stress. The model calculates the stress transfer caused by brittle failure in the upper lithosphere and ductile creep in the lower lithosphere and the resulting strain distribution. An initial horizontal stress σ_0 is applied uniformly to the lithosphere in the x-axis direction. The perpendicular horizontal axis is labelled y and the vertical axis z (measured positive downwards).

Conservation of the horizontal force arising from the applied stress gives the equation:

$$\int_0^L \sigma_x \, dz = \text{constant}$$

where σ_x is the horizontal stress in the lithosphere and L is the lithosphere thickness. Differentiation of this equation with respect to time gives:

$$\int_0^L \dot{\sigma}_x \, dz = 0.$$

The assumption that the various layers of the lithosphere are welded together and that the lithosphere undergoes a uniform horizontal strain with depth gives the equation:

$$\frac{d\epsilon_x}{dz} = 0$$

or differentiating with respect to time

$$\frac{d\dot{\epsilon}_x}{dz} = 0.$$

The lithosphere is assumed to behave as a Maxwell viscoelastic material in which stress is also relieved by brittle deformation. Stress and strain within the lithosphere are linked by the equation

$$\epsilon_x = \frac{1}{E}(\sigma_x - \sigma_x^0) - \frac{\nu}{E}(\sigma_y - \sigma_y^0) - \frac{\nu}{E}(\sigma_z - \sigma_z^0) + \epsilon_x^v$$

where ϵ_x is the total horizontal strain, σ_x is the total stress in the x-direction, σ_x^0 is the initial stress, ϵ_x^v is the ductile creep in the x-direction, E is Young's modulus and ν is Poisson's ratio. Initial stresses σ_x^0, σ_z^0 and σ_y^0 are used for modelling stress release by brittle fracture. Similar equations exist for strains ϵ_y and ϵ_z.

Plane strain in the y-direction gives the additional equation $\epsilon_y = 0$, while the vertical stress σ_z arising from the applied stress is zero, i.e. $\sigma_z = 0$. Manipulation and integration of the above equations gives the final equations for the temporal and spatial variations of σ_x and σ_y

$$\dot{\sigma}_x = \int_0^t \left(\frac{1}{L}\int_0^L k\dot{\epsilon}_V\, dz - k\dot{\epsilon}_V\right) dt' - \frac{1}{L}\int_0^L \sigma_x^0 \cdot dz + \sigma_x^0$$

$$\dot{\sigma}_y = \int_0^t \left[\nu\dot{\sigma}_x - E\frac{(2\sigma_y - \sigma_x)}{6\eta}\right] dt' + \sigma_y^0 - \nu\sigma_x^0$$

where $k = E/(1-\nu^2)$.

The derivation of these equations is described in greater detail by Kusznir (1982).

Ductile deformation within the lower and middle lithosphere is assumed to be accomodated by non-Newtonian power-law creep. For the mantle, ductile creep in olivine is assumed to provide the dominant creep mechanism. Following the experimental work of Kohlstedt & Goetze (1974), Goetze (1978) has suggested that dislocation (power-law) creep provides the dominant creep mechanism for olivine except at high deviatoric stresses ($\tau > 2$ kB). For higher levels of stress Goetze suggests that a Dorn law is more applicable. Post (1977) has shown that a dislocation creep mechanism is also applicable for (wet) dunite. Bodine *et al.* (1981), drawing on the olivine and dunite creep laws of Goetze and Post and on their own modelling of oceanic lithosphere flexure, propose the following relationship between creep rate, stress and temperature for dislocation and Dorn law creep in the mantle:

dislocation creep

$$\dot{\epsilon} = 7 \times 10^{10} \exp\left(\frac{-53\,030.3}{T}\right)(\sigma_1 - \sigma_3)^3\ \mathrm{s}^{-1} \qquad \text{for } (\sigma_1 - \sigma_3) < 2\ \mathrm{kB}$$

Dorn law

$$\dot{\epsilon} = 5.7 \times 10^{11} \exp\left[\frac{-55\,555.6}{T}\left(1 - \frac{(\sigma_1 - \sigma_3)}{85}\right)^2\right]\mathrm{s}^{-1} \qquad \text{for } (\sigma_1 - \sigma_3) > 2\ \mathrm{kB}$$

where $(\sigma_1 - \sigma_3)$ is in kB (1 kB = 100 MPa).

For the continental crust, dislocation creep in quartz is assumed to be the dominant mechanism controlling creep deformation. As with olivine, the amount of water strongly controls the creep rates; creep rates being greater for greater water content. The ductility of crust controlled by creep in quartz will consequently be dependent on the crustal water content and on the amount of quartz, both of which will decrease with depth. The upper crust is assumed to deform according to a wet quartz rheology with 50 per cent quartz composition while the lower crust, on the assumption of a granulite facies composition is assumed to deform according to a dry quartz model with 10 per cent quartz. The above model for the crustal rheology is of course a gross oversimplification and certain qualifications relating particularly to the lower crust should be pointed out: (1) the lower crust in certain situations may be wet; (2) creep in plagioclase may be important; and (3) cataclastic flow may be a significant mechanism. The creep rates used for wet and dry quartz are as follows and are based on the experimental work of Koch, Christie & George (1980):

wet quartz:

$$\dot{\epsilon} = 4.36 \exp\left(\frac{-19\,332.08}{T}\right)(\sigma_1 - \sigma_3)^{2.44}\ \mathrm{s}^{-1}$$

dry quartz:

$$\dot{\epsilon} = 0.126 \exp\left(\frac{-18\,244.65}{T}\right)(\sigma_1 - \sigma_3)^{2.86}\ \mathrm{s}^{-1}$$

where $(\sigma_1 - \sigma_3)$ is in kB.

Brittle deformation within the lithosphere has been predicted by the use of Griffith's theory (1924) as modified by McClintock & Walsh (1962) and described by Jaeger & Cook (1971). Three failure domains have been used – tensional failure, open crack compressional and closed crack compressional. The physical parameters within the modified Griffith theory which control failure are tensile strength, T_0; the frictional coefficient, μ and the critical stress, σ_{gc}, required to close the Griffith crack. Of these parameters T_0 and μ have the greatest influence on brittle failure.

Estimates of tensile strength, T_0, from laboratory experiments for crystalline rocks (Jaeger & Cook 1971; Brace 1964) lie predominantly in the range 0.1–0.4 kB. A value of 0.2 kB has been generally used in the calculation of this paper although in Section 4 and Fig. 8 the effect of a lower value is investigated.

Values of the coefficient of friction, μ, estimated from laboratory experiments (Jaeger & Cook 1971; Byerlee 1978) lie predominantly in the range 0.5–1.0. Tests on fault gouge clay material give a much lower value for μ of the order of 0.1 (Wang & Mao 1979). However such low μ material would only be present in the top few kilometres of the crust giving way with increase in depth and metamorphism to cataclasite material (Sibson 1983). Heat flow observations over the San Andreas Fault (Lachenbruch & Sass 1980) which show the absence of any significant heat flow anomaly have been interpreted to suggest a low faulting stress and consequently a low value of μ. The determination of μ by this technique is however extremely indirect and the reliability of the estimated value uncertain. The value of μ should, according to the Anderson theory of faulting, be related to the angle between a fault plane and the maximum principal stress, σ_1. Turcotte (1983) has used a dip of 35° for the Wind River Thrust to give a value of $\mu = 0.35$. However values of the angle between the fault plane and σ_1 commonly range for normal and thrust faults between 20° and 35° corresponding to a range of μ of 1.2–0.35. $\mu = 0.5$ may be taken as a representative estimate and this value has been generally used in the calculations of this paper. In addition, the effects of $\mu = 1$ have been investigated in Section 4 and Fig. 8 in order to include the higher laboratory estimates of μ, and as will be seen make little difference to the results.

The stress required to close the Griffith cracks, σ_{gc} has been reported by Murrell (1965) to be $-4.19\ T_0$ which gives an estimate for σ_{gc} of the order of 0.8 kB. However estimates of the crack closure stress from core samples from the Michigan basin (Wang & Simmons 1978) give a higher value of 1.45 kB. An intermediate value of 1.0 kB has been used in this paper.

Failure is dependent on stresses σ_x and σ_z. The stress σ_y, being the intermediate stress, is not required in the 2-D Griffith–McClintock and Walsh formulation. At failure the stress σ_x is returned to the failure envelope (the stress σ_z is simply lithostatic).

The model has been tested against a more elaborate 3-D plane strain finite element model and the results are identical. The formulation described above, however, provides for greater spatial and temporal resolution.

The temperature dependence of the ductile component of the lithosphere deformation suggests that the lithosphere temperature is a critical parameter. Continental lithosphere temperature structure has been calculated using the lithosphere temperature model of Pollack & Chapman (1977). The lithosphere temperature field is identified by the surface heat flow.

3 Application of the model to continental lithosphere

3.1 THE DISTRIBUTION OF STRESS WITH DEPTH

The mathematical model of lithosphere deformation described above has been applied primarily to the deformation of continental lithosphere. The response of continental shield lithosphere with a heat flow of $q = 45$ mW m^{-2} and thickness 150 km subjected to an initial tensional stress of 0.2 kB is shown in Fig. 2(a).

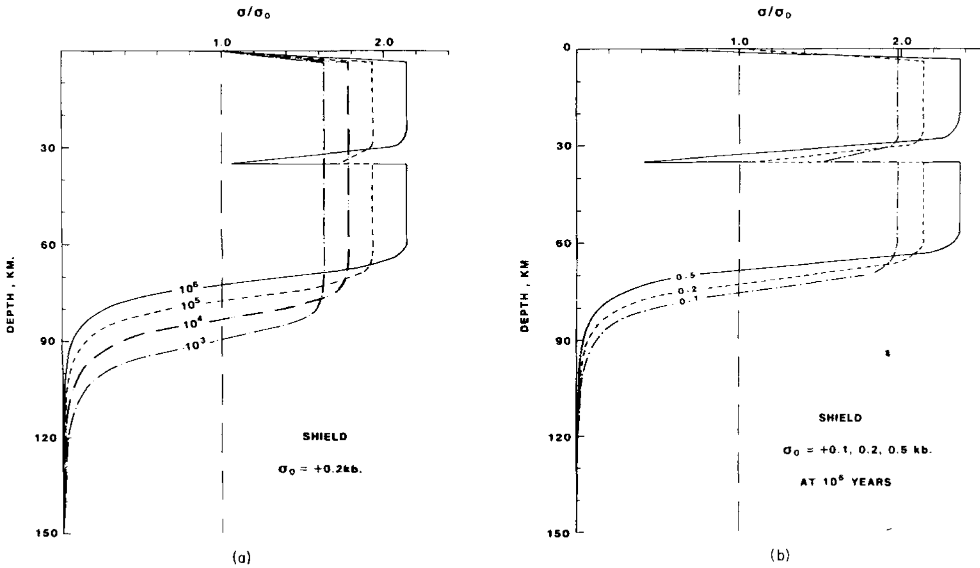

Figure 2. Horizontal stresses within continental shield type lithosphere plotted against depth: (a) at various times following the application of an initial stress $\sigma_0 = +0.2$ kB; (b) at time 10^6 yr after stress application, for initial applied stresses of $\sigma_0 = +0.1, +0.2$ and $+0.5$ kB.

The stress/depth profiles are shown at various times after the application of the stress. As time increases, ductile creep in the lower lithosphere leads to the decay of stress there and its transfer to the upper lithosphere. By 10^6 yr, stress decay in the lower half of the lithosphere is almost complete and the level of stress within the upper lithosphere has been increased by a factor of approximately $\times 2$. The amplification of stress in the upper lithosphere has also resulted in brittle fracture in the topmost lithosphere and the transfer downwards of the released stress. With increase in time, the high ductility zone at the base of the lower crust (with quartz rheology) becomes more apparent.

The stress response of a piece of lithosphere is dependent on the magnitude of the applied stress, since both the brittle and ductile deformation are dependent on it. In Fig. 2(b) stress in continental shield lithosphere is shown at 10^6 yr after the application of various levels of initial stress varying between 0.1 and 0.5 kB. For the greater initial stress values the ductile deformation in the lower lithosphere proceeds more rapidly and greater stress amplification in the upper lithosphere results. This arises primarily from the power-law dependence of strain rate on stress. The low stress region at the base of the continental crust also becomes more apparent for greater levels of applied stress.

The behaviour of lithosphere with a hotter temperature structure is shown in Fig. 3 for Basin-and-Range type lithosphere with $q = 95\ \mathrm{mW\,m^{-2}}$. In Fig. 3(a) stress is shown as a function of depth at times 10^3 and 10^4 yr after the application of an initial tensional stress of 0.2 kB. The hotter lithosphere has undergone effectively complete stress decay within the mantle and lowermost crust with resulting stress amplification in the middle crust by a factor of between $\times 8$ and $\times 11$. The large levels of amplified stress in the upper crust have resulted in extensive brittle failure. The stress profiles with depth show two subsidiary stress peaks or discontinuities below a stress minimum at approximately 15 km depth. These subsidiary peaks result from the discontinuities in rheology as composition changes from wet to dry quartz and from dry quartz to olivine respectively.

Fig. 3(b) shows the response of Basin-and-Range continental lithosphere to an applied compressive stress of 0.2 kB. Comparison of the stress profiles for both tensional and

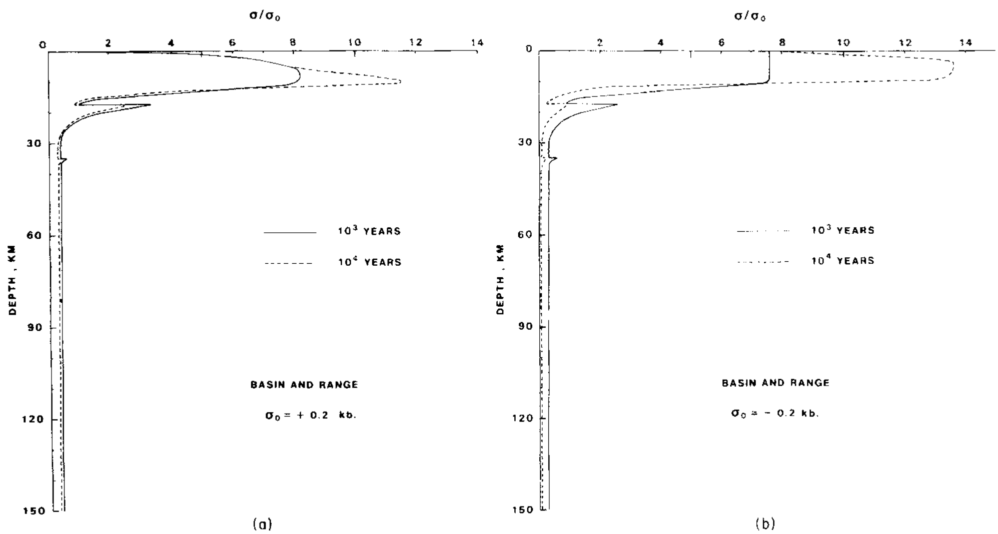

Figure 3. Horizontal stresses within Basin-and-Range type lithosphere plotted against depth at times 10^3 and 10^4 yr after the application of an applied stress: (a) $\sigma_0 = +0.2$ kB; (b) $\sigma_0 = -0.2$ kB.

compressive stresses at 10^3 yr shows that no failure has occurred for the compressive stress, while significant failure in the upper crust has occurred for the tensile case. The tensile stress case has a greater amplified stress showing that a significant contribution to stress amplification can arise in the middle crust due to brittle failure.

In Fig. 3(a) the curve for the tensile applied stress at 10^4 yr shows that the brittle failure envelope has intersected the top of the region in which ductile deformation has occurred, resulting in a sharp stress peak. The elastic core of the lithosphere for this model at this time consequently has ceased to exist with all of the lithosphere experiencing significant brittle or ductile deformation. The lithosphere in this model has consequently suffered *whole lithosphere failure* (WLF). In contrast, the stress profile for compressive applied stress at 10^4 yr (Fig. 3b) shows that WLF has not occurred.

In Fig. 4 the stress/depth profiles for continental shield and Basin-and-Range lithosphere are compared with those of ocean-basin lithosphere with a heat flow of 60 mW m^{-2}. Stresses are shown at 10^3 yr after the application of an applied stress of 0.2 kB. The rheology of the oceanic lithosphere is assumed to be controlled by olivine and the initial thickness of the oceanic lithosphere, over which the stress is applied, is 80 km. The oceanic lithosphere has undergone a similar amount of stress amplification to the continental shield lithosphere and has also suffered little brittle deformation compared with the Basin-and-Range model. While the oceanic lithosphere model has a higher heat flow than the continental shield model, it contains a greater proportion of lithosphere with the stronger olivine rheology.

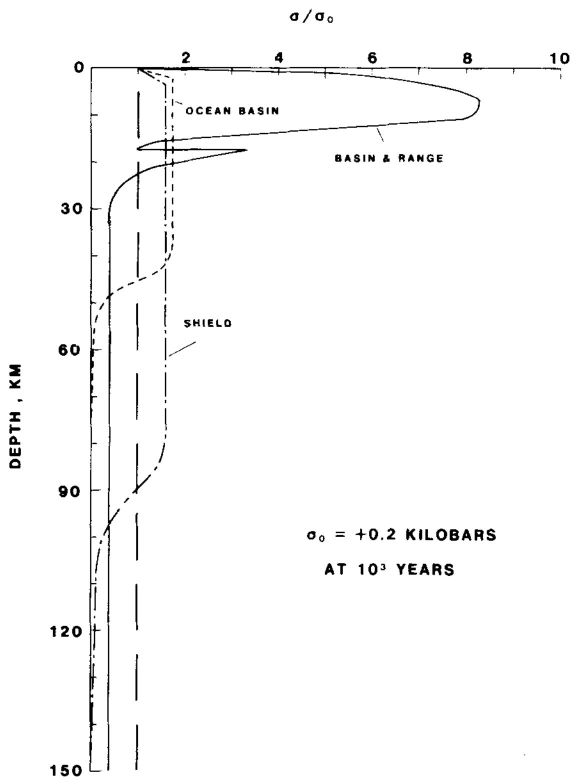

Figure 4. A comparison of stress as a function of depth for shield, Basin-and-Range and ocean-basin lithosphere at time 10^3 yr after the application of an initial stress $\sigma_0 = +0.2$ kB.

3.2 THE DEVELOPMENT OF LITHOSPHERE DEFORMATION

The ductile and brittle deformation of the lithosphere in response to the applied lateral stress will result in horizontal strains which for lithosphere undergoing WLF will become geologically significant. In Fig. 5(a), horizontal strain ϵ_x in the lithosphere, expressed as a percentage, is plotted as a function of time for various lithosphere models. At 1 Ma the strain of the hotter Basin-and-Range model subjected to 0.2 kB tension is approaching 100 per cent. In contrast, the strains in the cooler continental shield and oceanic basin models, at 10^6 yr, are of the order of 0.01 per cent. Such strains would not be geologically observable. Also shown in Fig. 5(a) is the strain–time curve for Basin-and-Range lithosphere subjected to an applied compressive stress of 0.2 kB. The strain in this model at 10^6 yr is only just approaching 1 per cent, and is significantly less than that of the tensile model. The upturn in the curve however suggests that WLF may be about to occur.

The dependence of the horizontal strain within the lithosphere both on the lithosphere temperature structure and on the sign of the applied stress is illustrated in Fig. 5(b) where strain is plotted against time for various models with heat flow values between 40 and 100 mW m^{-2}. The temperature structures were calculated using the Pollack & Chapman (1977) continental lithosphere temperature model. For the tensile applied stress curves, WLF occurs at about 10^3 yr for lithosphere with $q = 80$–100 mW m^{-2}. For cooler lithosphere with $q = 60$ mW m^{-2}, WLF occurs much later at about 10^5 yr. For compressional applied stress, only the curve with $q = 100$ mW m^{-2} shows WLF occurring by 1 Myr.

The dependence of the horizontal strain on the magnitude of the stress is demonstrated in Fig. 6 where strain–time curves are shown for lithosphere with $q = 60$ mW m^{-2} subjected to both tensile and compressive stresses between 0.1 and 0.5 kB. The curves for tensile applied stress of 0.2 and 0.5 kB show WLF by 1 Myr. However, for compression only the 0.5 kB curve shows geologically observable strains by 10^6 yr and strain rates in the geologically significant range.

4 The strength of intraplate lithosphere

In the previous section it has been shown that stress amplification is critical in explaining how the relatively small intraplate stresses available from known sources can overcome the high strength of the upper lithosphere to cause complete failure and high strains of the kind necessary to produce significant intraplate crustal deformation. The critical role of the geotherm in controlling the rate and extent of stress concentration is illustrated by the differences in the strain–time curves for shield and Basin-and-Range lithosphere (Fig. 5a). From Fig. 5(b) it may be deduced that geologically significant strain can be expected from lithosphere with $q > 60$ mW m^{-2} under a tensional applied stress of 0.2 kB but only from very hot lithosphere with $q > 80$ mW m^{-2} under a compressive applied stress of 0.2 kB.

It is clear from the above that for any given value of heat flow there will be a critical threshold value of both tensional and compressive applied stress which will cause *whole lithosphere failure* and thereby initiate large geologically significant strains. Fig. 7(a) summarizes the relationship between this critical stress σ_c and heat flow q indicating the fields in which significant deformation are predicted. The critical stress corresponds to that required to generate *whole lithosphere failure* by 1 Myr when initially applied over lithosphere 150 km thick. This diagram can thus be used to calculate, for a region of continental lithosphere of known heat flow, the critical applied stress necessary to cause significant deformation. The critical stress σ_c is very sensitive to relatively small changes in q in the range 40–80 mW m^{-2}. The strength of the brittle upper lithosphere, and consequently the whole lithosphere is controlled by the value of T_0 and μ used in the Griffith failure criterion.

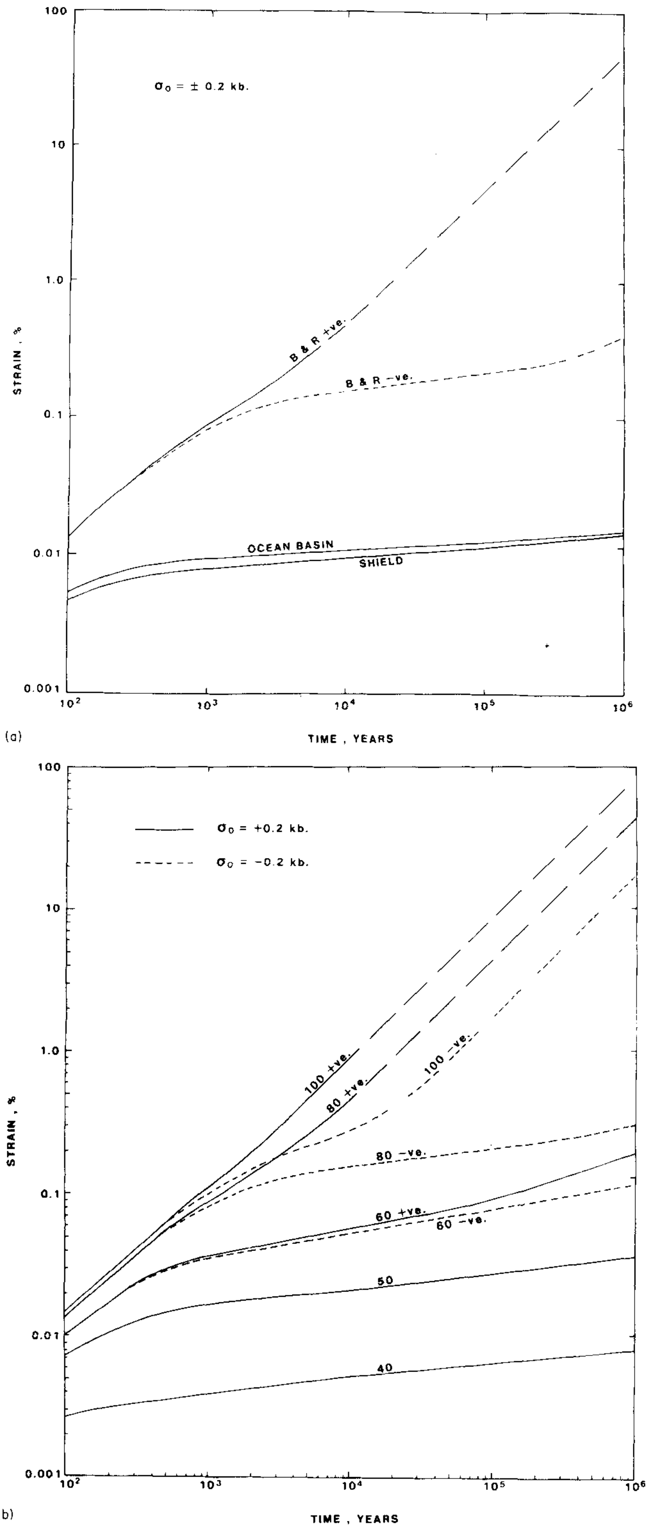

Figure 5. Strain–time curves for an applied stress of ± 0.2 kB: (a) For continental shield, ocean-basin and Basin-and-Range types of lithosphere. Only Basin-and-Range lithosphere shows geologically significant strains. (b) For continental lithosphere with different geothermal structures (characterized by their heat flow values measured in mW m^{-2}).

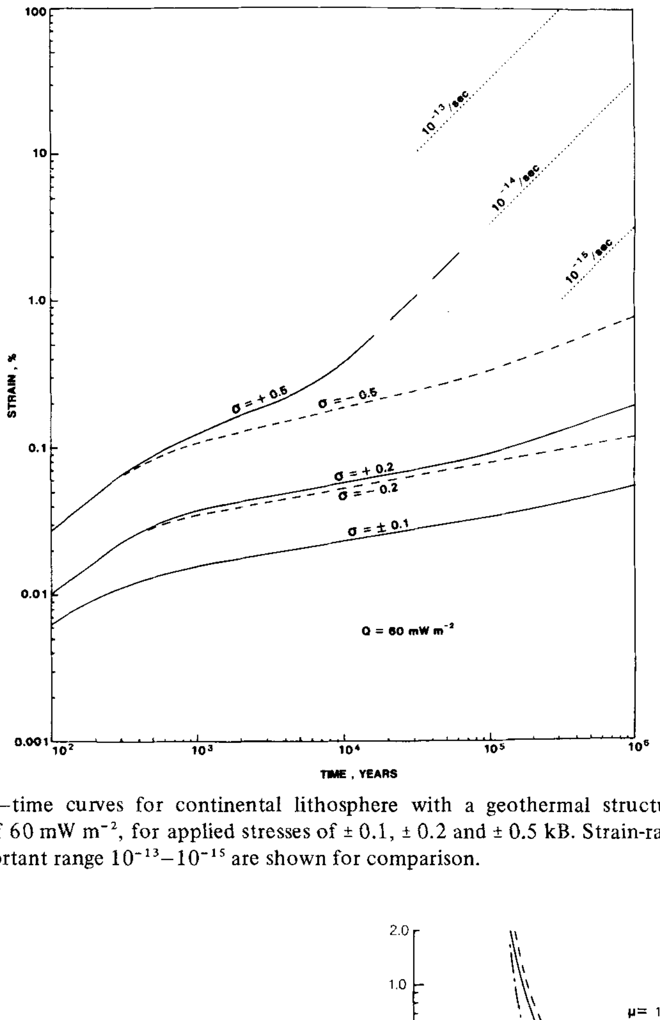

Figure 6. Strain–time curves for continental lithosphere with a geothermal structure corresponding to a heat flow of 60 mW m^{-2}, for applied stresses of ± 0.1, ± 0.2 and ± 0.5 kB. Strain-rate gradients in the geologically important range 10^{-13}–10^{-15} are shown for comparison.

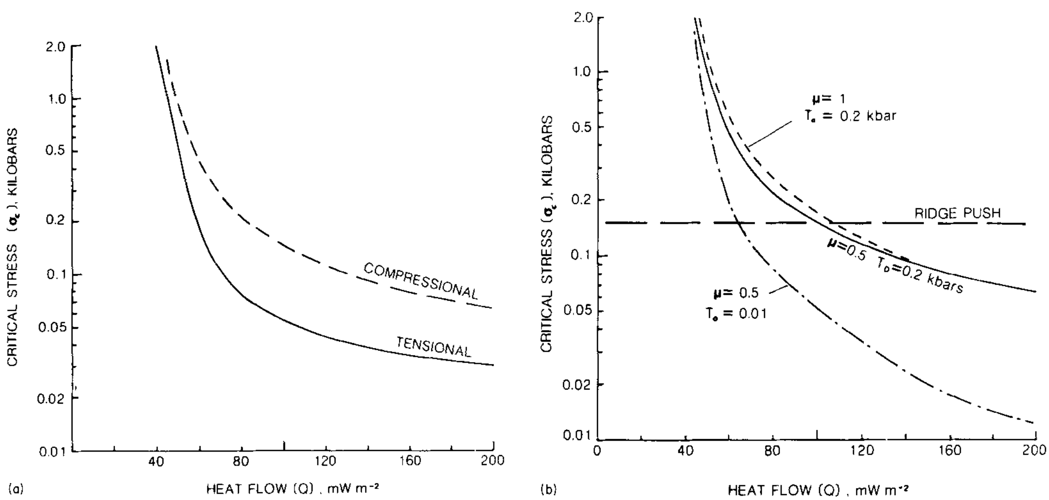

Figure 7. Curves showing the critical stress σ_C, (the initial stress applied over the whole lithosphere required to produce *whole lithosphere failure*) versus lithosphere heat flow q. (a) For both tensile and compressive lithosphere failure. The region above the curve represents the field where WLF occurs leading to significant geological deformation. (b) For compressional failure shown for various values of the parameters controlling brittle failure: T_0 and μ. The likely value of σ_C arising in continental lithosphere from the ocean ridge push force is shown for comparison.

Consequently the inevitable uncertainty is determining T_0 and μ produce corresponding uncertainties in σ_c. The curves of Fig. 7(a) have been calculated using values $T_0 = 0.2$ kB and $\mu = 0.5$. Weakening the model failure strength by choosing a much lower value of T_0 of 0.01 kB (corresponding to low cohesion within previously fractured lithosphere) has the effect of lowering σ_c significantly, especially at higher heat flow values (Fig. 7b). Changes in the value of the coefficient of friction μ within the probable range limits are less significant. The effect of increasing μ to 1.0, as shown in Fig. 7(b), is to increase the lithosphere strength particularly at lower heat flow values.

5 Expected levels of intraplate stress and a comparison with the strength of the lithosphere

The most important sources of tectonic stress in the lithosphere probably arise from plate boundary forces and from isostatically compensated loads. The plate boundary forces consist of *ridge-push, slab-pull* and *subduction suction.* The *ridge-push* force acts at ocean ridges causing a lateral compressive stress of about 0.2–0.3 kB, distributed over the adjacent oceanic lithosphere plate. The slab-pull force, resulting from the negative buoyancy of the sinking lithosphere, acts on the subducting plate and is opposed by lithosphere collision, bending and subduction resistance forces (see Forsyth & Uyeda 1975). The resulting stress in the subducting lithosphere consequently depends on the age of the subducting lithosphere and the rate of subduction. The resulting stress is expected to be generally tensional and in the range 0–0.5 kB. The precise nature of the suction force (Elsasser 1971; Forsyth & Uyeda 1975) is unclear but it is generally accepted that a tensional stress estimated at *c.* 0.2 kB is exerted in the upper (non-subducting) plate as a result of the subduction process. Like its counterpart the slab-pull force, the subduction suction force will be dependent on the age of the subducting lithosphere, on the rate of subduction, and probably in addition on the angle of dip of the subduction zone. Moving plates are also affected by a *mantle drag* force acting on the base of the lithosphere. However this force is considered to be probably an order of magnitude smaller than the plate boundary forces (Schubert *et al.* 1978; Richardson *et al.* 1976). For oceanic lithosphere, the net effect of the above stresses appears generally to be a net compression (see Richardson *et al.* 1976).

In addition to the above forces, the continental plates are affected by *isostatically compensated load stresses* due to topographic loading, crustal thickness variation and low density compensating mantle. These stresses will be associated both with passive continental margins with an estimated magnitude of *c.* 0.1 kB (Bott & Dean 1972) and with plateau uplifts within continents (*c.* 0.3 kB – Bott & Kusznir 1979). A tensional stress is exerted on the loaded compensated part of the lithosphere and a corresponding compressional stress in the adjacent lithosphere.

The stresses associated with the above forces will persist in lithosphere deforming as a consequence of their action. Such stresses have been called *renewable* stresses by Bott & Kusznir (1984). Such stresses are therefore capable of generating considerable tectonic deformation. In contrast, thermal stresses, membrane stresses and lithosphere flexure stresses, although large in magnitude, are dissipated by ductile and brittle lithosphere deformation and are incapable of generating horizontal lithosphere strains of more than a few per cent. Such stresses have been called *non-renewable* by Bott & Kusznir (1984).

It is important in considering the effect of these stresses to calculate their effect over the appropriate lithosphere thickness. Thus the ridge-push force may be calculated as a compressive stress of 0.3 kB when applied to an 80 km thick oceanic lithosphere but is reduced to 0.15 kB when applied to 150 km thick continental lithosphere. The expected levels of stress, within oceanic and continental lithosphere, arising from the main stress sources described above, are summarized in Table 1.

The likely levels of stress expected within continental plates can be approximated in two dimensions by summing the stresses for the various sources. Thus a continental plate with a ridge on each side would be in net compression throughout but the ridge-push element would be partly offset by a tensional continental margin element given a low net compressive stress of the order of 0.05 kB. A continental plate with a subduction zone on each side on the other hand might be expected to show a net tensional stress of up to

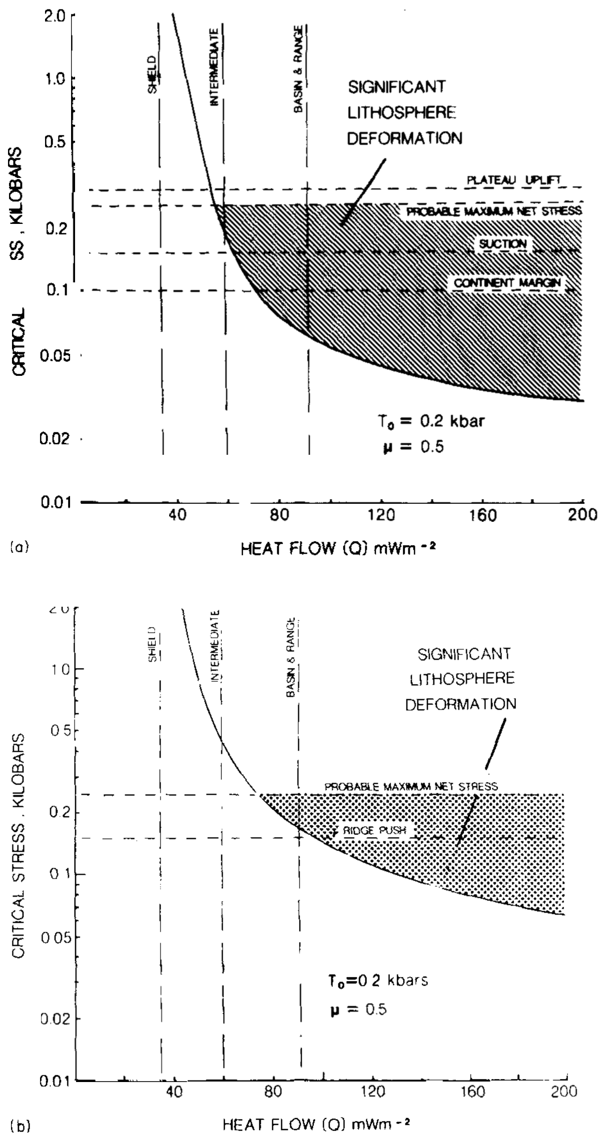

Figure 8. Curves of critical stress σ_c versus lithosphere heat flow, q, for (a) tensional and (b) compressional applied stress compared with possible stress source levels. $T_0 = 0.2$ kB, $\mu = 0.5$. (a) Field of significant tensional lithosphere deformation compared with estimated stress levels for likely sources of tensional stress (plateau uplift, subduction and continental margin stresses) and for the probable maximum net stress. (b) Field of significant compressional lithosphere deformation compared with the estimated stress level from ocean-ridge push, and for the probable maximum net stress.

c. 0.3 kB (*cf.* the break-up of Pangaea during the Mesozoic). In a more complex example like the present-day northern American plate, the state of stress would be expected to vary from net tensional within the Basin-and-Range plateau uplift to compressional in the eastern part of the continent affected by the mid-Atlantic ridge-push.

Considering only the sources of stress already discussed, it seems likely that the stress levels within present continental plates are within the range −0.25 to +0.25 kB – although locally these levels could be exceeded due to other contributions from non-renewable stresses (e.g. thermal or membrane stresses).

The expected levels of continental intraplate stress can be compared with the strength of the lithosphere predicted by the lithosphere deformation model. Fig. 8(a) indicates the field of likely extensional lithosphere deformation in relation to the theoretical stress levels associated with the main sources of tensional intraplate stress (plateau uplift, subduction suction and continental margin effects). In practice these tensional stresses would be partly offset by compressional stresses and it is unlikely that in present-day continental lithosphere a net (renewable) tensional stress exceeding 0.25 kB exists. In the case of compressional deformation (Fig. 8b) the likely maximum net stress level may be of the same order but would only be achieved in a piece of continental lithosphere affected by adjacent plateau uplift.

In summary, therefore, the lithosphere deformation model predicts significant extensional deformation in continental regions with heat flow values $q \geqslant c.\ 60\,\mathrm{mW\,m^{-2}}$ given a favourable combination of stress sources, and significant compressional deformation with $q \geqslant c.\ 75\,\mathrm{mW\,m^{-2}}$ under rather restricted conditions of stress combination. For more usual levels of compressive stress (*cf.* the ridge push estimate of 0.15 kB) failure would only occur in very hot or very weak lithosphere (*cf.* the lower curve of Fig. 7b).

6 The depth of the brittle-ductile transition

The application of stress to the lithosphere results in ductile deformation in the lower lithosphere and in brittle fracture in the upper lithosphere. If *whole lithosphere failure* has not occurred, the regions of brittle and ductile deformation are separated by a region of mechanically competent lithosphere which has suffered only elastic deformation (Fig. 1). However for increased values of applied stress, or with the progress of time as the stress amplification effect occurs, the regions of brittle and ductile deformation extend downwards and upwards respectively until they meet annihilating the elastic core of the lithosphere. This is the point at which WLF occurs. This process can be seen occurring in Fig. 3(a) and is represented schematically in Fig. 1. The position at which the regions of brittle and ductile deformation meet corresponds to the brittle-ductile transition.

The depth of the brittle-ductile transition can be determined from the deformational model and is dependent on the lithosphere temperature structure. In Fig. 9(a) the depth of the brittle-ductile transition is shown as a function of lithosphere heat flow. Separate curves are shown for tensile and compressional applied stress. The depth of the brittle-ductile transition can be seen to decrease with increase in heat flow. Tensile deformation can be seen to produce a slightly deeper brittle-ductile transition than compressional. For the tensile applied stress model, for heat flows less than approximately $60\,\mathrm{mW\,m^{-2}}$, two brittle ductile transitions are predicted by the model – one in the quartz rheology crust and the other in the olivine rheology mantle.

The curves shown in Fig. 9(a) correspond to models for which WLF occurs at 1 Myr after the application of the applied stress. The levels of stress required to produce such deformation are greater for lower levels of heat flow (see Fig. 7a). The curves are shown dashed for

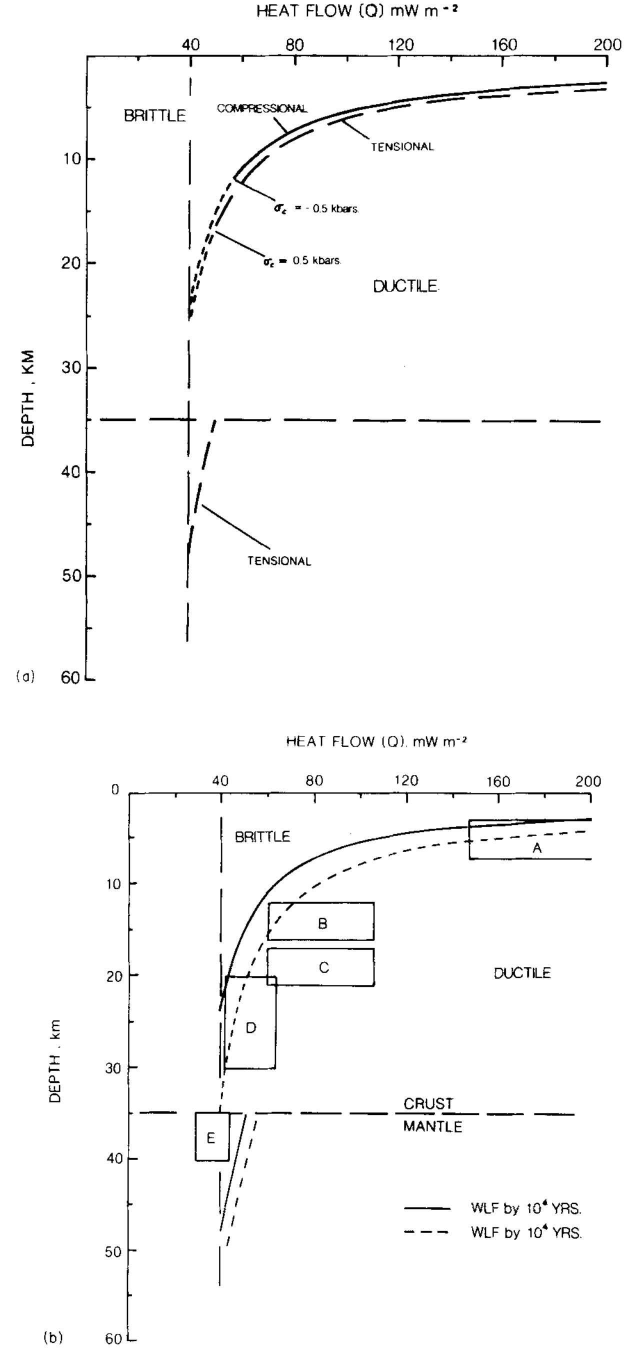

Figure 9. Plots of the calculated depth of the brittle-ductile transition against lithosphere heat flow. (a) Curves for compressive (solid line) and tensional (dashed line) deformation. The deformation rate corresponds to WLF by 1 Ma. The curves are shown dotted for deformation requiring an unrealistically large critical stress σ_C greater than $\pm$ 0.5 kB. (b) A comparison of the calculated brittle-ductile transition depth against observations of the brittle-ductile transition depths based on seismic evidence adapted from Sibson (1982). Seismic data areas are: (A) Geysirs and Clearlake Highlands. (B) Central California and Coso Range. (C) Wasatch Front. (D) Eastern US and Canada. (E) Sierra Nevada. Theoretical curves are shown for deformation rates corresponding to WLF by 10^4 (dashed line) and 10^6 yr (solid line).

models in which an applied stress greater than ±0.5 kB is required. Such large levels of stress are unlikely to be applied to the lithosphere (see Section 5) except in exceptional circumstances. Average strain rates of the models shown in Fig. 9 decrease with increasing heat flow ranging between approximately 0.1 and 1 per cent Ma^{-1} corresponding to strain rates of 10^{-16}–$10^{-15}\ s^{-1}$.

In Fig. 9(b) a composite curve for both tensile and compressive applied stress is shown for the relationship between brittle-ductile transition depth and heat flow. Also shown is a composite curve for tensile and compressional deformation for models in which WLF occurs at 10^4 yr after the initial application of stress. The latter models require greater levels of applied stress than the former. Average strain rates for this model vary between 100 and 10 per cent Ma^{-1}, decreasing with increase in heat flow. It can be seen that decreasing the time to WLF (and therefore increasing the strain rate) has the effect of deepening the brittle-ductile transition.

Also shown in Fig. 9(b) are estimates of the depth of the brittle-ductile transition depth as a function of heat flow, based on observations of the depth distribution of some continental earthquakes. The data shown are taken from Sibson (1982) and the brittle-ductile transition depth is estimated by assuming that it corresponds to the deepest observed seismic foci. The focal mechanisms correspond to extensional, thrust and strike-slip faulting. While the agreement with the transition depth predicted by the model is not perfect, the general dependence on heat flow is similar. The observed data would appear to correspond better to the faster strain-rate model. However the slower strain-rate curve could be made to fit the observed data by using a weaker brittle strength or a stiffer rheology for the crust.

7 Geological applications

7.1 INTRA-PLATE EXTENSION

Significant continental intra-plate extension appears to be confined to continental rift zones and rift-related basins. There is no general agreement among students of continental rift zones as to a simple mechanism for the initiation and evolution of such structures although crustal extension is now generally considered to be a major factor in their development. Active rift zones appear to be characterized by crustal thinning and by the formation of a 'low-velocity pillow' of hotter less dense asthenospheric material within the mantle part of the lithosphere (Illies 1970; Hermance 1982). There are great differences in the extent and character of magmatism related to rift zones. For example the total volume of volcanic products in the East African rift (*c.* 500 000 km^3 according to Baker, Mohr & Williams 1972) contrasts with only 5000 km^3 in the Baikal rift (Logatchev & Florensov 1978). Moreover the nature and extent of magmatism and the extent of crustal doming or uplift varies considerably along the length of individual rift systems and from one rift to another.

Some authors believe that many rifts result primarily from thermal anomalies below the lithosphere perhaps aided by favourable stress states in the overlying lithosphere; others believe that lithospheric extension is the primary cause and that thermo-magmatic effects are secondary and result from lithosphere thinning. A third possibility is that both mechanisms have operated and that some (weakly or non-volcanic) rifts are extensional in origin while others are primarily thermal in origin. The various models are discussed in summaries by Neumann & Ramberg (1978) and Mohr (1982). It is apparent from studies of individual rifts that the formation of a depression rather than crustal updoming is the first stage in the development of many rift zones (Mohr 1982) suggesting that the model of hot-spot generated, subsequently rifted, crustal domes (Burke & Dewey 1973) is not universally applicable.

Whether or not a thermal anomaly initiated the extension, the generation of any extensional rift structure must depend at least partly on the regional state of stress within the lithosphere and our model will therefore give estimates of the minimum stress conditions necessary for the initiation of continental rifts under specified thermal conditions, and will thus make some contribution to resolving the above dilemma. We consider the application of our model to five well-documented examples of intra-plate extensional tectonics: the Rhine graben, the Baikal and East African rifts, the North Sea basin, and the Basin-and-Range Province.

7.2 THE RHINE GRABEN

This is part of an extensive central European rift system formed in late Eocene–early Oligocene times with associated volcanic activity and intermittently active until the present day (Illies 1978; Ziegler 1982). According to Illies (1978) and Illies & Greiner (1978) initial subsidence took place in Eocene times, and the climax of tensional rifting in the late Eocene–early Oligocene coincided with the culmination of Alpine compression; this is seen as a reflection of the same stress field. Since mid-Pliocene times the stress axes have changed to a NW–SE σ_1 direction producing mainly sinistral strike-slip motion along the rift. Total extension across the rift is about 10 per cent according to Zeigler (1982). The present heat flow of 107 ± 35 mW m^{-2} in the upper Rhine graben compares with a value of 73 ± 20 for the Hercynian fold belts to the north and east (see Morgan 1982).

If we assume that the heat flow of 73 mW m^{-2} (similar to other areas of Hercynian orogenic crust) is representative of thermal conditions at the time of initiation of the rift, then according to Fig. 8(a) a tensional stress of just under 0.1 kB would be sufficient to initiate the rifting. An extensional stress of this magnitude could perhaps be envisaged in mid-Tertiary times if the effect of subduction at the Pacific end of the Eurasian plate more than offset the compressional element arising from the mid-Atlantic ridge (*cf.* Bott 1982). The effect of the north–south compression resulting from the Alpine collision, as suggested by Illies (1978), may have been an important contributory factor in raising the differential stress to the critical level.

However the initiation of the rift may be related to regional late Cretaceous–Palaeocene extension preceding the development of the Greenland–Norway spreading axis. The rift follows in part an old line of structural weakness, the Mjøsa–Mediterranean shear zone, which may also have played an important role in its initiation.

7.3 THE BAIKAL RIFT

This is situated in the central part of the Eurasian plate, about 3000 km north of the Himalayan suture zone. This 2500–3000 km long active rift has no obvious connection with any other rift system or with a plate boundary. The earliest volcanic activity associated with the rift is late Cretaceous in age but the bulk of the rift-related fissure eruption took place in Miocene to early Pliocene times (Logatchev *et al.* 1978; Logatchev & Florensov 1978). A figure of 10 km extension (*c.* 9 per cent) is given by these authors.

The heat flow in the rift is 97 ± 22 compared with 45 ± 10 mW m^{-2} in the Siberian platform to the west (Precambrian shield) and 55 ± 10 mW m^{-2} for the Caledonian fold belt to the SE (Morgan 1982). The rift is situated at the centre of a large uplifted region above a zone of abnormally low seismic velocity and presumably higher temperature in the upper mantle.

If the initiation of the extension preceded the thermal anomaly, we have to consider the likely extensional stress required for failure in crust with a heat flow of *c*. 55 mW m^{-2}. According to Fig. 8(a) a stress of *c*. 0.25 kB would be required which is about the limit of what might be expected by adding the effects of Pacific subduction suction and the Eurasian continental margin. The likely time of initiation of the rift coincides with the late Cretaceous to early Eocene collision between India and the Lhasa block (Allegre *et al.* 1984) which, by imposing a N–S compression on the central part of the Eurasian plate, may have been a contributory factor.

7.4 THE EAST AFRICAN OR KENYA RIFT

This is part of a rift system extending for about 3500 km through eastern Africa to connect with the Red Sea–Gulf of Aden rift, which has been an actively spreading plate boundary since about upper Oligocene times. Baker & Wohlenberg (1971) give a figure of 10 km extension for the Kenya rift since the Miocene (i.e. about 20 per cent extension). The rift is situated on a large regional uplift associated with a negative Bouguer anomaly with a width of more than 1000 km indicating the presence of a large low-density asthenosphere pillow (Fairhead 1976). The course of the rift network is strongly influenced by younger Precambrian tectonic trends and avoids the older Tanzanian craton. The average heat flow within the rift is 105 ± 51 mW m^{-2} compared with 52 ± 17 mW m^{-2} for the flank regions (Morgan 1982).

As Bott (1982) has pointed out, the African rift system appears to have developed within the continental part of a plate under general compressive stress arising from the ridge-push effect on each side. This is confirmed by compressional fault-plane solutions of earthquakes outside the rift zone (Fairhead & Stuart 1982). The initiation of the rift in Miocene times is therefore likely to be related to local extensional stress arising from the thermally induced plateau uplift. Assuming that the present flank heat flow approximates to the regional value over the thermal anomaly before rifting, a tensional stress of over 0.3 kB would be required for complete failure (Fig. 8b), near the upper limit of what might be expected. However the rift is continuous with the active spreading rift system in the Red Sea–Gulf of Aden through Ethiopia. The progressively more alkaline trend of the volcanicity southwards from the active spreading rift (Harris 1969) is associated with a progressively decreasing rate of widening southwards (McKenzie, Davies & Molnar 1970; Mohr 1982) suggesting a contribution to the extensional stress field from a wedging effect related to the plate boundary.

7.5 THE NORTH SEA BASIN

This may be taken as an example of the type of sedimentary basin considered in the model developed by McKenzie (1978) which envisages very rapid extension, with lithosphere stretching and thinning, followed by the upwelling of warm asthenosphere generating a thermal anomaly which subsequently cooled. The main extensional faulting phase in the North Sea lasted from mid-Jurassic to early Cretaceous times (about 60 Ma) with strains in the range 10–55 per cent (Wood & Barton 1983). The total extension estimated by considering the change in crustal thickness however, is up to 80 per cent (Wood & Barton 1983) and much of this extension relates to the initial phase of rifting which occurred in the Triassic (Zeigler 1982).

The early Tertiary onset of seafloor spreading in the Norwegian–Greenland sea caused the North Sea rift to become inactive, and the subsequent history of the basin may be interpreted as the effect of continued regional depression resulting from the cooling and subsequent disappearance of an anomalous upper mantle rift pillow of Jurassic age (*cf.* Bott 1982b; Zeigler 1982).

In order to apply the model to the North Sea basin, we must consider the conditions prevailing in Triassic times with lithosphere of normal thickness but unknown thermal gradient. The initial generation of the North Sea basin was part of a process of rifting which affected the whole of Pangaea prior to its break-up and has been discussed by Froidevaux & Schubert (1975), Bott (1982b) and Bott & Kusznir (1984). Tensile stresses might have arisen mainly from subduction suction effects around much of the contemporary continental margin providing a net stress of over 0.2 kB. According to Fig. 8(a) this would be sufficient for extensional rifting given intermediate heat flow values of *c.* 60 mW m^{-2} or over – similar to those in present-day Palaeozoic orogenic crust of western Europe.

7.6 THE BASIN-AND-RANGE PROVINCE

This is a large currently active extensional region situated near the western margin of the American plate, mainly in Nevada and Arizona. According to Zoback *et al.* (1981) the current phase of extensional deformation commenced about 10 Ma ago and has resulted in extensional strains of 15–30 per cent (an average strain rate of *c.* 10^{-15} s^{-1}). However this recent phase followed a more prolonged extensional phase in the period 30–10 Ma leading to much larger extensional strains of the order of 50–100 per cent or even more. Total extensions of as much as 300 per cent have been proposed by Wernicke (1981). The earlier extensional phase was initiated between 20 and 30 Ma ago in association with basaltic volcanism, and has been ascribed to back-arc processes related to subduction of the Farallon plate below the Pacific continental margin (Zoback *et al.* 1981). This tectonic setting suggests that a thermal anomaly would have accompanied the earlier rifting phase and that substantial structural and thermal weakening of the lithosphere may have taken place before the modern rifting phase began.

If the present heat flow of 92 ± 33 mW m^{-2} (see also the figure of 100 ± 15 for the related Rio Grande rift) (Table 2) is indicative of the thermal conditions accompanying the initiation of the modern rifting phase, Fig. 8(a) indicates that a very low tensional stress (*c.* 0.06 kB) would be sufficient to produce rifting. The heat flow in the flanking Colorado plateau is 60 mW m^{-2} (Chapman 1983). If the concentration of extensional effects in the Basin-and-Range Province resulted from a greater mid-Tertiary heating there compared with the Colorado plateau (*cf.* Morgan 1983) the heat flow at the time of initiation of the rifting was presumably somewhere between 60 and 90 mW m^{-2}. If we assume an initial heat flow of 70 mW m^{-2}, an extensional stress of 0.1 kB would be sufficient for failure according to Fig. 8(a). This stress level is lower than the likely tensional stress arising either from the plateau uplift, or from the suction force derived from subduction of the Farallon plate. A larger stress would produce more rapid extension.

7.7 DISCUSSION

These five examples of extensional deformation, four currently active and one inactive, were initiated at different times ranging from Triassic to Miocene and show extensions in the range 10–80 per cent over time periods of 10–100 Ma. The generally rather small extensions quoted yield low average strain rates of *c.* 10^{-16} s^{-1}, or 10^{-15} s^{-1} in the case of the Basin-and-Range Province (*cf.* Fig. 6) compared with typical plate boundary strain rates of *c.* 10^{-14} s^{-1}. The possibility that many rifts may be preceded by (relatively long?) periods of crustal depression and basin formation (*cf.* Mohr 1982) before 'active' rifting develops suggests that the period of initiation of a rift may be measurable in terms of tens of Ma rather than Ma but that after active rifting commences the rate of deformation presumably increases. It is noteworthy that the extension rate for the hot and more 'evolved' Basin-and-Range Province is an order of magnitude greater than those estimated for the other examples. The strain–time curve for 0.2 kB tension with a heat flow of 60 mW m^{-2} (Fig. 6) might be taken as a representative set of conditions leading to rifting. The curve shows WLF at about 10^5 yr. It is clear by extrapolating this curve that probably several tens of Ma will elapse before a geologically measurable strain of about 1 per cent is reached. An important geological implication of this aspect of our model is that observable evidence of intraplate extension may not appear until many tens of Ma after the imposition of the stress in lithosphere with average heat flow, and that the time of initiation of a rift cannot be simply correlated with the appearance of obvious extensional effects in the geological record.

The heat flow values in the active extensional regions are in the range 92–107 mW m^{-2}. Clearly with such high heat flows our model would predict extensional failure with very low values of extensional stress. However the model can strictly be applied only to the initial stage of rifting – starting from 'normal' lithosphere. Once significant crustal thinning has taken place, both the geometry and the rheology of the lithosphere are changed by the emplacement of warmer asthenosphere material in the lower part of the lithosphere (*cf.* McKenzie 1978) and in many cases by the development of vulcanicity. These changes

Table 2.

Region	Heat Flow, mWm^{-2}	Deformation state
A. Shield		
Superior Province[2]	34 ± 8	no failure
West Australia[2]	39 ± 8	no failure
West Africa (Niger)[2]	20 ± 8	no failure
South India[2]	49 ± 8	no failure
Mean Archaen + older Proterozoic[5]	41 ± 10	no failure
B. Intermediate		
Eastern U.S.A.[2]	57 ± 17	no failure
England and Wales[2]	59 ± 23	no failure
Central Europe (Bohemian massif)[2]	73 ± 18	local failure
Northern China[1]	75 ± 15	local failure
Mean Younger Proterozoic[5]	50 ± 5	-----
Mean Palaeozoic[5]	62 ± 20	-----
C. Thermally active		
Rhine graben[3]	107 ± 35	extensional failure
(flanks-Rhenish massif)[3]	(73 ± 20)	
Baikal rift[3]	97 ± 22	extensional failure
(S.E.flank-Older Palaeozoic)[3]	(55 ± 10)	
East African rift[3]	105 ± 51	extensional failure
(flanks)[3]	(52 ± 17)	
Basin-and-Range Province[2]	92 ± 33	extensional failure
(E.flank-Colorado plateau)[4]	(60)	

Heat flow data from Pollack & Chapman (1977)[1], Vitorello & Pollack (1980)[2], Morgan (1982[3], 1983[4], 1984[5]).

result in an increased thermal gradient which will in turn cause further structural weakening. The heat flow in an active rift would then be expected to be rather higher than in surrounding areas (e.g. compare the values of 107 ± 35 mW m^{-2} for the south Rhine graben with 73 ± 20 for the bordering Rhenish massif). To make a comparison of the data with the model results, it is necessary to use heat flow values which are representative of the regions *at the time of initiation* of the deformation.

Table 2 summarizes the heat flow data and tectonic status of a number of representative regions divided into (A) *continental shield* (Precambrian cratons), (B) *'intermediate'* (Palaeozoic orogenic crust) and (C) *thermally 'active'* (areas of current or recent rifting and vulcanicity). None of Group A with heat flow values in the range 34–49 mW m^{-2} show signs of significant current deformation (taking 'significant' to mean showing lateral crustal strains of *c.* 1 per cent or more). In group C, high heat flows ($q > 90$ mW m^{-2}) are associated with active volcanicity and extensional rifting. Group B shows a range of heat flow values derived from regions of Palaeozoic orogenic crust which probably correspond to the thermal conditions at the time of initiation of the rifts considered earlier, and which correspond rather closely to the range of 'flanking' heat flow values in the currently active rift areas (52 mW m^{-2} for East Africa to 73 mW m^{-2} for the Rhenish massif).

According to Fig. 8(a), significant extensional deformation should be possible in regions with a heat flow $q > c.$ 55 mW m^{-2} provided that favourable stress conditions exist, which is in good agreement with the data of Table 2.

These results suggest that a thermal anomaly is not an essential prerequisite for the formation of an extensional rift, although there are examples (the East African rift) whose initiation by an essentially thermal mechanism is easier to envisage because of the unfavourable stress conditions.

7.8 COMPRESSIONAL FAILURE

Significant intra-plate compressional deformation seems to be uncommon at present. Examples occur in Central Asia north of the Himalayan collision zone between India and Asia. Molnar & Tapponnier (1975) suggest that 200–300 km of crustal shortening and thickening have taken place within the Asian plate as a result of this collision and that much of the compressional deformation is concentrated in narrow fold and thrust belts like those of the Tien Shan and Nan Shan ranges, situated about 1500 km north of the plate suture.

The initial continental contact probably occurred in early to mid-Eocene times but the major effects of the collision appear to date from about the beginning of the Oligocene when large-scale vertical movements indicating crustal thickening and uplift occurred both in Tibet and in the more northerly ranges. At least some of the zones of compressional failure occur along previous (Mesozoic) subduction/collision sutures north of the main Indian suture (*cf.* Mitchell 1981; Allegre *et al.* 1984).

There are insufficient data available either about the heat flow pattern or the tectonic history of the interior of the Asian plate to allow our model to be adequately tested here.

The recently reported very high heat flow figures of 146 mW m^{-2} (Francheteau *et al.* 1984) attributed to high-level igneous intrusions are probably of only local significance. If we take a heat flow value of 75 mW m^{-2} to represent the likely thermal conditions during the initiation of compressional failure in the Oligocene in regions of Hercynian orogenic crust, a stress of -0.25 kB would be required (Fig. 8b) – too large to be attributed to the ridge-push effect alone. Larger compressive stresses could arise from the contribution of the Himalayan–Tibetan plateau uplift on the (presently unjustified) assumption that this preceded the intraplate failure to the north. Alternatively, much higher heat flow might be associated with residual effects of the older, Mesozoic, subduction zones within the Asian plate.

8 Conclusions

A mathematical model of viscoelastic intraplate lithosphere has been used to investigate lithosphere deformation in response to laterally applied stress and the resulting stress and strain distribution with time. The model incorporates the elastic, ductile and brittle behaviour of the lithosphere and the associated stress transfer resulting from stress release by ductile or brittle failure. Stress decay in the lower lithosphere due to ductile deformation leads to stress amplification in the upper lithosphere. Further amplification arises due to the release of the stress in the uppermost lithosphere by brittle failure and produces large amplified stresses in the middle and lower lithosphere. For sufficiently large levels of applied stress, or sufficiently hot lithosphere, the regions of significant ductile and brittle deformation meet, so destroying the elastic core of the lithosphere. This development has been named *whole lithosphere failure* (WLF) and only after this occurs can geologically significant deformation occur.

The deformation of the lithosphere and the magnitude of the applied stress required for WLF is critically dependent on the thermal structure of the lithosphere as represented by the surface heat flow. Significant, geologically observable, strains of *c.* 1 per cent or more may be produced through WLF over times of *c.* 1 Ma by an applied stress of +0.2 kB in lithosphere with an average heat flow ($q = 60\ \mathrm{mW\,m^{-2}}$). Much smaller stress levels are required in hotter lithosphere whereas for cooler shield or ocean-basin lithosphere WLF will not occur except for unrealistically high stress levels.

The magnitude of the applied stress required for WLF is much larger for compressive stress than for tensional. The critical level of applied tensional stress for lithosphere with an average heat flow of $60\ \mathrm{mW\,m^{-2}}$ is just under 0.2 kB. In contrast the critical compressive stress is 0.45 kB. These values are significantly lowered by using a much lower value of the failure strength T_0. For hotter lithosphere (e.g. Basin-and-Range Province) with $q = c.\ 90\ \mathrm{mW\,m^{-2}}$, the critical tensional stress is 0.065 kB and the critical compressive stress is 0.17 kB.

The main sources of intraplate stress arising from plate boundary forces and isostatically compensated loads are thought to give likely average net stress levels in the continental lithosphere in the range +0.25 to −0.25 kB. Using these expected maximum stress levels, the model predicts significant extensional deformation in regions with $q \geqslant c.\ 60\ \mathrm{mW\,m^{-2}}$ and significant compressional deformation for $q \geqslant c.\ 75\ \mathrm{mW\,m^{-2}}$ (under rather restricted conditions of stress combination). Thus extensional failure is predicted for areas of moderate heat flow (e.g. Central Europe, northern China) as well as for areas of high heat flow like the Basin-and-Range Province, whereas compressional failure is predicted only in areas of rather high heat flow. This is in good agreement with the observed rather widespread occurrence of extensional intraplate deformation and suggests that the much rarer compressional deformation may be restricted to regions of anomalously high heat flow or weak crust.

The model has also been used to calculate the depth of the brittle-ductile transition which is shown to decrease with increase in heat flow. This relationship may be tested against seismic evidence of the brittle-ductile transition depth. Comparison shows generally good agreement, although the seismic evidence shows a consistently deeper brittle-ductile transition depth than the model.

A deeper brittle-ductile transition in the model could be achieved by either using a weaker brittle failure criterion or a stronger rheology in the middle and lower crust. If the tensile and compressive strengths of the lithosphere in Sections 5 and 7 are of the right order, a combination of a weaker brittle failure criterion together with a stronger rheology would be required to satisfy the seismic brittle-ductile transition data.

In the above model, we have assumed for convenience that the lower crustal rheology is controlled by the deformation of dry quartz (whose rheology is well known). It is possible, however, that quartz is not present in sufficient quantity in the lower crust to form the rock matrix and control the ductile deformation. If so, plagioclase is likely to be the dominant mineral controlling the deformation and, while little is known about its rheology, it will be significantly stronger than quartz. Moreover the predominant deformation mechanisms in the lower crust may well be cataclastic flow, especially in lithosphere with lower heat flow values. There is at present insufficient information available to assess the effect of these factors on the model predictions.

References

Allègre, C. J. *et al.*, 1984. Structure and evolution of the Himalaya-Tibet orogenic belt, *Nature*, **307**, 17–22.

Baker, B. H., Mohr, P. A. & Williams, L. A. J., 1972. Geology of the eastern rift system of Africa, *Spec. Pap. geol. Soc. Am. 136*, **67** pp.

Baker, B. H. & Wohlenberg, J., 1971. Structure and evolution of the Kenya rift valley, *Nature*, **229**, 538–542.

Bodine, J. H., Steckler, M. S. & Watts, A. B., 1981. Observations of flexure and the rheology of the oceanic lithosphere, *J. geophys. Res.*, **86**, 3695–3707.

Bott, M. H. P., 1982a. The mechanism of continental splitting, *Tectonophys.*, **81**, 301–309.

Bott, M. H. P., 1982b. Origin of the lithosphere tension causing basin formation, *Phil. Trans. R. Soc. A*, **305**, 319–324.

Bott, M. H. P. & Dean, D. S., 1972. Stress systems at young continental margins, *Nature*, **235**, 23–25.

Bott, M. H. P. & Kusznir, N. J., 1979. Stress distributions associated with compensated plateau uplift structures with application to the continental splitting mechanism, *Geophys. J. R. astr. Soc.*, **56**, 451–459.

Bott, M. H. P. & Kusznir, N. J., 1984. Origins of tectonic stress in the lithosphere, *Tectonophys.*, **105**, 1–14.

Brace, W. F., 1964. Brittle fracture in rocks, in *State of Stress in the Earth's Crust*, pp. 111–174, ed. Judd, W. R., Elsevier, Amsterdam.

Bullard, E., Everett, J. E. & Smith, A. G., 1965. The fit of the continents around the Atlantic, *Phil. Trans. R. Soc. A*, **258**, 41–51.

Burke, K. & Dewey, J. F., 1973. Plume-generated triple junctions: key indicators in applying plate tectonics to old rocks, *J. Geol.*, **81**, 406–433.

Byerlee, E., 1978. Friction of rocks, *Pure appl. Geophys.*, **116**, 615–626.

Chapman, D. S., 1983. Colorado plateau: thermal-tectonic evolution (abstr.), *Int. U. Geodesy Geophys.*, Hamburg, p. 577.

Elsasser, W. M., 1971. Sea floor spreading as thermal convection, *J. geophys. Res.*, **76**, 1101–1112.

Fairhead, J. D., 1976. The structure of the lithosphere beneath the Eastern Rift, East Africa, deduced from gravity studies, *Tectonophys.*, **30**, 269–298.

Fairhead, J. D. & Stuart, G. W., 1982. The seismicity of the East African rift system and comparison with other continental rifts, in *Continental and Oceanic Rifts*, pp. 41–61, ed. Palmason, G., Geodynamics Series 8, American Geophysics Union.

Forsyth, D. & Uyeda, S., 1975. On the relative importance of the driving forces of plate motion, *Geophys. J. R. astr. Soc.*, **43**, 163–200.

Francheteau, J. *et al.*, 1984. High heat flow in southern Tibet, *Nature*, **307**, 32–36.

Froidevaux, C. & Schubert, G., 1975. Plate motion and structure of the continental asthenosphere: a realistic model of the upper mantle, *J. geophys. Res.*, **80**, 2553–2564.

Goetze, C., 1978. The mechanisms of creep in olivine, *Phil. Trans. R. Soc. A*, **288**, 99–119.

Griffith, A. A., 1924. Theory of rupture, *Proc. first int. Congr. Applied Mechanics*, Delft, A221, 163–198.

Harris, P. G., 1969. Basalt type and African rift valley tectonism, *Tectonophys.*, **8**, 427–436.

Heard, H. C., 1976. Comparison of the flow properties of rocks at crustal conditions, *Phil. Trans. R. Soc. A*, **283**, 173–186.

Hermance, J. F., 1982. Magnetotelluric and geomagnetic deep-sounding studies in rifts and adjacent areas: constraints on physical processes in the crust and upper mantle, in *Continental and Oceanic Rifts*, pp. 169–192, ed. Palmason, G., Geodynamics Series 8, American Geophysics Union.

Illies, J. H., 1970. Graben tectonics as related to crust-mantle interaction, in *Graben Problems*, pp. 3–27, eds Illies, J. H. & Mueller, St.

Illies, J. H., 1978. Two stages Rhinegraben rifting, in *Tectonics and Geophysics of Continental Rifts*, pp. 63–71, eds Ramberg, I. B. & Neumann, E. R., Reidel, Dordrecht.

Illies, J. H. & Greiner, G., 1978. Rhine graben and the Alpine system, *Bull. geol. Soc. Am.*, **89**, 770–782.

Jaeger, J. C. & Cook, N. G. W., 1971. *Fundamentals of Rock Mechanics*, Chapman & Hall, London.

Koch, P. S., Christie, J. M. & George, R. P., 1980. Flow law of 'wet' quartzite in the α-quartz Field, *Trans. Am. geophys. Un.*, **61**, 376.

Kohlstedt, D. L. & Goetze, C., 1974. Low-stress high-temperature creep in olivine single crystals, *J. geophys. Res.*, **79**, 2045–2051.

Kusznir, N. J., 1982. Lithosphere response to externally and internally derived stresses: a viscoelastic stress guide with amplification, *Geophys. J. R. astr. Soc.*, **70**, 399–414.

Kusznir, N. J. & Bott, M. H. P., 1977. Stress concentration in the upper lithosphere caused by underlying viscoelastic creep, *Tectonophys.*, **43**, 247–256.

Kusznir, N. J. & Park, R. G., 1982. Intraplate lithosphere strength and heat flow, *Nature*, **299**, 540–542.

Lachenbruch, A. H. & Sass, J. H., 1980. Heat flow and energetics of the San Andreas Fault zone, *J. geophys. Res.*, **85**, 6185–6222.

Le Pichon, X., 1968. Sea floor spreading and continental drift, *J. geophys. Res.*, **73**, 3661–3697.

Logatchev, N. A. & Florensov, N. A., 1978. The Baikal system of rift valleys, *Tectonophys.*, **45**, 1–13.

Logatchev, N. A., Rogozhina, V. A., Solonenko, V. P. & Zorin, Y. A., 1978. Deep structure and evolution of the Baikal rift zone, in *Tectonics and Geophysics of Continental Rifts*, pp. 49–61, eds Ramberg, I. B. & Neumann, E. R., Reidel, Dordrecht.

McClintock, F. A. & Walsh, J. B., 1962. Friction on Griffith cracks under pressure, *Proc. fourth U.S. Nat. Congr. Applied Mechanics*, pp. 1015–1021.

McKenzie, D., 1978. Some remarks on the development of sedimentary basins, *Earth planet. Sci. Lett.*, **40**, 25–32.

McKenzie, D. P. & Parker, R. L., 1967. The North Pacific: an example of tectonics on a sphere, *Nature*, **216**, 1276–1279.

McKenzie, D. P., Davies, D. & Molnar, P., 1970. Plate tectonics of the Red Sea and East Africa, *Nature*, **226**, 243–248.

Mitchell, A. H. G., 1981. Phaneozoic plate boundaries in mainland SE Asia, the Himalayas and Tibet, *J. geol. Soc. London*, **138**, 109–122.

Mithen, D. P., 1982. Stress amplification in the upper crust and the development of normal faulting, *Tectonophys.*, **83**, 259–273.

Mohr, P., 1982. Musings on continental rifts, in *Continental and Oceanic Rifts*, pp. 293–309, ed. Palmason, G., Geodynamics Series 8, American Geophysics Union.

Molnar, P. & Tapponnier, P., 1975. Cenozoic tectonics of Asia: effects of a continental collision, *Science*, **189**, 419–426.

Morgan, P., 1982. Heat flow in rift zones, in *Continental and Oceanic Rifts*, ed. Palmason, G., Geodynamics Series 8, American Geophysics Union.

Morgan, P., 1983. Uplift of the Colorado plateau and its relationship to volcanism and rifting in the adjacent Basin-and-Range and Rio Grande rift (abstr.), *Int. U. Geodesy Geophys.*, Hamburg, p. 576.

Morgan, P., 1984. The thermal structure and thermal evolution of the Continental Lithosphere, *Phys. Chem. Earth*, in press.

Murrell, S. A. F., 1965. The effect of triaxial stress systems on the strength of rocks at atmospheric temperatures, *Geophys. J. R. astr. Soc.*, **10**, 231–281.

Neumann, E. R. & Ramberg, I. B., 1978. Palaeorifts – concluding remarks, in *Tectonics and Geophysics of Continental Rifts*, pp. 409–424, eds Ramberg, I. B. & Neumann, E. R., Dordrecht.

Pollack, H. N. & Chapman, D. S., 1977. On the regional variation of heat flow, geotherms and lithosphere thickness, *Tectonophys.*, **38**, 279–296.

Post, R. L., 1977. High temperature creep of Mt Burnet Dunite, *Tectonophys.*, **42**, 75–110.

Richardson, R. M., Solomon, S. C. & Sleep, N. H., 1976. Intraplate stress as an indicator of plate tectonic driving forces, *J. geophys. Res.*, **81**, 1847–1856.

Schubert, G., Yuen, D. A., Froidevaux, C., Fleitout, C. & Sourian, M., 1978. Mantle circulation with partial shallow return flow: effects on stresses in oceanic plates and topography of the sea floor, *J. geophys. Res.*, **83**, 745–758.

Sibson, R. H., 1982. Fault zone models, heat flow, and the depth distribution of earthquakes in the continental crust of the United States, *Bull. seism. Soc. Am.*, **72**, 151–163.

Sibson, R. H., 1983. Continental fault structure and the shallow earthquake source, *J. geol. Soc. London*, **140**, 741–767.

Turcotte, D. L., 1983. Mechanisms of crustal deformation, *J. geol. Soc. London*, **140**, 701–724.

Turcotte, D. L. & Oxburgh, E. R., 1976. Stress accumulation in the lithosphere, *Tectonophys.*, **35**, 183–199.

Vitorello, I. & Pollack, H. N., 1980. On the variation of continental heat flow with age and the thermal evolution of continents, *J. geophys. Res.*, **85**, 983–995.

Wang, C. & Mao, N., 1979. Shearing of saturated clays in rock joints at high confining pressures, *Geophys. Res. Lett.*, **6**, 825–828.

Wang, H. F. & Simmons, G., 1978. Microcracks in crystalline rock from 5.3 km depth in the Michigan basin, *J. geophys. Res.*, **83**, 5849–5856.

Wernicke, B., 1981. Low-angle normal faults in the Basin and Range province: nappe tectonics in an extending orogen, *Nature*, **291**, 645–648.

Wernicke, B., Spencer, J. E., Burchfiel, B. C. & Guth, P. L., 1982. Magnitude of crustal extension in the southern Great Basin, *Geology*, **10**, 499–502.

Wood, R. & Barton, P., 1983. Crustal thinning and subsidence in the North Sea, *Nature*, **302**, 134–136.

Zeigler, P. A., 1982. Faulting and graben formation in western and central Europe, *Phil. Trans. R. Soc. A*, **305**, 113–143.

Zoback, M. L., Anderson, R. E. & Thompson, G. A., 1981. Cainozoic evolution of the state of stress and style of tectonism of the Basin and Range province of the western United States, *Phil. Trans. R. Soc. A*, **300**, 407–434.

Geophys. J. R. astr. Soc. (1984) 79, 539–553

Local and regional induction in the British Isles

R. J. Banks *Department of Environmental Sciences, University of Lancaster, Lancaster LA1 4YQ*

D. Beamish *Geomagnetism Unit, British Geological Survey, Murchison House, West Mains Road, Edinburgh EH9 3LA, Scotland*

Received 1984 March 28; in original form 1983 August 24

Summary. Electric currents induced in the shallow seas and deep ocean around the British Isles have a profound effect upon the electromagnetic fields observed at stations on the land. The configuration of anomalous currents changes with frequency, and causes corresponding changes in the geomagnetic transfer functions. Magnetic variations have been recorded at a dense network of sites in southern Scotland and northern England. Single-station transfer functions have been used to generate hypothetical event maps of the anomalous vertical field, and hence to infer the configuration of the anomalous internal currents. At periods exceeding 2000 s, the vertical field is dominated by the effects of electric currents to the west, presumably in the Atlantic Ocean. In the period range 400–2000 s, anomalous currents are concentrated in a thin sheet comprising the shallow seas, the thick sequences of post-Caledonian sedimentary rock which underlie them, and the extensions of the sedimentary basins into the land. The response of the individual basin is determined not only by its local conductivity structure, but also by the extent of its connection to the shallow seas, i.e. its regional importance within the conductive sheet. At periods less than 200 s on the other hand, the anomalous fields at inland sites are principally determined by the *local* geological structure. These results confirm conclusions reached from theoretical studies of electromagnetic induction in a heterogeneous surface layer (Park, Orange & Madden); that electromagnetic response data measured in a 3-D environment such as the Northumberland Basin must be interpreted using 3-D models. If one or 2-D models is used, the data must be corrected on the basis of regional measurements.

1 Introduction

The Atlantic Ocean and the shallow seas around the British Isles (Fig. 1) must strongly influence the electromagnetic fields observed on the land. Electric currents induced in the

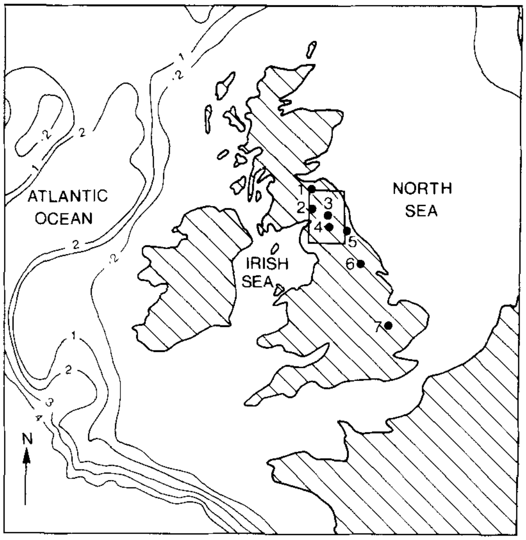

Figure 1. Location of the area investigated in relation to the shallow seas around the British Isles. Numbered stations are: 1 – Earlyburn, 2 – Eskdalemuir, 3 – Wark, 4 – Sinderhope, 5 – Durham, 6 – York, 7 – Cambridge. Bathymetric contours are labelled in kilometres.

sea-water produce magnetic fields which may contribute significantly to the total field at an inland site. In addition, the configuration of the shallow seas may modify the electric field within the land, and affect the response of bodies of conductive rock. Our aim in this investigation is to try to assess the effect of the seas on magnetic field variations with periods of 20–6000 s, and in particular to decide whether they must be included as an essential component of any model which attempts to simulate the electromagnetic fields at inland sites.

Edwards, Law & White (1971) determined single-station transfer functions at sites throughout the British Isles, and used an induction vector representation of their data to infer the approximate location of anomalous currents. At a period of 2400 s, they detected current concentrations in the Atlantic Ocean, in the North and Irish Seas, and also through the land beneath southern Scotland. Bailey & Edwards (1976) used the hypothetical event technique (Bailey *et al.* 1974) to represent the same data in a different way. They emphasized the distinction between the current systems generated in response to orthogonal polarisations of the horizontal magnetic field. With a northward magnetic field, the regional current flow should be from east to west, involving a significant component through the land, and exciting anomalous structures within the land. The regional current associated with an eastward field is approximately parallel to the coastline of the British Isles, and is most effective in exciting anomalous currents in the shallow seas.

More recently, Dosso, Nienaber & Hutton (1980) have used an analogue model to investgate the response of the British Isles to electromagnetic fields with periods in the range 1000–10 000 s. Their results confirmed the importance of both the period and polarization of the horizontal magnetic field in determining the configuration of the anomalous currents. The E-polarization case (magnetic field east–west) produces the most straightforward results. At the longest period (10 000 s) the vertical component of the magnetic field observed over the land is dominated by the induced currents in the Atlantic. As the period is reduced, there is a decrease in the spatial scale of the magnetic fields they produce. Consequently, at sites some distance from the continental edge, e.g. in Scotland and England, the relative importance of the current in the shallow seas increases, and is dominant at a period of 1000 s. When the magnetic field is north–south (the H-polarization case), the vertical field produced by the currents in the seas is much less important. There is some evidence that the varying geometry of the islands influences the amount of current which flows through different parts of the land. However, since the land has a uniform conductivity in the model, the effects of conductive structures such as sedimentary basins are not predicted.

We have used the analogue model results to help predict the frequency response of single-station transfer function data collected at a dense network of sites in northern England and southern Scotland. The area straddles the mainland from coast to coast (see Fig. 1). On its western side, the northern end of the Irish Sea is almost closed by southern Scotland, leaving only the narrow passage of the North Channel between Scotland and Ireland. It is possible that the constriction may cause more current to flow through the land between the Irish and North Seas than would be otherwise expected. This purely geometric effect may be enhanced further by the presence of a sedimentary basin, running east–west across northern England, linking the North and Irish Seas (Fig. 3).

Most of the data analysed in this paper are derived from an investigation of the Alston Block and Northumberland Basin (Beamish & Banks 1983). The single-station transfer function estimates are of particularly good quality, derived from large amounts of data, and covering a wide period range (20–7200 s). The reliability of the data can be judged from the fact that it is possible to generate smooth hypothetical event maps with a spacing of only 0.02 nT between contours for a horizontal field amplitude of 1 nT. The station spacing averages 10–15 km, enabling us to locate the internal currents very precisely, and to relate them with some confidence to known geological structures.

2 The frequency dependence of the transfer functions

The azimuth of the induction vector provides a useful indication of the geometry of the internal current system responsible for the anomalous vertical magnetic field (Banks 1973). Fig. 2 shows the frequency dependence of the azimuth of the real vector for representative stations in the area mapped in detail (numbers 1–4), and also for some widely separated sites on a north–south line parallel to the east coast of England (numbers 5–7).

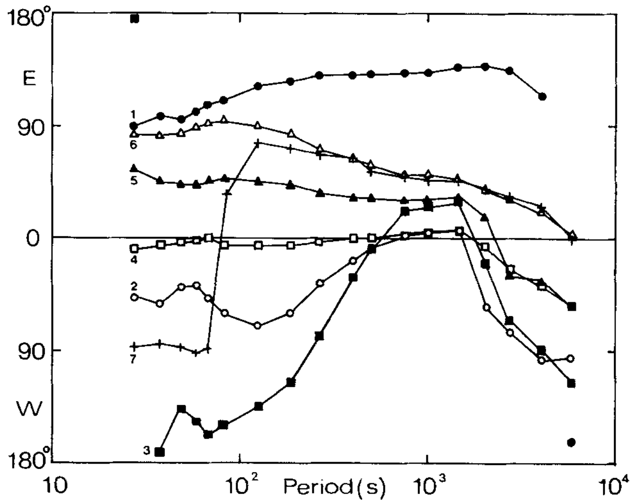

Figure 2. Azimuth of the real induction vector as a function of period. Station numbering as in Fig. 1.

At periods greater than 400 s, the frequency dependence of the azimuth is very similar at all the stations, with the exception of Earlyburn (1). As the period decreases from 10 000 to 1000 s, the vectors rotate from the NW to the NE quadrant. This behaviour agrees with that observed in the analogue model (Dosso *et al.* 1980). At 10 000 s, the magnetic fields are dominated by the current system in the deep ocean to the west and SW. As the period decreases, so does the spatial scale of the fields produced by the current in the Atlantic. The currents to the east in the North Sea are much closer, and their relative importance increases. The induction vectors at the most easterly stations (6 and 7) are the first to rotate as the period decreases, with the most westerly (3 and 4) the last to respond. The similarity in the behaviour of the real vector at all these sites strongly suggests that a common process controls the current which generates the magnetic fields. It is most unlikely that the strike of the local conductivity structure in the vicinity of each of these widely spaced stations is the same. It is much more probable that the common factor at all the sites is the dominant effect of currents induced in the shallow seas. However, the current system may not be confined to the seas alone, but extend inland by way of the sedimentary basins.

As the period falls to less than 400 s, the azimuths of the real vectors diverge, and below 100 s they stabilize around distinctly different directions. Such behaviour indicates that the local geological structure at each site controls the electromagnetic fields in the period range 30–100 s.

This simplified analysis of the frequency response of the magnetic field variations implies the existence of two distinct induction processes. Between 30 and 100 s, the induced current is controlled only by the *local* geological structure. In the range 400–2000 s, induction is a *regional* process involving the whole of a thin sheet comprising the shallow seas and conductive sediment both beneath the sea and on land. There is no sharp cut-off in the frequency ranges of the two modes of induction; their effects will overlap to some extent. The period ranges we are quoting are those in which each mode dominates the anomalous internal magnetic field at the majority of our sites.

To test the model, we need to investigate more closely the spatial correlation between the magnetic fields (and by implication the induced currents) and the local conductivity structure, in an area where the latter can be inferred from geological and other geophysical data. Fortunately, the structure of the region we have mapped in detail is relatively well known, both in terms of the surface geology, and from aeromagnetic, gravity and seismic surveys.

3 Spatial structure of the anomalous fields at intermediate periods

The area investigated in detail is shown in Fig. 3. It is bounded by the North Sea to the east and the Solway Firth to the west. Rocks of Ordovician and Silurian age, which were metamorphosed and folded in the Caledonian Orogeny, outcrop in the NW (the Southern Uplands), around the Cheviot volcanic centre in the NE, and in the SW (the Lake District). They are also present at very shallow depths in the SE, on the Alston Block. The Lake District, Alston Block, Cheviots and parts of the Southern Uplands, were all intruded by granite batholiths towards the end of the Caledonian Orogeny, and have subsequently formed relatively bouyant blocks of crust. The tendency of the Alston Block to rise relative to the surrounding areas has created major systems of faults along its northern, western and southern margins. By contrast, the crust in the areas between the granite-centred blocks has tended to subside, forming basins containing sediments of Upper Devonian to Permo–Triassic age. The thickness of the sediments is a maximum immediately to the north and west of the Alston Block, in the Northumberland Trough and Vale of Eden respectively. In both areas, the depth of the Caledonian basement is believed to reach 2–3 km (Lee 1982;

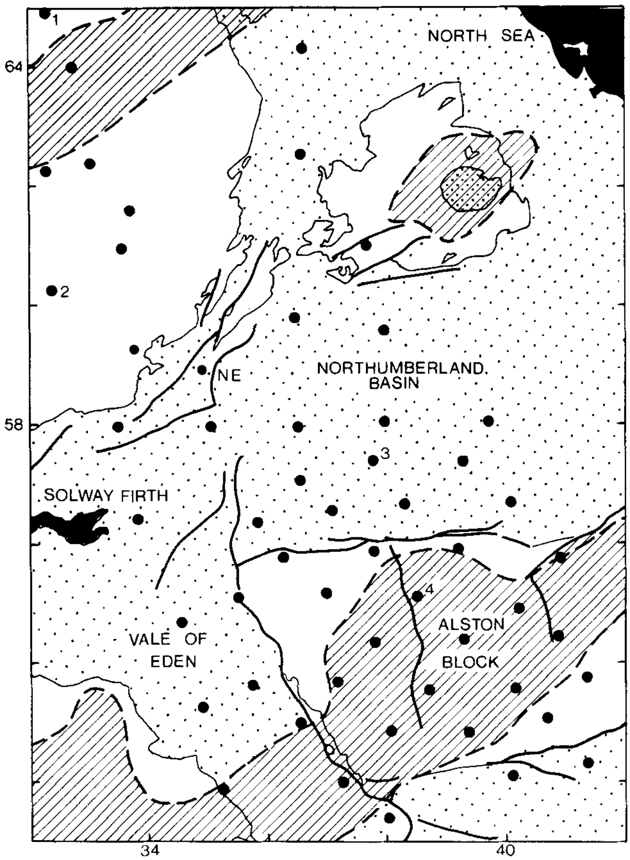

Figure 3. Station locations and geology. ● Magnetometer sites. — Major faults. Shading indicates areas underlain by granite batholiths. Stippled areas are underlain by substantial thicknesses of post-Caledonian sedimentary rock.

Bott 1974). The Carboniferous and Permo–Triassic sedimentary basins on the land are continuous with similar, but much thicker and more extensive basins beneath the North Sea and Irish Sea. The Caledonian metamorphic rocks, intruded by granite batholiths, can be expected to form a higher resistivity basement, over which there is a thin sheet of material with a high but laterally variable conductance, comprising both conductive sedimentary rocks and sea-water.

Two-frequency bands, centred on 750 and 60 s, were chosen on the basis of the frequency dependence of the real induction vector discussed in Section 2. Hypothetical event analysis (Bailey *et al.* 1974) was used to generate maps of the anomalous field associated with horizontal magnetic fields in the magnetic north and magnetic east directions (9°W and 81°E respectively). The azimuths are approximately parallel and perpendicular to the nearby east coast of England, and should correspond to H and E polarization induction in the North Sea. Single-station transfer functions (Banks 1973) are available at all the sites marked in Fig. 3. The data at 48 of the sites are derived from surveys by the authors and their colleagues (Beamish & Banks 1983; Grimes 1977); the remaining five are taken from Hutton & Jones (1980) and Ingham & Hutton (1982). The only anomalous field maps which can be generated from single-station transfer functions are of the real and imaginary parts of the vertical field. Unfortunately, the maps are only accurate if the horizontal field is uniform across the area, i.e. if the anomalous horizontal fields are only a small fraction of the total. Stations in the south of the area were operated simultaneously with a Rubidium magnetometer at Durham (see Fig. 1), and inter-station transfer functions were computed, linking the horizontal fields at each site to those at Durham (Beamish & Banks 1983). They showed that the anomalous horizontal fields at 750 s were generatlly less than 20 per cent of the total. At 60 s, however, the spatial variations in the horizontal fields are up to 100 per cent of the total field at Durham. These results suggest that hypothetical event maps based upon single-station transfer functions will given an adequate picture of the anomalous fields at 750 s, but that at 60 s the maps may be significantly distorted, and should be interpreted with care.

Fig. 4 is a map of the real part of the anomalous vertical field produced when the hori-

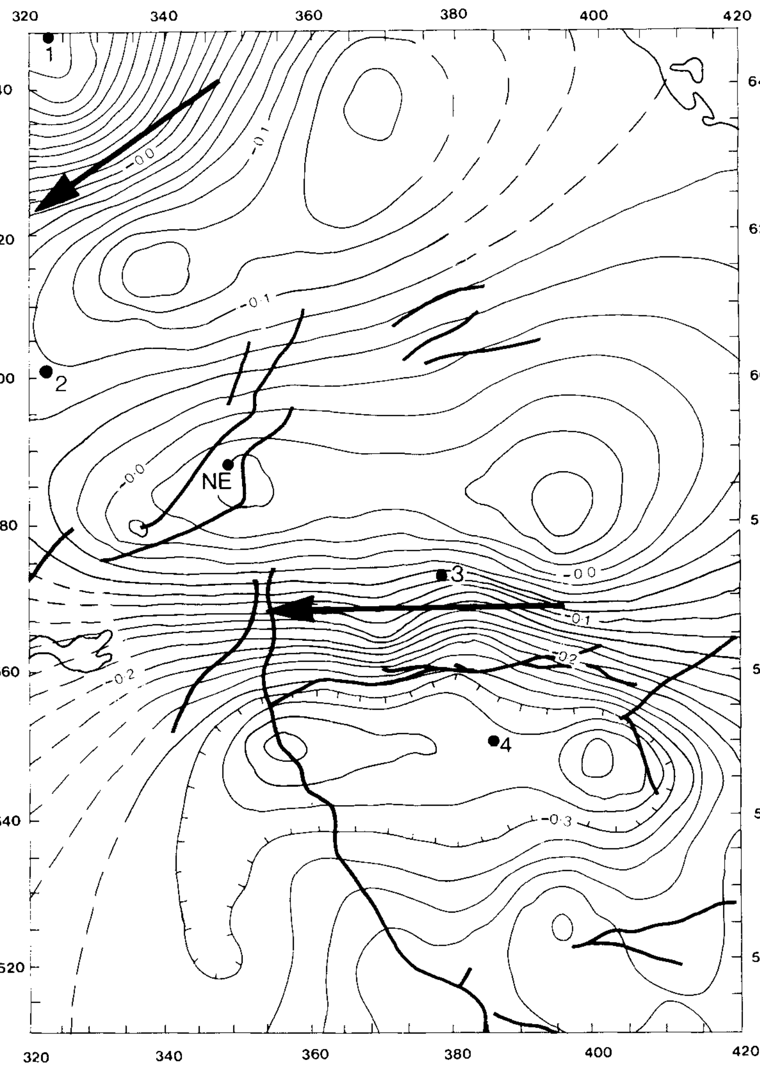

Figure 4. Hypothetical event maps of the anomalous vertical field. Period (T) = 750 s. Amplitude of the regional horizontal field = 1 nT. Azimuth (θ) of the regional field relative to magnetic north = 0°. Phase (ϕ) of the vertical field = 0°. Contour spacing = 0.02 nT. Heavy lines are major faults. Arrows indicate current concentrations.

zontal field at each site is directed magnetic north. The period is 750 s. The results for the imaginary part, which is very much smaller, are displayed in a different fashion in Section 5. A horizontal magnetic field with this azimuth should drive the current in the surface sheet from east to west through the land. Because the magnetic field is parallel to the coastline, no coast effect is expected, and none is observed. Instead, two intense anomalies are created over the land. The first of these, in the extreme NW of the map, is part of a NE to SW trending anomaly which runs across the entire width of Scotland beneath the Southern Uplands (see for example, Ingham & Hutton 1982). The second feature runs east–west, parallel to the southern margin of the Northumberland Trough, its maximum amplitude above the northern part of the Alston Block. The anomaly is asymmetric, possibly because of interference on its northern side from the other structure. The maximum current concentration is presumed to be in the position marked by the arrow, where the spatial gradient in the vertical field is greatest, and it coincides with the location of the greatest thickness of sediment in the Northumberland Trough. The steepness of the horizontal gradients in the magnetic field can be used to place constraints on the depth of the current. Alternatively, the vertical field map can be modelled by an equivalent current system in a thin sheet (Banks 1979). It turns out in this case that the sheet cannot be placed any deeper than 5 km; if it is, the current stream function is unstable. We interpret this to mean that at least a part of the current must be shallower than 5 km. The top 3 km of the crust is known to be formed from relatively conductive sedimentary rocks, which lie on top of a resistive metamorphic basement. A magnetotelluric station in the Northumberland Trough detected the surface conductor, which masked the deeper structure (Jones & Hutton 1979b). There is no positive evidence for the presence of any other conductive rocks in the upper crust, and, in view of the correlation between the anomalies and the near-surface structure, it seems most likely that the bulk of the current is flowing in the surface layer of sedimentary rock.

This superficial conductor is not isolated, but is linked at each end to more extensive bodies with greater conductivity–thickness products: the Irish and North Seas, and the underlying sedimentary basins of Permo–Triassic to Tertiary age. The question which naturally arises, is, whether the amplitudes of the anomalous fields around the Northumberland Basin would be as great as those observed if it were electrically isolated at both ends. If the connection to the rest of the sheet has no effects, the electromagnetic fields in and around the basin will be determined only by the 'local' geological structure, in this case the thickness, conductivity and horizontal extent of the Carboniferous sedimentary rocks. The Northumberland Basin runs east–west, and responds most strongly to a northward-directed horizontal magnetic field, just as we would expect if the induction were purely local. The very similar sedimentary basin in the Vale of Eden is aligned north–south, and if the induction is a local process, its response to an east magnetic field should be as strong as that of the Northumberland Basin to a northward field. However, if the link to the seas is important, the 'regional' situation of the conductor as part of the surface sheet should be just as important as the local conductivity structure in determining the basin's response. The Vale of Eden basin is linked at its northern end to the Solway Firth, but is an electrical dead-end to the south. Although it appears to connect to the Stainmore Trough, the sediment in both basins thins towards the junction, and the two conductors are effectively separate. There is, therefore, a significant contrast in the regional significance of the Vale of Eden and Northumberland Basins.

Fig. 5 shows the real part of the vertical field associated with a horizontal magnetic field directed eastward. The regional current should be driven from south to north, producing anomalous current concentrations in the North and Irish Seas. The resultant vertical field should be negative on the eastern side of the land, and positive on the west. The overall

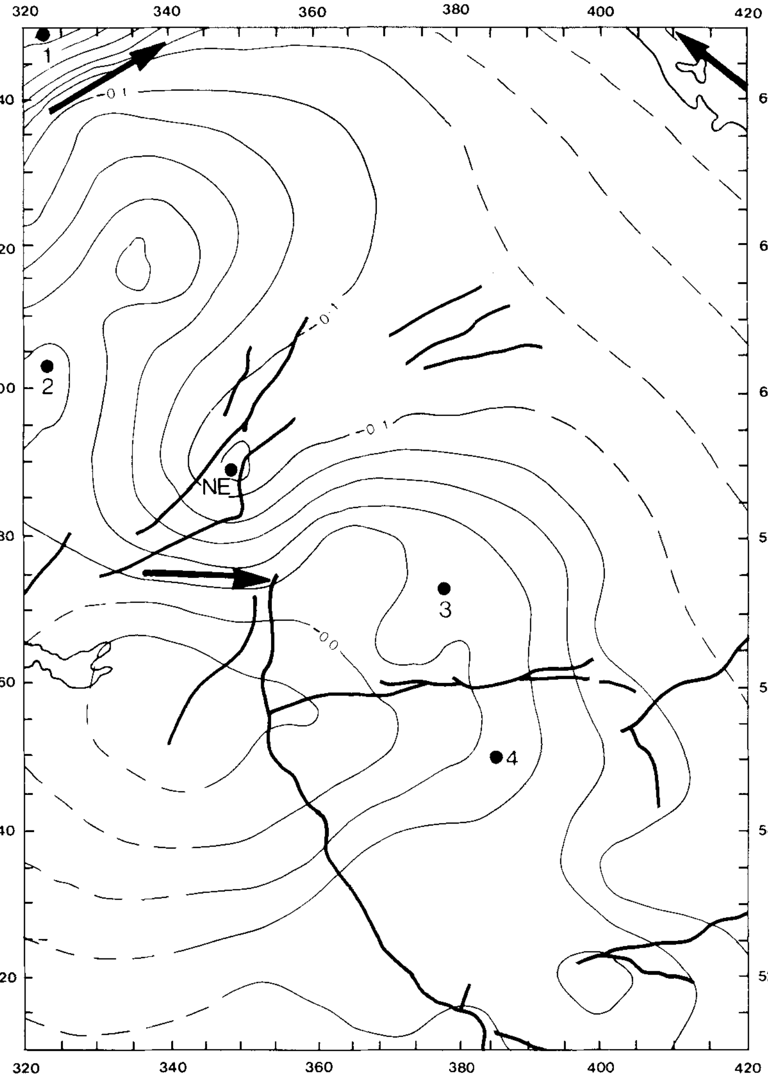

Figure 5. $T = 750$ s, $\theta = 90°$, $\phi = 0°$.

trend in the observations agrees with this prediction, although the field produced by the current in the North Sea is significantly stronger. However, superimposed on the broad pattern are features with much steeper spatial gradients. The Southern Uplands anomaly is still present in the NW corner, running from NE to SW. In addition, the influence of the conductor in the Northumberland Basin is plainly visible as an eastward bulge in the positive contours, indicating that the *eastward* magnetic field is able to induce a west-to-east current in the basin. Most significant of all, there is no sign of any anomaly running north–south along the eastern edge of the Vale of Eden, such as we would have expected if the local geological structure were the only factor determining the electromagnetic fields.

We conclude that, at a period of 750 s, the electromagnetic fields in northern England and southern Scotland are determined by induction in a thin sheet comprising both sea and sedimentary basins, and that the fields around a conductive structure on land are not only determined by its locally significant properties of conductance and lateral extent, but also by its regional importance with the sheet.

4 The spatial structure of the anomalous fields at short periods

Our analysis of the frequency dependence of the azimuth of the real induction vector led us to suggest that a profound change occurs in the mode of induction as the period of the magnetic field variations decreases to 100 s and less, and that the electromagnetic fields at shorter periods could well be much more closely related to the local geological structures. This assertion can be tested by investigating the fields around the two sedimentary basins at a period of 60 s.

Fig. 6 is a map of the real part of the vertical field associated with a northward horizontal magnetic field. The Southern Uplands anomaly in the NW has virtually disappeared, and the

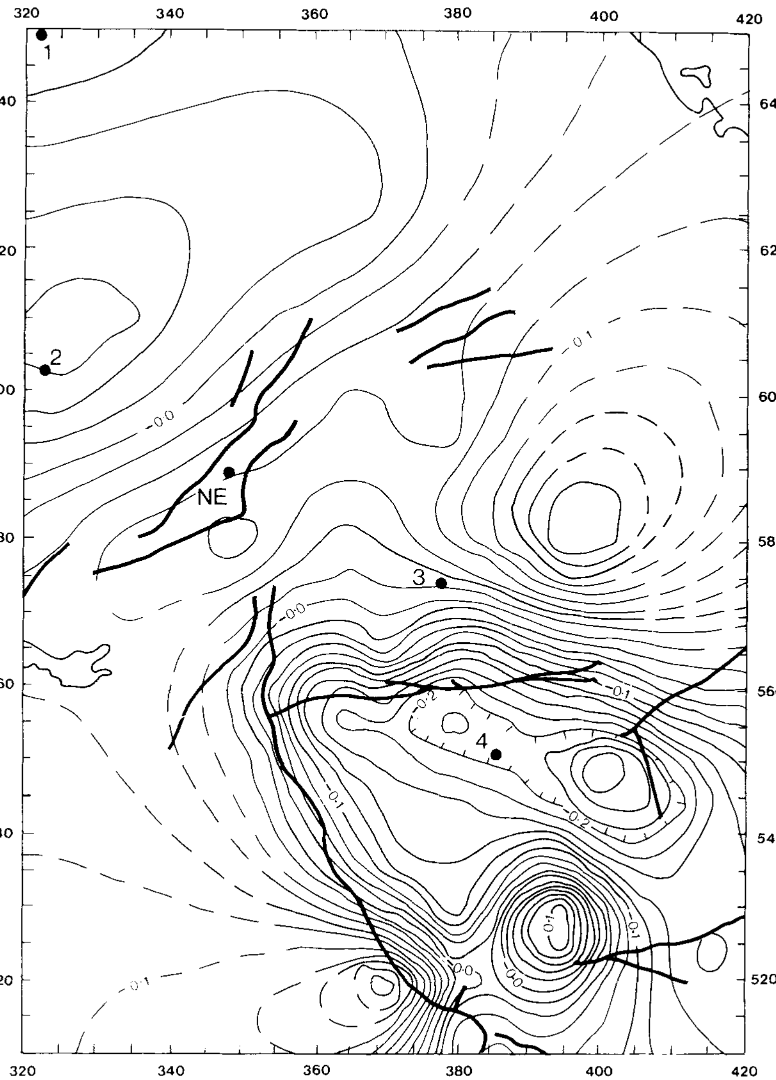

Figure 6. $T = 60$ s, $\theta = 0°$, $\phi = 0°$.

anomalies over the northern margin and centre of the Northumberland Basin are smoothly varying and of low amplitude. Intense anomalies running east–west are concentrated along the southern margin of the Northumberland Basin, where the sediment thickness is greatest, and where the boundary fault maximizes the contrast with the resistive rocks of the Alston Block. There is some indication of structures within the block, and a rather surprising apparent response from the western edge against the Vale of Eden. However, the station spacing of 10 km is barely adequate to resolve the structure over the southern part of the block, at the junction with the Stainmore Trough.

The response to an eastward magnetic field is shown in Fig. 7. The anomaly associated with the Northumberland Basin has virtually, though not entirely disappeared. However, at this frequency there is clear evidence of an anomaly running parallel to the western margin of the block, as we would expect if the induced fields in the Vale of Eden are determined by the local conductivity structure. The residual anomaly at the western end of the

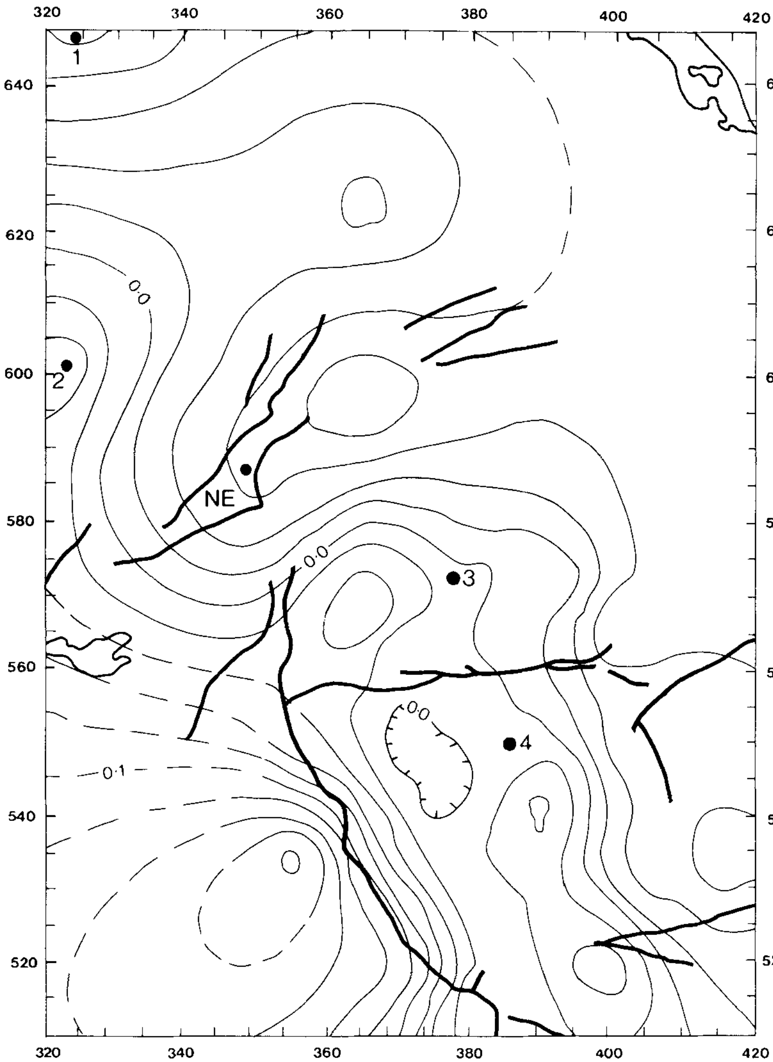

Figure 7. $T = 60$ s, $\theta = 90°$, $\phi = 0°$.

Northumberland Basin appears to correlate in position and trend with a SW to NE aligned anticline which causes the basement to shallow.

The observations of the Northumberland Basin and Vale of Eden at a period of 60 s support the view that electromagnetic fields with periods less than 200 s are predominantly determined by the *local* structure, and relatively uninfluenced by the regional setting of the basins within the surface sheet. It should therefore be entirely appropriate to model their response below 200 s by structures based upon the local geology.

5 The phase of the response at intermediate periods

So far, we have ignored the imaginary part of the anomalous field because its amplitude is generally much smaller than that of the real part. However, the phase of the fields observed at intermediate periods (i.e. 750 s) should be particularly significant if the model that has been proposed is correct. We have envisaged the anomalous fields at periods of 400–2000 s as arising from the perturbation of a regional current flow in a thin sheet of laterally variable conductance. The observed vertical field will be in phase with the perturbation currents created by the inhomogeneities. Provided the horizontal dimensions of the conductivity anomalies are small compared with the skin depth of the electromagnetic field, the perturbation current will itself be in phase with the regional current, which is common to all parts of the sheet. Consequently, the model predicts that the phase of the anomalous vertical field should be the same at every station, and only its amplitude will vary. The most direct approach to testing this idea is to plot an Argand diagram showing the real and imaginary components of the vertical field at each site which are produced when the horizontal field has a specified azimuth. If the phase is uniform, points for different sites will plot along a straight line which passes through the origin, and whose phase is that of the regional current.

Fig. 8 is an Argand diagram of the vertical fields associated with a northward horizontal field of amplitude 1 nT. Stations in the survey area are not labelled, but the more widely-spaced sites in Fig. 1 are indicated by their numbers. With three exceptions, the complex

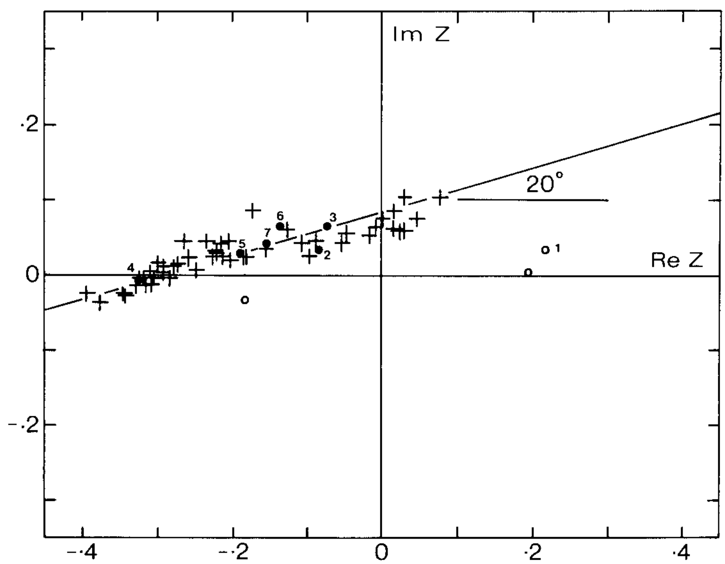

Figure 8. Argand diagram for the vertical field. $T = 750$ s, $\theta = 0°$. Numbers correspond to sites in Fig. 1.

values plot on a straight line. The exceptions are sites located in the extreme NW of the map, which are those most strongly influenced by the Southern Uplands anomaly. The distinction between the fields produced by this current, and those measured at the remaining sites, including some as far away as 300 km, is a strong indication that two quite separate current systems are involved. For instance, the Southern Uplands conductor may be significantly deeper than the surface sheet, and electrically isolated from it.

Although there is a linear relationship between the imaginary and real parts of the vertical field at the majority of the sites, the best-fitting line does not pass through the origin, as the sheet induction model would predict. The slope of the line corresponds to a phase of 20°. If a hypothetical event map is plotted with phase references of 20 and 110°, instead of the customary 0 and 90°, the map with 110° phase is essentially featureless, since all the stations display the same vertical field of approximately 0.08 nT. If the sheet model had been correct, this field at 110° phase would have been uniformly zero. A possible explanation of this behaviour is that the anomalous vertical field over the survey area is generated by two separate current systems. The major part is derived from the perturbation currents in the thin sheet, which are themselves in phase with a regional sheet current whose phase relative to the horizontal north magnetic field is 20°. The second part is a field of indeterminate magnitude and phase which is spatially uniform on a scale of several hundred kilometres.

Fig. 9 is an Argand plot of the vertical field associated with an eastward magnetic field. The amplitudes are much smaller in this case, and the points more scattered, but there is a hint of a correlation between the imaginary and real parts similar to that observed for the north magnetic field. Also, the magnitude of the offset created by the uniform field has diminished. This behaviour suggests that, by rotating the azimuth of the horizontal field, it may be possible to eliminate, or at least minimize the contribution of the uniform field, leaving only that of the current sheet. Experiment shows that a horizontal field with an azimuth of 115°E (i.e. 106°E geographic) comes closest to producing a set of data which plots along a straight line through the origin (see Fig. 10). The phase of the current sheet remains approximately 15–20°.

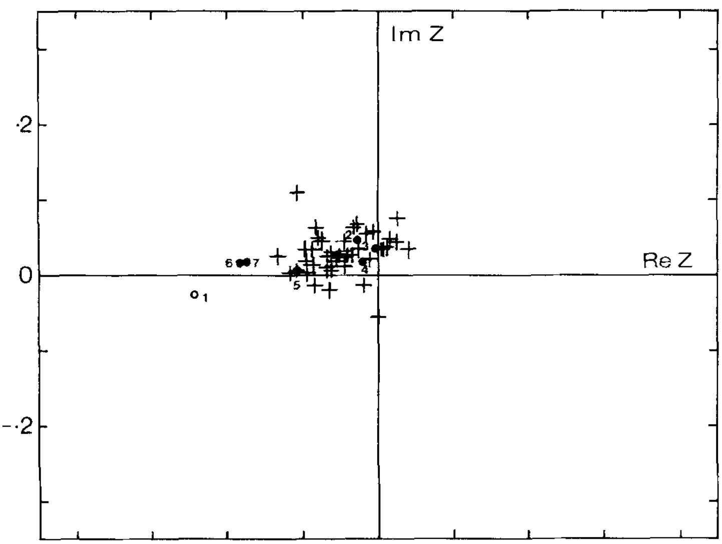

Figure 9. Argand diagram for $T = 750$ s, $\theta = 90°$.

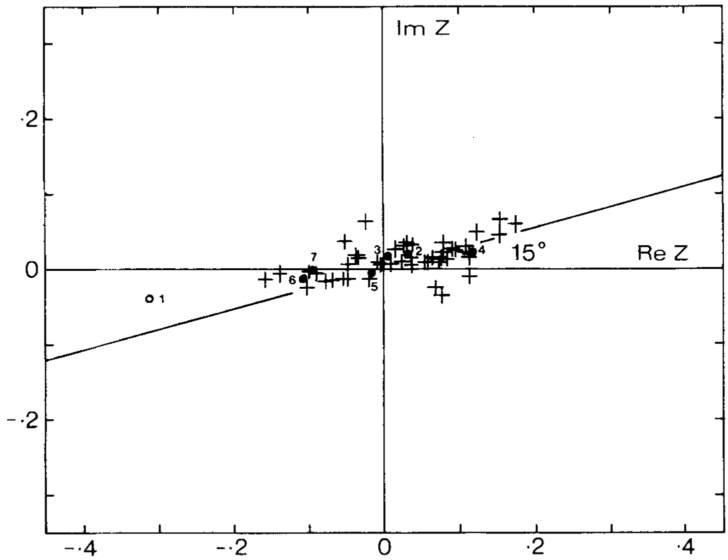

Figure 10. Argand diagram for $T = 750$ s, $\theta = 115°$.

The fact that the uniform field can be eliminated by choosing a magnetic field azimuth of 106°E gives a possible clue to its origin. The configuration of the continental edge around the British Isles is quite complex (see Fig. 1). Although the water depth is substantially greater to the west of Ireland than over the shelf, it is very variable, and never reaches anything like the full depth of the Atlantic. Only to the SW of the British Isles is there a true continental edge where the water depth increases very rapidly from 200 to 4000 m. It is this edge, with an azimuth of 110–120°E, which is likely to be the most important factor in controlling the induced current in the Atlantic Ocean. The vertical field of the Atlantic currents will be a minimum over the British Isles when the horizontal magnetic field is parallel to this edge, i.e. has an azimuth of 110–120°E. The stations we have analysed are nearly 1000 km from the edge, and at this distance the fields will be relatively uniform. We suggest therefore that the spatially uniform fields over north and eastern England at a period of 750 s are the residual direct fields of the current in the Atlantic Ocean.

6 Conclusions

Three distinct modes of induction control the electromagnetic fields observed in southern Scotland and in north and eastern England. The influence of each mode is most easily recognized in a specific period band, although the bands which the modes affect must overlap substantially. At periods greater than 2000 s, the transfer functions at the vast majority of sites are determined by electric current flowing to the west and SW in the Atlantic Ocean. This effect becomes more important with increasing period. In the period range 400–2000 s, the transfer functions are determined by currents induced in a thin sheet of laterally varying conductance, comprising the shallow seas and their underlying sediments, together with the landward extensions of the sedimentary basins. Other sources with different characteristics are locally important, such as the Southern Uplands anomaly, which is distinguished by its phase. At periods less than 200 s, the transfer functions are compatible with an induction process which is controlled only by the local geological structure.

We have called the intermediate period mode *regional induction*. We believe that our data show that the electromagnetic fields and transfer functions corresponding to this mode are not only determined by the local conductivity structure, but also by the role of the local conductor in the surface sheet which includes the shallow seas. The first step in attempting to interpret data from this band must involve a 3-D thin sheet model (e.g. Park, Orange & Madden 1983) which incorporates realistic estimates of the lateral variations in its conductance, based upon hydrographic, geological, and other geophysical data. Our results indicate that the choice of boundary to the area modelled may be rather critical, and the effects of placing it at different distances from the Northumberland Basin must be carefully investigated. In a 3-D environment such as the Northumberland Basin, magnetotelluric sounding curves covering this period band may be significantly distorted. It is not always obvious from impedance measurements at a single station that such distortion has occurred, and low values of skew and approximately isotropic apparent resistivity curves may tempt the interpreter to fit a 1-D model. The result may be false features in the resistivity profile at intermediate depths (Park *et al.* 1983). Response data from Newcastleton (station NE in Fig. 3) has been interpreted using a 1-D model to give a depth profile for the Northumberland Basin (Jones & Hutton 1979b). We think our results emphasize the importance of supporting an individual station response by an adequate *regional* coverage of soundings, so that the effects of the heterogeneous surface layer can be estimated and corrected for in the manner advocated by Park *et al.* (1983).

We have labelled the short-period mode, *local induction*. At most of the stations in our survey, it should be safe to interpret the response data from this and shorter period bands using models based on the geological structure in the immediate vicinity of the measurement sites. However, we must stress that this conclusion is specific to the area we have investigated. What is important is the relationship between the sheet thickness, the skin depth, and the 'adjustment length' (Park *et al.* 1983) of the electromagnetic fields, and these parameters are dependent on the particular geological structure.

Acknowledgments

We gratefully acknowledge support from the UK Natural Environment Research Council in the form of grant GR3/2371 and a grant from the Deep Geology Project. This paper is published with the approval of the Director, British Geological Survey (NERC).

References

Bailey, R. C. & Edwards, R. N., 1976. The effect of source field polarization on geomagnetic variation anomalies in the British Isles, *Geophys. J. R. astr. Soc.*, **45**, 97–104.

Bailey, R. C., Edwards, R. N., Garland, G. D., Kurtz, R. & Pitcher, D., 1974. Electrical conductivity studies over a tectonically active area in Eastern Canada, *J. Geomagn. Geoelectr.*, **26**, 125–146.

Banks, R. J., 1973. Data processing and interpretation in Geomagnetic Deep Sounding, *Phys. Earth planet. Int.*, **7**, 339–348.

Banks, R. J., 1979. The use of equivalent current systems in the interpretation of Geomagnetic Deep Sounding data, *Geophys. J. R. astr. Soc.*, **56**, 139–157.

Beamish, D. & Banks, R. J., 1983. Geomagnetic variation anomalies in northern England: processing and presentation of data from a non-simultaneous array, *Geophys. J. R. astr. Soc.*, **75**, 513–539.

Bott, M. H. P., 1974. The geological interpretation of a gravity survey of the English Lake District and the Vale of Eden, *J. geol. Soc. London*, **113**, 93–117.

Dosso, H. W., Nienaber, W. & Hutton, V. R. S., 1980. An analogue model study of electromagnetic induction in the British Isles region, *Phys. Earth planet. Int.*, **22**, 68–85.

Edwards, R. N., Law, L. K. & White, A., 1971. Geomagnetic variations in the British Isles and their relation to electric currents in the ocean and shallow seas, *Phil. Trans. R. Soc.*, **270**, 289–323.

Grimes, D. I. F., 1977. Geomagnetic Deep Sounding in north-west England, *MSc thesis,* University of Lancaster.

Hutton, V. R. S. & Jones, A. G., 1980. Magneto-variational and magnetotelluric investigations in Southern Scotland, *Adv. Earth planet. Sci.,* **9,** 141–150.

Ingham, M. R. & Hutton, V. R. S., 1982. Crustal and upper mantle electrical conductivity structure in southern Scotland, *Geophys. J. R. astr. Soc..,* **69,** 579–594.

Jones, A. G. & Hutton, V. R. S., 1979a. A multi-station magnetotelluric study in southern Scotland – I. Fieldwork, data analysis, and results, *Geophys. J. R. astr. Soc.,* **56,** 329–350.

Jones, A. G. & Hutton, V. R. S., 1979b. A multi-station magnetotelluric study in southern Scotland – II. Monte-Carlo inversion of the data and its geophysical and tectonic implications, *Geophys. J. R. astr. Soc.,* **56,** 351–368.

Lee, M. K., 1982. Interpretation of regional gravity and aeromagnetic data in the Northumberland-Borders-Cheviot area, *Geophys. J. R. astr. Soc.,* **69,** 281.

Park, S. K., Orange, A. S. & Madden, T. R., 1983. Effects of three-dimensional structure on magnetotelluric sounding curves, *Geophysics,* **48,** 1402–1405.

Geophys. J. R. astr. Soc. (1984) **79**, 555–563

On the excitation of the Earth's free wobble and reference frames

B. Fong Chao *Geodynamics Branch, Goddard Space Flight Center, Greenbelt, Maryland 20771, USA*

Received 1984 April 2; in original form 1983 May 17

Summary. In this paper we study the excitation of the Earth's polar motion in connection with problems that are associated with the diversity of reference frames involved in observations and theoretical computations. Thus, following the dynamics of the Earth's polar motion, the kinematics that relates observations from different reference frames are developed. The conventional procedures of studying the seismic excitation of polar motion are then re-examined accordingly – subject constantly to the question: relative to what reference frame? It is concluded that an inconsistency in the reference frames has prevailed in the literature. In particular, it is asserted that the computed change in the polar motion associated with a (sudden) seismic source is in fact what would be observed in Tisserand's mean frame. The latter has no real-world counterpart from the standpoint of observations, which are invariably made with respect to some geographic reference frame. While this inconsistency is indeed far from trivial in a philosophical sense, the resultant discrepancy is small for all practical purposes thanks to the nearly spherical configuration of the Earth.

1 Introduction

As any geodetic observations made on the surface of the Earth, the polar motion is a relative quantity; and the specification of reference frames is a common requirement for all investigations of the subject. In fact, now that the accuracy in geodetic measurements is being greatly improved thanks to modern techniques (see, e.g. Tapley 1983), the incorporation of various astronomical/geodetic reference frames has become a subject of great interest and significance, as attested by two International Astronomical Union (IAU) colloquia (No. 26, 1975 and No. 56, 1980). However, as will be shown in this paper, there has been a lack of consistency in the reference frames used in the study of the excitation of the Earth's Chandler wobble. This has happened among different investigators as well as in each individual study in the past. For example, theoretical computations are made with respect to reference frames that are defined dynamically while having no real-world counterpart from the standpoint of observations. The present paper is an effort to resolve this inconsistency and to assess the implications.

2 Dynamics of the Earth's free wobble

We should point out at the outset that in this paper the term 'polar motion' is used synonymously with the free (Chandler) wobble, with no regard to any forced motion (e.g. the meteorologically excited annual wobble); and that we shall study the excitation of the Chandler wobble by sources that are indigenous to the Earth. Thus, in the absence of external torques, the basic physical principle governing the Earth's free rotation is the conservation of angular momentum. In a reference frame which is under a rotation at angular velocity $\boldsymbol{\omega}$, the latter can be expressed as

$$\frac{d}{dt}\mathbf{H} + \boldsymbol{\omega} \times \mathbf{H} = \mathbf{0} \tag{1a}$$

where the angular momentum vector $\mathbf{H}$ can be resolved into two terms:

$$\mathbf{H} = (\text{moment of inertia tensor}) \cdot \boldsymbol{\omega} + (\text{relative angular momentum}). \tag{1b}$$

Equation (1) is known as the Liouville equation and is valid in any reference frame (Munk & MacDonald 1960). In reality, the departure of the Earth's rotational motion from the state of a constant rotation (the latter corresponds to zero polar motion and zero length-of-day variation) is infinitesimal, $\sim 0(10^{-6})$. Thus we define here a 'terrestrial frame' as a (non-inertial) reference frame whose origin resides at the centre of mass of the Earth (so that translational motions will not enter into our discussion) with the z-axis close to the rotation axis and whose departure from the state of constant rotation remains infinitesimal at all times. There is, of course, an infinite number of such terrestrial frames, and we shall discuss some interesting ones in sections to follow (and use the term in a stricter sense later in Section 4).

In a terrestrial frame, via a first-order perturbation scheme, a set of two disjoint, linearized equations of motion for the Earth's free rotation can be derived based on the Liouville equation (Munk & MacDonald 1960). They can be written in a Cartesian coordinate system as

$$(\dot{m} - i\sigma m) + (\dot{c} + i\Omega c) + (\dot{h} + i\Omega h) = 0 \tag{2}$$

$$\left(1 + \frac{\sigma}{\Omega}\right) \dot{m}_3 + \dot{c}_{33} + \dot{h}_3 = 0, \tag{3}$$

where the overdot denotes the time derivative, $\langle\ \rangle$ denotes the Cartesian vector, and

$\Omega = 2\pi/(1\ \text{day})$
$\sigma = \Omega\,(C-A)/A$
$A,\ A,\ C =$ three principal moments of inertia of the unperturbed (axial-symmetric) earth, $C > A$

$$\langle m_1, m_2, 1 + m_3 \rangle = \boldsymbol{\omega}/\Omega \tag{4}$$

$c = c_{13} + ic_{23}$

$$\begin{pmatrix} 1 + c_{11} & c_{12} & c_{13} \\ c_{12} & 1 + c_{22} & c_{23} \\ c_{13} & c_{23} & 1 + \sigma/\Omega + c_{33} \end{pmatrix} = (\text{moment of inertia})/A$$

$h = h_1 + ih_2,$

$\langle h_1, h_2, h_3 \rangle = (\text{relative angular momentum})/A\Omega.$

Equation (2) governs the polar motion m, and equation (3) governs the length-of-day variation m_3. Note that m, m_3 (the 'm-terms'), c, c_{33} (the 'c-terms'), and h, h_3 (the 'h-terms') are all dimensionless functions of time with infinitesimal magnitudes. As usual, we consider the c- and h-terms as the geophysical 'sources' that excite the m-terms which can be observed astronomically. We shall not take into account the 'feedback part' in the c- and h-terms from the m-terms due to the elastic yielding effect. The latter effect is responsible for lengthening the Chandler period from 10 to 14 month, but has no bearing on our forthcoming studies.

3 Kinematics of the Earth's free wobble

As stated earlier, equations (2) and (3) are valid in any (non-inertial) reference frame with respect to which the m-, c-, and h-terms remain infinitesimal. It is also obvious that these terms are all frame-dependent, that is, they will be given different quantitative descriptions by observers from different terrestrial frames. Let us now study the kinematic relations between these quantities as viewed from two terrestrial frames, frame (1) and frame (2). Let frame (2) be related to frame (1) by the set of three Eulerian angles (ϕ, θ, ψ), as depicted in Fig. 1. In general, these Eulerian angles are functions of time, and $\theta(t)$ stays infinitesimal throughout the motion. Now, to first order in θ, the transformation law (see, e.g. Goldstein 1950) for the angular momentum vector **H** can be written as

$$\mathbf{H}^{(2)} = \begin{pmatrix} \cos\Delta & \sin\Delta & \theta\sin\psi \\ -\sin\Delta & \cos\Delta & \theta\cos\psi \\ \theta\sin\phi & -\theta\cos\phi & 1 \end{pmatrix} \mathbf{H}^{(1)} \tag{5}$$

where the superscript (1) or (2) indicates reference frames, and

$$\Delta = \Phi + \Psi. \tag{6}$$

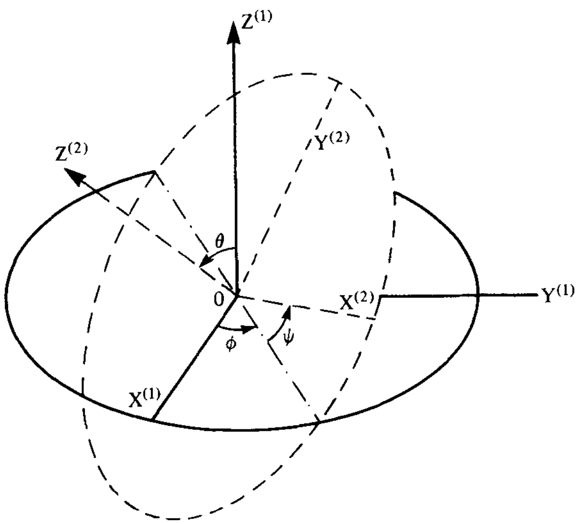

Figure 1. The Eulerian angles (ϕ, θ, ψ) between two reference frames, frame (1) and frame (2). For terrestrial frames, θ is infinitesimal.

Substituting equations (1b) and (4) into (5) and retaining only the first-order terms, we obtain the following basic kinematic relations that relates observations from two different terrestrial frames:

$$m^{(2)} + c^{(2)} + h^{(2)} = \exp(-i\Delta)\,(m^{(1)} + c^{(1)} + h^{(1)}) + i\left(1 + \frac{\sigma}{\Omega}\right)\exp(-i\psi)\,\theta \tag{7}$$

and

$$\left(1 + \frac{\sigma}{\Omega}\right) m_3^{(2)} + c_{33}^{(2)} + h_3^{(2)} = \left(1 + \frac{\sigma}{\Omega}\right) m_3^{(1)} + c_{33}^{(1)} + h_3^{(1)}. \tag{8}$$

We see that the quantity in equation (8) is frame-independent, or an invariant, to the extent that the actual frame-dependency is of second order. That the quantity is in fact also time-independent can be seen readily from equation (3). This, of course, is required by the conservation of (the z-component of) the angular momentum, and has served as the basis for a length-of-day study in relation to the atmospheric angular momentum variation (Rosen & Salstein 1983). We shall leave equations (3) and (8), and hence the length-of-day problem, as such without further discussions. Equation (7), on the other hand, is of central importance to forthcoming discussions. Note that, to first order in θ, Δ is simply the rotation angle between the two x–y planes belong to frames (1) and (2) about the (nearly coincident) z-axes (cf. Fig. 1). Hence the first term on the right side of equation (7) represents nothing but the rotation transformation about the z-axis through an angle Δ. It is the second term that has non-trivial implications, as we shall see presently.

4 Sudden indigenous excitation and reference frames

The solution to the polar motion equation (2) is

$$m(t) = -\exp(i\sigma t)\int_{-\infty}^{t} [i\Omega(c + h) + (\dot{c} + \dot{h})]\,\exp(-i\sigma\tau)\,d\tau. \tag{9}$$

For simplicity, let us assume that prior to time $t = 0$ all the m-, c- and h-terms as well as their time derivatives are identically zero, and the Earth simply rotates in space at the constant angular velocity $\mathbf{\Omega} = \Omega\,\hat{z}$ about its figure axis.

Suppose that at time $t = 0$ the (formerly unperturbed) Earth undergoes a sudden internal redistribution of mass that can be described by an infinitesimal displacement field, and that after the moment $t = 0$ the Earth 'freezes' into its perturbed configuration. This event inevitably induces a free wobble, known as the Chandler wobble. Now let us restrict ourselves to a particular subset of terrestrial frames, namely those 'evolve' at $t = 0$ and end up as a body frame of the Earth, so that the event can be described by

$$c(t) = c_0 H(t), \qquad h(t) = h_0\,\delta(t) \tag{10}$$

where $H(t)$ is the Heaviside step function and $\delta(t)$ is the Dirac delta function. We shall call such an event an H/δ event. Note that, after $t = 0$, the Eulerian angles (ϕ, θ, ψ) between any two terrestrial frames are now time-independent and that the dimension of h_0 is [time].

Substitute equation (10) into (9), we obtain the polar motion excited by an H/δ event:

$$m(t) = -\left(1 + \frac{\Omega}{\sigma}\right)(c_0 + i\sigma h_0)\exp(i\sigma t) + \frac{\Omega}{\sigma}\,c_0, \qquad t > 0. \tag{11}$$

Thus, in any given terrestrial frame, after the H/δ event that occurred at $t = 0$, the pole undergoes a prograde, circular motion at the angular rate σ and amplitude $(1 + \Omega/\sigma)\,|c_0 + i\sigma h_0|$ about the 'mean pole position' $(\Omega/\sigma)c_0$, starting from the point $-c_0 - (1 + \Omega/\sigma)\, i\sigma h_0$.

Now combine equations (7) and (11). By equating the time-dependent terms as well as the static terms, we obtain the following two conditions that relates observations with respect to a given H/δ event from two terrestrial frames, true to first order:

$$c_0^{(2)} = \exp(-i\Delta)\, c_0^{(1)} + i\frac{\sigma}{\Omega}\exp(-i\psi)\,\theta \tag{12a}$$

$$h_0^{(2)} = \exp(-i\Delta)\, h_0^{(1)} - \frac{1}{\Omega}\exp(-i\psi)\theta. \tag{12b}$$

It follows immediately from equations (12a, b) that the quantity $c_0 + i\sigma h_0$ acts as if it were a vector under the 2-D rotation through the angle Δ. In fact, it is an easy exercise to show that the two (complex) equations (12a, b) are equivalent to the following four (real) equations:

$$\theta = \Omega\,|c_0^{(2)} h_0^{(1)} - c_0^{(1)} h_0^{(2)}|/|c_0^{(1)} + i\sigma h_0^{(1)}| \tag{13a}$$

$$\psi = \arg(c_0^{(1)} + i\sigma h_0^{(1)}) - \arg(c_0^{(2)} h_0^{(1)} - c_0^{(1)} h_0^{(2)}) \tag{13b}$$

$$\phi = \arg(c_0^{(2)} + i\sigma h_0^{(2)}) + \arg(c_0^{(2)} h_0^{(1)} - c_0^{(1)} h_0^{(2)}) \tag{13c}$$

$$|c_0^{(1)} + i\sigma h_0^{(1)}| = |c_0^{(2)} + i\sigma h_0^{(2)}|. \tag{13d}$$

where arg denotes the argument of a complex quantity. Equations (13a–c) give the Eulerian angles between two terrestrial frames (1) and (2) induced by an H/δ event in terms of their respective c_0 and h_0. Equation (13d), on the other hand, states that the (real) quantity $|c_0 + i\sigma h_0|$ associated with an H/δ event is an invariant and, hence so is $(1 + \Omega/\sigma)\,|c_0 + i\sigma h_0|$, the amplitude of the polar motion induced by an H/δ event. Thus we see that while observers from two different terrestrial frames do not agree on the direction and magnitude of the static shift of the mean pole, nor on the direction of the instantaneous displacement of the pole that occurs at $t = 0$, they certainly agree on the amplitude of the polar motion. It implies that in any terrestrial frame c_0 and h_0 are not entirely independent quantities. The restriction is imposed by our physical requirement that the Earth 'freezes' after the event.

Now let us study the implication of equations (12a, b) with respect to some specific terrestrial frames. A trivial, but instructive, special case ensues when $\theta = 0$, i.e. when the two frames share the same z-axis. Then equations (12a, b) reduce to the kinematic transformation law for c_0 and h_0 under the 2-D rotation Δ in the x–y plane (cf. Fig. 1).

Two other special cases of terrestrial frame are of interest, namely the principal axes and the Tisserand's (mean) axes (Munk & MacDonald 1960):

(1) The principal axes (henceforth called the P-frame) correspond to the terrestrial frame in which $c = 0$. In the P-frame, The polar motion induced by the H/δ event (equation 11) reduces to

$$m^{(\mathrm{P})}(t) = -i(\Omega + \sigma)\, h_0^{(\mathrm{P})} \exp(i\sigma t). \tag{14}$$

The z-axis of the P-frame, about which the pole rotates, is the figure axis by definition.

(2) Tisserand's axes (henceforth called the T-frame) are defined as the terrestrial frame in which $h = h_3 = 0$. The polar motion (equation 11) in this case becomes

$$m^{(\mathrm{T})}(t) = \frac{\Omega}{\sigma}\, c_0^{(\mathrm{T})} - \left(1 + \frac{\Omega}{\sigma}\right) c_0^{(\mathrm{T})} \exp(i\sigma t). \tag{15}$$

We point out here that for the P- and T-frames, equations (13a) and (13b) reduce to

$$\theta_{\mathrm{PT}} = \Omega/\sigma \,|\, c_0^{(\mathrm{T})} \,| = \Omega \,|\, h_0^{(\mathrm{P})} \,|. \tag{16}$$

Fig. 2 illustrates, among other things, the polar motion with respect to both reference frames.

5 Are computations and observations compatible?

The foregoing mathematical treatment is valid with respect to the Earth to an accuracy within 10^{-6}; and an H/δ event is a convenient representation of an earthquake whose duration is generally much shorter than the Chandler period. In fact, in the study of seismic excitation of the polar motion, the conventional procedure connecting changes in the polar motion with the occurrence of major earthquakes has been as follows: (1) compute according to some theoretical formulae the c-term, the change in the product of inertia of the Earth, accompanying a given earthquake faulting with observed fault geometry; (2) neglect the h-term, use the computed c-term and the T-frame equation (15) to obtain the change in the polar motion m caused by the given earthquake; and (3) compare the resultant change in m with the observed polar motion. This procedure has been used by various investigators; among them, Mansinha & Smylie (1967), Ben-Menahem & Israel (1970), Smylie & Mansinha (1971), Dahlen (1971, 1973), Rice & Chinnery (1972), O'Connell & Dziewonski (1976) and Mansinha, Smylie & Chapman (1979). However, no strong conclusions have been drawn to

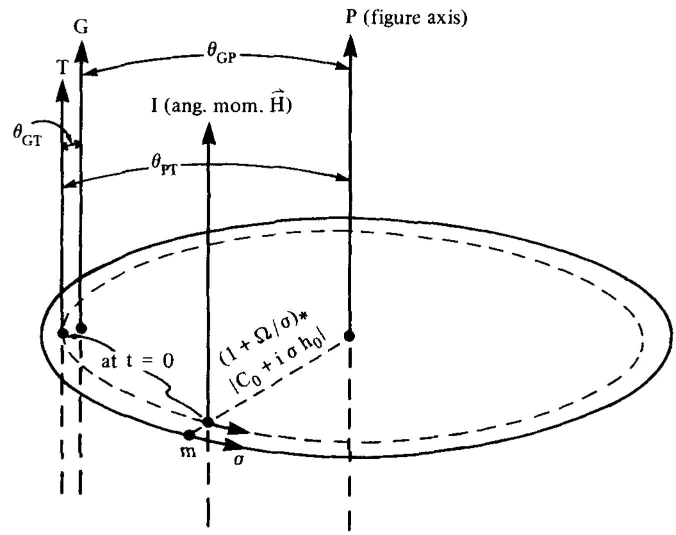

Figure 2. The z-axes of various reference frames and their relationship with the polar motion m. P: principal frame, T: Tisserand's frame, G: geographic frame, I: invariant frame. All these z-axis pass through the centre of mass of the Earth.

date. While there are indeed aspects that remain uncertain (for example, whether we know enough about the dynamics of seismic sources, or whether the available earth models are adequate), we shall here examine a fundamental problem associated with the above procedure, namely the compatibility between the polar motion observed astronomically and that computed according to geophysical observations of the seismic source. This problem arises from the diversity of reference frames involved. Indeed, as we have asserted, different terrestrial frames generally see different changes in polar motion excited by one given H/δ event; and in principle errors can arise from any inconsistency in the reference frames.

Now in order to relate computations with observations, we should bring in the so-called 'geographical frame' (henceforth the G-frame) (Munk & MacDonald 1960). A G-frame is a terrestrial frame defined with respect to a number of 'fixed' reference points on the surface of the Earth, from which all observations are made. Thus, corresponding to the said procedure (with steps (1) and (2) in reverse order), three levels of question should be raised:

(1) When is the h-term negligible from equation (11)?

(2) Given a fault geometry, what reference frame is used for the computation of the c-term (and the h-term if it is to be taken into account)?

(3) Are the two G-frames defined respectively by the seismic network and the astronomical/geodetic stations compatible?

For question (1), what we should really be concerned with is: in the presence of the c-term, is the h-term negligible in the G-frame? The neglect of the h-term is certainly valid in the T-frame where σh_0 is zero and the only contribution comes from c_0, while being evidently absurd in the P-frame where the converse is true. Note that, as we have asserted in equation (16), the magnitudes of $c_0^{(\mathrm{T})}$ and $\sigma h_0^{(\mathrm{P})}$ are in fact equal. This, as stated earlier, is a corollary of equation (13d) – that the quantity $|c_0 + i\sigma h_0|$ is frame-independent. It is the relative contribution of the two parts, c_0 and $i\sigma h_0$, that depends on the reference frame; and a look at equation (11) will convince us that in a given terrestrial frame the h-term is negligible if

$$\sigma |h_0| \ll |c_0|. \tag{17}$$

Now in terms of a given displacement field $\langle u_1, u_2, u_3 \rangle H(t)$ in the Earth, it can be shown that

$$c_0 = \frac{1}{A}\int dV \rho[-xu_3 - zu_1 - iyu_3 - izu_2] \tag{18a}$$

$$\sigma h_0 = \frac{\sigma}{\Omega}\,\frac{1}{A}\int dV \rho[yu_3 - zu_2 + izu_1 - ixu_3]. \tag{18b}$$

In general, the two integrals in equation (18) with respect to a terrestrial frame will have comparable magnitudes; and the factor $\sigma/\Omega(\sim 1/300)$ in (18b) will ensure the validity of condition (17). Alternatively, in terms of θ_{GT} and θ_{GP}, the departure angle between (the z-axis of) the G- and T-frame and that between the G- and P-frame respectively (Fig. 2), we see from equation (13a) that $\theta_{\mathrm{GT}} = \Omega\,|h_0^{(\mathrm{G})}|$ and $\theta_{\mathrm{GP}} = (\Omega/\sigma)\,|c_0^{(\mathrm{G})}|$. Therefore, $\theta_{\mathrm{GT}}/\theta_{\mathrm{GP}} = \sigma\,|h_0^{(\mathrm{G})}|/|c_0^{(\mathrm{G})}|$; and condition (17) is equivalent to

$$\theta_{\mathrm{GT}} \ll \theta_{\mathrm{GP}} \tag{19}$$

or, the condition that the z-axis departure of the G-frame from the T-frame is much smaller than that from the P-frame. In principle there is no *a priori* reason why condition (19) is true because the P- and T-frames are defined dynamically whereas the G-frame has a purely empirical definition. However, our quantitative argument above has ensured that (19), and hence (17), indeed holds, unless the terrestrial frame under consideration is extremely close to the P-frame – and for a 'reasonably' defined G-frame, the latter is not likely to happen. The situation is depicted in Fig. 2. Physically, the whole argument hinges upon the fact that the P-frame is very sensitive to any mass redistribution in the Earth in the sense that θ_{GP} has been 'magnified' by the factor Ω/σ, whose inverse essentially measures the Earth's deviation from spherical symmetry. Indeed, it is obvious that if the Earth were spherically symmetric, any (infinitesimal) redistribution of internal mass would in general shift the figure axis from the original z-axis by a finite angle. Notice, in passing, that, for the instantaneous displacement of the pole $-c_0 - (1 + \Omega/\sigma)\, i\sigma h_0$ at $t = 0$, the neglect of the h-term evidently yields a totally incorrect result. Fortunately, this quantity is itself $\sim 0(1/300)$ compared with the polar motion amplitude (see equation 11), and hence no serious error will be introduced in the polar motion. Therefore, we conclude that, thanks to the Earth's nearly spherical configuration, it is legitimate to use the T-frame formula (15) to calculate the polar motion with respect to a G-frame.

But is the theoretically predicted c-term truly $c_0^{(\mathrm{T})}$, as required by equation (15)? This leads us to question (2), which is of a strictly theoretical nature. Given a fault geometry, earlier investigations, despite differences in the actual approaches, have all computed the c-term (as they presumably would for the h-term) on a hypothetical non-rotating earth model with respect to the (non-rotating) inertial frame, $\boldsymbol{\omega} = \mathbf{0}$. In such a reference frame the total angular momentum of the non-rotating earth vanishes, $\mathbf{H} = \mathbf{0}$, which in turn, by equation (1b), gives zero relative angular momentum, $h = h_3 = 0$. In other words, if we were to compute the h-terms, which are uniquely determined by the displacement field that gives rise to our predicted c-terms, we will undoubtedly get $h = h_3 = 0$, simply because the latter condition is inherent in the equations of motion. The computed c-term is thus one that corresponds to the condition that $h = h_3 = 0$. Therefore, if we insist on using the same displacement field in computing the c-terms in a terrestrial frame (as did by the above-mentioned investigators), we are implicitly assuming $h = h_3 = 0$. The latter characterizes the T-frame, by definition.

A completely different procedure has been used by Smith (1977) for computing the polar motion m due to a given earthquake – the normal-mode approach. This is done in an 'invariant frame' (call it the I-frame), a frame that continues to rotate in space at the constant angular velocity $\boldsymbol{\Omega}$ regardless of what happens to the Earth. The I-frame is, again, defined dynamically; its z-axis coincides with the constant angular momentum vector $\mathbf{H}$. But unlike the two previously defined dynamical frames (the P- and T-frames), it is not a (body-fixed) terrestrial frame. Yet, contrary to what we might expect from Section 4, the computed mean pole shift by Smith (1977) relative to the I-frame are in good agreement with corresponding results by other investigators using the T-frame (see above). This, of course, is not a coincidence. The reason is that right after the moment the H/δ event occurs ($t = 0$) the I-frame is in fact coincident with the T-frame. This can be shown easily by, for example, comparing equation (15) with the Poinsot representation of a rigid body rotation (see, e.g. Lambeck 1980). After $t = 0$, as seen in a terrestrial frame, the I-frame starts to rotate about the figure axis, always keeping pace with the pole position m. Fig. 2 summarizes the relation among various reference frames.

Question (3) arises because even if we reduced all quantities to a seismic G-frame, the latter could still be different from an astronomical/geodetic G-frame. This, however, is a problem of an empirical nature, and can be answered simply by stating that, by increasing the geographical coverage and density of both networks, the two thus defined G-frames will in general approach coincidence in a statistical sense.

In conclusion, we have found a philosophical inconsistency in a diversity of reference frames employed in computation and in observation of Chandler wobble excitation by an H/δ source. Yet in practice, the resultant errors appear to be small because (1) all the computed c-terms, and hence the resultant changes in the polar motion m in the literature to date are in fact what would have been observed in the T-frame, and (2) it is legitimate to take the T-frame values to compare with the values observed in a G-frame – the error committed by so doing is on the order of 1/300 thanks to the nearly spherical configuration of the Earth. It is interesting to note that, in the T-frame under the constraint of vanishing h-terms, it is the relative (rather than the absolute) displacement at the fault, or the corresponding seismic moment tensor, that enters the computation of the c-term. Therefore, in principle, even the small difference between the T- and G-frames can be accounted for provided we can resolve the ambiguity in the absolute displacement as seen from a G-frame. This presumably can be achieved by means of geodetic techniques such as the San Andreas Fault Experiment (SAFE, see Smith *et al.* 1979) that uses satellite laser ranging to tie fault movements to a network of observatories that defines a G-frame.

Acknowledgments

Part of this work was completed during my tenure at the Goddard Space Flight Center as a Resident Research Associate sponsored by the National Academy of Sciences. I am also grateful to D. E. Smylie and an anonymous referee for suggestions.

Reference

Ben-Menahem, A. & Israel, M., 1970. Effects of major seismic events on the rotation of the Earth, *Geophys. J. R. astr. Soc.*, **19**, 367–393.

Dahlen, F. A., 1971. The excitation of the Chandler wobble by earthquakes, *Geophys. J. R. astr. Soc.*, **25**, 157–206.

Dahlen, F. A., 1973. A correction to the excitation of the Chandler wobble by earthquakes, *Geophys. J. R. astr. Soc.*, **32**, 203–217.

Goldstein, H., 1950. *Classical Mechanics*, Addison-Wesley, Reading, Massachusetts.

IAU Coll. No. 26, 1975. *On Reference Coordinate System for Earth Dynamics*, eds Kolaczek, B. & Weiffenbach, G.

IAU Coll. No. 56, 1980. *Reference Coordinate Systems for Earth Dynamics*, eds Gaposchkin, E. M. & Kolaczek, B.

Lambeck, K., 1980. *The Earth's Variable Rotation*, Cambridge University Press.

Mansinha, L. & Smylie, D. E., 1967. Effects of earthquakes on the Chandler wobble and the secular pole shift, *J. geophys. Res.*, **72**, 4731–4743.

Mansinha, L., Smylie, D. E. & Chapman, C. H., 1979. Seismic excitation of the Chandler wobble revisited, *Geophys. J. R. astr. Soc.*, **59**, 1–17.

Munk, W. H. & MacDonald, G. J. F., 1960. *The Rotation of the Earth*, Cambridge University Press.

O'Connell, R. J. & Dziewonski, A. M., 1976. Excitation of the Chandler wobble by large earthquakes, *Nature*, **262**, 259–262.

Rice, J. R. & Chinnery, M. A., 1972. On the calculation of changes in the Earth's inertia tensor due to faulting, *Geophys. J. R. astr. Soc.*, **29**, 79–90.

Rosen, R. D. & Salstein, D. A., 1983. Variations in atmospheric angular momentum on global and regional scales and the length of day, *J. geophys. Res.*, **88**, 5451–5470.

Smith, D. E., Kolenkiewicz, R., Dunn, P. J. & Torrence, M. H., 1979. The measurement of fault motion by satellite laser ranging, *Tectonophys.*, **52**, 59–67.

Smith, M. L., 1977. Wobble and nutation of the Earth, *Geophys. J. R. astr. Soc.*, **50**, 103–140.

Smylie, D. E. & Mansinha, L., 1971. The elasticity theory of dislocations in real earth models and changes in the rotation of the Earth, *Geophys. J. R. astr. Soc.*, **23**, 329–354.

Tapley, B. D., 1983. Polar motion and Earth rotation, *Rev. Geophys. Space Phys.*, **21**, 569–573.

Geophys. J. R. astr. Soc. (1984) 79, 565–572

The *P–SV* inverse problem for a layered elastic medium: what data are required?

Timothy J. Clarke *Department of Theoretical and Applied Mechanics, Thurston Hall, Cornell University, Ithaca, New York 14853, USA*

Received 1984 April 25; in original form 1984 January 27

Summary. In an earlier paper we described a method whereby the elastic parameters of a horizontally layered medium could be determined from a matrix of *P–SV* reflection seismograms for obliquely incident plane waves. We suggested that in order to obtain the required matrix, it would be necessary to measure the response, at many locations along a line, due both to a compressional source and to a source generating shear waves. By slant stacking such data, we could simulate the plane wave response at some slowness, and hence obtain the plane wave reflection seismograms for the structure, enabling us to use the algorithm described by Clarke to retrieve the wave speeds, density and thickness for each layer.

In this paper we consider the precise nature of the seismic sources required, and the data to be collected, in order to construct the *P–SV* reflection matrix. We show that it is possible to retrieve this information from three sets of data, each consisting of measurements, along a line, of the vertical or radial component of the response to a source possessing an appropriate degree of cylindrical symmetry. A certain amount of care is required, however, in choosing the three source/receiver combinations, since certain such pairs of data sets are not independent, and must be counted as a single set. As an example of three data sets which are independent, and hence sufficient, we show that measurements of the vertical and radial displacements caused by an explosive source, as well as the vertical component of the response to a vertical force, enable us to deduce the *P–SV* reflection seismograms, and hence to perform the structural inversion.

1 Introduction

In a previous paper (Clarke 1984), we described an algorithm whereby the matrix of *P–SV* reflection seismograms at oblique incidence for a horizontally layered elastic medium could be inverted to recover the elastic parameters in each layer. In the present paper we address the question of how to obtain the required plane wave seismograms, from measurements of vertical and radial components of the response to point sources at the surface of the Earth.

In Section 2 we consider the forward problem of a general point source near the surface of a layered elastic half-space. The response may be expressed as a Fourier transform over frequency ω, and a Hankel transform over slowness p, while the angular transform reduces to a summation over the five orders $m = 0, \pm 1, \pm 2$ (Hudson 1969).

As an intermediate stage in our inversion procedure we need to obtain the plane wave response, corresponding to a single value of slowness, and in Section 3 we introduce the idea of slant stacking the P–SV response to obtain these plane wave data. Although this is analogous to the process of slant stacking acoustic signals (Chapman 1981), the greater complexity of the P–SV problem would require us to perform an integration over the entire plane $z = 0$, rather than along a single line, to separate the contributions from different angular orders. To remove this difficulty we must restrict our sources to those generating radiation of a single angular order only, corresponding generally to cylindrical symmetry.

In Section 4 we show how to make use of the plane wave response to obtain the reflection seismograms required for our inversion scheme. We show that three independent slant stacks are required, all with the same stacking parameter but with a mixture of different sources or different displacement components. Thus it is not sufficient to measure the vertical component of the response to three different sources, nor to make use of single force sources only. The simplest example of three data sets from which it is possible to recover the P–SV reflection matrix consists of the vertical and radial components of the response to an explosive source, combined with the vertical displacement caused by a vertical force.

2 Surface response of a layered elastic half-space

We consider the surface response of a horizontally layered elastic medium, bounded above by a free surface and below by a homogeneous half-space, to a point excitation. The source is assumed to be just below the surface, and is described either by a point force $\mathbf{F}$ or by a moment tensor M. Following the notation of Kennett & Kerry (1979), we define cylindrical polar coordinates (r, ϕ, z), such that the z-axis passes through the source point, but we express the components of $\mathbf{F}$ and M within a Cartesian frame of coincident origin, whose x-axis corresponds to the line $\phi = 0$.

Adapting the expression derived by Kennett & Kerry (1979) to the case where source and receiver are both at the surface, we may write the displacement $\mathbf{w}_0$ in the frequency/slowness domain as

$$\mathbf{w}_0(\omega, p) = (M_U + M_D\tilde{R})\,[-\mathbf{\Sigma}_U + R_D(I - \tilde{R}R_D)^{-1}(\mathbf{\Sigma}_D - \tilde{R}\mathbf{\Sigma}_U)]. \tag{2.1}$$

Here $R_D(\omega, p)$ is the reflection matrix for the structure, for waves incident from above from a fictitious half-space occupying $z < 0$, while $\tilde{R}(p)$ is the free surface reflection matrix. $\mathbf{\Sigma}_U(p)$, $\mathbf{\Sigma}_D(p)$ represent respectively the contribution made by the source to up- and downgoing radiation, while $M_U(p)$ and $M_D(p)$ are matrices converting up- and downgoing wave amplitudes to displacement components. So far we have assumed that our source generates some combination of P–SV- and SH-waves. On the assumption that we know the surface values of the wave speeds and density, the matrices M_U, M_D, $\tilde{R}$ are known as functions of slowness, while the additional assumption that we know the source type and orientation allows us to calculate $\mathbf{\Sigma}_U$ and $\mathbf{\Sigma}_D$.

In the foregoing discussion we have, however, simplified matters somewhat. The relationship between the vertical displacement component U in the frequency/horizontal wavenumber domain and its time domain counterpart u_z is given by

$$u_z(r, \phi, t) = \frac{1}{2\pi} \int_{-\infty}^{\infty} d\omega \exp(-i\omega t) \int_0^{\infty} dkk \sum_{m=-2}^{2} U(k, m, \omega) J_m(kr) \exp(im\phi), \qquad (2.2)$$

(Hudson 1969) with analogous expressions for the other two components. For each angular order m the source generates different quantities of radiation, and although the reflection properties of the medium are independent of m, the total response will consist of a superposition of Hankel transforms of orders 0, 1 and 2. In the case of the radial component u_r, the situation is even more complicated, since it includes contributions from both *P–SV*- and *SH*-waves, and may thus be split into six separate portions.

The significance of this analysis becomes clear when we consider the first step in the inverse problem, which is to calculate the *P–SV* displacement variables U, V as functions of frequency for a particular slowness, from the vertical and radial components of the surface displacement. To invert the transforms in (2.2), we would need to integrate over r and ϕ, and hence to know the response over the whole plane $z = 0$, or at best over a segment. Such data are most unlikely to be available.

The solution we adopt is to restrict our attention to sources that generate only *P–SV* motion, and which excite radiation of only a single angular order. Thus, we consider only a vertical force, or a moment tensor with no off-diagonal terms, and for which $M_{xx} = M_{yy}$, the simplest example being a centre of dilatation. The only exception to cylindrical symmetry is the case of a horizontal force directed along the line $\phi = 0$, for which the vertical displacement on $\phi = 0$ may be written as a single Hankel transform of order one, and to which the *SH* field makes no contribution.

The simple sources represented either by a vertical force, or by a diagonal moment tensor, excite only *P–SV* radiation of angular order $m = 0$. We may thus write the vertical and radial components of the surface response as

$$u_z(t, r) = \frac{1}{2\pi} \int_{-\infty}^{\infty} d\omega \exp(-i\omega t)\, \omega^2 \int_0^{\infty} dp\, p\, U(\omega, p)\, J_0(\omega pr) \qquad (2.3a)$$

$$u_r(t, r) = \frac{-1}{2\pi} \int_{-\infty}^{\infty} d\omega \exp(-i\omega t)\, \omega^2 \int_0^{\infty} dp\, p\, V(\omega, p)\, J_1(\omega pr), \qquad (2.3b)$$

where U, V are the components of the $\mathbf{w}_0$ vector defined above, for *P–SV* motion (*cf.* Kennett 1980). The vertical component of motion due to a radially directed force may be written as a first-order Hankel transform, in the same form as (2.3b).

3 Slant stacking the *P–SV* response

In order to obtain the components U, V of the plane wave response for a particular slowness value, we may slant stack measurements of u_z, u_r along the line $0 \leqslant r \leqslant \infty$, thus inverting the Hankel transforms in (2.3a), (2.3b). For cylindrical geometry the slant stack in the time domain involves a convolution for each time point inside the stacking integral, and Chapman (1981) has given an explicit form of the convolution kernel as the Fourier transform of a Bessel function. The singularities of this kernel make the numerical integration difficult, however, and the existence of the fast Fourier transform makes such a procedure not only unnecessary, but also undesirable.

It is much more efficient first to Fourier transform the response at each receiver, and subsequently to perform the slant stack in the frequency domain, inverting (2.3a), (2.3b) via

$$\omega^2 U(\omega, p) = \int_0^\infty dr\, r\, J_0(\omega pr)\, u_z(\omega, r) \tag{3.1a}$$

$$\omega^2 V(\omega, p) = -\int_0^\infty dr\, r\, J_1(\omega pr)\, u_r(\omega, r), \tag{3.1b}$$

and performing a final Fourier transform to obtain the time series $U(t, p)$, $V(t, p)$.

In order to perform the Hankel transforms in (3.1a) and (3.1b) we would seem to require the displacement components u_z, u_r at closely spaced receiver locations along the entire line $0 < r < \infty$. Fortunately, this is not the case: although closely spaced receivers are, indeed, needed to preserve the high-frequency content of the data, as implied by the sampling theorem, the range of integration may be made finite with no significant loss of information, if we desire to reconstruct the medium only down to some finite depth. Such a result appears plausible, but more detailed analysis is required to establish it firmly.

Let the depth to which we require to determine the structure be D. We may define, for a slowness p, the time $T_p(D)$ after which even the multiple reverberations of the plane wave reflection seismogram become negligible. It is clear that T_p depends on the wave speeds within the medium, but we may assume it to be some small multiple of the two-way shear-wave travel time t_D to the depth D, given very approximately by $t_D = 2D(\beta_0^{-2} - p^2)^{1/2}$, with β_0 being the surface shear-wave speed. Thus we know the time T_p up to which we wish to reconstruct the plane wave response. We now assume that it is possible to estimate the maximum value α_m of the P-wave speed within the medium. By considering the simpler, 2-D slant stack integral, which is of the form

$$U(p, t) = \int_0^\infty dx\, u(x, t + px), \tag{3.2}$$

we see that no contribution will arise for $x > \alpha_m(T_p + px)$. We may thus replace the upper limit in (3.1a), (3.1b) by the finite value X_p, where $X_p = T_p/(p - 1/\alpha_m)$.

4 Retrieval of the reflection matrix from the slant stacked response

In Section 2 we related the surface response $\mathbf{w}_0$ in the frequency/slowness domain to the reflection matrix R_D for the structure. For the P–SV system, where $\mathbf{w}_0 = [U(\omega, p), V(\omega, p)]^{\mathrm{T}}$, we may rewrite (2.1) as

$$\mathbf{w}_0 = M_{\mathrm{F}}(-\boldsymbol{\Sigma}_{\mathrm{U}} + R_{\mathrm{F}}\boldsymbol{\Sigma}_{\mathrm{F}}), \tag{4.1}$$

where the suffix F indicates the influence of the free surface, through the reflection matrix $\tilde{R}$. The 2×2 matrices M_{F}, R_{F} are defined by

$$M_{\mathrm{F}} = M_{\mathrm{U}} + M_{\mathrm{D}}\tilde{R}, \tag{4.2}$$

$$R_{\mathrm{F}} = R_{\mathrm{D}}(I - \tilde{R}R_{\mathrm{D}})^{-1}, \tag{4.3}$$

while the source term $\boldsymbol{\Sigma}_{\mathrm{F}}$ is given by

$$\boldsymbol{\Sigma}_{\mathrm{F}} = \boldsymbol{\Sigma}_{\mathrm{D}} - \tilde{R}\boldsymbol{\Sigma}_{\mathrm{U}}. \tag{4.4}$$

The first term in (4.1) depends only on the properties of the source, and on surface values of the material constants, all of which we assume to be known. We may thus subtract this term, which corresponds to the direct source ray plus the ray once reflected at the surface, from the measured response, to obtain the free surface reflection seismogram $\mathbf{w}_F$, given by

$$\mathbf{w}_F(\omega, p) = M_F(p)\, R_F(\omega, p)\, \mathbf{\Sigma}_F(p). \tag{4.5}$$

Equation (4.5) is exact. In reflection seismology, however, it is customary to use an approximate form of (4.5), whereby the effect of the free surface is neglected. Within this approximation we obtain a seismogram $\mathbf{w}_H$, corresponding to what would be measured were the free surface to be replaced by a homogeneous half-space in $z < 0$, given by

$$\mathbf{w}_H(\omega, p) = M_U(p)\, R_D(\omega, p)\, \mathbf{\Sigma}_D(p). \tag{4.6}$$

Kennett (1979) has exploited this connection between R_D and R_F to derive an approximate transfer function for conventional, vertical component reflection seismology, which removes the effect of free surface multiples. In our treatment we assume, by contrast, that both components of the *P–SV* response are available. We may therefore eliminate the free surface effects entirely by inverting (4.3) to express R_D in terms of R_F as

$$R_D = (I + R_F\tilde{R})^{-1} R_F \tag{4.7}$$

where the elements of the free surface matrix $\tilde{R}$ are functions only of the known elastic parameters at the surface, and the slowness p.

In the following analysis we will limit our attention to the recovery of R_D from the displacement vector $\mathbf{w}_H$, via (4.6), although in practice an intermediate step is required in which we make use of (4.7) to obtain the multiple-free reflection matrix R_D from the observed matrix R_F. Although simple in theory, this step is far from trivial in practice, since to effect the transformation we must first remove the source time function from the reflection response by deconvolution. An alternative and simpler approach, in the absence of strongly reflecting interfaces, is to adopt the assumption made in conventional reflection seismology that such multiples are relatively small, and may be partially removed by careful filtering, although such an assumption is less readily tenable where large offset measurements are concerned.

We now consider the problem of extracting the time series contained in R_D from measurements of the response $\mathbf{w}_H$ to one or more known sources $\mathbf{\Sigma}_D$. We adopt the notation of Kennett & Kerry (1979), whereby the elements of R_D are ordered as

$$R_D(\omega, p) = \begin{pmatrix} R_D^{PP}(\omega, p) & R_D^{PS}(\omega, p) \\ R_D^{SP}(\omega, p) & R_D^{SS}(\omega, p) \end{pmatrix} \tag{4.8}$$

where R_D^{PS} is the reflected *P*-wave generated from an incident *S*-wave. M_U has the specific form (Kennett & Kerry 1979)

$$M_U = \begin{pmatrix} -iq_\alpha \epsilon_\alpha & p\epsilon_\beta \\ p\epsilon_\alpha & -iq_\beta \epsilon_\beta \end{pmatrix} \tag{4.9}$$

where $q_\alpha = (\alpha^{-2} - p^2)^{1/2}$, $\epsilon_\alpha = (2\rho q_\alpha)^{-1/2}$ and similarly for q_β, ϵ_β, while the source vector $\mathbf{\Sigma}_D$ is defined by

$$\mathbf{\Sigma}_D = [\phi_D, \psi_D]^T, \tag{4.10}$$

Table 1.

	Moment tensor $M = \mathrm{diag}(a, a, b)$	Force $\mathbf{F} = (0, 0, 1)^T$
ϕ_D	$-\epsilon_\alpha(p^2a - q_\alpha^2 b)$	$i\epsilon_\alpha q_\alpha$
ψ_D	$-\epsilon_\beta p q_\beta (a-b)$	$-\epsilon_\beta p$

(From Kennett & Kerry, 1979).

with ϕ_D being the *P*-wave amplitude and ψ_D the *SV*.

In Table 1 we list the values of ϕ_D, ψ_D for a cylindrically symmetric moment tensor and for a vertically applied force.

To make all the source terms independent of frequency, we have multiplied the values of ϕ_D, ψ_D for the force by a factor $(-i\omega)$, which corresponds to differentiating the seismograms produced by the point force before comparing them with those generated by the moment tensor source. Equivalently, we may view the source terms in Table 1 as those required to generate a step function response for the moment tensor, but an impulse for the force.

A formal solution to the problem of recovering R_D from $\mathbf{w}_H$ may now be easily obtained. Let $\mathbf{\Sigma}_D^1$, $\mathbf{\Sigma}_D^2$ be source vectors for two different sources, and $\mathbf{w}_H^1$, $\mathbf{w}_H^2$ the corresponding responses. Defining matrices W, Σ by the relations

$$W = [\mathbf{w}_H^1, \mathbf{w}_H^2], \quad \Sigma = [\mathbf{\Sigma}_D^1, \mathbf{\Sigma}_D^2] \tag{4.11}$$

we obtain the matrix form of (4.6),

$$W = M_U R_D \Sigma, \tag{4.12}$$

which may be formally inverted to yield

$$R_D = M_U^{-1} W \Sigma^{-1}. \tag{4.13}$$

In order to make use of (4.13), we must first check that the matrix inverses exist. The explicit form of M_U is given by (4.9), from which it is readily verified that its determinant is non-zero for real slowness values. The matrix Σ is also singular only if the source vectors $\mathbf{\Sigma}_D^1$, $\mathbf{\Sigma}_D^2$ are linearly dependent, contradicting our assumption of two independent sources.

Although (4.13) represents the simplest means of obtaining the reflection matrix R_D from the response W, it is not necessarily the most convenient in practice. By exploiting the symmetry of R_D, it is possible to make use of three, rather than four, sets of displacement data to derive the elements of the matrix. In addition, we do not necessarily wish to measure both components of the response for two sources, but might prefer to measure the vertical component only, for more than two sources. Such a procedure would be desirable when attempting to apply the inversion technique to small-scale laboratory experiments, where accurate horizontal component seismometers are difficult to construct. We should, therefore, investigate the question of how to decide whether three particular sets of data furnish sufficient information to delineate the elements of R_D.

We must first enumerate the possible sets of data which might be obtained in a seismic reflection experiment, under the restriction of a cylindrically symmetric source. Although any moment tensor of the form $M = \mathrm{diag}(a, a, b)$ is, in theory, permissible, we will restrict our attention to a pure explosive source $M = \mathrm{diag}(1, 1, 1)$, since it would be difficult to produce a more complicated source in practice. Under this assumption, we are led to consider five possible source/receiver combinations, which are listed in Table 2.

Table 2.

	Source	Displacement component
A	Explosion	Vertical
B	Explosion	Radial
C	Vertical force	Vertical
D	Vertical force	Radial
E	Radial force	Vertical

It appears at first sight that knowledge of any three of the five data sets listed in Table 2 enables us to obtain the reflection matrix R_{D}. Two particularly convenient combinations would be (A), (C), (E), requiring measurements of vertical motion only, and (C), (D), (E), corresponding to single force sources, which for an elastic medium are simpler to produce than a centre of dilatation. In both cases, however, the data are not independent, and are therefore insufficient to construct R_{D}.

To demonstrate that the data sets (A), (C), (E) are linearly dependent, we note that each source produces a quantity ϕ_{D} of P radiation, and a quantity ψ_{D} of SV radiation. Thus, the response of two independent, cylindrically symmetric sources may be used to predict the response to a third. In the case of data sets (C), (D), (E), we may use the reciprocity property of the Green tensor, in the form

$$G_{ij}(\mathbf{x}, t; \boldsymbol{\xi}, 0) = G_{ji}(\boldsymbol{\xi}, t; \mathbf{x}, 0) \tag{4.14}$$

to show that the radial response to a vertical force is the same as the vertical response to a radial force.

Although we have eliminated two combinations of data sets, several remain which are sufficient to enable us to construct R_{D}. The simplest case results from combining (A) and (B) with any of (C), (D), (E). Since the explosive source generates only P radiation, it is clear that measurements of the reflection seismogram give us $R_{\mathrm{D}}^{\mathrm{PP}}$, R_{D}^{SP} immediately, while symmetry furnishes R_{D}^{PS}. One further measurement then suffices to calculate the remaining element R_{D}^{SS}. It is thus possible to obtain the entire P–SV reflection matrix for the structure from measurements of the vertical component of the responses to an explosive source and a vertical force, plus the radial component of the response to either.

5 Discussion

We have shown that the data required to produce the P–SV reflection seismogram matrix, which forms the input to the inversion procedure described in Clarke (1984), consist of three sets of measurements along a line. These must include a mixture of vertical and radial component seismograms, and at least two different sources are needed. The cost of collecting such data, together with the requirement that the medium be horizontally layered, cast some doubt on the practical value of such a scheme, but future improvements in instrumentation could easily render it an effective technique, while the use of such an elastic inversion method locally to investigate the detailed structure of particular interfaces should also prove a useful adjunct to standard reflection profiling procedures.

Acknowledgments

The author is grateful to Professor Y. H. Pao for much useful discussion. This work was supported by the Office of Naval Research, under contract N00014-83-K-0051.

References

Chapman, C. H., 1981. Generalized Radon transforms and slant stacks, *Geophys. J. R. astr. Soc.*, **66,** 445–454.

Clarke, T. J., 1984. Full reconstruction of a layered elastic medium from *P–SV* slant stack data, *Geophys. J. R. astr. Soc.*, **78,** 775–793.

Hudson, J. A., 1969. A quantitative evaluation of seismic signals at teleseismic distances – 1. Radiation from point sources, *Geophys. J. R. astr. Soc.*, **18,** 233–249.

Kennett, B. L. N., 1979. The suppression of surface multiples on seismic records, *Geophys. Prospect.*, **27,** 584–600.

Kennett, B. L. N., 1980. Seismic waves in a stratified half space – II. Theoretical seismograms, *Geophys. J. R. astr. Soc.*, **61,** 1–10.

Kennett, B. L. N. & Kerry, N. J., 1979. Seismic waves in a stratified half-space, *Geophys. J. R. astr. Soc.*, **57,** 557–583.

Geophys,. J. R. astr. Soc. (1984) 79, 573–588

Evidence for detrital remanent magnetization carried by hematite in Devonian red beds from Spitsbergen; palaeomagnetic implications

R. Løvlie and T. Torsvik *Geophysical Institute, University of Bergen, Allegt. 70, N-5000 Bergen, Norway*

M. Jelenska and M. Levandowski *Polish Academy of Science, Institute of Geophysics, Pasteura 3, 00-973 Warzsawa, Poland*

Received 1984 April 25; in original form 1984 February 20

Summary. Palaeomagnetic investigation of the Devonian red bed succession of Central Spitsbergen, the Wood Bay Formation, uncovered stable magnetic directions associated with blocking temperatures above 600°C. Rock magnetic properties are characterized by features commonly found in hematite-bearing red sandstones. The scattered directional distribution of stable magnetic components show large, non-systematic spatial variations hardly compatible with magnetic overprinting processes. Petrographic observations (Friend), suggest a detrital origin of the hematite granules present, probably derived from a lateritic source area. A depositional origin of magnetizations carried by hematite is also inferred from almost coinciding azimuthal distributions of remanent directions and maximum axis of susceptibility ellipsoids. Effects of the depositional environment upon the acquisition of DRM carried by hematite is discussed. Subjective pattern recognition of directional distributions from sampling areas on both sides of the Dicksonfjorden, enables a tentative stratigraphic correlation reflecting the presence of pre-Middle Carboniferous faulting downthrowing to the east. A clockwise post-Devonian rotation of the Central Spitsbergen (uncertain magnitude) is inferred from an estimate of the Devonian palaeomagnetic meridian.

Introduction

The geology of the Svalbard archipelago reflects a number of geodynamic episodes related to the evolution of the North Atlantic region. Structural features reflect the superposition of four main episodes of deformation, of which the Caledonian orogeny was the most intense. The succeeding three tectonic events were associated with faulting and strike-slip movements rather than metamorphism. The geodynamic implications of these N–S striking fault patterns range from a pure fixistic interpretation (Krasil'scikov 1979) to a mobilistic model postulating differential movements of three separate blocks now constituting the Svalbard archipelago (Harland & Wright 1979). Palaeomagnetic directions residing in the Devonian Old Red Sandstone sequence, confined to the central graben of Spitsbergen, may elucidate the late post-Devonian tectonic history of the archipelago during which major strike-slip movements have been postulated (Harland & Wright 1979).

Previous palaeomagnetic investigations of the Devonian red bed formation on Spitsbergen have not been successful in retrieving acceptable distributions of remanent directions (Storetvedt 1972; Jelenska, Kruczyk & Kadzialko-Hofmokl 1979). This has been attributed to geomagnetic polarity changes during acquisition of chemical remanent magnetizations (CRM) associated with rather complex diagenetic oxidation/reduction processes of the magnetic minerals (Storetvedt 1972).

The origin of stable remanent directions in hematite-bearing red beds is still a matter of dispute. Hematite may occur both as relatively large, polycrystalline grains (specularite) and as a fine-grained pigment coating detrital grains. While specularite may be of both detrital and/or post-depositional origin (martite), pigment is exclusively attributed to precipitation of hematite associated with diagenetic processes in oxidizing environments. In order to discriminate between specularite and pigment as carriers of natural remanent magnetization acid leaching experiments have been applied. This approach rests on the assumption that the latest precipitated hematite (pigment) forms a coating on mineral grains and is selectively dissolved first by the action of acids. Experiments have demonstrated the presence of sometimes very complex systems of remanence directions (Roy & Park 1974) attributed to the acquisition of CRM in different palaeomagnetic field directions. Redeposition experiments of different fractions of crushed red beds has established characteristic thermal demagnetization features of depositional remanent magnetizations (DRM) carried by pigment and specularite (Collinson 1974).

A post-depositional origin of magnetization carried by pigment and/or specularite implies an unknown time of magnetization. Depending on the rate of hematite formation, red beds may be postulated to record substantial time-averages of geomagnetic field variations. Spectral analysis of reversal features within the Triassic Moenkopi formation, however, has been interpreted to reflect contemporaneous acquisition of stable remanent directions (Baag & Helsley 1974). Similar conclusions, regarding the time of magnetization, has been inferred from results of fold and conglomerate tests within the same formation (Purucker, Elston & Shoemaker 1980). Opposing views have been proposed from petrographic studies of the Moenkopi Formation which reports on five or possibly six different generations of hematite all suggested to be potential carriers of remanent magnetizations (Walker *et al.* 1981). Objections to contemporaneous acquisition of remanent magnetization in red beds is mainly based on the observation that Holocene hematite (pigment) carrying deposits are rare, as opposed to deposits showing different stages of red-staining interpreted to represent red-beds in the making (Walker 1974; Larson & Walker 1975).

Redeposition experiments of naturally disintegrated hematite-bearing sediments have recently (Tauxe & Kent 1984; Løvlie & Torsvik 1984) established that DRM carried by detrital hematite record the ambient magnetic field with errors in inclination described by the classical disc/sphere model (King 1955). Post-depositional rotation of hematite grains has been shown to result in remanent magnetizations parallel to the ambient magnetic field (Tauxe & Kent 1984). However, other experimental results suggest that remanence properties in hematite-bearing sand-silt sediments may depend on the experimental conditions (Løvlie & Torsvik 1984). Since sand-sized sediments are deposited in high energy environments a DRM is likely to be affected by randomizing processes acting during deposition.

Geology and sampling

The Late Silurian to Devonian sandstone succession which is confined within an area bounded by N–S striking faults in North Central Spitsbergen (Fig. 1) accumulated after major Caledonian folding and metamorphism and was subsequently exposed to the Upper Devonian (Svalbardian) phase of folding and faulting (Friend & Moody-Stuart 1972). The thickness of the various formations covers some 8 km, of which the investigated Wood Bay Formation amounts to some 3 km.

The environment of deposition include torrential alluvial fans, river flood-plains, brackish lagoons and inland lakes. No indications of marine conditions have been observed. Three river systems flowing towards a northern area of clay flats have been distinguished (Friend 1961).

Thin section analysis of the Wood Bay Formation sandstone has revealed the presence of red pellicles, composed of hematite granules (< 1 μm), which surround detrital grains. The red pellicles indicate a detrital origin of hematite derived from an area of lateritic weathering (Friend 1961). Post-depositional continuation of the oxidizing conditions has probably been low or moderate since in the coarser, grey-coloured sediment red pellicles are virtually absent (Friend 1961). This suggest that in high-energy environments, necessary for the accumulation of coarser beds, fine-grained hematite flakes were transported out of the area of deposition.

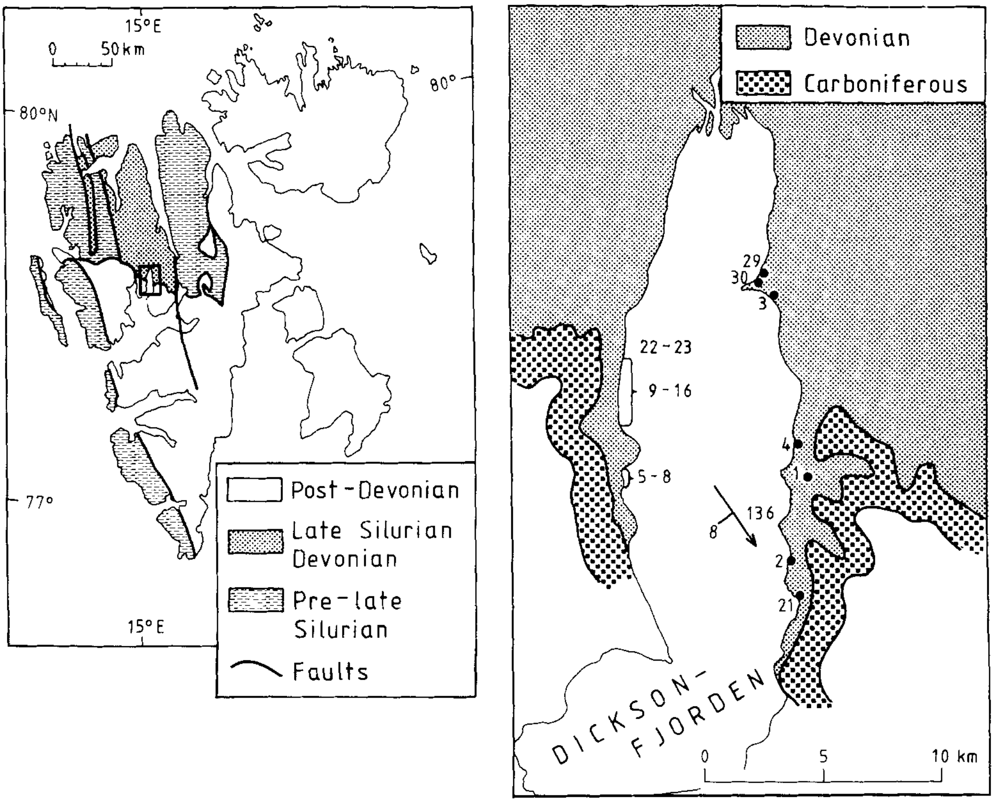

Figure 1. Maps of Spitsbergen and the Dicksonfjorden sampling area. Regional bedding of the Wood Bay Formation red beds (136/8) and sampling localities (numbers) are shown.

Palaeomagnetic samples of the Wood Bay Formation were collected in Dicksonfjorden, where the formation tilts slightly towards the SE (Fig. 1). The sampling localities are situated at shore level and covers the top 800 m of the red bed succession unconformably underlying Middle Carboniferous Limestones. Continuous stratigraphic sampling was prevented by areas of extensive surface weathering and scree coverage. One locality (site 16) consists of a coarse, grey-coloured rock, while the other localities are dominated by silt-sand deposits showing different hues of red to brown. Each locality is represented by 5–10 drill cores (19 mm in diameter). Sun compass orientations were only obtained occasionally due to weather conditions, but the available observations defined magnetic deviations close to zero which is in agreement with observatory measurements in Ny Ålesund some 60 km to the NE.

Rock magnetic properties

IRM-acquisition curves to 0.8 T of samples from all stratigraphic levels revealed identical features, as shown in Fig. 2(a). High coercivity minerals, which do not reach saturation in the maximum field available, associated with back-fields above 0.3 T, is indicative of fine-grained hematite (Dunlop 1972).

With the exception of samples from site 16 (coarse, grey-coloured rock), thermomagnetic curves exhibit identical features regardless of stratigraphy. A single, reversible Curie

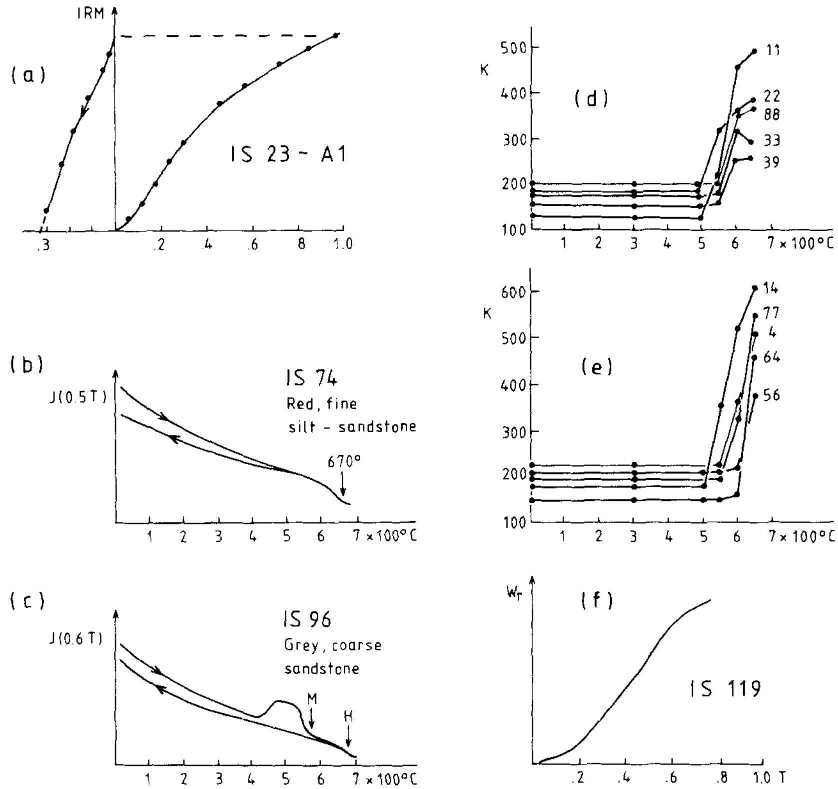

Figure 2. Plots of characteristic rock magnetic properties. (a) IRM-H acquisition and back-field curves. (b) and (c) thermomagnetic curves for red silt-sand samples and grey sand samples (arbitrary units). M and H, Curie points of magnetite and hematite respectively. (d) and (e) variation of reversible bulk susceptibility with temperature, (f) rotational hysteris curve, arbitrary units (W_r).

temperature around 670°C, indicative of almost pure hematite, is associated with a substantial paramagnetic contribution (Fig. 2b). Thermomagnetic curves obtained from site 16, show the characteristic increase in saturation magnetization upon heating to temperatures above 400°C indicative of magnetite production through the transformation of titanomaghemite. The magnetite Curie point (M, Fig. 2c) is not present upon cooling from 700°C, probably due to complete oxidation to hematite. The hematite Curie point (H, Fig. 2c) reflect the contribution from both the oxidation product of magnetite and the initial content of hematite.

Previous published thermomagnetic curves from the Wood Bay Formation (Storetvedt 1972), reflect the presence of substantial amounts of titanomaghemite. In the present material titanomaghemite was encountered only in coarse grey-coloured rocks, suggesting that previous thermomagnetic results of the Wood Bay Formation were obtained from coarser sequences than the present study. By magnetic extraction procedures of some recent flood-plain deposits, composed of disintegrated red sandstones from Dicksonfjorden, a small amount (<0.3 per cent) of titanomaghemite was obtained (Løvlie & Torsvik 1984). The presence of titanomaghemite within red bed deposits indicates that post-depositional oxidation of detrital grains has been minor.

Determination of the reversible bulk susceptibility in conjunction with progressive thermal demagnetization reveal a substantial increase in susceptibility above 500°C (Fig. 2d, e). This phenomenon is often encountered in hematite-bearing sediments and has been related to the production of magnetite by transformation of non-magnetic minerals (Stephenson 1967; Dunlop 1972). This conclusion has been questioned (Torsvik & Løvlie 1983) on the grounds that the amount of secondary magnetite relative to the primary content of hematite should enable a direct detection by thermomagnetic analysis, which remain to be established. In the present context it is emphasized that the Wood Bay Formation sandstone exhibits rock magnetic features characteristic of hematite-bearing sandstones in general.

Rotational hysteresis, determined on a few samples, also exhibit features indicative of hematite (Fig. 2f).

Although the present material is suggested to be dominated by hematite, titanomaghemite phases may contribute to remanence properties associated with blocking temperatures below 580°C.

Demagnetization experiments

Measurements of the remanent magnetization have been performed using three different magnetometers: a Digico balanced flux-gate spinner, a single axis SQUID and a JR-4 spinner magnetometer. The latter is situated at the Polish Academy of Sciences, Warsaw, while the former instruments are located at the University of Bergen. Anisotropy of magnetic susceptibility (AMS) was determined on an induction bridge (Kappabridge, KLY-1).

NRM intensities range between 1 and $10\,\mathrm{m\,A\,m^{-1}}$ and bulk susceptibilities between 12 and 60×10^{-5}. NRM directions within and between sites as well as from cylinders from identical drill-cores showed a high degree of non-systematic scatter.

Progressive alternating field demagnetization to 80 mT in a two-axis tumbler system, was not successful in reducing NRM intensities by more than 55 per cent. This partial demagnetization was associated by only minor directionl changes, *cf.* Fig. 3.

Chemical demagnetization by acid treatment turned out to be unsuccessful due to complete disintegration of the samples after only short exposures to dilute hydrochloric acid.

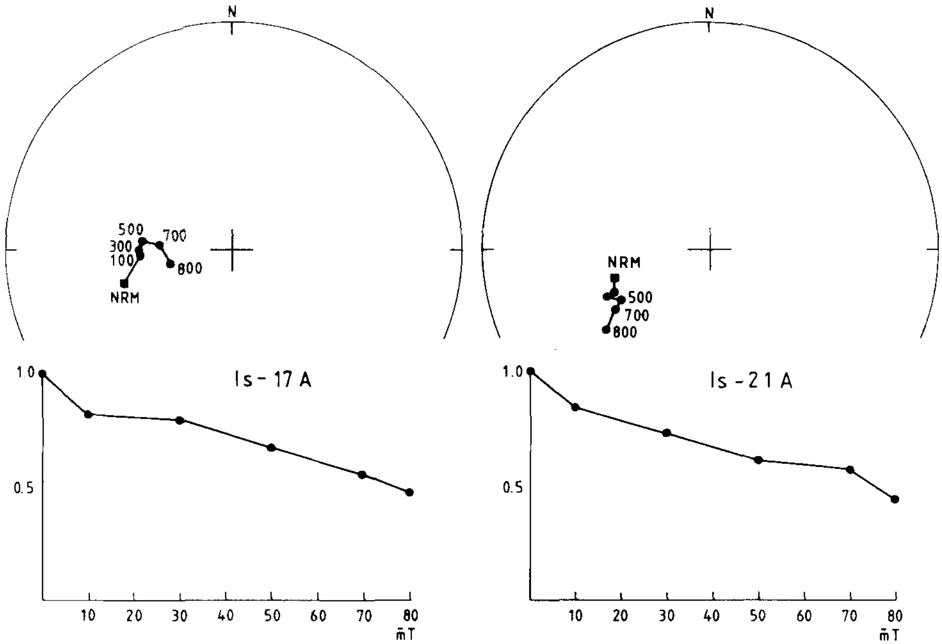

Figure 3. Results of af demagnetization to 80 mT.

The samples were thus subjected to thermal demagnetization treatment in two different furnaces, one Schonstedt Model TSD-1 Thermal Demagnetizer (Bergen) and one built by the Polish Academy of Sciences (Warsaw). In both furnaces, multiple permalloy shields are utilized to achieve close to field-free cooling environments (< 10 nT).

Directional properties

During progressive thermal demagnetization to 700°C non-systematic directional changes were encountered in less than half of the investigated samples. Characteristic behaviour during thermal demagnetization is shown in Fig. 4. The stereographic and vector plots (a), (b) and (d) show that an almost vertical component is removed below 625°C associated with slightly decreasing intensities. The final two steps, prior to reaching intensities comparable to the noise level of the instruments, define a significantly shallower component. Fig. 4(c) reveals a completely different behaviour, in that a continuous and gradual decrease in intentisity is associated by a shallow-dipping component below 600°C.

Fig. 5 demonstrates directional changes of two samples from site 3 determined in Warsaw (IS23-A2) and Bergern (IS22-B). Both samples define stable, coinciding directions after demagnetization to 600 and 200°C respectively. Pronounced different directional behaviour during demagnetization is attributed to small-scale spatial variations in the properties of remanence carrying minerals.

With few exceptions acceptable stable directions are associated with blocking temperatures above 575°C (Fig. 6). More or less systematic great-circle trends may precede terminal directions, indicate of at least a two component system in which one component is probably of viscous or chemical origin (IS4A, IS7B, Fig. 6). Demagnetization curves show a variety of patterns ranging from almost square-shaped (IS18A2, Fig. 6) to more linear decay curves (IS1 10A). The latter sample carries a stable, steeply dipping direction coinciding fairly well

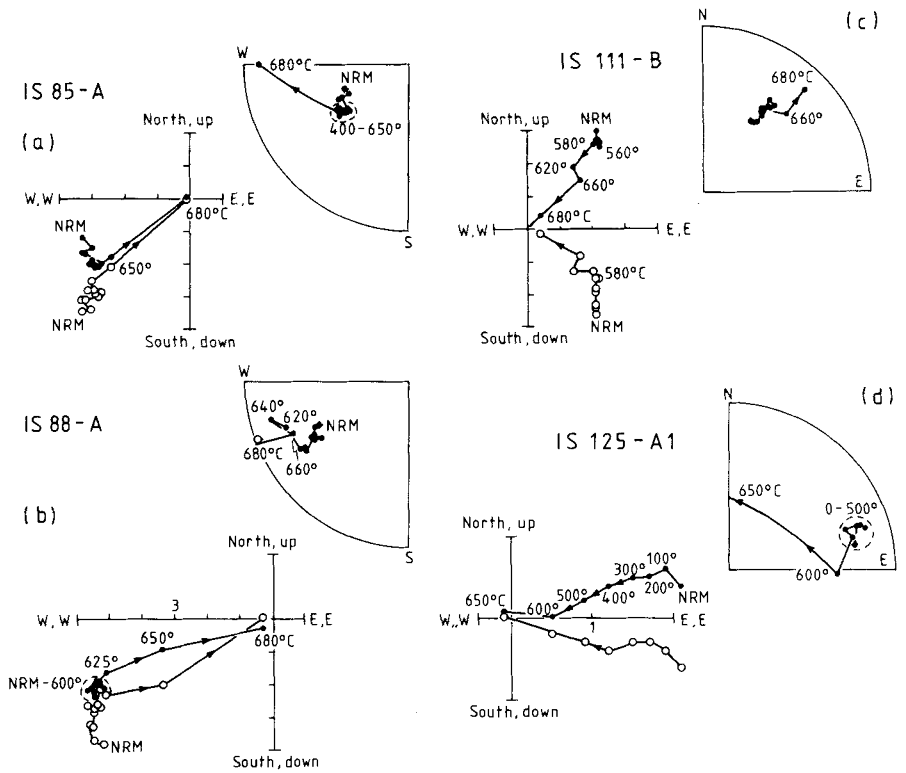

Figure 4. Stereographic and vector presentation of thermal demagnetization results. Unit on vector axis, 1 mA m⁻¹.

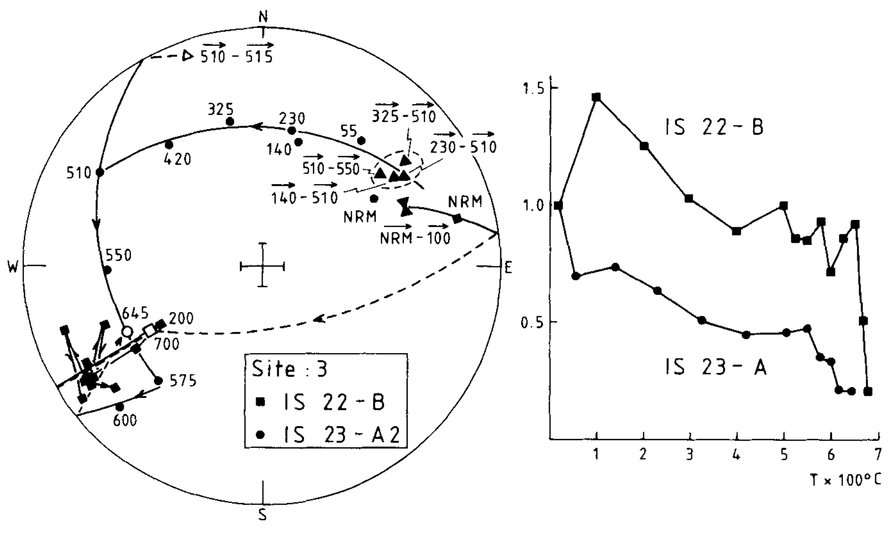

Figure 5. Thermal demagnetization results of two samples from site 3. Left: normalized intensity decay curves. Stereographic plot shows palaeomagnetic directions (open/filled circles) and removed vector components (triangles). Demagnetization temperatures in °C. Vector component intervals (°C) indicated by horizontal arrows.

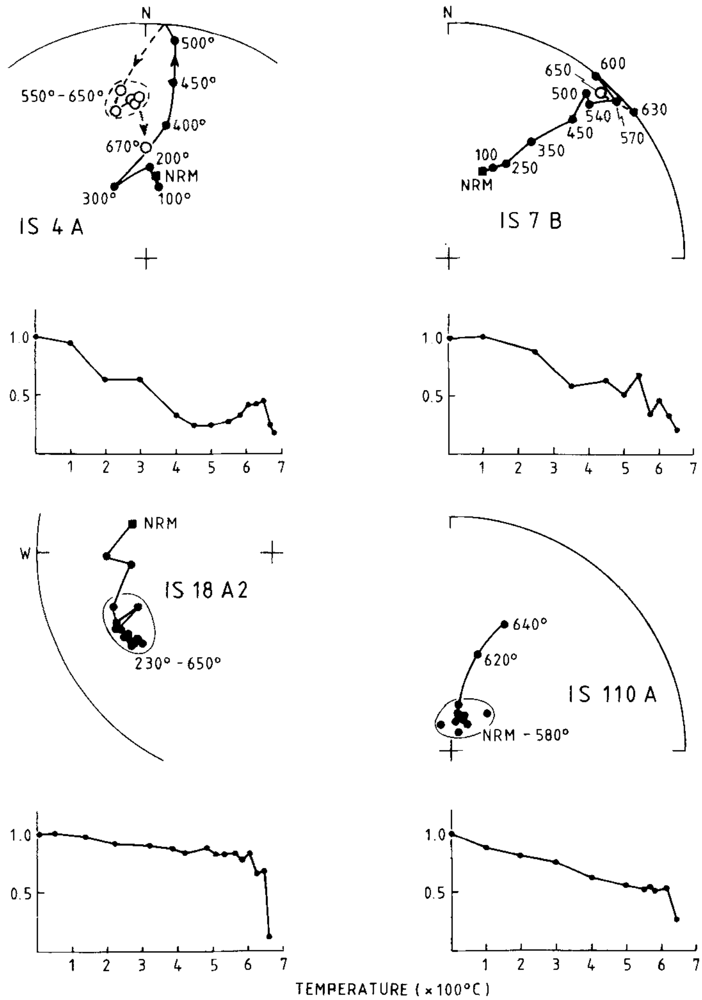

Figure 6. Characteristic thermal demagnetization results.

with the present geomagnetic field direction. This component is associated with blocking temperatures below 580°C, indicating a present-day CRM probably residing in titanomaghemite. Above 580°C the directional trend reflect the presence of a shallow dipping component.

A total of 130 samples were subjected to step-wise thermal demagnetization. Seventy-nine samples were accepted to carry stable or metastable directions, shown in Fig. 7. Results obtained in the two laboratories appear to agree fairly well (Fig. 5), but the directional scatter evidently does not justify a more analytical comparison to be carried out. Although the distribution of stable directions is rather scattered, a pronounced grouping is evident in the south-west quadrant. Standard great circle and vector subtraction analysis were unsuccessful in uncovering unambiguous systematic distributions of removed components, and no objective way of filtering has been attempted. The non-systematic directional distributions within sites and between cylinders from identical drill-cores suggest either that the stable directions represent systems of two or more superimposed components residing in minerals with overlapping blocking temperature spectra, or that stable directions do not necessarily reflect directions of the geomagnetic field. The latter alternative implies the

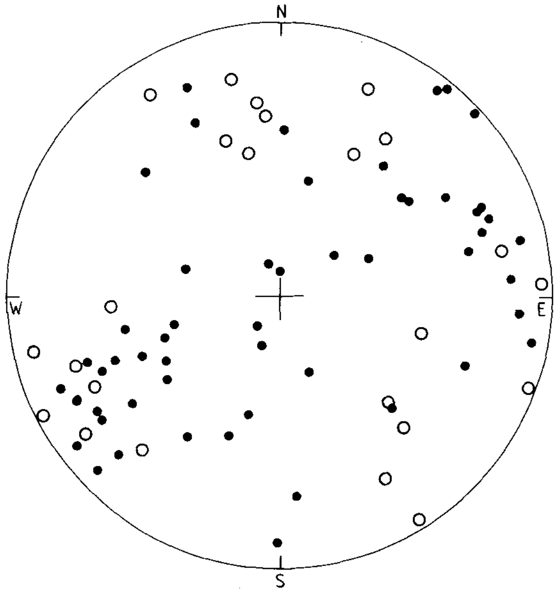

Figure 7. Distribution of accepted stable directions from the Wood Bay Formation, Dicksonfjorden.

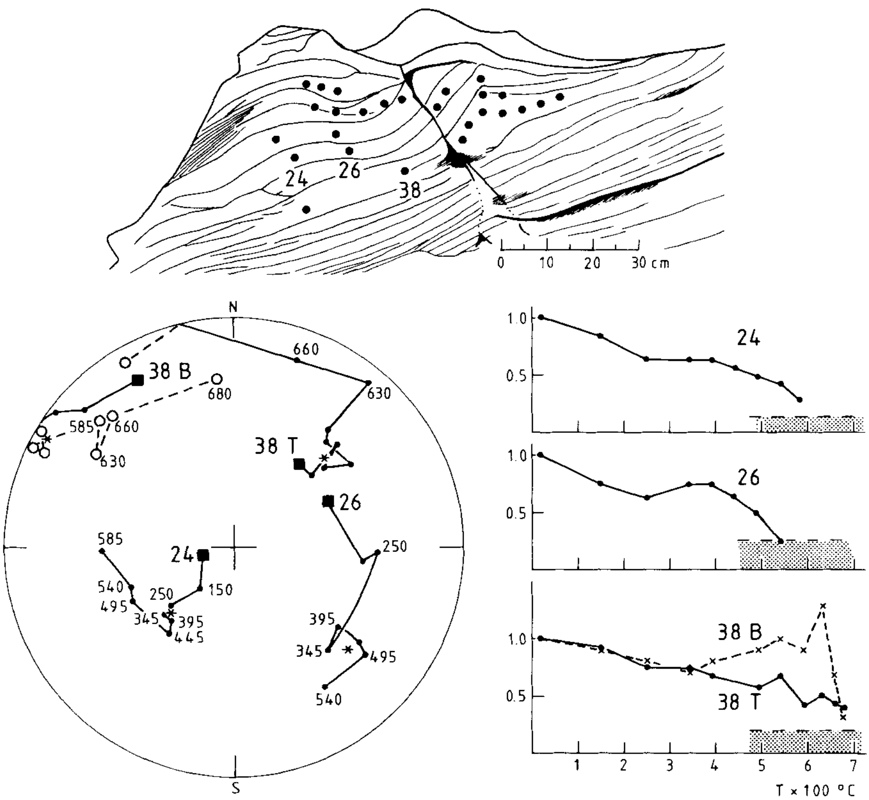

Figure 8. Schematic cross-section of primary slump structure. Sample positions indicated by filled circles. Directional variations and intensity decay curves shown for drill cores, 24, 26, 38T (top) and 38B (bottom). Accepted, metastable directions indicated by asterisks. Noise level of instrument indicated by the horizontal broken line.

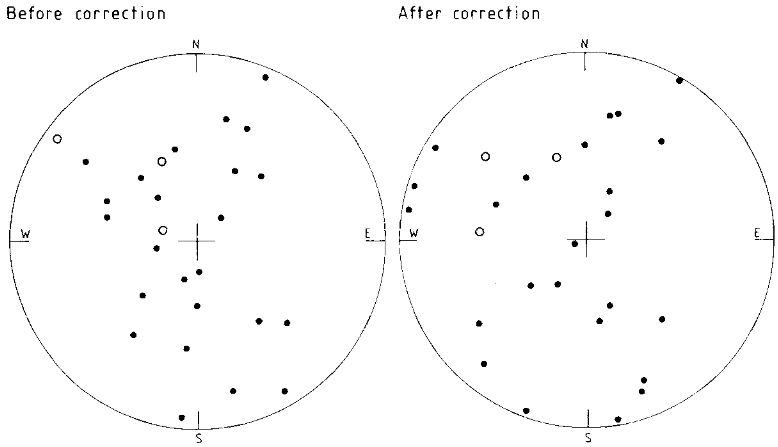

Figure 9. Distribution of metastable directions of primary slump feature. Left: *in situ* directions, right: after correction for local bedding.

action of randomizing processes in conjunction with the acquisition of stable remanent magnetizations. The origin of magnetization thus appear to be crucial in order to understand the obtained results.

During a second field season to the Dicksonfjorden area, a small, primary slump structure was located and sampled in detail. Fig. 8 shows a cross-section of this sedimentary feature with the positions of the 26 collected oriented samples. Results of progressive thermal demagnetization of two cylinders from the same drill-core, 38T (top) and 38B (bottom) (Fig. 8), illustrate the complexity of magnetization. Demagnetization curves are similar to 450°C, but while the bottom cylinder define a metastable direction below 580°C, the top cylinder of the same core carries a metastable component above 585°C. The large discrepency between directions residing in cylinders from the same core is suggested to reflect the scale of spatial inhomogeneity of the remanent magnetization. The highly scattered distribution of metastable directions are shown in Fig. 9.

It has been demonstrated that even after deformation (folding) of wet, cohesive clay-silt sediments the direction of the primary magnetization may be obtained by correcting for local folding (Verosub 1975). Applying a correction for the small-scale 'bedding' for each sample, results in a distribution of the stable directions shown in Fig. 9. It is apparent that this bedding test is negative with respect to elucidating the acquisition time of magnetization relative to the time of slumping.

Anisotropy of magnetic susceptibility

Determination of the AMS-ellipsoid directions and parameters of 80 samples from all stratigraphic levels resulted in distributions of minimum and maximum susceptibility axes shown in Fig. 10. The almost vertical distribution of the minimum axis defines a bedding plane almost coinciding with the observed sedimentary regional bedding plane. Almost flat-lying maximum axis define azimuthal distributions striking NE–SW. All AMS-ellipsoids are oblate ($E > 1$) with anisotropy factors ranging between 6 and 10 per cent. Foliation parameters have comparable magnitudes while lineations are significantly lower ($<1-2$ per cent).

Magnetic fabric properties of magnetite-bearing sediments deposited under different conditions are fairly well known (Hamilton & Rees 1970), as opposed to hematite-bearing

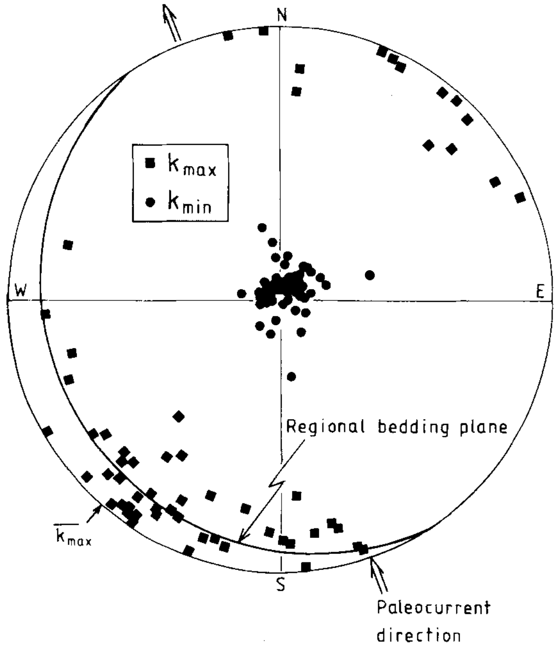

Figure 10. Directional distributions of maximum (k_{max}) and minimum (k_{min}) AMS axis. Flow direction of palaeocurrent (Friend & Moody 1972) shown by the double arrow. Mean azimuth of maximum susceptibility axis shown by the arrow. Projection of the measured mean regional bedding plane is on the lower hemisphere.

deposits. The origin of AMS in magnetite and hematite is fundamentally different in that the former is related to a geometric shape effect while the latter is due to magnetocrystalline effects. Hematite has a ferrimagnetic moment due to imperfect antiparallelism between crystallographic sub-lattices. This spin-canting effect gives rise to a weak spontaneous magnetization confined to lie in the basal-plane. This ferrimagnetic susceptibility is superimposed on an isotropic antiferromagnetic susceptibility which amounts to only 1/5 of the former for single domain grains (Stacey 1963). Hematite in effect has a uniaxial susceptibility with the maximum susceptibility restricted to lie in the basal plane.

The mean palaeocurrent direction for Dicksonfjorden (Friend & Moody-Stuart 1972), shown in Fig. 10, is almost along the strike of the regional bedding, and almost perpendicular to the mean direction of maximum susceptibility. The orientation of long axis of grains deposited in flowing water may be parallel or perpendicular to the water flow depending on the relative grain size distribution between the sediment surface and deposited grains (Rusnak 1957). AMS of magnetite is related to the geometric shape of individual grains and may reflect the statistical orientation of long axis. Similar considerations are not applicable for rocks carrying detrital hematite grains since the AMS of the latter is crystallographically controlled.

Discussion

ORIGIN OF MAGNETIZATION

Distributions of very scattered palaeomagnetic directions in red sandstones may be attributed to unresolved multicomponent systems, disturbed ambient field conditions during remananece acquisition (Collinson 1980) or to processes affecting the ability of a sedimentary rock to acquire and maintain a record of the ambient field. Since a disturbed geomagnetic field configuration is likely to be rather short-lived, it may be almost impossible to verify such interpretations.

Different diagenetic generations of hematite have been interpreted to favour a chemical origin of magnetic components associated with blocking temperatures in the 600–650°C range, and multicomponent systems have been proposed in order to explain complex directional behaviour in hematite-bearing rocks. Similar considerations, however, can also be applied to rocks containing detrital grains of hematite. Depending on grain-size distributions, hydrodynamic conditions during deposition may affect the alignment of different populations of hematite grains to different extents. Situations may arise in which the orientation of one fraction of grains is dominated by the magnetic field, while other grains fractions are predominantly affected by 'randomizing' forces acting during deposition (currents, turbulence). Since blocking temperatures are grain-size dependent, directional trends during thermal demagnetization may incorrectly be interpreted to reflect the effect of palaeomagnetic overprinting.

A DRM origin of magnetic components with blocking temperatures comparable to that of hematite, presumes that the composition of the source material can be determined. In the Wood Bay Formation, granules of hematite, usually attributed to post-depositional precipitation, appear to have been derived from a lateritic source area, implying a predominantly detrital origin of hematite.

DRM carried by hematite is characterized by systematic errors in inclination (Tauxe & Kent 1984; Løvlie & Torsvik 1984), which is likely to be grain-size dependent. Post-depositional realignment of hematite grains has been experimentally demonstrated (Tauxe & Kent 1984), but is suggested to be less effective than alignment during deposition due to the weak magnetic torque acting on hematite grains. In low-energy environments (still-water), DRM carried by hematite record the true azimuth of the ambient magnetic field, so even with errors in inclination a palaeomagnetic meridian may be determined.

The Dicksonfjorden stable directions appear to be distributed symmetrically along a NE–SW axis (Fig. 7). The large azimuthal scatter is attributed to remanent components residing in detrital grains partly disturbed by randomizing forces acting during deposition in the high energy environments (torrents, floods, rivers). This interpretation, in conjunction with results obtained from the primary slump feature (Fig. 9) implying negligible CRM acquisition or post-depositional realignment of detrital hematite grains, suggests a detrital origin of magnetization.

Redeposition experiments have demonstrated coinciding azimuths between directions of maximum susceptibility and DRM in hematite-bearing deposits (Løvlie & Torsvik 1984), probably related to the common origin of susceptibility and spontaneous magnetization in hematite grains. The mean azimuths of maximum susceptibility and stable directions (Figs 10 and 7) are seen to agree fairly well. It is concluded that the stable directions encountered in the investigated Wood Bay Formation are basically carried by detrital hematite.

Almost coinciding directions of stable magnetizations and the maximum axis of susceptibility have been reported previously from the Permian Dome de Barrot red beds (Van den Ende 1977), which was concluded to carry a depositional magnetization recording a time sequence of the contemporaneous geomagnetic secular variation.

STRATIGRAPHIC CORRELATION

The palaeomagnetic sampling localities are situated on both sides of the Dicksonfjorden. The base of the sequence in this area is not exposed, and the stratigraphic positions of the five sampling areas have been calculated relative to the Carboniferous Limestone sequence overlying the Devonian red bed succession. Fig. 11 shows the distributions of stable directions obtained from the five sampling areas. The large directional scatter within each group is apparent. Calculations of mean directions are not justified due to lack of objective criteria for filtering or sub-grouping. However, by subjective pattern recognition, the two stratigraphic lowermost groups on either side of the Dicksonfjorden appear to show almost identical directional patterns. The correlation between these groups (as suggested in Fig. 11) is admittedly highly speculative, but considering that contemporaneous deposition under still-water conditions across large lateral distances will result in sedimentary horizons carrying coinciding DRM directions reflecting the action of the ambient magnetic field, disturbances of DRM caused by similar depositional environments may turn out to generate corresponding directional patterns.

The correlation shown in Fig. 11 implies that the Dicksonfjorden may represent a topographic feature associated with a normal fault down-throwing to the east. To the south,

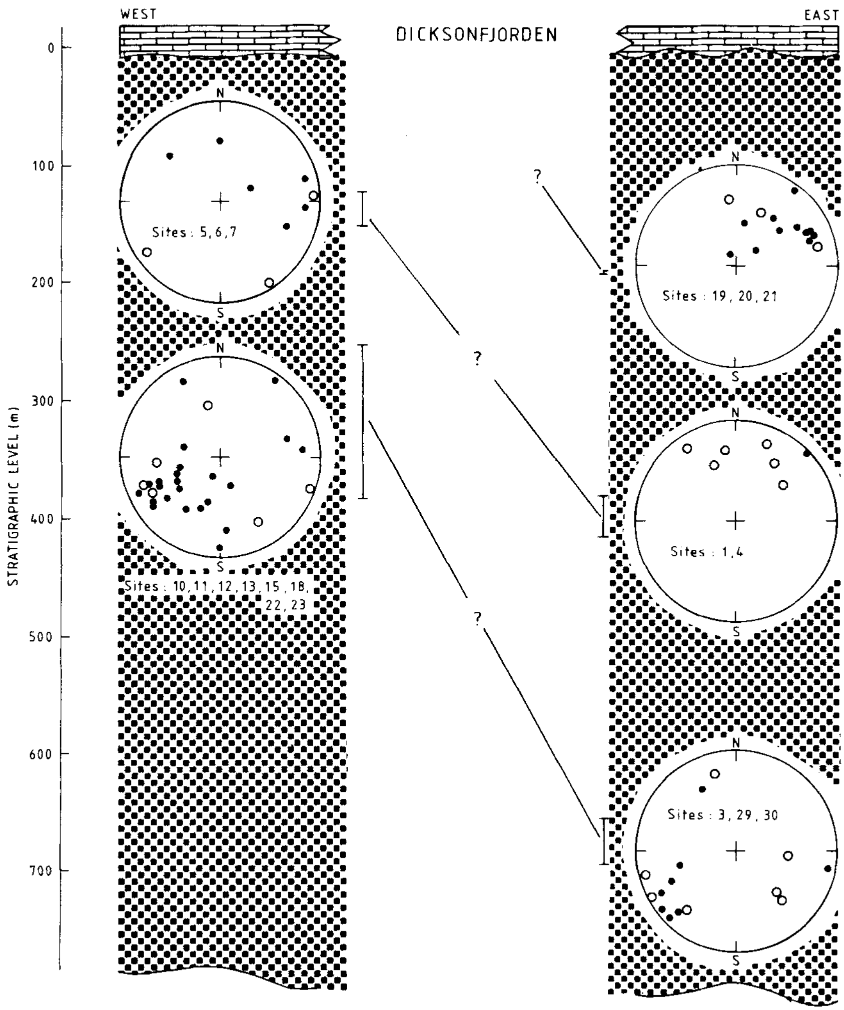

Figure 11. Distributions of stable directions from five sampling areas on both sides of the Dicksonfjorden. Tentative stratigraphic correlations based on subjective pattern recognition. Stratigraphic levels relative to base of overlying Middle Carboniferous Limestone.

Dicksonfjorden terminates into the Isfjorden and to the north continues into the Dickson Valley. The proposed N–S running normal fault may be related to the development of the post-Devonian N–S striking Billefjord fault system some 20 km to the east, which constitutes the eastern boundary of the Central Graben on Spitsbergen, within which the Devonian red bed succession is confined.

PALAEOMAGNETIC IMPLICATIONS

A detrital origin of remanent directions carried by hematite would imply an uncertainty with regard to the effect of inclination errors. DRM in hematite records the true azimuth of the ambient magnetic field, enabling a determination of the meridian of the palaeomagnetic pole. The application of palaeomagnetic directions in estimating the sense and magnitude of lateral fault movements may ultimately depend on comparing azimuths of declination.

The poor quality of the obtained distribution of stable directions from the Wood Bay Formation does not permit unambiguous comparisons with European palaeomagnetic poles in order to elucidate the post-Devonian tectonic relationship between Europe and Svalbard. Accepting the proposed detrital origin of the stable directions, it is reasonable to assume that the investigated section of the Wood Bay Formation was deposited and acquired remanent magnetizations in the same geomagnetic field (not necessarily of one polarity). The suggested randomizing effects of the depositional environments cannot be readily quantified, but are likely to be averaged out in the arithmetic mean of the azimuths of all stable directions. The mean azimuth around 240° defines an axis striking some 30° more easterly than the Devonian field azis for stable Europe recalculated to the present-day position of Spitsbergen. The unknown scatter of this inferred Devonian field axis for Spitsbergen may only justify the tentative conclusion of a clockwise rotation of the Central Spitsbergen relative to Europe since deposition in Devonian times.

Conclusion

The large scatter of stable palaeomagnetic directions can hardly be accounted for by magnetic overprinting processes alone. Petrographic and rock magnetic properties suggest a detrital origin of granules of hematite deposited in environments exposed to only minor, if any, post-depositional oxidization. Almost coinciding azimuths of remanence and maximum axis of susceptibility ellipsoids, also suggests a DRM origin residing in hematite. The large spatial variations of stable directions both between and within sites are attributed to randomizing effects caused by the high energy (hydrodynamic) environments acting during the accumulation of the Wood Bay Formation silt-sand sediments. It should be emphasized that post-depositional realignment on detrital hematite is likely to be strongly dependant on depositional environments (currents, floods) due to the weak magnetic torque acting on such grains.

Although the inferred influence of the proposed randomizing effects on the remanence directions due to the high energy depositional environments is rather conjectural, the almost symmetrical NE–SW distribution of stable directions (*cf.* Fig. 7) is tentatively concluded to reflect the geomagnetic meridian during accumulation of the Wood Bay Formation. This inferred Devonian axis for Spitsbergen strikes some 30° more easterly than the corresponding Devonian palaeomagnetic meridian for Europe. Taking into account the involved uncertainties, the result is nevertheless suggested to indicate a post-Devonian clockwise rotation of Central Spitsbergen relative to Europe.

Acknowledgments

During two field seasons we received logistic assistance from the Norwegian Polar Institute which is gratefully acknowledged. Laboratory assistance from K. Breyholtz is appreciated. The project has in part been financed from The Norwegian Research Council for Sciences and the Humanities.

References

Baag, C.-G. & Helsley, C. E., 1974. Evidence for penecontemporaneous magnetization of the Moenkopi Formation, *J. geophys. Res.*, **79**, 3308–3320.

Collinson, D. W., 1974. The role of pigment and specularite in the remanent magnetization of red sandstones, *Geophys. J. R. astr. Soc.*, **38**, 253–264.

Collinson, D. W., 1980. An investigation of the scattered remanent magnetization of the Dunnet Head sandstone, *Geophys. J. R. astr. Soc.*, **62**, 393–402.

Dunlop, D. J., 1972. Magnetic mineralogy of unheated and heated red sediments by coercivity spectrum analysis, *Geophys. J. R. astr. Soc.*, **27**, 37–55.

Friend, P. F., 1961. The Devonian stratigraphy of north and central Vestspitsbergen, *Proc. Yorks. geol. Soc.*, **28**, 77–118.

Friend, P. F. & Moody-Stuart, M., 1972. Sedimentation of the Wood Bay Formation (Devonian) of Spitsbergen: regional analysis of a late orogenic basin, *Norsk Polarinst., Skr. no. 157.*

Hamilton, N. & Rees, A. I., 1970. The use of magnetic fabric in paleocurrent estimation, in *Palaeogeophysics*, pp. 445–469, ed. Runcorn, S. K., Academic Press, London.

Harland, W. B. & Wright, N. J. R., 1979. Alternative hypothesis for the pre-Carboniferous evolution of Svalbard, *Norsk Polarinst., Skr. no. 167.*

Jelenska, M., Kruczyk, J. & Kadzialko-Hofmokl, M., 1979. Palaeomagnetic investigation of sedimentary and effusive rocks from Spitsbergen, Svalbard Archipelago, *Tech. Rep.*, The Institute of Geophysics of the Polish Academy of Sciences.

King, R. F., 1955. The remanent magnetism of artificially deposited sediments, *Mon. Not. R. astr. Soc. geophys. Suppl.*, **7**, 115–134.

Krasil'scikov, A. A., 1979. Stratigraphy and tectonics of the Precambrium of Svalbard, *Norsk Polarinst., Skr. No. 167*, 73–79.

Larson, E. E. & Walker, T. R., 1975. Development of chemical remanent magnetization during early stages of red bed formation in Late Cenozoic sediments, Baja California, *Bull. geol. Soc. Am.*, **86**, 639–650.

Løvlie, R. & Torsvik, T., 1984. Magnetic remanence and fabric properties of laboratory-deposited hematite bearing red sandstone, *Geophys. Res. Lett.*, **11**, 221–224.

Purucker, M. E., Elston, D. P. & Shoemaker, E. M., 1980. Early acquisition of characteristic magnetization in red beds of the Moenkopi Formation (Triassic), Grey Mountain, Arizona, *J. geophys. Res.*, **85**, 997–1012.

Roy, J. L. & Park, J. K., 1974. The magnetization process of certain red beds; vector analysis of chemical and thermal results, *Can. J. Earth Sci.*, **11**, 437–471.

Rusnak, G. A., 1957. Orientation of sand grains under conditions of unidirectional flow. 1. Theory and experiments, *J. Geol.*, **65**, 384–409.

Stacey, F. D., 1963. The physical theory of rock magnetism, *Adv. Phys.*, **12**, 45–113.

Stephenson, A., 1967. The effect of heat treatment on the magnetic properties of the old red sandstone, *Geophys. J. R. astr. Soc.*, **13**, 425–440.

Storetvedt, K. M., 1972. Old Red Sandstone palaeomagnetism of central Spitsbergen and the Upper Devonian (Svalbardian) phase of deformation, *Norsk Polarinst. Årb.*, pp. 59–69.

Tauxe, L. & Kent, D. V., 1984. Properties of a detrital remanence carried by hematite from study of modern river deposits and laboratory redeposition experiments, *Geophys. J. R. astr. Soc.*, **77**, 543–561.

Torsvik, T. & Løvlie, R., 1983. Formation of magnetic mineral(s) during laboratory heating of Devonian redbeds (Spitsbergen), palaeomagnetic implications, *IAGA Abstr.*

Van den Ende, C., 1977. Palaeomagnetism of Permian red beds of the Dome de Barrot-(S. France), *PhD thesis*, University of Utrecht.

Verosub, K. L., 1975. Palaeomagentic excursions as magneto-stratigraphic horizons. A cautionary note, *Science*, **190**, 48–50.

Walker, T. R., 1974. Formation of red beds in moisty tropical climates: a hypothesis, *Bull. geol. Soc. Am.*, **85**, 633–638.

Walker, T. R., Larson, E. E. & Hoblitt, R. P., 1981. Nature and origin of hematite in the Moenkopi formation (Triassic), Colorado plateau: a contribution to the origin of magnetism in red beds, *J. geophys. Res.*, **86**, 317–333.

Geophys. J. R. astr. Soc. (1984) 79, 589–612

Gaussian beam synthetic seismograms in a vertically varying medium

Raul Madariaga *UER Sciences Physiques de la Terre, Université Paris VII, and Laboratoire d'Etude Géophysique de Structures Profondes, associé au CNRS no. 195, Université Pierre et Marie Curie, Institut de Physique du Globe, 4, place Jussieu, 75230 Paris Cedex 05, France*

Received 1984 May 2; in original form 1984 January 25

Summary. We develop the Gaussian beam summation method for a medium in which velocity is only a function of depth. We show that in such a medium the kinematic and dynamic ray tracing equations, i.e. trajectories and amplitudes, may be solved in closed form for any initial wavefield specified at the source. The solution for an individual Gaussian beam is written in terms of the usual functions of ray theory: distance, travel time, intercept time and geometrical spreading. An important result of this analysis, confirmed by numerical experiments, is that one of the base functions selected by Červený, Popov & Pšenčík to solve the dynamic ray tracing equations should be modified to avoid causality problems. Finally, by means of a simple canonical transformation we rewrite all the equations in a geographical coordinate system independent of the particular ray trajectories. We then show that Gaussian beam summation is an analytical continuation to complex values of position and slowness of the WKB method proposed by Chapman. A simple computational method is developed in which it is not necessary to determine the coordinates of the observer in ray centred coordinates. This simplifies the computational effort so that Gaussian beam calculation becomes only slightly more expensive than WKB. With respect to the latter method Gaussian beam summation has the advantage that it is possible to control the amplitudes of the cut-off phases due to a finite range of slowness integration.

1 Introduction

Popov (1982), and Červený, Popov & Pšenčík (1982) have proposed, following a suggestion by Babic & Pankratova (1973), to calculate synthetic seismograms in general heterogeneous media by the summation of Gaussian beams. The technique would be applicable under the same general conditions of ray theory, i.e. short wavelengths compared to the scale of variation of the structure, but it would have the advantage that it would also work at caustics, shadows and other singularities of the ray field. The method contains two distinct parts.

In the first one, Gaussian beams are constructed around every single ray in a family of rays leaving the source in the direction of the recording stations. The method developed by Červený *et al.* (1982) to construct Gaussian beams was rather involved because it was obtained directly from the parabolic approximation to the wave equation. Simpler methods to construct Gaussian beams have been proposed by Keller & Streifer (1971), Deschamps (1971) and Felsen (1976) who obtained them by analytical continuation of the paraxial ray approximation to complex values of the slowness and source position. The second part of the method consists in the expansion of the source radiation into a family of Gaussian beams depending on the angle of radiation from the source. Červený *et al.* (1982) obtained this expansion by the matching of asymptotic expressions for the Gaussian beam to the classical far field radiation in a uniform medium. Gaussian beams, as defined by Červený *et al.* (1982), contain an arbitrary complex parameter whose effect on the computed seismograms was not very clear. The use of this complex parameter produces a distortion of the synthetic seismograms which must be carefully controlled.

Several examples of computation of wavefields by Gaussian beam summation have been presented by Červený *et al.* (1982) and Červený (1983). Nowack & Aki (1984) and Cormier & Spudich (1984) studied a number of geophysically interesting problems where Gaussian beam summation proved to be very useful.

In this paper we will study the Gaussian beam summation method in a medium where the velocity changes only in the vertical direction. A 2-D acoustical line source will be assumed. This simple model was chosen because it may be solved entirely in terms of standard results of ray theory. The role of the complex parameter of Gaussian beams may then be analysed analytically and numerically. We show by an exact solution of the dynamic ray tracing equations that one of the two independent solutions used by Červený *et al.* (1982) should be modified so that the asymptotic expansion of the wavefield be uniformly valid near caustics and shadows. The new solution corresponds to the vertical wave function used in Chapman's (1978) WKBJ seismograms. We show next that there is a canonical transformation that permits us to write Gaussian beams in geographical coordinates instead of ray centred ones. Similar coordinate transformations were discussed by Červený & Pšenčík (1984). The application of boundary conditions and the description of head waves should be greatly facilitated in this new representation. It does also simplify the numerical calculations since it is no longer necessary to calculate the normal distance from the station to the central ray. In geographical coordinates the Gaussian beam sum may be rewritten in a form that may be easily compared with WKBJ seismograms. When the complex parameter in the Gaussian beam expansion tends to zero (infinity in Červený *et al.*'s 1982 definition), it reduces to Chapman's WKBJ seismogram theory. Gaussian beam summation is simply an analytical continuation of the latter method for a particular choice of the complex horizontal slowness (ray parameter).

Although the presentation of the results would have been simpler if we had used the methods of Hamiltonian mechanics (Cisternas, private communication), we have preferred to develop our results following as closely as possible the theory as presented by Červený (1981), Popov (1982), Červený *et al.* (1982), Červený (1983) and Červený & Hron (1980). Hamilton's theory should allow us to simplify the extension of our results to general laterally heterogeneous media and will be further developed elsewhere.

2 Kinematic and dynamic ray tracing

The construction of Gaussian beams requires the calculation of a set of central rays for a given source. In this paper we study a line source at ($x = 0$, $z = 0$) so that the set of central

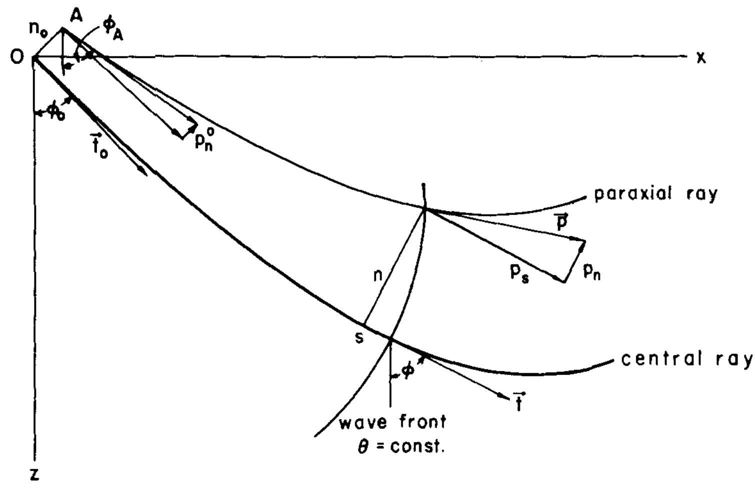

Figure 1. Geometry of paraxial ray coordinates (s, n, p_n) in the vicinity of a central ray of take-off angle ϕ_0. Dynamic or paraxial ray tracing consists in calculating $n(s)$, $P_n(s)$ along the central ray.

rays is obtained by the classical method of ray tracing in vertically heterogeneous media (Bullen 1961). Considering Fig. 1, let $p = \sin\phi/v$ be the ray parameter, then the position of the ray as a function of depth z is given by:

$$X(p, z) = \int_0^z \tan\phi \, dz \tag{1}$$

the travel time by:

$$T(p, z) = \int_0^z \frac{\sec\phi}{v} dz \tag{2}$$

and the intercept time by:

$$\tau(p, z) = T - pX = \int_0^z \frac{\cos\phi}{v} dz. \tag{3}$$

As is well known, these formulae may be continued without difficulty beyond the turning point $\cos\phi = 0$, where ϕ is the incidence angle between the ray and the vertical at any point along the ray. Initial values at $x = 0, z = 0$ are ϕ_0, $p = \sin\phi_0/v_0$.

Once kinematic ray tracing has been performed by any of the standard procedures (see Buland & Chapman 1983 for a recent review) it is necessary to do the dynamic ray tracing along each of the rays. Dynamic ray tracing consists in tracing a ray in the vicinity of a central one for a small initial perturbation of position and slowness (Červený & Pšenčík 1979). This procedure is usually known as paraxial ray tracing in other fields (Deschamps 1972). Červený & Pšenčík (1979) and Červený & Hron (1980) derived the equations for a paraxial ray in terms of ray centred coordinates (s, n) where n is the distance away from the central ray (see Fig. 1). The coordinate system (s, n) is orthogonal. Its scale factor for vertically varying media is:

$$h = 1 + pv_{,z}n \tag{4}$$

where p is the ray parameter and $v_{,z}$ is the local velocity gradient. h appears in the definition of local distance:

$$dr^2 = h^2 \, ds^2 + dn^2. \tag{5}$$

In order to write the dynamic ray tracing equations they introduced the slowness p_n which, in analytical mechanics terms, is the momentum conjugate to the position n. Then the total slowness vector in the vicinity of the central ray is (Červený 1981)

$$\mathbf{p} = p_s \mathbf{t} + p_n \mathbf{n} \tag{6}$$

where

$$p_s = (1 - p v_{,z} n)/v \tag{7}$$

is the slowness component along the tangent $\mathbf{t}$ to the central ray (see Fig. 1). Since on the central ray $p_n = 0$, then to first order in n p_n has to be of the form:

$$p_n = M(s) n \tag{8}$$

where $M(s)$ is related to the curvature of the wavefront at s. We may now obtain the travel time $\theta(s, n)$ in the vicinity of s from the standard definition:

$$\theta(s, n) = \theta(s, 0) + \int_0^n p_n(n)\, dn$$

writing $\theta(s, 0) = T(s)$, the travel time along the central ray, we find:

$$\theta(s, n) = T(s) + 1/2\, M(s) n^2. \tag{9}$$

Let us remark that slowness is expanded to first order while travel time is calculated to second order in n. As we will show, once $M(s)$ is known, all the rays in the vicinity of the central ray may be computed and if a particular ray may be traced then all others may be obtained by simple scaling.

As shown by Červený & Pšenčík (1979), the dynamic ray-tracing equations for a general 2-D medium are:

$$\frac{dn}{ds} = v p_n, \qquad \frac{dp_n}{ds} = -\frac{v_{,nn}}{v^2} n \tag{10}$$

where $v_{,nn}$ is the second derivative of the velocity with respect to n, calculated on the central ray. The system (10) is Hamilton's equations for the paraxial ray. An equation for $M(s)$ may be obtained by inserting (8) into the second of equations (10), but this is not the best way to find $M(s)$ since it yields a non-linear Ricatti equation. It is better to solve the system (10) for $n(s)$ and $p_n(s)$ and then to calculate $M(s)$ from (8).

Let us rewrite equation (10) for the vertically heterogeneous medium using:

$$d/ds = \cos\phi\, d/dz$$

$$d/dn = \sin\phi\, d/dz.$$

We find:

$$\frac{dn}{dz} = \frac{v}{\cos\phi} p_n, \qquad \frac{dp_n}{dz} = -\frac{p^2 v_{,zz}}{\cos\phi} n. \tag{11}$$

These equations have to be solved for a given set of initial conditions n_0, $p_n^0 = M(0)\, n_0$, where n_0 is the initial displacement of the paraxial ray in the direction of the normal and p_n^0 is the initial value of the normal slowness of the paraxial ray with respect to the central one. The solution of (11) for arbitrary initial conditions may be obtained from two sets of independent solutions of (11). Let (Q_1, P_1) and (Q_2, P_2) be these two sets of base functions. They satisfy:

$$\frac{dQ}{dz} = \frac{v}{\cos\phi} P, \qquad \frac{dP}{dz} = -\frac{p^2 v_{,zz}}{\cos\phi} Q. \tag{12}$$

The initial values for these two independent solutions may be arbitrary, but it is preferable to choose them in such a way that the two sets of base functions have a clear physical meaning. Once they have been found a general solution may be generated by:

$$\begin{aligned} n(s) &= A Q_1 + B Q_2 \\ p_n(s) &= A P_1 + B P_2 \end{aligned} \tag{13}$$

where A and B are two parameters to be determined from the initial conditions n_0 and p_n^0. Then $M(s) = p_n/n$ depends only on the ratio B/A.

We define a beam as a family of paraxial rays that share a common value of B/A and are centred around a central ray of parameter p. Once a paraxial ray $n_1(s)$ of initial conditions n_0, p_n^0 has been traced, the position $n_2(s)$ of any other paraxial ray in the beam may be found by simple scaling:

$$n_1(s)/n_2(s) = n_1(0)/n_2(0).$$

An important property of a beam is that geometrical spreading is common to all the paraxial rays. In fact, if we write:

$$\begin{aligned} Q(s) &= Q_1(s) + B/A\, Q_2(s) \\ P(s) &= P_1(s) + B/A\, P_2(s) \end{aligned}$$

then

$$n(s) = Q(s)/Q(0)\, n_0 \tag{14}$$

and a similar equation for $p_n(s)$. Solution (14) gives the relative position of a paraxial ray of initial normal distance n_0 to the central ray, in terms of the single function $Q(s)$. It may also be used to find n_0 when the final point of the ray $n(s)$ is given. We may then compute the paraxial ray belonging to a given beam that passes through a specified point in the vicinity of the central ray. Finally, 2-D geometrical spreading is defined by:

$$J = [n(s)/n(0)]^{1/2} = [Q(s)/Q(0)]^{1/2} \tag{15}$$

as shown by Červený & Pšenčík (1979). Thus, geometrical spreading depends only on the ratio B/A, just like the function $M(s)$. We may now write the asymptotic wave functions along the paraxial ray $n(s)$:

$$u(s, \phi_0, n) = \Phi(\phi_0) \left[\frac{Q(0)\, v(s)}{Q(s)\, v(0)}\right]^{1/2} \exp\left[i\omega\theta(s, \phi_0, n)\right] \tag{16}$$

where θ is the time delay function defined in (9). The factor $\Phi(\phi_0)$ is the excitation function of the paraxial rays near the central ray of take-off angle ϕ_0. As shown by (16) the wavefield in the vicinity of this ray is written in terms of $P(s)$ and $Q(s)$ so that it depends also on the ratio B/A.

We have defined a beam as the set of paraxial rays associated with a central ray of parameter $p = \sin\phi_0/v_0$, the form of the beam being controlled by the ratio B/A. Individual rays within the beam depend only on the normal distance $n(s)$. A Gaussian beam is an analytical continuation of a real beam to complex values of the ratio B/A. In order that the Gaussian beam be evanescent in the direction away from the ray, B/A has to be chosen such that $\operatorname{Im} M(s) < 0$ for all s. With this complex choice of B/A, (16) describes a Gaussian beam centred around the real ray of parameter p and complex curvature:

$$K(s) = M(s)/v(s). \tag{17}$$

3 Solution of the dynamic ray tracing equations

For general laterally heterogeneous media Červený *et al.* (1982) proposed to solve (12) numerically along the central ray for two particular sets of initial conditions $Q_1(0) = 1$, $P_1(0) = 0$ and $Q_2(0) = 0$, $P_2(0) = 1/v_0$. In vertically heterogeneous media the dynamic ray tracing equations may be solved in terms of quadratures. In order to do this we replace the first of equations (12) into the second to obtain:

$$\frac{d}{dz}\left(\frac{\cos\phi}{v}\frac{dQ}{dz}\right) = -\frac{v_{,zz}\,p^2}{\cos\phi}\,Q \tag{18}$$

which is a second-order Sturm–Liouville equation for Q. Equations of this type may be solved in terms of series expansions, but in the present case we can find a particular solution by inspection:

$$Q_a = \cos\phi \tag{19}$$

which may be easily verified by inserting it in (18) and using:

$$\frac{d\phi}{dz} = \frac{pv_{,z}}{\cos\phi}. \tag{20}$$

The other independent solution may now be found by a variation of the parameters; choosing $Q_b = \cos\phi\, f(z)$ one finds from (18)

$$\frac{df}{dz} = \frac{v}{\cos^3\phi}$$

and, after integration:

$$Q_b = \cos\phi \int_0^z \frac{v}{\cos^3\phi}\,dz \tag{21}$$

which considering equation (1), may be rewritten in the form:

$$Q_b = \cos\phi\, X'(p, z) \tag{22}$$

where

$$X'(p, z) = dX(p, z)/dp.$$

Q_b is the standard geometrical spreading function of ray theory for a point source (Chapman 1978; Červený & Pšenčík 1979).

We may write the general solution of (18) in the form:

$$Q(s) = A\cos\phi + B\cos\phi\, X'(p, z). \tag{23}$$

Reinserting this expression into the first of equations (12) we find:

$$P(s) = -A\,p^2 v_{,z} + B\,\frac{(1 - p^2 v_{,z} \cos\phi\, X')}{\cos\phi} \tag{24}$$

where we have used $dX'/dz = v/\cos^3\phi$.

Equations (23) and (24) yield a general solution to the system (12). We may now calculate:

$$M(s) = -\frac{p^2 v_{,z}}{\cos\phi} + \frac{B}{\cos^2\phi\,(A + B\,X')} \tag{25}$$

which shows that $M(s)$ contains a term that is independent of the choice of B/A. We could replace (23) and (25) into the Gaussian beam wavefield equation (16) and proceed to the next step which is the superposition of beams. It is preferable, however, to renormalize the solutions Q_1, P_1 and P_2, Q_2 so as to compare them to those chosen by Červený *et al.* (1982) and to the solutions used in the WKB method (Chapman 1978). A clear physical interpretation of each of these solutions will be given at the same time.

The WKB solution. For this solution, which we shall call Q_1, P_1 in the following, we choose $A = (\cos\phi_0)^{-1}$ and $B = 0$, where ϕ_0 is the take-off angle at the source. Then:

$$Q_1(s) = \cos\phi/\cos\phi_0$$

$$P_1(s) = -p^2 v_{,z}/\cos\phi_0 \tag{26}$$

writing $\cos\phi$ in terms of p, i.e.

$$\cos\phi = (1 - v^2 p^2)^{-1/2}$$

it may be easily verified that Q_1 is the square of the geometrical spreading appearing in the vertical WKB wave functions of Chapman (1978). The initial conditions satisfied by (26) are

$$Q_1 = 1, \qquad P_1 = -p^2 v_{,z}(0)/\cos\phi_0. \tag{27}$$

These initial conditions are different from those of Červený *et al.* (1982) who imposed $P_1(0) = 0$ for their first (initially plane) solution. The (Q_1, P_1) solution is described in Fig. 2(a), Q_1 is the normal coordinate of a paraxial ray of the same parameter p as the central ray but displaced at the source by a distance l along the normal to the ray. As shown in Fig. 2(a), (Q_1, P_1) are the base functions for a beam in which all the paraxial rays have the same ray parameter p. This wavefield appears in the standard plane wave decomposition of a general wavefield by Fourier transforms (Chapman 1978). This point will be clearer when we convert from ray coordinates to geographical ones. The initial value for P_1 may now be easily interpreted. The paraxial ray leaves the point A in Fig. 1 at the distance $Q_1 = 1$ from the central ray. Since both the central and the paraxial rays have ray parameter $p = \sin\phi_0/v_0$, the vertical coordinate of the point A is $z_A = -\sin\phi_0$ and the take-off angle of the paraxial ray at A is:

$$\phi_A = \phi_0 - d\phi/dz\,\sin\phi_0$$

using (20) for $d\phi/dz$ and equation (6) for **p** we find

$$p_n(z_A) = |\,\mathbf{p}\,|\,\sin(\phi_A - \phi_0)$$

so that:

$$P_1(0) = p_n(z_A) \approx -\frac{p^2 v_{,z}}{\cos\phi_0} \tag{28}$$

which is precisely the initial value (27) of P_1.

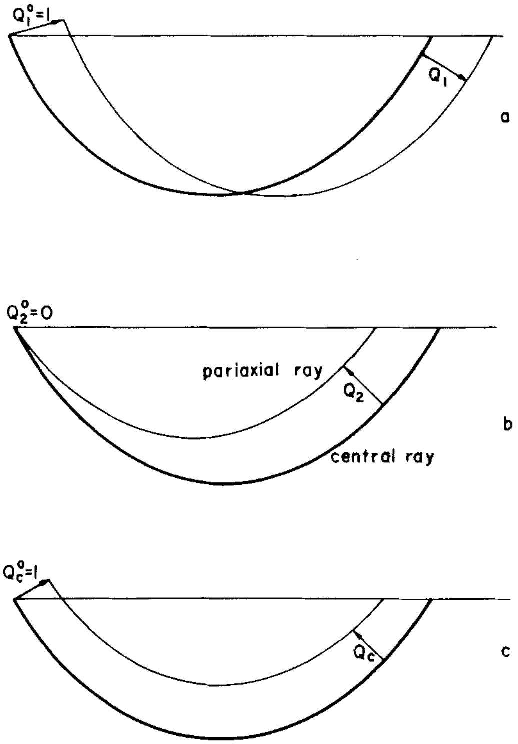

Figure 2. The base functions for the solution of paraxial ray tracing for arbitrary initial conditions. (a) WKB wavefunction or constant ray parameter beam in which the paraxial ray has the same ray parameter as the central ray. (b) The point source beam in which all rays diverge from the origin, this is the standard geometrical spreading function. (c) Červený *et al.* (1982) solution.

The beam defined by (Q_1, P_1) has a p-caustic (Chapman & Drummond 1983) at the bottoming depth for rays of ray parameter p, i.e. at z_B defined by $v(z_B) = p^{-1}$. At that depth $\cos\phi_B = 0$ and $Q_1(z_B) = 0$, so that the beam reduces to a point on the central ray. This caustic is at depth and it will not interfere with the calculation of wavefields at the surface, provided that ϕ is smoothly continued beyond $\pi/2$ so that on the upward moving part of the ray $\pi/2 < \phi < \pi$.

Červený et al. *(1978) solution.* They imposed $Q_1 = 1$, $P_1 = 0$ to their initial plane wave solution. To obtain this we put $A = 1/\cos\phi_0$, $B = p^2 v_{,z}^0$ and obtain:

$$Q_c(s) = \cos\phi(1/\cos\phi_0 + p^2 v_{,z}^0\, X')$$
$$P_c(s) = \frac{p^2 v_{,z}^0}{\cos\phi}\,(1 - p^2 v_{,z}\cos\phi\, X') - \frac{p^2 v_{,z}}{\cos\phi_0}. \tag{29}$$

This solution is more complicated than (26) but it has a simple physical interpretation as shown in Fig. 2(b). The angle ϕ_A has been forced to be equal to ϕ_0 so that $P_c(0) = 0$. Now the paraxial ray has a different ray parameter from the central beam and for a positive velocity gradient $v_{,z}^0$ the beam diverges at the origin. In general this beam has no caustic at depth so that Q_c does not change sign for the upward moving part of the ray trajectory.

Point source solution. The last solution presents no problem, we choose Červený *et al.*'s (1982) initial conditions $Q_2 = 0$, $P_2 = 1/v_0$. These are obtained for $A = 0$, $B = \cos\phi_0/v_0$

in (23) so that the solution is:

$$Q_2(s) = v_0^{-1} \cos\phi_0 \cos\phi \, X'$$

$$P_2(s) = \frac{\cos\phi_0}{v_0 \cos\phi}(1 - p^2 v_{,z} \cos\phi \, X'). \tag{30}$$

This solution describes a beam which diverges from the point source at (0, 0). The base function Q_2 is the square of the geometrical spreading function for a point source in a vertically heterogeneous medium (Červený & Pšenčík 1979). This solution is also depicted in Fig. 2(c). Using Q_2 and $M_2 = P_2/Q_2$ in the beam equation (16) we obtain the paraxial approximation for the radiation by a point source in a vertically heterogeneous medium.

Gaussian beam solution. We may now write a Gaussian beam solution of the paraxial or dynamic ray tracing equations. Such a solution may be written in general:

$$Q(s) = Q_1(s) + \delta Q_2(s)$$

$$P(s) = P_1(s) + \delta P_2(s) \tag{31}$$

where $\delta = A/B$ is the beam parameter. For real δ (31) represents the spreading of a beam that is intermediate between a WKB and a point source one. Gaussian beams are obtained for complex δ under the restriction $\mathrm{Im}\,\delta > 0$ so that the beam will be evanescent off the central ray. In the following we will only study imaginary δ and this will be considered as a small parameter. This definition is quite different from that of Červený who used Q_c instead of the WKB solution in (31) and used the imaginary coefficient $\epsilon = 1/\delta$. In their case ϵ had to be large and negative imaginary. Our choice of base functions and δ is deliberate, we consider Gaussian beams as a complex perturbation of WKB wave functions with a small Gaussian decay in the transverse direction to the central ray. This choice has a substantial effect upon the quality of the synthetics generated by Gaussian beam summation.

4 Gaussian beams in geographical coordinates

The previous analysis has strictly followed Červený *et al.*'s (1982) development of Gaussian beams, and we could proceed now to superpose them in order to simulate the radiation from a point source. However, in order to calculate the field of a Gaussian beam according to equation (16), we would have to calculate the position of the observation point in ray centred (s, n) coordinates. This has to be done for every central ray in the sum. The solution of this problem is more difficult than the solution of the dynamic ray tracing equations themselves and may only be performed numerically. The Gaussian beam method would be at a neat disadvantage when compared to Chapman's (1978) WKB method, in which the only elements which are needed are the ray functions, $X(p, z)$ and $T(p, z)$ defined in (1) and (3).

The calculations will be significantly simplified by a local rotation of the ray coordinates into geographical (x, z) coordinates. This rotation may be easily performed using the technique of canonical transformations of analytical mechanics. This transformation is not only convenient for computational purposes, it simplifies the application of boundary conditions and permits the proper calculation of interface waves, diffractions etc. . . . Most of all, it will show that Gaussian beams in vertically heterogeneous media are a simple analytical continuation of WKB seismograms.

Referring to Fig. 3, we rotate the ray centred coordinate system (s, n) $(s, Q$ for the base functions) into the local system (z, ξ). For this purpose we introduce the following canonical transformation.

$$n = \xi \cos\phi$$

$$p_n = -p^2 v_{,z} \xi + p_\xi / \cos\phi. \tag{32}$$

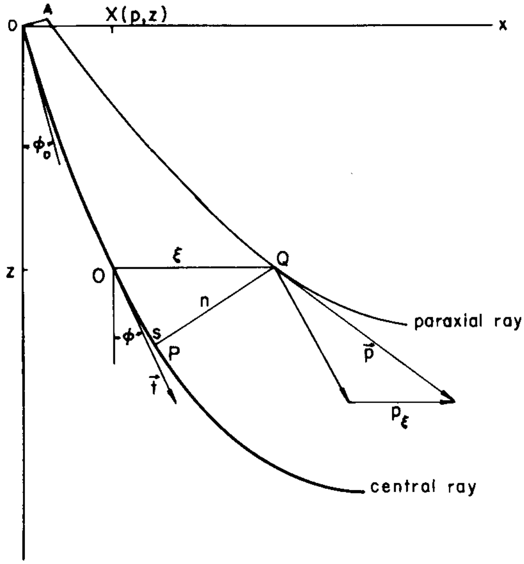

Figure 3. Geometry of the canonical transformation (32) in which the ray centred conjugate coordinates are rotated into geographical ones (ξ, p_ξ).

p_ξ is the slowness variable conjugate to ξ. It represents (see Fig. 3), the difference in ray parameter between the paraxial ray passing through Q and the central ray, i.e.

$$pQ = p + p_\xi. \tag{33}$$

Inserting (32) into the dynamic ray tracing equations (12) we find the following system in geographical coordinates:

$$\frac{d\xi}{dz} = \frac{v}{\cos^3\phi}\, p_\xi, \qquad \frac{dp_\xi}{dz} = 0. \tag{34}$$

These equations are much simpler than those in ray centred coordinates. Their general solution may be written in the form:

$$\xi = A + B\,X'(p, z)$$
$$p_\xi = B \tag{35}$$

where $X'(p, z)$ is defined in equation (22), and A and B are the same constants used in (23). The result p_ξ = constant is simple to interpret, along any ray in a vertical medium the horizontal slowness is conserved so that a paraxial ray conserves its difference in ray parameter with respect to the central ray.

We may now rewrite the solution for the base functions in these new coordinates:

WKB solution. In this case, from (26) we obtain:

$$\xi^1 = 1/\cos\phi_0$$
$$p_\xi^1 = 0. \tag{36}$$

Thus in this solution the paraxial ray has the same ray parameter as the central one and it is displaced laterally by a constant amount ξ^1. This is precisely the geometry shown in Fig. 2(a).

Červený et al. *(1982) solution.* Following equations (29) we find:

$$\xi^c = \cos^{-1}\phi_0 + p^2 v^0_{,z} X' \qquad p^c_\xi = p^2 v^0_{,z}. \tag{37}$$

This shows again that this solution is different from the WKB one when the initial gradient $v^0_{,z}$ is not zero. In a uniform medium where $v_{,z} = 0$, they coincide so that the problems associated with this choice of base functions do not appear in the models studied by Červený *et al.* (1982) and Červený (1983).

Point source solution. Following (30) we find:

$$\xi^2 = \cos\phi_0 v_0^{-1} X' \qquad p^2_\xi = \cos\phi_0 v_0^{-1}. \tag{38}$$

Let us note in passing that p^2_ξ is the derivative $dp/d\phi$ of the ray parameter.

Gaussian beam solution. From equation (31), we find:

$$Q(z) = \frac{\cos\phi}{v_0 \cos\phi_0}(v_0 + \delta\cos^2\phi_0 X') \tag{39}$$

a similar expression for $P(z)$ which we shall not use, and from (25):

$$M(z) = -\frac{p^2 v_{,z}}{\cos\phi} + \frac{\delta}{v_0 + \delta\cos^2\phi_0 X'}\,\frac{\cos^2\phi_0}{\cos^2\phi}. \tag{40}$$

We may now rewrite the equation for a beam (16) in the form:

$$u(z, \phi_0, \xi) = \Phi(\phi_0)\left[\frac{v(z)}{Q(z)\, v_0}\right]^{1/2} \exp\,[i\omega\theta(z, \phi_0, \xi)] \tag{41}$$

where we used $Q(0) = 1$, and since $n = \xi\cos\phi$

$$\theta(z, \phi_0, \xi) = T(s) - 1/2\, p^2 v_{,z} \cos\phi\, \xi^2 + 1/2\, N(z)\, \xi^2 \tag{42}$$

with

$$N(z) = \frac{p_\xi}{\xi} = \frac{\delta\cos^2\phi_0}{v_0 + \delta\cos^2\phi_0 X'}. \tag{43}$$

The function θ is the eikonal or travel-time along the paraxial ray to $(z, \xi) = (s, n)$. Following Fig. 3 we may now recalculate $T(s)$, the travel-time along the central ray to point P, in terms of travel-time $T(z, p)$ to 0. To second order this may be calculated as follows:

$$T(s) = T(z, p) + \int_{s_0}^{s_p} \frac{ds}{v(s)}.$$

Using a first-order development for the velocity Červený & Pšenčík (1984) showed that:

$$T(s) = T(z, p) + p\xi - 1/2\, p^2 v_{,z} \cos\phi\, \xi^2$$

so that (42) simplifies to:

$$\theta(z, \phi_0, \xi) = T(z, p) + p\,\xi + 1/2\, N(z)\, \xi^2 \tag{44}$$

which using $\xi = x - X(z, p)$ may be also written in the form:

$$\theta(z, \phi_0, \xi) = \tau(z, p) + px + 1/2\, N(z)\, \xi^2 \tag{45}$$

where τ is the intercept time (3). The time delay function $\theta(z, \phi_0, \xi)$ is the travel-time of beam centred around the ray of take-off angle ϕ_0 to the observer at (z, x). For imaginary $\delta > 0$, i.e. for Gaussian beams, $N(z)$ defined by (43) becomes complex and so does the time delay θ. This produces a Gaussian decay of the amplitudes away from the central ray.

Finally we consider the problem of boundary conditions. The propagation of a Gaussian beam across a boundary has been studied by Červený (1981) and by Popov (1982). Their method consisted in making a coordinate rotation to write the wavefront along the interface in terms of local geographical coordinates. This change of variables is entirely equivalent to ours. Since in vertically heterogeneous media all the interfaces are parallel to the (x, y) plane, geographical coordinates are the *natural* way of treating interfaces.

The boundary conditions are:

$$\xi \text{ and } p_\xi \text{ continuous at the boundary.} \tag{46}$$

If there is a first-order discontinuity we multiply the amplitude Φ by the appropriate transmission or reflection coefficient. The boundary conditions of Červený (1981) in terms of ray centred coordinates may be obtained returning in (46) from geographical to ray centred coordinates.

5 Gaussian beam summation

We may now represent the radiation from a point source in terms of Gaussian beams. The main problem for doing this is to determine the excitation coefficient for each beam. Červený *et al.* (1982) determined Φ by matching an asymptotic expansion of the Gaussian beam sum in a homogeneous medium to the far field radiation of a point source. Here we will adopt their expansion and we will verify later that it is closely related with the excitation function for plane waves in the WKB method.

The Fourier transformed expansion of a line source into Gaussian beams is, according to Červený *et al.* (1982):

$$u(\mathbf{r}, \omega) = \frac{i}{4\pi} \int \left[\frac{v(s)}{v(0)\, Q(s)}\right]^{1/2} \exp\left[i\omega\theta(s, \phi_0, n)\right]\, d\phi_0 \tag{47}$$

where $\theta(s, \phi_0, n)$ is in (9) and $Q(s)$ in (31).

In order to calculate (47) the integral is replaced by a sum over discrete values of the take-off angle ϕ_0. Each of the components of the sum constitutes a Gaussian beam calculated at the observation point $\mathbf{r}$. There is a major difficulty in using (47), the coordinates (s, n) of the observation point with respect to *every* ray in the expansion have to be calculated. This poses a severe computer problem because, as seen in Fig. 4, every ray has to be traced explicitly in order to calculate (s, n). The geographical coordinates introduced in the previous section eliminate the need to do this ray tracing, because both Q and θ may now be calculated in terms of the coordinates of the point where the ray breaks through the surface. From (47) we find:

$$u(\mathbf{r}, \omega) = \frac{i}{4\pi} \int \left[\frac{v(z)}{v(0)\, Q(z)}\right]^{1/2} \exp\left[i\omega\theta(z, \phi_0, \xi)\right]\, d\phi_0 \tag{48}$$

where, to first-order in ξ, we have replaced $Q(s)$ by $Q(z)$ given by (39), and θ is defined in (45). Both $Q(z)$ and $\theta(z, \phi_0, \xi)$ depend on the depth z of the observation point. This has

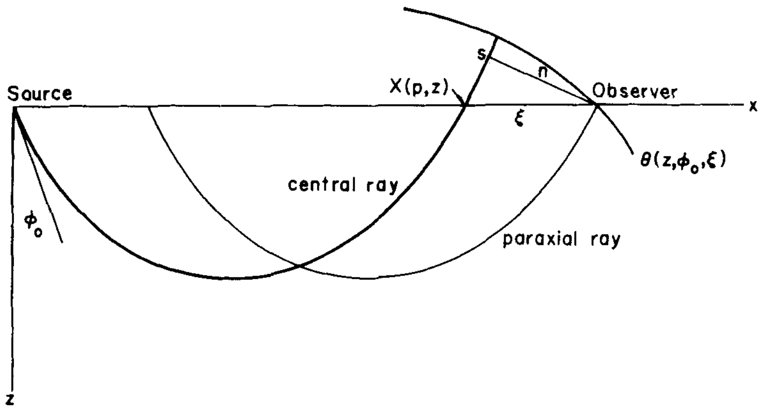

Figure 4. Computation of the contribution at a given observation point of the Gaussian beam centred around the ray ϕ_0. The formulation by Červený *et al.* (1982) requires the calculation of (s, n) while the geographical formulation proposed here requires $[X(p, z), \xi]$.

the advantage that when calculating synthetics at several points at the same depth (usually the free surface), only x and ξ change. There is *no need* to calculate the coordinates (s, n) of the stations with respect to the central rays any more so that the computational effort is greatly reduced.

We may now rewrite (48) as a slowness integral, changing variables to $p = \sin \phi_0 / v_0$:

$$u(\mathbf{r}, \omega) = \frac{i}{4\pi} \int_{-\infty}^{\infty} \left[\frac{v(z)}{v(0)\, Q(z)}\right]^{1/2} \exp\, [i\omega\theta(z, p, \xi)]\, \frac{dp}{q(0)} \tag{49}$$

where:

$$q(z) = v(z)^{-1} \cos \phi = [v(z)^{-2} - p^2]^{1/2}$$

$$Q(z) = \frac{v(z)\, q(z)}{v(0)\, q(0)}\, [1 + \delta\, v(0)\, q^2(0)\, X'(p, z)]$$

and in (45) $N(z)$ should be replaced by

$$N(z) = \frac{\delta\, v(0)\, q^2(0)}{1 + \delta\, v(0)\, q^2(0)\, X'(p, z)}.$$

This is our final expression for the Gaussian beam expansion of the Fourier transformed Green function for a line source in a vertically heterogeneous medium.

We may now find the limit of (49) when $\delta \to 0$:

$$u(\mathbf{r}, \omega) = \frac{i}{4\pi} \int_{-\infty}^{\infty} \frac{dp}{[q(0)\, q(z)]^{1/2}} \exp\, [i\omega(\tau + px)] \tag{50}$$

which is Weyl's expansion of a line source radiation into plane waves (Aki & Richards 1980, p. 194). In (49) and (50) we take as the limits of integration $(-\infty, \infty)$ in order to include inhomogeneous waves radiated by the line source. Equation (50) is the starting point for the WKB method proposed by Chapman (1978).

We may consider that the slowness integral (50) has been filtered in (49) by an anti-alias function of the Gabor (1946) type:

$$\text{filter} = \exp\, [i\, 1/2\, \omega\, N(z)\, \xi^2)]. \tag{51}$$

Filtering the slowness integral (50) had already been proposed by Wenzel, Stoffa & Buhl (1982), but their filter was much more complicated than the Gaussian beam one, and it was not derived from complex solutions of the eikonal equation.

The role of the parameter δ may be clarified if we consider the expression (49) on the source plane ($z = 0$). In this case $X'(p, 0) = 0$ and

$$u(x, 0, \omega) = \frac{i}{4\pi} \int_{-\infty}^{\infty} \frac{dp}{q(0)} \exp [\![i\omega[px + 1/2\, \delta\, v(0)\, q^2(0)\, x^2]]\!]. \tag{52}$$

When $\delta = 0$, this expression reduces to the plane wave expansion of the field of a line source in a homogeneous medium. In that case it is exactly the slowness transform of the Green function

$$u(x, 0, \omega) = \frac{i}{4} H_0^{(1)}(\omega \mid x \mid / v_0).$$

The exponential factor containing δ modifies this expansion distorting the plane waves, for positive imaginary δ they have a Gaussian decay away from $x = 0$. It is clear now that δ has to be small if we want (52) to represent approximately $H_0^{(1)}$.

We may also see what is the effect of using Červený *et al.*'s (1982) base function Q_c (ξ_c in geographical coordinates) instead of Q_1 (WKB). It is easy to see that this is equivalent to taking:

$$\delta = \frac{p^2 v_{,z} v_0}{\cos \phi_0} + (-i\epsilon)^{-1} \tag{53}$$

where ϵ is their parameter associated with the beam width. The real part of (53) produces a mismatch of the phases in (52) which is responsible for the non-causal behaviour observed in the synthetics calculated with their scheme.

We will be interested in computing the Gaussian beam sum in the time domain. As in the WKB technique we calculate the time domain transform before the slowness integral. As shown by Červený (1983), following Chapman (1978), we obtain from (48):

$$u(\mathbf{r}, t) = \frac{1}{4\pi} \int \frac{1}{\pi} \operatorname{Im} \left\{ \frac{i}{(t - \theta)} \left[\frac{v(z)}{v(0)\, Q(z)} \right]^{1/2} \right\} d\phi_0 \tag{54}$$

where θ is given by (44) or (45). For $\delta = 0$

$$\pi^{-1} \operatorname{Im} [(t - \theta)^{-1}] \rightarrow \delta(t - \theta)$$

and (54) reduces to Chapman's (1978) expressions for the WKB method. Calculating seismograms by straightforward discretization of (54) is not very practical because of the pole at $t = \theta$. It should be possible to regularize (54) by changing variables from ϕ_0 to t as proposed by Dey-Sarkar & Chapman (1978), but we prefer to use a source time function $s(t)$ of finite duration so that we actually calculate

$$U(\mathbf{r}, t) = s(t)_* u(\mathbf{r}, t) = \frac{1}{4\pi^2} \int s(t)_* \operatorname{Im} \left\{ \frac{i}{t - \theta} \left[\frac{v(z)}{v(0)\, Q(z)} \right]^{1/2} \right\} d\phi_0 \tag{55}$$

in our synthetics we have used Gabor's (1946) wavelets

$$s(t) = \exp [-(\omega_0 t/\gamma)^2] \cos \omega_0 t \tag{56}$$

as proposed by Červený (1983) because the convolution in (55) may be calculated by a simple approximation.

6 The constant gradient medium

We study, as a first example of the numerical method, a medium in which the velocity–depth law is given by $v(z) = v_0(1 + v_1 z)$. Rays in this medium are circular and all the relevant equations may be solved exactly (see, e.g. Ben-Menahem & Singh 1981, p. 510). In this case ray theory works without any problems and we could easily calculate synthetic seismograms by means of the ray theoretical approximation:

$$u(\mathbf{r}, t) = \frac{1}{2\pi}\left[\frac{v(z)}{2Q_2(z)}\right]^{1/2} [t - T(z, p)]^{-1/2} \tag{57}$$

where Q_2 is given by (30). Here $T(z, p)$ is the travel time along the ray passing through the observer and is given by (2).

We have calculated synthetic seismograms by converting (48) into a sum over equally spaced rays covering an angular sector $\phi_{max} - \phi_{min}$. This sector is determined in such a way that the exit points of the rays at the surface cover a distance much larger than that over which the observers are spread. For each of the rays we calculate p, $X(p, z)$, $T(p, z)$ and $X'(p, z)$ at their point of emergence. The ray trajectories are shown in Fig. 5 for the case $v_0 = 5\ \mathrm{km\ s^{-1}}$, $v_1 = 0.04\ \mathrm{km^{-1}}$.

Using a Gabor source function (56) with $\omega_0 = 2\pi f_0$, $f_0 = 4$ Hz and $\gamma = 3$ we calculate the contribution of each Gaussian beam to the integral (55). In Fig. 6 we show an example of the individual beam contributions to the synthetic calculated at $x = 70$ km. It may be observed that the Gabor wavelets are centred around the time Re $[\theta(z, \phi_0, \xi)]$ given by (45). We used to generate these rays a parameter $\delta = i \cdot 10^{-4}$, so that $\theta(z, \phi_0, \xi)$ differs little from the WKB time delay $\theta = \tau + px$. The effect of δ is clearly seen in Fig. 6. Near the minimum time $\theta_G = 11.4$ s, obtained for the geometrical optics angle $\phi_G = 36.13°$, the amplitude of the wavelets is maximum. When ϕ_0 is different from ϕ_G the amplitude of the wavelets diminishes and the pulses get broader. This is the main effect of using a complex time delay θ. Another important remark is that in this case, in which we perturb the WKB base function to obtain $Q(z)$ and $N(z)$, the arrival time Re θ increases when the angle ϕ_0 differs from the geometrical arrival ϕ_G. A similar behaviour is observed for the WKB arrival times (Chapman 1978). The result of summing the Gaussian beams is seen at the bottom of Fig. 6. The theoretical signal is indicated by dashed lines on the same figure.

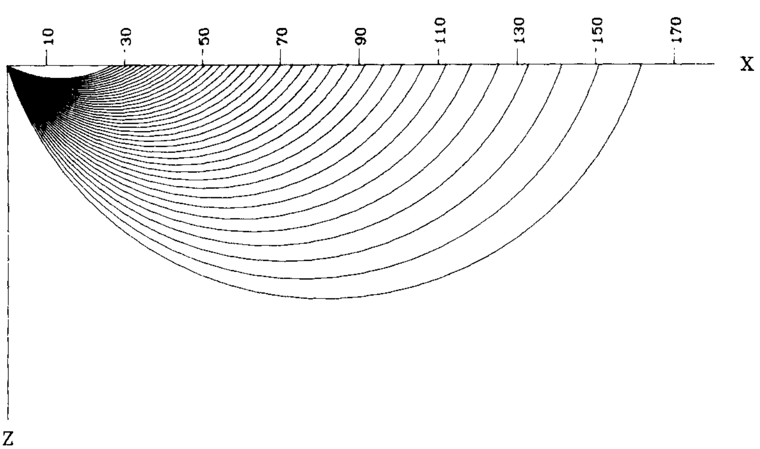

Figure 5. Set of central rays used to generate the synthetics in Figs 6 and 8. The medium is a half-space with a constant velocity gradient. The actual set of rays used in some of the computations has been reduced here for reasons of clarity.

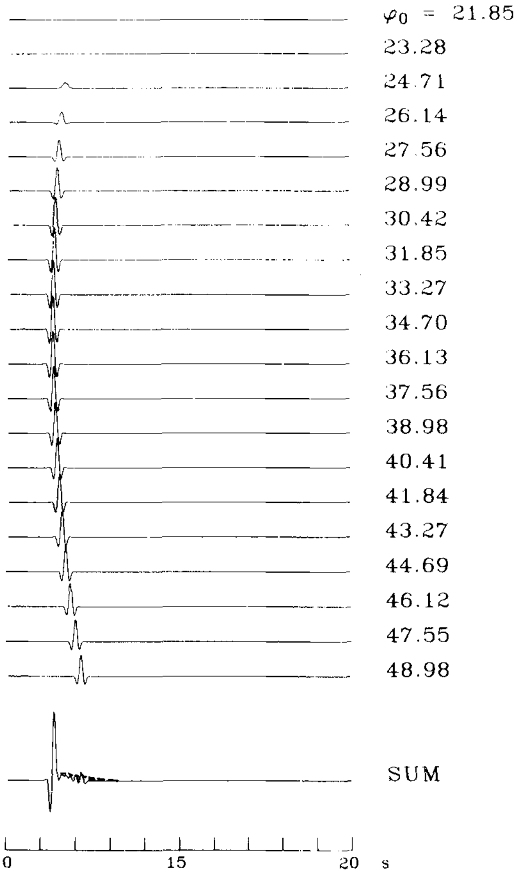

Figure 6. Individual Gaussian beam contributions for the synthetic seismogram shown at the bottom. The distance from the origin is 70 km. The medium is a half-space with a constant velocity gradient. In this figure we used the WKB base function in the generation of Gaussian beams. The geometrical arrival for the take-off angle $\phi_0 = 36.13°$ is minimum time, $\delta = 5 \times 10^{-4}$.

As we can see, the first part of the signal is undistinguishable from the theoretical one from which we conclude that Gaussian beams, as expected, work well near the geometrical arrival time. As we move further into the signal there are clear symptoms of aliasing: the density of rays is not enough to reproduce the decaying part of the tail of the Green function (57). There are three remedies to this problem: the first is to increase the number of rays to eliminate aliasing. The second one is to change variables in (48) to equal spacing in time which is the procedure advocated by Dey-Sarkar & Chapman (1978). The last possibility is to use large imaginary values of δ, close to the ideal beam width of Červený *et al.* (1982). The imaginary part of this ideal value is:

$$\delta_I = |Q_1(z)/Q_2(z)| = v(0)(\cos^2\phi_0 \, |X'|)^{-1}. \tag{58}$$

Using this value of δ has the effect of reducing the tail of the signals, i.e. the Green function decays more strongly than $t^{-1/2}$ for $t \gg T$ in (56). This is the method advocated by Červený *et al.* (1982). For the case studied here, the effect of using δ_I is to lose precision in the tail of the signal, for more complicated situations like triplications, the use of δ_I should be considered with great care because of the large variations of X' in (58). We will

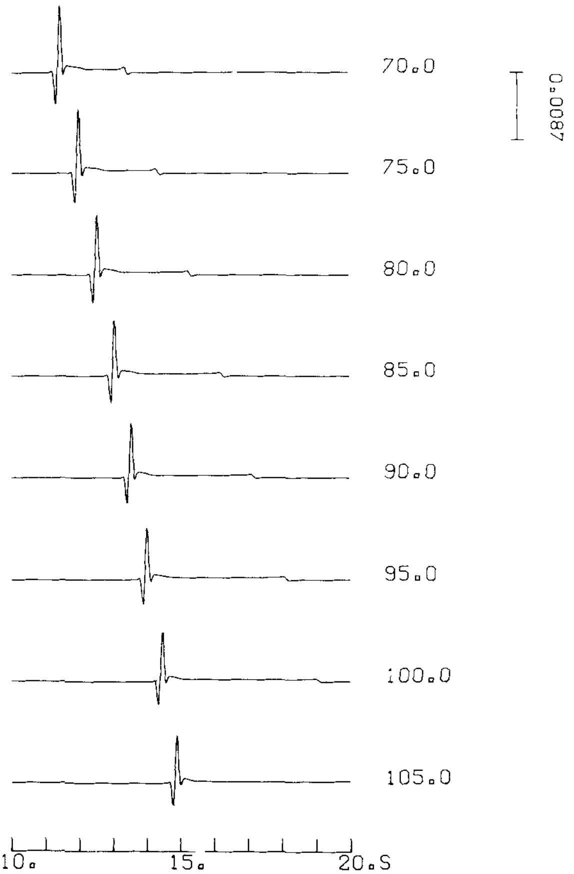

Figure 7. Synthetic seismic profile in a constant vertical velocity gradient medium, calculated with the Gaussian beam summation method using WKB base functions. $\delta = 10^{-3}$. Distance is indicated to the right of each record in kilometres. A clear cut off phase is observed a few seconds behind the signals.

come back to this problem in the next section. Our personal choice is intermediate between choosing a small $\Delta\phi_0$ and a large δ. For vertically heterogeneous models this is not very expensive computationally. We have calculated in this way the set of seismograms on Fig. 7 which show that the Gaussian beam summation method works very well for this very simple problem.

Finally, we address the problem of using Červený *et al.*'s (1982) base function Q_c instead of Q_1 in the expressions (39) for $Q(z)$. We showed that this is equivalent to choosing δ as in (53) and using the scheme as above to generate the synthetics. For a constant gradient medium the Q_c solution has no caustic at depth and the wavefront curvature is opposite to that of Q_1. This is the reason why the set of individual beam contributions calculated with the Červený *et al.* method on Fig. 8 is so different from that in Fig. 6. The wavelets are now centred around a curve Re $\theta(\phi_0)$ which has the opposite curvature to that of Fig. 6. The geometrical arrival time is a maximum now. In order to compensate for this effect the individual wavelets are Hilbert transformed ($\pi/2$ phase-shifted) with respect to those of Fig. 6. The final result for the Gaussian beam sum, also shown in Fig. 8, is still quite good near the arrival time but it deteriorates very rapidly. The worst problem is the appearance of non-causal arrivals ahead of the geometrical arrival time. These spurious arrivals are due

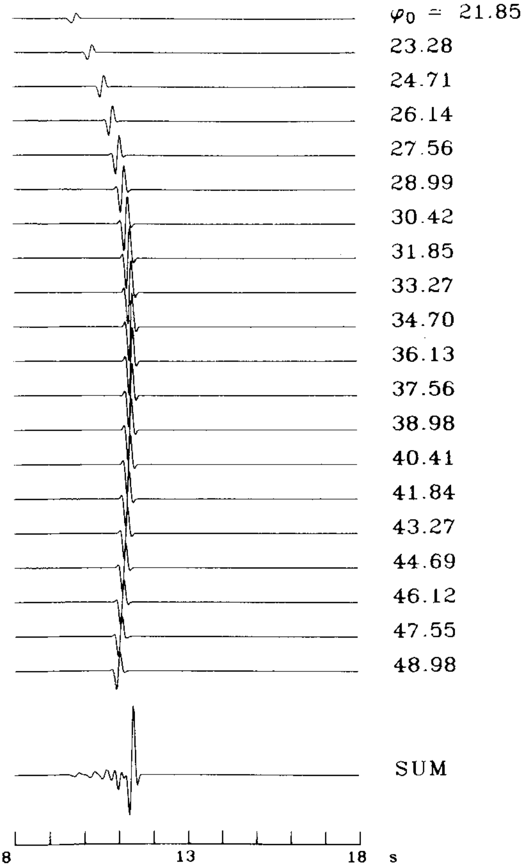

Figure 8. Same as Fig. 6 but with the Červený *et al.* (1982) base function (Fig. 2c). The geometrical arrival is still at 36.13° but it is a maximum time now. This creates the non-causal arrivals observed in the synthetic seismogram at the bottom.

to the modification of θ in (54) and they persist even if more rays are used. The only way to limit the non-causal arrivals is to use a very strong value for the imaginary part of δ. In the following, we consider that the use of the Červený *et al.* base function Q_c is undesirable and that the proper formulation is to use the WKB base function Q_1.

7 Modelling of a triplication

As a second example of the use of Gaussian beam summation we study a second-order velocity discontinuity. We consider a model of a constant velocity gradient layer of velocity $v(z) = v_0(1 + v_1 z)$, overlying a half-space of velocity $v(z) = v_2[1 + v_3(z - H)]$, where $H = 20$ km, $v_0 = 5$ km s^{-1}, $v_1 = 0.02$ km^{-1}, $v_2 = 9$ km s^{-1} and $v_3 = 0.05$ km^{-1}. Velocity is continuous at $z = H$, but because of the sudden change in gradient at this depth there is a triplication in the travel-time curve. A shadow is produced at 95 km by the discontinuity at 20 km and a caustic appears at 68 km. They are clearly visible in Fig. 9, where we show a set of rays calculated for this model. Classical ray theory fails in the vicinity of these travel-time singularities because the geometrical spreading function Q_2 in (57) varies very rapidly in their vicinity. Ray theory is practically useless in the range from 60 to 100 km, it is in this region that the Gaussian beam summation method is really useful. In Fig. 10 we plot Q_2 as

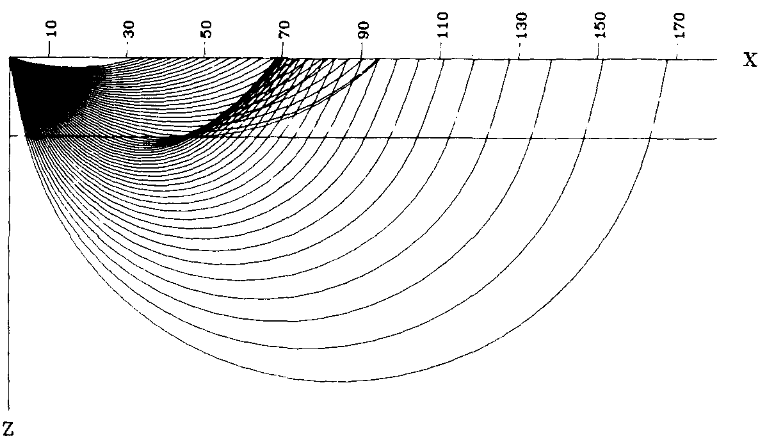

Figure 9. Central rays used to generate synthetics in a medium with a layer of constant velocity gradient overlying a half-space of similar characteristics. A shadow appears at 95 km and a caustic at 68 km.

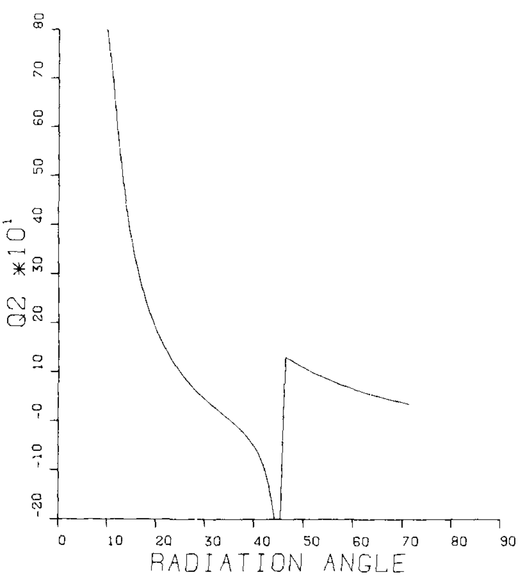

Figure 10. Geometrical spreading function for a point source in the medium of Fig. 9 as a function of take-off angle ϕ_0. At the caustic $\phi_0 = 35°$ and $Q_2 \to 0$; while at the shadow $\phi_0 = 46°$ and $Q_2 \to -\infty$.

a function of the radiation angle ϕ_0. It is observed that geometrical spreading is zero at the caustic so that (57) would predict an infinite amplitude there. On the other hand, Q_2 grows indefinitely on the reverse branch near the 95 km shadow, predicting zero amplitude for this branch. In reality neither of these results is correct because the field is dominated by interference effects in the vicinity of the singular points. Gaussian beam summation eliminates these problems because the individual beams behave regularly in the vicinity of the triplication; their singularities are now at depth near their turning points. Furthermore the Gaussian beam approach yields reasonable approximations for the diffracted waves observed ahead of the Airy caustic and beyond the shadow.

We have calculated the wavefield using both the Červený *et al.* (1982) formulation in ray centred coordinates (equation 47) and the new one in terms of geographical coordinates (equation 48). The results, as expected, are practically the same except for the diffraction from the shadow. This is due to the large values of the normal distance n to the central ray of the beam that causes the diffraction. The central ray of this beam is the ray that touches the interface at grazing incidence, which is also the ray that defines the position of the shadow at 98 km. Kinematic and dynamic ray tracing were done numerically using standard results for circular rays in a constant velocity gradient medium (see for instance Ben-Menahem & Singh 1981, p. 510). Synthetics were calculated using a Gabor (1946) source time function with $\omega_0 = 2\pi 4 \text{ rad s}^{-1}$ and $\gamma = 3$.

In Fig. 11 we present a seismogram section calculated between 60 and 110 km. One hundred and ten rays between $\phi_{min} = 0.1$ rad and $\phi_{max} = 1.4$ rad, were used in each seismogram. The range of distances $X(p)$ covered by these rays is shown by the extreme rays in Fig. 9, where for the purpose of clarity only 55 rays are shown. The large number of rays used was dictated by the need to eliminate aliasing without changing Červený *et al.*'s (1982)

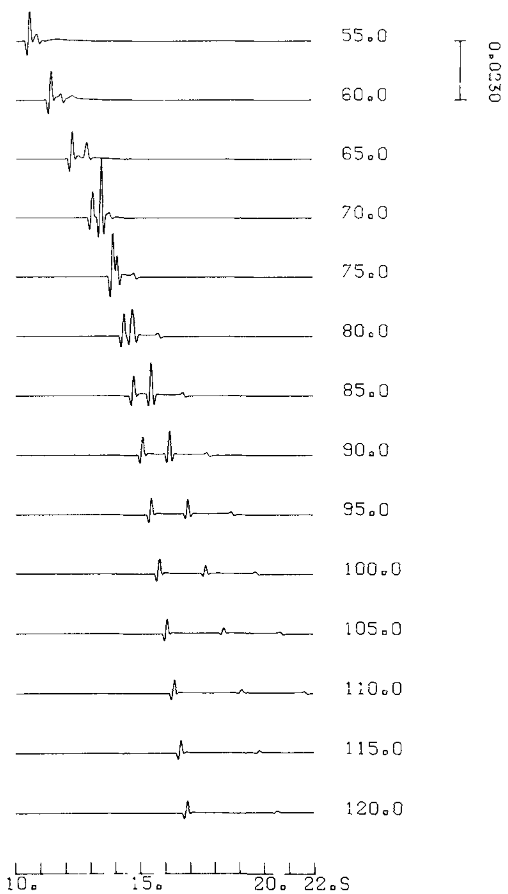

Figure 11. Seismic profile computed for the model of Fig. 9. Distance from the source is marked in kilometres to the right of each record. Diffraction ahead of the caustic is clearly seen at 60 km, while the diffraction from the shadow is observed up to 120 km. In this figure $\delta = 10^{-3}$. A clear cut-off phase is observed in this figure behind the main arrivals at distances greater than 70 km. This is due to the finite range of integration over angle.

formulation. A more sensible approach would be to change variables from ϕ_0 to the arrival time t. The last alternative discussed in the previous section would be to use larger values of $\mathrm{Im}(\delta)$ but this is not a good solution in this case because, as we will see later, the waves diffracted by the shadow would be poorly modelled. In order to generate Fig. 11 we used $\mathrm{Im}(\delta) = 10^{-3}$, the largest value beyond which the diffracted arrivals become severely distorted.

In Fig. 11 we observe very clearly the crossing near 70 km of the arrivals returned from the upper layer and those coming from the lower half-space. These first arrivals are of the same form as those of the simpler uniform gradient example calculated in Fig. 7. Ray theory appropriately models them. The second and third arrivals within the triplication are not easily identified in the synthetics. This is because of the finite frequency source function used to generate them. The diffracted signal in front of the caustic is very obvious in this figure and there is a clear enrichment in low frequencies as the distance to the caustic increases. Note also that the diffracted wave presents a $\pi/4$ phase shift with respect to the direct arrivals as predicted by Airy's theory for the diffraction from a caustic. An even more prominent diffraction is observed beyond the shadow at 95 km. This wave is diffracted by the second-order discontinuity and may be modelled by geometrical theory of diffraction

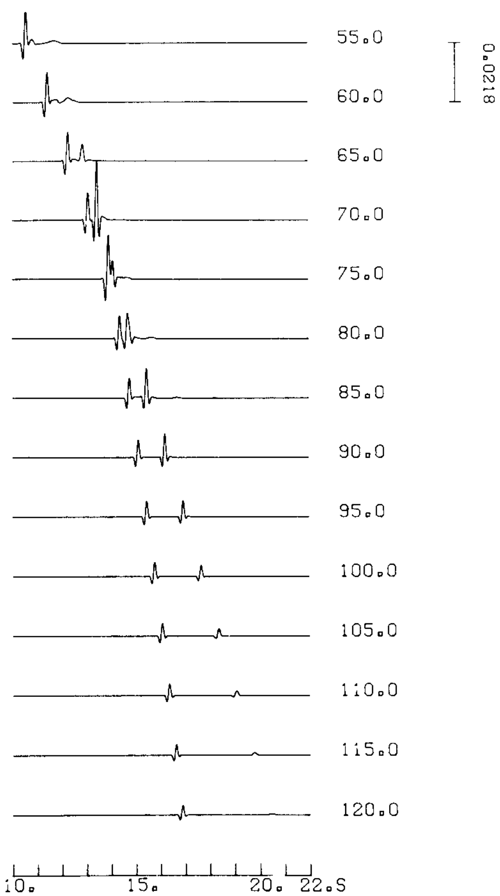

Figure 12. Similar to Fig. 11 but with $\delta = 10^{-2}$. The spurious cut-off phase has been greatly reduced, it is barely seen between 75 and 90 km.

as a creeping wave along the interface. The third arrival in the synthetics for $x > 70$ km is a cut-off phase due to the finite range of integration over ϕ_0.

Let us discuss now the role of the complex parameter δ. Červený *et al.* (1982) suggested using the optimum value δ_I defined by (58), although it is not clear from their paper whether they proposed to use the optimum value of δ for each beam, or whether a single value of δ should be chosen for all the beams contributing to a particular observation point. We prefer the latter approach because in the former case the asymptotic value of the Gaussian beam integral (48) would not be the ray approximation (57), since it would contain additional terms containing derivatives of δ with respect to ϕ_0. An even more important problem is that the minimum width criteria developed by Červený *et al.* (1982) is of little use in the case of a triplication because of the rapid variation of Q_2 with ϕ_0 observed in Fig. 10. If we adhere strictly to the optimum value δ_I (58) for δ, then $\delta_I = \infty$ at the caustic ($Q_2 = 0$) and $\delta_I = 0$ at the shadow where $Q_2 = \infty$. In fact, near the latter point any finite value of δ will make $Q(z) \to \infty$ and the integral representation (49) will not be a small perturbation of the WKB representation (50) any more. In practice, fortunately, we never sample exactly the ray grazing the interface – for which $Q_2 = \infty$ – and the effect on Gaussian beam synthetics remains limited. Extreme care should thus be exerted in the choice of δ. We proceeded in the following way: we chose an initial value for δ obtained from (58) using the average of Q_2 in the region of the triplication and a first set of seismograms was calculated. Then we increased δ by a factor of 10 and recalculated the synthetics which are shown in Fig. 12. The main effect is a reduction of amplitude of the later phases in Fig. 11, these include both the waves diffracted by the shadow and the cut off phases due to the finite range of integration over ϕ_0. This is the main advantage of the Gaussian beam method with respect to WKB: by properly adjusting δ the spurious effects of the finite integration range are greatly reduced, while an adequate precision is maintained for the physically significant arrivals.

8 Conclusion

We have presented the Gaussian beam summation method for a vertically heterogeneous medium. This solution is interesting for a number of reasons: first, it permits us to study in detail the properties of Gaussian beams in a non-trivial medium in which a number of interesting phenomena occur, for instance caustics, shadows, etc. Second, the solution of the dynamic ray tracing equations may be obtained in terms of quadratures using standard functions of classical kinematic ray theory (distance, travel time, intercept time and geometrical spreading). Third, the connection to other spectral decomposition methods for the calculation of synthetic seismograms may be clearly established. For instance, we demonstrate that Gaussian beam summation is an analytical continuation to complex values of relative position and slowness of Chapman's (1978) WKB method. Finally, a new, much simpler formulation could be obtained in geographical coordinates which eliminates the need to do explicit ray tracing in order to determine the local ray coordinates of each observation point.

We discussed in detail the problem of the choice of the arbitrary complex parameter ϵ (or $1/\delta$ in the terminology that we prefer) that appears in the formulation by Červený *et al.* (1982). We demonstrated that the real part of δ has to be chosen in such a way that when $\mathrm{Im}\,\delta \to 0$, a Gaussian beam reduces to a WKB vertical wave function. This may be simply imposed by choosing the WKB wavefunction as one of the base functions for the solution of the dynamic ray tracing equations. In this case the real part of δ is identically zero. If $\mathrm{Re}\,\delta \neq 0$, causality problems appear in the Gaussian beam summation. This happens in particular if one uses the base function proposed by Červený *et al.* (1982). The role of $\mathrm{Im}\,\delta$ is important since it allows to eliminate spurious phases in the synthetics due to the evaluation of the integral over a finite range of take-off angles. The choice of the value of δ was also discussed noting that the ideal beam-width criterion is not applicable in the vicinity of singular points of the ray expansion. For instance, at caustics the ideal beam width is always infinite, while it is zero at shadows. We propose that δ be considered as a small perturbation parameter measuring the deviation of Gaussian beam summation from the WKB expansion. δ may then be chosen by a series of numerical tests.

With the help of these results an efficient computer algorithm was written following very closely the propositions of Červený (1983). We studied two simple numerical examples that prove that Gaussian beam summation is a powerful tool to calculate synthetic seismograms in the presence of caustics, shadows or other singularities of the ray field. Furthermore, existing WKB programs may be easily modified to perform Gaussian beam summation.

Most of the results presented here may be extended to laterally heterogeneous media and to elastodynamic waves. For that purpose it is necessary to rewrite the paraxial ray tracing equations in geographical coordinates. Although the transformation from ray centred coordinates to general coordinates will be more difficult in laterally heterogeneous media, we believe that this may be done with the help of canonical transformations in phase space.

Acknowledgments

Many extremely helpful discussions with K. Aki, R. Nowack and V. Cormier at MIT are gratefully acknowledged. This work was funded by CNRS through a contract with ATP Geophysique Appliquée. IPG Contribution No. 757.

References

Aki, K. & Richards, P. G., 1980. *Quantitative Seismology, vol. I,* Freeman, San Francisco.

Babic, V. M. & Pankratova, T. F., 1973. On discontinuities of the Green function of mixed problems for the wave equation with variable coefficients, in *Problems of Mathematical Physics,* **6,** 9–27, Leningrad (in Russian).

Ben-Menahem, A. & Singh, S. J., 1981. *Seismic Waves and Sources*, Springer-Verlag, New York.

Buland, R. & Chapman, C. H., 1983. The computation of seismic travel times, *Bull. seism. Soc. Am.,* **73,** 1271–1302.

Bullen, K. E., 1961. Seismic ray theory, *Geophys. J. R. astr. Soc.,* **4,** 93–105.

Červený, V., 1981. Dynamic ray tracing in 2-D media and dynamic ray tracing across curved interfaces, *Stanford Explor. Project Rep. No. 28*, Stanford University, California.

Červený, V., 1983. Synthetic body wave seismograms for laterally varying layered structures by the Gaussian beam method, *Geophys. J. R. astr. Soc.,* **73,** 389–426.

Červený, V. & Hron, F., 1980. The ray series method and dynamic ray tracing systems for 3-D inhomogenous media, *Bull. seism. Soc. Am.,* **70,** 47–77.

Červený, V., Popov, M. M. & Pšenčík, I., 1982. Computation of wave fields in inhomogenous media. Gaussian beam approach, *Geophys. J. R. astr. Soc.,* **70,** 109–128.

Červený, V. & Pšenčík, I., 1979. Ray amplitudes of seismic body waves in laterally inhomogenous media, *Geophys. J. R. astr. Soc.,* **57,** 91–106.

Červený, V. & Pšenčík, I., 1984. Gaussian beams in elastic 2-D laterally varying layered structures, *Geophys. J. R. astr. Soc.,* **78,** 65–91.

Chapman, C. H., 1978. A new method for computing synthetic seismograms, *Geophys. J. R. astr. Soc.,* **64,** 321–372.

Chapman, C. H. & Drummond, R., 1983. Body-wave seismograms in inhomogenous media using Maslov asymptotic theory, *Bull. seism. Soc. Am.,* **72,** 5277–5917.

Cormier, V. F. & Spudich, P., 1984. Amplification of ground motion and waveform complexity in fault zones: examples from the San Andreas and Calaveras faults, *Geophys. J. R. astr. Soc.,* submitted.

Deschamps, G. A., 1971. Gaussian beams as a bundle of complex rays, *Electronics Lett.,* **7,** 684.

Deschamps, G. A., 1972. Ray techniques in electromagnetics, *Proc. IEEE,* **60,** 1022–1035.

Dey-Sarkar, S. K. & Chapman, C. H., 1978. A simple method for the computation of body wave seismograms, *Bull. seism. Soc. Am.*, **68,** 1577–1593.

Felsen, L. B., 1976. Evanescent waves, *J. opt. Soc. Am.*, **66,** 751–760.

Gabor, D., 1946. Theory of communications, *J. IEEE*, **93,** 429–441.

Keller, J. B. & Streifer, W., 1971. Complex rays with an application to Gaussian beams, *J. opt. Soc. Am.*, **61,** 40–43.

Nowack, R. & Aki, K., 1984. The 2-D Gaussian beam method: testing and application, *J. geophys. Res.*, submitted.

Popov, M. M., 1982. A new method of computation of wave fields using Gaussian beams, *Wave Motion*, **4,** 85–97.

Wenzel, F., Stoffa, P. L. & Buhl, P., 1982. Seismic modeling in the domain of intercept time and ray parameter, *Proc. IEEE Trans. acoust. Speech Sign.*, *ASSP-30*, 406–422.

Geophys. J. R. astr. Soc. (1984) 79, 613–633

The kinematics of the plate boundary zone through New Zealand: a comparison of short-and long-term deformations

R. I. Walcott* *Geology Department, Victoria University of Wellington, Private Bag, Wellington, New Zealand*

Received 1984 May 4; in original form 1984 March 5

Summary. Surveys of shear strain rates derived from repeated triangulation cover about one-quarter of the area of the plate boundary zone through New Zealand and are well distributed within it. Using a method developed by Haines relating shear strains to the total strain and velocity fields, the dilatational and rotational strain rates and the velocities within the deformed zone are derived. The plate boundary zone is shown to be two-dimensional, for the most part, in that gradients of the velocity along the length of the zone are small or zero. The shear strain rates are not uniform, however; they reach a maximum along a central axis and decrease gradually to zero toward the sides. Nor are the two independent components of strain, one involving shortening (or extension) perpendicular, and the other shear parallel, to the zone equally developed everywhere; there is a clear geographic separation with shortening developed over the subduction thrust and shear developed behind in a zone of wrench faulting. Time variations in the strain field in part of the region above the subduction interface are related to changes in the degree of coupling across the interface. A velocity field is computed: the relative velocity of the two plates from this data agree very well with that derived from seafloor spreading data. These strain and velocity fields derived from geodetic studies give the short-term kinematics of the plate boundary zone. The long-term kinematics of the zone are estimated from: (1) uplift and subsidence data which are related to changes in crustal thickness and hence to dilatational strain, and (2) variation in the declination of primary magnetization in rocks of known age, related to the rotational strain. The rate of rotational strain has increased in time from about 2 to $3^\circ\,\mathrm{Myr}^{-1}$, 10 Myr ago, to about $9^\circ\,\mathrm{Myr}^{-1}$ today. The increase can be understood as a secondary effect of a developing compressional component increasing the coupling between the plates so that more of the motion parallel to the zone is accommodated by distributed shear and less by aseismic slip. The rates of strain averaged over the last 1 Myr or so, and at a scale length of a few tens

* Present address: Department of Earth Sciences, University of Cambridge, Downing Street, Cambridge CB2 3EQ.

of kilometres, are closely similar in distribution and magnitude to the strain rates derived from short-term kinematics. While, therefore, at scale lengths of a few hundred metres or so faulting is very important and the deformation is discontinuous with unstrained blocks faulted, with large but uncertain slip, against adjacent blocks, the deformation at these longer-scale lengths is continuous and regular. The two consequences of this study are that: (1) strain from geodetic data can be directly related to the average long-term deformation and therefore can be an important tool in the study of deformation in regions of current tectonic activity, and (2) at scale lengths of a few tens of kilometres the deformation of a region can be described as the deformation of a continuum and we can ignore the effects of faulting.

1 Introduction

I infer the pattern and rates of strain, and the relative velocities (i.e. the kinematics) developed in a deforming region between two major plates from estimates of the shear rate obtained from triangulation survey data. Because faulting, through earthquakes and perhaps creep, dissipates elastic strain and consequently may modify the pattern and style of deformation, I distinguish between short-term and long-term kinematics of a plate boundary zone. In New Zealand the characteristic recurrence interval for fault movements on a major fault (i.e. the time between slip events of about the same size at the same location on a major fault) is around 10^3 yr; short term is taken to mean less than about 10^2 yr and long term is taken to mean greater than about 10^4 yr. Short-term deformation is therefore that accumulated in the period between major earthquakes whereas long-term deformation is the deformation accumulated over a considerable period of time that must include a very large number of faulting events. I show that the long-term and the short-term kinematics are essentially the same at scale lengths of tens of kilometres and that both are well described by the strain of a continuum.

2 Short-term kinematics

In early 1983 the last of seven narrow belts of first-order geodetic surveys was observed and completed a 10 yr project that has been adopted by the Department of Lands and Survey under the general Earth Deformation Programme of the Royal Society of New Zealand (1973). These are the Earth Deformation Studies (EDS) networks (Bevin 1981) and are shown in Fig. 1. While it is intended to repeat each of these surveys after about 10 yr to obtain information on earth deformation, many pre-existing first-order triangulation stations, surveyed mainly in the period 1925–1940, were reoccupied. Estimates of the shear strain accumulated in the intervening period can therefore be obtained. In addition, there have been other surveys within the standard control survey programme that have reoccupied old triangulation stations, some of which date from around 1880 and these also give estimates of shear strain. Previously published shear strain estimates (Bibby 1975, 1976, 1981a; Walcott 1978a, b, 1979) are, in general, consistent with the new data. The new data, however, are more homogeneous than those earlier in that each estimate of shear strain covers a similar area around $40 \times 40\ km^2$ and both surveys are of about the same accuracy.

In this paper the new shear strain data are given and, together with some earlier data, are interpreted in terms of the relative horizontal velocity of the surface of the Earth at regularly spaced points between the Pacific and Australian plates. In addition the shear strain

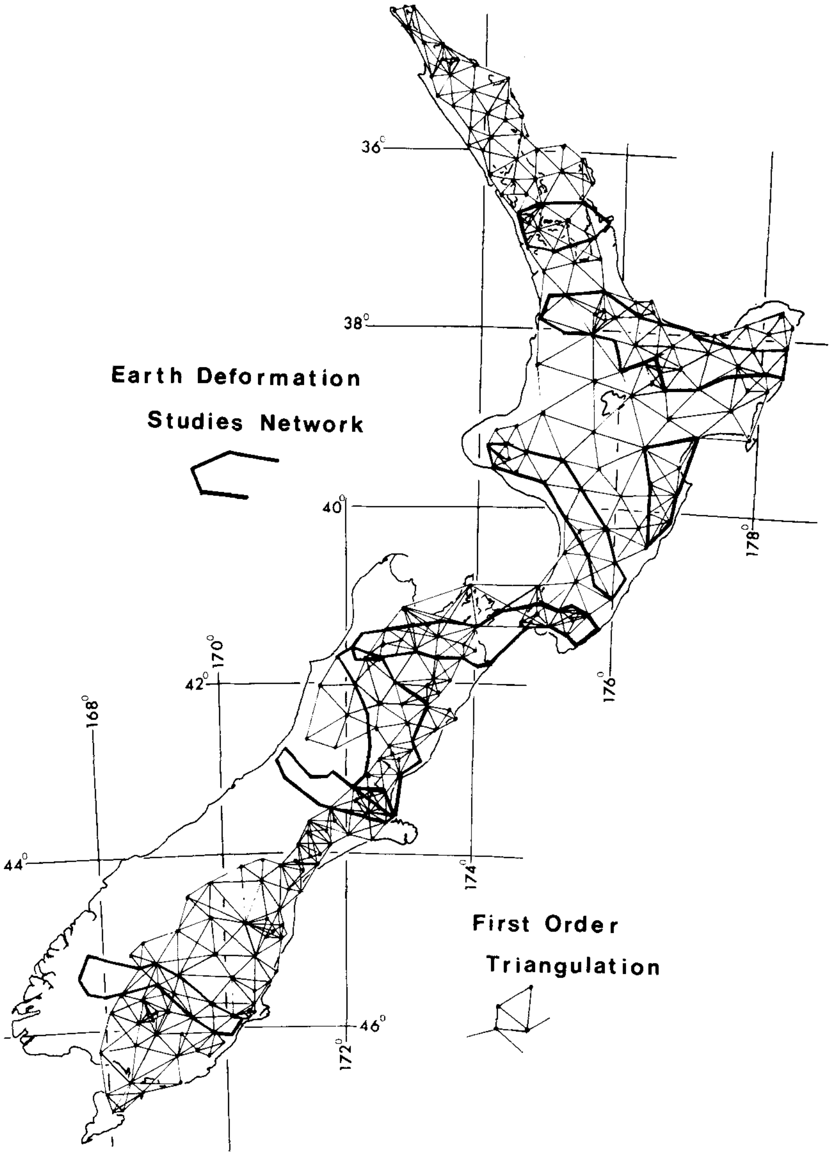

Figure 1. The first-order triangulation network established mostly in the period 1925–1941. Those parts of the network repeated in the Earth Deformation Studies programme are outlined.

rates provide estimates of the dilatational and rotational strain rate components within the plate boundary zone.

2.1 DATA

2.1.1 Estimation of the components of shear strain rate

The two methods used in the paper to obtain estimates of shear strain rate from survey data, 'Frank's Method' and the 'Method of Simultaneous Reduction' are described in detail in Frank (1966) and Bibby (1973, 1981b); only sufficient background material is given here to define the parameters discussed in the paper and illustrate the general features of the methods.

In a horizontal coordinate system (x, y), with (x) positive to the east and (y) positive to the north, in which deformation is occurring with components of velocity (u) along the (x)-axis and (v) along the (y)-axis, the components of strain rate are:

$$\frac{\partial u}{\partial x} - \frac{\partial v}{\partial y} = \dot{\gamma}_1 \text{ shear strain rate}$$

$$\frac{\partial u}{\partial y} + \frac{\partial v}{\partial x} = \dot{\gamma}_2 \text{ shear strain rate} \tag{1}$$

$$\frac{1}{2}\left(\frac{\partial u}{\partial x} + \frac{\partial v}{\partial y}\right) = \dot{\sigma} \text{ dilatational strain rate}$$

$$\frac{1}{2}\left(\frac{\partial u}{\partial y} - \frac{\partial v}{\partial x}\right) = \dot{\omega} \text{ rotational strain rate}$$

with the dot indicating differentiation with time.

Frank's Method is based on the observation equation relating change of an observed angle $\delta\phi$ defined by rays of azimuth θ_1 and θ_2 with the two shear strains, assuming that the strain is uniform over the area of the triangulation

$$\delta\phi = \gamma_1 \cos(\theta_1 + \theta_2) \sin\phi - \gamma_2 \sin(\theta_1 + \theta_2) \sin\phi \tag{2}$$

the solution being given by least squares of N observations and the rates given by dividing through by the time between the two surveys. The advantage of Frank's Method is that the calculations can be easily performed on a hand calculator which allows great flexibility and rapidity in obtaining solutions involving different combinations and numbers of angles. The disadvantage is that in using only reobserved angles it does not make use of all the information related to strain that may be available.

Simultaneous reduction is a procedure whereby all observational data of repeated surveys are reduced simultaneously to determine the station coordinates of one epoch and the derivable components of strain. Arbitrary minimal constraints are assumed consisting usually of a fixed origin, an azimuth and a distance scale. Although the displacements between stations of one epoch and the other will vary depending on these assumptions, strain is an invariant of the system of equations and can therefore be estimated free of bias (Bibby 1981b, p. 167). The advantage of this method is its generality: each survey does not have to be self-contained; only angles can be measured in one survey and only distances in the other; all observations relevant to the networks are relevant to the strain analysis. The disadvantage is that some considerable time is required to enter the observations free of error into the computer files. Where only reobserved angles are available it offers no advantages over Frank's Method.

The standard errors quoted here are determined from the diagonal terms of the covariance matrix and the sum of the squared residuals.

For purposes of illustration it is convenient to use the maximum shear atrain rate $\dot{\Gamma}$ and the orientation of the strain ellipse given by direction ψ the azimuth of the principle axis of compression

$$\dot{\Gamma} = (\dot{\gamma}_1^2 + \dot{\gamma}_2^2)^{1/2}$$

$$\psi = \tfrac{1}{2} \tan^{-1}\left(-\frac{\dot{\gamma}_2}{\dot{\gamma}_1}\right). \tag{3}$$

It is also convenient to refer to the two components of shear strain rate related to axes rotated through an angle β, by primes

$$\dot{\gamma}_1' = \dot{\Gamma} \cos(2\psi - 2\beta)$$
$$\dot{\gamma}_2' = -\dot{\Gamma} \sin(2\psi - 2\beta). \tag{4}$$

2.1.2 *Triangulation surveys and shear strain rates*

Shear strain rates determined from New Zealand triangulation data are listed in Table 1 and illustrated in Fig. 2(b). The area of each triangulation is outlined in Fig. 2(a), the numbers being the location identified in the first column of Table 1.

Modern control survey practise in New Zealand recognizes three orders of triangulation depending on size and accuracy. First-order triangulation has an average misclosure of 1″ with a maximum of 3″ and the average side length is not less than 40 km. For second-order the respective values are 3″, 5″ and 10 km and for third-order 5″, 8″ and 5 km. It is usual to refer to older surveys as fourth-order and most, but not all of the older surveys were inferior in accuracy to modern third-order.

Table 1. Shear strain rates.

Ref.	Surv.′	T″	$\dot{\gamma}_1'$ *	$\dot{\gamma}_2'$ *	$\dot{\Gamma}$ *	ψ **
1	1,1	50	-0.02±0.05	0.00±0.07	-	-
2	1,1	50	-0.10±0.10	-0.31±0.12	0.33±0.12	054±9
3	1,1	50	-0.03±0.05	-0.38±0.05	0.38±0.05	048±4
4	1,1	50	-0.10±0.12	-0.02±0.16	-	-
5	1,1	52	0.14±0.05	-0.13±0.06	0.19±0.05	068±6
6	1,1	50	-0.02±0.05	-0.14±0.06	0.14±0.06	049±11
7	1,1	50	-0.06±0.04	-0.17±0.04	0.18±0.04	055±6
8	2,2	33	-0.20±0.08	0.03±0.08	0.21±0.08	094±11
9	2,2	22	0.03±0.03	0.02±0.03	-	-
10	2,2	50	0.00±0.08	-0.04±0.08	-	-
11	1,1	50	-0.04±0.05	0.10±0.06	0.10±0.06	123±14
12	1,1	50	-0.13±0.08	-0.32±0.10	0.34±0.10	056±7
13	1,1	53	-0.39±0.03	0.12±0.05	0.41±0.03	098±3
14	1,1	53	-0.24±0.04	0.31±0.04	0.39±0.04	116±3
15	2,1	80	-0.34±0.14	0.53±0.14	0.63±0.14	119±6
16	1,1	45	-0.38±0.12	0.27±0.13	0.47±0.12	108±8
17	1,1	45	-0.38±0.11	0.22±0.07	0.44±0.10	105±5
18	2,2	50	-0.14±0.10	-0.06±0.10	0.15±0.10	078±19
19	2,2	50	-0.16±0.12	-0.11±0.11	0.19±0.12	073±17
20	4,3	80	0.03±0.12	0.20±0.11	0.20±0.11	134±17
21	4,3	80	0.02±0.11	0.32±0.11	0.32±0.11	137±10
22	1,2	45	-0.25±0.06	0.09±0.06	0.26±0.06	100±7
23	1,1	45	-0.08±0.06	0.03±0.06	0.08±0.06	102±20
24	4,3	95	0.02±0.13	0.02±0.12	-	-
25	4,3	95	-0.27±0.06	0.14±0.06	0.31±0.06	104±5
26	4,2	96	-0.39±0.10	0.54±0.10	0.67±0.10	117±4
27	4,2	96	-0.38±0.12	0.56±0.13	0.68±0.13	118±5
28	4,2	96	-0.46±0.09	0.29±0.09	0.55±0.09	106±5
29	1,1	38	0.03±0.08	0.02±0.08	-	-
30	1,1	38	0.04±0.08	-0.05±0.08	-	-
31	1,1	38	-0.08±0.06	0.04±0.06	0.09±0.06	103±18
32	1,1	38	-0.04±0.04	0.05±0.05	-	-

*Units of 10^{-6} rad yr^{-1} with standard error.
**Azimuth in degrees from true north with standard error.
′Order of surveys, 1 = first, 2 = second, 3 = third: see text.
″Years between first and second survey.

Figure 2. Map (a) shows the areas covered by triangulation data used in the calculation of the shear strain rates on map (b). The numbers on map (a) refer to Table 1, column 1: the numbers on map (b) are the rates of maximum shear in units of 10^{-6} rads yr^{-1}. The azimuth of the principal axis of compression is given by the bar.

As far as possible the shear strain rates given are for areas of $40 \times 40\,km^2$, that is for an average braced quadrilateral of first-order size. Thus in comparing two surveys of first-order triangulation there will be typically eight observations of changes of angle used in the estimate of the shear strain rate or many more for second- and third-order triangulations covering the same area. The increase in number of observations for second, and third orders of triangulation offsets, to some extent, their inferior accuracy. Also, as the standard error of shear strain rate is inversely proportional to the amount of time between the surveys, the low accuracy, older surveys give similar values of standard error to those of high accuracy, but more recent, surveys.

The period over which the strain rates are determined differ in the North and South Islands. In the North Island, apart from the first-order belt westwards of East Cape (Figs 1 and 8) the strain rates are determined for the period since 1930. A great earthquake in 1931 in the vicinity of Hawkes Bay (Fig. 8) of mag 7.9 separates periods of a quite different strain rate pattern (Walcott 1978b): before 1931 relative compression perpendicular to the north-eastward trend of the subduction zone occurred and after 1931 there was relative extension. Thus the data of Table 1 in the North Island refer only to the pattern established since that earthquake. In the South Island most of the data cover the period from the first surveys of around 1880. Where it is possible to compare strain rates over different periods in the South Island similar values are obtained (Bibby 1981a).

The pattern of maximum shear strain rate is simple and the changes appear to be smoothly varying functions of position. The maximum shear strain rate reaches its greatest values of around 0.6 μrad yr^{-1} in a belt that extends north-eastward from Fiordland (Fig. 8) toward East Cape and decreases smoothly north-westward and south-eastward to low values adjacent to the undeformed Australian and Pacific Plates. The orientation of the strain ellipse is uniform throughout the South Island and southern part of the North Island. The orientation is also uniform throughout north-eastern North Island but the direction of the principal axis of compression is to the NE and not WSW as elsewhere.

The physical meaning of the shear strain rates is most readily understood by the components $\dot{\gamma}_1'$, $\dot{\gamma}_2'$ resolved to axes oriented parallel (x) and normal (y) to the plate boundary zone (Fig. 3). In the South Island the trend of the Alpine Fault is 050° and there y is taken to be oriented 140° azimuth. Along the east coast of the North Island the trend of the fold and fault belt is about 035°, therefore y is taken to be 125° azimuth. The boundary between the two different trends is taken to be Cook Strait between the North and South Island. These orientations differ somewhat from the trends of folds and faults in small parts of the plate boundary zone, notably in Nelson (NW South Island) where the trend is about 010° and in the Central Volcanic Region of the North Island where the trend is 040°.

The plate boundary zone can be treated as 2-D (Section 2.2.1) in that the gradients of the

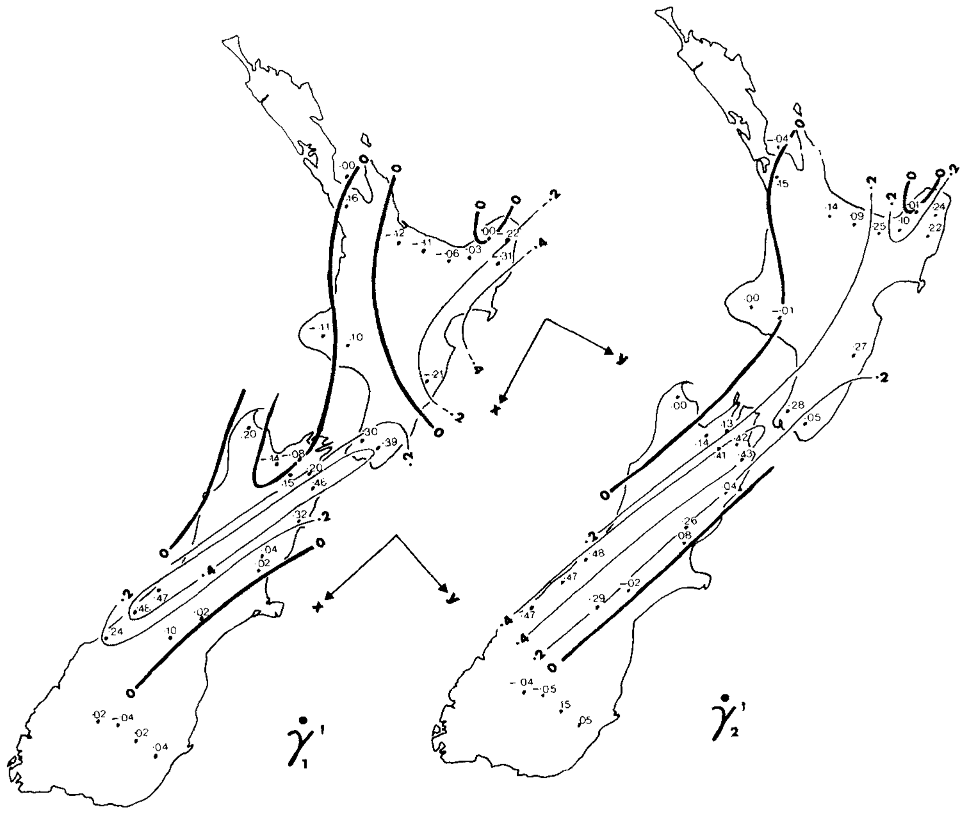

Figure 3. Shear strain rates components $\dot{\gamma}_1'$ and $\dot{\gamma}_2'$ derived for the particular orientation of axes shown (which differ in the North and South Islands). The data are contoured at intervals of 0.2×10^{-6} rad yr^{-1}. The $\dot{\gamma}_1'$ component corresponds to compression (+ve) or extension (−ve) in the y-direction; the $\dot{\gamma}_2'$ component corresponds to shear (+ve = dextral).

velocity components along the length of the zone are very much smaller than the gradients perpendicular to the zone, i.e.

$$\left|\frac{\partial(u, v)}{\partial x}\right| \rightarrow 0$$

then

$$\dot{\gamma}_1' \simeq \frac{-\partial v}{\partial y}, \quad \dot{\gamma}_2' \simeq \frac{-\partial u}{\partial y}$$

and $\dot{\gamma}_1'$ is a measure of the rate of compression (positive) or extension (negative) perpendicular to the zone and $\dot{\gamma}_2'$ is a measure of the simple shear, positive being shear in a dextral sense along the x-axis.

2.1.3 *The calculation of velocity and components of strain rate*

Haines (1982) gives the general solution to the partial differential equations relating shear strain rate to velocity (equations 1) and shows that given the velocity along one boundary of a deforming region within which the shear strain rates are known then the velocity everywhere is uniquely determined. Specifically, if we take a boundary ($y = 0$) to lie within a plate and set $U = V = 0$ there then the velocities within the region are relative to that plate. Thus from Haines (1982, equation 1, p. 204)

if

$$\frac{\partial \dot{u}}{\partial x} - \frac{\partial \dot{v}}{\partial y} = \dot{\gamma}_1(x, y); \quad \frac{\partial \dot{u}}{\partial y} + \frac{\partial \dot{v}}{\partial x} = \dot{\gamma}_2(x, y)$$

and

$$U(x, 0) = V(x, 0) = 0 \tag{5}$$

then

$$\dot{u}(\dot{x}, y) + i\dot{v}(x, y) = \int_0^y \overline{\dot{\gamma}}_2 \{x + i(y-y'), y'] \, dy - \int_0^y \overline{\dot{\gamma}}_2 [x + i(y-y'), y'] \, dy$$

where $\overline{\dot{\gamma}}_1$, $\overline{\dot{\gamma}}_2$ are analytic complex valued functions of complex argument corresponding to the real valued functions of real argument $\dot{\gamma}_1$, $\dot{\gamma}_2$. The remaining two components of strain rate, $\dot{\sigma}$, $\dot{\omega}$ (equations 1) are also determined; alternatively given $\dot{\sigma}$, $\dot{\omega}$ we can calculate $\dot{u}$, $\dot{v}$, $\dot{\gamma}_1$ and $\dot{\gamma}_2$.

Therefore with $\dot{\gamma}_1$, $\dot{\gamma}_2$ given as analytic functions (e.g. polynomials in x and y to order N) we can perform the integrations of equation (5) and obtain the velocity within the region and also the remaining components of strain rate.

This is a general solution to the linear equations of deformation to which the solutions of Walcott (1978a) and McKenzie & Jackson (1983) are for a special case in which the components of strain rate are uniform everywhere within the deforming region.

A network of evenly spaced points giving a grid of 40 km sides is placed over the plate boundary zone between the edges of the Pacific and Australian plates defined as the outer limit of significant crustal seismicity over the 20 yr period 1956–1976 (Hatherton 1980). Values of shear strain rate are assigned to those grid elements where data are available; in addition all four components of strain rate are assigned zero value in those parts of the grid beyond the plate boundary zone. Surfaces of order N are fitted to the values of strain rate

$$\dot{\gamma}_1(x, y) = \sum_{p=0}^{N} \sum_{q=0}^{P} G_{pq}\, x^{p-q}\, y^q$$

$$\dot{\gamma}_2(x, y) = \sum_{p=0} \sum_{q=0} H_{pq}\, x^{p-q}\, y^q. \tag{6}$$

Haines shows that the components of velocity are

$$U(x, y) = \sum_{p=0}^{N+1} \sum_{q=0}^{p} U_{pq}\, x^{p-q}\, y^q$$

$$V(x, y) = \sum_{p=0}^{N+1} \sum_{q=0}^{p} V_{pq}\, x^{p-q}\, y^q \tag{7}$$

where the coefficients are given by the recurrence formulae

$$U_{(p+1)(q+1)} = [H_{pq} - (p+1-q)\, V_{(p+1)q}]/q+1$$

$$V_{(p+1)(q+1)} = [(p+1-q)\, U_{(p+1)q} - G_{pq}]/q+1. \tag{8}$$

We take the velocity along that side of the grid along the edge of the Australian plate to be zero so that the velocities calculated for the plate boundary zone are relative to the Australian Plate.

In the calculation of the coefficients G and H the data for shear strain rates are weighted by the inverse of their standard errors. Fourth-, fifth- and sixth-order surfaces all fit the strain rate data and give similar levels of significance by way of an F test. A fifth-order surface illustrated by the four derived components of strain rate is shown in Fig. 4.

2.2 INTERPRETATION

The shear strain rates derived from the surface fitting procedure compared with the input data (Fig. 3) show a satisfactorily similar pattern but, as to be expected in fitting a polynomial, the peak values are smoothed and the zone of shear is spread: the peak values are only about one-half, and the zone is twice as wide, as observed. While the surface fitting procedure will not have a large effect on the computation of velocities, as these are derived by the integration of strain rates against distance, the strain rates themselves are not well represented by Fig. 4.

2.2.1 *Two-dimensionality of the plate boundary zone*

We note in Fig. 3 that to a good approximation both $\dot{\gamma}_1'$ and $\dot{\gamma}_2'$ are functions of y only so that $\partial(u, v)/\partial x$ are small or zero. Hence the dilatational strain rate is approximately $-\tfrac{1}{2}\dot{\gamma}_1'$ and the rotational strain rate is approximately $\tfrac{1}{2}\dot{\gamma}_2'$. Thus, when in the following I refer to present day strain rates I mean the shear strain rates of Fig. 3 and the dilatational and rotational strain rates so derived from them.

2.2.2 *Non-uniformity of the strain field*

Both Walcott (1978a, b) and McKenzie & Jackson (1983) have modelled a plate boundary zone by uniform strain fields (i.e. the gradients of velocity are uniform everywhere within

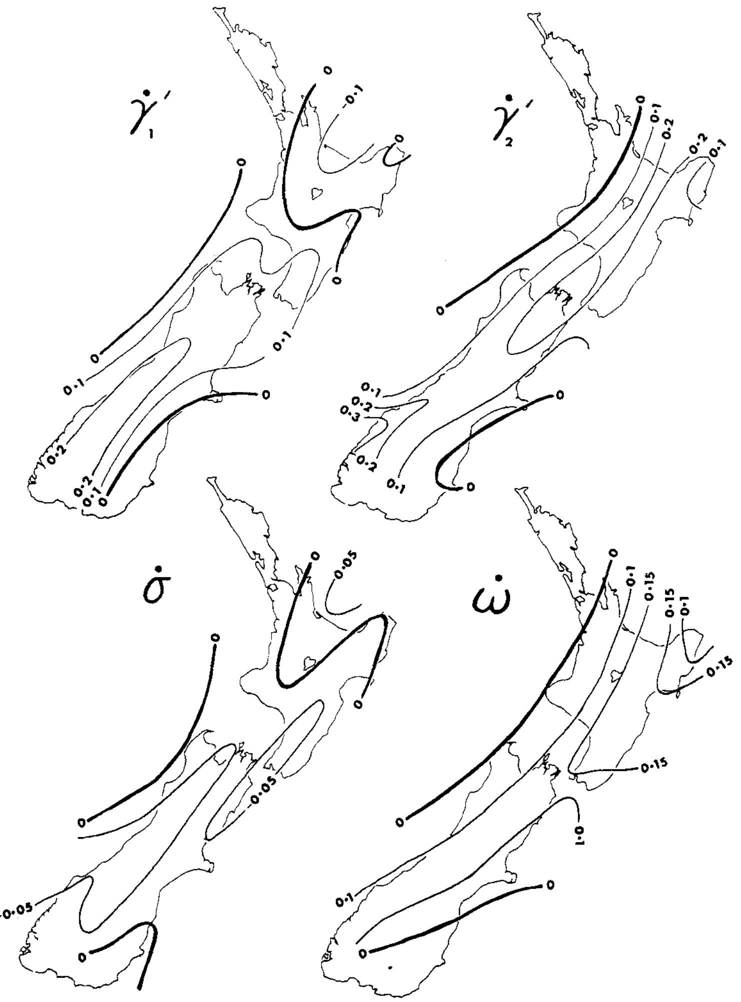

Figure 4. The four components of strain rate derived from the data of Table 1 by fitting a fifth-order polynomial to the shear strain rate data. Compare the observed (Fig. 3) and modelled shear strain rates.

the zone) and such uniformity is to be expected for a homogeneous block of material subjected to deformation by uniform relative motion of its boundaries. But the strain fields of Figs 3 and 4 are far from being uniform; strain rates reach a maximum along a central axis and decrease gradually towards the edges of the zone. Moreover the distribution of the two components of the shear strain rate are not the same indicating that the relative motion of the boundary is accommodated in different ways in different parts of the plate boundary zone. This is shown most clearly in data from the northern part of the South Island described by Bibby (1981a). I plot this data in profile (Fig. 5) with the measured values of $\dot{\gamma}_1'$ and $\dot{\gamma}_2'$ plotted against distance normal to the plate boundary zone from the edge of the Pacific Plate; the non-uniform distribution of strain is evident as is the relative offset in the two components of shear strain rate.

The offset in position illustrates variation in the accommodation of relative motion of the plates, with the motion in the y direction (compression) being largely accommodated in the

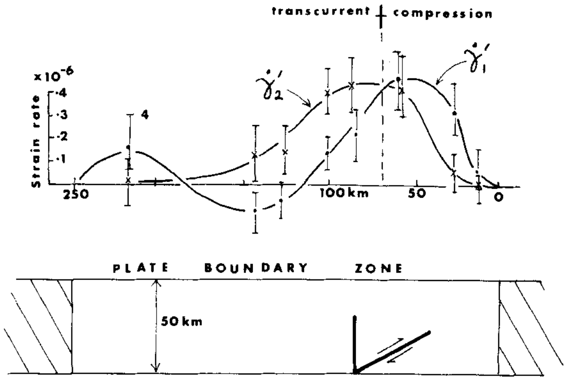

Figure 5. The non-uniformity and unequal distribution of shear strain rates in the northern part of the South Island from data given by Bibby (1981a). Note that compression ($\dot{\gamma}_1$) predominates to the right (east) and transcurrent movement ($\dot{\gamma}_2$) predominates on the left (west). Also that both components are not uniform but reach a maximum near the centre of the deforming zone. A possible model involving stress-free cuts in an otherwise uniform slab could explain this pattern in the lower diagram, but other possibilities exist such as a change in physical properties of the crust.

right of the profile (presumably by thrusting) and motion in the x (normal to the paper) accommodated in the left by wrench faulting.

We can explain the non-uniform distribution of strain by supposing that the zone is heterogeneous in its mechanical properties being somewhat weaker (or thinner) under regions of high strain rate. A possible model is illustrated in Fig. 5 where an otherwise uniform slab between the two plates has two cuts which allow slip: the strain will be concentrated in the thinner part of the slab above the cuts and there will be a spatial separation of the two components of shear strain rate. The model is not totally *ad hoc* as the inclined cut could be the subduction thrust and the vertical, the root zone of the wrench faults that occur in this part of the boundary zone but it is *ad hoc* to the extent that it is speculation to suppose that there is slip on these features at depth. We can equally well model the strain rate distribution by any other form of heterogeneity. Certainly the basement rocks exposed in the region of highest shear strain rate in the northern part of the South Island are very strongly sheared and therefore presumably weaker: this could however be both cause and consequence of the high shear strain rates.

2.2.3 The velocity field

The velocity field for the plate boundary zone through New Zealand has been computed from the shear strain rates using the method of Haines (Fig. 6). The velocities along the edge of the grid against the Australian Plate are held to zero so that the computed velocities are relative to that plate. The direction is given by the arrows and the rate by the length of the arrows. The standard error in speed is given by the radius of the ellipse (drawn at the end of each vector) in the direction of motion and the standard error in direction is given by the tangent to the ellipse from the vector origin.

Bibby (1981a, b) has carefully integrated the shear strains across the northern part of the South Island (Fig. 5) to obtain a velocity of 54 ± 9 mm yr^{-1} in a direction of $264 \pm 10°$ for the motion of the Pacific relative to the Australian Plate. The velocity computed from sea-floor spreading data for the same location using the Chase (1978) parameters of the Euler rotation ($-62.0°$, $174.3°$, $1.27°$ Ma^{-1}) are 47 ± 5 mm yr^{-1} at $270 \pm 5°$ azimuth. The two are

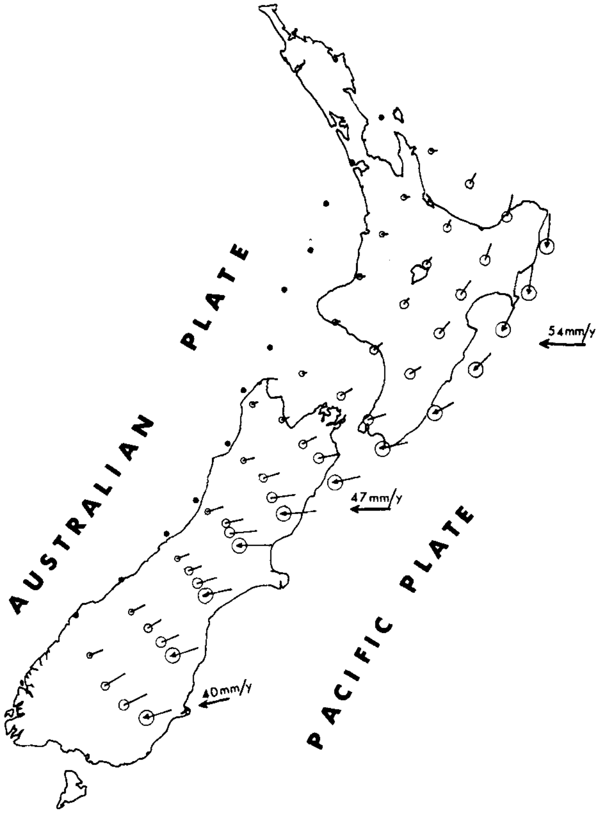

Figure 6. Velocities calculated on a grid from the shear strain rates of Table 1. The NW side of the grid, the line of dots, is fixed to the Australian Plate so that the velocities are relative to that plate. The length of the arrows is proportional to speed and the direction is given by the arrow. The standard error in direction (tangents) and rate (length) is shown by the ellipses (generally very close to being circles) at the end of each velocity. Also shown are the velocities of the Pacific with respect to the Australian Plate from Chase (1978).

identical within limits of error, a somewhat surprising result given that the two are derived from very different data and for very different periods of time; the former based on data for a period of not more than 100 yr, the latter from the separation of magnetic anomalies at least 3 Ma old. Note that the errors given for the seafloor spreading data are formal errors derived for a large and redundant data set. They are model dependent; a change in the particular model of plates (e.g. the introduction of a plate boundary along the Ninety East Ridge) does result in computed velocities rather different to those given (see discussion in Walcott 1979).

Knowing the velocity of the Pacific relative to the Australian Plate it is a straightforward procedure to transform the plate boundary zone velocities relative to one plate to those relative to the other. The two kinematically equivalent velocity models are shown in Fig. 7 where I have used the Chase (1978) rotation parameters to effect the transformation.

The velocity field is not in itself particularly informative – the more useful information for deformation studies is given by the strain and strain rates. However the two diagrams of Fig. 7 do show at a glance the relative simplicity of the kinematics of the plate boundary zone, and the major characteristics of the deformation. In the South Island the velocities

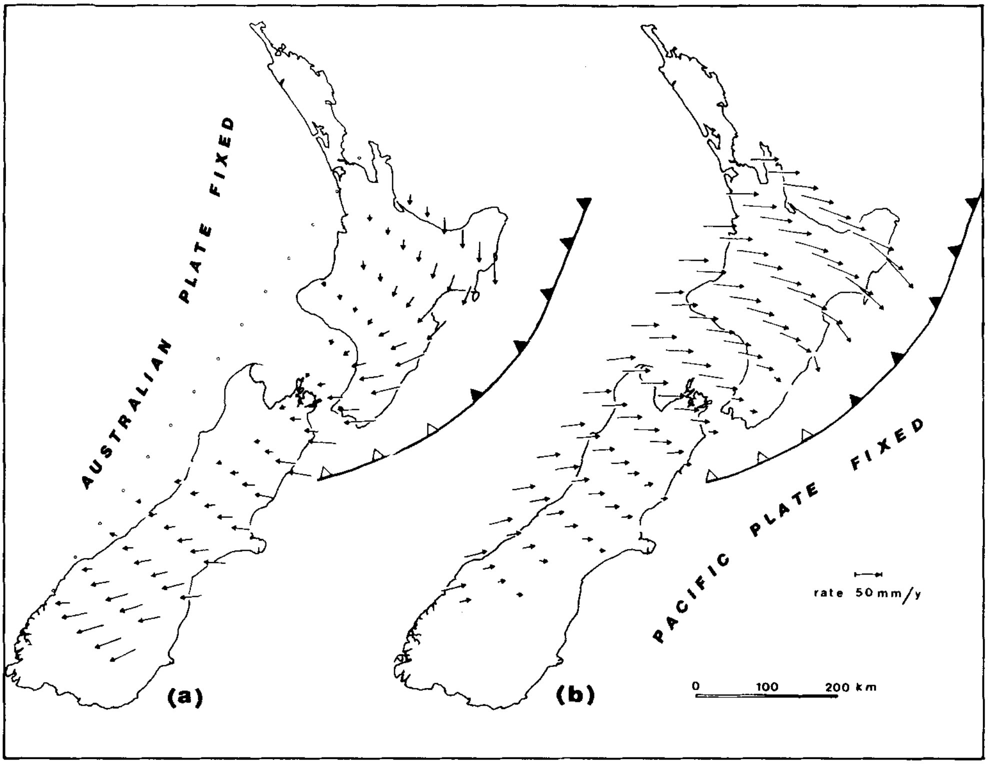

Figure 7. Velocities relative to the Australian (a) Pacific Plates (b). The velocity discontinuity at the Hikurangi Trough (solid line) is identified by the solid teeth. Open teeth indicate that part of the Trough currently locked so that the relative movement of the plates is accommodated wholly by deformation in the crust overlying the subduction.

are oblique to the plate boundary zone, the relative velocities abruptly decrease across the zone to zero. In the North Island the velocity vectors are bent (Fig. 7b) to become orthogonal to the trend of the plate boundary zone where the subducted plate directly underlies, and is in contact with the obducted plate. This is presumably a consequence of the subduction obduction process and is discussed in Walcott (1978b) and below.

2.2.4 The locked southern and unlocked northern parts of the Hikurangi Subduction Zone

Subducted oceanic lithosphere exists the full length of the Tonga–Kermadec–Hikurangi subduction zone, terminating in the northern part of the South Island along a line extending westward of the northern edge of the continental crust of the Chatham Rise (Bibby 1981a). The termination is abrupt and is manifest in the distribution of intermediate depth earthquakes. The Hikurangi Subduction Zone is that part adjacent to New Zealand and is named from the Hikurangi Trough (indicated by the line in Fig. 7 with saw teeth) a rather shallow trough (*c.* 3 km deep) east of the North Island and equivalent to the Kermadec Trench to the north.

The northern and southern parts of the zone behave mechanically very differently. In the north a velocity discontinuity must exist across the trough because of the very large component of velocity orthogonal to the plate boundary (Fig. 7b). To the south the velocities are near zero so that the relative motion between the plates is being accommodated by strain in the lithosphere above the subducted plate. To distinguish these two regions, I use open saw teeth to indicated a locked subduction thrust and solid saw teeth to indicate a freely slipping subduction thrust.

2.2.5 Short-term variation of the strain field

During the 1931 Hawkes Bay earthquake (*M* 7.9; Richter 1958) thrust motion involving shortening of some 3 m in a NW direction occurred on a fault about 200 km in length. For most of its length the fault did not break the surface but an elongate, domal uplift developed

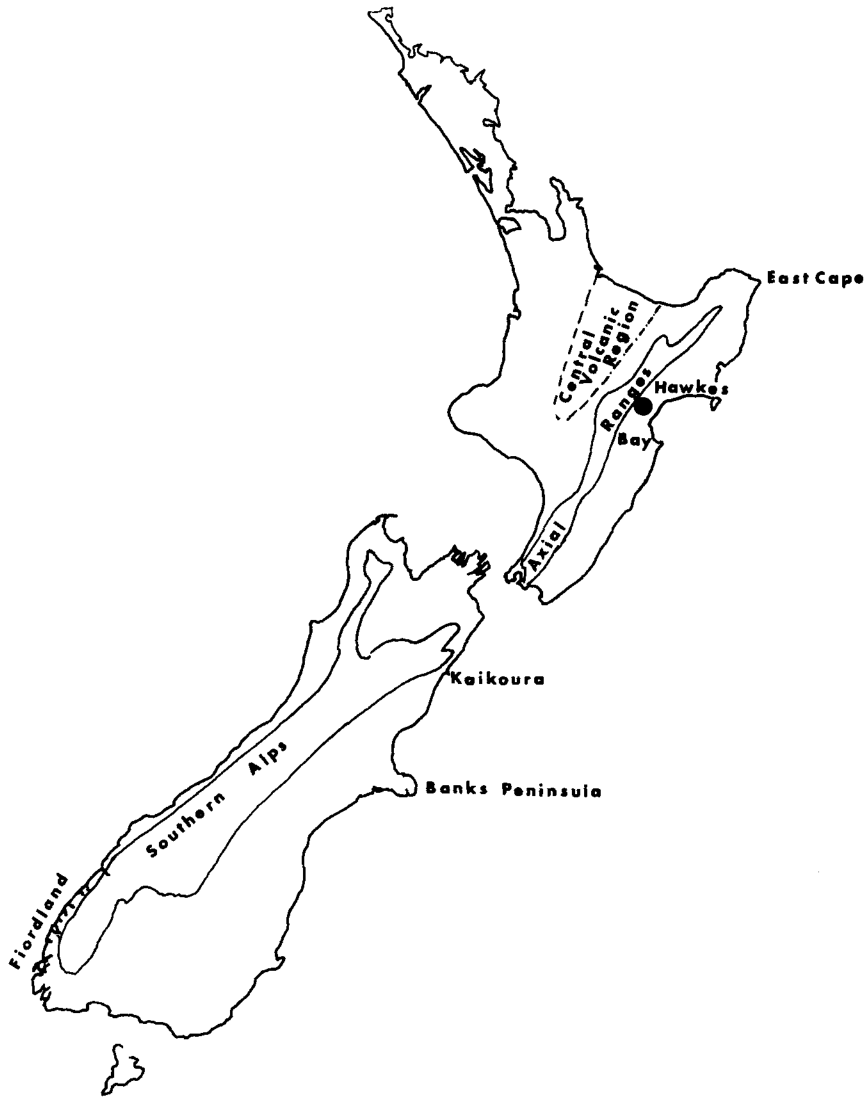

Figure 8. A summary of uplift and subsidence in New Zealand over the last 1 Myr or so. The Central Volcanic Region has been subsiding, elsewhere uplift occurs in the land area. The most rapid uplift coincides with the highest elevation since New Zealand mountains are geologically young: the 2000 m contour is drawn. The epicentre for the 1931 Hawkes Bay Earthquake is marked by the large solid circle.

on the down dip (NW) side of the fault. Before the earthquake the pattern of strain was very different to that since (Walcott 1978b). The principal axis of compression is, today, NE/SW where prior to 1931 it was NW/SE (i.e. the $\dot{\gamma}_1'$ strain component is today negative, before the earthquake it was positive). The data coverage is insufficient to determine the full extent of the region of positive $\dot{\gamma}_1'$, but it may have extended most of the length of the east coast from East Cape to Kaikoura (Fig. 8). In the Central Volcanic Region however, the γ_1' component was negative as normal faulting with NE strike occurred in this period (Grange 1932). A repeated sequence of compression/earthquake/extension is inferred to be due to locking of the subduction interface that dips under Hawkes Bay from the Hikurangi Trough (Walcott 1978b). During a period in which the interface is locked the relative plate motion is accumulated as compression of the obducted crust (positive $\dot{\gamma}_1'$) leading eventually to rupture and an earthquake. During a period in which the interface is unlocked the deformed obducted crust gradually relaxes its accumulated deformation. The deformation on the east coast on the North Island is therefore inferred to involve episodic changes in the sign of $\dot{\gamma}_1'$ but with $\dot{\gamma}_2'$ largely unaffected. Over a period of a few cycles the net effect must be to shorten the crust (i.e. net compression, or positive $\dot{\gamma}_1'$) in the region west of the coastline as this has been a region of net uplift in the last few thousand years (Fig. 8).

3 Long-term kinematics

While it is the two components of shear strain that are useful in the study of short-term kinematics, it is the two other components of areal strain, the dilatational and rotational components that are most useful for long-term studies. Over long periods of time the accumulated dilatations give rise to changes in the thickness of the crust that are manifest as uplift or subsidence at the surface. Similarly rotational strain accumulates over geological time and can be measured from the anomaly in declination of primary magnetization in palaeomagnetic studies. In practice, however, there are considerable difficulties in relating uplift or subsidence to crustal thickness changes and, due to lack of suitable rocks, declination anomalies are available in only a part of the plate boundary zone.

3.1 DILATATION

By the conservation of mass

$$\frac{\partial \dot{u}}{\partial x} + \frac{\partial \dot{v}}{\partial y} + \frac{\partial \dot{w}}{\partial z} = 0$$

so that

$$\frac{\partial \dot{w}}{\partial z} = -\left(\frac{\partial \dot{u}}{\partial x} + \frac{\partial \dot{v}}{\partial y}\right)$$

$$= \dot{\gamma}_1 \qquad \text{when } \frac{2\dot{u}}{\partial x} = 0.$$

The vertical extensional strain rate, $\partial \dot{w}/\partial z$ is given by $\Delta \dot{w}/W$ where $\Delta \dot{w}$ is the rate of change of crustal thickness W.

Given estimates of $\Delta \dot{w}$ from uplift and subsidence observations we can estimate values of the 'long-term' component of shear strain rate $\dot{\gamma}_1'$ and compare them to the 'short-term' components given in Fig. 3.

There is an obvious close correspondence between the relative rate, and sign, of uplift and the uplift implied by the short-term $\dot{\gamma}_1'$ strain rate. The mountains of New Zealand are geologically very young, less than 5 Myr old, and the highest mountains and the most rapidly uplifting regions, like the Southern Alps (Fig. 8) lie close to the highest value of $\dot{\gamma}_1'$. Along the eastern half of the North Island negative values of $\dot{\gamma}_1'$ exist today but these are unusual; positive values are to be expected on average (see Section 2.2.5). In the Central Volcanic Region of the North Island (Fig. 8) the values of $\dot{\gamma}_1'$ are negative ($-0.11 \times 10^{-6}\,\mathrm{yr}^{-1}$, Fig. 3) implying subsidence, and substantial subsidence has occurred there in the last 1 Myr.

The quantitative relationship between uplift and the change in the thickness of the crust will however vary. Where the rate of uplift is balanced by the rate of erosion the vertical motion of the surface is equal to the rate of change in thickness of the crust so that uplift rate $= \partial\dot{w}/\partial z \cdot W = \Delta\dot{w}$. Where, however erosion is unimportant and the resulting topographic load is compensated by crustal thickening and the development of topographic roots $\Delta\dot{w} = \text{uplift}.\ \rho_a/(\rho_a - \rho_c)$ where ρ_a is the density of the asthenosphere (say 3.3) and ρ_c is the density of the crust (say 2.8), then $\Delta\dot{w}$ may be 6.6 x uplift rate.

Thus depending on the importance of erosion and the degree of compensation for the increasing topographic loads the rate of change of crustal thickness due to compression may be equal to, or as much as 6.6 times, the rate of uplift. This is an important point as it demonstrates that the conversion of the $\dot{\gamma}_1'$ strain component to uplift, or vice versa, is very strongly dependent of the particular model of compensation. Along the crest of the Southern Alps the erosion rate is about equal to the rate of uplift, according to Adams (1978), so that the uplift of around $6\,\mathrm{mm\,yr}^{-1}$ with peak values of about $17\,\mathrm{mm\,yr}^{-1}$ (Wellman 1979) implies a long-term strain rate for the $\dot{\gamma}_1'$ component of $0.2 \times 10^{-6}\,\mathrm{yr}^{-1}$ with peak values of $0.6 \times 10^{-6}\,\mathrm{yr}^{-1}$. Further east, where the mountains are flat topped and the erosion rate is very much less, the uplift is about $1\,\mathrm{mm\,yr}^{-1}$ (Wellman 1979) and using the factor of 6 as being appropriate, the implied strain rate for the long-term component is again $0.2 \times 10^{-6}\,\mathrm{yr}^{-1}$. The effect of the lateral changes in erosion rate and compensation, therefore, is to make the derived long-term $\dot{\gamma}_1'$ component much smoother, less peaked and more spread out than the topography.

In the Central Volcanic Zone a subsidence of about 2 km in the last 1 Myr is indicated (Stern 1984). A part of this subsidence is contributed by the infilling volcanics of density ρ_v. The relationship between the rate of change of crustal thickness $\Delta\dot{w}$ and rate of subsidence $\dot{d}$ is therefore $\Delta\dot{w} = \dot{d}(\rho_a - \rho_v)/(\rho_a - \rho_c)$ and taking $\rho_a = 3.2$, $\rho_c = 2.5$, $\rho_c = 2.8$, $\Delta\dot{w} = 2(0.7/0.5)\,\mathrm{mm\,yr}^{-1}$ so that for a crustal thickness of 20 km (Stern 1984) the long-term $\dot{\gamma}_1'$ component is $0.14 \times 10^{-6}\,\mathrm{yr}^{-1}$. This is the same magnitude as the short-term strain rate but because of the uncertainties in the model the error must be about 50 per cent.

The pattern and rates of the long-term dilatational strain all over New Zealand are therefore closely similar to those of the short term. But this pattern and these rates have not been maintained for more than about 1 Myr. Before that, the dilatation component (and by implication, the γ_1' shear strain component) must have been small or zero, since throughout most of the Tertiary New Zealand was covered by marine sedimentary rocks. A gradual increase in the component of compression across the plate boundary zone is indicated by seafloor spreading data (Stock & Molnar 1982) and has been discussed by Walcott (1984).

3.2 ROTATION

Palaeomagnetic studies of Tertiary sedimentary rocks on the east coast of the North Island and in north-eastern South Island show rotations of the declination of the primary remanent magnetization about vertical axes that increase with age. Details of the techniques, collection

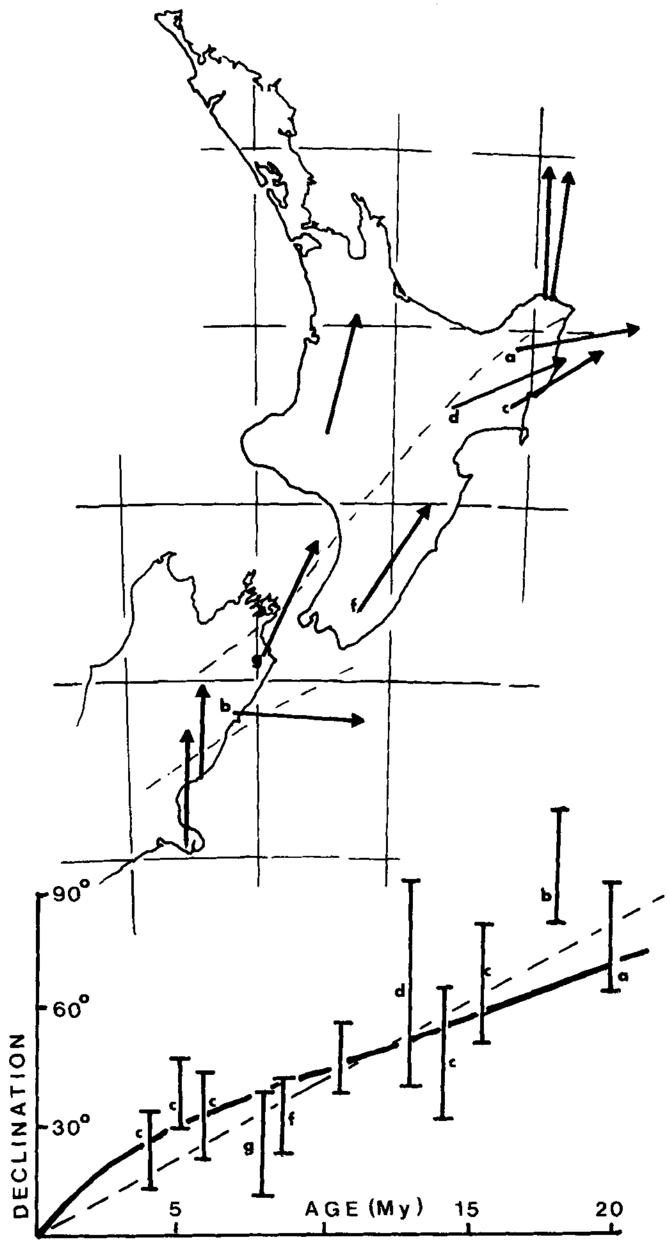

Figure 9. The declination of primary magnetization in sedimentary rocks in New Zealand. In the top diagram the dashed line outlines the zone of large rotations and can be compared to the zone of current deformation (Fig. 3). Outside that zone rotations are small or zero. The lower diagram plots declination against age for sites within the zone of deformation. The rate of rotation in the south at locality b is greater than the rate in the north at a. The average rate of rotation for the whole zone is about 4° Myr^{-1} (dashed line) but an increasing rate towards the present (solid line) is a preferred interpretation as it fits the 5 Myr old data better. The lower case letters in the upper diagram show the localities from which the data in the lower diagram are obtained. Not all data are plotted in the upper diagram.

methods and rock ages and properties are given in Walcott, Christoffel & Mumme (1981) and Walcott & Mumme (1982) and further work will be given in Mumme & Walcott (in preparation). The results are summarized in this paper.

The cores have been collected from Tertiary sedimentary rocks (mudstone, siltstones and less commonly, sandstones) of known palaeontological age with a strike and dip close to that of the regional structure. Generally the dip increases with age being about 30° for rocks around 10 Myr and up to 50° for rocks around 20 Myr old.

A strong viscous remanence is present in most samples but it can generally be removed by thermal or magnetic cleaning. Unless the primary magnetization is reversed, however, it is not generally possible to distinguish between a hard and persistent magnetization in the present-day field and a normal primary magnetization. For this reason most of the samples regarded as showing a primary magnetization are reversed.

The data are summarized in Fig. 9. The top map shows the locations of the sampled rocks and the dashed line marks the boundaries of the zone of strong rotation. Outside the dashed lines no rotations greater than 20° (and generally very much less than that) are found in rocks younger than 20 Myr. The bottom graph shows declinations and 95 per cent confidence limits plotted against age (known to about ±2 Myr). The letters relate the data on the map and the graph. The youngest declinations are obtained from data obtained by N. D. Watkins from the Mangapoike River (locality c, Fig. 9) a summary of which is reported in Kennett & Watkins (1974). The declination shown in the map at Banks Peninsula on the east coast of the South Island is from the work of Evans (1970); the remainder is reported in the papers cited in the beginning of this section.

Because of polar wander relative to the Australian Plate (Embleton 1981) the axial dipole field in New Zealand will show a progressive clockwise change in declination of about $1^\circ\,\mathrm{Myr}^{-1}$. There is, however, no significant change in declination in the New Zealand region due to polar-wander relative to the Pacific Plate. Thus the site west of the deformed zone in the central North Island (Fig. 9) shows no tectonic rotation and the sites to the north of the zone on East Cape indicate a counter-clockwise tectonic rotation of no more than 10°. The average rate of rotation within the deformed zone is given by the dashed line and is $4^\circ\,\mathrm{Myr}^{-1}$ or an average tectonic rotation of between 3 and $4^\circ\,\mathrm{Myr}^{-1}$ (the rotation of the axial dipole field due to polar wander will be $1^\circ\,\mathrm{Myr}^{-1}$ for sites on the Australian Plate, $0^\circ\,\mathrm{Myr}^{-1}$ for sites on the Pacific Plate and intermediate rates of rotation for intermediate sites).

The rate of tectonic rotation is however probably neither uniform in time nor in location. The rate of rotation in the NE of the South Island judging from site 'b' is about $5^\circ\,\mathrm{Myr}^{-1}$ as compared to less than $4^\circ\,\mathrm{Myr}^{-1}$ appropriate to site 'a'. Also the average rate of rotation over the last 5 Myr is about $6^\circ\,\mathrm{Myr}^{-1}$ and therefore the rate of rotation has probably increased with time. Both of these variations bring the long-term rotation into better agreement with the short-term rotation rate of about $8^\circ\,\mathrm{Myr}^{-1}$ ($0.13 \times 10^{-6}\,\mathrm{rad\,yr}^{-1}$), derived from the $\dot{\gamma}_2'$ component (Fig. 3) which has a value of about $0.26 \times 10^{-6}\,\mathrm{yr}^{-1}$ along most of the east coast of the North Island.

4 Discussion

The most important observation to be made in this study is the close similarity in pattern and in rate of short- and long-term kinematics. The dilatational component derived from shear strain rate data is close to that inferred from uplift studies based on geological data appropriate to a 10^6 yr time-scale: in the vicinity of the Southern Alps the average short-term value for $\dot{\gamma}_1'$ is $0.3 \times 10^{-6}\,\mathrm{yr}^{-1}$ whereas the average long-term rate for the same region is about

$0.2 \times 10^{-6}\,\mathrm{yr}^{-1}$ assuming that the rate of erosion over the last 10^4 yr is equal to the rate of uplift. The small difference is not significant given the uncertainties in the relationship between $\dot{\gamma}_1'$ and uplift rate. The short-term rotational strain rate is about $8^\circ\,\mathrm{Myr}^{-1}$ and for the long-term rotational strain rate the average over the last 5 Myr is about $6^\circ\,\mathrm{Myr}^{-1}$, and over the last 20 Myr it averages about $4^\circ\,\mathrm{Myr}^{-1}$ although it may be somewhat higher in the north-eastern part of the South Island. The rate of rotation has therefore apparently increased with time from around $3^\circ\,\mathrm{Myr}^{-1}$ in the period 5–20 Myr to the present-day value. Such an increase in the rate of rotation (and hence in the shear strain rate $\dot{\gamma}_2'$) is to be expected: in mid-Tertiary times when the relative plate motion was parallel to the plate boundary zone and the compressional component of strain (the $\dot{\gamma}_1'$ component of shear strain rate) was small or zero a large part of the relative plate motion could have been taken up by aseismic slip on the transform fault (as is happening in parts of California today): the amount of distributed shear parallel to the fault was probably small and, hence, so was the rotation. As compression increased perpendicular to the plate boundary, and the mountains commenced to rise, the degree of coupling between the plates would increase and the plate motion would be accommodated over a wider zone and the rate of shear ($\dot{\gamma}_2'$) and rotation ($\dot{\omega}$) would also increase.

4.1 THE ROLE OF FAULTING

The close similarity of short- and long-term kinematics raises the question of the role of faulting in the deformational process, for long-term deformation is the accumulated effect of a very large number of earthquakes whereas short-term deformation is that developed wholely within an interseismic period. It would appear that while earthquakes may dissipate the shear strains over small volumes of the plate boundary zone and fragment the zone into an assemblage of blocks, they affect the rotations and dilatations developed in the zone not at all. It is presumably a matter of scale. At a scale of a few hundred metres the shear, dilatational and rotational strains have been dissipated by fault movements at the boundaries of the blocks so that within an individual block the rocks are unstrained. But the motion on the faults at the boundaries of the blocks must be such as to produce a net rotation, and dilatation, and shear between the blocks, which at a scale of tens of kilometres can be modelled as if the faults did not exist. We can therefore treat the plate boundary as if it were a continuum, with a ductile deformation.

6 Conclusion

Continental crust in New Zealand, and in general, deforms in a very different manner to oceanic crust. Plate boundary zones are broader in the continents and the relative plate motion is accommodated by a widely distributed, although not necessary uniform, deformation. Instead of subduction at compressional boundaries crustal thickening occurs with consequent uplift; at extensional boundaries the motion is achieved by crustal thinning and possible subsidence instead of the creation of new crust: and at transform boundaries a very broad zone of shear, pervasive down to dimensions of a few kilometres, may develop within which unstrained crustal blocks of smaller dimensions may rotate. The study of deformation therefore involves the study of the rates, pattern and history of uplift or subsidence and of rotation from palaeomagnetic studies. Knowledge of rotation and crystal thickness changes gives quantitative information of the kinematics of the plate boundary zone.

The most important information for the study of present-day deformation is provided by geodetic surveys where they are available. A detailed knowledge of the shear strains throughout a plate boundary zone gives a very precise and complete picture of the present-day kinematics. Earthquake studies in continental plate boundary zones, while of undisputed value, may be very incomplete as only a fraction of the total slip across the zone in the case of New Zealand (Walcott 1979) and probably elsewhere, is accommodated by seismic slip. At the present time very few plate boundary zones have repeated geodetic surveys analysed in terms of shear strain although many must possess an initial survey of adequate accuracy to provide useful information if it were repeated. This paper, and previous work in New Zealand (Bibby 1975, 1976) has shown that the earlier surveys do not have to be of the most precise sort, for the relative inaccuracy of the older surveys is more than offset by the large time interval between the initial and repeated surveys.

Acknowledgments

The work on this paper was largely done while I was at Geophysics Division, DSIR, Wellington, and the paper was written while I was on leave from Victoria University of Wellington at the Department of Earth Sciences, Cambridge with assistance of an Anglo-Australasian Fellowship from the Royal Society and a Visiting Overseas Scholarship at St John's College, Cambridge. I am indebted to Hugh Bibby's critical insight for not being more wrong than I am, and to stimulating discussions with Dan McKenzie, Geof King and James Jackson.

References

Adams, J., 1980. Contemporary uplift and erosion of the Southern Alps, New Zealand, *Bull. geol. Soc. Am.*, **91**, 2–4.

Bevin, A. J., 1981. Geodetic surveys for earth deformation, in *Misc. Series*, **5**, *R. Soc. N.Z.*, pp. 87–96.

Bibby, H. M., 1973. The reduction of geodetic survey data for the detection of earth deformation, *Dept Sci. Indus. Res. Wellington, Geophys. Div. Rep. 84.*

Bibby, H. M., 1975. Crustal strain from triangulation in Marlborough, New Zealand, *Tectonophys.*, **29**, 529–540.

Bibby, H. M., 1976. Crustal strain across the Marlborough faults, New Zealand, *N.Z. Geol. Geophys.*, **19**, 407–425.

Bibby, H. M., 1981a. Geodetically determined strain across the Southern end of the Tonga-Kermadec-Hikurangi Subduction Zone, *Geophys. J. R. astr. Soc.*, **66**, 513–533.

Bibby, H. M., 1981b. Unbiased estimate of strain from triangulation data using the method of simultaneous reduction, *Tectonophys.*, **82**, 161–174.

Chase, C. G., 1978. Plate kinematics: the Americas, East Africa and the rest of the world, *Earth planet. Sci. Lett.*, **37**, 353–368.

Embleton, B. J. J., 1981. A review of the palaeomagnetism of Australia and Antarctica, in *Paleomagnetism of the Continents*, pp. 77–92, eds McElhinny, M. W. & Valencio, D. A., American Geophysical Union, Geodynamics Series, 2.

Evans, A. Ll., 1970. Geomagnetic polarity reversals in the Late Tertiary lava sequence from Akaroa Volcano, New Zealand, *Geophys. J. R. astr. Soc.*, **21**, 163–183.

Frank, F. C., 1966. Deduction of earth strains from survey data, *Bull. seism. Soc. Am.*, **56**, 35–42.

Grange, L. I., 1932. Taupo Earthquakes, 1922, *N.Z. Jl Sci. Technol.*, **14**, 139–141.

Haines, A. J., 1982. Calculating velocity fields across plate boundaries from observed shear rates, *Geophys. J. R. astr. Soc.*, **68**, 203–209.

Hatherton, T., 1980. Shallow seismicity in New Zealand, 1956–75, *J. R. Soc. N.Z.*, **10**, 19–25.

Kennett, J. P. & Watkins, N. D., 1974. Late Miocene – Early Pliocene palaeomagnetic stratigraphy, paleoclimatology and biostratigraphy in New Zealand, *Bull. geol. Soc. Am.*, **85**, 1383–1398.

McKenzie, D. & Jackson, J., 1983. The relationship between strain rates, crustal thickening, palaeomagnetism, finite strain and fault movements within a deforming zone, *Earth planet. Sci. Lett.*, **65**, 182–202.

Richter, C. F., 1958. *Elementary Seismology*, W. H. Freeman, San Francisco.

Royal Society of New Zealand, 1973. *Report on Earth Deformation Studies,* National Committee for Geological Sciencies, Royal Society of New Zealand.

Stern, T. A., 1984. A back-arc basin formed within continental lithosphere; the Central Volcanic Region of New Zealand, *Tectonphys.,* in press.

Stock, J. & Molner, P., 1982. Uncertainties in the relative positions of the Australia, Antarctica, Lord Howe and Pacific Plates since the Late Cretaceous, *J. geophys. Res.,* **87,** 4697–4714.

Walcott, R. I., 1978a. Present tectonics, and late Cenozoic evolution of New Zealand, *Geophys. J. R. astr. Soc.,* **52,** 137–164.

Walcott, R. I., 1978b. Geodetic strains and large earthquakes in the axial tectonic belt of North Island, New Zealand, *J. geophys. Res.,* **83,** 4419–4429.

Walcott, R. I., 1979. Plate motion and shear strain rates in the vicinity of the Southern Alps, *Bull. R. Soc. N. Z.,* **18,** 5–12.

Walcott, R. I., 1984. Reconstruction of the New Zealand region for the Neogene, *Palaeogeogr. Palaeoclim., Palaeoecol.,* **46,** 217–231.

Walcott, R. I., Christoffel, D. A. & Mumme, T. M., 1981. Bending within the axial tectonic belt of New Zealand in the last 9 My from paleomagnetic data, *Earth planet. Sci. Lett.,* **52,** 427–434.

Walcott, R. I., & Mumme, T. M., 1982. Paleomagnetic study of the Tertiary sedimentary rocks from the East Coast of the North Island, New Zealand, *Dept Sci. indus. Res., Geophys. Div. Rep. 189,* 44 pp.

Wellman, H. W., 1979. An uplift map for the South Island of New Zealand and a model for uplift of the Southern Alps, *Bull. R. Soc. N.Z.,* **18,** 13–20.

Geophys. J. R. astr. Soc. (1984) **79**, 635–649

Electrical resistivity structure of the Senegal basin as determined from magnetotelluric and differential geomagnetic soundings

M. Ritz *Office de la Recherche Scientifique et Technique Outre-Mer, B.P. 1386, Dakar, Sénégal, West Africa*

Received 1984 May 8; in original form 1983 July 11

Summary. The methods of magnetotelluric (MT) and differential geomagnetic soundings (DGS) have been applied to study the electromagnetic response of the structure of the Senegal sedimentary basin. The measurements at 10 sites were carried out along a profile running perpendicularly across a zone of north–south flexures and faults over the period range 10–1000 s. Variation of periods up to 10 000 s were obtained at two sites. The anomalous geomagnetic variation field across the major fault zone is characterized by an increase in the magnetic eastward component. Two-dimensional modelling of the apparent resistivities and phases reveals a highly anomalous upper crustal structure involving a low-resistivity zone in the central part of the basin (less than 30 Ωm). To satisfy the additional long-period data at two sites, a deep conductor is also required at a depth below 300 km with a resistivity less than 10 Ωm. The crustal discontinuity located ~ 200 km off the coast is possibly related to the opening of the Atlantic Ocean. The difficulty in resolving the question of the nature of the crust in this region results in part from the limitations of the methods used at present for this determination.

1 Introduction

During the last 3 yr, the time-varying electric and magnetic fields have been measured by the Office de la Recherche Scientifique et Technique Outre-Mer (ORSTOM) at 10 sites along a profile crossing the Senegal basin and extending along the 14th parallel. A schematic cross-section of the sedimentary basin as redrawn from De Spengler, Castelain & Leroy (1966) and Liger (1980) shows the general pattern of the area from the Atlantic coast to the Mauritanides along the latitude of the Dakar Peninsula (Fig. 1). That cross-section shows a Precambrian crystalline basement dipping to the west under a wedge of post-Palaeozoic sedimentary rocks of more than 5 km (Mesozoic and Cenozoic sediments). The motivation for the field experiment was to determine the resistivity values associated with the zone of N–S flexures and faults along longitude 15°W and to see if changes in electrical character of the crust and/or upper mantle can be expected to occur between the deep basin and the zone outside of the actual post-Jurassic sedimentary basin. The present paper reports on

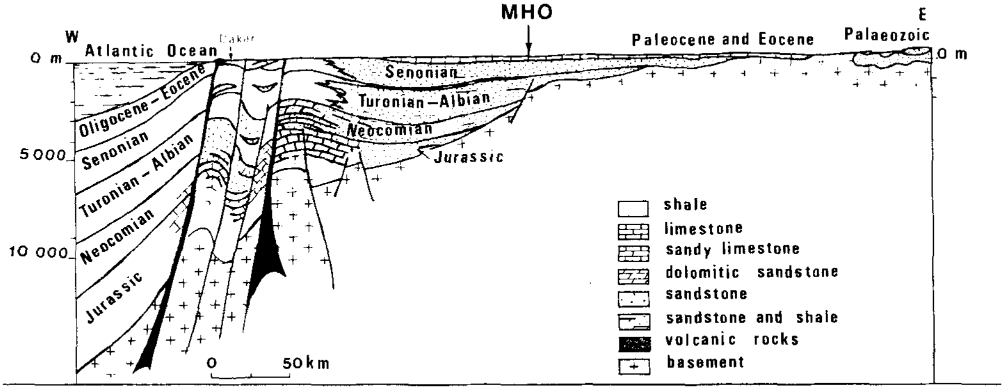

Figure 1. Cross-section of the Senegal basin from De Spengler *et al.* (1966) and Liger (1980).

the MT and DGS results from sites referred to in Table 1. The locations of the recording sites of this study are shown in Fig. 2. The full names, abbreviated station names as used in Fig. 2 and the station coordinates are given in Table 1.

The Senegal coastal basin situated on the western edge of Western Africa broadly extends to the boundaries of Senegal as it lies between the 10 and 21° northern parallels (Guinea Bissau and Mauritania). It is bounded in the east by the West African mobile belt (Hercynian orogenic belt–Mauritanides). This basin was formed during the Jurassic period before the transgression of the Cretaceous period, then extended to the Tertiary with a great subsidence towards the west (Dillon & Sougy 1974). During this period, between 210 and 170 Myr, at the end of the different stages of rifting of the Trias, one witnesses the aperture of the Atlantic Ocean with the formation of a new oceanic crust (Le Pichon & Fox 1971). The subsidence and the Mesozoic rifting of the West African margin responsible for the formation of the Senegal basin was very likely accompanied by the intrusion of magmatic material into predominantly coast-parallel fissures and fractures (Van der Linden 1981).

Geophysical studies have been carried out in Senegal basin: gravity studies, electrical soundings, drillings and aeromagnetic profiles. The area between KAH and MBM showing a strong gravity gradient is interpreted in terms of thick mafic intrusions within the basement

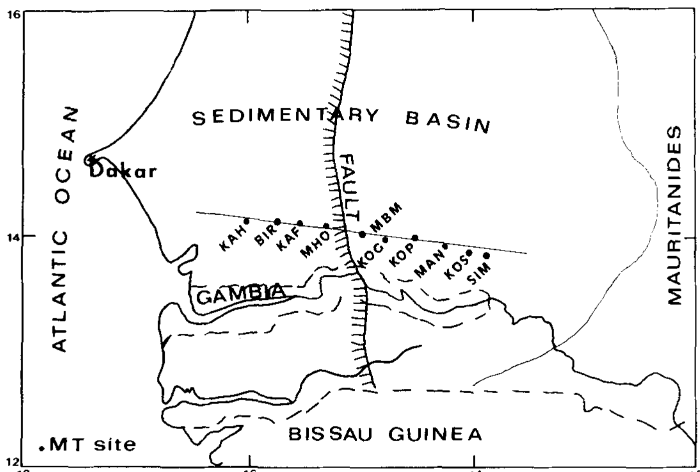

Figure 2. Location map of the magnetotelluric sounding sites in relation to the major fault.

Table 1. Mt sites, code names and geographic coordinates.

Station name	Code	Long. (W)	Lat. (N)
Kahone	KAH	16° 02′	14° 09′
Birkelane	BIR	15° 45′	14° 08′
Kaffrine	KAF	15° 33′	14° 06′
Malème Hodar	MHO	14° 18′	13° 56′
Mbaye Mbaye	MBM	15° 00′	14° 00′
Koungheul	KOG	14° 58′	13° 59′
Koumpentoum	KOP	14° 33′	13° 59′
Malème Niani	MAN	14° 18′	13° 56′
Koussanar	KOS	14° 03′	13° 52′
Sinthiou Malème	SIM	13° 55′	13° 50′

complex (Liger 1980). Many electrical soundings carried out with line AB of 6000 m give us an idea of the thickness of the sedimentary series above the basement (Compagnie Générale de Géophysique 1957). However, the depth of the investigation through the electrical soundings is relatively weak (of the order of 1000 m) and the resistant basement easily visible to the east, disappeared in the west from the meridian 15 °W. Below the deep basin, the nature and depth of the basement are generally unknown.

2 Observations and processing

Magnetic variations were measured using Mosnier sensors which give the *H* and *D* components of the magnetic field (Mosnier & Yvetot 1972). These are horizontal variometers with suspended magnet and feedback. The sensitivity is 10 mV γ^{-1}. Telluric variations trending N–S and E–W were detected through the measurement of the potential difference between pairs of lead electrodes situated 500 m apart and at a depth of 1.50 m. Magnetic and telluric signals were filtered and amplified in the period band ranging from 10 to 1000 s before reaching the recording equipment, which is composed of two 'Sefram' graphic recorders. The same equipment is found at the moving station and at the reference station. Recordings were made simultaneously at a reference station (SIM). The electromagnetic fields were recorded for one week at each site. Approximately one month of long-period MT data was recorded simultaneously at the two sites SIM and MHO. The analogue traces were digitized at 3 s intervals, by means of a trace-follower digitizing table.

Two methods have been used to study the structure basin:

(a) *Magnetotellurics*: the horizontal and orthogonal components of the electric and magnetic fields, which are measured at the surface, are combined by a complex transfer function, the impedance tensor *Z*. The elements of *Z* depend on the resistivity distribution and the orientation of the measuring coordinate system (Cantwell 1960; Madden & Nelson 1964; Vozoff 1972; Beblo & Björnsson 1978). Two parameters, the apparent resistivity $\rho_a(T)$ and the phase difference between the electric and magnetic field $\phi(T)$ are calculated as functions of period from the impedance tensor. For a two-dimensional earth (2-D), the principal impedance values are calculated with axes parallel and perpendicular to the strike of the 2-D structure (TE and TM directions). From these are derived the parallel and perpendicular resistivities and phases (Thayer 1975). For each period, the angular rotation of the impedance tensor yields an estimate of the structural strike. For each site, apparent resistivities and phases in the principal directions are computed and are plotted in Figs 3, 4 and 5.

(b) *Differential geomagnetic soundings*: the geomagnetic variation field produced by lateral variations in the telluric current system has a vertical component and produces anomalous variations in the regional horizontal field. The total geomagnetic variations field is thus composed of a source component and an induced component produced by the telluric current system. Consequently, to study the variation field, a reference site is located so that it can be assumed to be influenced only by the regionally uniform telluric current system and by the source field, which is assumed to be uniform over the study area. By subtracting the horizontal field observed at this base station from the fields observed at the field stations, the anomalous field due to the non-uniform component of the telluric current can be determined (Babour & Mosnier 1977). Telluric current concentrations are controlled by the electrical conductivity structure of the crust and upper mantle. Under the assumption of a uniform source with infinite spatial wavelengths, the observed field field variations, comprised of normal and anomalous field variations, can be fitted statistically to the frequency-domain relation (Schmucker 1970):

$$\begin{pmatrix} H_a \\ D_a \end{pmatrix} = \begin{pmatrix} h_H & h_D \\ d_H & d_D \end{pmatrix} \begin{pmatrix} H_n \\ D_n \end{pmatrix} + \begin{pmatrix} \delta_H \\ \delta_D \end{pmatrix}$$

(H_a, D_a) is the Fourier transform of the anomalous field, i.e. the field associated with the lateral conductivity inhomogeneities, (H_n, D_n) denotes the Fourier transform of the normal field, and (δ_H, δ_D) is a residual field.

Geomagnetic field variations at Sinthiou Maleme (SIM) were chosen as the reference in calculations of the anomalous geomagnetic variation field across the basin. Site SIM is about 200 km east of the major fault (Fig. 2). At each station the azimuth θ of a linearly polarized, horizontal reference field that maximizes the correlated part of the anomalous field, is calculated. This direction is the preferential induction direction (Vasseur *et al.* 1977). In order to know the frequency dependence of the anomaly, we have computed the transfer function $G(f)$ linking the anomalous field at each site, to the normal field (SIM) projected on the induction direction. The response will be a maximum (or minimum) along this axis (Banks & Ottey 1974).

3 Results

3.1 MAGNETOTELLURIC RESULTS

We have calculated 10 tensor MT soundings covering the period range from 10 to 1000 s. The resulting principal axis orientation proved to be quite stable across the entire period band and the average principal direction is given in Table 2 for each station. We note a sudden change in the principal axis orientation between sites KOG and KOP. The axes are oriented N–S in the deep basin and at both MBM and KOG (this direction is roughly parallel to the strike of the prominent N–S trending fault), but are more E–W for all other sites (except KOS). It can be seen (Fig. 1) that the significant rotation occurs outside of the actual post-jurassic sedimentary basin and it is probable that this indicates the presence of boundaries between two structures of different electrical conductivity, mainly near the surface, but also at greater depths (Ritz 1983). Figs 3 and 4 show the calculated values for the apparent resistivities and phases from rotated impedance for all the 10 sites, separately for the TE and TM directions. The values of resistivities at the site KOP are elevated by a factor of 2 compared to the adjacent site KOG. At site KAF, which is about 40 km west

Table 2. Orientation of the principal axes of the impedance tensors (clockwise from north).

Station	KAH	BIR	KAF	MHO	MBM	KOG	KOP	MAN	KOS	SIM
Orientation	33°	13°	13°	7°	16°5	17°	48°	66°	Undefined	62°

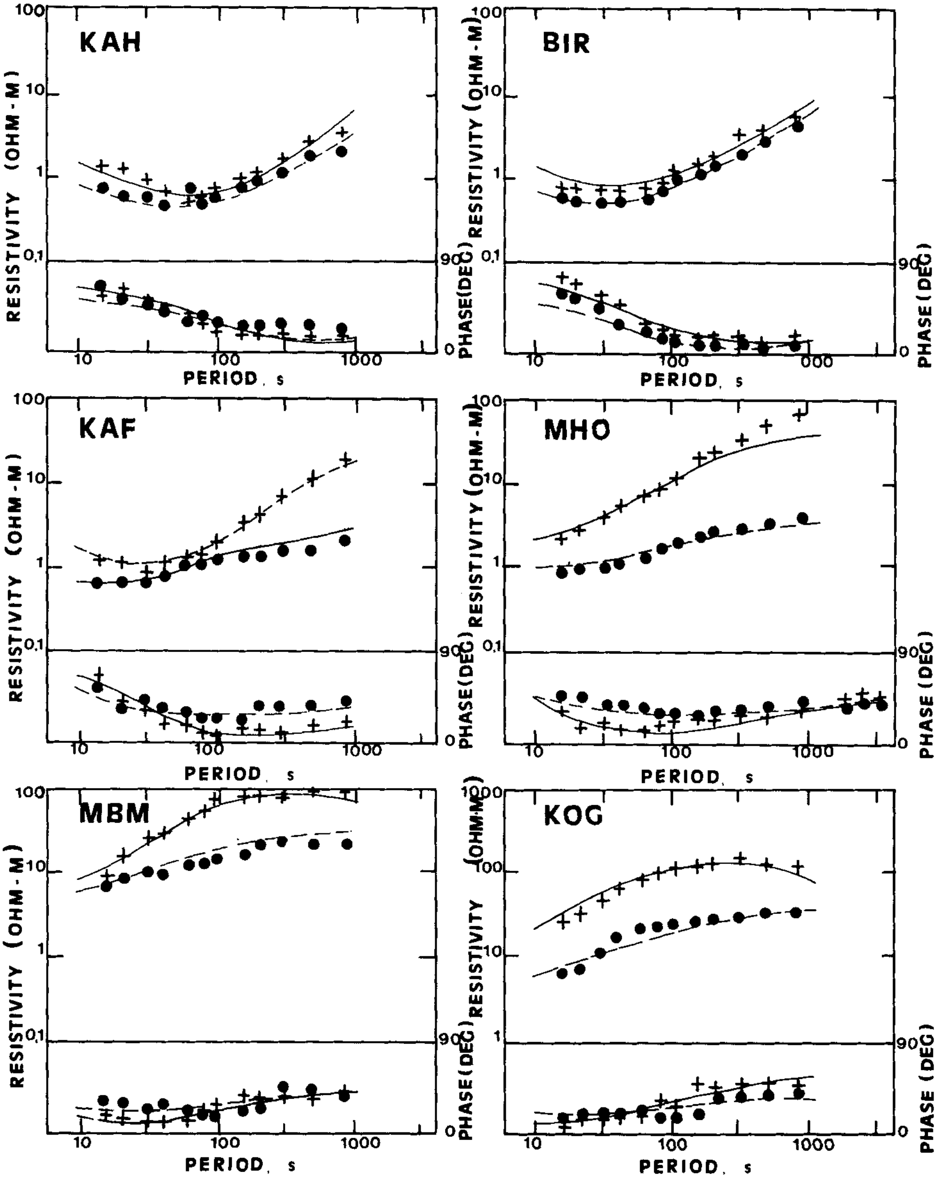

Figure 3. Apparent resistivities and phases for the MT sites on the Senegal basin. The principal resistivities and phases for the TE and TM directions are shown by crosses and solid circles, respectively. Solid and dashed lines through the measured values are theoretical curves calculated from the model shown in Fig. 10.

of the fault, the significant divergence of the TE and TM amplitudes at periods above 100 s shows clearly the effect of lateral resistivity variations. This type of behaviour continues in a progressively increased manner, from west to east, up to the site KOG (about 30 km east of the fault). The long-period MT data at the two sites MHO and SIM, until about 10 000 s, are presented in Fig. 5. The long-period data for site MHO display increasing anisotropy with increasing period. The azimuths of the maximum resistivity principal direction are nearly invariant over all the period bands analysed.

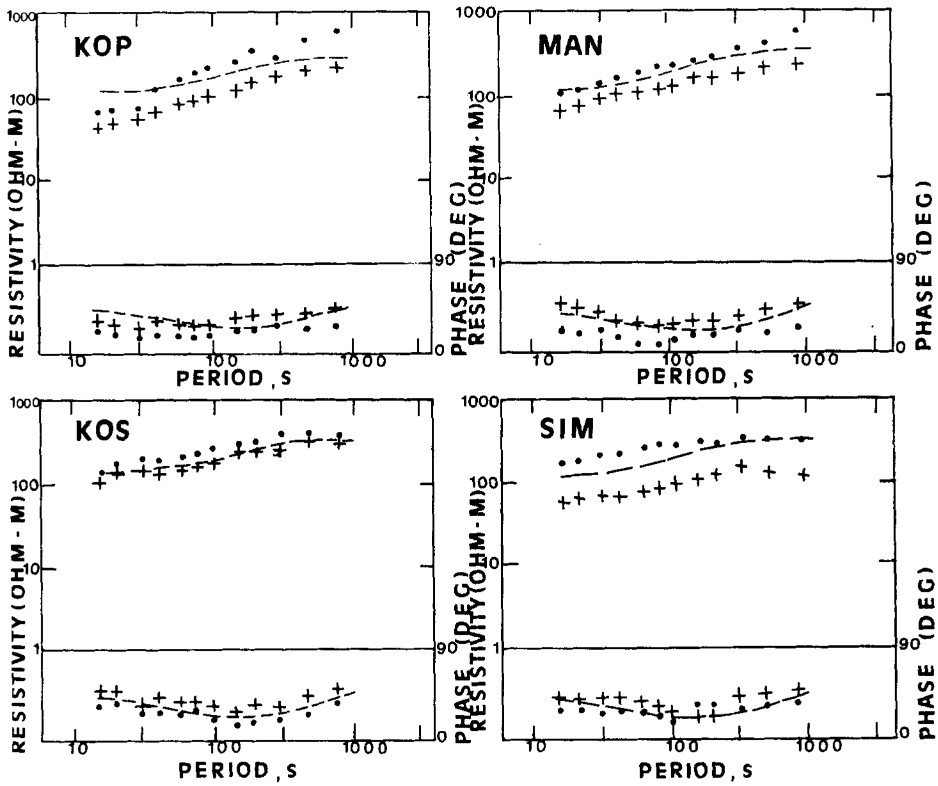

Figure 4 – *continued.*

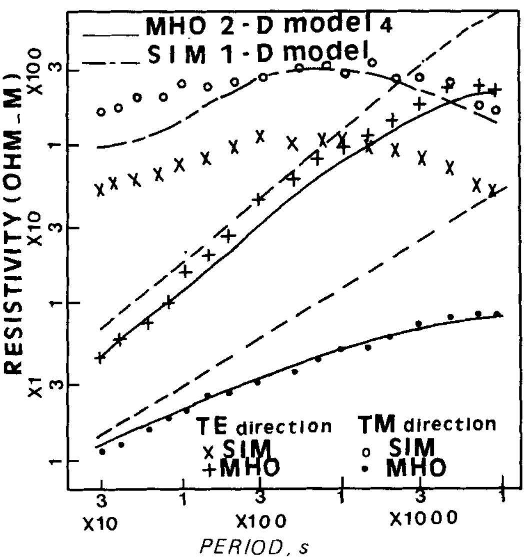

Figure 5. TE and TM sounding curves at the long-period MT sites. Solid and dashed curves are the result of the 2-D model calculations at MHO with upper crustal conductor present (model 4) and removed (model 1), respectively. The curve defined by the long and short dashes is the response of the 1-D model shown in Fig. 10 at SIM.

For the region to the east of KOG, the data for site KOS are the most nearly 1-D, as can be seen from the near coincidence of the major and minor apparent resistivities. The data for sites KOP, MAN and SIM show splits between the TE and TM amplitudes, but the phase data practically coincide (except MAN). Through site SIM, difference between resistivity values for the two directions, is relatively constant throughout the period range (Fig. 5). In this region, with a thin sedimentary cover (Fig. 1), there are possibly some 2- or 3-D features maintaining the separation in the data. Theoretical calculations show that local 2- or 3-D surface inhomogeneities have a strong influence on the amplitude data and but a weak influence on the phase data. In this situation the major curve (TE or TM) will be closer to the 1-D curve without shallow heterogeneity (Berdichevsky & Dimitriev 1976). The maximum apparent resistivity observations through sites KOP, MAN, and SIM are practically identical with the observations at site KOS (Fig. 4), where data are not distorted

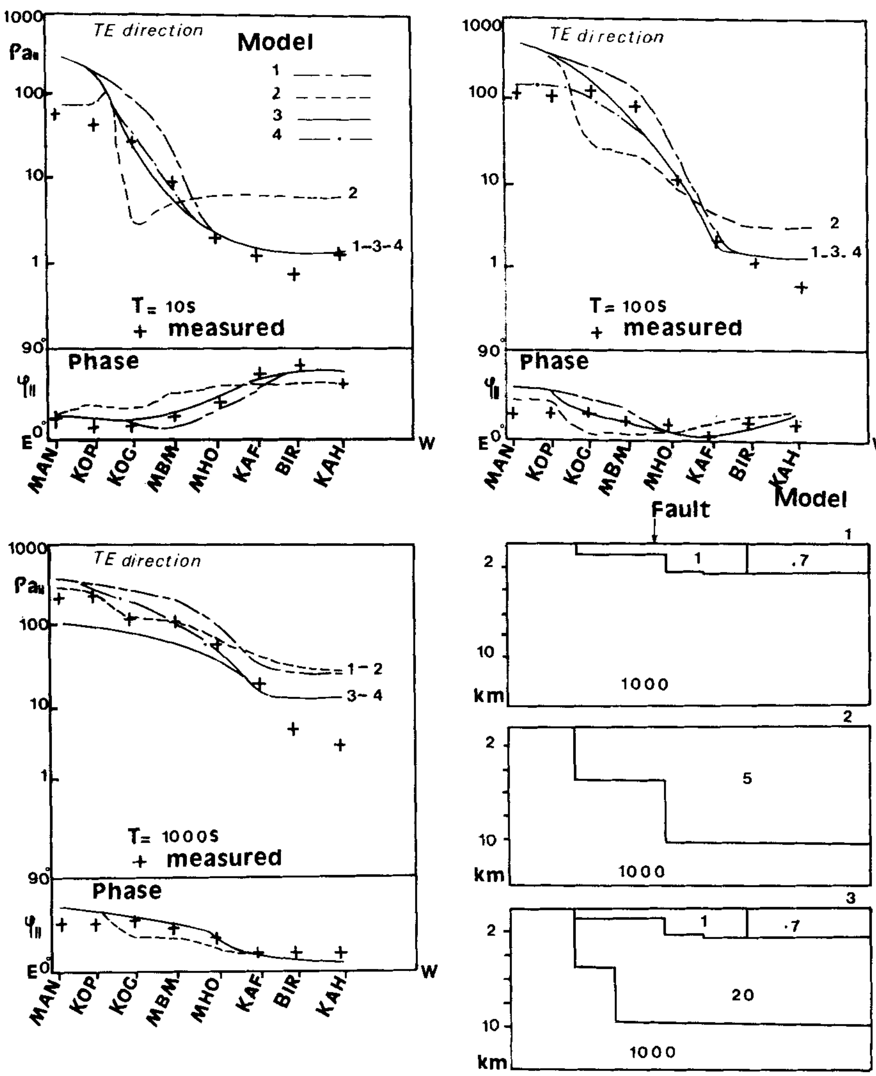

Figure 6. Variation of MT data along the profile for the TE direction case, for periods 10, 100 and 1000 s and results of calculation for three models shown at the right side of the figure. (The overburden is not displayed in these models.) At 1000 s, the phase curves are similar for the models 1 and 3.

significantly by the presence of the lateral near-surface inhomogeneities. This obvious similarity therefore point to a similar 1-D conductivity structure under these four stations. The apparent anisotropy at KOP, MAN and SIM indicates distortion of the electromagnetic field due to lateral heterogeneities which are shallower than the penetration depth of the shortest period measured.

Electromagnetic fields penetrate into the Earth to depths which vary depending on the Earth conductivity and the period of the signals. The depth of sounding can be related to period by use of the concept of the penetration depth [$p(\text{km}) = \sqrt{10\,\rho T}/2\pi$, ρ is the resistivity in ohm metres, T is the period in seconds]. The sedimentary layers of the Senegal deep basin were expected to have low resistivity. Over a 1 Ωm basin, we measured the resistivity from the surface to a depth of about 1500 m at 10 s, 5000 m at 100 s and to about 16 km at 1000 s. Figs 6 and 7 show the observed values of the TE and TM apparent resistivities and phases along the profile between MAN and KAH for 10, 100 and 1000 s. The TE resistivities form a gradual transition between the high resistivity (towards the east) to low resistivity region (towards the west). The apparent resistivity along the profile, for the sites to the west of KOG, rises somewhat with the penetration depth indicating layers.

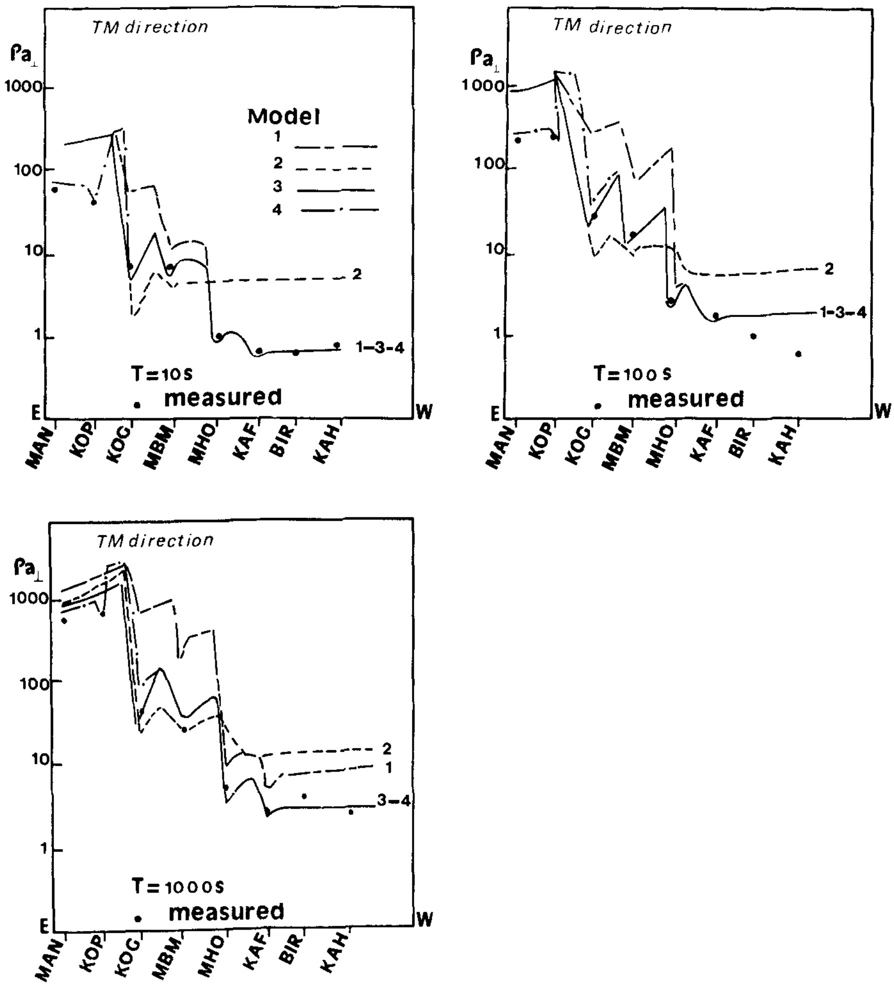

Figure 7. As Fig. 6 for the TM direction (apparent resistivities only).

When the period increases at site MHO from 10 to 100 s ($p \sim 1.5-6$ km), both TE and TM apparent resistivities increase, indicating penetration of the electromagnetic fields into a resistive layer. The variation in apparent resistivity is insignificant for KAF, BIR and KAH, reflecting lateral homogeneity of the surface sediments within the vicinity of these sites. No detailed knowledge of the deep basin is available; however, the basement slopes down from about 800 m in the east (KOS) to about 10 km in the Dakar area (Fig. 1). The top of the basement is a layer boundary at which the resistivity is increased by a factor between 10 and 1000 (Losecke, Knödel & Müller 1979). It seems reasonable to assume that the resistive layer under MHO could be associated with the basement at depths between 1.5 and 6 km, and that the horizon of the layer continuously deepens towards KAF, BIR and KAH (at some depth greater than 6 km). In the case of TM direction, on the western border of the profile, Figs 6 and 7 show steep resistivity gradients as the basement front is approached. Apparent resistivities of several hundred ohm metres are associated with the crystalline or metamorphic basement.

3.2 MAGNETIC RESULTS

The amplitude of the magnetic eastward geomagnetic variation field (D component) increases for KOG, MBM, MHO, KAF, BIR and KAH, with the result that the amplitude of the D component at MHO is about twice that of the reference station SIM. The variations in the horizontal north (H) component appear to be identical at the 10 stations. We have calculated the induction direction for these sites. These directions lie between 90° and 110° in the period range from 30 to 1000 s. Fig. 8 shows the frequency dependence of the induction direction at a representative site (KAF). The residual geomagnetic variation field D_a is linked only to the horizontal east (D_n) component. We have calculated the transfer function $G(f)$ and the phase linking D_a, obtained at each site, to the normal field (SIM), projected on the induction direction 100°. The modulus of the maximum response and the phase of $G(f)$ as a function of the period are presented for the site KAF in Fig. 8. The anomalous geomagnetic variation field along the profile with the period of 100 s is displayed in Fig. 9. The anomalous field D_a/D_n has a maximum between MHO and KAF at 100 s. The anomalous geomagnetic field variation across the fault could be accounted for by one or more of the following: concentration of currents by conductive structures (sediments), direct induction in the underlying structures so that the 2-D modelling could

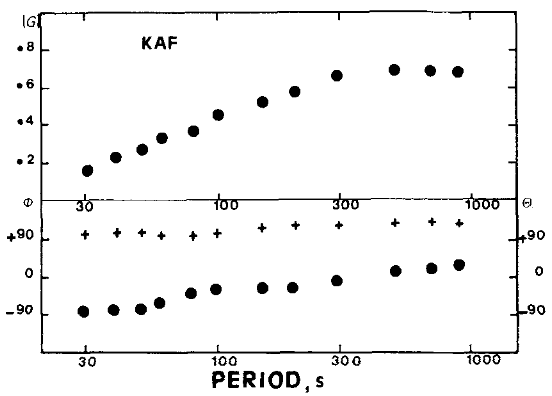

Figure 8. Transfer function G as a function of period (modulus and phase) computed between the anomalous geomagnetic variation field D_a (KAF) and the normal horizontal field (SIM) projected on the induction direction θ (crosses indicate the induction direction).

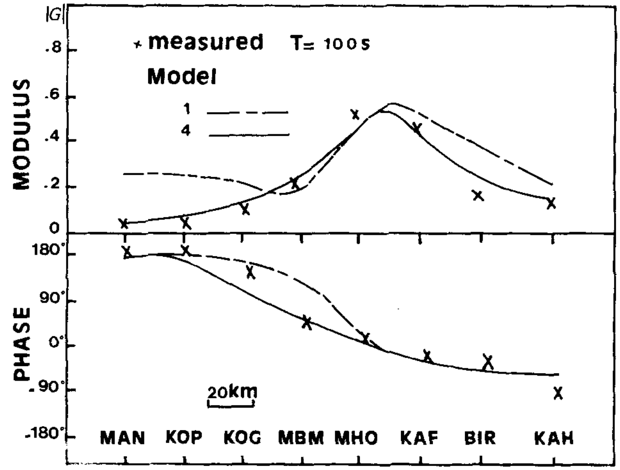

Figure 9. Observed anomalous horizontal field along the profile with a period of 100 s. The lines through the measured values are theoretical curves calculated from models presented in Fig. 6. Model 4 not represented in Fig. 6 (*cf.* p. 645).

be used to fit the observed anomaly (Bailey *et al.* 1974; Gough 1981; Gregori & Lanzerotti 1982). Whatever the inductive mechanism, a maximum depth for the current system can be made from the well-defined anomaly of the Fig. 9 (Gough 1973). Estimate gives a maximum depth of 25 km. In differential geomagnetic sounding basins with well conducting sediments can be recognized by large disturbances of the normal geomagnetic field. This is due to telluric currents, which are induced in the conductive sediments of the basin in addition to the large-scale uniform telluric current system in the area. As the additional electric current system in the basin flows only in the striking direction of the basin (that is about N–S for the Senegal basin), the anomalous geomagnetic variation field is only measured in the *D* component of the magnetic variations. The *H* component is not affected by the non-uniform component of the telluric current system (Babour & Mosnier 1979). The Senegal basin consists of two parts along the profile, an eastern thin part and a western thicker part (Fig. 1). At a first glance, it appears that electric current flow in the sediments of the deep basin might cause this anomalous horizontal field.

4 Modelling

On the basis of the above observations, modelling for the 10 sites was done by using a combination of inverse 1-D computations (Jupp & Vozoff 1975), and 2-D forward modelling (Stodt 1978). In constructing the 1- or 2-D models in order to fit the electromagnetic data the following assumptions were made.

(1) In the region at some distance of the fault, about 60 km east and more, the resistivity is a function of depth only (similarity of the major and minor apparent resistivity at KOS).

(2) The electrical conductivity structure beneath a part of the basin is 2-D, so that a line from KOG to KAH direct would be at right angle to the N–S trending fault.

(3) An overburden of average resistivity 15 Ωm extends down to 800 m, overlaid the region. This assumption is supported by the electrical soundings for the uppermost sedimentary layer and corresponds to the known structure of the basin.

(4) The zone of N–S flexures and faults along longitude 15 °W marks the line of division between two contrasting regions. This is based on the sudden decrease of the apparent resistivity between KOG and MHO at 10 s (Figs 6 and 7).

The inversion was done on both the major apparent resistivity and phase data simultaneously for stations east of the site KOG. A layered earth model of four layers is adequate to describe the major data (Fig. 4). For SIM, there is improvement of fit at periods greater than 1000 s if the number of layers is increased to one (Fig. 5). This model indicates a resistive crust underlain by material of 50 Ωm starting at a depth of about 20 km (Fig. 10). For site SIM, the model was developed to estimate the highly conducting portion of the mantle. A five-layered model suggests a conducting layer of approximately 10 Ωm beginning at 300 km.

At the right side of Fig. 6 three of the several 2-D models constructed are shown as a simple approximation to the resistivity distribution. The simplest model is the model 1 with a major lateral conductivity change between MBM and MHO: On the hand basement, on the other hand the deep basin extending to a depth of 1.5–3 km with $\rho = 1-0.7$ Ωm. Model 2 consists of well-conducting material with several kilometres thickness (until 10 km) beneath the deep basin. Model 3 is a combination of models 1 and 2 with various conductors added to the sedimentary basin at crustal depths. Model 4 (not displayed in Fig. 6) is similar to model 3 with a conductive crustal layer (~ 50 Ωm) at a depth between 20 and 30 km under

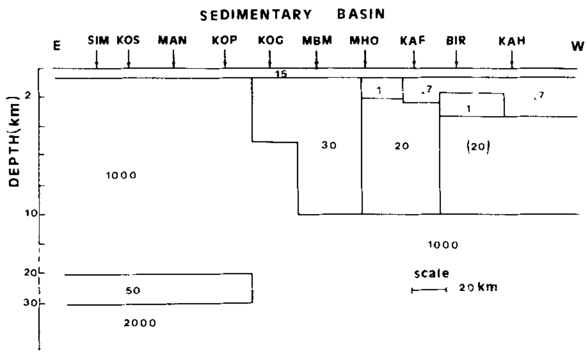

Figure 10. East–west 2-D resistivity model for Senegal basin. The conducting portion of the mantle beginning at 300 km is not represented. The numbers indicate assumed resistivities in ohm metres. The parameter in brackets is poorly resolved.

KOP and MAN. Observations and model calculations have been made with the periods, 10, 100 and 1000 s (Figs 6 and 7). The apparent resistivities are shown for both TE and TM direction cases, the phases are shown for the TE direction case only. The phases for model 4 are not illustrated here. For the TE and TM directions the results of measurements and the calculated curves fit best for model 4. However, between MHO and KAH at periods less than 100 s, the same apparent resistivity curves are obtained for the models 1 and 3. At 1000 s, the difference between these resistivity curves is relatively little, the periods of variations are not long enough to discriminate between a resistant layer (model 1) and a good conducting one (model 3). The distinction between these two models cannot be estimated accurately at this stage so that we are not convinced that an anomalously good conducting layer exists under the deep basin. Long-period MT data for site MHO and the results for models 1 and 4 are represented in Fig. 5 for the purpose of comparing the model resistivities with the measured resistivities. These model calculations for long-period variations have mainly been made to see if a well-conducting zone may be assumed below the deep basin. For periods of 1000 to 10 000 s, there is a significant difference in the form of the apparent resistivity curves (TE and TM directions) calculated for the models 1 and 4. It is interesting to note the increase in the discrepancy between the results of measurements and the calculated curves for model 1. A resistant layer below the deep basin at MHO is inadequate to fit the TE and TM values at long periods. Two-dimensional modelling of the long-period data from this site shows that the class of models which fit the MHO observations suggests that there is an anomalously good conductive layer in the upper crust. Because of the lack of long-period MT data at BIR and KAH, the horizontal extension of the well-conducting layer can be reliably determined only to a distance of about 45 km to west of the major fault. On the basis of the model studies (Figs 5, 6 and 7), it seemed to be reasonable to assume the existence of a good conductor in the upper crust (< 10 km thick) to a distance of about 45 km to each side of the N–S trending fault.

Model 4, between KOG and KAF, was adapted to provide a reasonable fit for the MT data (Fig. 10). The results for final model are also shown in Figs 3 and 5 along with the field results (TE and TM directions). At long periods adjustment of the model can be achieved by placing the transition from high to low mantle resistivity at approximately 300 km at SIM and MHO.

For the geomagnetic data two simple 2-D models are used. They correspond to the models 1 and 4 (see Fig. 6). Model 4 is not presented in Fig. 6 (*cf.* p. 645). If we assume the models to strike in a N–S direction, we can compare the calculated data with the magnetic eastward component of the field measurements. The modulus and phase of D_a/D_n are plotted along the profile for 100 s in Fig. 9. Model 1 shows that electric current flow in the well-conducting sediments of the basin produces excessive anomalous horizontal fields at the westernmost sites.

The observed values of D_a/D_n along the profile best fit the model 4, where a crustal conductive structure is added to the sedimentary model. The response of this type of model across the basin is shown with the observed anomalous geomagnetic variation field in Fig. 9. The study of the anomalous geomagnetic variation field along the profile partly contributes to a more exact determination of the upper crustal layer under KAF, BIR and KAH and suggests that an anomalously well-conducting layer is quite likely below the deep basin.

Final adjustment of the model 4 was made to provide an adequate fit for the values of the TE and TM apparent resistivities and phases (Figs 3 and 4). Although the final model (Fig. 10) gives results which approximately correspond to the field results, the uniqueness of this model cannot be guaranteed because of the number of assumptions involved.

To summarize, the following can be said: the MT measurements can be interpreted in a satisfactory way only if an anomalously well-conducting layer is assumed below the sedimentary basin between KOG and KAF. This layer begins close to the surface beneath the eastern basin (KOG and MBM) and dips to the west under a wedge of Mesozoic and Cenozoic sediments of more than 2 km; it has a resistivity of about 20–30 Ωm, and a thickness of less than 10 km. Geomagnetic measurements suggest the lateral extension of this layer under BIR and KAH. It is interesting to note that the two methods are necessary to show the existence in this region of the upper crustal conductor. Crustal electrical resistivity structure in Senegal basin derived from MT and DGS measurements is shown in Fig. 10.

5 Discussion

5.1 NATURE OF THE CRUSTAL RESISTIVITY ANOMALIES

The zone of enhanced electrical conducting which has been inferred at lower crustal depths beneath the eastern basin is common. High conductivities for depths of about 15–35 km have been found by many investigators using the magnetotelluric, geomagnetic and controlled source experiments below different tectonic provinces of the Earth (see, for example: Blohm, Worzyk & Scriba 1977; Van Zijl 1977; Jones & Hutton 1979; Connerney, Nekut & Kuckes 1980; Edwards, Bailey & Garland 1981; Ingham & Hutton 1982; Kurtz 1982). Regarding conducting zones in a depth of 15 km and more, several theories exist: partial melting in the presence of a small quantity of water of the moderate temperatures (Lebedev & Khitarov 1964), hydration processes (Hyndman & Hyndman 1968), a combination of basic rock type and high pore fluid pressures (Lee, Vine & Ross 1983). In this area no measurement of the heat flow has been obtained and higher than normal temperatures in the crust cannot be ruled out as a possible interpretation of the crustal conducting layer below the eastern basin. In order to determine the nature of the conducting layer in the crust, it is very desirable to couple electromagnetic methods with seismic investigations.

An important feature of the electromagnetic results is that the entire upper crust down to about 10 km has a resistivity less than 30 Ωm (in western basin, Fig. 10). The sedimentary unit represents the actual post-Jurassic basin with Cenozoic and Mesozoic sediments. Resistivity of this unit is of about 1 Ωm. In Canada, the Mesozoic–Cenozoic sediments of the Coastal Plain may have resistivities as low as a few ohm metres (Greenhouse & Bailey 1980). Beneath this sedimentary sequence the resistivity is anomalously low (20–30 Ωm). A range of possible interpretations for this zone is summarized here. Resistivities of 30 Ωm or less can be related to the presence of the thermal fluids (Thayer 1975). Electrolytic conduction in pore fluids is the dominant conduction mechanism in the upper 8 km and a shallow conductor at crustal depth can then be explained by increased porosity in the host rock, increased temperature, or increased salinity of the fluid. The conductor under the deep basin could be associated with saline water, slight variations in porosity could then provide resistivity variations as suggested by Fig. 10. The low resistive zone could be also in relations with the existence of a fractured zone with high water content along the zone of N–S faults. The difference between the low (20 Ωm) and the relatively low (30 Ωm) zone might arise from a difference in degree of fracture and degree of water content. This zone can be also connected with the presence of conducting minerals (Gough 1981).

5.2 TECTONIC IMPLICATIONS

The most significant result of the present experiment is the existence of a crustal discontinuity in the basin located ~200 km off the Atlantic. The tectonic history of the basin accounts perhaps for the present-day variations in electrical characteristics and depth of conductors located in the lower crust below the eastern basin and in the upper crust beneath the deep basin.

In the basin, the expected crustal thinning in the transition from continental crust in the east to an oceanic type crust in the Dakar area (Rabinowitz 1979; Liger 1980) makes it is difficult to say whether the good conductor below the deep basin marks an anomalous layer in the upper crust or the crust–mantle boundary. Liger (1980) interprets the coastal positive Bouguer gravity values in terms of a considerable thinning of crust and gives a crustal thickness of 12 km under the Cape Verde peninsula (Dakar). Burke (1976, fig. 1) reveals the existence of a deep, sediment-filled graben in Senegal (Casamance graben) between 50 and 100 km wide striking for 400 km well within the basin. The development of this graben is associated with the opening of the Atlantic Ocean between 210 and 170 Myr ago. The geology of the graben is poorly known, drilling on one of salt diapirs produced a basement rock of altered basalt (Hayes *et al.* 1971). It is quite likely that the Mesozoic rifting was widely accompanied by rapid accumulation of several kilometres of sediment and intrusion of magmatic material into fractures (Dillon & Sougy 1974).

Does the MT model support this view? Cenozoic and Mesozoic sediments, with resistivities as low as 1 Ωm may well be associated with saline water in rift fractures. Below the actual post-Jurassic sedimentary basin, the anomalously low resistivity could reflect the presence of fractured wet and possibly altered magmatic material in association with the Ocean opening. The crust in this region was of continental origin, with strong contamination by basaltic intrusions. The measuring site of KOG probably marks the boundary of the Triassic graben in the Precambrian basement and extends over a distance of about 100 km. It is possible that the conductive zone in the upper crust delineates an old zone of weakness which was associated with magmatic activity over a long time during the formation of the Senegal basin. It appears, however, that definite conclusions seem to be still premature or largely speculative. More detailed results may be reached in the future by additional MT soundings, seismic investigations and measurements of the heat flow.

Acknowledgments

Thanks are due to J. Vassal and M. Chauvin for their assistance in this study; especially L. Mollard, the Technical Engineer for the MT equipment since 1972. I am also grateful to P. Perichon and other personnel of the Bondy Laboratory, for computational assistance.

References

Babour, K. & Mosnier, J., 1977. Differential geomagnetic soundings, *Geophysics*, **42**, 66–76.

Babour, K. & Mosnier, J., 1979. Differential geomagnetic soundings in the Rhinegraben, *Geophys. J. R. astr. Soc.*, **58**, 135–144.

Bailey, R. C., Edwards, R. M., Garland, G. D., Kurtz, R. & Pitcher, D., 1974. Electrical conductivity studies over a tectonically active area in eastern Canada, *J. Geomagn. Geoelect.*, **26**, 125–146.

Banks, R. J. & Ottey, P., 1974. Geomagnetic deep sounding in and around the Kenya rift valley, *Geophys. J. R. astr. Soc.*, **36**, 321–335.

Beblo, M. & Björnsson, A. J., 1978. Magnetotelluric investigation of the lower crust and upper mantle beneath Iceland, *J. Geophys.*, **45**, 1–16.

Berdichevsky, M. N. & Dimitriev, V. I., 1976. Basic principles of interpretation of magnetotelluric sounding curves, in *Geoelectric and Geothermal Studies*, pp. 163–221, ed. Adam, A., Akademiai Kiado, Budapest.

Blohm, E. K., Worzyk, P. & Scriba, H., 1977. Geoelectrical depth soundings in southern Africa using the the Cabora Bassa power line, *J. Geophys.*, **43**, 665–679.

Burke, K., 1976. Development of graben associated with the initial ruptures of the Atlantic Ocean, *Tectonophys.*, **36**, 93–112.

Cantwell, T., 1960. Detection and analysis of low frequency magnetotelluric signals, *PhD thesis*, Massachusetts Institute of Technology.

Compagnie Générale de Géophysique, 1957. *Reconnaissances hydrauliques et structurales par sondages électriques au Sénégal, en Mauritanie et en Casamance*, Paris.

Connerney, J. E. P., Nekut, A. & Kuckes, A. F., 1980. Deep crustal electrical conductivity in the Adirondacks, *J. geophys. Res.*, **85**, 2603–2614.

De Spengler, A. J., Castelain, J. & Leroy, M., 1966. Le bassin secondaire-tertiaire du Sénégal, in *Bassins Sédimentaires du Littoral Africain, Littoral Atlantique*, pp. 80–94, ed. Reyre, D., Symp. Ass. Serv. Géol. Africain, New Delhi, 1964.

Dillon, W. P. & Sougy, M. A., 1974. Geology of West Africa and Canary and Cape Verde Islands, in *The Ocean Basins and Marings, 2. The North Atlantic*, pp. 315–390, eds Nairn, A. E. M. & Stehli, F. G., Plenum Press.

Edwards, R. N., Bailey, R. C. & Garland, G. D., 1981. Conductivity anomalies: lower crust or asthenosphere?, *Phys. Earth planet. Int.*, **25**, 263–272.

Gough, D. I., 1973. The interpretation of magnetometer array studies, *Geophys. J. R. astr. Soc.*, **35**, 83–98.

Gough, D. I., 1981. Magnetometer arrays and geodynamics, in *Evolution of the Earth, Geodynamics Series, Am. geophys. Un.*, **5**, 87–95.

Greenhouse, J. P. & Bailey, R. C., 1981. A review of geomagnetic variation measurements in the eastern United States: implications for continental tectonics, *Can. J. Earth Sci.*, **18**, 1268–1289.

Gregori, G. P. & Lanzerotti, L. J., 1982. Electrical conductivity structure in the lower crust, *Geophys. Surveys*, **4**, 467–499.

Hayes, D. E., Pimm, A. C., Benson, W. E., Berger, W. H., Von Rad, U., Sapko, P. R., Beckmann, J. P., Roth, P. H. & Musich, L. F., 1971. Deep sea drilling project, Leg 14, *Geotimes*, **16**, 14–17.

Hyndman, R. D. & Hyndman, D. W., 1968. Water saturation and high electrical conductivity in the lower continental crust, *Earth planet. Sci. Lett.*, **4**, 427–432.

Ingham, M. R. & Hutton, V. R. S., 1982. The interpretation and tectonic implications of the geoelectric structure of Southern Scotland, *Geophys. J. R. astr. Soc.*, **69**, 595–606.

Jones, A. G. & Hutton, V. R. S., 1979. A multistation magnetotelluric study in Scotland – II. Monte-Carlo inversion of the data and its geophysical and tectonic implications, *Geophys. J. R. astr. Soc.*, **56**, 351–368.

Jupp, D. L. B. & Vozoff, K., 1975. Stable iterative methods for the inversion of geophysical data, *Geophys. J. R. astr. Soc.*, **42**, 957–976.

Kurtz, R. D., 1982. Magnetotelluric interpretation of crustal and mantle structure in the Greenville Province, *Geophys. J. R. astr. Soc.*, **70**, 373–397.

Lebedev, E. B. & Khitarov, N. T., 1964. Dependence of the beginning of melting of granite and the electrical conductivity of its melt on high vapour pressure, *Geochem. Int.*, **1**, 193–197.

Lee, C. D., Vine, F. J. & Ross, R. G., 1973. Electrical conductivity models for the continental crust based on laboratory measurements on high-grade metamorphic rocks, *Geophys. J. R. astr. Soc.*, **72**, 353–371.

Le Pichon, X. & Fox, P. J., 1971. Marginal offsets, fracture zones, and the early opening on the North Atlantic, *J. geophys. Res.*, **76**, 6294–6307.

Liger, J. P., 1980. Structure profonde du bassin côtier sénégalo-mauritanien. Interprétation des données gravimétriques et magnétiques, *Thèse 3ème cycle*, University Aix-Marseille III.

Losecke, W., Knödel, K. & Müller, W., 1979. The conductivity distribution in the North German sedimentary basin derived from widely spaced areal magnetotelluric measurements, *Geophys. J. R. astr. Soc.*, **58**, 169–179.

Madden, T. & Nelson, P., 1964. A defense of Cagniard's magnetotelluric method, *Geophys. lab. O.N.R., Project NR*, pp. 371–401, Massachusetts Institute of Technology.

Mosnier, J. & Yvetot, P., 1972. Nouveau type de variomètre à aimant asservi en direction, *Annls Géophys.*, **28**, 219–224.

Rabinowitz, P. D., 1974. The boundary between oceanic and continental crust in the western North Atlantic, in *The Geology of Continental Margins*, pp. 67–84, eds Burk, C. A. & Drake, C. L., Springer-Verlag.

Ritz, M., 1983. The distribution of electric conductivity on the eastern border of the West African craton (Republic of Niger), *Geophys. J. R. astr. Soc.*, **73**, 475–488.

Schmucker, U., 1970. Anomalies of geomagnetic variations in the south-western United States, *Bull. Scripps Inst. Oceanogr.*, **13**, University of California Press.

Stodt, J. A., 1978. Documentation of a finite element program for solution of geophysical problems governed by the inhomogeneous 2-D scalar Helmholtz equation, *Rep. AER 76-11155, Dept Geol. Geophys.*, University of Utah, Salt Lake City.

Thayer, R. E., 1975. Telluric-magnetotelluric investigations of regional geothermal processes in Iceland, *PhD thesis*, Geological Sciences at Brown University.

Van der Linden, W. J. M., 1981. The crustal structure and evolution of the continental margin off Senegal and the Gambia, from total-intensity magnetic anomalies, *Geologie Mijnb.*, **16**, 257–266.

Van Zijl, J. S. V., 1977. Electrical studies of the deep crust in various provinces of South Africa, in *The Earth's Crust*, ed Heacock, J. G., *Geophys. Monogr. Am. geophys. Un.*, **20**, 470–500, Washington DC.

Vasseur, G., Babour, K., Menvielle, M. & Rossignol, J. C., 1977. The geomagnetic variation anomaly in the northern Pyrénées: study of the temporal variation, *Geophys. J. R. astr. Soc.*, **49**, 593–607.

Vozoff, K., 1972. The magnetotelluric method in the exploration of sedimentary basins, *Geophysics*, **37**, 98–141.

Geophys. J. R. astr. Soc. (1984) 79, 651–690

UK National Report for the Quadrennium 1979–1983 to the International Association of Geomagnetism and Aeronomy

At its meeting on 1983 March 14 the Geomagnetism and Aeronomy Sub-Committee of the Royal Society decided that the United Kingdom report to the IAGA for the four years 1979–1983 should take the form of a bibliography of papers published in the period 1979 June to 1983 June excluding any papers previously reported in 'Geomagnetism and Aeronomy Research in the United Kingdom 1975–1979' published by the Royal Society, and submitted to the International Association of Geomagnetism and Aeronomy at the XVII General Assembly of IUGG, Canberra, 1979 December. Letters requesting information were circulated to 53 research groups in the UK and the bibliography which follows was compiled by B. R. Leaton and K. M. Creer from returns from 38 of these research groups.

ABRAHAMSEN, N. & READMAN, P.W., 1980. Geomagnetic variations recorded in Older (> 23,000 B.P.) and Younger Yoldia Clay (ca. 14,000 BP) at Norre Lyngby, Denmark, **Geophys. J. R. astr. Soc., 62,** 329-344.

AITKEN, M.J., ALCOCK, P.A. , BUSSELL, G.D. & SHAW, C.J., 1981. Archaeomagnetic determination of the past geomagnetic intensity using ancient ceramics: allowance for anisotropy, **Archaeometry, 23,** 53-64.

BALOGH, A., HEDGECOCK, P.C., SMITH, E.J. & TSURUTANI, B.T., 1983. The magnetic field investgation of the International Solar Polar Mission, **ESA SP-1050.**

BANKS, R.J., 1981. Strategies for improved global electromagnetic response estimates, **J. Geomag. Geoelectr., 33,** 569-585.

BANKS, R.J., BEAMISH, D. & GEAKE, M.J., 1983. Magnetic variation anomalies in northern England and southern Scotland, **Nature, 303,** 516-518.

BARBETTI, M., TABORIN, Y., SCHMIDER, B. & FLUDE, K., 1980. Archaeomagnetic results from late Pleistocene hearths at Etiolles and Marsangy, France, **Archaeometry, 22,** 25-46.

BARKER, F.S., BARRACLOUGH, D.R. & MALIN, S.R.C., 1981. World magnetic charts for 1980 - spherical harmonic models of the geomagnetic field and its secular variation, **Geophys. J. R. astr. Soc., 65,** 525-533.

BARNETT, J.J., HOUGHTON, J.T. & PESKETT, G.D., 1979. Observations of the stratosphere and mesosphere from Nimbus satellites, **Printed from (COSPAR) Remote Sounding of the atmosphere from space,** 83-88, (Innsbruck).

BARNETT, J.J., 1980. Satellite measurements of middle atmosphere temperature structure, **Phil. Trans. R. Soc. Lond., A296,** 41-57.

BARRACLOUGH, D.R., 1981. The 1980 geomagnetic reference field, **Nature, 294,** 14-15.

BARRACLOUGH, D.R., 1982. Historical observations of the geomagnetic field, **Phil. Trans. R. Soc. Lond., A306,** 71-78.

BARRACLOUGH, D.R., 1982. Evaluation of IGRF 1980 candidate models, **J. Geomag. Geoelectr., 34,** 383-385.

BARRACLOUGH, D.R. & MALIN, S.R.C., 1979. Geomagnetic secular acceleration, **Geophys. J. R. astr. Soc., 58,** 785-793.

BARRACLOUGH, D.R. & MALIN, S.R.C., 1981. An algorithm for synthesizing the geomagnetic field, **Computers & Geosciences, 7,** 401-405.

BARRACLOUGH, D.R. & MALIN, S.R.C., 1981. A definitive model of the geomagnetic field and its secular variation for 1965 - II. Dip poles from surface to core, **Geophys. J. R. astr. Soc., 65,** 467-473.

BARRACLOUGH, D.R. & MALIN, S.R.C., 1981. 150 years of the North Magnetic Pole, **Nature, 291,** 377.

BARRACLOUGH, D.R., HODDER,B.M. & MALIN, S.R.C., 1982. The IGS proposal for the new international geomagnetic Reference Field, **J. Geomag. Geoelectr, 34,** 351-356.

BEAMISH, D., 1979. Source field effects on transfer functions at mid-latitudes, **Geophys. J. R. astr. Soc., 58,** 471-493.

BEAMISH, D., 1980. Diurnal characteristics of transfer functions at pulsation periods, **Geophys. J. R. astr. Soc., 61,** 623- 643.

BEAMISH, D., 1982. A geomagnetic precursor to the 1979 Carlisle earthquake, **Geophys. J. R. astr. Soc., 68,** 531-543.

BEAMISH, D., 1982. The time-dependence of electromagnetic response functions, **Geophys. Surv., 4,** 405-434.

BEAMISH, D., 1982. Anomalous geomagnetic variations on the island of South Georgia, **J. Geomag. Geoelectr., 34,** 479 -490.

BEAMISH, D., 1983. A comparison of time and frequency domain geomagnetic sounding, **Geophys. J. R. astr. Soc., 73,** 689-704.

BEAMISH, D. & HAMILTON, R.A., 1983. The influence of tectonic boundaries on geomagnetic variations in the Scotia Sea, **British Antarctic Survey Bulletin, 59,** 1-8.

BEAMISH, D., HANSON, H.W.& WEBB, D.C., 1979. Complex demodulation applied to Pi2 geomagnetic pulsations, **Geophys. J. R. astr. Soc., 58,** 471-493.

BEAMISH, D., HEWSON-BROWNE, R.C., KENDALL, P.C., MALIN, S.R.C. & QUINNEY, D.A., 1980. Induction in arbitrarily shaped oceans, IV: Sq. for a simple case, **Geophys. J. R. astr. Soc., 60,** 435-443.

BEAMISH, D., HEWSON -BROWNE, R.C., KENDALL, P.C., MALIN, S.R.C. & QUINNEY, D.A., 1980. Induction in arbitrarily shaped oceans, V: the circulation of Sq-induced currents around land masses, **Geophys. J. R. astr. Soc., 61,** 479-488.

BEAMISH, D. & JOHNSON, P.M., 1982. Difficulties in the application of magnetic field gradient analysis to induction studies, **Phys. Earth Planet. Inter., 28,** 1-13.

BECKMANN, G.E.J., 1979. A review of Nagssugtoqidian palaeomagnetism, **Rapp. Gronlands geol. Unders., 89,** 115-124.

BECKMANN, G.E.J., 1981. Comments on The Palaeomagnetism of the Central Zone of the Lewisian foreland, north-west Scotland by J.D.A. Piper, **Geophys. J. R. astr. Soc., 66,** 463-470.

BECKMANN, G.E.J., 1982. Palaeomagnetism of nine dated Phanerozoic dykes in south-east Greenland, **Geophys. J. R. astr. Soc., 69,** 355-368.

BECKMANN, G.E.J., 1983. Palaeomagnetism of some Precambrian rocks in south-east Greenland, **Phys. Earth Planet. Inter., 32,** 85-99.

BERING, E.A. ROSENBERG, T.J., BENBROOK, J.R., DETRICK, D., MATTHEWS, D.L., RYCROFT, M.J., SAUNDERS, M.A. & SHELDON, W.R., 1980. Electric fields, electron precipitation and VLF radiation during a simultaneous magnetospheric substorm and atmospheric thunderstorm, **J. geophys. Res., 85,** 55-72.

BEYNON, SIR GRANVILLE, 1981. The Upper Atmosphere, **Proc. R. Institution,** 229-262.

BIRD, C.F. & PIPER, J.D.A., 1981. Opaque petrology, magnetic polarity and thermodynamic properties in the Reydarfjordur dyke swarm, eastern Iceland, **Jokull, 30,** 34-41.

BORRADAILE, G.J. & TARLING, D.H., 1981. The influence of deformation mechanisms on magnetic fabrics in weakly deformed rocks, **Tectonophys., 77,** 151, 168.

BRIDEN, J.C., 1979. The Earth' s magnetic memory, **Univ. Leeds Rev., 22,** 19-31.

BRIDEN, J.C., 1981. Precambrian orogenies and polar wandering, **Nature, 289,** 125-126.

BRIDEN, J.C. & ARTHUR, G.R., 1981. Precision of measurement of remanent magnetization, **Canadian J. Earth Sci., 18,** 527-538.

BRIDEN, J.C., CLARK, R.A. & FAIRHEAD, J.D., 1981. Gravity and magnetic studies in the Channel Islands, **J. Geol. Sci., 139,** 35-48.

BRIDEN, J.C., DUFF, B.A. & KRONER, A., 1979. Palaeomagnetism of the Koras Group, Northern Cape Province , South Africa, **Precam. Res., 10,** 43-57.

BRIDEN, J.C. & DUFF, B.A., 1981. Pre-Carboniferous palaeomagnetism of Europe north of the Alpine orogenic belt, in: **Palaeoconstruction of the Continents, eds. McElhinny, M.W. and Valencio, D.A., Amer. Geophys. Union, Geodynamic Series, 2,** 137-149.

BRIDEN, J.C. & PIPER, J., 1982. Late Precambrian-Palaeozoic palaeomagnetism and evolution of the Caledonides, **Terra Cognita, 2,** 10-11.

BRIDEN, J.C., REX, D.C., FALLER, A.M. & TOMBLIN, J.F., 1979. K-Ar geochronology and palaeomagnetism of volcanic rocks in the Lesser Antilles island arc, **Phil. Trans. R. Soc. Lond., A291,** 485-528.

BRIDEN, J.C., REX, D.C., FALLER, A.M. & TOMBLIN, J.F., 1979. K-Ar geochronology and palaeomagnetism of volcanic rocks in the Lesser Antilles Island Arc, **Geophys. J. R. astr. Soc., 57,** 272.

BRIDEN, J.C., SMITH, A.G. & HURLEY, A.M., 1981. Palaeomagnetism and Mesozoic-Cenozoic Palaeocontinental maps, **J. geophys. Res., 86,** B12, 631-656.

BROOM, S.M. & RODGER, A.S., 1982. The nocturnal intermediate layer over South Georgia: solar and magnetic influence on occurrence, **J. atmos. terr. Phys., 44,** 713-717.

BROWN, C. & GIRDLER, R.W., 1982. Structure of the Red Sea at 20^{o}N from gravity data and its implication for continental margins, **Nature, 298,** 51-53.

BROWN, G.M., 1979. New methods for predicting the magnitude of sunspot maximum, Solar-Terrestrial Prediction Proceedings, **U.S. Dept. of Commerce, 2,** 264-279.

BROWN, G.M., 1981. Prediction techniques for forthcoming solar maxima, **The Physical Basis of the Ionosphere in the Solar-Terrestrial System, AGARD CP295,** 31/ 1-31/ 7.

BROWN, G.M., 1981. Possible use of (a) solar faculae and (b) the interplanetary magnetic field as heralds of a solar cycle peak, **Solar Phys., 74,** 125-129.

BROWN, G.M. & BUTCHER, E.C., 1981. The use of abnormal quiet days in Sq(H) for predicting the magnitude of sunspot maximum at the time of the preceding sunspot minimum, **Planet. Space Sci., 29**, 73-77.

BROWN, G.M. & EVANS, D.R., 1980. The use of solar faculae in studies of the sunspot cycle, **Solar Phys., 66**, 233-243.

BROWN, G.M. & EVANS, D.R., 1980. Latitude variations of photospheric activity areas with particular reference to solar faculae, **Solar Phys., 68**, 141-149.

BROWN, G.C. & MUSSETT, A.E., 1981. **The Inaccessible Earth, Allen and Unwin, London**, 235pp.

BROWN, M.G., 1981. Towards the Numerical Atmosphere, **Nature, 292**, 290.

BROWN, M.G. & DUNGEY, J.W., 1983. Economising plasma simulation by total neglect of the displacement current, **J. Computational Phys.,**

BROWNSCOMBE, J.L. & SCHLAPP, D.M., 1983. The lunar semi-diurnal tide observed by stratospheric sounding units on the TIROS-N series of satellites, **J. atmos. terr. Phys., 45**, 27-32.

BRYANT, D.A., 1981. Rocket studies of particle structure associated with auroral arcs, **AGU Geophysical Monograph, 25**, 103.

BRYANT, D.A., 1982. The hot electrons in and above the auroral ionosphere - observations and physical implication, **Proc. Nobel Symp. on Problems in magnetospheric/ionospheric Plasma Physics and Strategies for their solution, Kiruna.**

BUTCHER, E.C. & BROWN, G.M., 1980. Abnormal quiet days and the effect of the interplanetary magnetic field on the apparent position of the Sq focus, **Geophys. J. R. astr. Soc., 63**, 783-789.

BUTCHER, E.C. & BROWN, G.M., 1981. On the nature of abnormal quiet days in Sq(H), **Geopyhys. J. R. astr. Soc., 64**, 513-526.

BUTCHER, E.C. & BROWN, G.M., 1981. The variability of Sq(H) on normal quiet days, **Geophys. J. R. astr. Soc., 64**, 527-537.

CANNON, P.S. & RYCROFT, M.J., 1982. Schumann resonance frequency variations during sudden ionospheric disturbances, **J. atmos. terr. Phys., 44**, 201-206.

CARRIGAN, C.R. & GUBBINS, D., 1979. The source of the Earth's Magnetic Field, **Sci. Amer. Feb.,** 118-130.

CHRISTIANSEN, P.J. & GOUGH, M.P., 1980. Electron cyclotron waves in the Earth's Magnetosphere, **The Polar Ionosphere, Reidel.**

CHRISTIANSEN, P.J., GOUGH, M.P, MARTELLI, G. & BLOCH, J.J., 1979. GEOS 1 observations of electrostatic waves and their relationship with plasma parameters, **Advances in Magnetospheric physics with GEOS 1 and ISEE, Reidel**, 63.

CHROSTON, P.N., EVANS, C.J. & LEE, C., 1979. Laboratory measurements of compressional wave velocities and electrical resistivity of basalts from DSDP Leg 49, **in Initial Reports of the Deep Sea Drilling Project**, Luyendyk, B.P., et al., 49, 761-763, US Government Printing Office, Washington.

CISOWSKI, S.M., COLLINSON, D.W., RUNCORN, S.K., STEPHENSON, A. & FULLER, M., 1983. A review of lunar palaeointensity data and implications for the origin of lunar magnetism, **J. geophys. Res., 88**, A691-704.

CLARK, D.H. & STEPHENSON, F.R., 1980. Establishing the case for Maunder Minimum, **Nature, 284**, 592.

COLLIN, H.L., SHARP, R.D., SHELLEY, E.G. & JOHNSON, R.G., 1981. Some general characteristics of upflowing ion beams over the auroral zone, and their relationship to auroral electrons, **J. geophys. Res., 86**, 6820-6826.

COLLINSON, D.W., 1979. On the possibility of using Lunar fines to determine the intensity of the ancient Lunar magnetic field, **Phys. Earth Planet. Inter., 20**, 312-316.

COLLINSON, D.W., 1980. An investigation of the scattered remanent magnetization of the Dunnet Head sandstone, **Geophys. J. R. astr. Soc., 62**, 393-402.

COLLINSON, D.W., 1982. Methods in Rock Magnetism and Palaeomagnetism, **Chapman and Hall, London, 0-412-22980-3.**

COWLEY, S.W.H., 1980. Plasma populations in a simple open model magnetosphere, **Space Sci. Rev., 26**, 217-275.

COWLEY, S.W.H., 1980. A closer look at Saturn's magnetosphere, **Nature, 285**, 302-303.

COWLEY, S.W.H., 1980. The problem of defining a substorm, **Nature, 286**, 332-333.

COWLEY, S.W.H., 1980. Jupiter's magnetosphere, **Nature, 287**, 775-776.

COWLEY, S.W.H., 1981. Magnetospheric asymmetries associated with the Y-component of the IMF, **Planet. Space Sci., 29**, 79-96.

COWLEY, S.W.H., 1981. Magnetospheric and ionospheric flow and the interplanetary magnetic field, **The Physical Basis of the Ionosphere in the Solar-Terrestrial System, AGARD-CP-295**, pp.4-1 to 4-14.

COWLEY, S.W.H., 1981. A new magnetic reconnection experiment in the laboratory, **Nature, 291**, 191-192.

COWLEY, S.W.H., 1981. Asymmetry effects associated with the X-component of the IMF in a magnetically open magnetosphere, **Planet. Space Sci., 29,** 809-818.

COWLEY, S.W.H., 1982. The causes of convection in the Earth's magnetosphere: A review of developments during the IMS, **Rev. Geophys. Space Phys., 20,** 531-565.

COWLEY, S.W.H., 1982. Substorms and the growth phase problem, **Nature, 295,** 365-366.

COWLEY, S.W.H. & HUGHES, W.J., 1983. Observation of an IMF sector effect in the Y magnetic field component at geostationary orbit, **Planet. Space Sci., 31,** 73-90.

COWLEY, S.W.H & SCHULL, P. Jr., 1983. Current sheet acceleration of ions in the geomagnetic tail and the properties of ion bursts observed at the lunar distance, **Planet. Space Sci., 31,** 235-245.

COWLEY, S.W.H. & SOUTHWOOD, D.J., 1980. Some properties of a steady-state geomagnetic tail, **Geophys. Res. Lett., 7,** 833-836.

CREER, K.M., 1981. Long period geomagnetic secular variations since 12000 yr B.P., **Nature, 292,** 208-212.

CREER, K.M., 1982. Lake sediments as recorders of geomagnetic field variations - applications to dating post-Glacial sediments, **Hydrobiologia, 92,** 587-596.

CREER, K.M., 1983. Palaeomagnetism through the lifetime of Geophysical Journal - a brief personal view, **Geophys. J. R. astr. Soc., 74,** 159-161.

CREER, K.M., 1983. Computer synthesis of geomagnetic palaeosecular variations, **Nature, 304,** 695-699.

CREER, K.M., HOGG, E., MALKOWSKI, Z., MOJSKI, J.E., NIEDZIOLKA-KROL, E., READMAN, P.W. & TUCHOLKA, P., 1979. Palaeomagnetism of Holocene lake sediments from north Poland, **Geophys. J. R. astr. Soc., 59,** 287-313.

CREER, K.M., HOGG, T.E., READMAN, P.W. & REYNAUD, C., 1980. Palaeomagnetic secular variation curves extending back to 13,400 B.P. recorded by sediments deposited in Lac de Joux, Switzerland, **J. Geophys., 48,** 139-147.

CREER, K.M. & PAPAMARINOPOULOS, S., 1983. The palaeomagnetism of Cave sediments, Section 4.7 (pp.243-249) in **Geomagnetism of Baked Clays and Recent sediments (eds. K.M. Creer, P. Tucholka and C.E. Barton), Elsevier,** 324 pp.

CREER, K.M., READMAN, P.W. & JACOBS, A.M., 1980. Palaeomagnetic and palaeontological dating of a section at Gioia Tauro, Italy:

identification of the Blake Event, **Earth Planet. Sci. Lett., 50,** 303-314.

CREER, K.M., READMAN, P.W. & PAPAMARINOPOULOS, S., 1981. Geomagnetic secular variations in Greece through the last 6000 years obtained from lake sediment studies, **Geophys. J. R. astr. Soc., 66,** 193-219.

CREER, K.M. & TUCHOLKA, P., 1982. Construction of type curves of geomagnetic secular variation for dating lake sediments from east-central N. America, **Can. J. Earth Sci., 19,** 1106-1115.

CREER, K.M. & TUCHOLKA, P., 1982. Secular variation as recorded in lake sediments: a discussion of North American and European Results, **Phil. Trans. R. Soc. Lond., A306,** 87-102.

CREER, K.M. & TUCHOLKA, P., 1982. The shape of the geomagnetic field through the last 8500 years over part of the Northern Hemisphere, **J. Geophys., 15,** 188-198.

CREER, K.M. & TUCHOLKA, P., 1983. On the current state of lake sediment palaeomagnetic research, **Geophys. J. R. astr. Soc., 74,** 223-238.

CREER, K.M. & TUCHOLKA, P., 1981. Epilogue - chapter 5 (pp. 273-305) in **Geomagnetism of Baked Clays and Recent Sediments (eds. K.M. Creer, P. Tucholka and C.E. Barton), Elsevier,** 324 pp.

CREER, K.M., TUCHOLKA, P., VALENCIO, D.A., SINITO, A.M. & VILAS, J.F.A., 1983. Palaeomagnetism of lake sediments - results from Argentina Section 4.5 (pp.231-236) in **Geomagnetism and Baked Clays and Recent Sediments, (eds. K.M. Creer, P. Tucholka and C.E. Barton,)** Elsevier, 324 pp.

CREER, K.M., VALENCIO, D.A., SINITO, A.M., TUCHOLKA, P. & VILAS, J.F.A., 1983. Geomagnetic secular variations 0-14000 bp as recorded by lake sediments from Argentina, **Geophys. J. R. astr. Soc., 74,** 199-221.

DABROWSKI, A., TKACZ, M. & TUCHOLKA, P., 1980. Magnetostratigraphical elements of Vistulian glaciation in Poland, **Quaternary Studies in Poland, 2,** 7-12.

DAGLEY, P. & MUSSETT, A.E., 1981. Palaeomagnetism of the British Tertiary igneous province: Rhum & Canna, **Geophys. J. R. astr., Soc., 65,** 475-491.

DAGLEY, P., MUSSETT, A.E., WILSON, R.L. & HALL, J.M., 1978. The British Tertiary igneous province: palaeomagnetism of the Arran Dykes, **Geophys. J. R. astr. Soc., 54,** 75-91.

DELDERFIELD, J., SCHOFIELD, J.T. & TAYLOR, F.W., 1980. Radiometer for the Pioneer Venus Orbiter, **IEEE Transactions on Geoscience and Remote Sensing, GE-18,** 70-76.

DENBY, M., BULLOUGH, K., ALEXANDER, P.D. & RYCROFT, M.J., 1980. Observational and theoretical studies of a cross meridian refraction of VLF waves in the ionosphere and magnetosphere, **J. atmos. terr. Phys., 42,** 51-60.

DICKINSON, P.H.G., BAIN, W.C., THOMAS, L., WILLIAMS, E.R., JENKINS, D.B. & TWIDDY, N.D., 1980. The determination of the atomic oxygen concentration and associated parameters in the lower ionosphere, **Proc. R. Soc. Lond., A369,** 379-408.

DICKINSON, P.H.G., WILLIAMS, E.R. & JENKINS, D.B., 1981. Rocket-borne experiments for simultaneous measurement of atomic oxygen concentration, electron density and gas temperature, **Bundesministerium fuer Forschung und Technologie, 81/052,** 340-350, University of Wuppertal.

DODSON, M.H. & McCLELLAND BROWN, E., 1980. Magnetic blocking temperatures of single domain grains during slow cooling, **J. geophys. Res., 85,** 2625-2637.

DOMINGO, V., HYNDS, R.J. & STEVENS, G., 1979. A solar proton event of possible non-flare origin, **Proc. 16th Int. Cosmic Ray Conf. Kyoto, 5,** 192.

DOWNEY, W.S. & MITCHELL, J.G., 1981. K-Ar ages of Mylonites from the Moine Thrust Zone, Eriboll, Scotland, **Geophys. J. R. astr. Soc., 65,** 247.

DRAKE, C.L. & GIRDLER, R.W., 1982. History of Rift Studies, in 'Continental and Oceanic Rifts' (ed. G. Palmason), **Geodynamics Series (A.G.U. - G.S.A.), 8,** 5-15.

DUDENEY, J.R., 1981. The ionosphere - a view from the pole, **New Scientist, 91,** 714-717.

DUDENEY, J.R., CROWLEY, G. & JONES, T.B., 1979. Large simultaneous disturbances in Antarctic ionosphere, **Antarct. J.U.S., 14,** 213-214.

DUDENEY, J.R., JARVIS, M.J., KRESSMAN, R.I., PINNOCK, M., RODGER, A.S. & WRIGHT, K.H., 1982. Ionospheric troughs in Antarctica, **Nature, 295,** 307-308.

DUFF, B.A., 1979. The palaeomagnetism of Cambro-Ordovician red beds, the Erquy Spilite Series and the Tregastel-Ploumanac'h granite complex, Amorican Massif (France and the Channel Islands), **Geophys. J. R. astr. Soc., 59,** 345-365.

DUFF, B.A., 1979. Peaked thermomagnetic curves for hematite-bearing rocks and concentrates, **Phys. Earth Planet. Inter., 19,** 1-4.

DUFF, B.A., 1980. The palaeomagnetism of Jersey volcanics and dykes, and the Lower Palaeozoic apparent wanderpath for Europe, **Geophys. J. R. astr. Soc., 60,** 355-375.

DUFF, B.A., 1980. Palaeomagnetism of Late Precambrian or Cambrian diorites from Leicester, UK, **Geol. Mag., 117,** 479-483.

DUFF, B.A., 1981. Scattered palaeomagnetic directions acquired during dioritization and stoping of the diorite-metagabbro complex, Jersey, C.I., **J. Geol. Soc., 138,** 485-492.

DUFF, B.A., 1982. Comment on 'Palaeomagnetism and the mid-European Ocean - an alternative interpretation of Lower Palaeozoic apparent polar wander' by C.F. Burrett, **Geophys. J. R. astr. Soc., 72,** 535.

DUNGEY, J.W., 1979. First evidence and early studies of the Earth's bow shock, **Il Nuovo Cimento, 20,** N.6.

DUNGEY, J.W., 1981. Magnetospheric plasmas, **Phil. Trans. R. Soc., London, A300,** 489-496.

DUNGEY, J.W., 1982. A formulation for computation of a class of collision-free plasmas in two dimensions, **J. Plasmas Phys., 28,** 141-147.

DUNGEY, J.W., 1982. Thinning of field-aligned currents, **Geophys. Res. Lett., 9, 11,** 1243-1245.

EDWARDS, K.J., KERSLEY, L. & SHRUBSOLE, L.F., 1981/2. Sporadic-E propagation at VHF, **Report to Home Office, Directorate of Radio Technology,** (i) 62.25MHz (1981), (ii) 77.25MHz (1981), (iii) 59.25 MHz(1982), (iv) Comparative studies (1982).

ELLIS, P. & SOUTHWOOD, D.J., 1983. Reflection of Alfven waves by non-uniform ionosphere, **Planet. Space Sci., 31,** 107-117.

ESSEX, E.A., KERSLEY, L., et al. 1981. A global response of the total electron content of the ionosphere to the magnetic storm of 17 and 18 June 1972, **J. atmos. terr. Phys., 43,** 293-306.

ETCHETO, J., CHRISTIANSEN, P.J., GOUGH, M.P.& TROITIGRION, J.G., 1982, Terrestrial continuum radiation observations with GEOS 1 and ISEE 1, **Geophys. Res. Lett., 9,** 1239.

EVANS, C.J., CHROSTON, P.N. & TOUSSAINT-JACKSON, J.E., 1982. A comparison of laboratory measured electrical conductivity in rocks with theoretical conductivity based on derived pore aspect ratio spectra, **Geophys. J. R. astr. Soc., 71,** 247-260.

EYKEN, A.P. van, WILLIAMS, P.J.S., MAUDE, A.D. & MAJID, A., 1980. A regular and sustained wave in the ionosphere, **J. atmos. terr. Phys., 42,** 513-516.

EYKEN, A.P. van, WILLIAMS, P.J.S., MAUDE, A.D. & MORGAN, W.G., 1982. Atmospheric gravity waves and sporadio-E, **J. atmos. terr. Phys., 44,** 25-30.

FABIANO, E.B., PEDDIE, N.W., BARRACLOUGH, D.R. & ZUNDE, A., 1982. International Geomagnetic Reference Field 1980 and Grid Values, **Bull. Int. Assoc. Geomag. Aeron., No.47.**

FALLER, A.M. & SOPER, N.J., 1979. Palaeomagnetic evidence for the origin of the coastal flexure and dyke swarm in central E. Greenland, **J. Geol. Soc., 136,** 737-744.

FALLICK, A.E., PILLINGER, C.T. & STEPHENSON, A., 1979. Hydrolysable carbon magnetic susceptibility and isothermal remanent magnetization measurements of highland sample 68501: Comments on carbon content and size distribution of finely divided lunar iron, **Proc. 10th Lunar Planet. Sci. Conf. Geochim. et Cosmochim. Acta., suppl.10, vol.2,** 1469-1481.

FARMAN, J.C. & PIGGOTT, W.R., 1982. The Earth's atmosphere as seen from Antarctica, **Impact of Science on Society, 32,** 281-291.

FELLGETT, P.B. & USHER, M.J., 1980. Fluctuation phenomena in instrumental sciences, **J. Phys. E. (Sci. Instrum.), 13,** 1041-1046.

FOSS, C.A., 1981. Graphical methods for rapid vector analysis of demagnetization data, **Geophys. J. R. astr. Soc., 65,** 217-221.

FOX, J.M.W. & AITKEN, M.J., 1980. Cooling-rate dependence of thermoremanent magnetisation, **Nature, 283,** 462-463.

FREER, R. & O'REILLY, W., 1980. The diffusion of Fe^{2+} ions in spinels with relevance to the process of magnetization, **Miner. Mag., 43,** 889-899.

FREUND, R.E., & TARLING, D.H., 1979. Preliminary Mesozoic palaeomagnetic results from Israel and inferences for a microplate structure in the Lebanon, **Tectonophys., 60,** 189-205.

FULLER-ROWELL, T.J. & REES, D., 1981. A three-dimensional, time-dependent simulation of the global response of the thermosphere to a geomagnetic substorm, **J. atmos. terr. Phys., 43,** 701-721.

FURNES, H., HERTOGEN, J., MITCHELL, J.G., AUSTRHEIM, H. & SINHA-ROY, S., 1983. Trace element geochemistry and ages of mafic and felsic dykes from the Kerala region, India, **Neues Jahrbuch Miner. Abh., 146,** 82-100.

GADSDEN, M., 1980. A meteoric nightglow? **Mon. Not. R. Soc., 192,** 581-594.

GADSDEN, M., 1981. The silver-blue cloudlets again: nucleation and growth of ice in the mesosphere, **Planet. Space Sci., 29,** 1079-1087.

GADSDEN, M., 1982. Noctilucent clouds, **Space Sci. Revs., 33,** 279-334.

GADSDEN, M., 1983. A note on the orientation and size of noctilucent cloud particles, **Tellus, 35B,** 73-75.

GAMES, K.P., 1980. The magnitude of the archaeomagnetic field in Egypt between 3000 and 0 BC, **Geophys. J. R. astr. Soc., 63,** 45-56.

GAMES, K.P., 1981. The Earth's magnetism - in bricks, **New Scientist, 90,** 678-681.

GAMES, K.P. & BAKER, M.E., 1981. Determination of geomagnetic archaeo-magnitudes from clay pipes, **Nature, 289,** 478-9.

GANGULY, S., WALKER, J.C.G. & RISHBETH, H., 1980. The dynamic F2-layer over Arecibo, **J. atmos. terr. Phys., 42,** 553-562.

GARDINER, G.W., LANE, J.A. & RISHBETH, H., 1982. Radio and space research at Slough 1920-1981, **The Radio and Electronic Engineer, 52, No.3,** 111-121.

GOLIKOV, Y.Y., PLYASOVA-BAKOUNINA, T.A., TROITSKAYA, V.A., CHERNIKOV, A.A., PUSTOVALOV, V.V. & HEDGECOCK, P.C., 1980. Where do solar wind-controlled micropulsations originate? **Planet. Space Sci., 28,** 535-543.

GOSLING, J.T., ASHBRIDGE, J.R., BAME, S.J., FELDMAN, W.C., ZWICKL, R.D., PASCHMANN, G., SCKOPKE, B. & HYNDS, R.J., 1981. Interplanetary ions during an energetic storm particle event: the distribution functions from 400 eV to 1.6 MeV, **J. geophys. Res., 86,** 547-554.

GOUGH, M.P., 1982. Non-thermal continuum emissions associated with electron injections: remote plasmapause sounding, **Planet. Space Sci., 30,** 657-668.

GOUGH, M.P., CHRISTIANSEN, P.J. & GERSHUNY, E., 1980. E.S. wave morphology near the geostationary orbit, **Space Research: Advances in Space Exploration 1, Pergamon Press.**

GOUGH, M.P., CHRISTIANSEN, P.J., MARTELLI, G. & GERSHUNY, E., 1979. Interaction of electrostatic waves with warm electrons at the geomagnetic equator, **Nature, 279,** 515.

GOUGH, M.P., CHRISTIANSEN, P.J. & THOMAS, R., 1980. E.S. emissions studied in high resolution, **Space Research: Advances in Space Exploration 1, Pergamon Press.**

GOUGH, M.P. & KORTH, A., 1982. New light on the equatorial source of pulsating aurora, **Nature, 298,** 253-255.

GOUGH, M.P., MAEHLUM, B., MARTELLI, G., SMITH, P.N. & VENTURA, G., 1980. Bunching of 8-10 keV auroral electrons in the vicinity of an artificial electron beam, **Nature, 287,** 15-17.

GOUGH, M.P., MAEHLUM, B., MARTELLI, G., SMITH, P.N. & VENTURA, G., 1980.

Bunching of 8-10 keV auroral electrons at megahertz frequencies in the vicinity of an artificial electron beam, **ESA SP-152**, 331.

GOUGH, M.P. & URBAN, A., 1983. Auroral beam/plasma interaction observed directly, **Planet. Space Sci., 31**, 875-883.

GREEN, C.A., 1979. Observations of Pg pulsations in the northern auroral zone and at lower latitude conjugate regions, **Planet. Space Sci., 27**, 63-77.

GREEN, C.A., 1981. Continuous magnetic pulsations on the IGS array of magnetometers, **J. atmos. terr. Phys., 43**, 883-898.

GREEN, C.A., 1982. The role of ground arrays of magnetometers in the study of pulsation resonance regions, **Planet. Space Sci., 30**, 1199-1209.

GREEN, C.A. & HAMILTON, R.A., 1981. An ionospheric effect on the conjugate relationship of Pi2 magnetic pulsations, **J. atmos. terr. Phys., 43**, 1133-1141.

GREEN, C.A., ODERA, T.J. & STUART, W.F., 1983. The relationship between the strength of the IMF and the frequency of magnetic pulsations on the ground and in the solar wind, **Planet. Space Sci., 31**, 559-567.

GUBBINS, D., 1979. The Earth's precessional Dynamo, **The Observatory, 99**, 113.

GUBBINS, D., 1981. Planetary magnetism and the thermal evolution of planetary cores, **Evolution of the Earth, Geodynamics Series 5**, 105-109, American Geophysical Union.

GUBBINS, D., 1981. Rotation of the Inner Core, **J. geophys. Res., 86**, 11695-11699.

GUBBINS, D., 1982. Finding core motions from magnetic observations, **Phil. Trans. R. Soc. Lond., A306**, 247-254.

GUBBINS, D., 1983 Geomagnetic field analysis - I. Stochastic inversion, **Geophys. J. R. astr. Soc., 73**, 641-652.

GUBBINS, D. & MASTERS, T.G., 1979. Driving mechanisms for the Earth's dynamo, **Advances in Geophysics**, 21, 1-50.

GUBBINS, D., MASTERS, T.G. & JACOBS, J.A., 1979. Thermal evolution of the Earth's core, **Geophys. J. R. astr. Soc., 59**, 57-99.

GUBBINS, D. & ROBERTS, N., 1983. Use of the frozen flux approximation in the interpretation of archaeomagnetic and palaeomagnetic data, **Geophys. J. R. astr. Soc., 73**, 675-687.

GUBBINS, D., THOMSON, C.J. & WHALER, K.A., 1982. Stable regions in the

Earth's liquid core, **Geophys. J. R. astr. Soc., 68,** 241-251.

GUNN, N.M. & MURRAY, A.S., 1980. Geomagnetic field magnitude variations in Peru derived from archaeological ceramics dated by thermoluminescence, **Geophys. J. R. astr. Soc., 62,** 345-66.

HAILWOOD, E.A., HAMILTON, N. & MORGAN, P.D., 1980. Magnetic polarity dating of tectonic events at passive continental margins, **Phil. Trans. R. Soc. Lond., A294,** 189-208.

HAJEB-HOSSEINIEH, H., KERSLEY, L. & EDWARDS, K.J., 1980. Ionospheric protonospheric electron content studies using ATS-6, **Beacon Satellite Measurements of Plasmaspheric and Ionospheric Properties (Ed. P.F. Checcacci)**, Florence, Italy, 191-198.

HAJKOWICZ, L.A., BRAMLEY, E.N. & BROWNING, R., 1981. Drift analysis of random and quasi-periodic scintillations in the ionosphere, **J. atmos. terr. Phys., 43,** 723-733.

HALL, D.S., 1980. The influence of energy diffusion on auroral particle distributions, **ESA Report, SP-152,** 285.

HAMILTON, N., 1979. A palaeomagnetic study of sediments from Site 397 northwest African continental margin, **Initial Reports of the Deep Sea Drilling Project, 47,** 463-477.

HAMILTON, N., 1979. Preliminary magnetic fabric studies of lower Cretaceous sediments from DSDP Site 397, Northwest African continental margin, **Initial Reports of the Deep Sea Drilling Project, 47,** 481-482.

HAMILTON, R.A., 1982. The morphology of magnetic pulsations at Halley Bay, 1974-1976, **British Antarctic Survey Bull.,** 51-75.

HANSON, H.W., WEBB, D.C. & BEAMISH, D., 1979. A high resolution study of continuous pulsations in the European sector, **Planet. Space Sci., 27,** 1371-1382.

HAPGOOD, M., 1980. Infrared observation of a persistent meteor train, **Nature, 286,** 582-583.

HAPGOOD, M., COLLIN, H.L. & ROTHWELL, P., 1980. TV observations of the Barium-Geos ion jet experiment, **Proceedings of the ESA / PAC symposium, ESA-SP152,** 293.

HAPGOOD, M.A. & ROTHWELL, P., 1981. Fragmentation of a meteor in near earth space, **Nature, 290,** 385-386.

HAPGOOD, M.A. & ROTHWELL, P., 1982. Structure of small meteoroids, deduced from two station low light level TV observations of meteor trails, **Comparative Study of the Planets (Ed. Coradini),** Reidel, 311-315.

HAPGOOD, M.A., ROTHWELL, P. & ROYRVIK, O., 1982. Television observations of

Perseid meteors, **Mon. Not. R. astr. Soc., 201,** 569-577.

HAPGOOD, M.A. & TAYLOR, M.J., 1982. Analysis of airglow image data, **Ann. Geophys., 38,** 805-813.

HARGRAVES, R.B., COLLINSON, D.W., ARVIDSON, R.E. & CATES, P.M., 1979. Viking magnetic properties experiment: Extended mission results, **J. geophys. Res., 84,** 8379-8384.

HARRIES, J.E., 1980. Spectroscopic observation of middle atmosphere composition, **Phil. Trans. R. Soc., A296,** 161.

HART, A.M., HONEBON, C.D. & ROSSER, W.G.V., 1983. Local contributions to the M_2 lunar geomagnetic variations in the South West of England, **Phys. Earth Planet. Inter., 32,** 60-64.

HART, A.M., KRAUSE, P. & ROSSER, W.G.V., 1983. Possible contributions of leakage currents from the Atlantic Ocean to the magnetic field variations observed in Devon, **Phys. Earth Planet. Inter., 32,** 107-113.

HAYWARD, D.H. & DUNGEY, J.W., 1983. An Alfven wave approach to auroral field-aligned currents, **Planet. Space Sci., 31,** 579-585.

HEWSON-BROWNE, R.C., 1981. The numerical solution of oceanic electromagnetic induction problems, **Geophys. J. R. astr. Soc., 67,** 235-238.

HEWSON-BROWNE, R.C. & KENDALL, P.C., 1980. Induction in arbitrarily shaped oceans II: edge correction for the case of infinite conductivity, **J. Geomag. Geoelectr., 32,** 51-58.

HEWSON-BROWNE, R.C. & KENDALL, P.C., 1981. Electromagnetic induction in the earth in electrical contact with the oceans, **Geophys. J. R. astr, Soc., 66,** 333-349.

HIDE, R., 1979. On the magnetic flux linkage of an electrically conducting fluid, **Geophys. Astrophys. Fluid Dynam., 12,** 171-176.

HIDE, R., 1979. Dynamo Theorems, **Geophys. Astrophys. Fluid Dynam., 14,** 183-186.

HIDE, R., 1981. The magnetic flux linkage of a moving medium: a theorem and geophysical applications, **J. geophys. Res., 86.,** 11681-11687.

HIDE, R., 1981. Self-exciting dynamos and geomagnetic polarity changes, **Nature, 293,** 728-729.

HIDE, R., 1982. On the role of rotation in the generation of magnetic fields by fluid motions, **Phil. Trans. R. Soc. Lond., A306,** 223-234.

HIDE, R., 1982. The giant planets, **Phys. Bull., 33,** 358-361.

HIDE, R., 1983. Magnetic analogue of Ertel's potential vorticity theorem, **Annales Geophysicae, 1,** 59-60.

HIDE, R., 1983. On kinematic self-exciting dynamo theories: a summary of some recent work, **Planetary and Stellar Magnetism (Ed. A.M. Soward),** 259-261.

HIDE, R., & MALIN, S.R.C., 1981. On the determination of the size of the Earth's core from observations of the geomagnetic secular variation, **Proc. R. Soc. Lond., A374,** 15-33.

HIDE, R. & PALMER, T.N., 1982. Generalization of Cowling's theorem, **Geophys. Astrophys. Fluid Dynam., 19,** 301-309.

HIJAB, B.R. & TARLING, D.H., 1982. Lower Jurassic palaeomagnetic results from Yorkshire, England, and their implications, **Earth Planet. Sci. Lett., 60,** 147-154.

HOBBS, B.A., 1981. A comparison of Sq analyses with model calculations, **Geophys. J. R. astr. Soc., 66,** 435-444.

HOBBS, B.A., 1982. Automatic model-finding for the one-dimensional magnetotelluric problem, **Geophys. J. R. astr. Soc., 168,** 253-266.

HOBBS, B.A. & DAWES, G.J.K., 1979. Calculation of the effect of the oceans on geomagnetic variations with an application to the Sq field during the IGY, **J. Geophys., 46,** 273-289.

HOBBS, B.A. & DAWES, G.J.K., 1980. The effect of a simple model of the Pacific Ocean on Sq variations, **J. Geomag. Geoelectr., 32,** 59-66.

HOBBS,, B.A. & PARKINSON, W.D., 1979. Conditions for the geomagnetic induction relationship, **Phys. Earth Planet. Int., 19,** 5-6.

HORNE, R.E.B., CHRISTIANSEN, P.J., GOUGH, M.P., RONMARK, K., JOHNSON, J.F.E., SOJKA,J. & WENN, G., 1980. ECH wave dispersion - effects of suprathermal electron distribution, **Space Research/Advances in Space Exploration 1 (Ed. K. Knott),** Pergamon Press.

HORNE, R.B., CHRISTIANSEN, P.J., GOUGH, M.P. & RONMARK, R., 1981. Amplitude variations of ECH waves - a comparison between theory and experiment, **Nature, 294,** 338-340.

HOULISTON, D.J., LOUGHLIN, J., WAUGH, G. & RIDDICK, J.C., 1983. A high -speed data logger for geomagnetic applications, **Computers and Geosciences, 9,** 471-480.

HROUDA, F., STEPHENSON, A. & WOLTAR, L., 1983. On the standardization of measurements of the anisotropy of magnetic susceptibility, **Phys. Earth Planet. Inter., 32,** 203-208.

HUTTON, V.R.S., DAWES, G., INGHAM, M., KIRKWOOD, S., MBIPOM, E.W. & SIK, J.,

1981. Recent studies of time variations of natural electromagnetic fields in Scotland, **Phys. Earth Planet. Inter., 24**, 66-87.

HUTTON, V.R.S., DOSSO, H.W. & NEINABER, W., 1980. An analogue model study of electromagnetic induction in the British Isles, **Phys. Earth Planet. Inter., 22**, 68-85.

HUTTON, V.R.S., INGHAM, M.R. & MBIPOM, E.W., 1980. An electrical model of the crust and upper mantle in Scotland, **Nature, 287**, 30-33.

HUTTON, V.R.S. & JONES, A.G., 1979. A multi-station magnetotelluric study in S. Scotland - Part I - Fieldwork, data analysis and results, **Geophys. J. R. astr. Soc., 56**, 329-349.

HUTTON, V.R.S. & JONES, A.G., 1979. A multi-station magnetotelluric study in S. Scotland - Part II - Monte-Carlo inversion of the data and its geophysical and tectonic implications, **Geophys. J. R. astr. Soc., 56**, 351-368.

HUTTON, V.R.S. & JONES, A.G., 1980. Magnetovariational and magnetotelluric investigations in S. Scotland, **J. Geomag. Geoelectr., 32**, 141-149.

HYNDS, R.J. & DOMINGO, V., 1981. Intensity decay patterns for proton particle increases associated with interplanetary shock waves, **Proc. 17th Int. Cosmic Ray Conf., Paris, 3**, 447.

INGHAM, M.R. & HUTTON, V.R.S., 1982. Crustal and upper mantle electrical conductivity structure in Southern Scotland, **Geophys. J. R. astr. Soc., 69**, 579-594.

INGHAM, M.R. & HUTTON, V.R.S., 1982. The interpretation and tectonic implications of the geoelectric structure of Southern Scotland, **Geophys. J. R. astr. Soc., 69**, 595-606.

JACOBS, J.A., 1979. Planetary magnetic fields, **Geophys. Res. Lett., 6**, 632.

JACOBS, J.A., 1979. The core and the Earth, **GEOS Summer**, 9-11.

JACOBS, J.A., 1980. When did the Earth's core form? **Geol. Soc. Can. Spec. Paper 20**, 35-48.

JACOBS, J.A., 1980. The evolution of the Earth's core and the geodynamo, **Proc. Int. School Phys. Course LXXVIII, Acad. Press**, 508-530.

JACOBS, J.A., 1981. Heat flow and reversals of the Earth's magnetic field, **J. Geomag. Geoelectr., 33**, 527-529.

JACOBS, J.A., 1982. The Earth's core: its structure, evolution and magnetic field. Introductory remarks, **Phil. Trans. R. Soc. Lond., A306**, 9-10.

JACOBS, J.A., 1983. Reversals of the Earth's magnetic field, **Publ. Observ.**

del Ebro, Mem. No. 14, 277-298.

JADY, R.J., MARSHALL, R.T. & MORGAN, K., 1979. Comparison of analyses of Dst variations, **Phys. Earth Planet. Inter., 20,** 6-10.

JADY, R.J., PATERSON, G.A. & WHALER, K., 1983. Inversion of the electromagnetic induction problem using Parker's algorithms with both precise and practical data, **Geophys. J. R. astr. Soc., 75,** 125-142.

JAMES, R.W., ROBERTS, P.H. & WINCH, D.E., 1980. The Cowling anti-dynamo theorem, **Geophys. Astrophys. Fluid Dynam., 15,** 149-160.

JOHNSON, H.P., KARSTEN, J.L., VINE, F.J., SMITH, G.C. & SCHOENHARTING, G., 1982. A low-level magnetic survey over a massive sulfide ore body in the Troodos Ophiolite complex, Cyprus, **Mar. Tech. Soc. J., 16(3),** 76-80.

JOHNSON, J.F.E. & SOJKA, J.J., 1981. Electrostatic analyser measurements made in a laboratory 'ionospheric' plasma, **J. Phys. E. Sci. Inst., 14,** 432-438.

JONES, D., 1980. Latitudinal beaming of planetary radio emissions, **Nature, 288,** 225-229.

JONES, D., 1981. Beaming of terrestrial myriametric radiation, **Adv. Space Res., 1,** 373-376.

JONES, D., 1981. First remote sensing of the plasmapause by terrestrial myriametric radiation, **Nature, 294,** 728-730.

JONES, D., 1981. Radio wave emission from the Io torus, **Adv. Space Res., 1,** 333-336.

JONES, D., 1981. Xe^+-induced ion-cyclotron harmonic waves, **Adv. Space Res., 1,** 103-106.

JONES, D., 1982. Plasma waves in the earth's magnetosphere, **Adv. Space Res., 2,** 25-31.

JONES, D., 1982. Terrestrial myriametric radiation from the earth's plasmapause, **Planet. Space Sci., 30,** 399-410.

JONES, D., KORTH, A., RONMARK, K. & YOUNG, D., 1981. Helium cyclotron harmonic waves in the magnetospheric plasma, **Adv. Space Res., 1,** 319-324.

JONES, T.B. & HAYHURST, P.L., 1982. A mode direction sounder, **I.E.E. HF Communications Systems and Techniques Conf. Publ. No.206,** 36-40.

JONES, T.B. & MOWFORTH, K.E., 1980. Experimental validation of the ONSOD Omega prediction method, **AGAARD Conf. Proc. No.295.**

JONES, T.B. & MOWFORTH, K.E., 1981. A review of the analytical techniques for determining the phase and amplitude of a VLF radio wave propagating in the earth-ionosphere waveguide, **AGAARD Conf. Proc. No.305.**

JONES, T.B. & MOWFORTH, K.E., 1981. The effects of propagation on the accuracies of positions determined using Omega in the U.K., **AGAARD Conf. Proc. No.305.**

JONES, T.B., ROBINSON, T., KOPKA, H. & STUBBE, P., 1982. Phase changes induced in a diagnostic radio wave passing through a heated region of the auroral ionosphere, **J. geophys. Res., 87,** 1557-1564.

JONES, T.B., ROBINSON, T., STUBBE, P. & KOPKA, H., 1982. Anomalous absorption effects produced by high power radio waves, **AGAARD Conf. Proc. No. 332.**

JONES, T.B., ROBINSON, T., STUBBE, P. & KOPKA, H., 1983. Non linear effects in the ionospheric propagation of high power radio waves, **I.E.E. Antennae and Propagation Conf. Publ. No.219,** 304-307.

KAO, D. & ORR, D., 1982. Magnetotelluric studies in the Market Weighton area of Eastern England, **Geophys. J. R. astr. Soc., 70,** 323-337.

KAO, D., & ORR, D., 1982. Magnetotelluric response of a uniformly stratified earth containing a magnetized layer, **Geophys. J. R. astr. Soc.; 70,** 339-347.

KENDALL, P.C. & QUINNEY, D.A., 1983. Induction in the oceans, **Geophys. J. R. astr. Soc., 74,** 239-255.

KERSLEY, L., 1980. An empirical model of ionospheric slab thickness, **Propagation Effects in Space/Earth Paths, AGAARD-CPP-284,** 231-238.

KERSLEY, L., 1981. Studies of the plasmasphere/protonosphere by satellite radio beacon and other techniques, **Scientific and Engineering Uses of Satellite Radio Beacons (Ed. A.W. Wernik),** Warsaw, 149-159.

KERSLEY, L., AARONS, J. & KLOBUCHER, J.A., 1980. Night time enhancements in total electron content near Arecibo and their association with VHF scintillations, **J. geophys. Res., 85,** 4214-4222.

KERSLEY, L. & KLOBUCHER, J.A., 1980. Storm associated protonospheric depletion and recovery, **Planet. Space Sci., 28,** 453-458.

KERSLEY, L. & KLOBUCHER, J.A., 1980. Average response of protonospheric content to geomagnetic storm activity, **Beacon Satellite Measurements of Plasmaspheric and Ionospheric Properties (Ed. P.F. Checcacci),** Florence, 181-187.

KERSLEY, L. & REES, P.R., 1982. Tropospheric gravity waves and their possible association with medium-scale travelling ionospheric disturbances, **J. atmos. terr. Phys., 44,** 147-159.

KIRKWOOD, S.C., HUTTON, V.R.S. & SIK, J., 1981. A geomagnetic study of the Great Glen Fault, **Geophys. J. R. astr. Soc., 66,** 481-490.

KIVELSON, M.G. & SOUTHWOOD, D.J., 1981. Plasma near Io: estimates of some physical parameters, **J. geophys. Res., 86,** 10122-10126.

KIVELSON, M.G. & SOUTHWOOD, D.J., 1983. Charged particle behaviour in low frequency geomagnetic pulsations III: Spin phase dependence, **J. geophys. Res., 88,** 174.

KOPKA, H., STUBBE, P., JONES, T.B. & ROBINSON, T., 1982. Nonlinear reflectivity of high power radio waves in the ionosphere, **Nature, 295,** 680.

LAIRD, M.J., 1981. Reflection of electromagnetic waves by density gradients in a magnetised plasma, **J. atmos. terr. Phys., 43,** 81-86.

LANCHESTER, B.S., 1980. Mapping of Auroral forms from an Allsky coordinate grid, **ESA SP152,** 313.

LEE, C.D., VINE, F.J. & ROSS, R.G., 1983. Electrical conductivity models for the continental crust based on laboratory measurements on high-grade metamorphic rocks, **Geophys. J. R. astr. Soc., 72,** 353-371.

LEMAIRE, J . & RYCROFT, M.J., 1982. Solar system plasmas and fields, **Adv, Space Res., 2,** 87.

LEMBEGE, B. & JONES, D., 1982. Propagation of electrostatic upper-hybrid emission and Z mode waves at the geomagnetic equatorial plasmapause, **J. geophys. Res., 87,** 6187-6201.

LEPINE, D.R., BRYANT, D.A. & HALL, D.S., 1980. A 2.2 Hz modulation of auroral electrons imposed at the geomagnetic equator, **Nature, 286,** 469-471.

LEPINE, D.R., HALL, D.S., BRYANT, D.A., JOHNSTONE, A.D., CHRISTIANSEN, P.J., GOUGH, M.P. & GIBBONS, W., 1980. 2.2 Hz oscillations in auroral electrons, **ESA SP-152,** 317.

LEsTER, M. & ORR, D., 1981. The Spatio-temporal characteristics of Pi2's, **J. atmos. terr. Phys., 43,** 947-974.

LESTER, M. & ORR, D., 1983. Correlations between ground observations of Pi2 geomagnetic pulsations and satellite plasma density observations, **Planet. Space Sci., 31,** 143-160.

LESTER, M. & SMITH, A.J., 1980. Whistler duct structure and formation, **Planet. Space Sci., 28,** 645-654.

LESTER, M. & SMITH, A.J., 1980. A whistler study of the bulge region of the plasmapause, **IMS in Antarctica (Ed. Hirasawa), Natl. Inst. Polar Res.**, Tokyo, 113-127.

LIRITZIS, Y. & THOMAS, R., 1980. Palaeointensity and thermoluminescence measurements on Cretan kilns from 1300 to 2000 B.C., **Nature, 283,** 54-55.

LIU, C.H., KLOSTERMYER, J., YEH, K.C., JONES, T.B., ROBINSON, T., HOLT, O., LEITINGER, R., OGAWA, T., SINNO, K., KATO, S., BEDARD, A.J. & KERSLEY, L., 1982. Global dynamic response of the atmosphere to the eruption of Mount St. Helens on 18 May 1980, **J. geophys. Res., 87,** 6281-6290.

LIVERMORE, R.A., VINE, F. J. & SMITH, A.G., 1983. Plate motions and the geomagnetic field - I. Quaternary and late Tertiary, **Geophys. J. R. astr. Soc., 73,** 153-171.

LOCKWOOD,, M., 1981. A simple model of the effects of the mid-latitude trough in the bottomside F layer on HF radiowave propagation, **Radio Sci., 16,** 385.

LOCKWOOD, M., 1982. Thermal ion flows in the topside auroral ionosphere and the effects of low-altitude transverse acceleration, **Planet. Space Sci., 30,** 595-609.

LOCKWOOD, M., 1983. Field aligned plasma flow in the quiet mid-latitude ionosphere deduced from topside soundings, **J. atmos. terr. Phys., 45,** 1.

LOCKWOOD, M. & TITHERIDGE, J.E., 1981. Ionospheric origin of magnetospheric O^+ ions, **Geophys. Res. Lett., 8,** 381.

LOCKWOOD, M. & TITHERIDGE, J.E., 1982. Departures from diffusive equilibrium in the topside F-layer from satellite soundings, **J. atmos . terr. Phys., 44,** 425-440.

LOVLIE, R. & MITCHELL, J.G., 1982. Complete remagnetisation of some Permian Dykes from Western Norway induced during burial uplift, **Phys. Earth Planet. Inter., 30,** 415-421.

LOWES, F.J., 1979. Comment on 'The relationship between mean anomaly block sizes and spherical harmonic representations' by Richard H. Rapp, **J. geophys. Res., 84,** 4781-4782.

LOWES, F.J., 1979. Comment on 'On the shape of directional data sets' by David C. Engebretson and Myrl E. Beck,Jr., **J. geophys. Res., 84,** 6303.

LOWES, F.J., 1981. The ground-state conductivity profile of the core-mantle system of the Earth - comment, **Phys. Earth Planet. Inter., 25,** 177.

LOWES, F.J., 1981. Grand unification magnetic monopoles inside the Earth,

Nature, 292, 273.

LOWES, F.J., 1982. On magnetic observations of electric trains, **The Observatory, 102,** 44.

McCLELLAND BROWN, E., 1981. Palaeomagnetic estimates of temperatures reached in contact metamorphism, **Geology, 9,** 112-116.

McFADDEN, P.L. & LOWES, F.J., 1981. The discrimination of mean directions drawn from Fisher distributions, **Geophys. J. R. astr. Soc., 67,** 19-33.

McPHERSON, P.H. & RISHBETH, H., 1979. Thermospheric temperatures over Malvern: a comparison of incoherent scatter data with two global thermospheric models, **J. atmos. terr. Phys., 41,** 1021-1029.

MALIN, S.R.C., 1979. Geomagnetism, **Phys. Bull. 30,** 476-577.

MALIN, S.R.C., 1982. Sesquicentenary of Gauss's first measurement of the absolute value of magnetic intensity, **Phil. Trans. R. Soc. Lond., A306,** 5-8.

MALIN, S.R.C., 1983. Modelling the geomagnetic field, **Geophys. J. R.astr. Soc., 74,** 147-157.

MALIN, S.R.C. & BARRACLOUGH, D.R., 1981. Exploiting geomagnetic data, **Nature, 293,** 337.

MALIN, S.R.C. & BARRACLOUGH, D.R., 1982. 150th anniversary of Gauss's first absolute magnetic measurement, **Nature, 297,** 285.

MALIN, S.R.C., BARRACLOUGH, D.R. & HODDER, B.M., 1982. A compact algorithm for the formation and solution of normal equations, **Computers & Geosciences, 8,** 355-358.

MALIN, S.R.C. & BULLARD, SIR EDWARD C., 1981. The direction of the Earth's magnetic field at London 1570-1975, **Phil. Trans. R. Soc. Lond., A299,** 357-423.

MALIN, S.R.C. & GUBBINS, D., 1983. The need for archival magnetic measurements, **J. Hist. Astron., 14,** 70-75.

MALIN, S.R.C. & HIDE, R., 1982. Bumps on the core-mantle boundary: geomagnetic and gravitational evidence revisited, **Phil. Trans. R. Soc. Lond., A306,** 281-289.

MALIN, S.R.C. & HODDER, B.M., 1982. Was the 1970 geomagnetic jerk of internal or external origin? **Nature, 296,** 726-728.

MALIN, S.R.C., HODDER, B.M. & BARRACOUGH, D.R., 1983. Geomagnetic secular variation: a jerk in 1970, Contibuciones Cientificas para Comemorar el 75 Aniversario del Observatorio del Ebro (Ed. J.O. Cardus), **Publ. Obs. Ebro. Memoria No.14,** 239-256.

MALIN, S.R.C. & SCHLAPP, D.M., 1980. Geomagnetic lunar analysis by least squares, **Geophys. J. R. astr. Soc., 60,** 409-418.

MASTERS, G., 1979. Observational constraints on the chemical and thermal structure of the Earth's deep interior, **Geophys. J. R. astr., Soc., 57,** 507-534.

MATTHEWS, J.P., SMITH, A.J. & SMITH, I.D., 1979. A remote unmanned ELF / VLF gonimeter receiver in Antarctica, **Planet. Space Sci., 27,** 1391-1401.

MATTHEWS, J.P. & YEARBY, K.H., 1980. Magnetospheric VLF line radiation observed at Halley, Antarctica, **Mem. Nat. Inst. Polar. Res. Tokyo,** 95-112.

MATTHEWS, J.P. & YEARBY, K.H., 1981. Magnetospheric VLF line radiation observed at Halley, Antarctica, **Planet. Space Sci., 29,** 97-106.

MATTHEWS, J.P. & YEARBY, K.H., 1981. Siple VLF transmissions and their magnetospheric effects observed at Halley, Antarctica, **Adv. Space Res., 1,** 209-212.

MBIPOM, E.W. & HUTTON, V.R.S., 1983. Geoelectromagnetic measurements across the Moine Thrust and the Great Glen in northern Scotland, **Geophys. J. R. astr. Soc., 74,** 507-524.

MIER-JEDREZJOWICZ, W.A.C. & HUGHES, W.J., 1980. Phase skipping and packet structure in geomagnetic pulsation signals, **J. geophys. Res., 85,** 6888.

MIER-JEDREZJOWICZ, W.A.C. & SOUTHWOOD, D.J., 1981. Comparison of Pc3 and Pc4 pulsation characteristics on an East-West mid-latitude chain of magnetometers, **J. atmos. terr. Phys., 43,** 911.

MORGAN, G.E. & BRIDEN, J.C., 1981. Aspects of Precambrian palaeomagnetism with new data from the Limpopo Mobile Belt and Kaapvaal Craton in southern Africa, **Phys. Earth Planet. Inter., 24,** 142-168.

MORGAN, G.E. & SMITH, P.P.K., 1981. Transmission electron microscope and rock magnetic investigations of remanence carriers in a Pre-cambrian metal dolerite, **Earth Planet. Sci. Lett., 53,** 226-240.

MORRIS,, W.A., 1980. A palaeomagnetic study of Cambrian red beds from Cartaret, Normandy, France, **Geophys. J. R. astr. Soc., 62,** 577-590.

MOWFORTH, K.E. & JONES,T.B., 1983. The determination of the propagation characteristics of very long low frequency radio waves, **I.E.E. ICAP 83, Conf. Proc. No. 219,** 12-15.

MUSSETT, A. E., 1981. Palaeomagnetism and dating of the British Tertiary Igneous Province, **Open Earth, 15.**

NEINABER, W., DOSSO, H.W. & HUTTON, V.R.S., 1981. Electromagnetic induction in the British Isles region: analogue model and field station results, **Phys. Earth Planet. Inter., 27,** 122-132.

NIELSEN, E., GUTTLER, W., THOMAS, E.C., STEWART, C.P., JONES, T.B. & HEDBERG, A., 1983. SABRE - A new radar auroral backscatter experiment, **Nature, 304,** 712-714.

NIELSEN, E., WHITEHEAD, J.D., HEDBERG, L.A. & JONES, T.B., 1983. Test of the cosine relationship of radar auroral doppler velocity measurements, **Radio Sci., 18,** 230.

NIELSEN, T.F.D., SOPER, N.J., BROOKS, C.K., KENT, C., FALLER, A.M., HIGGINS, A.C. & MATTHEWS, D.W., 1981. The pre-basaltic sediments and the lower basalts at Kangerdlugssuaq, East Greenland: their stratigraphy , lithology, palaeomagnetism and petrology, **Meddlelser om Gronland, Geoscience, 6.**

NORRIS, A.J., JOHNSON, J.F.E., SOJKA, J.J., WRENN, G.L., CORNILLEAU-WEHRLIN, S., PERRAUT, S. & ROUX, A., 1983. Experimental evidence for the acceleration of thermal electrons by ion cyclotron waves in the magnetosphere, **J. geophys. Res., 88,** 889-898.

O'DONOVAN, J.B. & O'REILLY, W., 1983. Magnetic properties of basalts from hole 504B, DSDP Leg 69, **Init. Reps. Deep Sea Drilling Project, 69,** 721-726.

OFFERMANN, D., BRUCKLEMANN, H.G.K., BARNET, J.J., LABITZKE, K., TORKER, K.M. & WIDDEL, H.U., 1982. A scale analysis of the D region winter anomaly, **J. geophys. Res., 87,** 8286-8306.

O'REILLY, W., 1983. The identification of titanomaghemites: model mechanisms for the maghemitization and inversion processes and their magnetic consequences, **Phys. Earth Planet. Inter., 31,** 65-76.

ORR, D. & HANSON, H.W., 1981. Geomagnetic pulsation phase patterns over an extended latitudinal array, **J. atmos. terr. Phys., 43,** 899-910.

OZDEMIR, O. & O'REILLY, W., 1981. High-temperature hysteresis and other magnetic properties of synthetic monodomain titanomagnetites, **Phys. Earth Planet. Inter., 25,** 406-418.

OZDEMIR, O. & O'REILLY, W., 1982. Magnetic hysteresis properties of synthetic monodomain titanomagnetites, **Earth Planet. Sci. Lett., 57,** 437-447.

OZDEMIR, O. & O'REILLY, W., 1982. An experimental study of the intensity and stability of thermoremanent magnetization acquired by synthetic monodomain titanomagnetite substituted by aluminium, **Geophys. J. R. astr. Soc., 70,** 141-154.

OZDEMIR, O. & O'REILLY, W., 1982. An experimental study of thermoremanent magnetization acquired by synthetic monodomain titanomaghemites, J. **Geomag. Geoelectr., 34,** 467-478.

PALUMBO, A. & MALIN, S.R.C., 1979. Campo geomagnetico L. Catalogo delle fonti, **Bollotino della Societa dei Naturalisti in Napoli, 88,** 1-31.

PARKER, R.L. & WHALER, K.A., 1981. Numerical methods for establishing solutions to the inverse problem of electromagnetic induction, **J. geophys. Res., 86,** 9574-9584.

PEDEIRA, E., KELLEY, M., REES, D., MIKKELSEN, I.S., JORGENSEN, T.S. & FULLER-ROWELL, T.J., 1980. Observations of neutral wind profiles between 115- and 275-km altitude in the dayside auroral oval, **J. geophys. Res., 85,** 2935-2940.

PIPER, J.D.A., 1978. Geological and geophysical evidence relating to continental growth and dynamics and the hydrosphere in Precambrian times: **Earth's rotation**, Ed. Brosche, P. and Sundermann, J., Springer-Verlag, Berlin, 1978, 197-241.

PIPER, J.D.A., 1979. A palaeomagnetic survey of the Jotnian dolerites of central-east Sweden, **Geophys. J. Roy. astr. Soc., 56,** 461-71.

PIPER, J.D.A., 1979. Outline volcanic history of the region west of Vatnajokull, Central Iceland, **J. Volc. Geotherm. Res., 5,** 87-98.

PIPER, J.D.A., 1979. Aspects of Caledonian palaeomagnetism and their tectonic implications, **Earth Planet. Sci. Lett., 44,** 176-192.

PIPER, J.D.A., 1979. Palaeomagnetism of the Ragunda intrusion and dolerite dykes, central Sweden, **Geol. Foren. Stockh. Fordh., 101,** 139-148.

PIPER, J.D.A., 1979. Palaeomagnetic study of late Precambrian rocks of the middle craton of England and Wales, **Phys. Earth Planet. Int., 19,** 59-72.

PIPER, J.D.A., 1979. Palaeomagnetism of the central zone of the Lewisian foreland, north-west Scotland, **Geophys. J. R. astr. Soc., 59,** 101-102.

PIPER, J.D.A., 1980. Palaeomagnetic study of the Swedish Rapakivi Suite: Proterozoic tectonics of the Baltic Shield, **Earth Planet. Sci. Lett., 46,** 443-461.

PIPER, J.D.A., 1980. Analogous Upper Proterozoic apparent polar wander loops, **Nature, 283,** 845-847.

PIPER, J.D.A., 1980. A palaeomagnetic study of Svecofennian basic rocks: Middle Proterozoic configuration of the Fennoscandian, Laurentian and Siberian Shields, **Phys. Earth Planet. Int., 23,** 165-187.

PIPER, J.D.A., 1980. Comments on 'Palaeomagnetism in the Coronation Geosyncline and arrangement of continents in the middle Proterozoic' by E. Irving and J.C. McGlynn, **Geophys. J. R. astr. Soc., 62,** 473-477.

PIPER, J.D.A. & SMITH, R.L., 1980. Palaeomagnetism of the Jotnian lavas and sediments and post-Jotnian dolerites of central Scandinavia, **Geol. Foren. Stockh. Fordh., 102,** 67-81.

PIPER, J.D.A., 1981. Palaeomagnetic study of the (Late Precambrian) west Greenland kimberlite-lamprophyre suite: definition of the Hadrynian track, **Phys. Earth Planet. Int., 27,** 164-186.

PIPER, J.D.A., 1981. The altitude dependence of magnetic remanence in the slowly-cooled Precambrian plutonic terrain of west Greenland, **Earth Planet. Sci. Lett., 54,** 449-466.

PIPER, J.D.A., 1981. Magnetic properties of the Alnon Complex, **Geol. Foren. Stockh. Fordh., 103,** 9-15.

PIPER, J.D.A., 1981. Palaeomagnetism of pseudotachylites from the Ikertoq shear belt, and their relationship to the kimberlite-lamprophyre province, central west Greenland, **Dansk. Geologisk. Foren., 30,** 57-67.

PIPER, J.D.A., 1982. The Precambrian palaeomagnetic record: the case for the Proterozoic Supercontinent, **Earth & Planet. Sci. Lett., 59,** 61-89.

PIPER, J.D.A., 1982. A palaeomagnetic investigation of the Malvernian and Old Radnor Precambrian, Welsh Borderlands, **Geol. J., 17,** 69-88.

PIPER, J.D.A., 1982. Movements of the Continental Crust and Lithosphere-Aesthenosphere Systems in Precambrian Times, Contribution to **Tidal Friction and the Earth's Rotation II,** P. Brosche & J. Sundemann (eds.) (Springer-Verlag Berlin Heidelberg New York) 153-315.

PIPER, J.D.A., 1983. Rock and roll on a massive scale, **Times Higher Ed. Supplement,** 12-13.

PLYSOVA-BAKUNINA, T.A., TROITSKAYA, V.A., STUART, W.F. & KHARCHENKO, I.P., 1983. Generation of Pc4 in the solar wind and at the magnetopause, **J. Sib. Dept. Acad. Sci., U.S.S.R., 62,** 103-108.

PRITCHARD, H.M. & MITCHELL, J.G., 1979. K-Ar data for the age and evolution of Gettysburg Bank, North Atlantic Ocean, **Earth Planet. Sci. Lett., 44,** 261-268.

QUEGAN, S., BAILEY, G.J., MOFFETT, R.J., HEELIS, R.A., FULLER-ROWELL, T.J., REES, D. & SPIRO, R.W., 1982. A theoretical study of the distribution of ionisation in the high latitude ionosphere and the plasmasphere: first results on the mid-latitude trough and light-ion trough, **J. atmos terr. Phys., 44,** 619-640.

QUINN, J. & SOUTHWOOD, D.J., 1982. Observations of parallel ion energization in the equatorial region, **J. geophys. Res., 87**, 10536-10540.

RATHORE, J.S., 1979. Application of magnetic susceptibility anisotropy technique to the study of geological structures in the Armorican Massif, France, **Tectonophys., 60**, 207-216.

RATHORE, J.S., 1980. The application of magnetic susceptibility analyses to the study of tectonic events on the Periadriatic Line - Project Tiefbau der Ostalpeh, **Mitt. oster. Geol. Ges., 71/72**, 275-290.

RATHORE, J.S., 1980. A study of secondary fabrics in rocks from the Lizard Peninsula and adjacent areas in South-West Cornwall, England, **Tectonophys., 68**, 147-160.

RATHORE, J.S., 1980. The magnetic fabrics of some slates from the Borrowdale volcanic group in the English Lake District and their correlation with strain, **Tectonophys., 67**, 207-220.

REES, D., 1979. Mid-latitude winds and electric fields in the lower thermosphere and their relationship with the global Sq ionospheric current system, **J. Geomag. Geoelectr., 31**, 267-285.

REES, D., CHARLETON, P., LLOYD, N., STEEN, A. & WITT, G., 1983. Interferometric and doppler imaging studies of the auroral thermosphere from Kiruna Geophysical Institute, **Proc. VIth ESA Symposium on Rocket and Balloon Programmes and Related Research, ESA SP-183**, 53-57.

REES, D., FULLER-ROWELL, T.J. & ROUNCE, P.A., 1980. Asymmetric global circulation systems following geomagnetic substorms, **Proc. Vth ESA-PAC Symposium on European Rocket and Balloon Programmes and Related Research, Bournemouth, 1980, ESA SP-152**, 81-88.

REES, D. & MAYNARD, N.C., 1980. Mid-latitude measurements of the ionospheric electric field during the ALADDIN programme, **J. atmos. terr. Phys., 42**, 577-582.

REES, D., SCOTT, A.F.D., CISNEROS, J.M., SATRUSTEGUI, J.M., WIDDEL, H. & ROSE, G., 1979. Relationships between the local dynamic structure of the atmosphere and ionospheric absorption during the West European Winter Anomaly Campaign 1975/76, **J. atmos. terr. Phys., 41**, 1063-1074.

RICHARDSON, I.G. & HYNDS, R.G., 1981. Low energy (ca. 35 keV) proton enhancements associated with co-rotating solar wind streams at 1 AU, **Proc. 17th Int. Cosmic Ray Conf., Paris, 3**, 430.

RICHARDS, M.L., 1980. Electromagnetic sounding with long submarine cables, **Proc. of the 17th Assembly of the ESC, Budapest, 1980, Akademiai Kiado, Budapest**, 363-367.

RICHARDS, M.L., SCHMUCKER, U. & STEVELING, E., 1982. Electrical conductivity in the Urach Geothermal Area, A geomagnetic induction study using pulsations, **The Urach Geothermal Project, Schweiserbartsche Verlagsbuch-handlung, Stuttgart**, 301-311.

RIJNBECK, R.P., COWLEY, S.W.H., SOUTHWOOD, D.J. & RUSSELL, C.T., 1982. Observations of reverse polarity flux transfer events at the Earth's dayside magnetopause, **Nature, 300**, 23-26.

RISHBETH, H., 1979. Ion-drag effects in the thermosphere, **J. atmos. Terr. Phys., 41**, 885-894.

RISHBETH, H., 1980. Winds in the polar thermosphere, **Nature, 284**, 398-399.

RISHBETH, H., 1981. Fifty years of Slough's ionosphere, **Nature, 289**, 638.

RISHBETH, H., 1981. The F-region dynamo, **J. atmos. terr. Phys., 43**, 387-392.

RISHBETH, H., 1982. Europe probes the auroral atmosphere, **Nature, 295**, 93-94.

RISHBETH, H. & WALKER, J.G.G., 1982. Directional currents in nocturnal E-region layers, **Planet. Space Sci., 30**, 209-214.

ROBERTSON, Y.C., COWLEY, S.W.H. & DUNGEY, J.W., 1981. Wave-particle interactions in a magnetic neutral sheet, **Planet. Space Sci., 29**, 399-403.

ROBINSON, P.R., 1983. Improvements to the system of four equiradial coils for producing a uniform magnetic field, **J. Phys. E: (Sci. Instrum.), 16**, 39-42.

RODGER, A.S., 1982. Union Radio Mark II ionosondes in Antarctica, **British Antarctic Survey Bulletin**, 69-77.

RODGER, A.S., BOTELER, D.H. & DUDENEY, J.R., 1981. The importance of the maximum plasma frequency of the ionosphere in controlling the occurrence of blackout, **J. atmos. terr. Phys., 43**, 1243-1247.

RODGER, A.S., FITZGERALD, P.H. & BROOM, S.M., 1981. The nocturnal intermediate layer over South Georgia, **J. atmos. terr. Phys., 43**, 1043-1050.

RODGER, A.S. & PINNOCK, M., 1980. The variability and predictability of the main ionospheric trough, **Exploration of the polar upper atmosphere, Reidel**, 463-469.

ROGERS, J., FOX, J.M.W. & AITKEN, M.J., 1979. Magnetic anisotropy in ancient pottery, **Nature, 277**, 644.

ROGERS, J. & SHARE, J., 1979. A microprocessor controlled superconducting magnetometer for palaeomagnetic research, **Geophys. J. R. astr. Soc., 57**, 267.

RONMARK, K., CHRISTIANSEN, P.J. & GOUGH, M.P., 1979. Banded electron cyclotron harmonic instability - a first comparison of theory and experiment, **Advances in Magnetospheric Physics with GEOS 1 and ISEG, Reidel,** 81.

RUNCORN, S.K., 1980. Lunar Polar Wandering, **Geochimica et Cosmochimica Acta, Suppl. 14,** 1867-1877.

RUNCORN, S.K., 1980. Some comments on the mechanism of continental drift, **Mechanisms of continental drift and plate tectonics (Eds. P.A. Davies and S.K. Runcorn), Academic Press,** 193-198.

RUNCORN, S.K., 1981. Wegener's Theory: The role of geophysics in its eclipse and triumph, **Geol. Rundschau, 70,** 784-793.

RUNCORN, S.K., 1982. Lunar palaeomagnetism, **The Comparative Study of the Planets** (Eds. A. Coradini and M. Fulchignoni, Reidel,) 291-294.

RUNCORN, S.K., 1982. Primeval displacements of the lunar pole, **Phys. Earth Planet. Inter., 29,** 135-147.

RUNCORN, S.K., 1982. The Moon's deceptive tranquility, **New Scientist, 96, 1328,** 174-180.

RUNCORN, S.K., COLLINSON, D.W. & STEPHENSON, A., 1981. Palaeomagnetism and Planetology, **Phys. Earth Planet. Inter., 24,** 205-217.

RUNCORN, S.K., COLLINSON, D.W. & STEPHENSON, A., 1983. Lunar palaeomagnetism and its implications, **Advances in Space Research, 2, No. 12,** 12-29.

RUNCORN, S.K., LIBBY, W.F. & LIBBY, L.M., 1980. Superheavy-element fission tracks in iron meteorites, **Nature, 287,** 565.

RUNCORN, S.K. & SUESS, H.E., 1982. Investigating Solar Activity, **Science, 218,** 842.

RUSSELL, C.T., LUHMANN, J.G., ODERA, T.J. & STUART, W.F., 1983. The rate of occurrence of dayside Pc3, 4 Pulsations: The L- value dependence of the IMF Cone Angle Effect, **IGPP Publ. No. 2409.**

RUSSELL, C.T., LUHMANN, J.G., ODERA, T.J. & STUART, W.F., 1983. The rate of occurrence of dayside Pc3, 4 pulsations: The L- value dependence of the IMF Cone Angle Effect, **Geophys. Res. Lett., 8,** 663-666.

RUSSELL, C.T. & RYCROFT, M.J., 1982. Energetic charged particle and electromagnetic wave injections into space, **Adv. Space Res., 2,** 55-58.

RYCROFT, M.J., 1982. Antarctic observations available for IMS correlative analyses, **IMS source book, AGU,** 196-210.

RYCROFT, M.J., CANNON, P.S. & TURUNEN, T., 1981. ELF radio signals produced in the auroral ionosphere by non-linear demodulation of signals from high-power amplitude-modulated transmitters, **Adv. Space Res., 1,** 449-454.

SANDERSON, T.R., DOMINGO, V., WENZEL, K.-P., van ROOIJEN, J.J., STEVENS, G., BALOGH, A. & HYNDS, R.J., 1979. Magnetospheric bursts measured upstream of the Earth at distances up to ca. 260 R_E, **Eos, 60,** 368.

SAUNDERS, M.A., 1983. Recent ISEE observations of the magnetopause and low latitude boundary layer: a review, **J. Geophys., 52,** 190.

SAUNDERS, M.A., SOUTHWOOD, D.J., HONES, E.W., Jr. & RUSSELL, C.T., 1981. A hydromagnetic vortex seen by ISEE 1 and 2, **J. atmos. terr. Phys., 43** 927-932.

SCHLAPP, D.M., 1980. Lunar tides in the middle atmosphere from NIMBUS 5 data, **J. atmos. terr. Phys., 42,** 529-532.

SCHLAPP, D.M., 1981. Lunar tides in the stratosphere and mesosphere from NIMBUS 6 data, **J. atmos. terr. Phys., 43,** 205-207.

SCHLAPP, D.M. & MALIN, S.R.C., 1979. Some features of the seasonal variation of geomagnetic lunar tides, **Geophys. J. R. astr. Soc., 59,** 161-170.

SCHLAPP, D.M. & MANN, R.J., 1983. The spatial scale of correlation of the day-to-day variability of Sq, **Geophys. J. R. astr. Soc., 73,** 671-673.

SCHLOESSIN, H. & JACOBS, J.A., 1980. Dynamics of a fluid core with inward growing boundaries, **Can. J. Earth Sci. 17,** 72-89.

SELLEK, R., 1981. A differencing method for the determination of the lunar daily geomagnetic variation from short data series, **Geophys. J. R. astr. Soc., 67,** 229-233.

SELLEK, R. & MALIN, S.R.C., 1982. Geomagnetic lunar analysis - the estimation of errors, **Geophys. J. R. astr. Soc., 70,** 793-796.

SHAW, C.J. & WIDMAR, F.J., 1982. Magnetic investigation of a wall at the Akhenaten Temple Site, Karnak, **Proceedings of the 22nd Symposium on Archaeometry, Bradford,** 102-111.

SHAW, J., DAGLEY, P. & MUSSETT, A.E., 1982. The magnitude of the palaeomagnetic field in Iceland between 2 and 6 Myr ago, **Geophys. J. R. astr. Soc., 68,** 211-218.

SHAW, J., 1979. Rapid changes in the magnitude of the archaeomagnetic field, **Geophys. J. R. astr. Soc., 58,** 107-116.

SHURE, L., WHALER, K., GUBBINS, D. & HOBBS, B., 1983. Physical constraints for the analysis of the geomagnetic secular variation, **Phys.**

Earth Planet. Inter., 32, 114-131.

SIK, J.M., HUTTON, V.R.S., DAWES, G.J.K. & KIRKWOOD, S.C., 1981. A geomagnetic variation study of Scotland, **Geophys. J. R. astr. Soc., 66,** 491-512.

SINGER, H.J., HUGHES, W.J., STUART, W.F. & GREEN, C.A., 1981. Dayside pulsations related to nightside pi2's, **EOS, 62,** 1014.

SINGER, H.J., SOUTHWOOD, D.J., WALKER, R.J. & KIVELSON, M.G., 1981. Alfven wave resonance in a realistic magnetic field geometry, **J. geophys. Res., 86,** 4589-4596.

SMALL, L. & RYCROFT, M.J., 1983. The Q-value and resistance of the heliospheric resonator model for the 22 year solar cycle, **Planet. Space Sci., 31,** 701-704.

SMITH, A.G., HURLEY, A.M. & BRIDEN, J.C., 1981. Phanerozoic palaeo-continental world maps, **Cambridge University Press,** 102 pp.

SMITH, A.J. & CARPENTER, D.L., 1982. Echoing mixed-path whistlers near the dawn plasmapause, observed by direction-finding receivers at two Antarctic stations, **J. atmos. terr. Phys., 44,** 973-984.

SMITH, A.J., CARPENTER, D.,L. & LESTER, M., 1981. Longitudinal variations of plasmapause radius and the propagation of VLF noise within small extensions of the plasmasphere, **Geophys. Res. Lett., 8,** 980-983.

SMITH, M.J., BRYANT, D.A. & EDWARDS, T., 1980. Pulsations in auroral electrons and positive ions, **J. atmos. terr. Phys., 42,** 167-178.

SMITH, P.A. & KING, J.W., 1981. Long-term relationships between sunspots, solar faculae and the ionosphere, **J. atmos. terr. Phys., 43,** 1057-1063.

SMITH, R.L., 1979. A high pressure cell for chemical demagnetization of sediments, **Geophys. J. R. astr. Soc., 59,** 605-608.

SMITH, R.L., 1979. Palaeomagnetism of the Sarna alkaline body, **Geol. Foren. Stockh. Fordh., 101,** 167-168.

SMITH, R.L. & PIPER, J.D.A., 1982. Palaeomagnetism of the southern zone of the Lewisian (Precambrian) Foreland, NW Scotland, **Geophys. J. Roy. astr. Soc.** 325-347.

SMITH, R.L., STEARN, J.E.F. & PIPER, J.D.A., 1983. Palaeomagnetic studies of the Torridonian sediments, NW Scotland, **Scott. J. Geol. 19,**(1), 29-45.

SOUTHWOOD, D.J., 1980. Thunderstorms and substorms; Any connection? **Nature, 284,** 599.

SOUTHWOOD, D.J., 1980. Low frequency pulsation generation by energetic particles, J. **Geomag. Geoelectr., 32, SII,** 75.

SOUTHWOOD, D.J., 1980. Report from the IUGG Assembly: IAGA Sessions on Pulsations, **EOS, 61,** 476.

SOUTHWOOD, D.J., 1983. Wave generation in the terrestrial magnetosphere, **Space Sci. Rev., 34,** 259.

SOUTHWOOD, D.J. & HUGHES, W.J., 1983. Theory of hydromagnetic waves in the magnetosphere, **Space Sci. Rev., 35,** 301.

SOUTHWOOD, D.J. & KIVELSON, M.G., 1981. Charged particle behaviour in low frequency geomagnetic pulsations I: Transverse Waves, **J. geophys. Res., 86,** 5643-5655.

SOUTHWOOD, D.J. & KIVELSON, M.G., 1982. Charged particle behaviour in low frequency geomagnetic pulsations II: Graphical approach, **J. Geophys. Res., 87,** 1707-1710.

SOUTHWOOD, D.J., KIVELSON, M.G., WALKER, R.J. & SLAVIN, J.A., 1980. Io and its plasma environment, **J. geophys. Res., 85,** 5959-5698.

STEPHENSON, A., 1980. Rotational remanent magnetization and the torque exerted on a rotating rock in an alternating magnetic field, **Geophys. J. R. astr. Soc., 62,** 113-132.

STEPHENSON, A., 1980. The measurement of the magnetic torque acting on a rotating sample using an air turbine, **J. Phys., E: Sci. Instrum., 13,** 311-314.

STEPHENSON, A., 1980. Gyromagnetism and the remanence acquired by a rotating rock in an alternating field, **Nature, 284,** 48-49.

STEPHENSON, A., 1980. A gyroremanent magnetization in anisotropic magnetic material, **Nature, 284,** 49-51.

STEPHENSON, A., 1981. Gyromagnetic remanence and anisotropy in single domain particles, rocks and magnetic recording tape, **Phil. Mag. B., 44,** 635-664.

STEPHENSON, A., 1981. Gyroremanent magnetization in a weakly anisotropic rock sample, **Phys. Earth Planet. Inter., 25,** 163-166.

STEPHENSON, A., 1983. Changes in the direction of the remanence of rocks produced by stationary alternating field demagnetization, **Geophys. J. R. astr. Soc., 73,** 213-239.

STRANGEWAYS, H.J., 1980. Systematic errors in VLF direction-finding of whistler ducts I , **J. atmos. terr. Phys., 42,** 995-1008.

STRANGEWAYS, H.J., MADDEN, M.A. & RYCROFT, M.J., 1983. High latitude observations of whistlers using three spaced goniometer receivers, **J. atmos. terr. Phys., 45,** 387-399.

STRANGEWAYS, H.J. & RYCROFT, M.J., 1980. Systematic errors in VLF direction-finding of whistler ducts - II. **J. atmos. terr. Phys., 42,** 1009-1023.

STRANGEWAYS, H.J. & RYCROFT, M.J., 1980. Trapping of whistler-mode waves through the side of ducts, **J. atmos. terr. Phys., 42,** 983-994.

STRANGEWAYS, H.J., RYCROFT, M.J. & JARVIS, M.J., 1982. Multi-station VLF direction-finding measurements in eastern Canada, **J. atmos. terr. Phys., 44,** 509-522.

STUART, W.F., 1979. On arrival of the initial movements of Pi2's at conjugate stations, **J. atmos. terr. Phys., 41,** 1223-1232.

STUART, W.F., 1982. Arrays of magnetometers operated in NW Europe, **The I.M.S. Source Book, A.G.U. Publications.**

STUART, W.F. & BARSCZUS, H.G., 1980. Pi's observed in the daylight hemisphere at low latitudes, **J. atmos. terr. Phys., 42,** 487-497.

STUART, W.F., BRETT, P.M. & HARRIS, T.J., 1979. Mid latitude secondary resonance in Pi2's, **J. atmos. terr. Phys., 41,** 65-75.

STUART, W.F. & LANZEROTTI, L.J., 1982. Long period hydromagnetic wave inside the plasmasphere, **J. geophys. Res., 87,** 1703-1706.

STUBBE, P.., KOPKA, H., JONES, T.B. & ROBINSON, T., 1982. Wide band attenuation caused by powerful radio waves, **J. geophys. Res., 87,** 1551-1555.

STUBBE, P., KOPKA, H., LAUCHE, H., RIETVELD, M.T., BREKKE, A., HOLT, O., JONES, T.B., ROBINSON, T., HEDBERG, A., THIDE, B., CROCHET, M. & LOTZ, H.J., 1982. Ionospheric modification experiments in northern Scandinavia, **J. atmos. terr. Phys., 44,** 1025-1041.

SUMMERS, D., 1981. Interpreting the magnetic fields associated with two-dimensional induction anomalies, **Geophys. J. R. astr. Soc., 65,** 535-552.

SUMMERS, D., 1982. On the frequency response of induction anomalies, **Geophys. J. R. astr. Soc., 70,** 487-502.

TAMSETT, D. & GIRDLER, R.W., 1982. Gulf of Aden axial magnetic anomaly and the Curie temperature isotherm, **Nature, 298,** 149-151.

TARLING, D.H., 1979. Palaeomagnetic reconstructions and the Variscan Orogeny, **Proc. Ussher Soc., 4, 3,** 233-261.

TARLING, D.H., 1980. Upper Palaeozoic Continental Distributions based on Palaeomagnetic Studies, **The Terrestrial Environment and the Origin of Land Vertebrates (Ed. A.L. Panchen,) Academic Press,** 11-37.

TARLING, D.H., 1980. The tectonic evolution of the Earth's surface and changing lithospheric properties, **Mechanisms of Continental Drift and Plate Tectonics (Eds. P.A. Davies and S.K. Runcorn), Academic Press**, 61-73.

TARLING, D.H., 1981. Introduction: in **Plate Tectonics, Economic Geology and Geotectonics (Ed. D.H. Tarling), Blackwell**, 1-30.

TARLING, D.H., 1981. Palaeomagnetic considerations and general conclusions, **Economic Geology and Geotectonics (ed. D.H. Tarling), Blackwell**, 193-213.

TARLING, D.H., 1981. The geologic evolution of South America with special reference to the last 200 million years, **Evolutionary biology of the new world monkeys and continental drift (Eds. R.L. Ciochon and A.B. Chiarelli), Plenum**, 1-41.

TARLING, D.H., 1981. Geophysics and Universities, **Geology Teaching, 6**, 58-60.

TARLING, D.H., 1982. Palaeomagnetism and sedimentology, **Open Earth, 16**, 19-20.

TARLING, D.H., 1982. The archaeomagnetic properties of coins, **Archaeometry, 24**, 76-79.

TARLING, D.H., 1982. Geomagnetic cores and secular effects, **Nature, 296**, 394-395.

TARLING, D.H., 1982. The possible utilisation of the magnetisation of archaeological metallic artefacts, **J. Archaeo. Sci., 10**, 41-42.

TAYLOR, F.W., 1982. Comparisons between the atmospheres of the terrestrial planets, **ESA SP-185.**

TAYLOR, M.J., 1981. A wide field, low light level TV system to measure the state of polarization of light, **J. Phys. E. Sci. Instr., 14**, 865-869.

THOMAS, L., 1979. A study of the enhanced electron concentrations in the mid-latitude D region on winter days in terms of the positive-ion chemistry, **J. Geomag. Geoelectr., 31**, 567-583.

THOMAS, L., 1982. The neutral and ion chemistry of the upper atmosphere, **Handbuch de Physik (Ed. K. Rawer), Springer-Verlag, 49/6**, 7-127.

THOMAS, L., 1983. Modelling of the ion composition of the middle atmosphere, **Ann. Geophysicae, 1**, 61-73.

THOMAS, R.W. & ROTHWELL, P., 1979. A latitude effect in the periodicity of auroral pulsating patches, **J. atmos. terr. Phys., 41** 1179-1184.

THOMAS, R.W. & STEINBAEK-NIELSEN, H.C., 1981. Recurrent propagating auroral forms in pulsating aurora, **J. atmos. terr. Phys., 43,** 243-254.

THOMPSON, R., 1982. A comparison of geomagnetic secular variation as recorded by historical, archaeomagnetic and palaeomagnetic measurements, **Phil. Trans. R. Soc. Lond., A306,** 103 -112.

THOMPSON, R. & BARRACLOUGH, D.R., 1982. Geomagnetic secular variation based on spherical harmonic and cross validation analyses of historical and archaeomagnetic data, **J. Geomag. Geoelectr., 34,** 245-263.

THOMPSON, R., BLOEMENDAL, J. DEARING, J.A., OLDFIELD, F., RUMMERY, T.A., STOBER, J.C. & TURNER, G.M., 1980. Environmental applications of magnetic measurements, **Science, 207,** 481-486.

THOMPSON, R., BLOEMENDAL, J . & OLDFIELD, F., 1979. Magnetic measurements used to assess sediment influx at Llyn Goddionduon, **Nature, 280,** 50-53.

THOMPSON, R. & CLARK, R.M., 1980. Author's reply to a comment on 'An objective method for smoothing palaeomagnetic data,' **Geophys. J. R. astr. Soc., 60,** 315-317.

THOMPSON, R. & CLARK, R.M., 1981. Fitting polar wander paths, **Phys. Earth Planet. Inter., 27,** 1-7.

THOMPSON, R. & CLARK, R.M., 1982. A robust least squares Gondwanan apparent polar wander path and the question of palaeomagnetic assessment of Gondwanan reconstructions, **Earth Planet. Sci. Lett., 57,** 152-158.

THOMPSON, R., LONGWORTH, G., BECKER, L.W., OLDFIELD, F., DEARING, J.A. & RUMMERY, T.A., 1979. Mossbauer effect and magnetic studies of secondary iron oxides in soils, **J. Soil Sci., 30,** 93-110.

THOMPSON, R. & MORTON, D.J., 1979. Magnetic susceptibility and particle size distribution in recent sediments of the Loch Lomond drainage basin, Scotland, **J. Sed. Pet., 49,** 801-812.

THOMPSON, R. & OLDFIELD, F., 1979. Geomagnetic polarity measurements from Pleistocene deposits in Southwest France and their chronological implications, **Geol. J., 14, 2,** 117-126.

THOMPSON, R., OLDFIELD, F., & APPLEBY, P.G., 1980. Palaeoecological studies of lakes in the Highlands of Papua, New Guinea, **J. Ecol., 68,** 457- 477.

THOMPSON, R., OLDFIELD, F. & BROWN, A., 1979. The effect of micro-topography and vegetation on the catchment of airborne particles measured by remanent magnetism, **Quaternary Res., 12,** 326-332.

THOMPSON, R., OLDFIELD, F., RUMMERY, T.A. & WALLING, P.E., 1979.

Identification of suspended sediment sources by means of magnetic measurements: some preliminary results, **J. Water Resource Res., 15, 2,** 211-218.

THOMPSON, R., RUMMERY, T.A., BLOEMENDAL, J., DEARING, J. & OLDFIELD, F., 1979. The persistance of fine induced magnetic oxides in soils and lake sediments, **Ann. de Geophysique, 35,** 103-107.

THOMPSON, R., SCOULLES, M. & OLDFIELD, F., 1979. Magnetic monitoring of marine particulate pollution in the Elefsis, Gulf, Greece, **Marine Pollution Bull., 10,** 287-291.

THOMPSON, R. & STOBER, J.C., 1979. Magnetic remanence acquisition in Finnish lake sediments, **Geophys. J. R. astr. Soc., 57,,** 727-739.

THOMPSON, R. & STOBER, J.C., 1979. An investigation into the source of magnetic minerals in some Finnish lake sediments, **Earth planet. Sci. Lett., 45,** 464-474.

THOMPSON, R. & TURNER, G.M., 1979. British geomagnetic master curves 10,000-0 yr BP for dating European sediments, **Geophys. Res. Lett., 6,** 249-252.

THOMPSON, R., WALLING, D.E., PEART, M.R. & OLDFIELD, F., 1979. Suspended sediment sources identified by magnetic measurements, **Nature, 281,** 110-113.

TODESCHUCK, J.P. & ROCHESTER, M.G., 1980. The effect of compressible flow on anti-dynamo theorems, **Nature, 284,** 250-251.

TUCHOLKA, P., 1980. Short period secular variations (SPSV) of the geomagnetic field recorded in highly scattered palaeomagnetic records of Holocene lake sediments from North Poland, **Earth planet. Sci. Lett., 48,** 379-384.

TUCKER, P., 1979. Selective post-depositional realignment in a synthetic sediment, **Phys. Earth planet. Inter., 20,** 11-14.

TUCKER, P., 1980. A grain mobility model of post-depositional realignment, **Geophys. J. R. astr. Soc., 63,** 149-163.

TUCKER, P., 1980. Stirred remanent magnetization: A laboratory analogue of post-depositional realignment, **J. Geophys., 48,** 153-157.

TUCKER, P., 1981. Low temperature magnetic hysteresis properties of multidomain single-crystal titanomagnetite, **Earth planet Sci. Lett., 54,** 167-172.

TUCKER, P., 1981. Palaeointensities from sediments: normalization by laboratory redepositions, **Earth planet. Sci. Lett., 56,** 398-404.

TUCKER, P. & O'REILLY, W., 1980. The laboratory simulation of deuteric oxidation of titanomagnetites: Effect on magnetic properties and stability of thermoremanence, **Phys. Earth Planet. Inter., 23**, 112-133.

TUCKER, P. & O'REILLY, W., 1980. Reversed thermoremanent magnetization in synthetic titanomagnetites as a consequence of high temperature oxidation, **J. Geomag. Geoelctr., 32**, 341-355.

TURNER, G.M. & THOMPSON, R., 1979. Behavoiur of the Earth's magnetic field as recorded in the sediment of Loch Lomond, **Earth planet. Sci. Lett., 42**, 412-426.

TURNER, G.M. & THOMPSON, R., 1981. Lake sediment record of the geomagnetic secular variation in Britain during Holocene times, **Geophys. J. R. astr. Soc., 65**, 703-725.

TURNER, G.M. & THOMPSON, R., 1982. Detransformation of the British geomagnetic secular variation record for Holocene times, **Geophys. J. R. astr. Soc., 70**, 789-792.

TURNER, P., METCALFE, I. & TARLING, D.H., 1979. Palaeomagnetic studies of some Dinantian limestone from the Craven Basin and a contribution to Asbian magnetostratigraphy, **Proc. Yorkshire Geol. Soc., 42, 3, 21**, 371-396.

TURUNEN, T., CANNON, P.S. & RYCROFT, M.J., 1980. ELF radio signals in the auroral ionosphere generated by non-linear demodulation of LF and/or MF transmissions, **Nature, 286**, 375-377.

URRUTIA-FUCAGAUCHI, J., 1981. Some observations on short-term magnetic viscosity behaviour at room temperature, **Phys. Earth Planet. Inter., 26**, 1-5.

URRUTIA-FUCAGAUCHI, J. & TARLING, D.H., 1983. Palaeomagnetic properties of Eocambrian sediments in northwestern Scotland, **Palaeogeog. Palaeoclim. Palaeoecol., 41**, 325-334.

VALENCIO, D.A., CREER, K.M., SINITO, A.M., VILAS, J.F.A., MAZZONI, M.M., SPALLETI, L.A., ROMERO, E.J. & FERNANDEZ, C.A., 1982. Estudio palaeomagnetico, sedimentologico y palinologico de ambientes lacustres, part 1 Lago El Trebol, **Asociacion Geologica Argentina, Revista, XXXVII (2)**, 183-204.

VAN der VOO, R., BRIDEN, J.C. & DUFF, B.A., 1980. Late Precambrian and Palaeozoic palaeomagnetism of the Atlantic-bordering continents, **26th International Geological Congress, Paris, Proceedings, Coll. 6(4)**, 203-212.

VAN EYKEN, A.P, et al. 1982. Interaction of gravity waves with sporadic E layers, **J. atmos. terr. Phys., 44**, 25-29

WALDOCK, J.A., JONES, T.B., NEILSEN, E. & SOUTHWOOD, D.J., 1983. First results of micropulsation activity observed by SABRE, **Planet. Space Sci., 31**, 573-578.

WALKER, A.D.M., GREENWALD, R.A., STUART, W.F. & GREEN, C.A., 1979. STARE auroral radar observations of Pc5 geomagnetic pulsations, **J. geophys. Res., 84**, 3373-3388.

WALKER, R.J. & SOUTHWOOD, D.J., 1982. Momentum balance and flux conservation in model magnetospheric magnetic fields, **J. geophys. Res., 87**, 7460-7466.

WALTON, D., 1982. Errors and resolution of thermal techniques for obtaining the magnetic intensity, **Nature, 295**, 512-515.

WARD, I.A., LESTER, M. & THOMAS, R.W., 1982. Pulsing hiss pulsating aurora and micropulsations, **J. atmos. terr. Phys., 44**, 931-938.

WATTS, D.R., 1982. A multicomponent , dual-polarity palaeomagnetic regional overprint from the Moine Assemblage, North West Scotland, **Earth Planet. Sci. Lett., 61**, 190-198.

WATTS, D.R. & BRAMALL, A.M., 1980. Palaeomagnetic investigation in the Ellesworth Mountains, **Antarctic Journal of United States, XV, No. 5**, 34-46.

WATTS, D.R. & BRAMALL, A.M., 1982. Palaeomagnetic evidence for a displaced terrain in Western Antarctica, **Nature, 293**, 638-641.

WHALER, K.A., 1980. Does the whole of the Earth's core convect? **Nature, 287**, 528-530.

WHALER, K.A., 1982. Geomagnetic secular variation and fluid motion at the core surface, **Phil. Trans. R. Soc. Lond., A306**, 235-246.

WHALER, K.A. & GUBBINS, D., 1981. Spherical harmonic analysis of the geomagnetic field: An example of a linear inverse problem, **Geophys. J. R. astr. Soc., 65**, 645-693.

WHITE, R. & LARID, M.J., 1980. Rays and foci in a magneto-ionic medium with linearly varying magnetic field, **Planet. Space Sci., 28**, 837-846.

WILKINS, G.A., 1979. Presentation in the primary literature of data derived from observations in the geosciences, **CODATA Bull., No. 32**.

WILLIAMS, E.R., 1980. A series of daytime Lyman-alpha extinction measurements at middle-latitude, **J. atmos. terr. Phys., 42**, 307-315.

WILLIAMS, P.J.S., EYKEN, A.P. van & BERTIN, F., 1982. A test of the Hines dispersion equation for atmospheric gravity waves, **J. atmos. terr. Phys., 44**, 573-576.

WILLIS, D.M., 1982. A direct analytic method of calculating the quadrupole parameters of a planetary magnetic field, **Geophys. J. R. astr. Soc., 68**, 751-764.

WILLIS, D.M. & OSBORNE, A.D., 1982. Quadrupole and octupole parameters of Jupiter's main magnetic field, **Geophys. J. R. astr. Soc., 68.** 765-776.

WILSON, R.L., HALL, J.M. & DAGLEY, P., 1982. The British Tertiary igneous province, palaeomagnetism of the dyke swarm along the Sleat Coast of Skye, **Geophys. J. R. astr. Soc.,68,** 317-323.

WOOD, B.J. & STRENS, R.G.J., 1979. Diffuse reflectance spectra and optical properties of some sulphides and related minerals, **Min. Mag., 43,** 509-518.

WRENN, G.L., JOHNSON, J.F.E. & SOJKA, J.J., 1979. Stable pancake distributions of low energy electrons in the plasma trough, **Nature, 279,** 512.

WRENN, G.L., JOHNSON, J.F.E. & SOJKA, J.J., 1981. The Suprathermal Plasma Analyser on the ESA GEOS Satellites, **Space Sci. Instru., 5,** 271-293.

YALLOP, B.D. & HOHENKERK, C.Y., 1980. Distribution of sunspots 1874-1976, **Solar Phys., 68,** 303-305.

YEARBY, K.H., MATTHEWS, J.P. & SMITH, A.J., 1981. VLF line radiation observed at Halley and Siple, **Adv. Space Res., 1,** 445-448.

YEARBY, K.H.,SMITH, A.J., KAISER, T.R.& BULLOUGH, K., 1983. Power line harmonic radiation in Newfoundland, **J. atmos. terr. Phys., 45,** 409-419.

YOUNG, D.T., PERRAUT, S., ROUX, A., DE VILLEDARY, C., GENDRIN, R., KORTH, A., KREMSER, G. & JONES, D., 1981. Wave-particle interactions near ω_{He^+} observed on GEOS-1 and 2: Propagation of ion, cyclotron waves in He^+ -rich plasma, **J. geophys. Res., 86,** 6755- 6772.

I.G.S. GEOMAGNETIC BULLETINS

No.10 **Annual Mean Values of Geomagnetic Elements,** 1981.

No.11 **Geomagnetic Results 1978-79; Eskdalemuir, Hartland and Lerwick Observatories,** 1981.

No.12 **A bibliographical guide to the production of local and regional charts,** 1981.

No.13 **Geomagnetic Results 1980; Eskdalemuir, Hartland and Lerwick Observatories,** 1982.

No.14 **Geomagnetic Results 1981; Eskdalemuir, Hartland and Lerwick**

Observatories, 1983.

No.15 **Geomagnetic Results 1982; Eskdalemuir, Hartland and Lerwick Observatories**, 1983.

1:250,000 SERIES, AEROMAGNETIC ANOMALY MAP OF THE UK,

Institute of Geological Sciences, Keyworth, UK.

Each sheet covers an area of 1° latitude by 2° longitude and the co-ordinates designate its SW corner.

Lundy	51°N	06° W	1980
Bristol Channel	51°N	04°W	1980
Chilterns	51°N	02°W	1980
Thames Estuary	51°N	00°	1982
Cardigan Bay	52°N	06°W	1980
Wales and Marches	52°N	04°W	1980
East Midlands	52°N	02°W	1980
East Anglia	52°N	00°	1982
Flemish Bight	52°N	02°E	1983
Spurn	53°N	00°	1983
Indefatigable	53°N	02°E	1983
Tyne-Tees	54°N	02°W	1981
Tyne-Tees (2nd.ed.)	54°N	02°W	1983
Clyde	55°N	06°W	1980
Borders	55°N	04°W	1980
Farne	55°N	02°W	1981
Tiree	56°N	08°W	1983
Argyll	56°N	06°W	1983
Tay-Forth	56°N	04°W	1981
Marr Bank	56°N	02°W	1983
Devil's Hole	56°N	00°	1983
Little Minch	57°N	08°W	1983
Peterhead	57°N	02°W	1983
Lewis	58°N	08°W	1983
Fair Isle	59°N	02°W	1979
Shetland	60°N	02°W	1980
Halibut Bank	60°N	00°	1983

Geophys. J. R. astr. Soc. (1984) **79**, 691–696

Research note

Low-frequency electromagnetic induction in the Moon: linearized inverse theory and lunar core calculations

B. A. Hobbs*, L. L. Hood, F. Herbert and C. P. Sonett†
Lunar and Planetary Laboratory, University of Arizona, Tucson, Arizona 85721, USA

Received 1984 January 25; in original form 1983 September 1

Summary. Day-side lunar electromagnetic transfer function estimates of Hood, Herbert & Sonett are analysed using the linearized inverse theory of Backus & Gilbert. A smooth conductivity distribution exponentially increasing with depth in the range 260–1200 km is found to fit the data. The conclusions are compatible with the forward model calculations of Hood *et al.* Further calculations explore the compatibility of a silicate or metallic lunar core with the data. A metallic lunar core of radius 438 km is allowed but not required.

Introduction

One method of obtaining information on the electrical conductivity of the Moon is by analysing the day-side lunar electromagnetic transfer function, a new determination of which has been made by Hood, Herbert & Sonett (1982a) at 19 frequencies in the range 10^{-5}–10^{-3} Hz; the values and associated errors are tabulated in Hobbs *et al.* (1984). Hobbs *et al.* (1984) used these data to place an upper bound on the radius of a highly conducting lunar core. In addition to discussing the lunar core, Hood *et al.* (1982a) estimated conductivity as a function of depth within the Moon using forward modelling techniques. For completeness, linearized inverse theory (Backus & Gilbert 1970) is here applied to the data and some additional forward model calculations examine further the question of a lunar core.

The transfer function $T(f)$ is defined as the amplitude of the ratio of the total tangential magnetic field at the lunar surface to the same magnetic field component measured in the solar wind (e.g. Sonett 1982). At low frequencies, $f < 10^{-3}$ Hz, calculations are independent of the tangential direction. In Hobbs *et al.* (1984) the values of $T(f_i)$, $i = 1, 2, \ldots, 19$ are given along with their upper and lower bounds (determined from $T^2(f_i)$ and their associated one standard deviation estimates). The one standard deviation estimate for T is taken to be the difference between the upper bound and T at each frequency. Thus the data consist of $T(f_i) \pm \delta T(f_i)$, $i = 1, 2, \ldots, 19$. For a given conductivity of the Moon, $\sigma(r)$, the theoretical

* On leave from Department of Geophysics, University of Edinburgh, James Clerk Maxwell Building, Mayfield Road, Edinburgh EH9 3JZ.
† Also Department of Planetary Sciences.

response $M(f_i)$ may be calculated and compared with $T(f_i)$. A measure of misfit between model calculations and data is provided by

$$\chi^2 = \sum_{i=1}^{19} \{[T(f_i) - M(f_i)]/\delta T(f_i)\}^2.$$

If the 19 data estimates were independent, we would be willing to consider models $\sigma(r)$ whose responses yield $\chi^2 < 19$ as acceptable solutions. However, as shown in Hobbs *et al.* (1984), the 19 estimates of Hood *et al.* (1982a) are not independent, and acceptable solutions should be regarded as those for which $\chi^2 < 2.4$. (Using the method of Parker 1980 and Parker & Whaler 1981 the best fitting solution to this data set has $\chi^2 = 0.43$ – Hobbs *et al.* 1984.) In view of the data dependence, an alternative more objective measure is to require the data to be satisfied at the one standard deviation level, namely

$$T(f_i) - \delta T(f_i) \leqslant M(f_i) \leqslant T(f_i) + \delta T(f_i) \qquad i = 1, 2, \ldots, 19$$

Inverse calculations: the model search

Linearized inverse schemes require a model whose responses fit the data to within either or both of the above measures. Usually a starting model is first found whose responses crudely approximate the data. Subsequent perturbations then transform this starting model to one whose responses fit the observations to the required measure.

The search for a suitable starting model began with a uniform Moon describable by one parameter, the conductivity σ_0. The uniform Moon which best fits the data is given by $\log \sigma_0 = -3.1$ and the associated χ^2 is 371. This model gives a very poor fit to the data and was found unsuitable as a starting model.

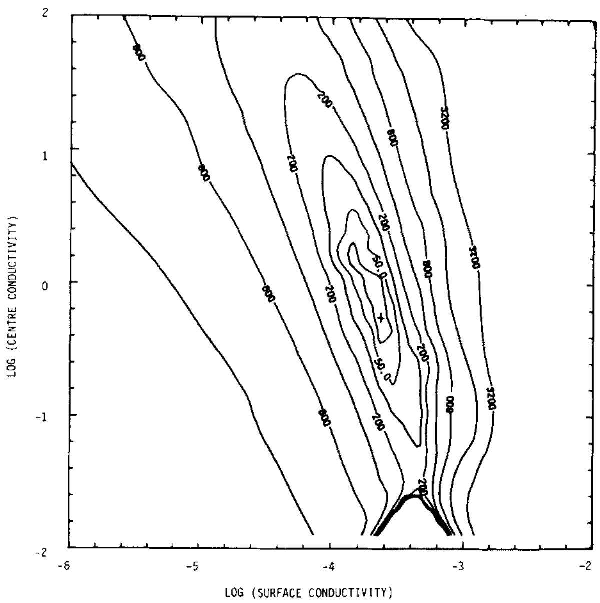

Figure 1. Contours of the misfit χ^2 as a function of the logarithm of the centre and surface conductivities. For each model, $\log \sigma$ is linear between the centre and the surface. A cross marks the position of the minimum χ^2.

An alternative smooth starting model is one in which the logarithm of conductivity, instead of remaining constant throughout the Moon as above, varies linearly with depth. The conductivity is thus exponential in form and is describable by two parameters σ_1, the conductivity at the centre of the Moon and σ_2 the surface conductivity. Values of the parameters $\log \sigma_1$ in the range -2 to 2 and $\log \sigma_2$ in the range -6 to -2 were considered and for each pair (σ_1, σ_2) the response and resulting misfit X^2 were calculated. The result is Fig. 1, in which X^2 is contoured as a function of $\log \sigma_1$ and $\log \sigma_2$. χ^2 is generally large (>100) but there is a region in which $\chi^2 < 20$. A cross marks the minimum χ^2 obtained and this corresponds to the values $\log \sigma_1 = -0.28$, $\log \sigma_2 = -3.64$. The associated χ^2 is 2.4, indicating that this model is already an acceptable solution which requires no further refinement. The model, response and data are shown in Fig. 2.

This bland solution, fitting the data so well, was most unexpected. It presupposes definitive statements on detailed structure within the Moon using the present data set – for whatever structure may be found in a particular model, this solution is a counter-example satisfying the data extremely well. The solution is both simple and powerful. The solution is compared in Fig. 2 with the forward calculations of Hood *et al.* (1982a). Except at the surface, the linear model lies within the envelope suggested by them. With an acceptable model obtained, inferences may now be drawn from the trade-off calculations discussed in the following section.

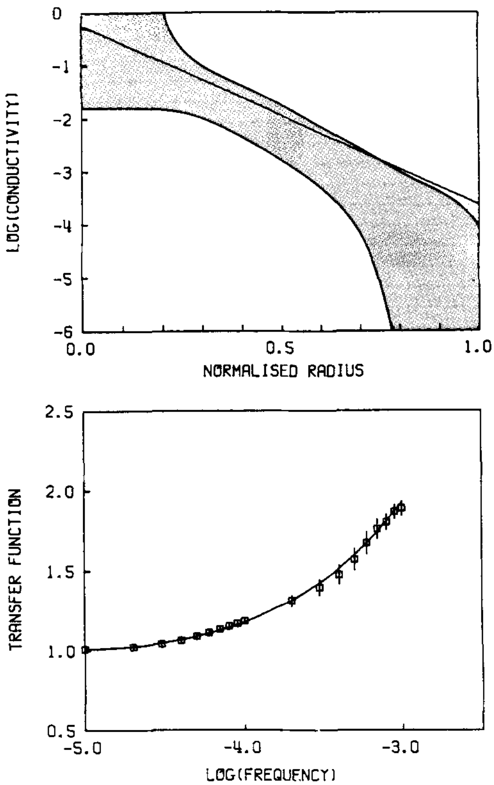

Figure 2. The best-fitting exponential model ($\log \sigma$ is the straight line, upper diagram) corresponding to the minimum χ^2 in Fig. 1, together with its response (solid line, lower diagram). Superimposed on the lower diagram are the data with their one standard deviation error bars. Superimposed on the upper diagram is the envelope of acceptable models determined by Hood *et al.* (1982a).

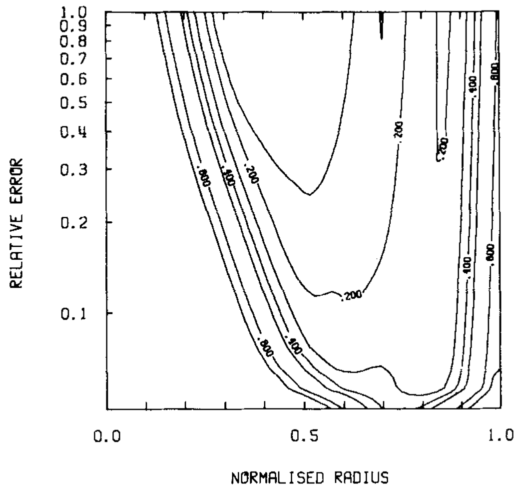

Figure 3. The trade-off calculations showing contours of normalized spread as a function of the relative error $\Delta\sigma/\sigma$ and the normalized radius within the Moon.

Inverse calculations: model interpretation

The exponential model of Fig. 2 was used as a basis for the trade-off calculations of Backus & Gilbert (1970). Fig. 3 is the resulting trade-off diagram in which spread is contoured as a function of relative error $\Delta\sigma/\sigma$ and normalized radius within the Moon. The term 'spread' is that used by Backus & Gilbert (1970) and is essentially a length scale over which the conductivity model has been averaged – it thus represents the depth resolution of the conductivity estimate. The spread is normalized by the radius of the Moon. Fig. 3 shows that the normalized spreads are smallest (giving the best resolution) between the normalized radii 0.30 and 0.85 (260–1200 km depth) and that the data do not resolve conductivity above 260 km or below 1200 km. Since the model conductivity varies by 3 orders of magnitude between the surface and centre of the Moon, a rather large value of relative error seems appropriate. A value of 60 per cent is associated with spreads of < 0.15 between depths of 480 and 1200 km. Adopting this value, examples of the conductivity, spread and error estimates are presented in Fig. 4 and are again compared to the forward modelling

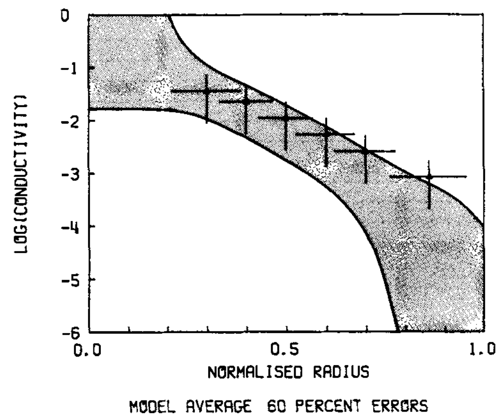

Figure 4. Lunar conductivity estimates with associated error limits and spreads corresponding to a constant relative error in conductivity of 60 per cent. The envelope of acceptable models determined by Hood *et al.* (1982a) is superimposed.

calculations of Hood *et al.* (1982a). Except near the surface, the two approaches yield much the same information. Certainly the lunar conductivity cannot depart significantly from the model of Fig. 2 consistently over regions larger than about 260 km. Structure on a finer scale than this is possible.

The lunar core

The envelope of Hood *et al.* (1982a), shown in Fig. 2, was obtained from nine special conductivity profiles fitting the data (out of 25 000 such trial profiles). Hood *et al.* (1982a) considered the possibility of a highly conducting lunar core by adding uniform cores (of 10^2 and 10^7 S m^{-1}) to their existing profiles and noting the effect on the calculated transfer functions. As the size of the core is increased so too is the transfer function at the lowest frequencies. The maximum core radius compatible with the data at the one standard deviation level is in fact the model for which the response at the lowest frequency is the maximum bound $T(f_1) + \delta T(f_1)$. In this way, Hood *et al.* (1982a) determined the maximum core radius as 360 km. (In a later analysis, Hood, Herbert & Sonett (1982b), an upper limit of 375 km was estimated.)

A similar approach is adopted here, except that when a core is added, the conductivity between the core and surface is recalculated to give the best fitting solution. In this way the 'mantle' conductivity compensates for the core. The model is now describable by four parameters. σ_2 is again the surface conductivity but σ_1 is now the conductivity at some radius r_0. Below r_0 the model is constant with conductivity σ_0, above r_0 $\log \sigma$ is again linear with r. For a given core conductivity σ_0, the maximum value of r_0 was determined such that parameter pairs (σ_1, σ_2) could still be found satisfying all the data at the one standard deviation level. In this way the largest values of r_0 compatible with the data were found for a range of values of σ_0.

Hood *et al.* (1982a) chose two values for the lunar core conductivity. Their value of 10^2 S m^{-1} probably represents the smallest value appropriate to a metallic core, whereas their value of 10^7 S m^{-1}, at the frequencies of interest, is effectively perfectly conducting. Using the above exponential model plus the uniform core, for $\sigma_0 = 10^2$ S m^{-1} the maximum core radius is 438 km and for $\sigma_0 = 10^7$ S m^{-1} the maximum is 431 km. These values compare favourably with the rigorous upper bound for a perfectly conducting lunar core of 435 km determined by Hobbs *et al.* (1984). Fig. 5 shows the relation between σ_0 and the associated

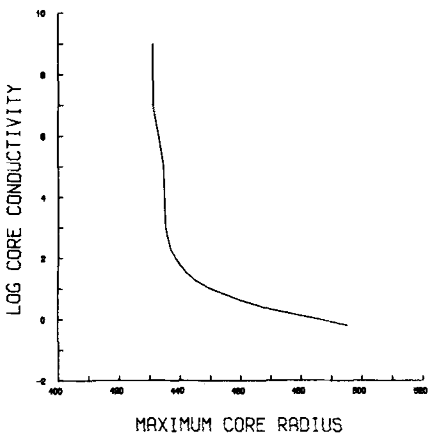

Figure 5. The maximum permissible core radius as a function of core conductivity (for linear functions of log conductivity in the 'mantle').

maximum core radius for $\sigma_0 = 10^0 - 10^9\ \mathrm{S\,m^{-1}}$. The core size is insensitive to σ_0 for $\sigma_0 > 10^3\ \mathrm{S\,m^{-1}}$. Below $\sigma_0 = 10^2\ \mathrm{S\,m^{-1}}$ the core might be considered silicate and for example for a silicate core of conductivity $10\ \mathrm{S\,m^{-1}}$, Fig. 5 indicates the maximum radius as 450 km. The above maximum sizes are not definitive with respect to this dataset and associated errors, since there may be other (non-linear) distributions of log conductivity between the core and surface that allow a larger core size. However the values are probably good approximations in view of the compatibility of this approach and the rigorous method (Hobbs *et al.* 1984) for large σ_0.

Conclusions

The day-side lunar electromagnetic transfer function for low frequencies (10^{-5}–10^{-3} Hz) has now been analysed by forward modelling (Hood *et al.* 1982a) and by inverse theory. The two approaches yield compatible conclusions, the average lunar conductivity increases more or less exponentially with depth in the range 260–1200 km. Moreover, it is possible to fit the lunar data with a smooth conductivity distribution, thereby implying that it is not necessary to consider discontinuous or complex electrical structures for the lunar interior. Fine-scale structure is always possible, but the average conductivity in regions thicker than about 260 km will not differ significantly from the proposed exponential increase. The smooth solution also shows that it is not necessary to invoke a lunar core. A core is not precluded however, and forward calculations suggest the maximum radius for a metallic core is 431–438 km (a rigorous value of 435 km for a perfectly conducting core is determined elsewhere – Hobbs *et al.* 1984).

References

Backus, G. & Gilbert, F., 1970. Uniqueness in the inversion of inaccurate gross Earth data, *Phil. Trans. R. Soc.*, **A266,** 123–192.

Hobbs, B. A., Hood, L. L., Herbert, F. & Sonett, C. P., 1983. An upper bound on the radius of a highly electrically conducting lunar core, *J. geophys. Res., Suppl.*, **88,** B97–B102.

Hood, L. L., Herbert, F. & Sonett, C. P., 1982a. The deep lunar electrical conductivity profile: structural and thermal inferences, *J. geophys. Res.*, **87,** 5311–5326.

Hood, L. L., Herbert, F. & Sonett, C. P., 1982b. Further efforts to limit lunar internal temperatures from electrical conductivity determinations, *J. geophys. Res., Suppl.*, **87,** A109–A116.

Parker, R. L., 1980. The inverse problem of electromagnetic induction: Existence and construction of solutions based upon incomplete data, *J. geophys. Res.*, **85,** 4421–4428.

Parker, R. L. & Whaler, K. A., 1981. Numerical methods for establishing solutions to the inverse problem of electromagnetic induction, *J. geophys. Res.*, **86,** 9574–9584.

Sonett, C. P., 1982. Electromagnetic induction in the Moon, *Rev. Geophys. Space Phys.*, **20,** 411.

Geophys. J. R. astr. Soc. (1984) 79, 697–703

Research note

A further earthquake on the Kerguelen Plateau

R. D. Adams* and B. M. Zhang† *International Seismological Centre, Newbury, Berkshire RG13 1LZ*

Received 1984 May 11

Summary. The 'search' procedure of the International Seismological Centre for previously unreported earthquakes has located a further earthquake on the eastern edge of the Kerguelen Plateau, about 1200 km SSE of Kerguelen Island. This event (M_b 4.7) occurred on 1981 April 6, and was about 65 km west of a larger event (M_b 5.2) that occurred in 1973. These two earthquakes are the only ones known to have occurred on the Plateau, apart from three events close to Kerguelen Island. The position of the new event is about mid-slope on the steep eastern edge of the Plateau, and analysis of depth phases confirms that it occurred in a water depth of 2.2 km, with a focal depth of 10–12 km beneath the seafloor. Similar analysis of the earlier event, which is beneath the bottom of the slope, places it at a depth of 20–25 km, near the base of the crust, and indicates that there is a likely thickness of about 1 km of unconsolidated sediment in this area.

Kerguelen–Gaussberg Plateau

The broad area of shallow water extending SSE from Kerguelen Island towards Antarctica is variously known as the Kerguelen or Gaussberg Plateau or Ridge. Its structure and topography are described by Houtz, Hayes & Markl (1977) and more recently by Schlich (1982). In its northern part it includes the islands of Kerguelen and Heard and is shallower than 1000 m for a length of about 800 km. Beyond a NE–SW trending col between 55 and 58°S the southern part of the plateau continues towards Antarctica near 85°E.

The plateau is generally classified as an 'aseismic ridge'. The northern part has a rather complex basement topography, whereas the southern part is smoother with more uniform sedimentation (Schlich 1982). Magnetic anomalies indicate a shallower basaltic basement, and gravity measurements that the ridge is nearly compensated with a crustal thickness of about 20 km (Houtz *et al.* 1977). Such thicknesses are commonly found in other areas of similar depth, such as the Campbell Plateau to the south of New Zealand (Adams 1962).

SEISMICITY

Fig. 1 shows the general pattern of seismicity in the southern Indian Ocean (Barazangi &

*Also at Department of Geology, University of Reading, Reading RG6 2AB.
† Permanent address: Institute of Geophysics, State Seismological Bureau, Beijing, China.

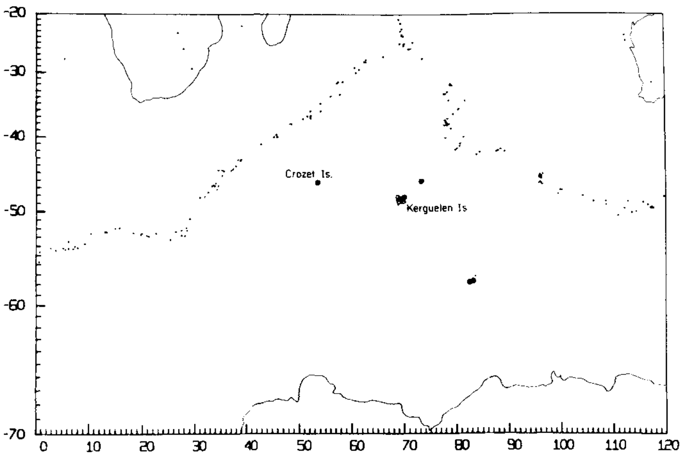

Figure 1. Seismicity of South Indian Ocean (Barazangi & Dorman 1969) with additional earthquakes from ISC files.

Dorman 1969), delineating the Atlantic–Indian and Indian–Antarctic active spreading ridges. Also shown are those earthquakes held on the International Seismological Centre files for the area south of the ridges. These include an event near Crozet Island, an isolated event north east of Kerguelen Island, and three events close to Kerguelen Island, as well as the two earthquakes to the SSE which are the main topic of this paper. These events are listed in Table 1. Okal (1981) has discussed the two shocks of 1973.

Earthquakes to the SSE of Kerguelen Island

In 1973 the Preliminary Determination of Epicenter service of the US Geological Survey located an earthquake about 1200 km SSE of Kerguelen Island in an area of no known previous activity. Its position was later redetermined by ISC using readings from 36 stations and a magnitude of 5.2 (M_b) was allocated. A second, smaller event has now been located in the same area. This event, on 1981 April 6, was found from 12 previously unassociated readings by the 'search' procedure carried out at ISC (Adams, Hughes & McGregor 1982). The solution and readings are given in Table 2.

ISC solutions for these two events are included in Table 1; both earthquakes are well-determined from a good azimuthal distribution of stations, and their formal location errors are about ±5 km. The earthquakes lie beneath the steep slope of the Plateau (Fig. 2); the larger, earlier, event is near the bottom of the slope where the water depth is shown as

Table 1. ISC determinations of earthquakes in south Indian Ocean.

Date	Lat °S	Long °E	Depth km	Mb	Area
1973 Mar 20	57.82	83.59	33	5.2	SE of Kerguelen Is
1973 May 03	46.14	73.22	18	5.5	NE of Kerguelen Is
1974 Sep 21	46.15	53.63	33	-	Crozet Is
1980 Apr 24	48.78	69.24	10	4.6	Kerguelen Is
25	48.72	69.17	10	4.7	Kerguelen Is
25	48.56	69.47	10	4.9	Kerguelen Is
1981 Apr 06	57.99	82.50	0	4.7	SE of Kerguelen Is

Table 2. Solution and station readings for earthquake 1981 April 6 on Kerguelen Plateau.

1981 April 06d 21 hr 53 min 21.6 ± 0.25 s 57.99 ± 0.052°S 82.50 ± 0.079°E h = 0 km (restrained)

Station	Distance (Deg)	Azimuth (Deg)	Phase	Arrival Time h. m. s.	Residual s.
Mawson	13.09	215	eP	21 56 30	-1.3
			eS	58 43	-16
South Pole	32.18	180	eP	21 59 54.2	1.2
Young	49.10	91	P	22 02 13.4	1.0
Alice Springs	50.01	69	eP	22 02 19	-0.5
Chiredzi	52.02	293	eP	22 02 35	0.3
Rhoboro Hills	52.91	116	iP	22 02 42.0	0.9
Warramunga Arr	53.38	67	P	22 02 44.1	-0.9
Bulawayo	54.22	291	P	22 02 51.0	0.0
Mount Isa	55.34	73	eP	22 02 59	-0.3
Brisbane	56.83	89	eP	22 03 09	-0.9
Charters Towers	59.31	79	P	22 03 27.0	-0.4
Chieng Mai	77.71	16	eP	22 05 21.2	-0.4
Kabul	92.87	349	eP	22 06 38.2	1.3
Danmarks Havn	147.92	335	iPKP	22 13 07.9	4.2

4.2 km, and the smaller, later, event is some 65 km to the west, in shallower water about 2.2 km deep.

Interpretation of depth phases

Usual geometrical location methods are not adequate to determine focal depths without observations from close stations, and the depths assigned in Table 1 are conventional values. Analysis of reflections following the initial P phase, however, gives good determinations of focal depth below the seafloor and the thickness of the liquid layer (Fig. 3). Such techniques have been used by Mendiguren (1971) and Pearce (1981). In the terminology of Mendiguren, we use pP to denote the phase reflected from the solid–liquid interface at the seafloor, and PwP to denote the phase which in addition has travelled through the water to be reflected at the sea surface. Multiple water-wave reflections are termed $PmwP$.

For the small event of 1981, the only available record adequate for such analysis is that from Warramunga Array in Australia, at a distance of 53°. This record (Fig. 4) clearly shows arrivals following the initial P phase at intervals of 4.0, 7.0 and 10.0 s. Interpreting the first of these as pP gives a focal depth of 10–12 km beneath the seafloor, depending on the sub-bottom velocity, and the two later arrivals, when interpreted as PwP and $PwwP$, give a water depth of 2.2 km in good agreement with that shown on the bathymetric charts.

No array records could be found for the 1973 event, but this was large enough for good records to be available on film chips from World Network Stations. A selection of these is shown in Fig. 5. The most prominent arrival at all stations is about 13.7 s after P, and is interpreted as PwP. Over the range of distances concerned the expected variation in this time interval is small compared with errors of measurement. The smaller arrival about 6.7 s after P gives a focal depth of 20–25 km when interpreted as pP. The interval of about 7 s between this phase and PwP corresponds to a liquid depth of 5.2 km, or about 1 km more than the water depth shown on the charts.

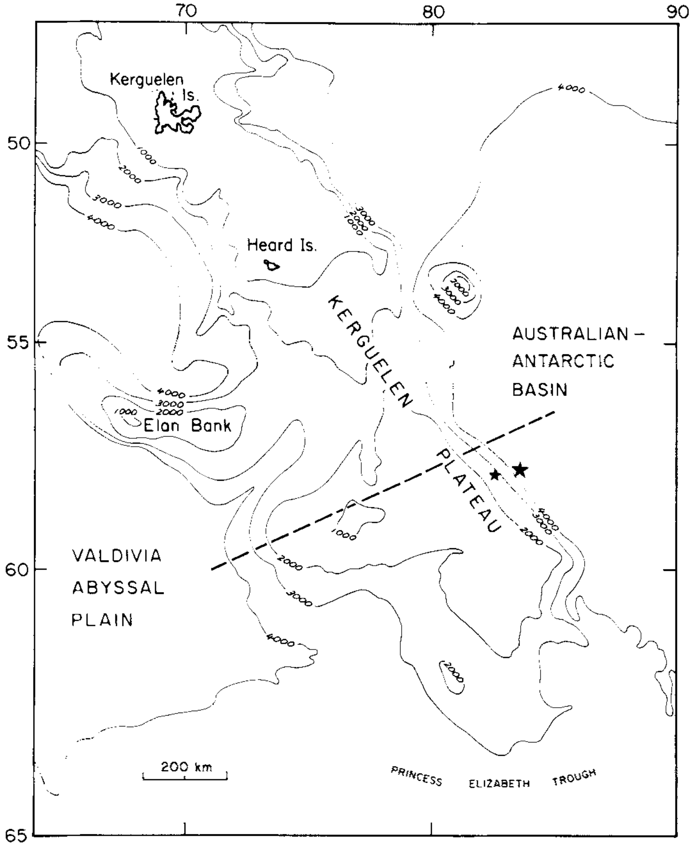

Figure 2. Position of earthquakes of 1973 (large star) and 1981 (small star) on Kerguelen Plateau. Bathymetry from GEBCO (1981). Broken line shows position of cross-section in Fig. 6. Depth in metres.

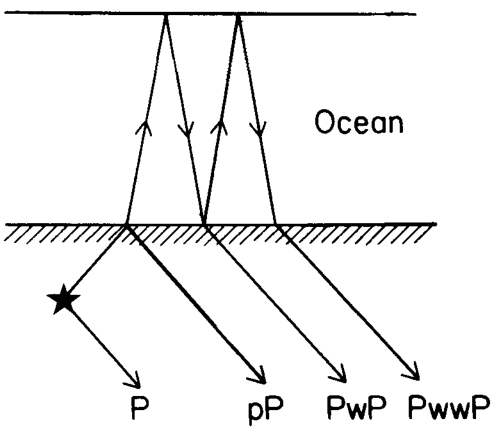

Figure 3. Adopted nomenclature for surface reflections from earthquakes in oceanic areas.

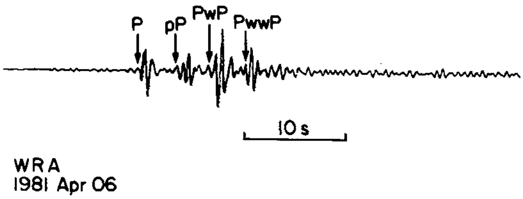

Figure 4. Record at Warramunga array of earthquake of 1981 April 6.

A cross-section derived from a marine geophysical traverse close to this area is reported by Houtz *et al.* (1977, fig. 15). It is reproduced in Fig. 6, which also shows the positions and depths of the two earthquakes. The line of the cross-section is marked in Fig. 2.

The 1981 event at a depth of 10–12 km is beneath the steep slope of the Plateau in an area where no sediment is shown, and the water depth determined from *PwP* phases agrees well with that of 2.2 km on the charts.

The 1973 event is deeper, near the base of the crust postulated by the marine survey. It lies beneath the bottom of the steep slope of the Plateau, where the survey shows a thickness of about 1 km of low-velocity sediment in addition to the 4.2 km of water shown on the charts. The existence of this sediment layer is confirmed by the liquid depth of 5.2 km found from the depth phases which would correspond to the total thickness of water and unconsolidated sediment, with the *pP* phase being reflected from the base of the unconsolidated sediment, and not from the water–sediment interface.

Mechanism

The earthquake of 1981 was not well enough recorded to give any useful information about source mechanism. For the larger event of 1973 the first motions recorded at distant

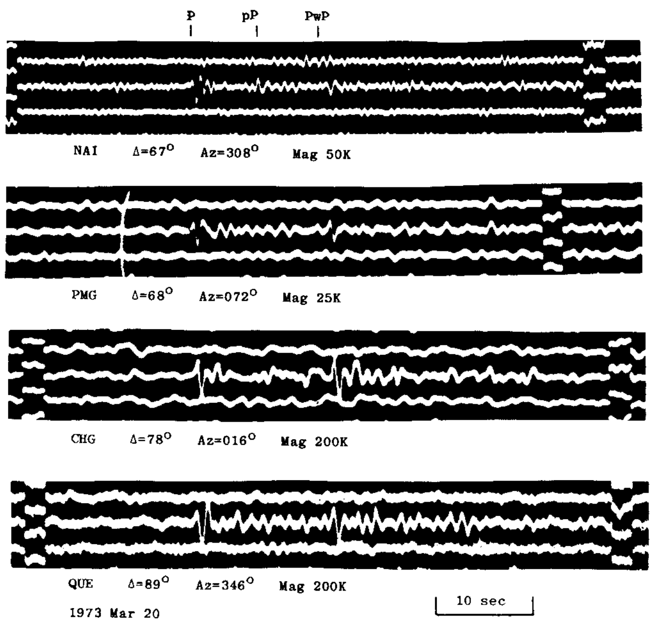

Figure 5. Records of earthquake of 1973 March 20 written at selected stations of the world-wide standard seismograph network (Nairobi, Port Moresby, Chieng Mai, Quetta).

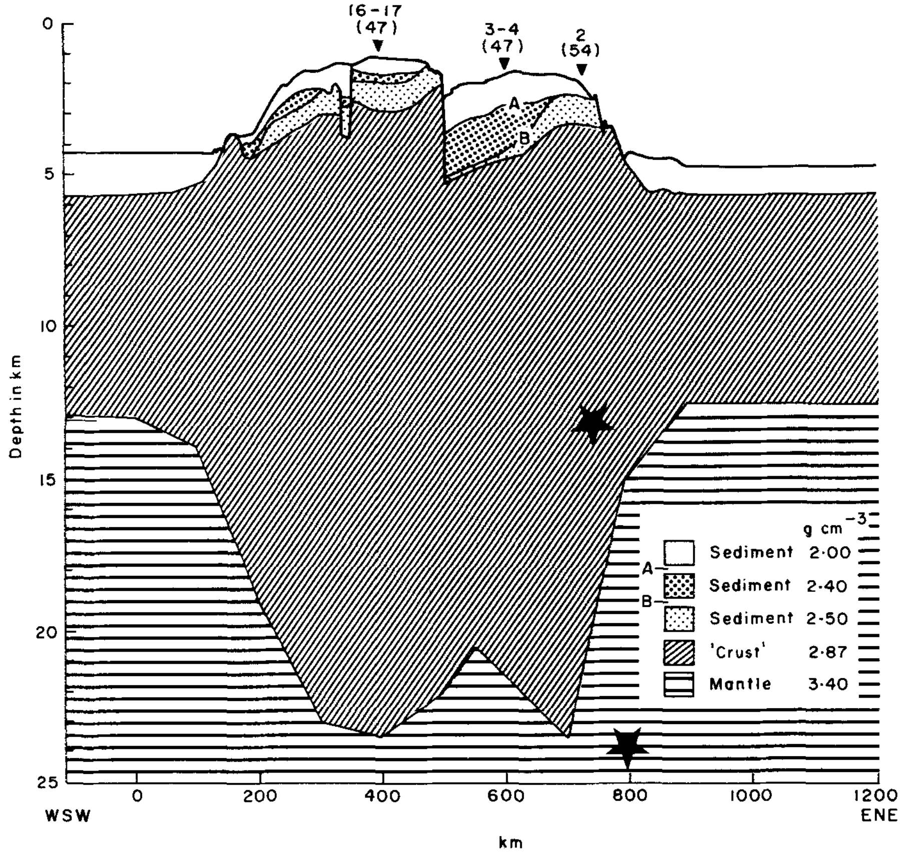

Figure 6. Cross-section of the Kerguelen Plateau from Houtz *et al.* (1977) showing position and depth of earthquakes of 1973 (deeper) and 1981 (shallower). Position of cross-section is shown in Fig. 2.

stations were predominantly compressions (Fig. 5), indicating a source of thrust type. The distribution of stations was such that no details of orientation could be determined. This indeterminacy was also reported by Okal (1981) who in addition noted that surface waves were not well enough developed for source analysis.

Such compressive sources are commonly found for intraplate earthquakes, including those in the oceans that are not close to spreading ridges. Okal (1981), however, found that the larger event to the NE of Kerguelen Island on 1973 May 3 had a tensional mechanism, which he interpreted as indicating possible magmatic activity.

Conclusion

Intraplate earthquakes in the south Indian Ocean are rare, but those that do occur tend to be associated with some feature such as an island where tectonism or volcanism has occurred, or as reported here, with a structural discontinuity such as the edge of a plateau. These two earthquakes, separated by eight years and 65 km, are far enough apart in time and position that they cannot be considered closely related, such as mainshock and aftershock, yet they are close enough to show that their particular area is under stress that was not relieved entirely by the first event. Such stress could arise from residual movement of the plateau relative to the adjoining seafloor, or from the accumulation of sediment at the base of the slope.

With continuing improvements in recording techniques and the consequent lowering of the threshold of detection, the pattern of earthquake occurrence in this and other areas of low activity should become clearer over the years.

Acknowledgment

We thank Dr P. D. Marshall of MOD(PE), Blacknest, for providing the Warramunga seismogram, and for helpful advice.

References

Adams, R. D., 1962. Thickness of the Earth's crust beneath the Campbell Plateau, *N. Z. Jl Geol. Geophys.*, **5**, 74–85.

Adams, R. D., Hughes, A. A. & McGregor, D. M., 1982. Analysis procedures at the International Seismological Centre, *Phys. Earth planet. Int.*, **30**, 85–93.

Barazangi, M. & Dorman, J., 1969. World seismicity maps compiled from ESSA, Coast and Geodetic Survey epicenter data, 1961–1967, *Bull. seism. Soc. Am.*, **59**, 369–380.

GEBCO, 1981. *General bathymetric chart of the oceans*, sheet 5.13, Canadian Hydrographic Service, Ottawa.

Houtz, R. E., Hayes, D. E. & Markl, R. G., 1977. Kerguelen Plateau bathymetry, sediment distribution and crustal structure, *Mar. Geol.*, **25**, 95–130.

Mediguren, J. A., 1971. Focal mechanism of a shock in the middle of the Nasca Plate, *J. geophys. Res.*, **76**, 3861–3879.

Okal, E. A., 1981. Intraplate seismicity of Antarctica and tectonic implications, *Earth planet. Sci. Lett.*, **52**, 397–409.

Pearce, R. G., 1981. Complex *P* waveforms from a Gulf of Aden earthquake, *Geophys. J. R. astr. Soc.*, **64**, 187–200.

Schlich, R., 1982. The Indian Ocean: aseismic ridges, spreading centres, and oceanic basins, in *Ocean Basins and Margins, 6, The Indian Ocean*, pp. 51–147, eds Nairn, A. E. M. & Stehli, F. G., Plenum Press, New York.